EGG-NPR-10631
September 1990

INFORMAL REPORT

IN-SITU STRESS AND NATURAL FRACTURING AT THE INEL SITE, IDAHO

EGG-NPR-10631
September 1990

IN-SITU STRESS AND NATURAL FRACTURING AT THE INEL SITE, IDAHO

by

Danial Moos and Colleen A. Barton
Rock and Borehole Geophysics Project
Department of Geophysics
Stanford University
Stanford, California

Prepared for U.S. Department of Energy
Office of New Production Reactors
Under DOE Idaho Field Office
Contract No. DE-AC07-76ID01570

INFORMAL REPORT NUMBER → EGG-NPR-10631
September 1990

In-situ Stress and Natural Fracturing at the INEL Site, Idaho

A Report to
EG&G Idaho, Inc.

Daniel Moos
Colleen A. Barton

Rock and Borehole Geophysics Project
Department of Geophysics
Stanford University

September 10, 1990

Executive summary

It has long been noted that, although Basin-Range extension is active on both sides of the Eastern Snake River Plain (ESRP), only micro-earthquakes have been detected beneath the plain itself. To help understand this observation, borehole televiewer (BHTV) logs were recorded in four wells previously drilled at the Idaho National Engineering Laboratory, with the principal goal of detecting stress-induced wellbore breakouts to help constrain the magnitudes and determine the orientations of the horizontal principal stresses. These data also provide a detailed look at fracturing and lithostratigraphy within the volcanic rocks of the ESRP.

Wells USGS-17, USGS-7, and NONAME-1 were drilled to relatively shallow depths (less than 1000') and penetrate only the uppermost basaltic flows. These wells were logged over the intervals 390-567 feet, 757-890 feet, and 265-549 feet, respectively. The INEL-1 well, drilled to a total depth of 10,333 feet, was logged over the interval 6780 to 10,243 feet, within the underlying silicic volcanics. Analog BHTV data recorded during logging were digitized and interactively processed utilizing specially developed software which provides an integrated environment for analyzing borehole shape and features.

Analyses of the depth distribution and orientation of fractures intersecting USGS-17, USGS-7, and NONAME-1 provide a detailed picture of flow stratigraphy within the basalts. Although there are some interesting differences between the data from each of these wells, a characteristic lithostratigraphy within each flow unit emerges. At the base of each flow is a narrow zone of rubbly material, which grades into a massive interior cut by near-vertical fractures, possibly columnar joints. Near the top is a narrow zone a few meters thick of shallow dipping fractures. This pattern of fractures detected in the basalts penetrated by the shallow wells is most likely due to thermal stresses generated during cooling. Individual flows identified on the bases of this characteristic pattern have thicknesses on the order of 85 feet. However, it was not possible to positively match specific flow units between wells.

The positions, orientations and apparent apertures of macroscopic fractures intersecting the INEL-1 well within the interval 6780 to 10,243 ft were determined to study their distribution and to investigate their effect on the physical properties of the silicic volcanics. The majority of fractures encountered in the well strike ENE-WSW and dip steeply NNW. Most are sealed, providing evidence of past hydrothermal flow at this site. Fracture frequency does not systematically decrease with depth in the study interval. These steeply dipping fractures are interpreted as relict structures related to caldera collapse, and thus were not formed in the present-day stress field. Furthermore, they

strike in the direction of the least horizontal stress inferred from earthquake focal mechanisms outside of the plain. However, until we have direct knowledge of the orientations and magnitudes of the principal horizontal stresses, we cannot determine their potential for re-activation.

In addition to these fractures, numerous more shallow-dipping fractures were found. These tend to cluster within specific depth intervals. This pattern is similar to that found in the extrusive basalts, suggesting that the cyclic repetition of high density fracturing with intervening zones of moderate to low fracture density may be a consequence of processes occurring during deposition and cooling of the silicic volcanics.

No breakouts were found in the logged interval within the INEL-1 well. This requires a normal faulting stress regime beneath the ESRP based on the analysis of the stresses necessary to cause breakouts. However, until precise measurements of the strengths of these rocks are made we cannot discriminate between a hydrostatic (i.e. $S_{hmin} \approx S_{Hmax} \approx S_v$) and an incipient faulting (i.e. both S_{hmin} and $S_{Hmax} << S_v$) environment. Thus we cannot determine based on breakout analysis whether the lack of earthquakes greater than $M_S = 3$ within the SRP is due to low stress differences at depth, or to the greater strength of crustal rocks.

We suggest that hydraulic fracturing stress measurements be made in the INEL-1 well to measure the magnitudes of the horizontal stresses. The BHTV logs obtained in this study could be used to select unfractured intervals for those tests.

Table of Contents

Introduction

This report presents the results of analyses of borehole televiewer (BHTV) data recorded in four wells drilled on the Idaho National Engineering Laboratory plant site in the Eastern Snake River Plain (ESRP) near Idaho Falls, Idaho. The data was collected in holes USGS-7, USGS-17, NONAME-1, and INEL-1, all of which had been drilled previously for other purposes. The locations of the holes are shown in Figure 1.

The report is written in two sections. The main section briefly describes the geology and tectonics of the ESRP, to place the measurements in the proper context. We then briefly describe the technique of logging with the BHTV, outline the measurement sequence, and present the principal results. Finally, we suggest additional work which would help to quantify the conclusions, and propose some measurements which are a logical adjunct to the BHTV data acquisition and which would resolve the principal question posed by the study, that is, what is the state of stress at depth beneath the ESRP, and what are the consequences for seismic hazard to structures. The second section is a series of appendices which present the primary data, and include detailed chronologies of the data acquisition, reprints of previously published reports that describe the methods in detail, and documentation of the calibrations, data acquisition procedures and analysis methods used in this study.

The primary purpose of recording BHTV data in the four study wells was to determine the state of stress beneath the Eastern portion of the SRP. Although data was acquired in four wells, only data from the deepest of these, INEL-1 (drilled to a depth of 10,333'), could be used for this purpose. In this study we relied on the anticipated presence of stress-induced wellbore breakouts to provide information about the orientations and magnitudes of the in situ stresses beneath the ESRP. Breakouts (Bell and Gough, 1979) are wellbore enlargements oriented in the direction of the least horizontal principal stress, due to compressive shear failure of the wellbore where the circumferential stress concentration is greatest (e.g., Zoback et al., 1985). Recent work indicates that the presence (or absence) of wellbore breakouts can also provide estimates of the horizontal stress magnitudes (see Appendix V; Moos and Zoback, 1990). For example, breakouts are much more likely in a highly compressive (reverse-faulting) environment than in an extensional (normal faulting) one. Previous experience in a wide variety of stress regimes and regions had suggested that, at the depth reached by the INEL-1 well in particular, stress-induced wellbore failure is common (Stock et al., 1985; Hickman et al., 1985; Plumb and Cox, 1987; Moos et al., 1988).

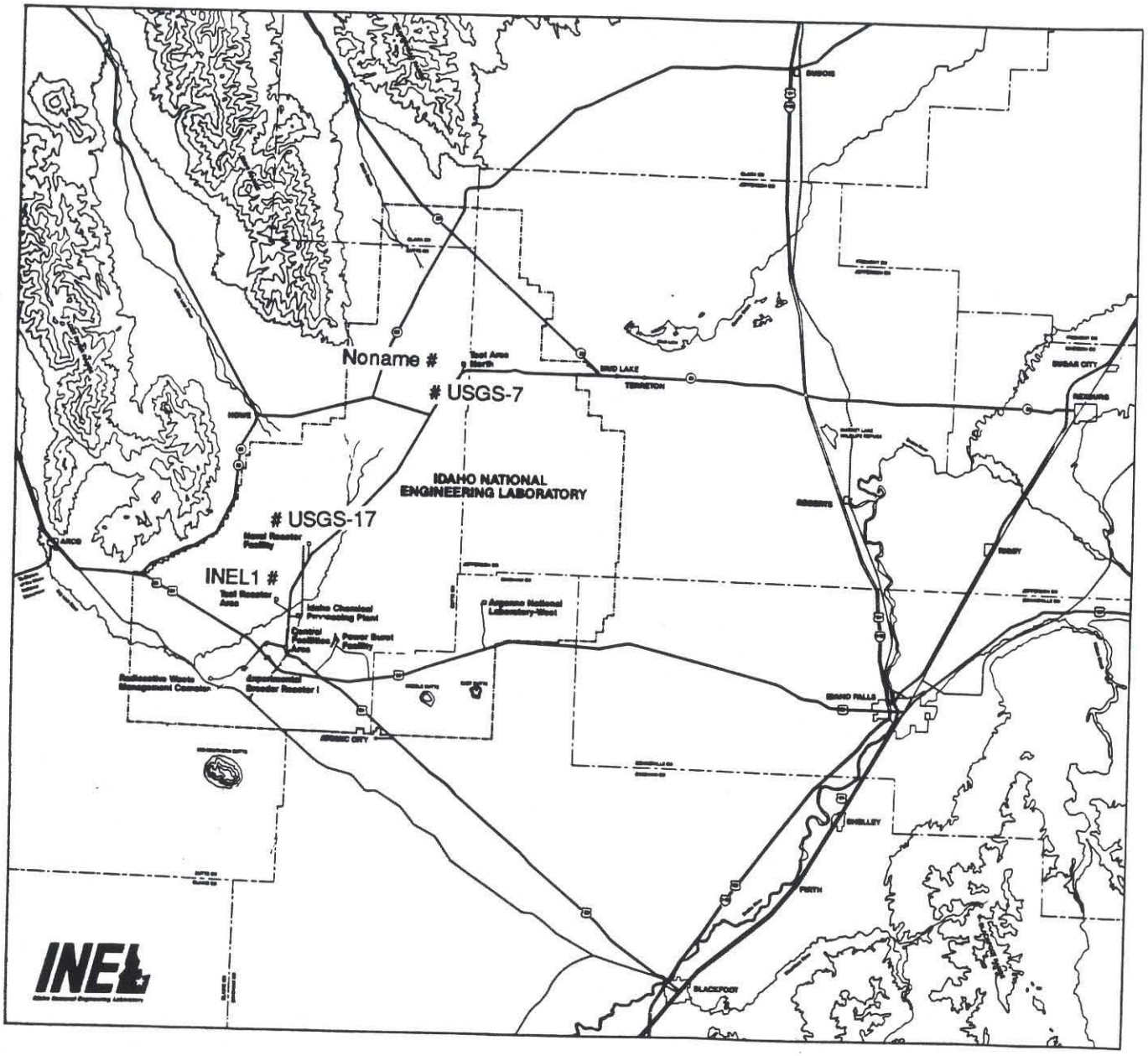

Figure 1: Location of the INEL plant site and positions of the wells used in this study.

A secondary objective of logging all four wells with the BHTV was to determine the orientations and characteristics of fractures and other discontinuities intersecting the wellbores. Fractures are particularly important in crystalline rock in determining the hydrologic, mechanical and seismic properties of the rock mass. In an otherwise competent material fractures provide permeable pathways, and if fluid filled may result in detectable seismic anisotropy. Furthermore, in active tectonic environments earthquakes typically occur on planes of weakness preferentially aligned with the principal stress directions. If fractures are found to have a strong preferred orientation which is aligned with the present-day stress field, then these fractures are potentially seismically active. In instances in which fracture orientations are not related in any obvious way to the present stress field, they record a history of cooling and/or paleo-tectonic activity which can reveal much about the history of a given region.

Geologic Setting

The Idaho National Engineering Laboratory is sited on the Eastern Snake River Plain (ESRP) just west of Idaho Falls, ID (Figure 1). The Snake River Plane cuts a concave Northward arc across the northern Basin and Range physiographic province, the trace of a hotspot whose present position is marked by the Yellowstone caldera (e.g., Morgan, 1972). In the ESRP, initial silicic volcanism has since given way to extensive extrusion of basalts which now overlie the silicic volcanics. This volcanism is still active; flows within the Craters of the Moon National Monument a few miles West of the INEL are less than 100 years old.

Information regarding the composition of the materials that underlie the ESRP has generally been obtained from interpretations of surface geophysical investigations. Analyses of cores and cuttings obtained during drilling of the INEL-1 well provide one of the few direct observations of the subsurface (Prestwich and Bowman, et al., 1980). Based on these analyses, more than 2000 feet of basalts have been extruded onto the ESRP. Sands and gravels are interlayered with these basalts. The underlying silicic volcanics extend to the total depth of more than 3.1 km. These include more than 5500 feet of welded tuffs, with minor amounts of cinders and tuffaceous interbeds. Dense, recrystallized hydrothermally altered rhyodacite ash-flows were found in the well below about 8000 feet. Below this depth the rock becomes increasingly dacitic; at 9460 feet an abrupt change to dacites was inferred from an increase in logged density. At greater depths, basaltic intrusions comprise as much as 25% of the present 40 km thick crust, based on interpretations of seismic refraction data (e.g., Sparlin, et al, 1982).

Basin and Range tectonic activity characterizes the regions on both sides of the ESRP, as characterized by the 1983 Borah Peak earthquake immediately to the North of the INEL. Although significant activity appears to be concentrated within a parabolic arc with its head beneath Yellowstone National Park, no earthquakes larger than $M_S = 3$ have been detected in the period since 1961 beneath the plain itself (Figure 2, after Anders et al., 1989). However, feeder vents for the extrusive basalts are aligned in a north-northwest direction, suggesting that the plain is extending in the same direction as the surrounding province. A number of ideas have been proposed to explain the lack of seismic activity beneath the plain. These include that the plain is undergoing ductile deformation, a consequence of elevated subsurface temperatures (e.g., Furlong, 1979), or alternatively that the basalts are simply too strong to fail (Anders et al., 1989). A recent alternative explanation proposed by Thompson et al. (in press) is that magmatic overpressure accompanying intrusion of dikes applies a large enough lateral stress to raise the least horizontal compression above the value necessary to allow normal faulting. Resolving between these competing explanations requires measurements of the stress state beneath the ESRP.

Unfortunately, there is a pronounced lack of information regarding the in situ stress state in the immediate region of the INEL plant. This is a consequence largely of the lack of seismicity. Figure 2 shows the locations of earthquakes larger than $M_S = 3$ in the region surrounding the ESRP. Figure 3 shows the stress data for a larger region surrounding the plain. This figure was compiled from the World Stress Data Base and includes data through 1989. Three earthquakes in northern Nevada indicate a roughly NE-SW direction of principal horizontal compression in the Basin and Range and a normal faulting environment. A series of earthquakes near the Idaho/Utah border suggests a similar magnitude and orientation of the principal stress field immediately to the SE of the plain. Immediately to the North of the SRP, maximum compression trends NW-SE, as illustrated by the stress directions inferred from the 1983 Borah Peak normal faulting event (indicated by a solid triangle). Not surprisingly, focal plane solutions surrounding the ESRP (Figure 3) yield maximum compression directions paralleling the trends of the latest Quaternary surface (normal) faults on which they presumably occurred (Figure 2). These point slightly towards the Yellowstone hot-spot, rather than being exactly perpendicular to the axis of the plain, a consequence of their origin along the "wake" of the hotspot trace.

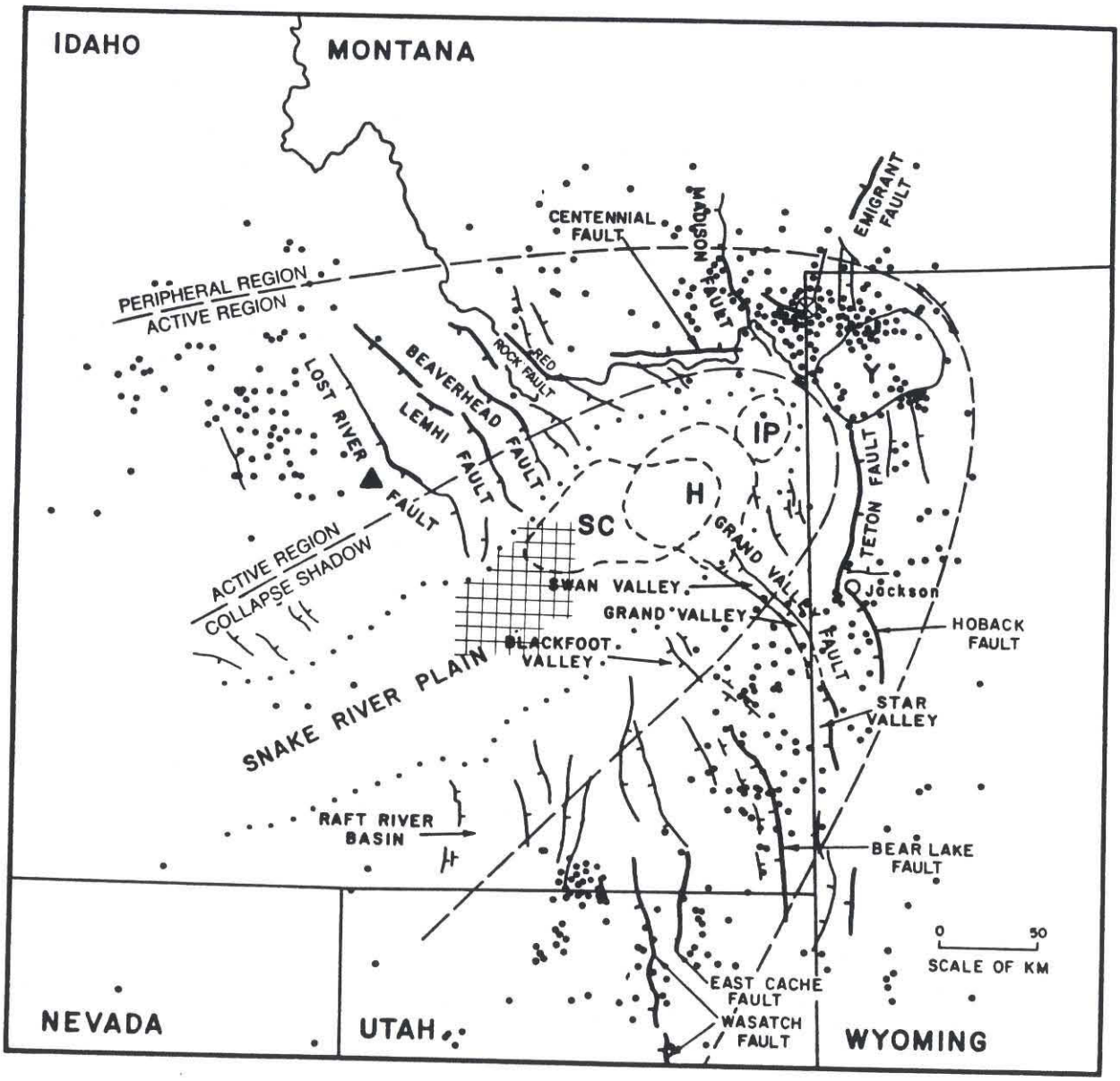

Figure 2: Distribution of earthquakes greater than $M_S = 3$ in the region of the eastern Snake River Plain, after Anders et al., 1989. The triangle shows the location of the 1983 Borah Peak earthquake, and the boundary of the INEL is marked.

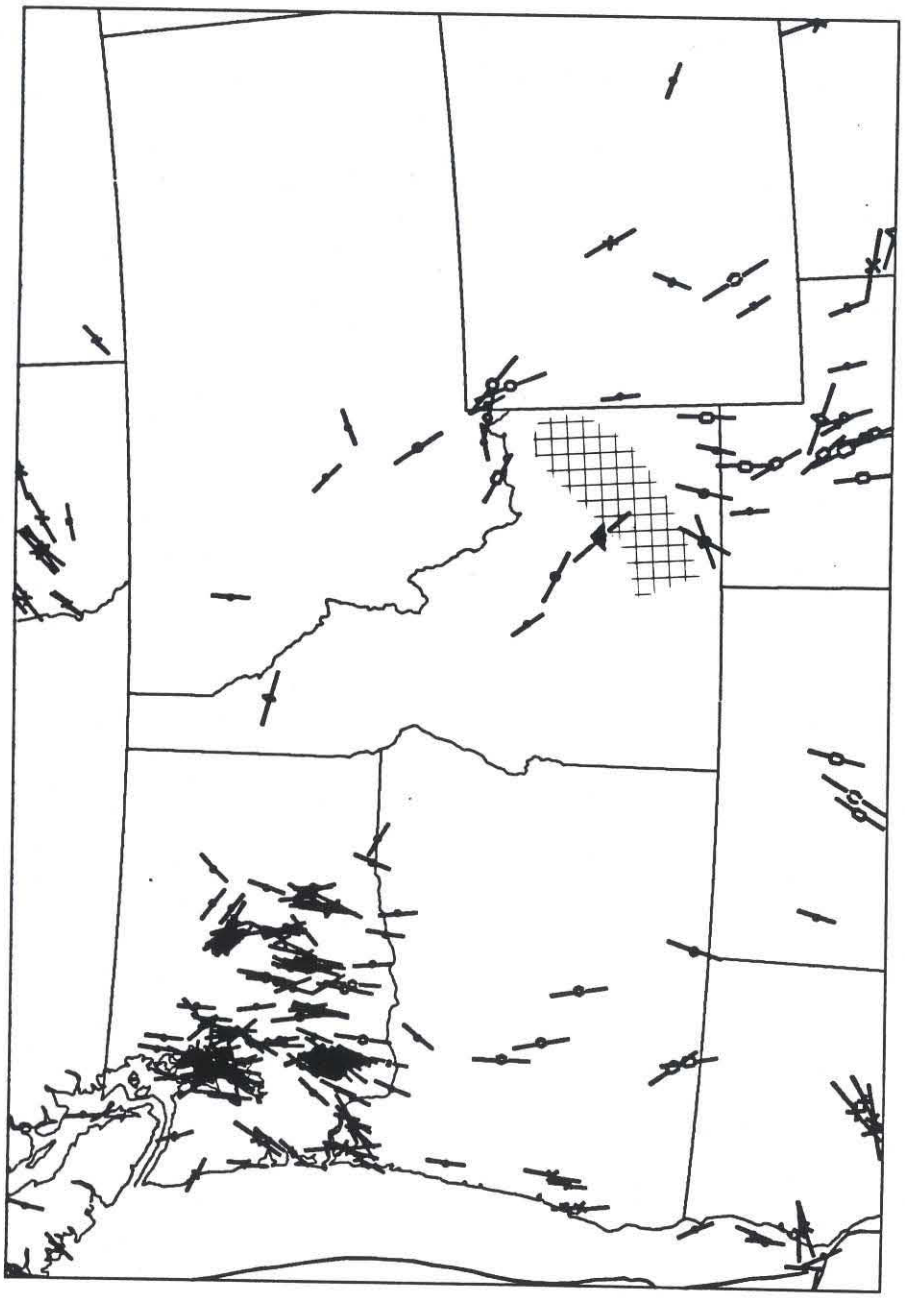

Figure 3: Stress data for the region surrounding the SRP, compiled from the 1989 World Stress Database (Zoback, et al., 1989). The triangle shows the location of the 1983 Borah Peak earthquake, and the boundary of the Snake River Plain is marked.

Description of the wells used in this study

Four wells were reoccupied for BHTV log data acquisition. Table I shows the depths, hole sizes and logged intervals in each of these wells. Three of these (USGS-17, USGS-7, and NONAME-1) penetrate to shallow depths in the basalts. Figures 4, 5 and 6 are well summaries for the shallow wells. The fourth (INEL-1) reached a total depth during drilling of 10,333 feet, and bottomed in silicic volcanics (Figure 7). Data in this hole was collected only in the open-hole interval below 9 5/8" casing. Thus only the silicic volcanics were logged in INEL-1 during the course of this study.

The intervals logged in these wells were constrained by the depth of the water table or of casing, and the total depth of the well. In each case we lowered the logging sonde until it was resting on the bottom of the well. The distance between the transducer measurement point and the end of the tool is about 4 feet. Therefore, the present total well depth can be found by adding 4 feet to the tabulated bottom of the logged interval. As the acoustic pulse generated by the transducer must propagate through the wellbore fluid to be reflected from the borehole wall, we can determine water table very precisely from the depth at which the signal return is lost. In each case the water table was measured a number of times; the numbers presented in Table I are the averages of these observations.

Table I: Well descriptions and summary of the intervals logged in the course of this study:

Well Name	Water Table (BHTV, ft)	Casing Depth (Driller's, ft)	Total Depth (Driller's, ft)	Interval Logged (open-hole, ft)	Hole size (in)
USGS-7	207	760	940	757-890	5.5
USGS-17	392	≈30	600	390-567	18
NONAME-1	204	272*	549*	265-549	12.25
INEL-1	303††	6796†	10,333†	10,243-6780	12.25

*inferred from BHTV log results

†referenced to Kelly Bushing, 20 feet above ground level

††from depths logged running into the well only

We briefly summarize the geological information available for each drillhole in the sections describing the televiewer data acquired in each. These descriptions were obtained from copies of well geometry figures and lithologic summaries provided by R. P. Smith (EG&G) prior to the start of logging.

Well Summary: USGS-7

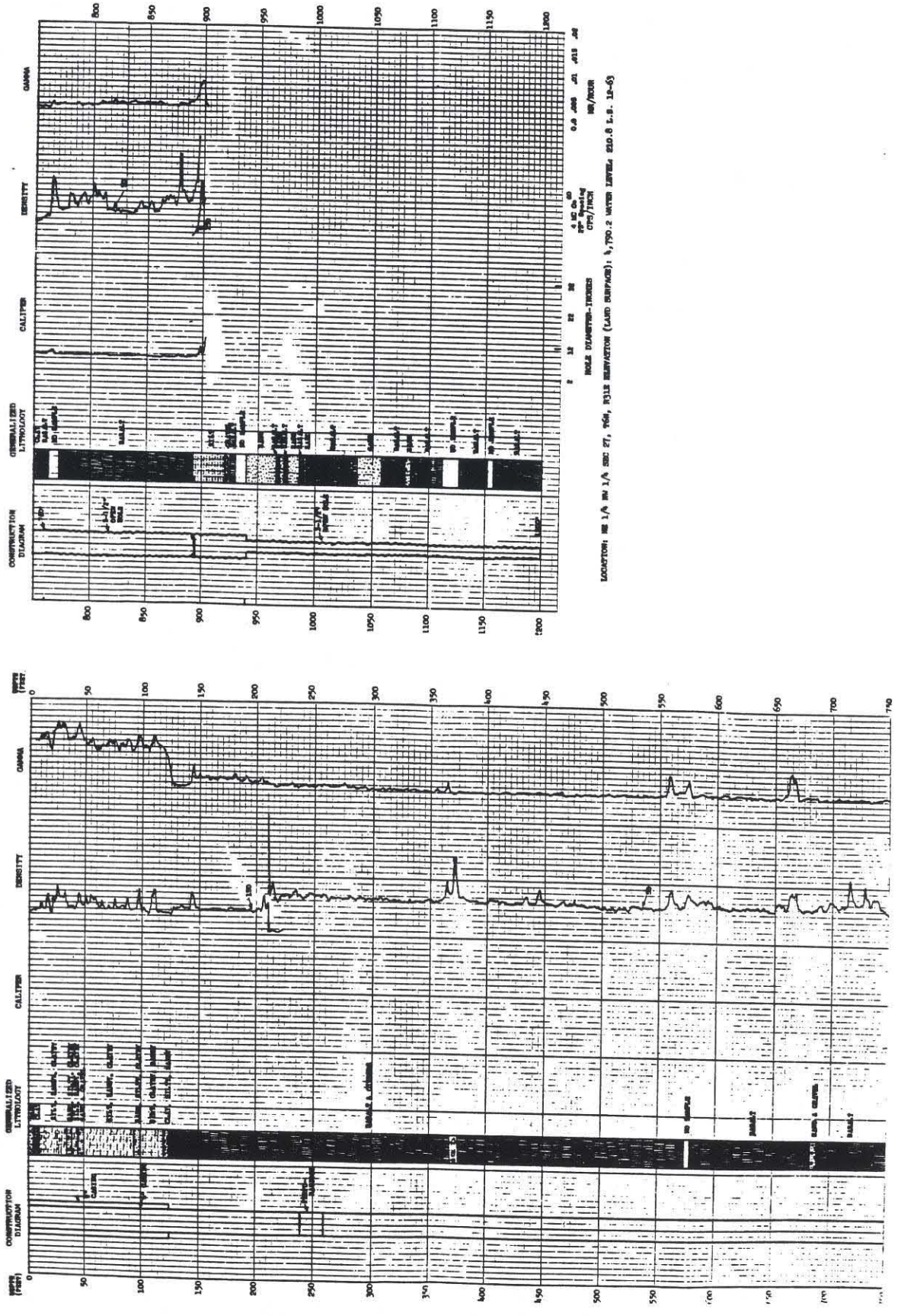

Figure 4: Construction diagram for well USGS-7

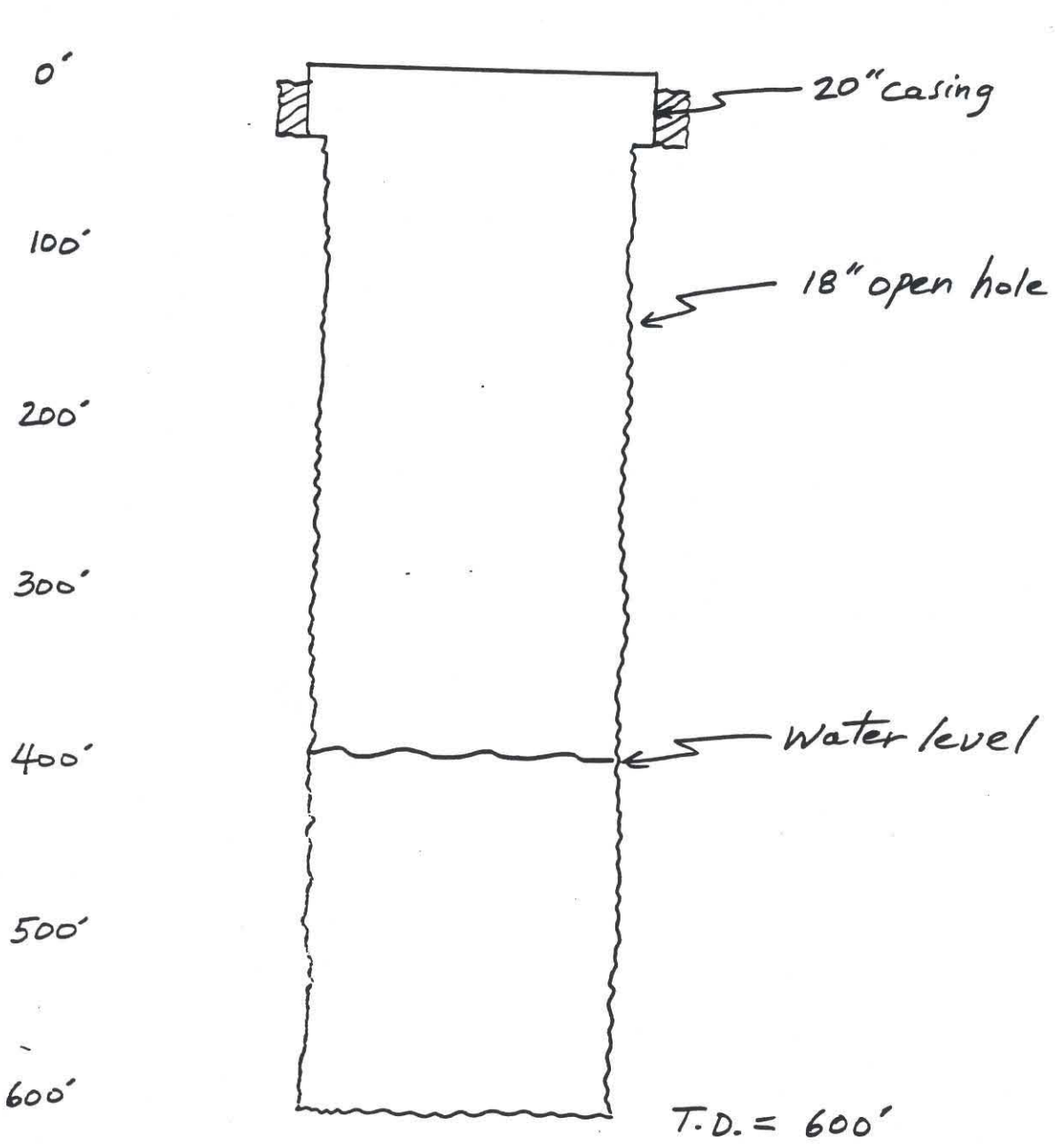

Figure 5: Construction diagram for well USGS-17

Well Summary: Noname

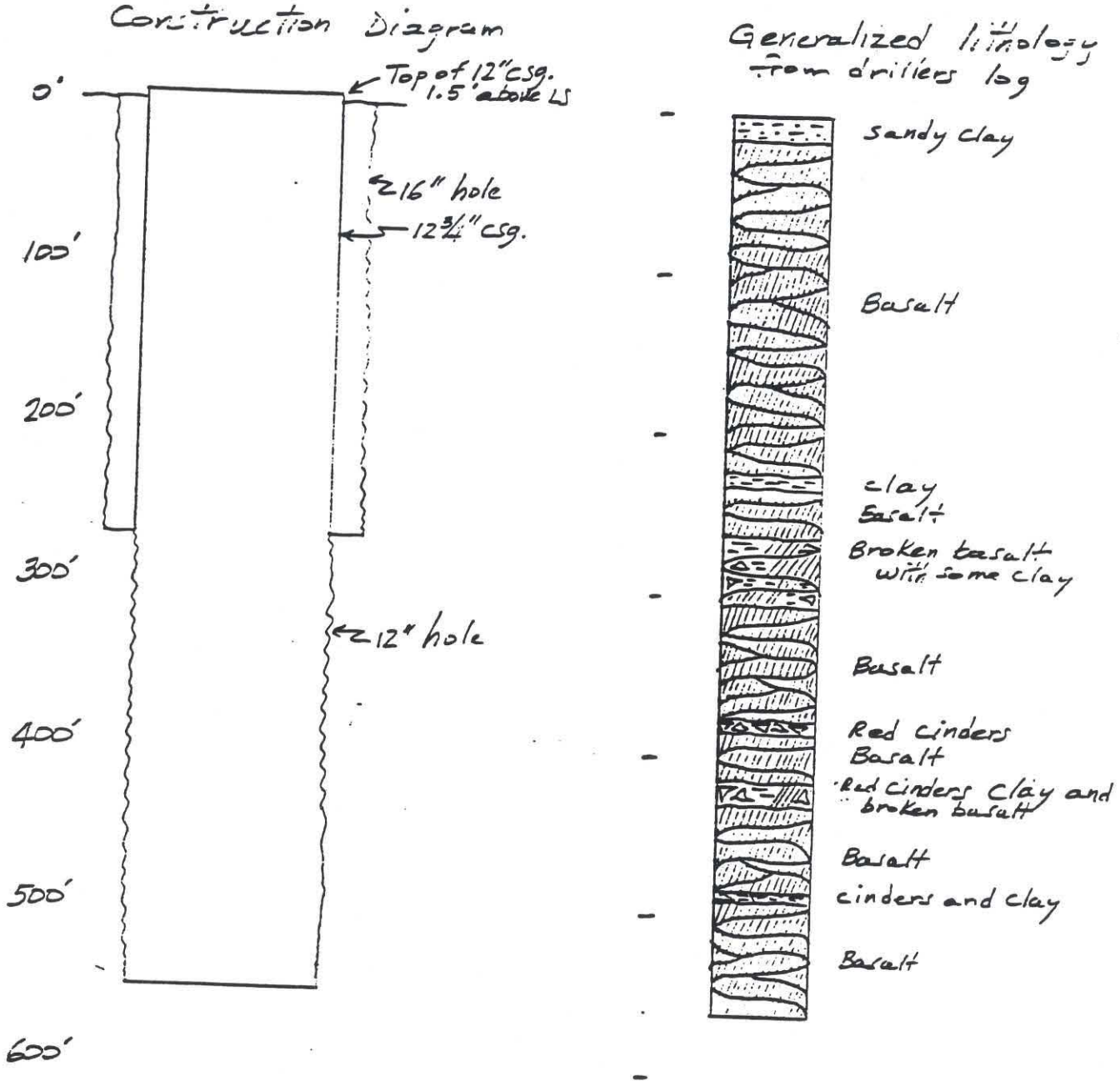

Figure 6: Construction diagram for well NONAME-1

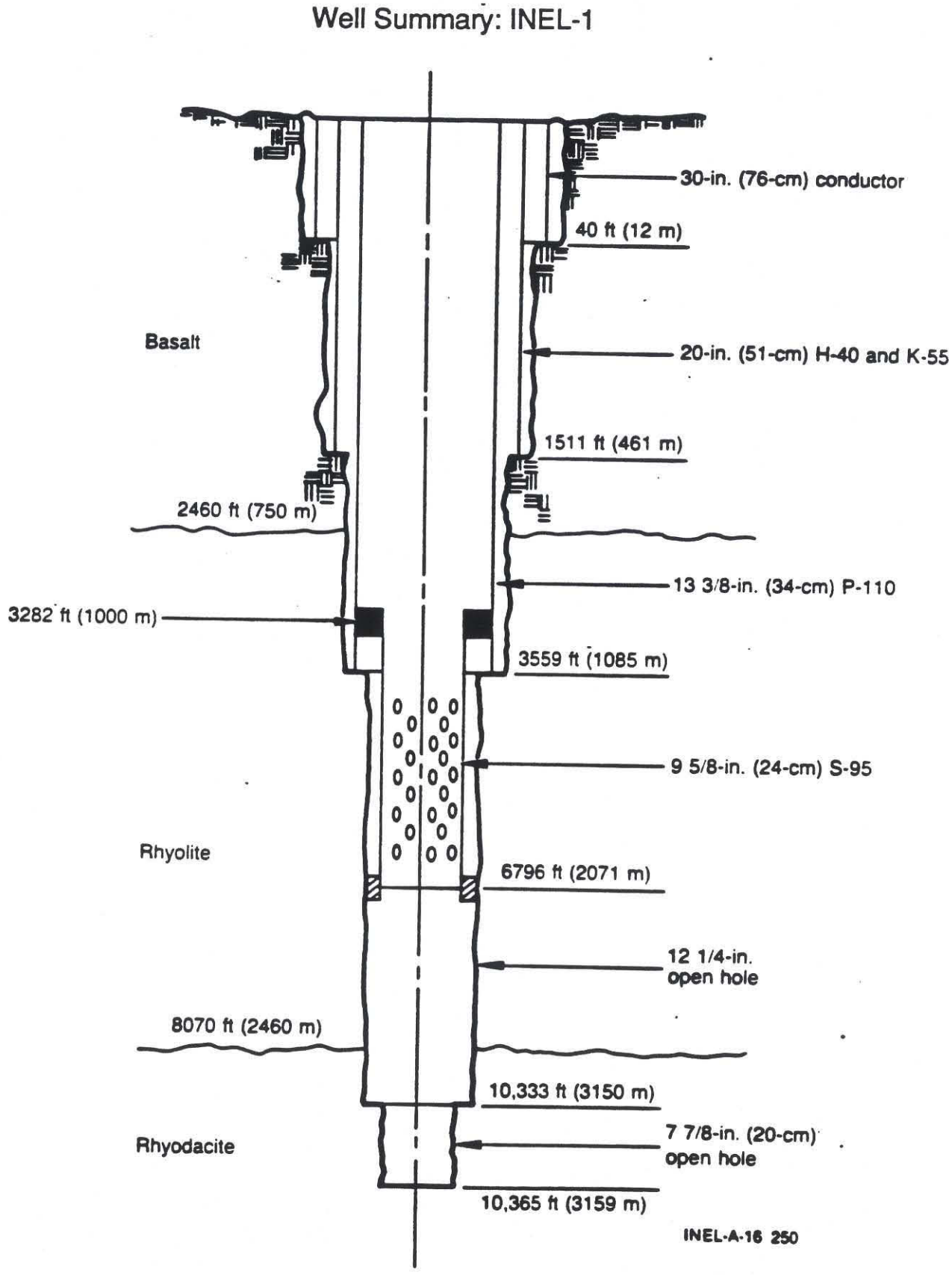

Figure 7: Construction diagram for well INEL-1

Previously Recorded Televiewer Data

The USGS Denver Water Resources Group collected BHTV data at INEL-1 during and shortly after the completion of drilling operations. Their depths are all referenced to the Kelly Bushing, 20' above ground level. Unfortunately, the USGS logs do not provide complete coverage of the INEL-1 hole. Furthermore, the data is available only as photographic copies of polaroids taken during logging, and thus is not appropriate for quantitative analysis. The depth intervals for which this data is available are 7100-7250, 7300-7380, 7420-7500, 7580-7780, 7980-8030, 8540-8600, 8900-9060, 9680-9800, and 10045-10200 feet.

These logs clearly show the effects of eccentering of the televiewer sonde as dark stripes running vertically along the images (Georgi, 1985). However, large numbers of sub-vertical fractures striking within 20° of EW can be seen in the images. No stress-induced breakouts were observed in these early logs.

A completely new set of borehole televiewer data was collected in this study for several reasons. First, the original logs are incomplete. Second, the quality of the new generation BHTV is superior to that available in 1981, through use of better centralizers and a newly designed, focussed transducer assembly. Furthermore, wellbore breakouts are often detectable in digitized data where they are invisible in the analog photographs. Also, there is some evidence elsewhere (for example, in the Kola well; L. Vernik, pers. comm.) that breakouts develop in time, and thus it was suspected that the 9-year interval between the early logs and the present date may have allowed new breakouts to occur. Finally, the BHTV data can be used to select intervals for later hydraulic fracturing stress measurements, and can be compared to televiewer logs made after successful tests to image the resultant hydrofracs.

DATA ACQUISITION

The borehole televiewer is an ultrasonic well-logging tool useful for imaging lithostratigraphic features and for measuring the orientation and distribution of fractures as well as the orientation and width of stress-induced wellbore breakouts. The analog televiewer, originally designed by Mobil Oil, Inc. (Zemanek et al., 1970), contains a rotating transducer that emits an acoustic pulse at the rate of 1800 times a second (See Figure 1, Appendix IV). The 1.4 Mhz transducer is mounted on a shaft which rotates at three revolutions per second. The logging sonde is centered in the wellbore using bowsprings, and is drawn upwards at a speed of 2.5 cm/s. Thus the reflection point describes a helical path as the tool moves up the wellbore, with repeat samples at each

azimuth obtained approximately every 0.8 cm. A fluxgate magnetometer within the tool fires at each crossing of magnetic north, making it possible to orient the data. The raw data displayed as a function of azimuth and depth in the hole presents a N-E-S-W-N unwrapped section of the amplitude of the reflected pulse in the borehole. A schematic of the tool and a sample of the data recorded during logging is presented in Figure 8.

Borehole televiewer data were collected in USGS-17, USGS-7, NONAME-1 and INEL-1 in late May and early June of 1990. Appendix I summarizes the data acquisition sequence, and the depth intervals for which data were acquired in each well are presented in Table I. Two different logging sondes were used to acquire the data. A 1 3/4" diameter sonde designed for use in small holes was used in USGS-17, USGS-7, and NONAME-1. Excellent data was recorded in USGS-7 and NONAME-1, but as described below the 18" hole size of USGS-17 was too large to adequately center the tool. Regardless, the piezoelectric source is powerful enough to return reflections even in this hole, provided the pulse strikes the borehole at normal incidence. Thus we were still able to extract useful information from the digitized and processed data. Data was recorded in INEL-1 using a 3 5/8" diameter, newly designed, high temperature televiewer. As this was our first use of this new tool, a number of electronic and mechanical failures plagued the recording effort. Even though we spent one week at the manufacturer prior to logging at the INEL, recording a complete log in that hole required a visit to the site by a technician from the manufacturing company. A detailed discussion of the procedures we used to verify the correct operation of this tool is presented in Appendix II.

The raw televiewer data recorded in the field on videotape were digitized at Stanford prior to analysis. This process is described in detail by Barton (1988) and in Appendix IV of this report. In post logging digitization the recorded BHTV signal is examined within a specified window to determine the peak amplitude and its associated travel time (Barton, 1988). Figure 1b of Appendix IV is an oscilloscope image of the playback of the analog wave train recorded on videotape for each pulse firing of the BHTV tool. The signal below the BHTV wave train represents the Mhz frequency clock used to discretely sample the windowed borehole wall reflection. The peak amplitude and associated travel time are measured for each pulse firing, for later display as false-color images of reflection amplitude and wellbore radius.

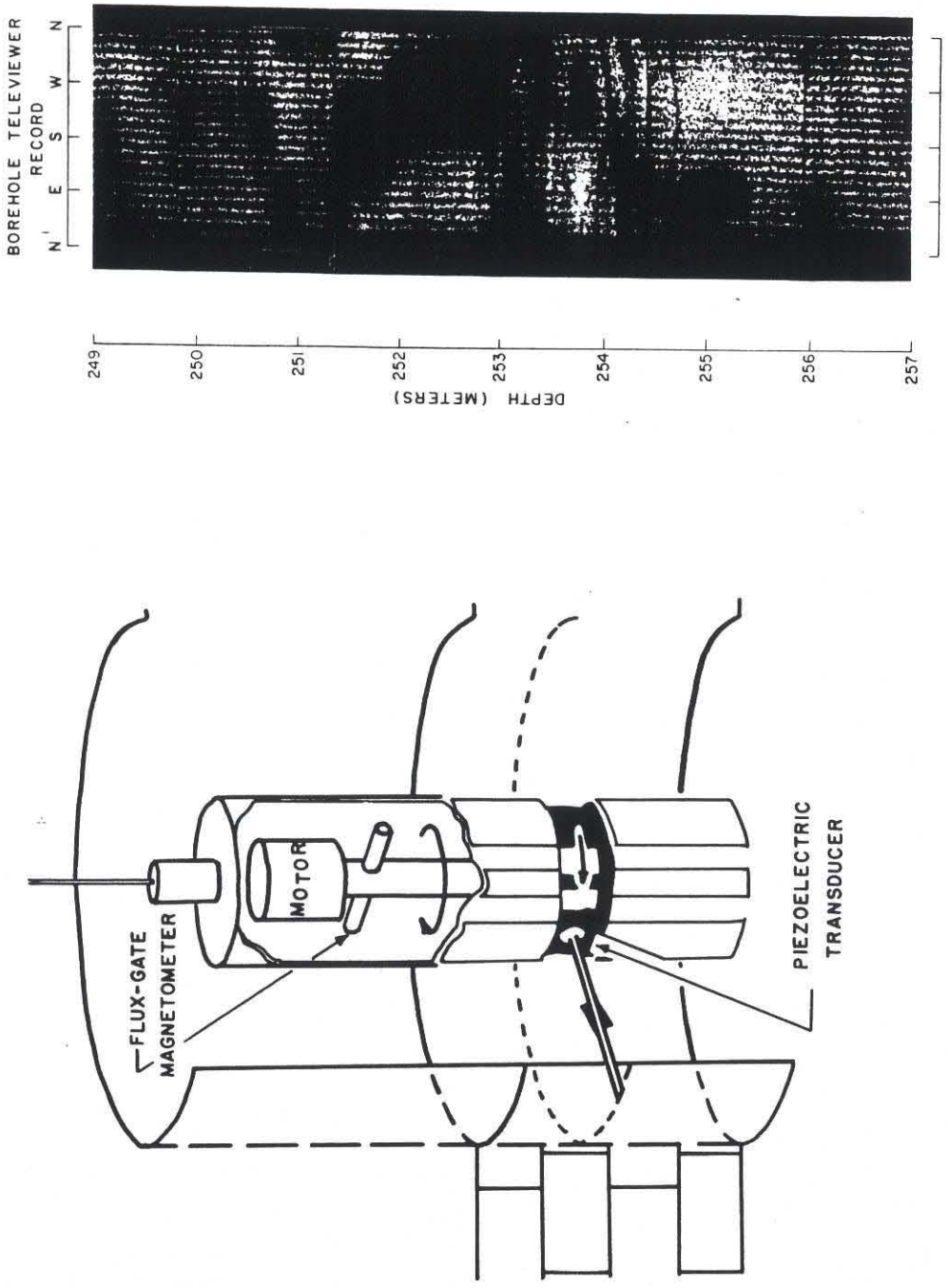

Figure 8: Schematic of the operation of the borehole televiewer, showing a sample Polaroid image recorded during logging.

The digital data are preprocessed before display. Preprocessing involves visual editing of the data for unwanted scans, median filtering to remove noise, and removal of the effects of off-centered tools. The data are shifted to correct for the magnetic declination at the logging site or of any other azimuthal data shift, and the amplitude and travel time values are scaled to the range 0 to 256. The editing and preprocessing procedures followed for the digital data recorded in INEL-1 and the three shallow wells of this study are described in detail in Appendix IV.

Conversion of travel time to true borehole radius requires prior calibration of the BHTV, as each tool is slightly different. These calibrations are carried out prior to and following each logging run, as described in Appendix II. Correct hole size determination requires knowing the speed of sound in the fluid in the wellbore, and thus these calibrations are generally carried out using samples of the mud in the hole. All four wellbores logged at the INEL were filled with clear water, so we simply used tap water for this study. The calculations required to convert travel time to borehole radius are thoroughly discussed in Appendix IV.

Stresses Beneath the ESRP

The data from the INEL-1 well was studied in detail to determine if stress-induced spalling of the wellbore (wellbore breakouts) had occurred. Appendix V describes the process of formation of breakouts, and outlines a methodology whereby the magnitudes of the horizontal stresses can be determined from the depth at which they begin to become common in a given well or region. These developments are briefly summarized below.

The process of drilling a wellbore into the earth's crust results in the concentration of stresses at the borehole wall. The equation relating the principal far-field horizontal stresses (S_{Hmax} and S_{hmin}) to the resulting circumferential stress ($\sigma_{\theta\theta}$) at the wellbore were derived by Kirsch (1898), and can be generalized to include wellbore fluid pressure (P_{mud}) different from the pore pressure (P_p):

$$\sigma_{\theta\theta}(\theta)=S_{Hmax} + S_{hmin} -2(S_{Hmax} -S_{hmin})\cos 2\theta - P_p - P_{mud} \qquad (1)$$

The maximum circumferential stress is attained at the azimuth of the minimum far-field horizontal stress ($\theta=90^o$), and the minimum circumferential stress is attained at the azimuth of the far-field maximum stress ($\theta=0^o$). The assumptions implicit in this equation are that the borehole is drilled in a vertical direction, that the vertical stress is a principal stress, and that the effective stress law is valid.

In general, wellbore failure can occur as a result of either compressive or tensile stress concentrations around the borehole, and, as described by Moos and Zoback (1990), observations of wellbore failure can provide information about the magnitudes of the in situ stresses.

Compressive stress failures at the azimuth of the least principal horizontal in situ stress (where the compressive stress concentration is greatest) are termed stress-induced wellbore breakouts (Bell and Gough, 1979) and have proven to be a reliable measure of stress orientation on land in many areas (see summary by Zoback et al., 1989). Breakouts have been identified both in uncomputed dipmeter logs (e.g., Bell and Gough, 1979) and in borehole televiewer logs (e.g., Zoback et al., 1985). Where both logs are run in the same hole, similar results have been obtained (e.g., Plumb and Hickman, 1985).

Wellbore breakouts occur by compressive shear failure wherever $\sigma_{\theta\theta}$ exceeds the strength of the rock, C (e.g., Zoback et al., 1985). If the two horizontal stresses are different, failure will occur at the azimuth of Shmin, where:

$$\sigma_{\theta\theta}^{max} = 3S_{Hmax} - S_{hmin} - P_p - P_{mud} \geq C \qquad (2)$$

From this equation and knowledge of the appropriate rock strength, C, constraints can be placed on the magnitudes of S_{Hmax} and S_{hmin}.

Tensile failures around the wellbore form at the azimuth of the greatest principal horizontal in situ stress (where the stress concentration around the well is least compressive). The hydraulic fracturing stress measurement technique takes advantage of this effect (Hubbert and Willis, 1957). However, tensile fractures may form adjacent to the wellbore simply as a consequence of drilling the hole. As is the case for wellbore breakouts, observations of tensile failure at the wellbore provide information about both stress orientation and magnitude.

Tensile fractures will occur whenever the minimum value of circumferential stress at the azimuth of SHmax is less than the tensile strength of the rock, T:

$$\sigma_{\theta\theta}^{min} = 3S_{hmin} - S_{Hmax} - P_p - P_{mud} < -T \qquad (3)$$

Thermally-induced tensile stresses due to cooling of the borehole wall by circulation of relatively cold drilling fluids can also promote tensile failure while drilling (Allison and Nielson, 1988; Morin et al., 1990). In these cases the fractures cannot propagate significant distances away from the wellbore unless the wellbore fluid pressure exceeds the least principal in situ stress (c.f., Stock et al., 1985; Moos and Zoback, 1990). Thus in

some cases tensile fractures can be formed at the wellbore but will not be observed during drilling because they are not associated with pronounced fluid loss. These can sometimes be observed by scanning logs such as the borehole televiewer or the formation microscanner.

As described above, the stress regime within the Basin and Range surrounding the ESRP is an extensional one. Thus breakouts were not expected to occur until a significant depth below ground level. It was still surprising, however, that no breakouts were detected in the INEL-1 well to its total depth of more than 3.1 km. Figure 9 illustrates the range of horizontal stresses allowed by the frictional strength of the crust for a depth in the INEL-1 well of 2.5 km. Superimposed on the figure are lines which subdivide the stress fields based on the presence or absence of breakouts, if the strength of the rocks is 100 MPa. Two strength criteria are illustrated. The first is the biaxial strength criterion employed by Moos and Zoback (1990). The second is the criterion suggested by Vernik and Zoback (submitted) to apply to rocks at depths below which microcracks are entirely closed and permeability and porosity approach zero.

Resolving the question of which of these two criteria is appropriate for the case at INEL-1 requires the determination of the so-called Biot coefficient, α, in the effective stress equation:

$$P_{eff} = P_c - \alpha P_p \qquad (5)$$

If $\alpha = 1$ the effective stress law applies, the fluid pressure in the wellbore offsets the rock pore pressure, Eqn's. 1-3 are appropriate to describe the wellbore stress concentration, and the rock strength for the case in which $P_{mud} = P_p$ is the biaxial strength (at the wellbore wall $S_1 = \sigma_{\theta\theta}$, $S_2 = S_v$; $S_3 = 0$). If $\alpha = 0$, the wellbore fluid pressure, P_{mud}, acts as a boundary condition on the wellbore, Eqn's. 1-3 must be modified to treat the total stresses, and the appropriate strength is approximately 1/2 the ultimate strength for the polyaxial stress case, C_p (at the wellbore wall $S_1 = \sigma_{\theta\theta}$, $S_2 = S_v$; $S_3 = P_{mud}$). This value ($\approx 0.5C_p$) is the point at which dilatent microcracks begin to develop, which for the wellbore case will lead immediately to failure and the formation of breakouts. The failure criterion then becomes (after Vernik and Zoback):

$$\sigma_{\theta\theta}^{max} = 3S_{Hmax} - S_{hmin} - P_{mud} \geq C_{ef} \; (\approx 0.5C_p) \qquad (6)$$

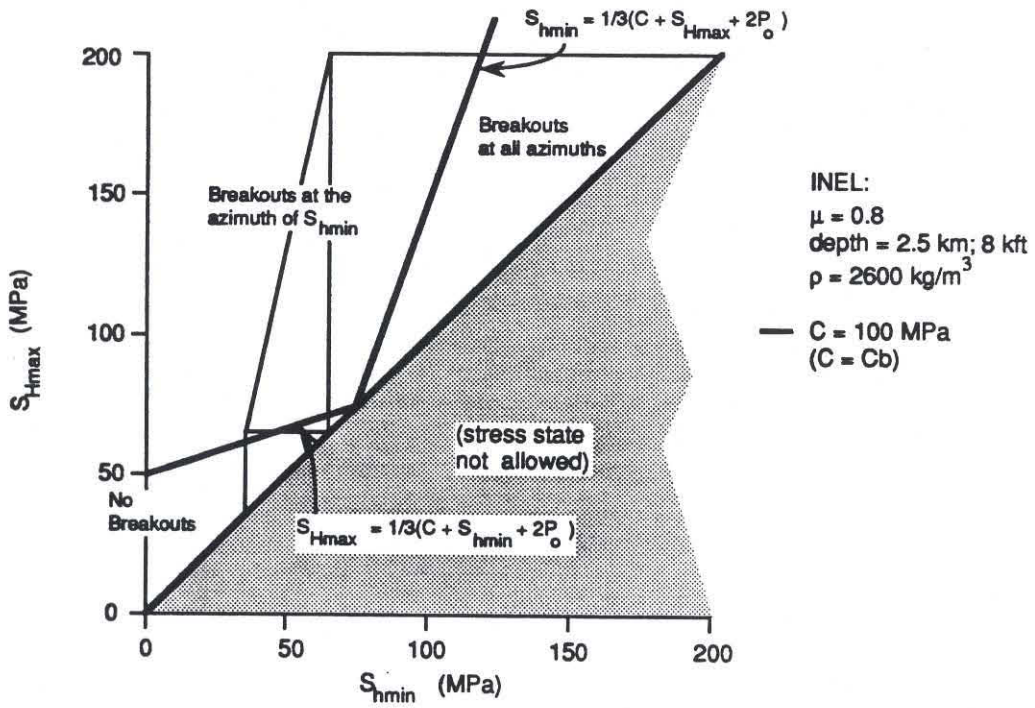

ASSUMING EFFECTIVE STRESS GOVERNS FAILURE
(Moos and Zoback, 1990)

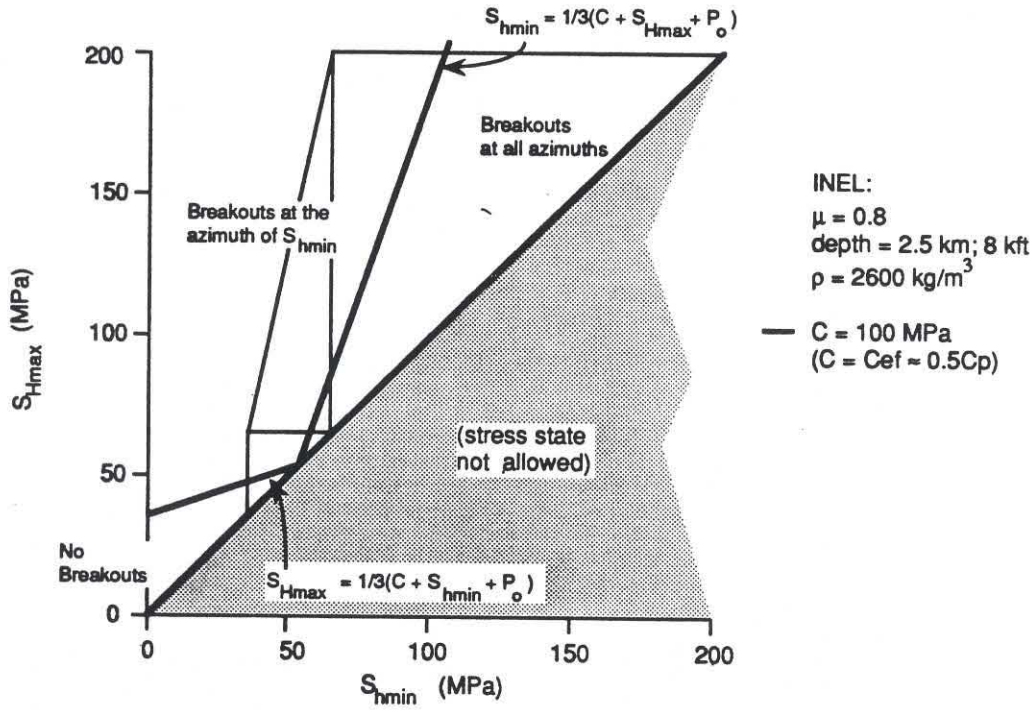

ASSUMING TOTAL STRESS GOVERNS FAILURE
(Vernik and Zoback, submitted)

Figure 9: Frictional constraints on the horizontal principal stresses appropriate for the INEL site, along with the fields within which breakouts are or are not expected. The upper figure illustrates the range of stresses at 2.5 km depth that would be expected to cause or not to cause breakouts, if the effective stress law applies. The lower figure is the same, but assumes that the effective stress law does not apply.

As a first estimate of the value of α, the ratio Vp/Vs provides a useful discriminator. Low values of this ratio are typical of rock with few microcracks, and indicate that the appropriate value is $\alpha = 0$. Higher values result from the presence of microcracks which enhance the porosity and permeability of the rock and lead to values of α closer to 1. Unfortunately, no measurements of V_p/V_s at the wellbore are available for the INEL-1 well. However, values of $\alpha \approx 0$ are associated with resistivities (which are sharply lower in the presence of microcracks) above 10,000 ohm-m. Examination of resistivity logs recorded in the INEL-1 well, therefore, should allow determination of which method should be used to estimate stress magnitudes.

As lithologies are variable within the INEL-1 well, it is reasonable to expect that rock strengths are also. A wide variety of values for welded tuffs are reported. For illustration, therefore, we choose strengths of 100 MPa, within the range reported for crystalline rocks. For strengths close to these, the absence of breakouts requires a normal faulting stress regime. Large horizontal stress differences are unlikely. However, more precise strength values are required to discriminate between a between a hydrostatic (i.e. $S_{hmin} \approx S_{Hmax} \approx S_v$) and an incipient faulting (i.e. both S_{hmin} and $S_{Hmax} << S_v$) stress regime.

As there are no breakouts within the depths penetrated by the INEL-1 well, we next asked the question of whether the drillers reported anything that might suggest that hydraulic fractures were created in the wellbore during drilling. As described by Moos and Zoback (1990) and others, the likelihood of tensile failure in a wellbore increases if cold drilling fluids are juxtaposed against warmer rocks, as the cooling of the wellbore which results causes the generation of circumferential tension. The preponderance of vertical fractures in the INEL-1 well, and their strong preferred orientation, is characteristic of drilling induced hydraulic fracturing observed elsewhere (for example, Stock et al., 1985).

However, there was no evidence of lost circulation within the depths logged by the BHTV. Furthermore, all the available evidence suggests that the fractures we saw in the INEL-1 data are old. Thus we conclude that the horizontal stresses were not sufficiently different to cause hydraulic fracturing. This places a lower bound on the horizontal stress difference, as it requires that strike-slip faults cannot be active in the current stress regime.

Thus the results of borehole televiewer logging in the INEL-1 well, although they require low (normal faulting) horizontal stresses and only a modest horizontal stress difference, do not resolve the issue of either the orientation of the horizontal principal stresses, or their precise magnitudes.

Fracturing in INEL-1

High quality borehole televiewer (BHTV) data were available from the INEL-1 drillhole for detailed analysis over the interval 6780 to 10,243 ft. The analog BHTV logs indicated that the data were generally of very good quality. In the following discussion we present the results for the data from INEL-1. The analog data were digitized and interactively processed prior to analysis using the techniques summarized above and described in more detail in Appendix IV.

While our study provides detailed data of fracture distribution at only a single location, it provides 3505 feet of continuous sampling in the silicic volcanics. The strike, dip and apparent aperture of 2568 natural fractures encountered over the depth range studied are reported below. The large number of fractures provides a representative sample of fracturing at the INEL site and presents an opportunity to examine their statistical distribution.

Measurement of Fracture Orientation and Apparent Aperture

Fracture orientations and apparent apertures were measured throughout the 3505 feet of hole logged in INEL-1. An example of the measurement of fracture orientation and apparent aperture for data typical of the INEL-1 BHTV log is presented in Figure 10. The left window of Figure 10 shows the fit of a sinusoid to the trace of a steeply dipping fracture at 9725 ft and the right window the interactive measurement of fracture aperture. A detailed description of the measurement technique is given in Appendix IV.

All fractures with apertures in the range from 0.2 in to 20 in were detected and measured. Many fractures with smaller apertures were also detected but their widths could not be accurately measured. Shear zones more than 20 in wide cause such disruption of wellbore conditions that the apparent fracture aperture cannot be measured with the televiewer. In total, 2568 macroscopic fracture orientations were analyzed from the INEL-1 image data. Of the 2568 fractures studied 2273 apertures were measured.

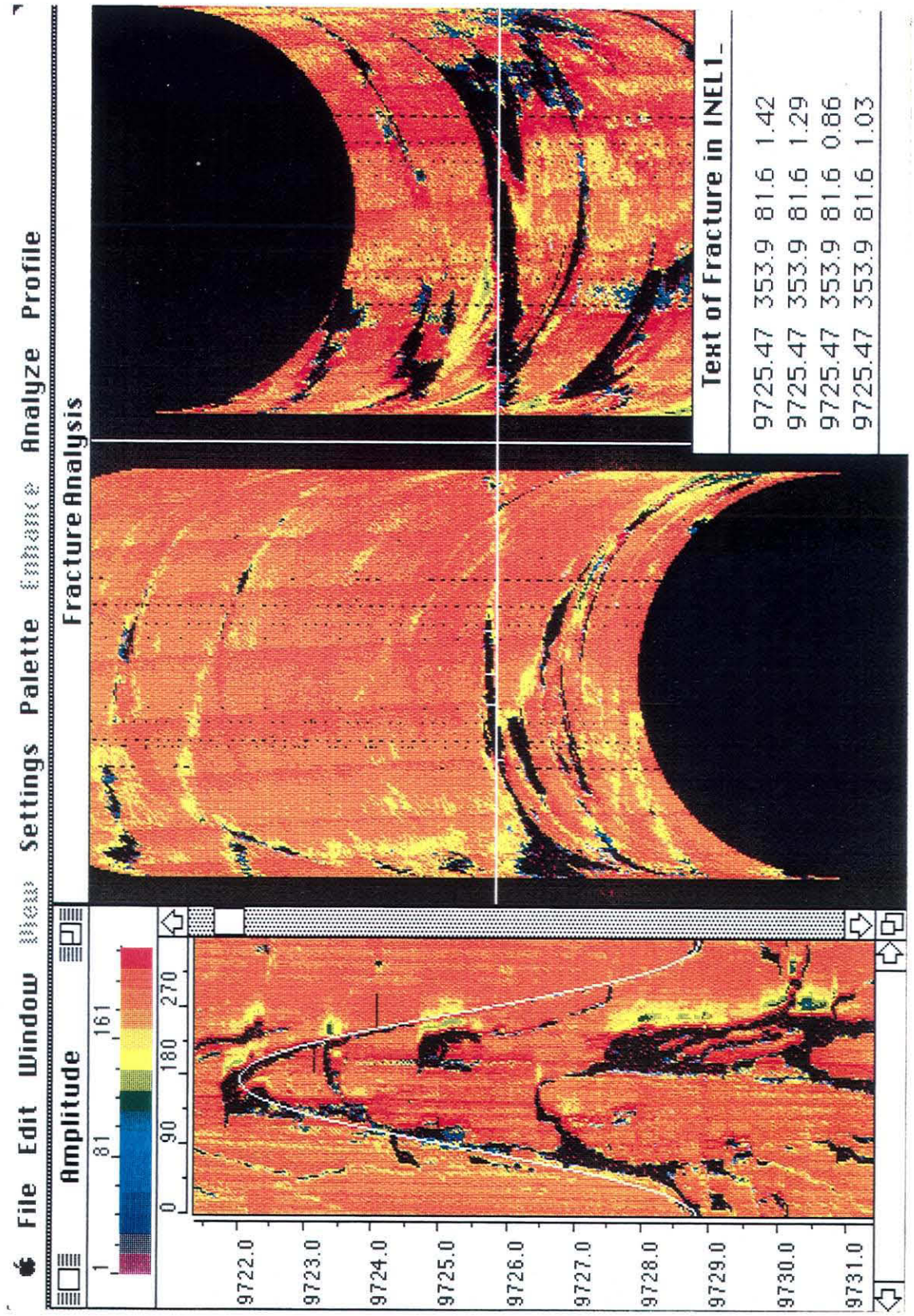

Figure 10: Interactive workstation screen showing the measurement of fracture orientation and apparent aperture for data typical of the INEL-1. The left window shows the fit of a sinusoid to the trace of a steeply dipping fracture at 9725 ft and the right window the interactive measurement of fracture aperture.

The BHTV reflectivity image data indicate that a different, often lower, reflectivity material infills the majority of fractures in the well. Figure 11 is an example of the acoustic character of the infill found in most fractures measured in the INEL-1 well. The fracture between 8505.5 and 8508.5 ft is only defined at its peak and trough. Little of this fracture trace can be discriminated in the corresponding travel time section. Toward the bottom of this interval between 8513.5 and 8514.5 a fracture is clearly filled with a material of lower reflectivity. Again, this fracture causes only minor changes in the borehole radius. The enlarged fracture from 8515 to 8516 ft appears to be partially infilled and substantially eroded. The most convincing evidence that these fractures are sealed is that in most cases it is only possible to distinctly discriminate the peak and trough of a fracture where the mechanical erosion of these steep features is the greatest. The remaining segments of the sealed fractures can be seen only by careful examination of the enhanced reflectivity image data.

The character of fractures shown in Figure 11 is typical for much of the logged section of INEL-1. Thus, most of fractures imaged by the BHTV in this study appear to be sealed, probably with calcite. The large number of fractures and the extent of their infilling and connectivity provides evidence for the past movement of groundwater.

Fracture Distribution

Plotted in Figure 12 is the fracture frequency per foot over the interval 6780 to 10,245 feet. The fracture distribution tends to be clustered with intermittent high fracture densities (c.f. 7725 ft; 8340 ft; 9525 ft; 10,200 ft). Several zones of intense fracturing are indicated by the hashed lines. Many of these correlate with a high measured fracture density, although over some highly fractured intervals the BHTV signal is reduced resulting in the inability to discriminate fractures. Data on apparent fracture aperture is shown in Figure 12 as the cumulative amount of fracture aperture (in inches) per 1 foot of depth. Comparing this profile to that of fracture density, several intervals with a high frequency of fractures correspond to a low cumulative width per foot. However, where the apparent aperture per foot is large there are usually a large number of fractures. Although mechanisms acting to close fractures would be expected to reduce the number of open fractures with increasing depth, the data do not show this trend.

There appears to be a cyclic repetition of high density fracturing followed by moderate to low fracture density throughout the logged interval (c.f. 7725 - 8325 ft; 9525 - 10,100 ft). These apparent cycles may be associated with repeated deposition of the volcanics and with the associated compositional changes.

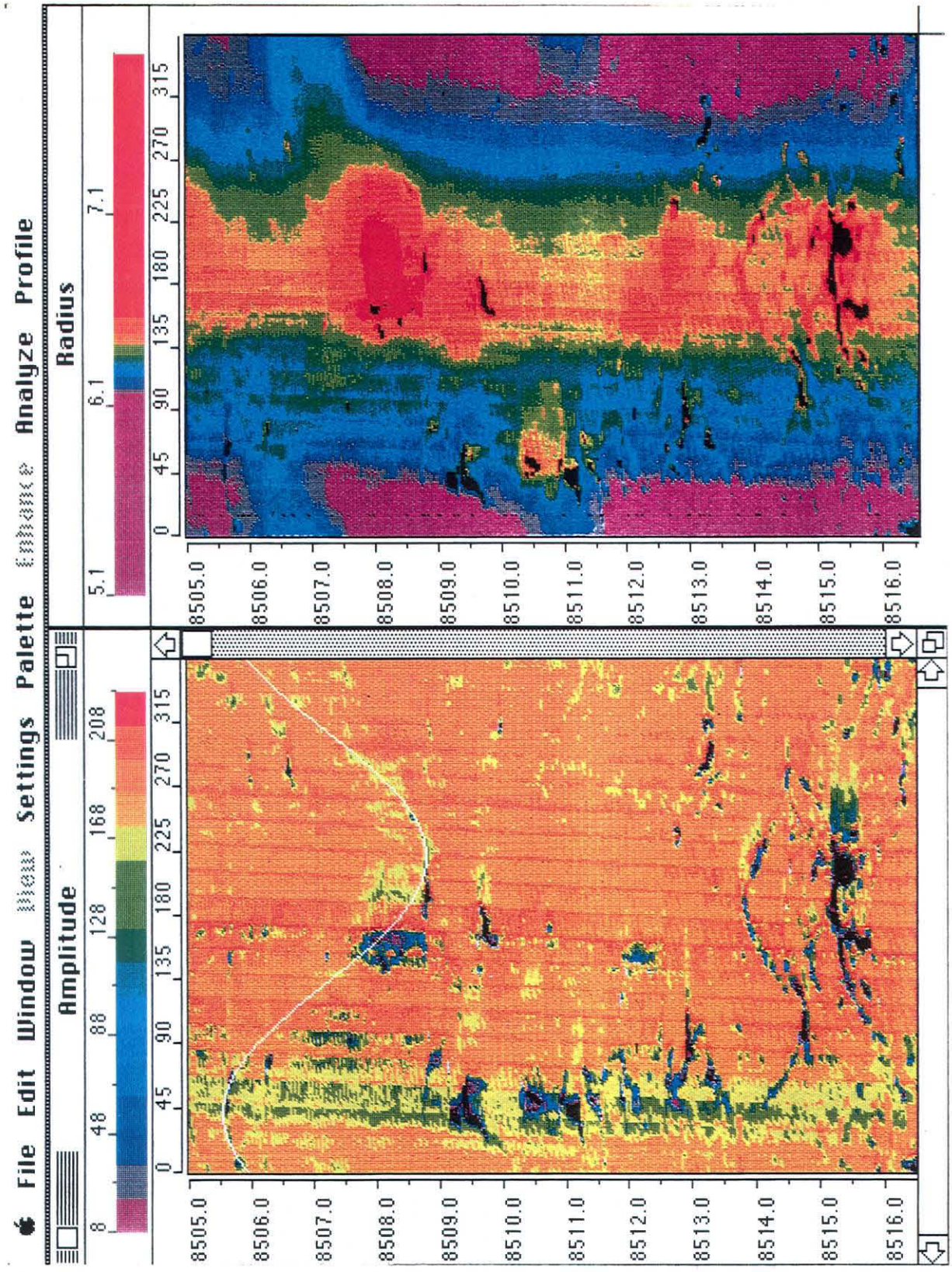

Figure 11: An example of the acoustic character of the infilling material found in most fractures measured in the INEL-1 well. Left window of the amplitude of the reflected energy indicates the fracture trace visible at its peak and trough while the wellbore radius image (right window) shows little of the fracture trace.

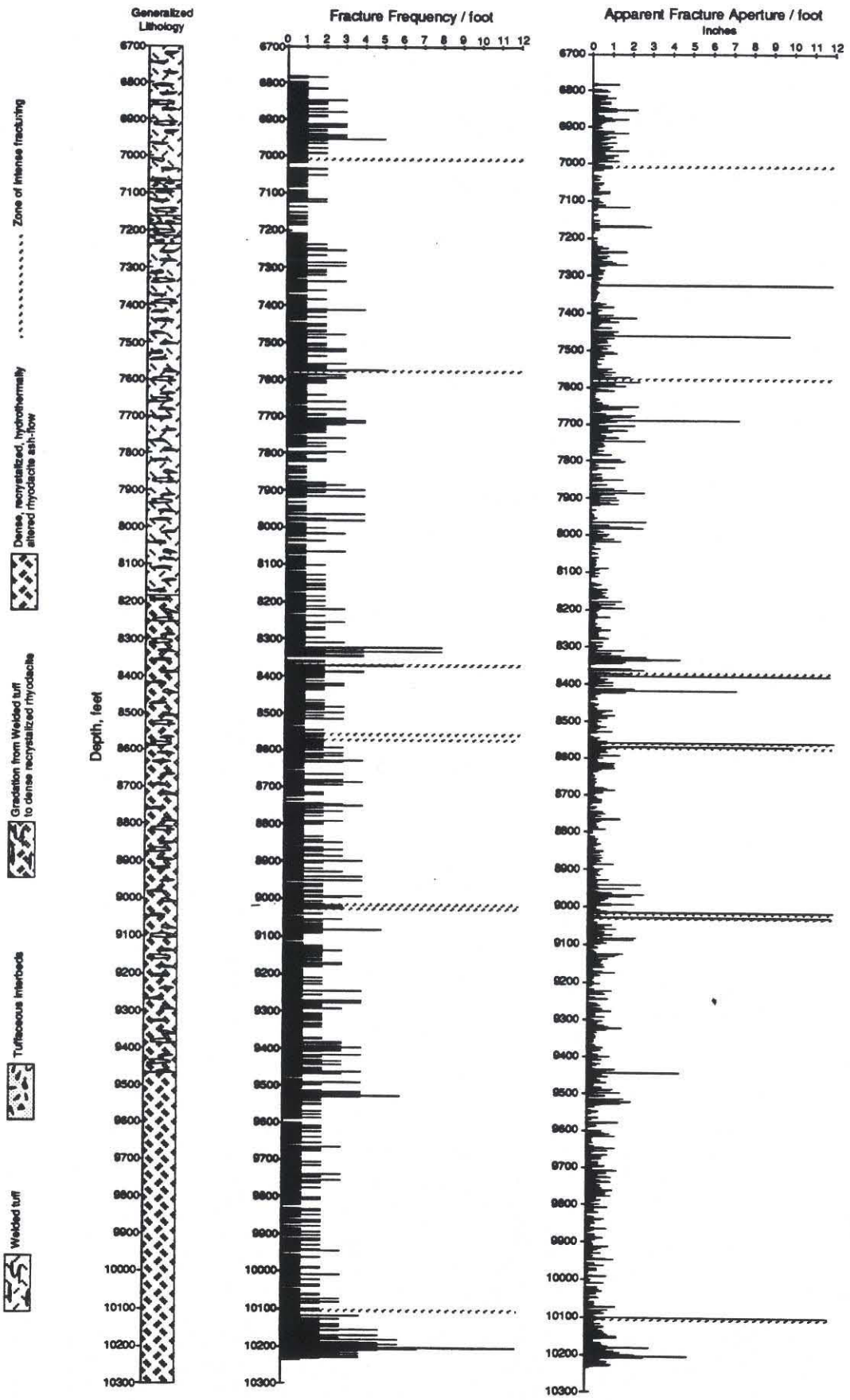

Figure 12: Generalized lithology, fracture frequency and apparent aperture per foot over the interval 6780 to 10,245 feet. in well INEL-1

Fracture Orientation

Orientations of all of the macroscopic fractures detected in the INEL-1 well are shown in Figure 13 in a lower hemisphere stereographic projection. On the left side the data are presented as poles to fracture planes and on the right side they are presented as a contour diagram of pole densities. A step function method was used to contour pole densities. The contour shading shown in the legend in Figure 13 represents the percentage of points that fall within the area of the point counting circle.

While there is clearly a random component of fracture orientations, a statistically significant concentration of fractures strikes East-southeast and dips steeply to the Northwest. The primary concentration of fractures strike at an azimuth of 155° and dip 78° Northwest. A secondary significant population is comprised of subhorizontal fractures dipping from 5° to 30°.

The strike of fracture planes for 500 foot depth intervals within the INEL-1 well is presented in Figure 14. This includes all fractures, regardless of their dip angle. Aside from the interval between 7500 and 8500 ft, where the azimuth of the predominant fracture strike is 250°, the predominant fracture strike azimuth in the INEL-1 well is 265°. There is no clear relationship between fracture strike (Figure 14) and either lithology or fracture frequency (Figure 12).

A summary of fracture orientation with depth is presented in Figure 15 as a tadpole plot. The dip of the fracture is plotted along the x-axis, and the dip direction of each fracture is indicated by the compass angle along which the tail of the tadpole points. The size of the tadpole sphere represents the aperture of the fracture. Open spheres indicate a fracture too small to accurately measure apparent aperture. There is a predominance of steeply dipping fractures throughout the logged interval. There is also a significant number shallow dipping fractures. This representation of the data shows larger fractures have steeper dip than smaller fractures and that it is the majority of large macroscopic fracture that comprise the overall ENE trend that dips North-northwest. Although data are compressed in this representation the cyclic repetition of fracturing is again clear.

The large number of near-vertical fractures, and their strong preferred orientations, suggest a common origin for these features. One likely explanation is that the INEL-1 well penetrated a zone of intense fracturing related to the collapse of a caldera within the silicic volcanics. The fact that these fractures are largely filled supports this inference. This is perhaps the first direct evidence for the existence of collapse structures buried beneath the flow basalts mantling the plain. Although the lack of breakouts in the INEL-1 well suggests that the magnitude of horizontal stresses is low, we cannot determine the potential for re-activation of these fractures (or of others penetrated by the INEL-1 well) until we

Figure 13: Lower hemisphere stereographic projection of the orientations of all of the macroscopic fractures detected in well INEL-1.

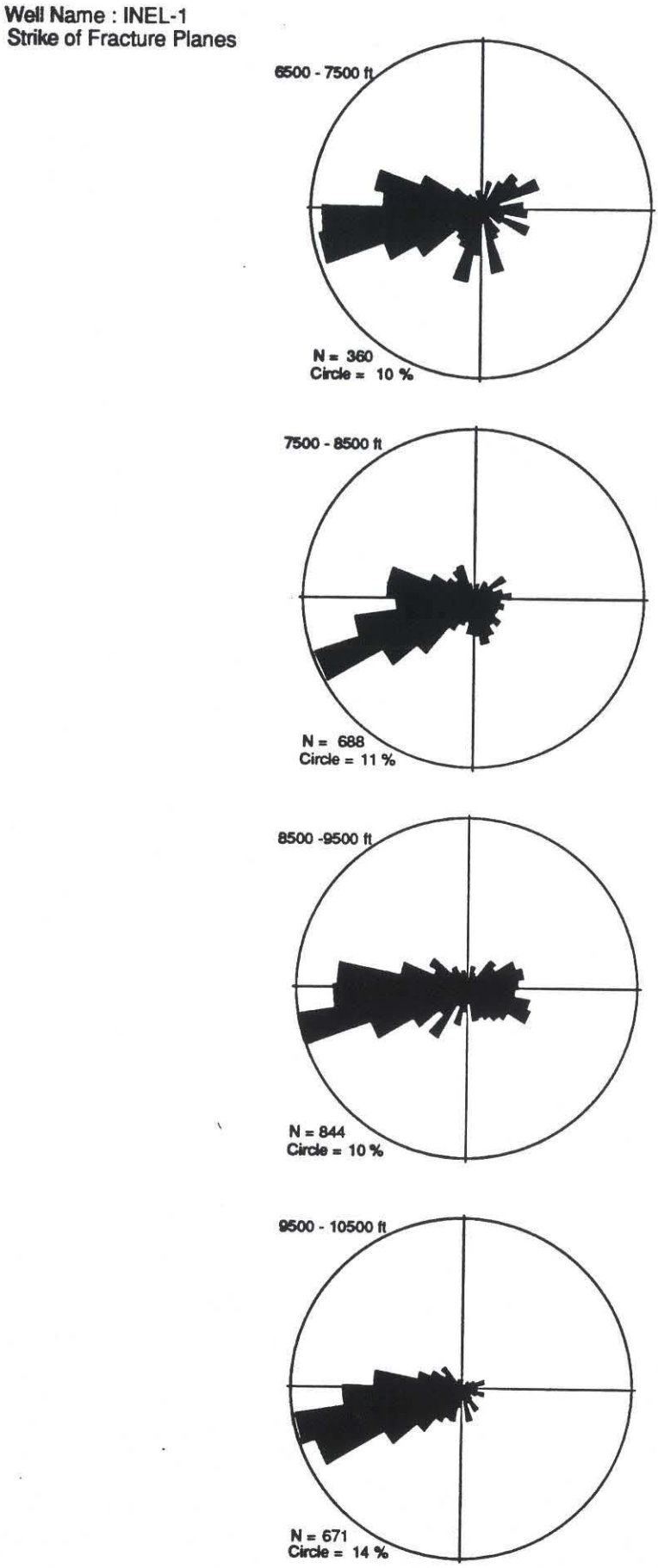

Figure 14: The strike of fracture planes for 500 foot depth intervals within the INEL-1 well.

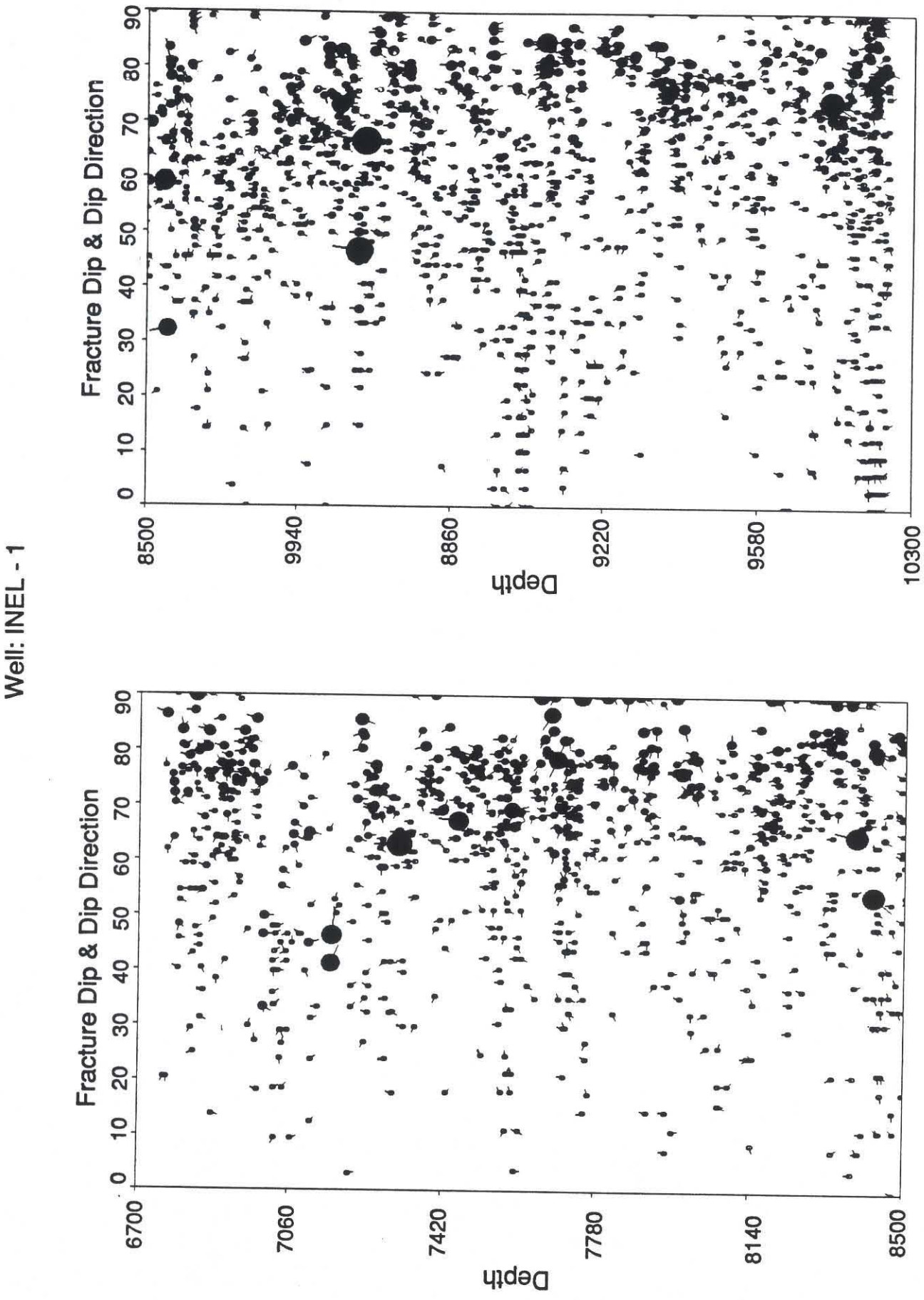

Figure 15: Tadpole plot of fracture orientation with depth for well INEL-1. Fracture dip is plotted along the x-axis, and the dip direction of each fracture is indicated by the compass angle of the tadpole tail.

have direct knowledge of the orientations and magnitudes of the principal horizontal stresses. However, for these fractures to be reactivated as normal faults the least horizontal stress beneath the plain would have to be oriented perpendicular to its axis.

Fractures and Lithology

Figure 12 includes a sketch of the major lithologic units (based on a report by Prestwich and Bowman, et al., 1980) provided at the scale of the fracture density profile. The generalized lithology over the interval of recorded BHTV data in the INEL-1 drillhole consists of an upper unit of welded tuffs with interbeds of reworked tuffaceous sands, non-welded ash-flow tuff, and air-fall ash. Below approximately 9000 ft there is a gradual change to dacite. Although fracture density does not have a strong correlation with lithology at this very generalized scale this does not rule out a possibility of better correlation and lithologic control of fracturing at a smaller scale.

In order to investigate the relationship between fracturing and lithology we subdivided the interval at the logged top of the dacites, picked at 9460 ft (Prestwich and Bowman, et al., 1980), and present the orientations of fractures above and below this boundary in stereographic projection. Figure 16a represents those fractures above the lithologic boundary, and 16b those fractures below this boundary. A population of shallow dipping fractures appears in the data from below 9460 ft (Figure 16b) that is not well developed above that depth (Figure 16a). However, from the tadpole plot of Figure 15 it is clear that these shallow dipping fractures are also found above the dacite, and that the significance of this cluster in the data from below the dacite is a statistical fluke due to the shorter depth interval. High densities of sub-horizontal fractures are found at 8450, 9400 and 10,200 ft.

Physical Properties and Fracturing

Prestwich and Bowman, et al. (1980) present only a brief summary of the geophysical logs recorded in the INEL-1 well over the depth interval of this study. Although we do not have access to the log data itself, it is worth while to compare their description of the log responses to the BHTV data we discuss here. Unfortunately, comparison of geophysical log anomalies with fracturing is often quite difficult, as variations in lithology or vein fill material, foliation, grain size, degree of alteration, or geologic contacts can produce variations in geophysical log measurements that are not related to the presence of fractures but could resemble those that are (Paillet, 1985; 1988).

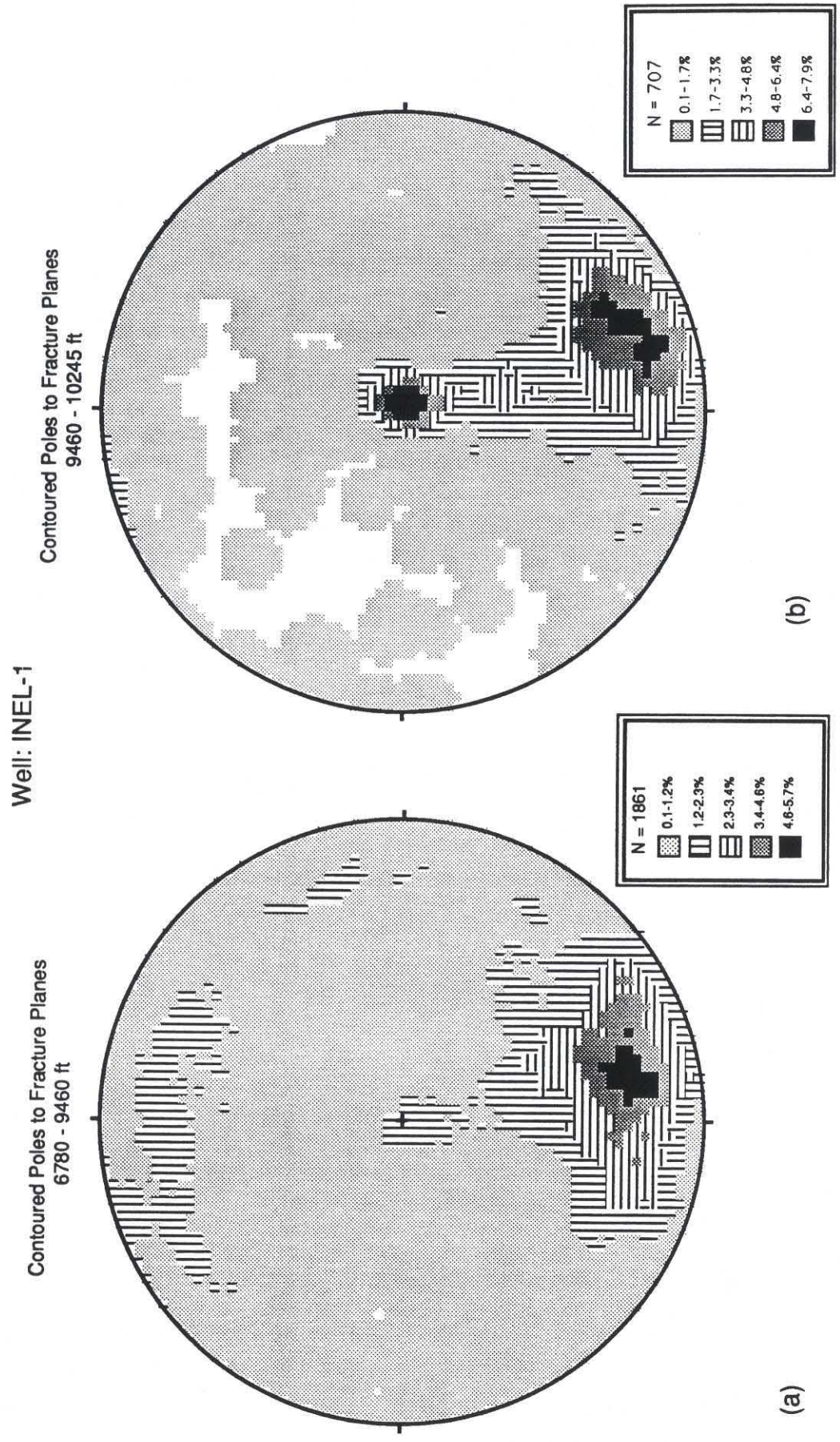

Figure 16: (a) Lower hemisphere stereographic projection of measured fractures above the lithologic boundary at 9460 ft in well INEL-1 and (b) measured fractures below this boundary.

The most valuable logs to augment fracture data are temperature, resistivity, sonic, neutron porosity and natural gamma. The following paragraph briefly summarizes the usefulness of each of these logs to the interpretation of the fracture data.

Both compressional and shear sonic velocities often decrease markedly at fractured horizons, with an accompanied increase in V_p/V_s, which is an expected result of the decrease in stiffness associated with fracturing (Moos and Zoback, 1983). Sonic data is extremely useful in the characterization of fracturing when used in conjunction with borehole image data as it generally provides information about which fractures persist away from the borehole. Gamma values often increase at depths of greater fracture frequency. The comparison of BHTV identified fractures to gamma anomalies is significant in that the BHTV often detects open fractures while the gamma tool is most sensitive to the potassium content of infilling clay minerals and to the presence of uranium which is often concentrated in fractures due to hydrothermal activity. Thus the presence or absence of a gamma increase reveals much about the nature of the infilling material. Neutron porosity logs, which measure the concentration of atomic hydrogen, should not be very sensitive to fractures as the associated porosity increase is small; however, the roughness of the borehole at the intersection of a fracture may cause a porosity anomaly (Paillet, 1988). High porosity values in basalts are probably due to hydration of the basalts around fractures and the associated borehole enlargement and not representative of true fracture porosity. It is not possible to discriminate between neutron porosity anomalies associated with true fracture porosity and those caused by infill or alteration however these logs usually present a good empirical relationship between anomalies and the location of fractures. Electrical logging can usually locate natural fractures in a wellbore because alteration minerals associated with fractures provide exchange cations for the conduction of current even if the adjacent intact rock may be resistive. The association between the electrical response and fracture permeability remains qualitative due to the similarity between the electrical response due to clay alteration around fractures and that due to brine infilled fractures (see Paillet, 1985; Pezard, 1988; Pezard et al., 1990; and references therein). Anomalies detected in temperature logs associated with fractures provide evidence for fluid flow into or out of the well, giving an anomalous change in thermal gradient. Thus temperature logging is perhaps the most reliable survey technique to assess hydrogeologic properties.

Although the log data from INEL-1 have not yet been made available to perform an in depth analysis of the relationship between physical properties measurements and fracturing the following relationship between fracturing and log response was noted.

The interbedded zone of porous and dense rock from 7070 to 7231 ft detected in the geophysical logs (sonic, neutron and resistivity) is a zone of low to moderate fracture frequency but with isolated large aperture fractures. The anomaly at 7110 feet marks a 15 foot wide fracture zone visible in the BHTV image data. This depth correlated exactly with the depth of a recorded temperature anomaly. The BHTV image data at another temperature anomaly near 7285 ft reveals a number of open fractures. Although several large steeply dipping fractures occur at a lower depth (7500 ft) these fractures appear to be at least partially filled. Temperature anomalies between 9600 and 9750 ft are associated with a depth interval where the majority of fractures are in fact open in contrast to the obviously sealed fractures previously discussed.

Changes in the sonic and neutron signature at 8081 ft correspond to a region of low fracture frequency and cumulative aperture. The BHTV data is in general agreement with the geophysical log data which indicate few open fractures for geothermal production. As mentioned previously, there is strong evidence of past hydrothermal flow inferred from the extent to which the fractures are sealed.

Analysis of fracturing in USGS-17, USGS-7, and NONAME-1

Wells USGS-17, USGS-7, and NONAME-1 were all drilled to shallow depths (less than 1000') and encountered basalt flows, rubble, and intercallated sediments. Borehole televiewer data were obtained in these wells primarily to study the fracturing and lithostratigraphy of the basalt section. The results provide an opportunity to study in a localized area changes in the character of individual flow units. The well geometry and the intervals logged in each well are presented in Table I, and the detailed operational procedures are described in the Appendices I and II. The procedures used to analyze these data are identical to those used for the data from INEL-1, with the exception that fracture apertures were not determined.

USGS-7

USGS-7 was drilled to a depth of 940 feet using a 5 1/2" drill-bit (Fig. 4). The hole was logged with the 1 3/4" televiewer over the interval from its present total depth of 895' and the bottom of 6" casing at 760' (driller's depth). The loss of the hole below that depth is most likely due to wellbore collapse within a silt sequence in the interval 885 to 940 feet (Fig. 4). The geologic section interpreted from cuttings and geophysical logs in this hole indicates a thick sequence of undifferentiated basalts within the entire logged interval. The BHTV results, however, present a quite different picture.

The amplitude of the reflected signal and the wellbore radius calculated from the calibrated travel-times are presented as false-color images in Appendix III. Examination of these images reveals a characteristic lithostratigraphy within the logged section. The intervals from 890 to 857 feet and 802 to 773 feet are characterized by chaotic, partially missing reflections, either due to a large number of intersecting fractures or a brecciated or blocky fabric. In the interval 857 to 802 feet, a thick interval of massive basalt is cut by a series of near-vertical fractures. Near the top of this interval, a series of sub-horizontal fractures occur with spacings of a few feet. The interval above 773 feet seems to repeat this sequence, but the top of the interval, where the sub-horizontal fractures presumably occurred, is now behind casing.

The orientations of fractures intersecting the wellbore were picked interactively from the image data. In this exercise we attempted to extract fracture planes from the chaotic images presented in the intervals 890 to 857 and 802 to 773 feet. Figures 17 to 19 display the results. In Figure 17 fracture frequency is plotted as a function of depth. Concentrations of fractures occur in the chaotic zones (the intervals 890 to 857 and 802 to 773 feet). It is not at all clear that these are fractures, but by treating them as such we can gain a more quantitative idea of the degree of "brecciation". Figure 18 shows a tadpole plot of fracture orientations as a function of depth. With the exception of the chaotic zones, the majority of the fractures are steeply dipping (more than 60 degrees), and most of the fractures in the massive interval 857 to 815 feet dip more than 80 degrees.

Plots of fracture orientations (Figure 19) reveal three clusters of fractures, striking NS, about N30°E, and S50°E. These all dip more than 60°, and in the case of the N30°E set are nearly vertical. Furthermore, these fractures are concentrated in the centers of the massive basalts. This, combined with the fact that the strike directions of these sets are approximately 120° apart, suggests that these are columnar joints formed by cooling of the thick basalt flows.

In this context, the origins of the other characteristic layers in the image can be inferred to be due to processes occurring during emplacement and cooling. The chaotic zones may correspond to the rubbly base of the flows, while the discrete sub-horizontal fractures are typical of fractures found below flow tops. The same characteristic patterns can also be found in NONAME-1.

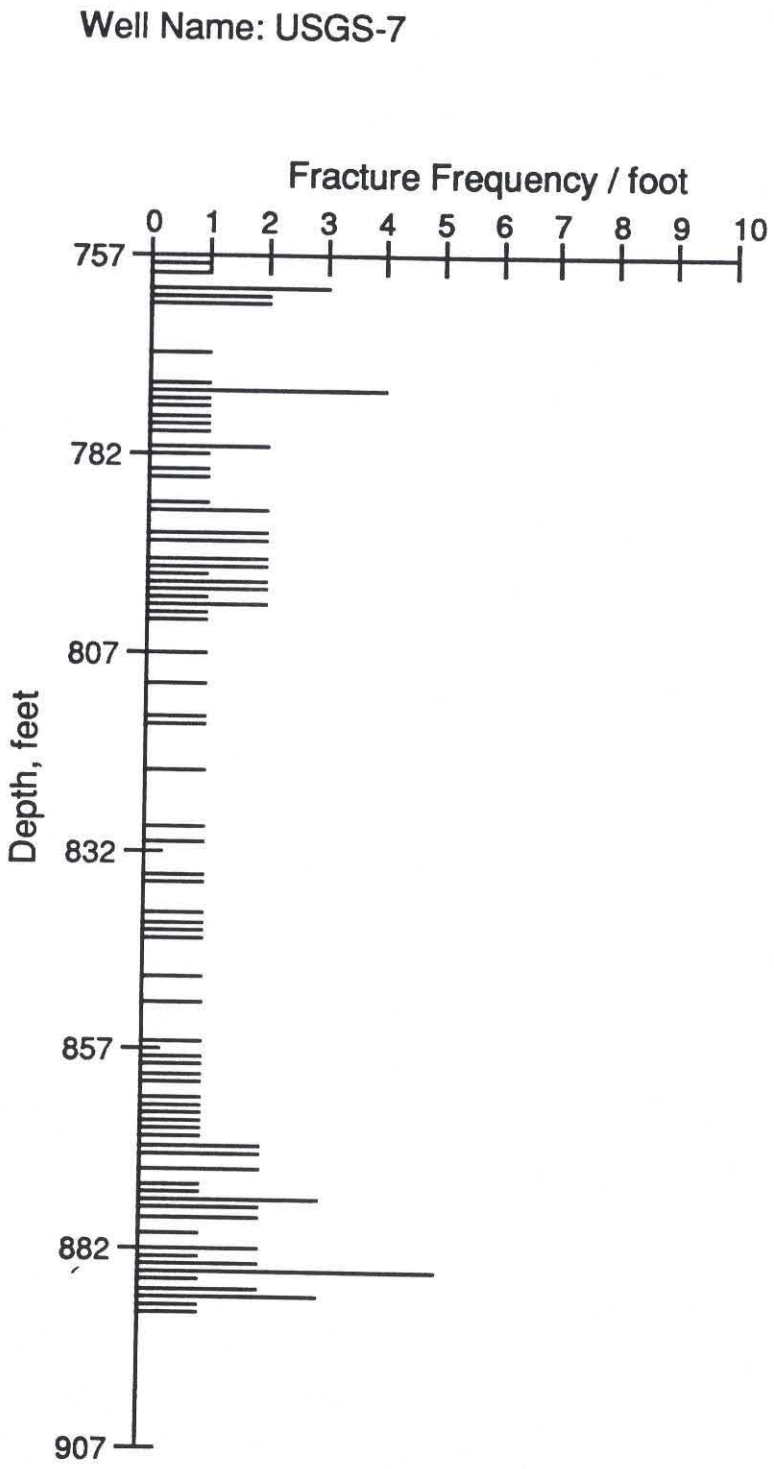

Figure 17: Fracture frequency plotted as a function of depth for well USGS-7.

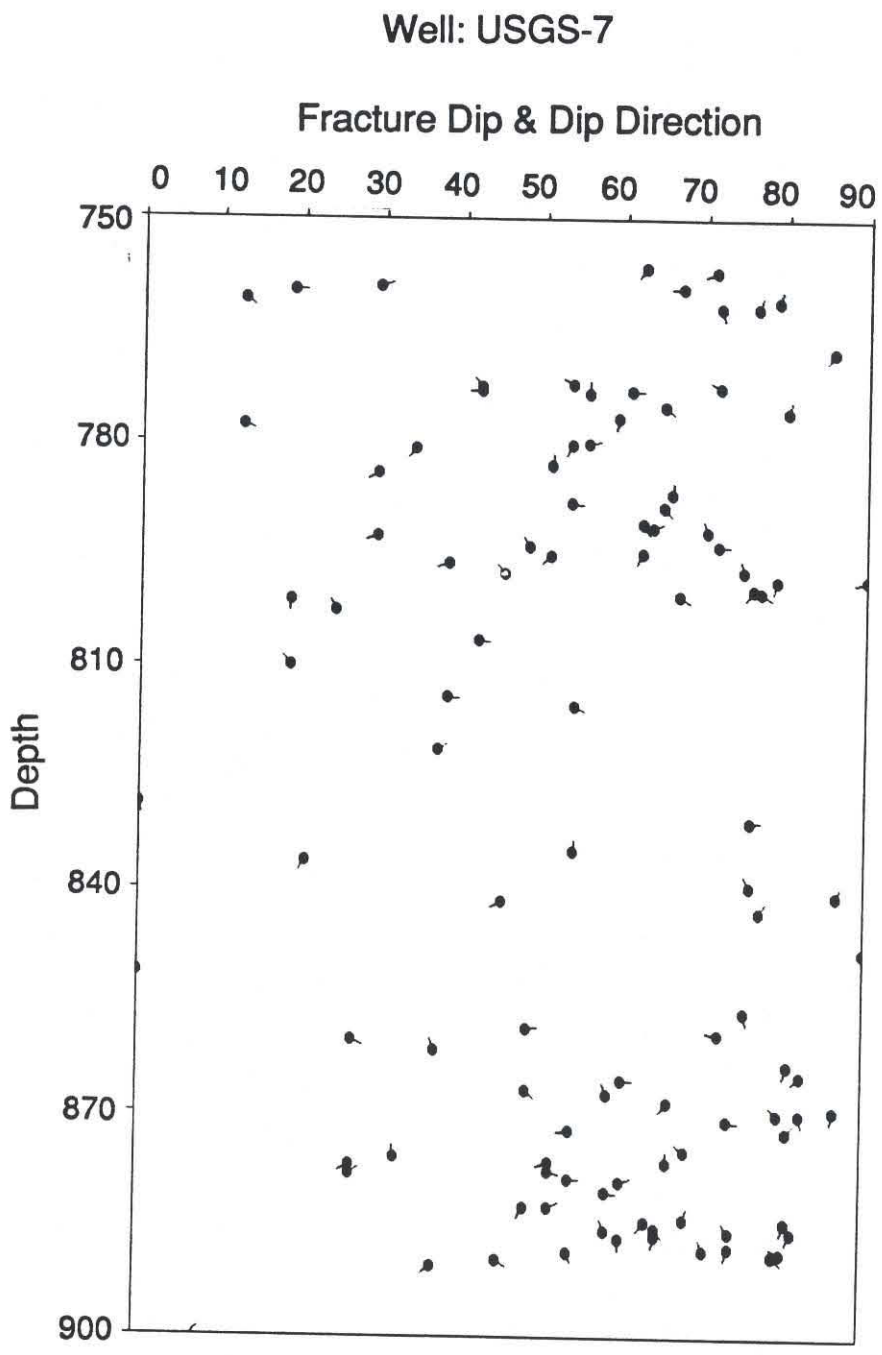

Figure 18: Tadpole plot of fracture orientation with depth for well USGS-7. Fracture dip is plotted along the x-axis, and the dip direction of each fracture is indicated by the compass angle of the tadpole tail. Tadpole plot of fracture orientations as a function of depth.

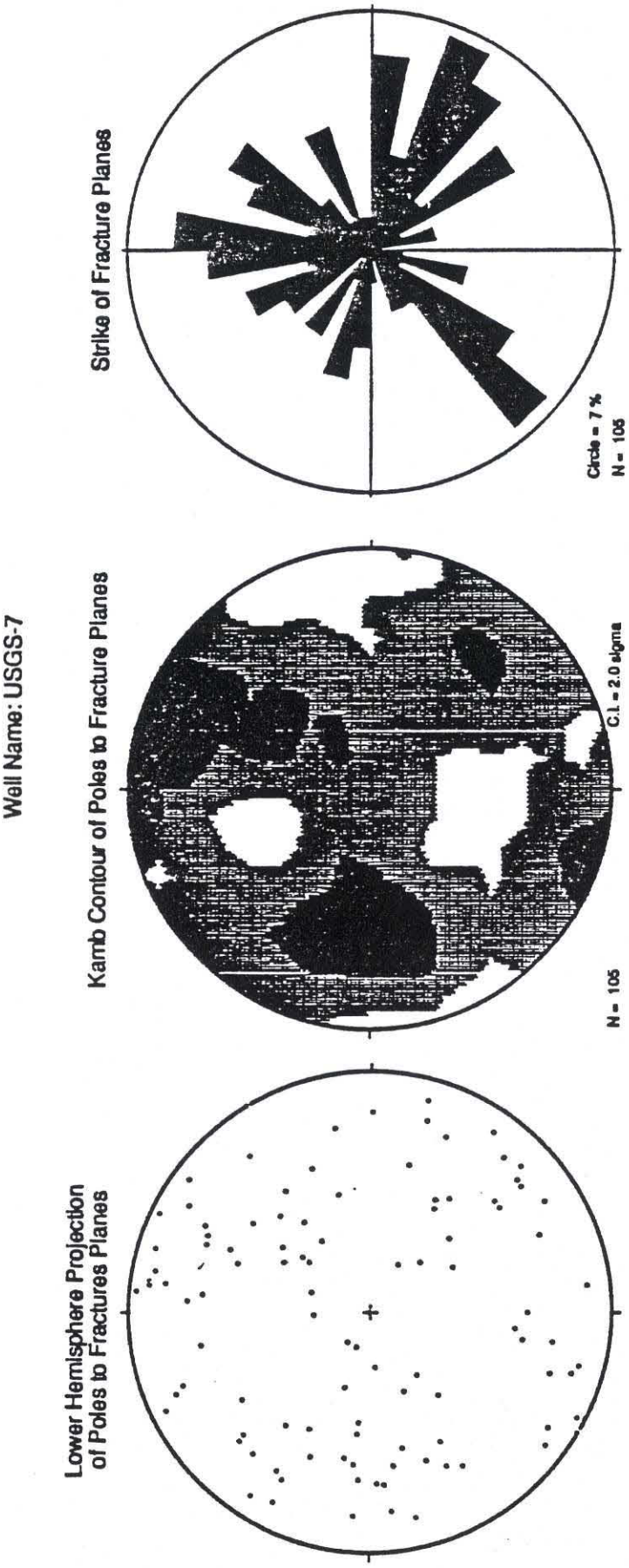

Figure 19: Lower hemisphere stereographic projections of poles to fracture planes, contoured poles to planes and strike of all fractures measured in well USGS-7.

NONAME-1

The NONAME-1 well was drilled using a 12" bit to a total depth of approximately 550 feet. The well geology interpreted from the driller's log is displayed in Figure 5. The interval is comprised primarily of basalts, with broken basalts, red cinders, and/or clay in the intervals 272-300', 380-385', 415-425', and 495-490' (depths approximate). Again, analyses of the BHTV data allowed these intervals to be related to structural features of the basalts.

The interval from 549' to 265' was logged in this well, again with the 1 3/4" (slim-hole) televiewer. The results in NONAME-1 are the best of those recorded in the basalts. Appendix III includes false-color images of the reflected amplitude and wellbore radius determined from the digitized data. In these images the intervals 549-543', 522-518', 494-492', 437-440', 424-428', 381-378', 317-325', and 287-291' contain subhorizontal fractures or enlarged sections of hole. Some of these correspond to the intervals of broken basalts, red cinders, or clay noted in the driller's logs. Some of these were not noted, however. Massive basalts with only a few near-vertical fractures are found in the intervals between these zones.

The positions and orientations of fractures picked interactively from the image data are presented in Figures 20 to 22. Figure 20, which shows fracture frequency plotted as a function of depth, reveals that fractures are not evenly distributed in this well, as inspection of the images suggests. The zones of densest fracturing have generally shallowly dipping fractures (less than 40°, Fig 21). However, some of these (for example, the interval 317-325') also contain fractures which dip more steeply (50 to 70 degrees).

In contrast to the results at USGS-7, the preponderance of fractures detected in NONAME-1 are sub-horizontal. These fractures contribute to a cluster with an approximate N50°W strike and dip between 10° and 30° NE (Figure 22). The rose diagram reveals two secondary maxima, one striking about 20°N of East and the other about 30°S of East. These have intermediate dips (between 40° and 70°).

However, as in the case of USGS-7, several vertical fractures were detected. These subtend chords in the well, rather than diameters (for example, at 490') and have a variety of strikes. Although most of these strike roughly E-W, two strike NS, and three strike approximately S30°E. Furthermore, as is the case at USGS-7, these fractures are found near the centers of otherwise massive intervals. Thus, although these do not reveal the strong pattern suggestive of columnar joints found in the data from USGS-7, we prefer this explanation of their origin in this well also.

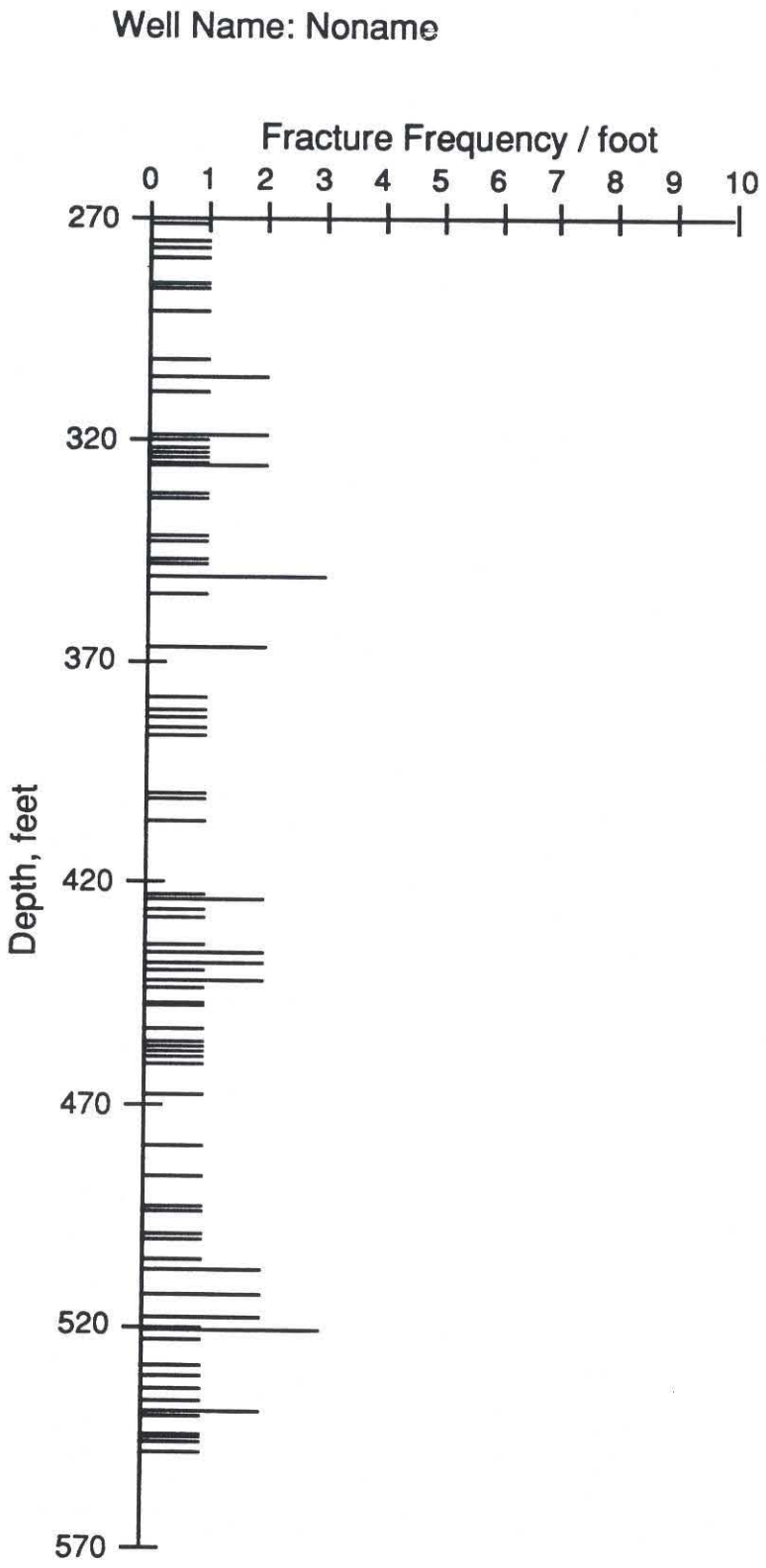

Figure 20: Fracture frequency plotted as a function of depth for well NONAME-1.

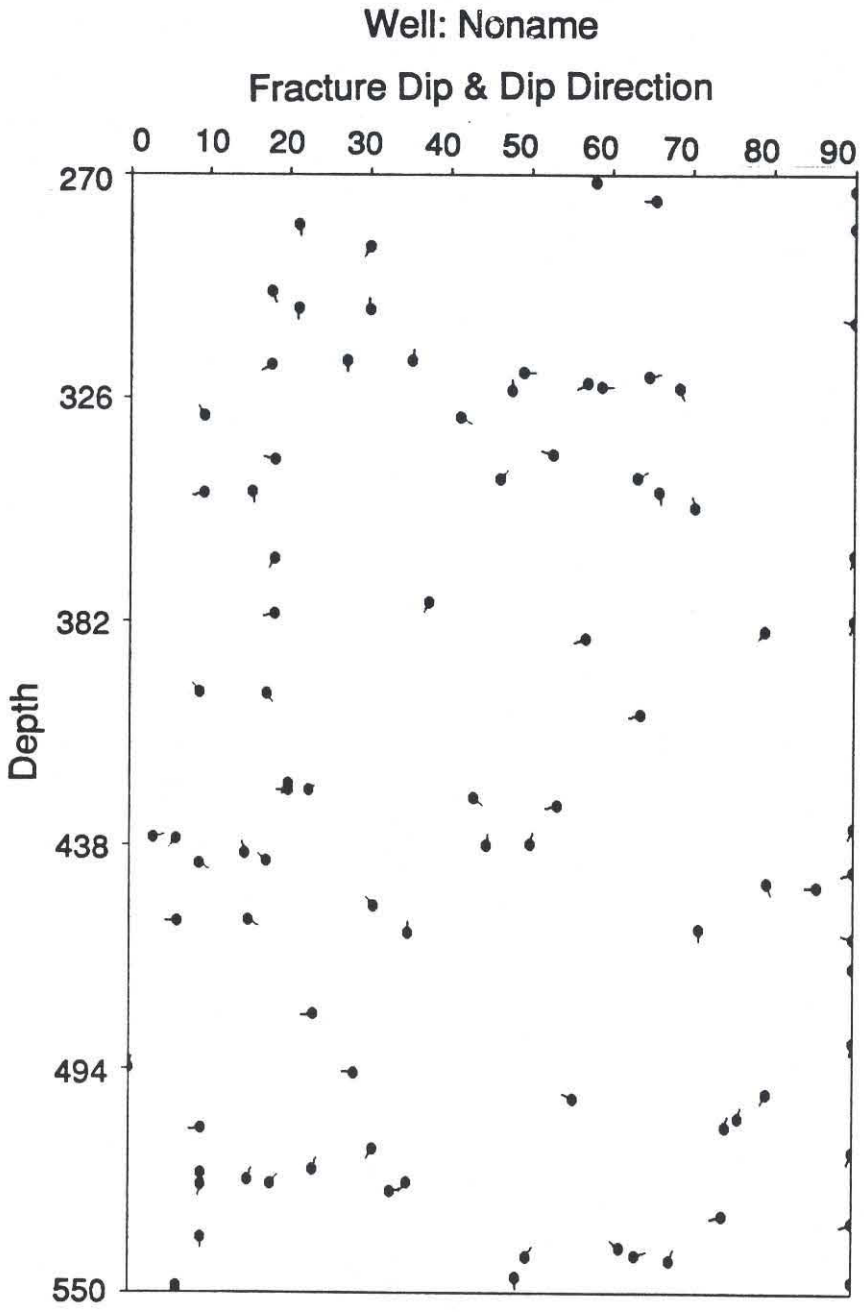

Figure 21: Tadpole plot of fracture orientation with depth for well NONAME-1. Fracture dip is plotted along the x-axis, and the dip direction of each fracture is indicated by the compass angle of the tadpole tail.Tadpole plot of fracture orientations as a function of depth.

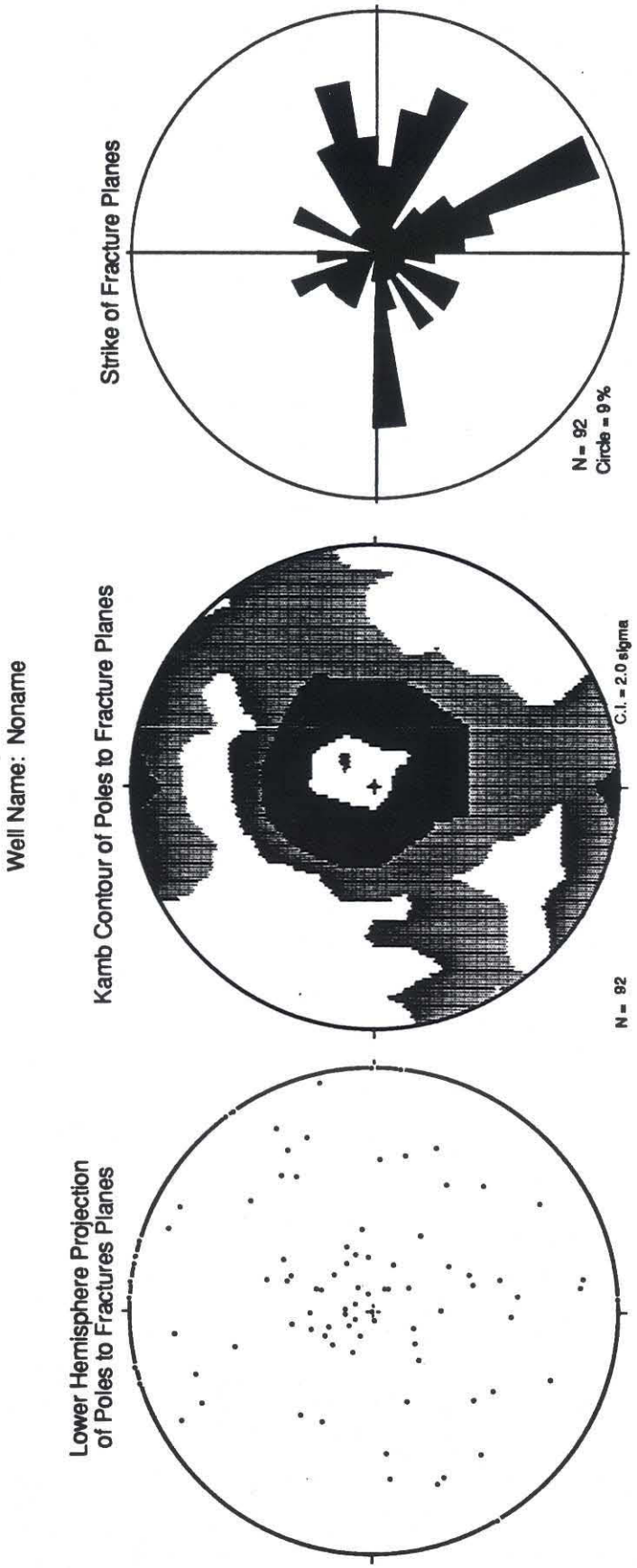

Figure 22: Lower hemisphere stereographic projections of poles to fracture planes, contoured poles to planes and strike of all fractures measured in well NONAME-1.

USGS-17

The USGS-17 well was drilled using an 18" bit to a total depth of 600 feet (Figure 6). No data is available for this well regarding the lithostratigraphy of the penetrated section. However, based on the results from the other wells, the interval penetrated presumably consists of interlayered basalt flows and more chaotic or brecciated intervals.

USGS-17 was logged with the 1 3/4" (slim-hole) televiewer over the interval between its present depth of 567 feet and the static water table at 390 feet. The data were digitized and are displayed as false-color images of wellbore radius and reflected amplitude in Appendix III. Because of the large diameter of the wellbore, the televiewer sonde could not be adequately centered in the hole. This resulted in incomplete azimuthal coverage of the hole, as can be seen in the false-color images (see Georgi, 1985 for a description of the effects of eccentering on BHTV images). Consequently, fractures are more difficult to detect in these data than in data from the other three wells. However, the orientations of those fractures that could be detected were picked interactively (as described above for INEL-1) and the results are presented in Figures 23 through 25.

Figure 23 presents a plot of detected fracture frequency versus depth in USGS-17. In general, fractures are detectable only intermittently across the 275' depth interval logged. Most of the fractures dip steeply to the South, (more than 80°) and strike essentially E-W, as can be seen in the tadpole plot (Figure 24) and the stereonets and rose diagrams (Figure 25). This apparent strong preferred orientation may result from the fact that the fractures are most easily imaged in their up- and down-dip directions, and that the data returned from this well is primarily in a band of azimuths centered roughly on North and South. Thus any steeply dipping fractures with dip azimuths more than 20 degrees from a N-S line are less likely to be detected. A small subsidiary maximum strikes approximately S50°E and dips about 40°SW.

The remaining few fractures are sub-horizontal. Most of these occur within the interval 470 to 480 feet, although single shallow-dipping features are also detected at about 400' and near the total depth of 565' (Figure 24); the bottom of the logged interval is characterized by a broad subhorizontal band of missing data (Appendix III). If these sub-horizontal features are interpreted as fracturing near flow tops (in the case of the feature detected at 400') and/or as inter-flow materials (in the case of the intervals 470-480 and 565-567'), as analysis of the much better data from USGS-7 and NONAME-1 implies, then it suggests that the interval 565 to 480 feet may be a complete section of a single basalt flow, and the top of the logged interval may be near the top of the overlying flow. The fact that the logging sonde could not penetrate to total depth in the well may be a consequence of hole collapse within the weaker materials at the base of the lower flow.

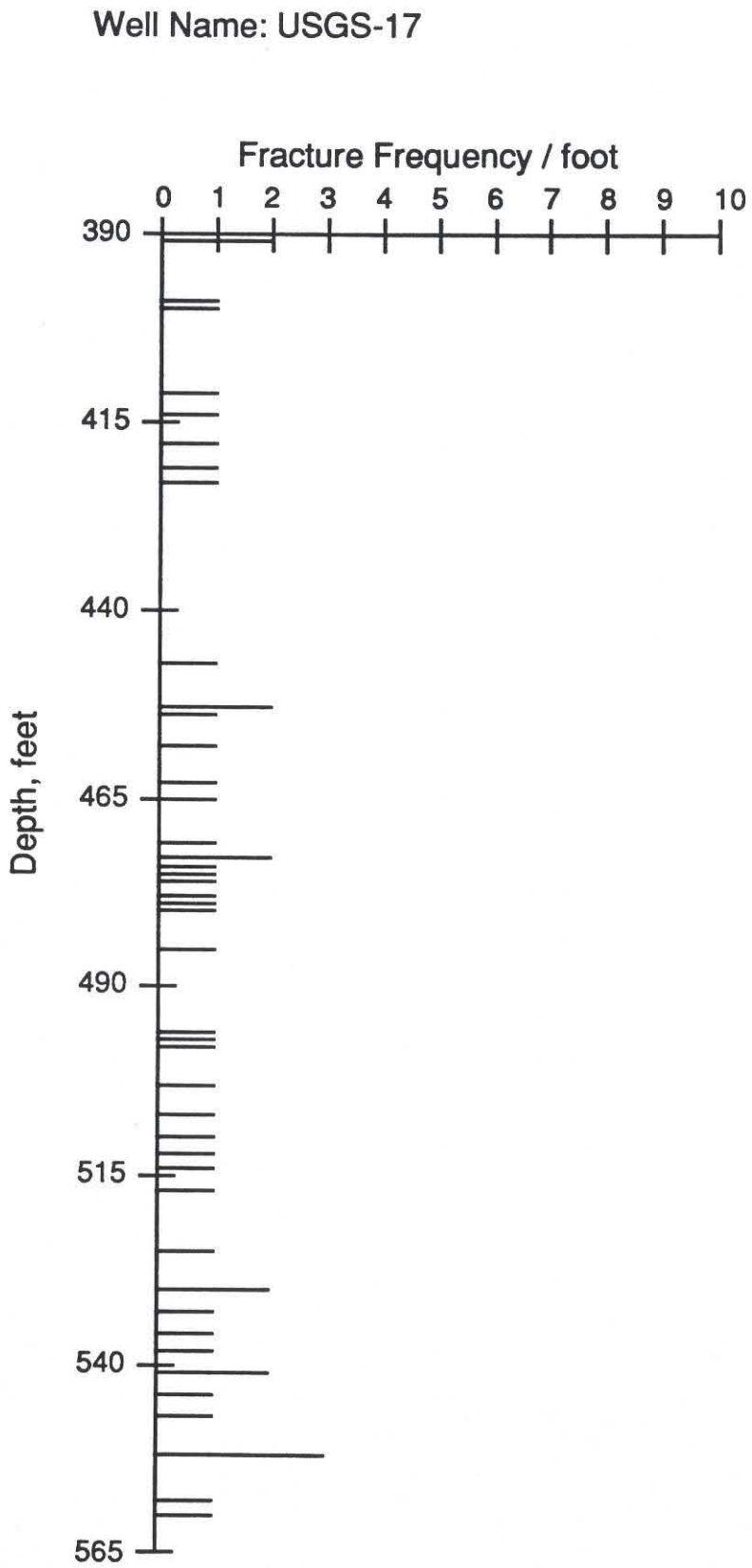

Figure 23: Fracture frequency plotted as a function of depth for well USGS-17.

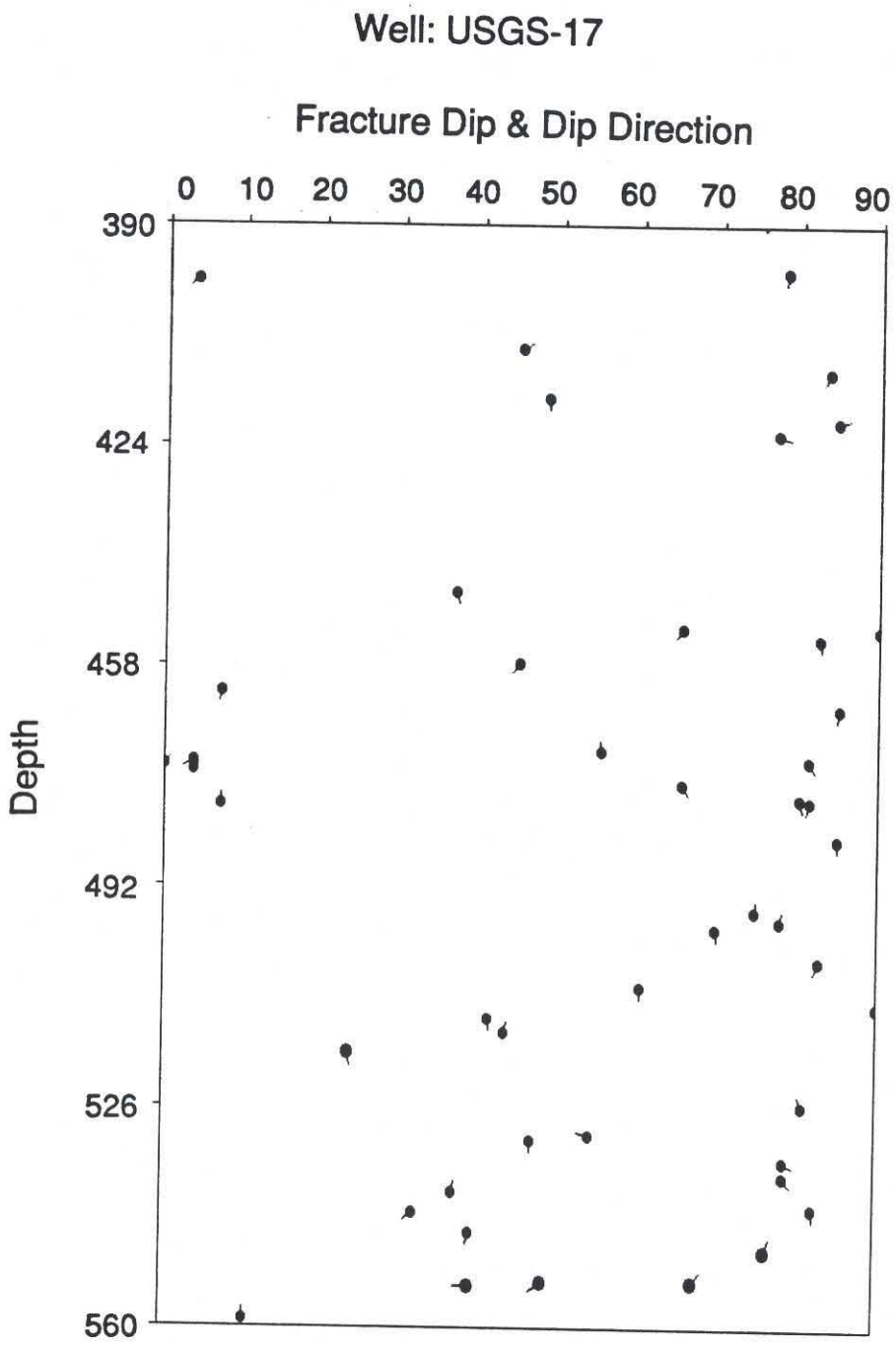

Figure 24: Tadpole plot of fracture orientation with depth for well USGS-17. Fracture dip is plotted along the x-axis, and the dip direction of each fracture is indicated by the compass angle of the tadpole tail.Tadpole plot of fracture orientations as a function of depth.

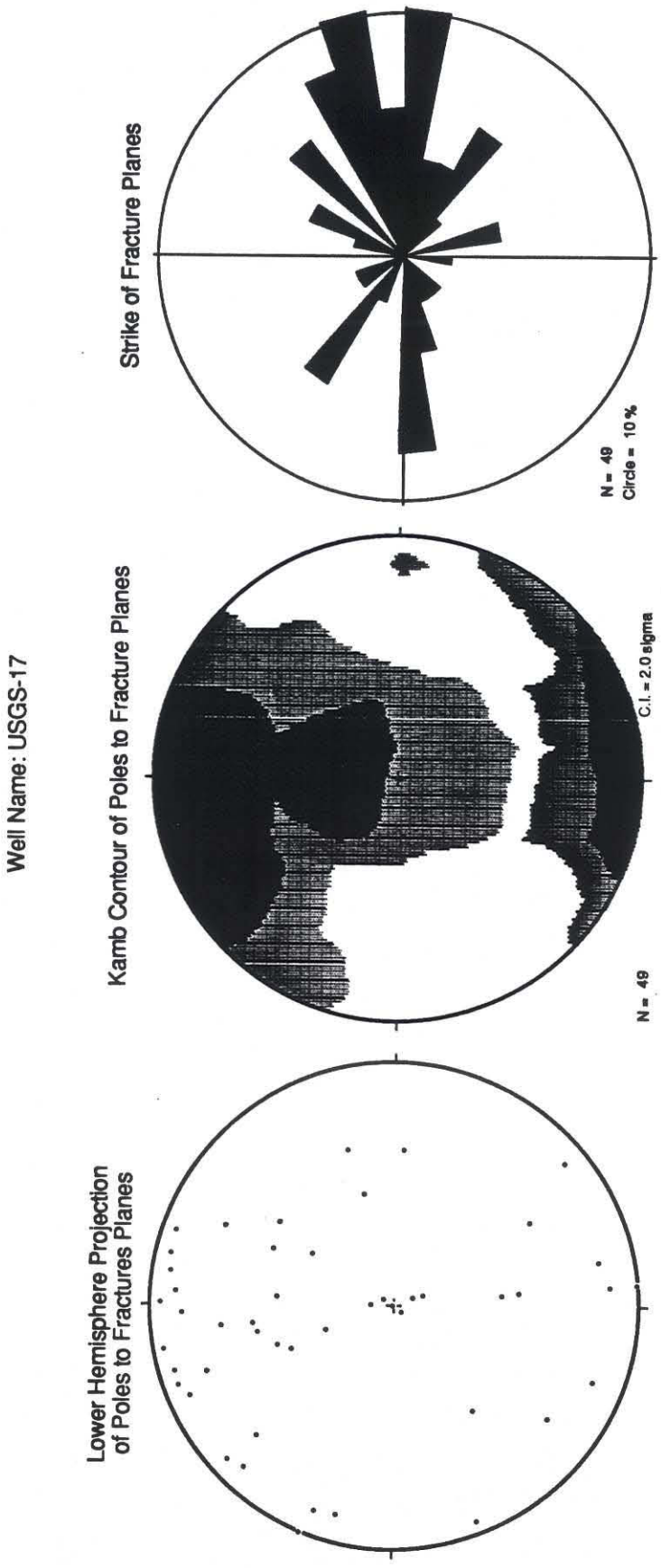

Figure 25: Lower hemisphere stereographic projections of poles to fracture planes, contoured poles to planes and strike of all fractures measured in well USGS-17.

The approximately 85' thickness of the intervals between sub-horizontal features may correspond to a characteristic thickness for the flow units. The steeper fractures detected at intervals throughout the well would then be, as in the other wells, columnar joints within the massive flow interiors.

Summary of results for the basalts

No wellbore breakouts were detected in wells USGS-17, USGS-7, and NONAME-1. This can be ascribed to the shallow depths of these wells, and the fact that they were drilled through basalts, which are quite strong and thus unlikely to fail in compression at the shallow depths studied.

The logs in the three holes drilled into basalts reveal a characteristic pattern of fracturing, related to emplacement and cooling of the basalts. This pattern was also noted by Paillet and Kim (1987) for televiewer data recorded in basalts on the Columbia River Plateau. At the base of each flow is a narrow zone of rubbly material, which grades into a massive interior cut by near-vertical fractures, possibly columnar joints. Near the top is a narrow zone a few meters thick of shallow dipping fractures. Based on this pattern in two of the wells the average flow thickness is slightly less than 100 m. Although this overall pattern is apparent in each of the wells studied, differences between the wells will need to be studied in more detail before possible inter-well interpretations can be made.

Recommendations for Related Studies

The results borehole televiewer logging in INEL-1, USGS-7, USGS-17, and NONAME-1 provide a detailed look at the lithostratigraphy and fracturing within the basalts and underlying silicic volcanics beneath the Eastern Snake River Plane. However, the primary purpose of obtaining BHTV data, to determine the orientations and constrain the magnitudes of the crustal stresses, requires the collection of some additional data and more complete analysis of the data already in hand.

Systematic comparison of these results to geophysical well logs (particularly temperature, resistivity, sonic waveform, and natural gamma) could reveal additional valuable information about the fractures, filling, permeability, and lithostratigraphy of the silicic volcanics. Furthermore, such analysis is required to determine the appropriate equations to use to describe the wellbore stress concentration and related failure.

Strength measurements on cores from the INEL-1 well are necessary to apply the techniques of Moos and Zoback (1990) to the determination of stress magnitudes from the

lack of breakouts. Although the absence of breakouts in INEL-1 to 3.1 km requires that both horizontal stresses be less than the vertical stress, it does not distinguish between an incipient normal faulting environment (ie $S_h << S_v$) and a more nearly hydrostatic one (ie $S_h \approx S_v$). It is therefore necessary to obtain a more detailed knowledge of the range of uniaxial compressive strengths appropriate for the rocks penetrated by the INEL-1 well, coupled with careful analysis of the logs to infer the Biot α.

Finally, to determine quantitatively the magnitudes of the horizontal stresses, there is no substitute for hydraulic fracturing stress measurements. The BHTV data acquired as part of the work described herein can be used to select unfractured intervals for testing. In this (normal-faulting) environment it should be relatively easy to hydrofrac the rock to total depth. Furthermore, standard analyses (e.g. Hickman and Zoback, 1983) should suffice to provide determinations of S_{hmin}, as this stress is the least principal stress. The temperature at total depth in INEL-1 of $\approx 150^{o}C$ should not be a factor, as hydraulic fracturing stress measurements have been made at similar temperatures elsewhere (for example, in the Cajon Pass Scientific Drillhole, Healy and Zoback, 1988).

References Cited

Allison, M.L. and D.L. Nielson, Stress in active geothermal systems, in *Advances in Geothermal Reservoir Technology,* Lawrence Berkeley Lab - ESL-88027-JP, 1988.

Anders, M.H., J.W. Geissman, L.A. Piety, and J.T. Sullivan, Parabolic distribution of circumeastern Snake River Plain seismicity and latest Quaternary faulting: Migratory pattern and association with the Yellowstone hotspot, *J. Geophys. Res., 94*, 1589-1621, 1989.

Barton, C.A., *Development of in-situ stress measurement techniques for deep drillholes*, PhD. Thesis, Stanford University, 192 pp, 1988.

Bell, J. S. and D.I. Gough, Northeast-southwest compressive stress in Alberta: Evidence from oil wells, *Earth Planet. Sci. Lett.*, 45, 475-482, 1979.

Furlong, K.P., An analytic stress model applied to the Snake River Plain (Northern Basin and Range Province, USA), *Tectonophysics, 58*, T11-15, 1979.

Georgi, D.T., Geometrical aspects of borehole televiewer images, *Trans. 26th Ann. SPWLA Logging Symposium*, 1-C, 1985.

Healy, J.H. and M.D. Zoback, Hydraulic fracturing in situ stress measurements to 2.1 km depth at Cajon Pass, California, *Geophys. Res. Lett., 15(9)*, 1005-1008, 1988.

Hickman, S.H., and M.D. Zoback, The interpretation of hydraulic fracturing pressure-time data for in situ stress determination, in *Proceedings of the Workshop on Hydraulic Fracturing Stress Measurements*, U.S. National Committee on Rock Mechanics, Washington, D.C., 11 pp., 1983.

Hubbert, M.K., and D.G. Willis, Mechanics of hydraulic fracturing, *J. Petrol. Tech., 9*, 153-168, 1957.

Kirsch, G., Die Theorie der Elastizitat und die Bedurfnisse der Festigkeitslehre, VDI Z, 42, 707, 1898.

Moos, D., and M.D. Zoback; In situ studies of velocity in fractured crystalline rocks; *J. Geophys. Res., 88*; p. 2345-2358, 1983.

Moos, D., M.D. Zoback, F. Paillet, and C. Barton, Stress orientation and magnitude from wellbore breakouts in the Moodus Research Borehole -- comparison with regional data, (abs), *EOS, Trans. AGU (69)*, p. 492, 1988.

Moos, D., and M.D. Zoback, Utilization of observations of wellbore failure to constrain the orientation and magnitude of crustal stresses: Application to continental, DSDP and ODP borehole, *J. Geophys. Res., 95*, 9305-9325, 1990.

Morgan, J.W., Deep mantle convection plume and plate motions, *Am. Assoc. Pet. Geol. Bull., 56*, 203-312, 1972.

Morin, R.H., R.L. Newmark, C.A. Barton, and R.N. Anderson, State of lithospheric stress and borehole stability at DSDP Site 504B, eastern equatorial Pacific, *J. Geophys, Res., 95*, 9293-9303, 1990.

Paillet, F.L., Problems in fractured-reservoir evaluation and possible routes to their solution, *The Log Analyst, 26*, 6, 26-41, 1985.

Paillet, F.L., and K. Kim, Character and distribution of borehole breakouts and their relationship to in situ stresses in deep Columbia River basalts, *J. Geophys. Res., 92*, 6223-6234, 1987.

Paillet, F. L., Fracture characterization and fracture-permeability estimation at the underground research laboratory on southwestern Manitoba, Canada, U.S.G.S., *Water Resources Investigations Report, 88-4009*, 1988.

Pezard, P.A., R.N. Anderson, J.J. Howard, and S.M. Luthi, Electrical properties of mid ocean ridge basalt and implications for the structure of the upper oceanic crust in Hole 504B, *J. Geophys. Res., 95, B6*, 9237 - 9264, 1990.

Pezard, P.A., Fracture distribution and basement structure from measurements of electrical resistivity in the basement of the Cajon Pass scientific drillhole, California, *Geophys. Res. Lett., 15*, 9, 1021 - 1024, 1988.

Plumb, R.A., and S.A. Hickman, Stress-induced wellbore elongation: A comparison between the four-arm dipmeter and the borehole televiewer in the Auburn Geothermal Well, *J. Geophys. Res., 90*, 5513-5521, 1985.

Plumb, R. A. and J.W. Cox, Stress directions in eastern North America determined to 4.5 km from borehole elongation measurements, *J. Geophys. Res., 92*, 4805-4816, 1987.

Prestwich, S.M., and Bowman, J.A., et al., Completion and testing report: INEL geothermal exploratory well one (INEL-1), U.S. Dep't. of Energy, Report #IDO-10096, 1980.

Sparlin, M.A., L.W. Braile, and R.B. Smith, Crustal structure of the eastern Snake River Plain from ray tracve modeling of seismic refraction data, *J. Geophys. Res., 87*, 2619-2633, 1982.

Stock, J.M., J.H. Healy, S.H. Hickman, and M.D. Zoback, Hydraulic fracturing stress measurements at Yucca Mountain, Nevada, and the relationship to the regional stress field, *J. Geophys. Res., 90*, 8691-8706, 1985.

Thompson, G.A., Parsons, T., and Smith, R.B., Examples of magma overpressure suppressing normal faulting and inhibiting seismicity: Snake River Plain, Idaho,

Yucca Mountain, Nevada, and Mono Craters, California, (abs) *EOS, Trans. AGU*, in press.

Vernik, L. and M.D. Zoback, Estimation of maximum horizontal principal stress magnitude from stress-induced wellbore breakouts in the Cajon Pass Scientific Research Borehole, submitted to *J. Geophys. Res.*

Zemanek, J., E.E. Glenn, Jr., J.J. Norton, and R.L. Caldwell, Formation evaluation by inspection with the borehole televiewer, *Geophys. 35*, 254-269, 1970.

Zoback, M.D., D. Moos, L. Mastin and R.N. Anderson, Wellbore breakouts and in situ stress, *J. Geophys. Res.*, 90, 5523-5530, 1985.

Zoback, M. L., M.D. Zoback, J. Adams, M. Assumpção, S. Bell, E.A. Bergman, P. Blümling, N.R. Brereton, D. Denham, J. Ding, K. Fuchs, N. Gay, S. Gregersen, H.K. Gupta, A. Gvishiani, K. Jacob, R. Klein, P. Knoll, M. Magee, J.L. Mercier, B.C. Müller, C. Paquin, J. Rajendran, O. Stephansson, G. Suarez, M. Suter, A. Udias, Z.H. Xu, and M. Zhizhin, Global patterns of intraplate stress: A status report on the world stress map project of the International Lithosphere Program, *Nature*, 341, 291-298, 1989.

Appendix I - Field Chronology

Operations at the INEL were carried out in two separate phases. The first phase occupied the period between May 14 and May 21. During that time span holes USGS-17, USGS-7 and NONAME-1 were logged with the 1 3/4" televiewer tool, and the lowermost portion of INEL-1 (from 10243 to 9250 feet) was logged with the 3 3/8" geothermal tool. Operations terminated after repeated attempts to log INEL-1 with both the 1 3/4" tool and the 3 3/8" geothermal tool failed to recover a complete log of the hole. The second phase of operations commenced June 3 with the arrival on-site of an engineer from M&W Instruments (the manufacturer of the televiewers) to effect repairs on the 3 3/8" geothermal tool, and ended June 8 with the successful recovery of a complete log of INEL-1.

Tables A-1-I and A-1-II are chronologies of field operations at the INEL site for phases one and two, respectively. Table A-1-III summarizes the data collected in each of the holes during the course of operations. All of this data was digitized for analysis. As described elsewhere in this report, the final log from INEL-1 was a composite of the phase one and two logs. Otherwise, each data set was recorded in a single pass. Furthermore, with the exception of the data from NONAME-1 and INEL-1, both pre- and post-logging calibrations were obtained.

Appendix II presents the color renderings of the calibrations used to correct the data for magnetic declination and for the offset between apparent magnetic North determined by the tool and its true azimuth. Appendix III presents the final color figures showing borehole radius and reflected amplitude as a function of depth and azimuth in USGS-17, USGS-7, NONAME-1 and INEL-1. These displays have been corrected for declination and for the offset between apparent magnetic North determined by the tool and its true azimuth. The field data sheets and the post-logging digitization data sheets are included in Appendix VI.

TABLE A-1-I: INEL Phase I operations – May 14 to May 21

May 14 - truck and personnel arrive Idaho Falls (1900 hrs)
May 15 - arrive INEL plant, obtain badges, BHTV log of USGS-17
logging truck and boom truck on site at USGS 17 1040 hrs
Rig up
Attempt operation with geothermal BHTV 1200 - 1500 hrs
Record pre-log calibration
Log USGS 17 with small BHTV 1500 - 1750 hrs
Record post-log calibration
May 16 - BHTV logs of USGS-7 and NONAME-1
move to USGS 7 site and rig up 0930 - 1230 hrs
Record pre-log calibration
log USGS 7 with 1 3/4" BHTV 1230 - 1430 hrs
(while on site at USGS 7 review quality assurance)
Record post-log calibration
rig down; move to Noname 1; rig up 1430 - 1645 hrs
Record pre-log calibration
log Noname 1 with 1 3/4" BHTV 1645 - 1800 hrs
Post-log calibration failed
move equipment to INEL 1 1800 - 1900 hrs
May 17 - set up on INEL 1 - attempt log with 1 3/4" BHTV
run pig into well - hung up at top of liner 1015 - 1100 hrs
rehead cable 1130 - 1600 hrs
RIH with small BHTV: Compass failed while running in hole;
we ran to TD to test operations at high temperature
and successfully logged 300 feet at 10'/minute,
but without compass orientations . 1735 - 2200 hrs
Problems with the tool were traced to a flooded cable head.
May 18 - repair and testing of equipment 0900 - 1715 hrs
rehead cable
inspect and repair minor connector damage in the 3 3/8" geothermal tool
confirm tool operations.
May 19 - Log lower portion of INEL-1 with 3 3/8" geothermal tool
RIH with geothermal tool - tool sticking just below casing 1230 hrs
POOH
move upper centralizers to relaxed position 1640 hrs
RIH to TD. @ TD 1910 hrs
Log 10,234 to 9,250' - At 9400' we encountered problems with the tool
Tried adding a DC power supply without success
left tool in casing at 6000' 0100 hrs, May 20
May 20 - Attempt to continue logging INEL-1
added DC power supply borrowed from the EG&G shop
RIH to 9300' - tool failed in same mode 1245 hrs ->
POOH w/ geothermal tool 1315 hrs
RIH with small BHTV 1450 ->
tool failed in compass mode just below liner (as before)
Pulled small tool out of the hole 1640 hrs
May 21 - Shut down operations: return crane, move truck to staging area, fly home

TABLE A-1-II: INEL Phase II Operations – June 3 to June 8

June 3 - Stanford crew arrives Idaho Falls 1800 hrs
June 4 - refuel truck, technician arrives from M&W Instruments
work on 3 3/8" geothermal tool at EG&G office 0730 - 1800 hrs
June 5 - complete tool repair
return to INEL site and prepare for logging 0730 - 2130 hrs
June 6 - successful pre-log calibration.
record log of INEL-1 0630 ->
June 7 - log continues - attempted post-log calibration failed 0500 hrs
rigged down
returned to EG&G to work on tool again 1100 - 1800 hrs
June 8 - return to Stanford

TABLE A-1-III: Data recovered in each well:

Well Name	Date	Depth Interval, ft	Logging Tool	Comments
USGS-17	May 15	567-390	1 3/4"	pre- and post-log cal
USGS-7	May 16	895-850	1 3/4"	pre-log cal &
USGS-7	May 16	895-750	1 3/4"	post-log cal (higher gain settings - tool never left the hole)
NONAME-1	May 16	550-265	1 3/4"	pre-log cal only
INEL-1	May 17	10133-9800	1 3/4"	no orientations
INEL-1	May 19	10243-9250	3 1/8"	pre-log cal only tool failed at 9250' - log orientations identical to USGS log
INEL-1	May 20	none	1 3/4"	compass orientation failed, ending attempt
INEL-1	June 6-7	10243-6780	3 1/8"	pre-log cal only complete log - but orientations invalid below 9946'

Appendix II - Tool Calibration

As part of standard field procedures with the borehole televiewer, a calibration of the compass orientation and of the conversion of travel-time to radius is made both prior to and after completion of a logging operation. In the case of operations at INEL, pre- and post-log calibrations were obtained at USGS-7 and USGS-17. A pre-log calibration only was obtained at NONAME-1. A pre-log calibration only was obtained for both Phase I and Phase II logging runs in INEL-1. The lack of a post-log calibration for INEL-1 and NONAME-1 is not deemed to be critical, as in each instance in which pre- and post-log calibrations were obtained, the calibrations agree to within a few degrees and a fraction of an inch radius.

The details and figures illustrating the results of these calibrations are discussed in this section.

In the case of USGS-7, USGS-17, and NONAME-1, the logs we obtained are the only data available with which the orientations of features within the boreholes can be determined. Thus there is no independent data to compare to our results. Consequently, the tool calibrations are necessary to validate the orientations we obtained. In the case of the INEL-1 well, a previous borehole televiewer log was recorded by the U.S. Geological Survey. Thus we can compare our orientations to those obtained independently by the USGS. As it turns out, this exercise is critical in selecting the data to analyze in the INEL-1 well, as described in more detail below.

Field Calibrations

This section describes the compass and radius calibrations we obtained in the field for each of the logging runs at the Idaho National Engineering Laboratory. These calibrations are designed to verify tool operation and are run as standard operating procedures both before and after logging in each hole. In general, orientations and radius corrections do not change over the course of a field survey. Copies of the checklists completed in the field for each logging run are provided in Appendix VI, Quality Assurance Documentation.

Instrument calibrations are obtained by placing the televiewer tool in an aluminum tank with 1/2"-thick walls, of interior diameter 6.5". Four aluminum bars are placed at 90° intervals around the tank, and an interior sleeve of 1/2"-thick aluminum is placed in one half of the tank. The entire tank is placed as far away as possible from sources of magnetic fields, and oriented wrt magnetic North. The tank is typically buried to prevent its tipping over, and the tool is placed into a hole in its center. The top of the tool is also centered, by means of an aluminum ring. A schematic drawing of the orientation device is shown below.

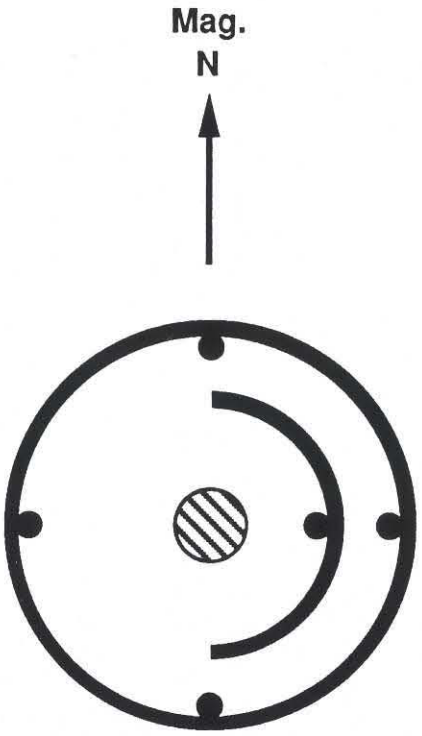

Fig A-II-1: Schematic drawing of the calibration tank used to verify the operation of the magnetic orientation device of the borehole televiewer.

Once the tool is in the orientation tank power is applied and the tool is allowed to warm up for a short time. The pre-log orientation calibration is obtained by recording the signal for approximately one minute. The procedure for calibrating the 1 3/4" tool is as follows: First the tool is placed in magnetic orientation mode, and a short section of data is recorded on videotape and on film. To assist in rapid interpretation of the photographic image the signal is first gated to display only reflections from the insert (early times) and then to display both the reflections from the outer and inner section, and finally to display only sections from the outer wall. The tool is then switched to "mark" mode and then back to "compass" mode, to verify that both modes are working. This procedure had to be modified for the large tool due to its use of focussed transducers, which do not produce a clear image for radii smaller than the focussing point, by inserting into the tank an absorbing rod at a known orientation.

After completion of the pre-log calibration, the tool is removed from the tank and run into the hole, with power applied to the tool the entire time. While running into the hole gain settings are adjusted to obtain an optimal image, and thus a post-calibration log is required. This log also allows us to assess possible drift due to changes in temperature of the tool electronics. The post-log calibration procedure is identical to the pre-log procedure. To assure the best assessment of the tool operation, power is applied to the tool from the start of the pre-log calibration to the end of the post-log calibration.

USGS-17

A successful log was obtained in USGS-17 using the 1 3/4" (slimhole) borehole televiewer. Pre and post log calibrations were obtained and are presented along with the field data sheets in Appendix VI. As can be seen from the images, the orientation correction did not change during the course of the log, and the azimuth correction determined from the post-log calibration was applied to the data prior to display and analysis. Figure A-II-2) shows a color rendering of the corrected (azimuthally and for radius conversion) calibration image. On this figure and in the final data a further correction for the magnetic declination at the site was also made.

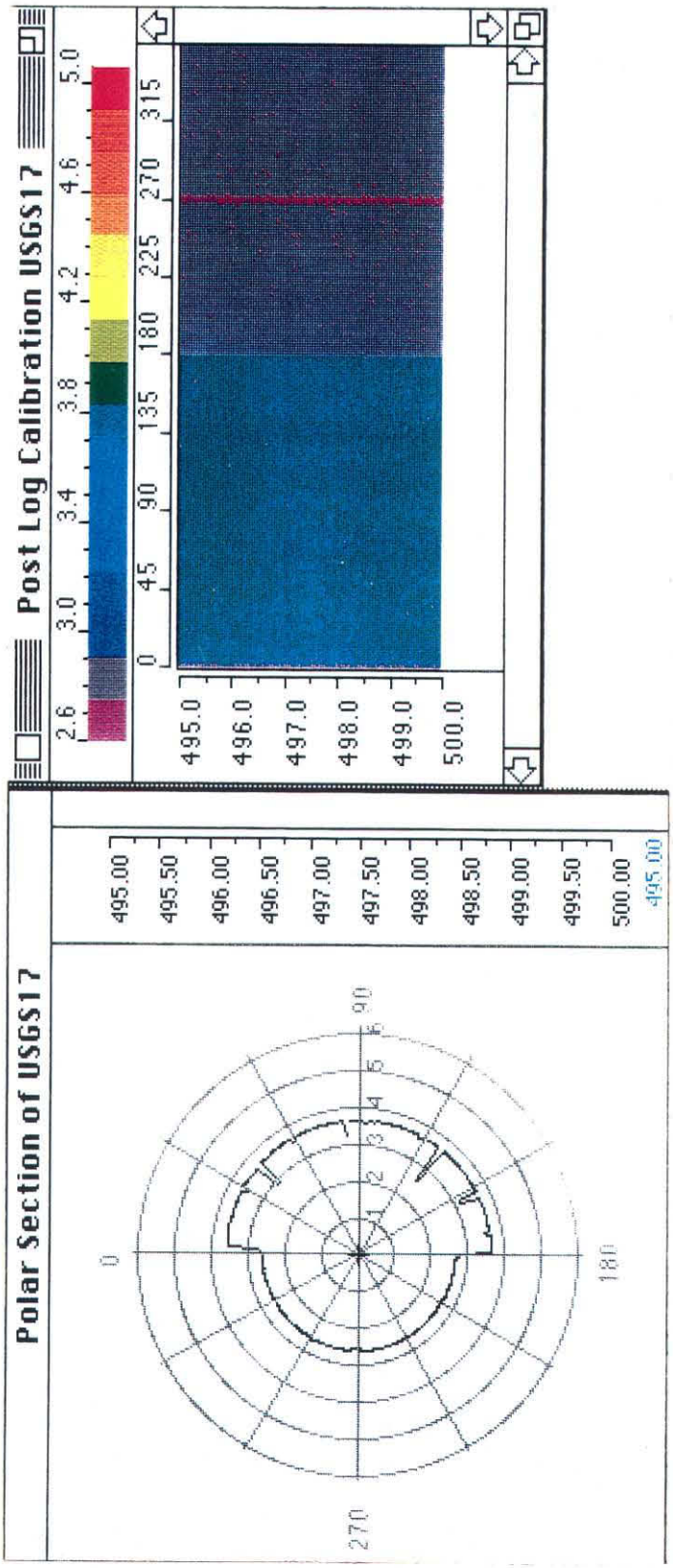

Figure: A-II-2: Polar projection (left window) and unwrapped view of the post log calibration recorded for well USGS-17.

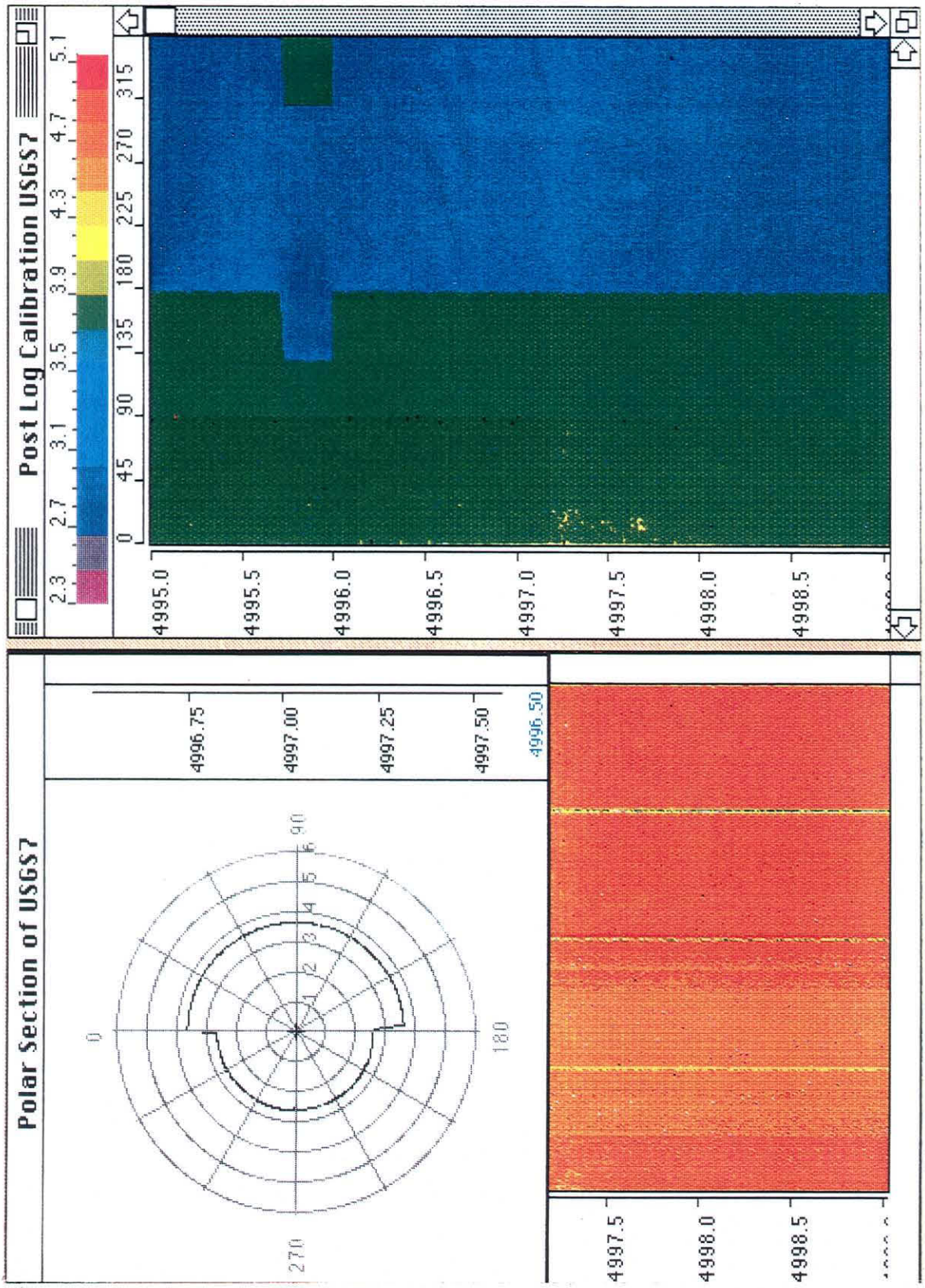

Figure A-II-3: Polar projection (left window) and unwrapped view of the post log calibration recorded for well USGS-7.

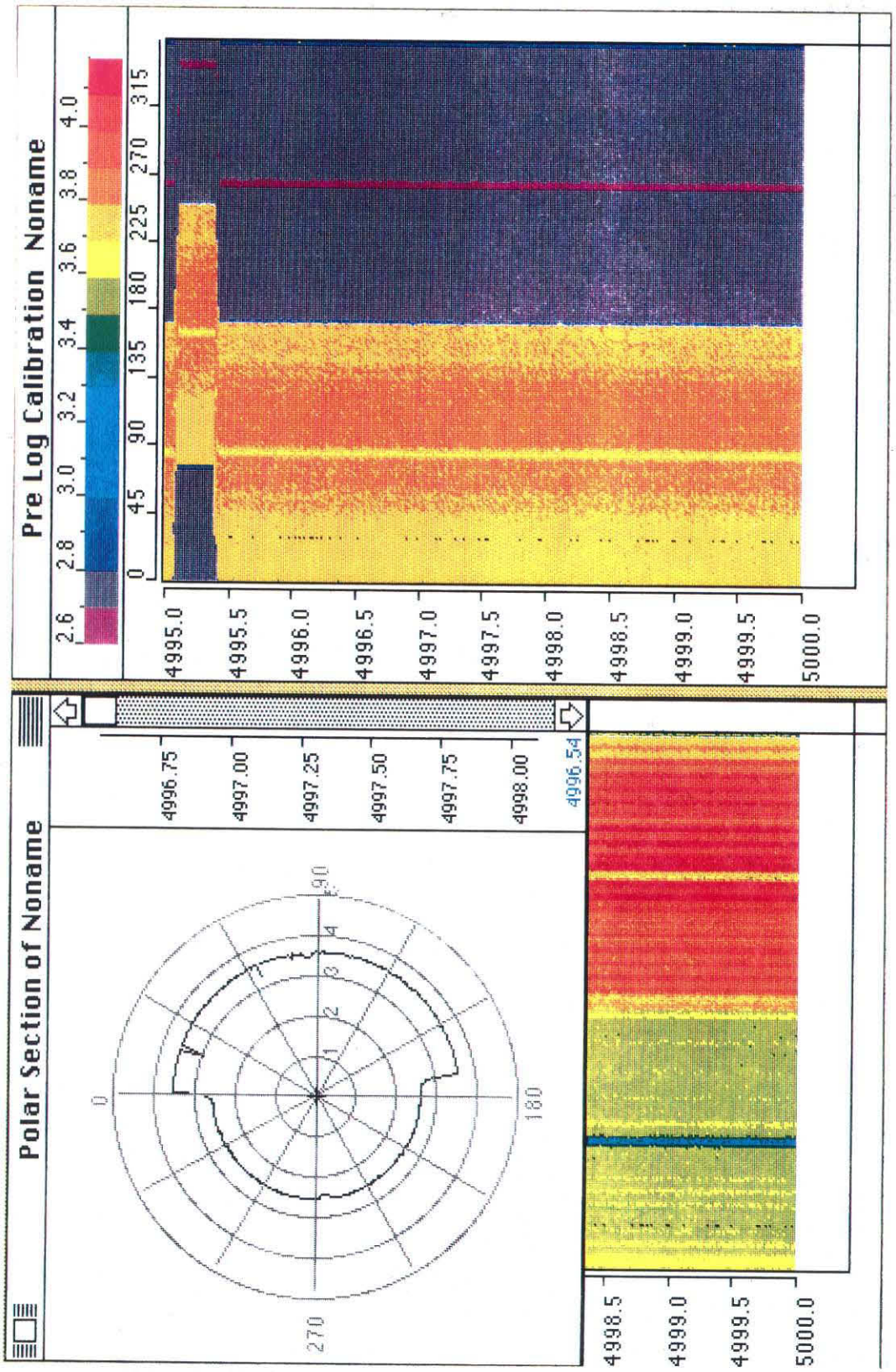

Figure A-II-4: Polar projection (left window) and unwrapped view of the post log calibration recorded for well NONAME-1.

USGS-7

A successful log was obtained in USGS-7 using the 1 3/4" (slimhole) borehole televiewer. Pre and post log calibrations were obtained and are presented along with the field data sheets in Appendix VI. As can be seen from the images, the orientation correction did not change during the course of the log, and the azimuth correction determined from the post-log calibration was applied to the data prior to display and analysis. Figure A-II-3 shows a color rendering of the corrected (azimuthally and for radius conversion) calibration image. On this figure and on the final data a further correction for the magnetic declination at the site was also made.

NONAME-1

A successful log was obtained in NONAME-1 using the 1 3/4" (slimhole) borehole televiewer. No post log calibration was obtained in this well, however, due to the failure of the compass after completion of the log. The symptom of that failure was the complete loss of an orienting signal, rather than its progressive deterioration. Thus we are confident that the log was obtained with the correct compass orientation. Furthermore, the lack of drift for the pre- and post- log calibrations at the previous two wells suggests that no drift is associated with the azimuth data obtained here. The pre-log calibration is presented along with the field data sheets in Appendix VI. The azimuth correction determined from this pre-log calibration was applied to the data prior to display and analysis. Figure A-II-4 shows a color rendering of the corrected (azimuthally and for radius conversion) calibration image. On this figure and on the final data a further correction for the magnetic declination at the site was also made.

Orientation Verification - INEL-1

The 3 3/8" geothermal tool was used to obtain the borehole televiewer data at INEL-1. Calibrations for this tool were difficult to obtain, and in fact no post-log calibrations were obtained for either the Phase I or Phase II logs of the hole. Fortunately, a previously recorded log (by the U.S. Geological Survey) provided images of the hole which overlapped a substantial portion of the open-hole interval. Checks of the orientations of these images vs. the new logs provided an additional test of the orientation data, as described below.

Pass I: 10243 - 9250 feet.

The pre-log calibration of the near-focus transducer (the one used to record the data) is presented in Appendix VI along with the field data sheets. In this calibration an absorbing rod was attached to the tool at magnetic East, and the window was gated on the far reflection from the East side of the tank. The insert was placed on the West side of the tank for this test. The edge of the inner sleeve was located by the tool at $\approx 180^{o}$, and the rod was located $\approx 90^{o}$, indicating that no orientation correction was necessary for this tool, except to correct for the magnetic declination at the site. Attempts to digitize the calibration for analysis interactively were unsuccessful. Thus the radius calibration was made within the 9 7/8" o.d. liner, which is presumed based on a wall thickness of 1/4" to have an i.d. of 9 3/8". The velocity of sound in the fluid was assumed to be 1494 m/s..

Pass II: 10243 - 6780 feet.

Pre-log calibration of the orientation was made for the phase two log in INEL-1 in the aluminum tank with a phenolic rod placed at magnetic West. The gain was varied as described in the figure (Appendix VI). Magnetic West was determined to be aligned correctly for the tool, and thus no static correction was applied to the data, except to correct for magnetic declination at the site. Attempts to digitize the calibration for analysis interactively were unsuccessful. Thus the radius calibration was made within the 9 7/8" o.d. liner, which is presumed based on a wall thickness of 1/4" to have an i.d. of 9 3/8". The velocity of sound in the fluid was assumed to be 1494 m/s.

Comparison of Phase I, Phase II, and USGS logs of INEL-1:

Because of the lack of post-log calibrations for the data recorded at INEL-1, we compared the orientations of data recorded in the well during three different logging runs (the earlier USGS log, and our Phase I and Phase II logs). If all three logs agreed then we

could assume that the pre-log calibration suggesting that there was no error in compass orientation was reliable. If only two of the three logs agreed then we could assume that the third log was in error, and attempt to trace the source of that error. The results of this comparison indicated that three orientations agree to within measurement error within the interval 9946 to 9250 feet, but the Phase II log orientations differed from the other two logs in the interval below 9946 feet. Accompanying this difference are abrupt changes in orientation over short intervals in the Phase II log, that were revealed in the travel-time images from that data set. We studied the voice-over comments recorded during the Phase II log and traced a problem in that log to a level of DC power delivered to the tool that may have been too low to operate the magnetic orienting device. The DC level was increased at a depth of 9946 feet, the point above which the logs agreed.

In the course of this analysis we discovered that our depth reference at ground level resulted in a systematic 20' discrepancy between the depths in the USGS log and those in our two surveys. The USGS depths were uniformly deeper than those we recorded for the identical intervals. This is most likely due to the reference depth of the USGS log at a rig floor 20' above the ground level. All depths we report in this document are those we recorded.

The results for the tie points we selected are tabulated in Table A-II-1. At some of those depths we also provide figures, as noted in the table.

Table A-II-1: Tie points for orientation checks in INEL-1*:

Description	Phase I		Phase II	USGS	
	depth	azimuth	azimuth	depth	azimuth
	7130	-	190	7150	185-190
	7572	-	314	7592	330
	7995	-	129	8015	130
	8949	-	128	8973	128
(see Figure A-II-5)	9513	130	122	no data	
	9520	340	340	no data	
fracture					
(see Figure A-II-6)	9714	110-130	110-130	9738	110-124
	9730	90	90	9752	94
(see Figure A-II-7)	9942	130	130	no data	
	9949	120	257	no data	
	9955	180	296	no data	
(see Figure A-II-8)	9975	302	118	no data	
hourglass					
(see Figure A-II-9)	10032	148	342	10053	148

*all azimuths w.r.t. magnetic North

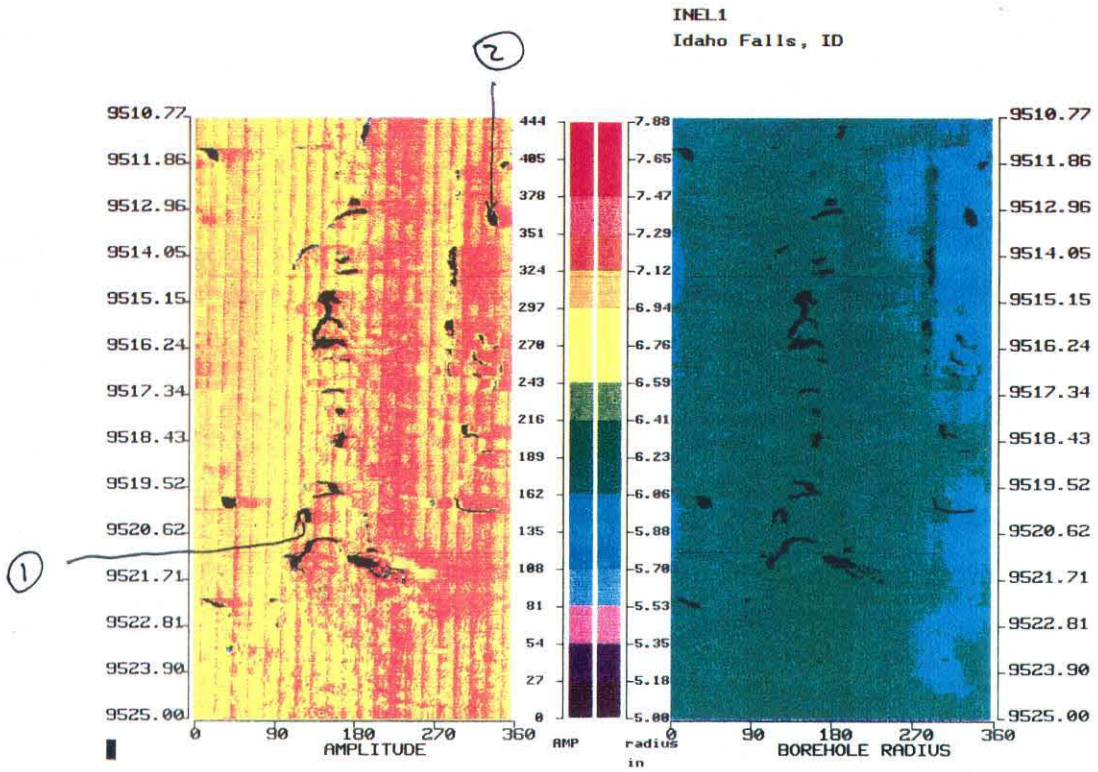

AZIMUTH CALIBRATION

① @ 9520'

azimuth phase 2 122°

azimuth phase 1 ~~285°~~ 130°

② @ 9513'

azimuth phase 2 340°

azimuth phase 1 340°

Figure A-II-5: Comparisons of the phase one and phase two azimuths of features observed in the INEL-1 well at depths of 9513 and 9520 feet. No data is available at this depth from the USGS log.

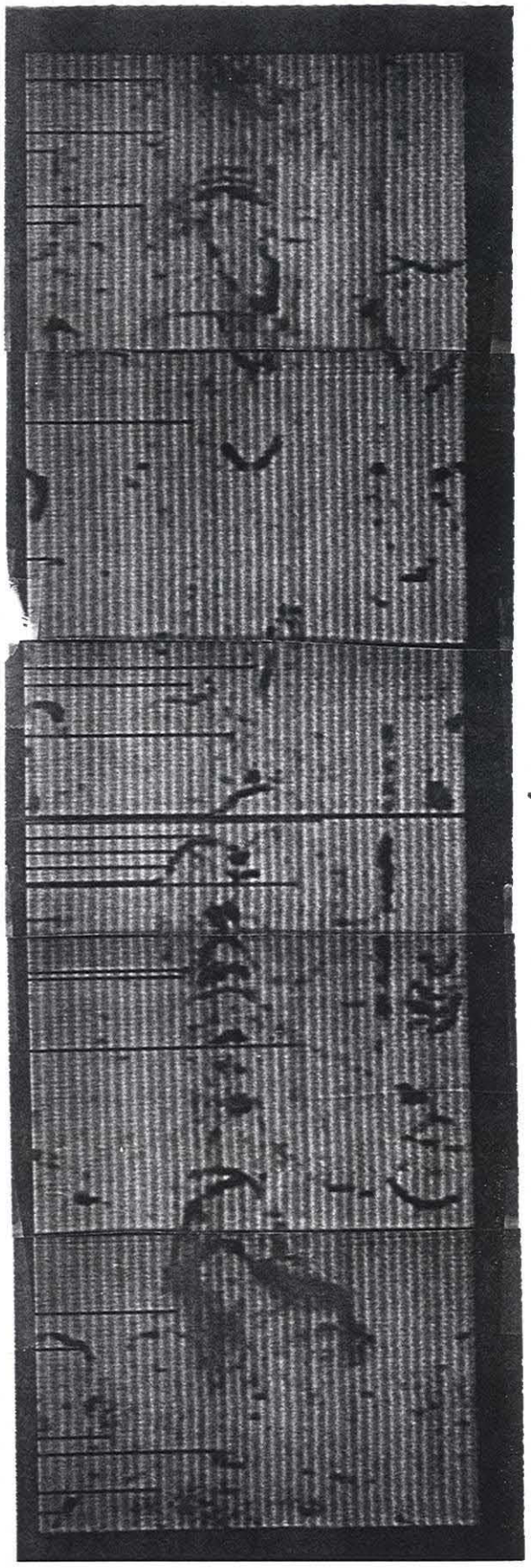
9500
2
1
9525

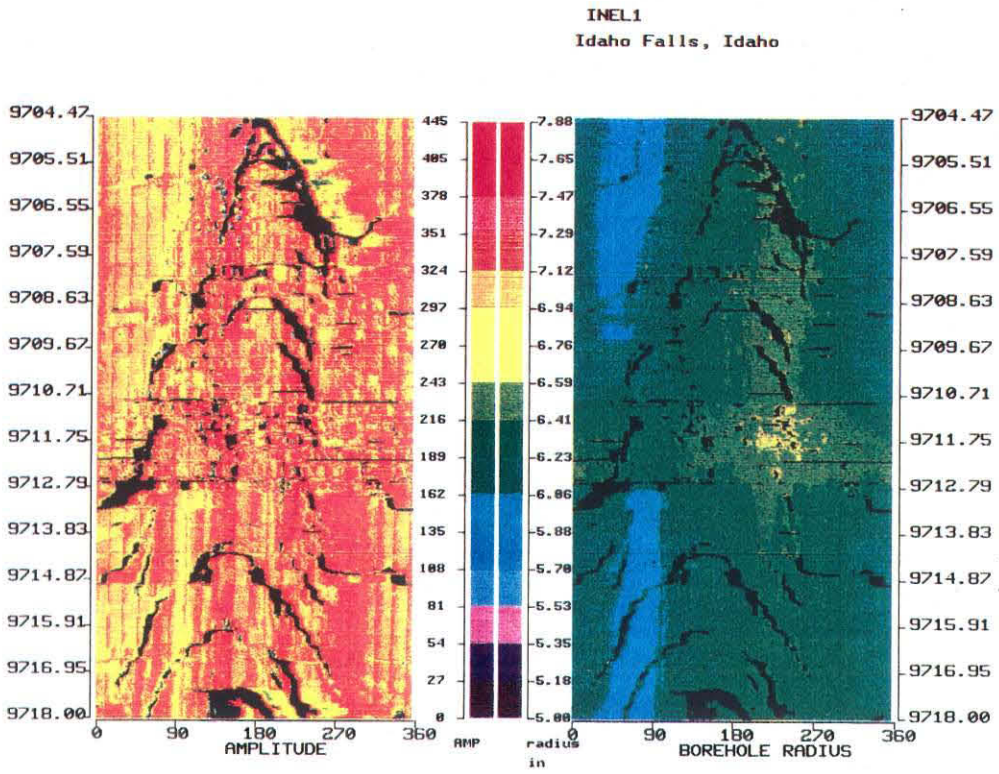

] fracture ~110° - 130°

ORIENTATION COMPARISON

AT DEPTH:

Paillet: 9718'

Pass 1: 9718'

Pass 2: (corrected to Pass 1 depths)
9715'

Figure A-II-6: Comparisons between the azimuths of features observed in the phase one, phase two and USGS logs of the INEL-1 well at depths of 9714 and 9730 feet.

Idaho Falls, Idaho INEL #1
June 21, 1980
10045 - 10095

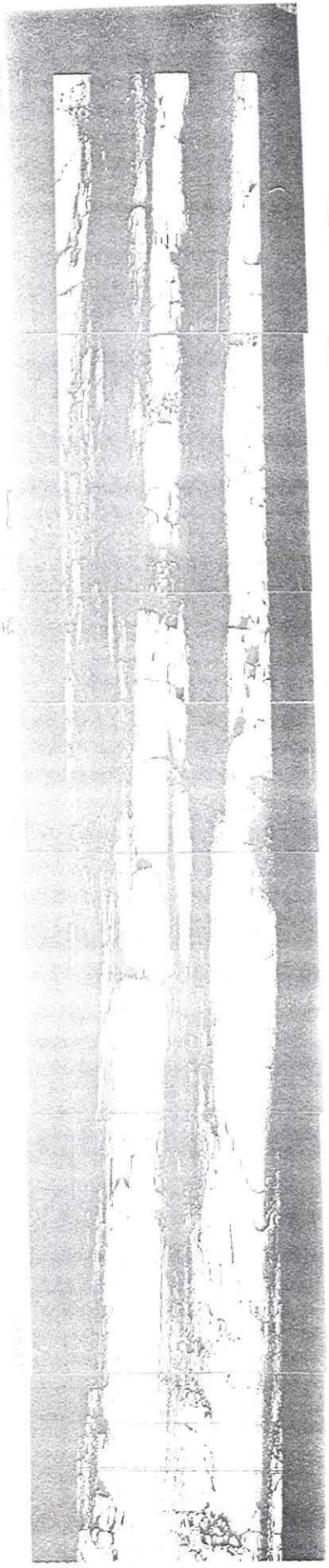

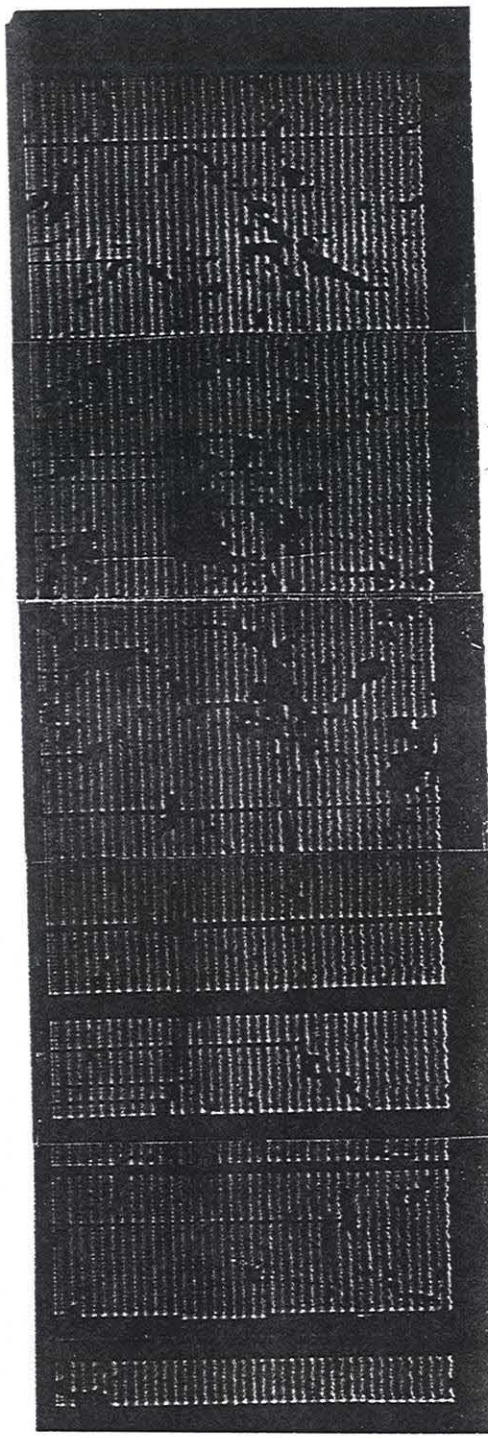

INEL-1 PASS 1
PHOTOGRAPH

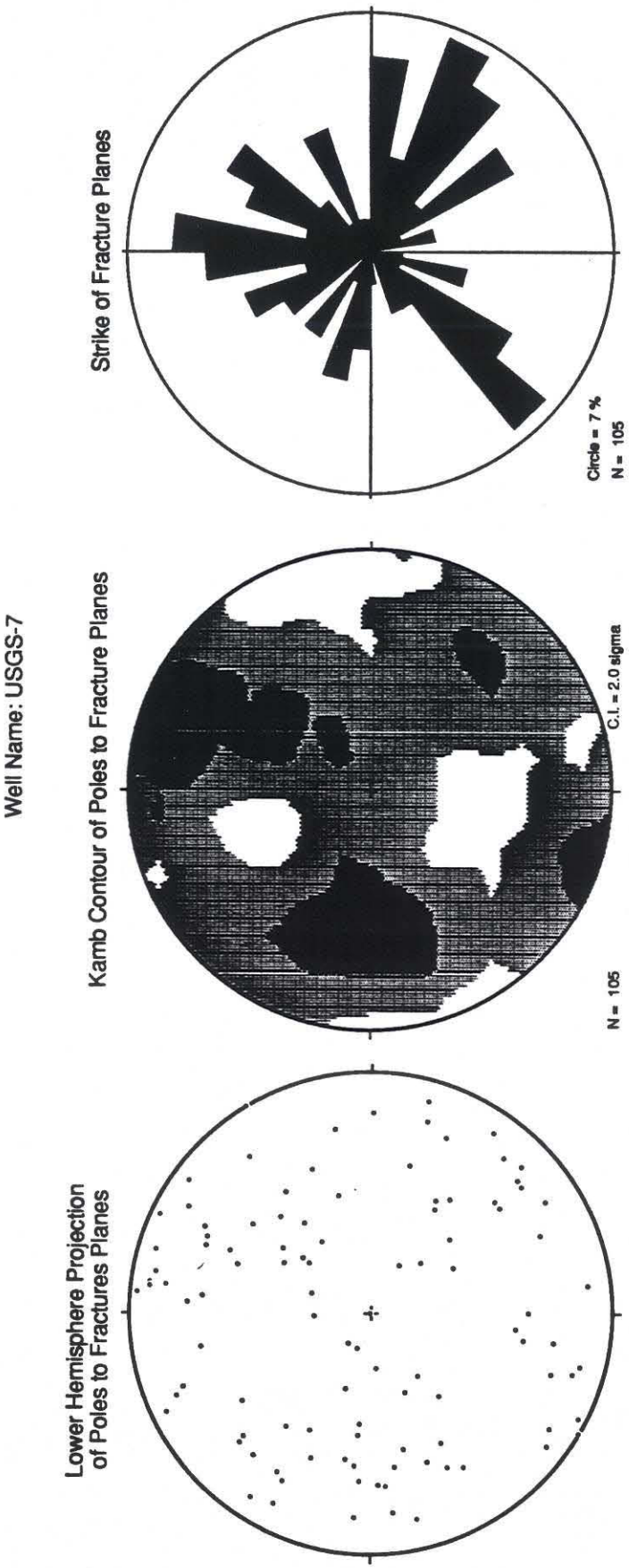

Figure 19: Lower hemisphere stereographic projections of poles to fracture planes, contoured poles to planes and strike of all fractures measured in well USGS-7.

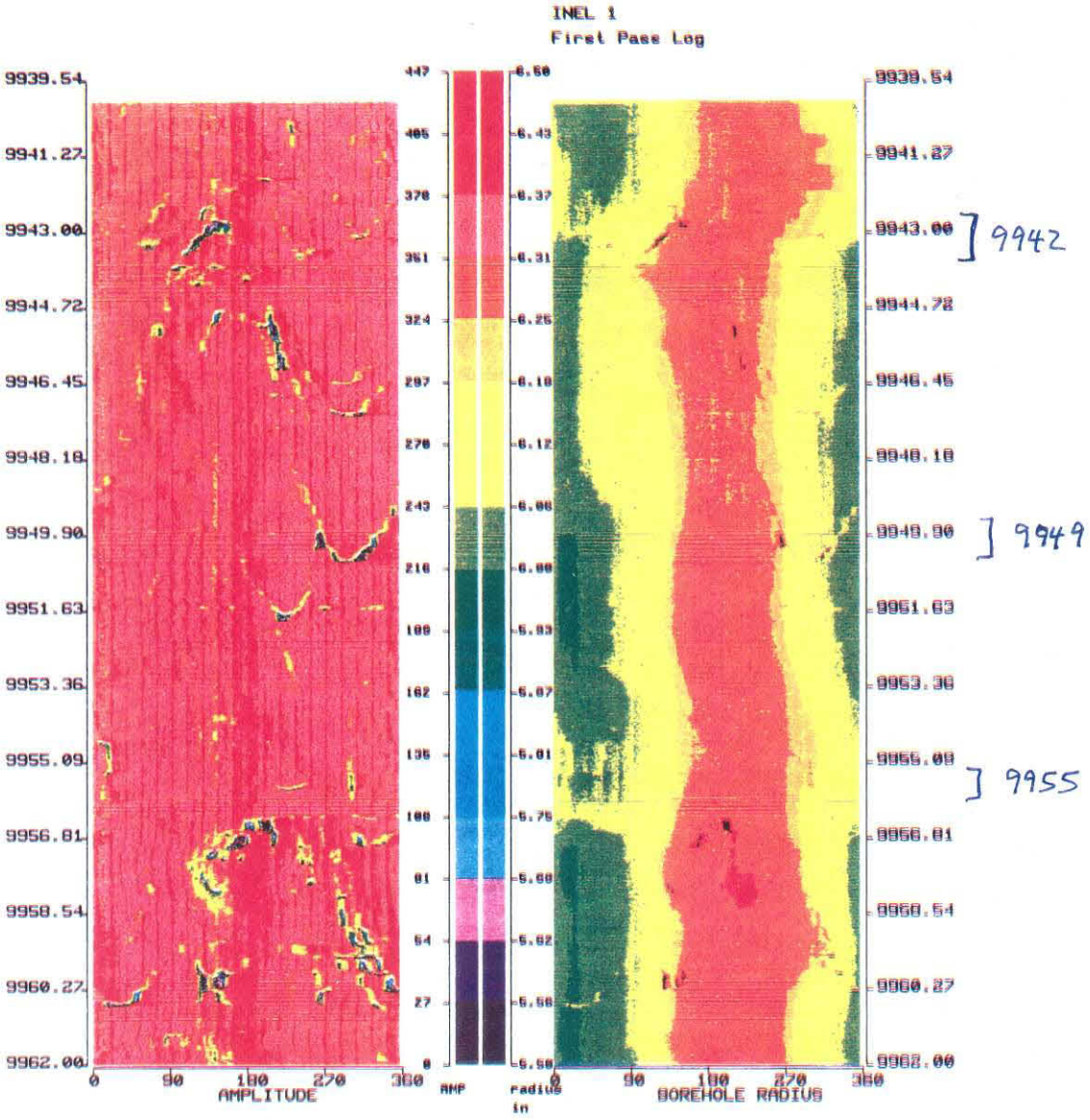

Figure A-II-7: Comparisons of the phase one and phase two azimuths of features observed in the INEL-1 well at depths of 9942 (where the azimuths agree), and 9949 and 9955 feet, where a different amount of offset in the azimuths is observed. No data is available at this depth from the USGS log.

INEL#1
Idaho Falls, Idaho

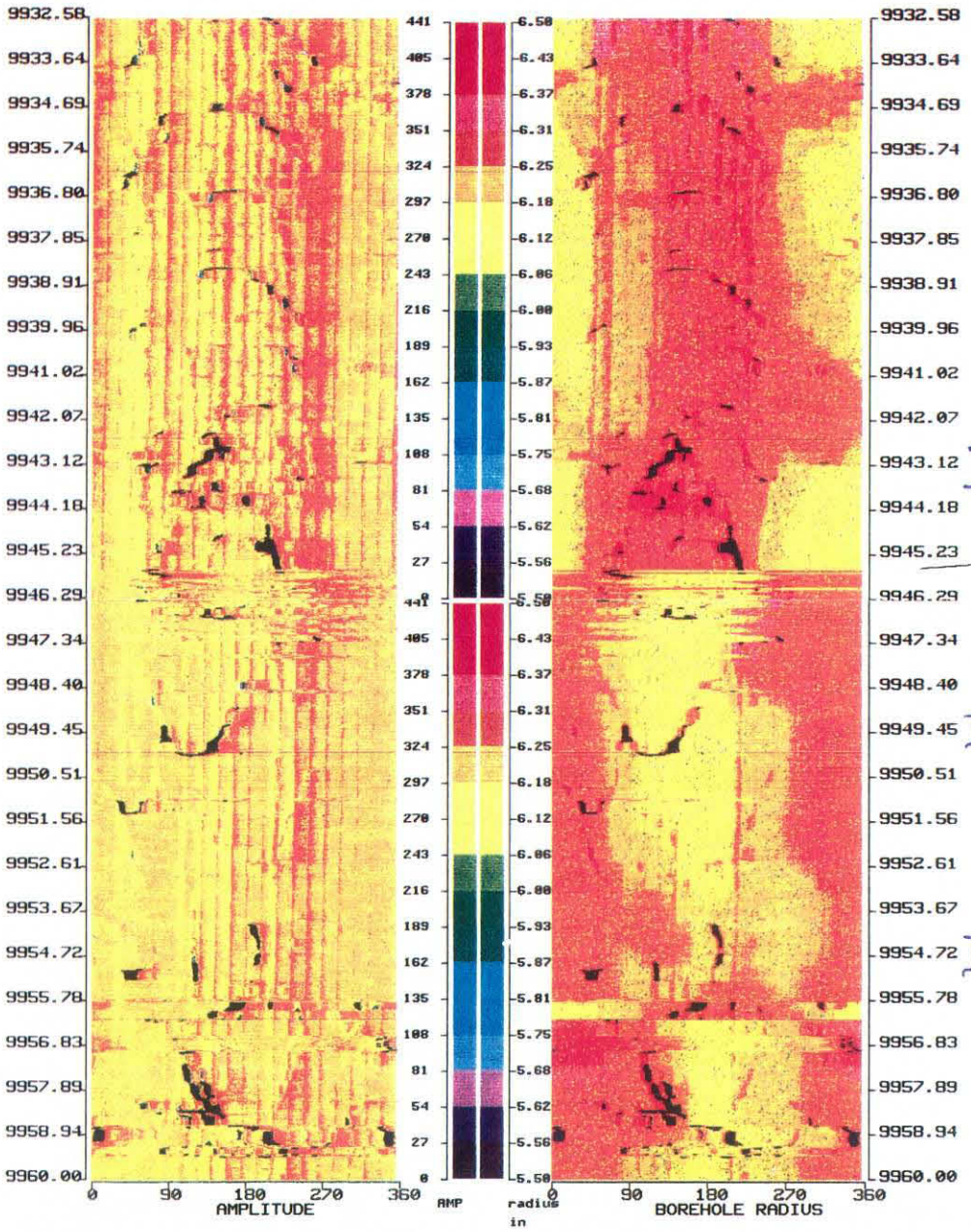

] 9942

orientation jump

(adjusted borehole DC during recording)

] 9949

radius ~6.25

] 9955

= orientation jump

= orientation jump

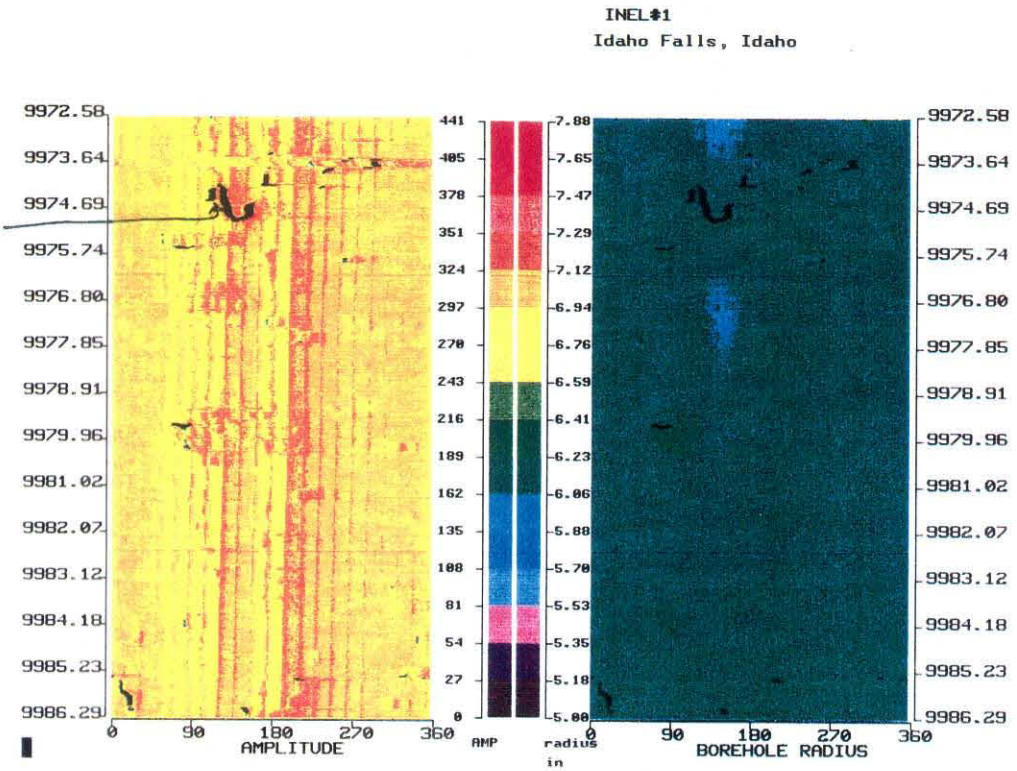

turn in center of ntical black

118°

ORIENTATION CHECK:

digitized pass 2 118°

photos pass 1 302°

@ 9974.5 subtract 176° from digitized to match

Pass 1

Figure A-II-8: Comparison of the phase one and phase two azimuths of features observed in the INEL-1 well at a depth of 9975 feet, where the orientations do not agree. No data is available at this depth from the USGS log.

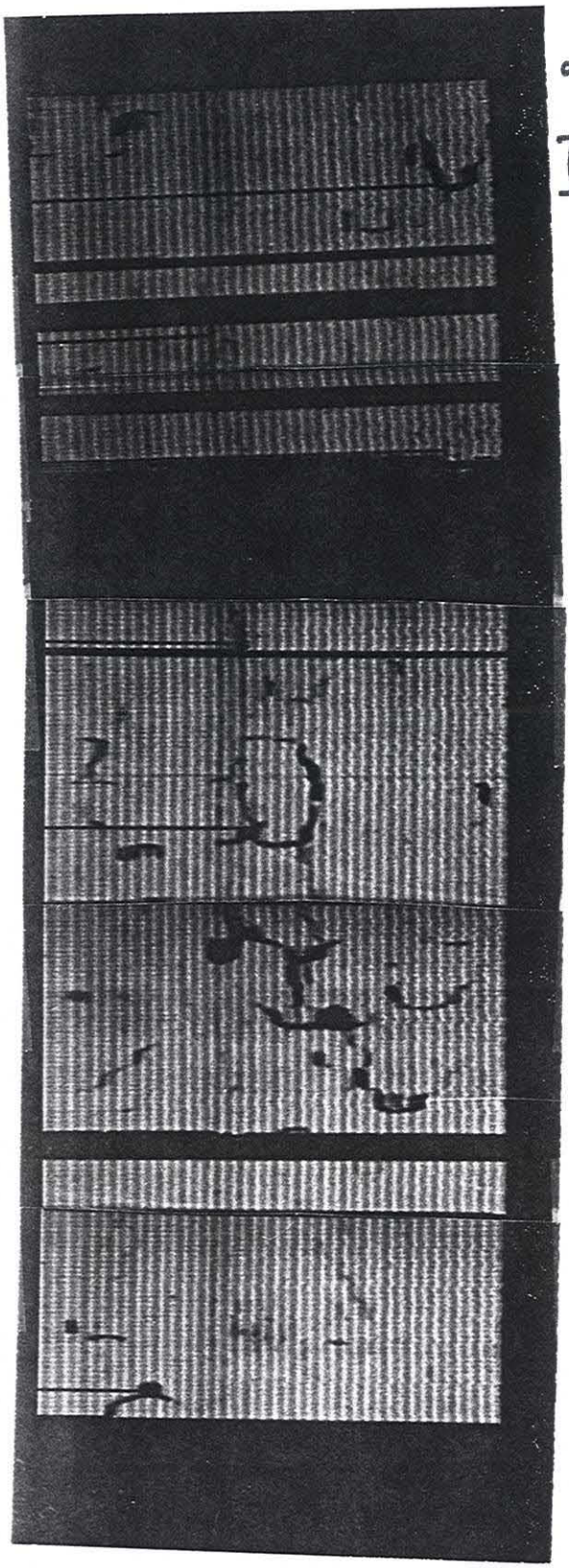
9975
10,000

Digitized data Pass 2

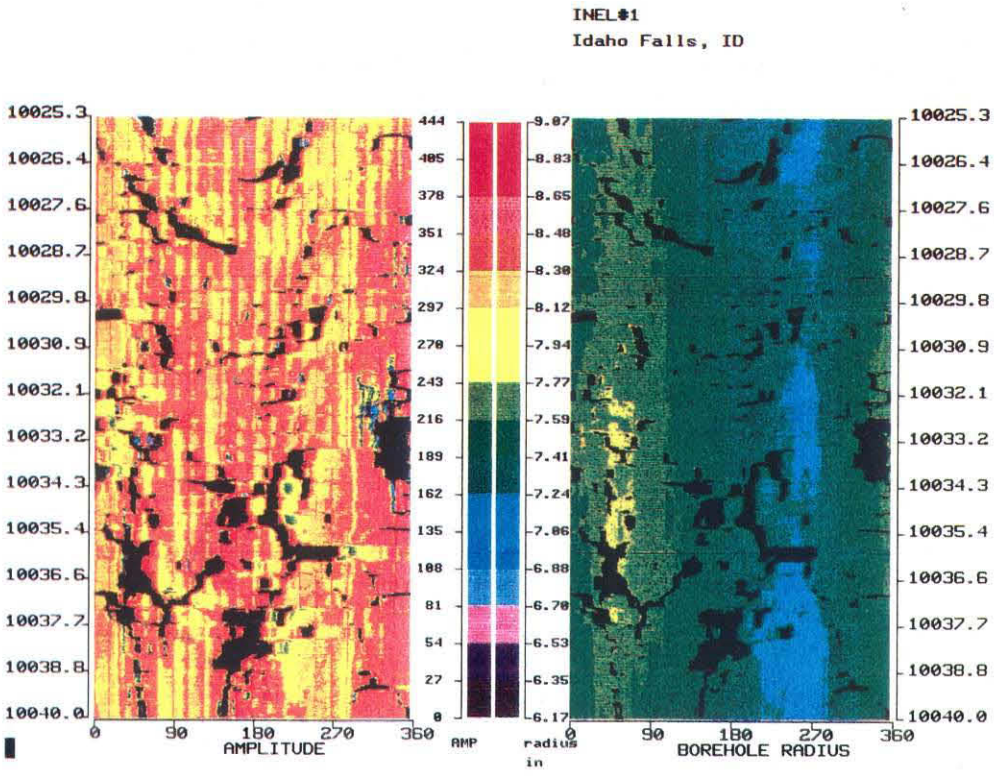

] "hourglass" @ 342°

ORIENTATION COMPARISON AT DEPTH:

Paillet	Pass 1	Pass 2
148°	148°	342°

(subtract 194° from pass two to equal other logs)

Paillet: 10,053'

Pass 1: 10,032'

Pass 2: (corrected to pass 1 depths) no photos @ this depth during the log

Figure A-II-9: Comparison of the phase one, phase two, and USGS azimuths of features observed in the INEL-1 well at a depth of 10,032 feet. Note that the orientations of the USGS and phase one logs are the same, whereas that of the phase two log is different.

acoustic televiewer log
Idaho Falls, Idaho EXEL #1
June 21, 1980
9730 - 9780

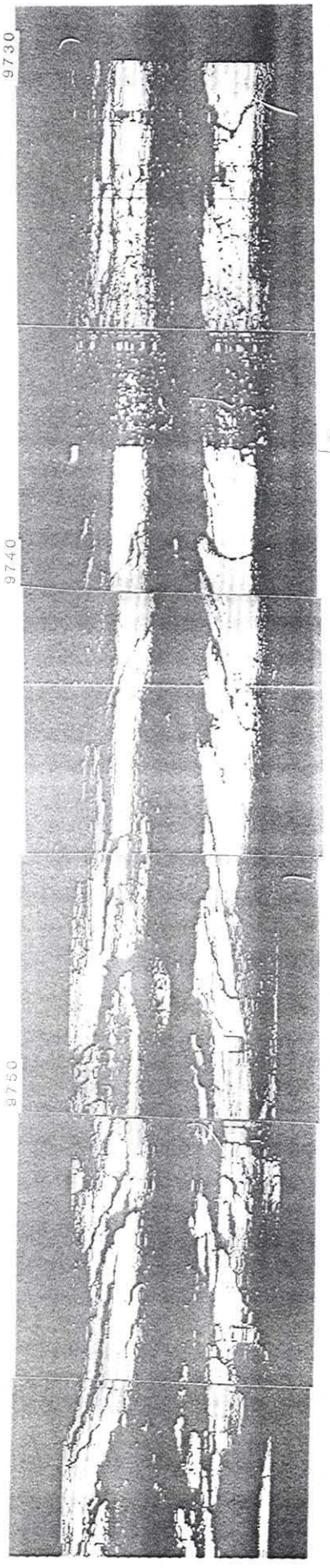

9737

depth tie

9716.5

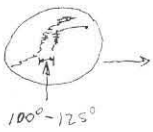

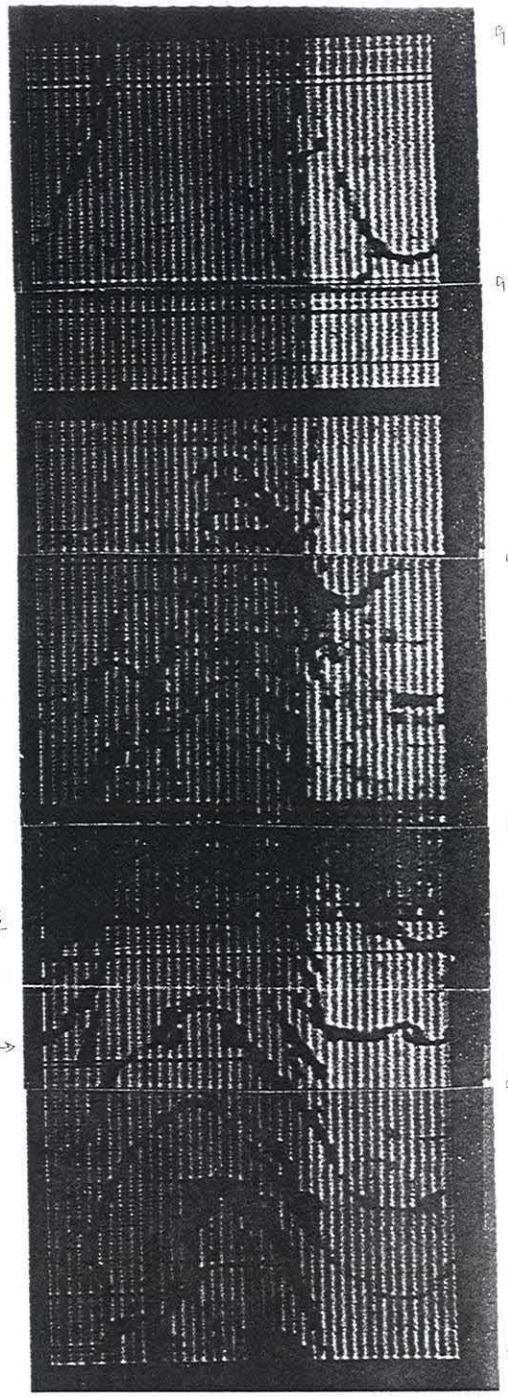

Appendix III - Color Images

BHTV image data from USGS-7, USGS-17 and Noname was shipped to R. Smith on July 15, 1990. Image data from INEL-1 was shipped to R. Smith on August 8, 1990.

Appendix IV - Barton et al., BHTV analysis paper

The paper included here as Appendix IV is in press (Springer-Verlag). It describes in detail the algorithms used to digitize, calibrate, and filter the televiewer data prior to analysis. Also described are the algorithms used to analyze the data, and the interactive front end which simplifies the analysis.

INTERACTIVE IMAGE ANALYSIS OF BOREHOLE TELEVIEWER DATA

by

Colleen A. Barton, Lawrence G. Tesler

and Mark D. Zoback

ABSTRACT

This chapter describes an interactive graphics system designed for borehole televiewer (BHTV) image analysis. The software provides one of the first comprehensive tools for borehole image data analysis available to exploration and research scientists on a low cost and easy-to-use personal computer, the Apple Macintosh II.

The program, called BHTVImage, provides an integrated environment for analyzing borehole shape and features. Images of BHTV data are displayed in false color on a graphics screen and are manipulated with a mouse pointing device. A variety of two and three-dimensional displays of borehole radius and acoustic reflectivity are used to display the data. Tens of meters of borehole wall can be rapidly viewed by scrolling through the data within a graphics window. Interactive measuring tools are provided to quickly measure and record wellbore features. The values of the scales, units, and grid intervals can be modified interactively during program execution. Gross scale features can be easily extracted from the images through interactive thresholding to produce a scaled comparison with complementary log data such as resistivity or sonic recordings. Alternatively, full resolution images can be analyzed to investigate the fine details of fractures or cross-bedding intersecting the well.

One of the reasons Macintosh applications are easy to use is that there is remarkable human interface consistency among applications. To help meet that standard of consistency, the BHTV analysis software was implemented using an Apple product called MacApp. MacApp is an "object-oriented framework", i.e., a "generic" application that defines standard "objects" like windows and views. Any desired Macintosh application can be derived from MacApp by describing in code only the differences between that application and the generic one. The resulting program achieves consistency with other Macintosh applications without special effort on the part of the programmer. MacApp, as well as the bulk of the BHTV analysis program, is written in the object-oriented language Object Pascal. Certain BHTV analysis subroutines are written in the language C.

The software discussed has provided the primary analysis tool for the BHTV image data recorded in the Cajon Pass and KTB research wells. The Cajon Pass Well, located in Southern California near the San Andreas fault, was drilled to investigate the paradox of low stress, low heat flow measurements along an active plate boundary. The KTB deep

drilling project located in the Oberpfalz zone of West Germany was undertaken to evaluate an ancient continental suture. The accurate determination of borehole shape and the characterization of wellbore breakouts and fractures with depth have been essential to understanding fault mechanics and tectonic stresses and to the interpretation of geophysical and core data from these and many other wells.

INTRODUCTION

The borehole televiewer is an ultrasonic well-logging tool useful for imaging lithostratigraphic features and for measuring the orientation and distribution of fractures as well as the orientation and width of stress-induced wellbore breakouts. The analog Televiewer, originally designed by Mobil Oil, Inc. (Zemanek et al., 1970), contains a rotating transducer that emits an acoustic pulse at the rate of 1800 times a second. Figure 1 is a schematic diagram of the acoustic mechanism of the Televiewer tool. The 1.4 Mhz transducer rotates at three revolutions per second and moves vertically up the borehole at a speed of 2.5 cm/s. The transducer diameter is about 1.27 cm (0.5 in) however the emitted sound is focused to a narrow beam of about 3^{o} due to the high frequency. A fluxgate magnetometer within the tool fires at each crossing of magnetic north, making it possible to orient the data.

Prior to the 1980's and the emergence of downhole digital imaging tools, borehole wall images were limited to analog photographs. Image analysis was a static, tedious process. With the inception of the microprocessor, digital images of the borehole wall have become the standard data presentation format.

Image photographs are still routinely collected in standard field operation of the analog BHTV tools. The analog televiewer tool transmits ultrasonic seismograms through a standard wireline logging cable which are recorded on videotape. The analog data are channeled into a three-axis oscilloscope where the horizontal sweep represents the scan of the rotating transducer around the borehole, the vertical sweep represents the rise of the tool in the borehole and the intensity is modulated by the reflected energy from the borehole wall. The oscilloscope then produces an unwrapped 360^{o} gray scale image of about 1.52 m (5 ft) of the borehole wall. The BHTV "log" is constructed from Polaroid photographs taken of successive oscilloscope screens as the tool progresses uphole during field logging. Each 3x5 photograph is then assembled into a composite log. The analog "north pulse" is recorded on one of the two audio channels of the video recorder. Depth is also analog analog on the remaining audio track of the video recorder.

The analog Televiewer tool has not undergone any major design changes since it was first introduced to geophysical logging in 1970. Interpretation of the photographic log has been limited to estimations of gross structure from the reflected image. The primary use of Televiewer data had been to determine the orientation of fractures in granitic rocks, analyses which involved tedious and inaccurate measurements. No capability existed in the analog data to correct the measured orientations of planar features for the effects of off-center tools or elliptical boreholes, conditions which can lead to substantial measurement error. With the rising use of wellbore breakouts to determine in situ stress, televiewer data has become increasingly important.

Digital televiewers have recently been designed that contain downhole processors to reduce the received signal to a peak amplitude and associated travel time before digital transmission (Heinz and Schepers, 1985; Schlumberger, Inc.). In digital tools, the horizontal resolution of the data is generally reduced by about one half of that of the analog tools. However, precision is gained by eliminating noise problems such as analog signal degradation in the cable. The marker pulse at magnetic north and depth readings are encoded automatically in the data recorded by the digital tools. The tilt of the tool is monitored by two inclinometers and an accelerometer provides continuous data on tool speed. Although the resolution is completely dependent upon hole size and logging speed, the Televiewer typically will provide horizontal resolution of a few millimeters and a one centimeter vertical resolution in a 30.5 cm (12 in) borehole.

Uphole data processing schemes for analog borehole image data have been operational since the early 1980's. Early post logging processing of the images was accomplished by fiber optics recording hardware (Wiley, 1980; Broding, 1982). At the outset of the development of uphole digitization systems specialized equipment was built; today inexpensive off the shelf data acquisition boards are available for workstations and most personal computers. In post logging digitization the recorded BHTV signal is examined within a specified window to determine the peak amplitude and its associated travel time. The determination can be performed by efficient software algorithms (Barton, 1988) or electronically measured by edge detection hardware (Pasternack and Goodwill, 1983; Taylor, 1983; Rambow, 1984; Wong et al., 1989; Faraguna et al., 1989). The time required to capture and record each pair of values is generally within 0.5 microseconds.

Digitization of standard analog data results in dual measurement of acoustic reflectivity of the borehole wall and the ultrasonic travel time of the imaging pulse at a spatial resolution well above conventional logging tools. The software and techniques described herein to analyze and interpret BHTV data are applicable to any digital televiewer

data set whether obtained directly from a digital tool or derived by analog-to-digital conversion from an analog wave train (Figure 1b).

Advantages of Digital Interactive BHTV Data Analysis

Digitizing and digital processing of the analog Televiewer data has opened a new dimension in the interpretation of BHTV data, most significantly, the precise measurement and display of the travel time of the reflected pulse. Assuming a known mud velocity along the raypath for the source and reflected pulses, the two-way travel time can be converted to distance to give the detailed topography of the borehole wall. Another advantage of digital data is that it can be enhanced and corrected for geometric effects. Borehole features can be displayed in a way that best suits the type of feature under investigation. For example, wellbore breakouts are best represented in polar cross section. Finally, it is possible to make systematic quantitative measurements quickly and accurately.

BHTVImage utilizes various two- and three-dimensional displays of the borehole radius and acoustic reflectivity to facilitate data analysis. It allows the user to make quantitative measurements of borehole features such as breakouts, fracture orientation and apparent aperture, and lithologic features. The analysis software has been implemented on a Macintosh II personal computer. The program provides an integrated environment for analyzing borehole shape and features where images of BHTV data are displayed in false color on a graphics screen and are manipulated by graphics mouse and keyboard commands.

The primary advantages to interactive data analysis are that it gives the geophysicist the ability to (1) interactively manipulate the data to obtain an optimal view of a particular feature, (2) look at the same data interval simultaneously from a variety of perspectives and (3) make decisions as the analysis proceeds.

Menu driven commands and analysis operations provide an ease of use factor to the software. Tens of meters of borehole wall image can be rapidly viewed by scrolling through the data within a graphics window. Images can be enlarged to the full resolution of the screen and scrolled to search for fine features. Alternatively, larger sections of the well can be displayed at the scale of standard logs. Interactive measurement tools are provided to quickly measure wellbore features. The values of the scales, units, and grid intervals can be modified interactively during program execution. Menu-operated window management provides easy access to the various views the user is interpreting.

BHTV File Format

A common aspect to all borehole image data is the physical size of the data set and the associated difficulties in managing the volume of data generated. The voluminous size of image data controls the configuration of the computer hardware and impacts software design along every step of the acquisition, display, enhancement and analysis process. Computer speed and memory capacity are rapidly increasing, however, these constraints remain a significant consideration in the design of an image processing system. Data compression is a widely used and widely researched topic in computer science. Compression and decompression algorithms exist for computer systems common to oil industry, research and government facilities. They are at present too costly in computational time to be useful in interactive image analysis.

The data input consists of header information followed by arrays of amplitude and travel time values. Careful thought is required in header format design given the extreme variability in image data and the fact that other scientists may use the data. For example, image enhancement involves filtering and other processing that results in permanent transformation of the data. It is important to keep a history of the transformations that a particular image data set has undergone to preserve the ability to interpret the data. In header format design it is beneficial to consider extensibility, that is, the flexibility to extend the header at a later time it to include more, fewer or different header parameters. Table I summarizes header specifications used in this system. The header parameters can be inspected by choosing a menu command which presents a dialog box, a display of the current settings of the header parameters. These parameters can be edited as necessary to adjust the data to the proper depths, compass azimuth, etc.

In the uphole digitization scheme developed at Stanford the returned reflection is windowed and discretely sampled (Figure 1b). The peak amplitude and associated travel time are measured for each pulse firing. The conversion of travel time to true borehole radius is completely dependent on the BHTV tool and transducer frequency used to record the data. The mud fluid velocity in the borehole, V_f, the correct radius of the televiewer tool, T_r, must also be known. The transit time between the transducer and the outside of the window housing the transducer, T_{off}, must be known for the particular tool and transducer frequency used to record the data. For example, T_{off} is 16 μs for the large diameter high frequency Simplec Inc. televiewer and 9.81 μs for the Schlumberger Inc. high frequency large diameter tool. Conversion of the travel time data to borehole radius is then:

$$R = \frac{((S*T_i*W/N) + D - T_{off})}{2} * V_f + T_r \qquad (1)$$

where T_i is the two-way travel time, S the sample rate in samples/μs, D is the digitizing delay time in μs, W the digitization window length in μs and N the number of samples digitized per pulse. To assure accuracy in the conversion of travel time to radius for each logging run a calibration adjustment can be added to equation (1). The calibration constant is obtained from a calibration test of the tool in a specially designed tank before each logging run. A calibration tank requires at least two different radius values, for example, a smaller radius from 0° to 180° circumference and a larger radius from 180° to 360°. The measured travel time values measured at known radius values can be used to compute the calibration constant and the fluid velocity. Data recorded in this tank may also be used to calibrate the compass azimuth of the transducer with respect to magnetic north.

Conversion to the format for BHTVImage includes resampling of variable scan length data to a fixed length, shifting the data to correct for the magnetic declination at the logging site or any other azimuthal data shift, and scaling of the amplitude and travel time values to the range 0 to 256 expected by the program. An essential consideration during data acquisition is the threshold detection level imposed during data acquisition. When no reflection is detected above the noise threshold that particular pulse must be flagged within the data set to signify that no energy returned to the transducer. These values of missing data are important elements of the BHTV data format.

HUMAN INTERFACE DESIGN

Experience with a predecessor to BHTVImage on a different computer had shown that the utility and appeal of the program would be quite limited unless the user could interact freely with an image, i.e., display it alone or alongside other images, scroll through it to study its features, decide whether to correct for geometric distortion and do so if desired, decide whether to enhance the image in one or more ways and do so if desired, choose views that seem at the time to be useful, and make measurements of any desired features in any order at all. Achievement of these goals required a highly interactive graphical user interface.

Another goal we chose was to make the BHTVImage software accessible to other researchers. Two factors were important to achieve this goal: affordability and ease of use. The Macintosh II computer met all the above criteria as well as technical requirements such

as sufficient memory capacity to hold multi-megabyte images and a high-fidelity color display.

One of the reasons Macintosh applications are easy to use is that there is remarkable human interface consistency among applications. After a user has learned one or two applications, the knowledge he or she has gained about how to interact with them can be generalized to other applications. Studies have shown this to result in reduced learning time. To accrue the advantages of consistency, BHTVImage was designed to follow Apple's user interface guidelines wherever feasible.

The Macintosh user interface is based on a number of principles. One is modelessness. A mode is a state of an interactive system that affects the meaning of user actions. If the user takes an action in one mode thinking the system is in another mode, undesired effects can result. As a result, the Macintosh guidelines discourage modes, and insist that when modes are unavoidable, the current mode be inescapably obvious to the user. If BHTVImage, for example, had been designed so that the user specified a filter command and then the borehole section to filter, then between the first and second specification, the system would have been in a mode expecting the section to be specified. Instead, in analogy with other Macintosh applications, BHTVImage was designed so that the user first specifies ("selects") a borehole section and then any operation on it—or several sequential operations, or none. Between the selection and the operation, there is no mode. The user may scroll or move the window, run other Macintosh applications, peruse the menus in search of a desired command, select a different section of the borehole for the operation, or even change one's mind and never specify the operation.

Another principle of the Macintosh user interface is that everything the user must think about should be visible. When we added the ability to measure a fracture or breakout, our first thought was to write the measurement data directly to a text file. However, if we had done so, the user would not have been able to see the measurements until after the file was saved and another program was run to examine it. Instead, we decided to display the measurements in a text window immediately after they were made. In addition to providing the desired visibility, we discovered the additional benefit that the measurements could be edited using a standard text window editor to delete a mistaken measurement or for other useful purposes.

One other principle of the Macintosh user interface is that applications should be tested on typical users, revised in response to difficulties they encounter, retested, revised again, etc., until the ease of use level meets expectations. In the case of BHTVImage, one target user (an author of this paper) was involved in the detailed design and implementation of the program. Thus, it was not surprising that all of the twenty-odd geophysicists who

have tried it thus far—some with no help but a ten-page preliminary manual--have reported extreme satisfaction with the user interface.

Key components of the Macintosh user interface, and their expression in BHTVImage (discussed below), include:

Macintosh	BHTVImage
Windows:	Amplitude window, borehole radius window, correction window, etc.
Views:	Unwrapped view, polar cross-section view, cylindrical projection, etc.
Selections:	Selection of text, of one fracture, or of all data between two depths
Menus:	File, Edit, Windows, Views, Settings, Palette, Analyze, and Profile
Dialogs:	Dialogs to provide control over the display of scales, filter options, etc.
Keyboard shortcuts:	
	The escape key to record a fracture, command-X to remove a section
Palettes:	Palette of 16 hues, gray scale or black and white

OVERVIEW OF PROGRAM USAGE: A Scenario of the Analysis of BHTV Data

Open a Data File

The standard representation of borehole image data has been a 2-D unwrapped 360° view of borehole azimuth versus depth. The interpretation of borehole image data involves the display of different borehole features in an optimal geometry so that they can be viewed and most accurately measured. Planar features that intersect the borehole appear as sinusoids on the 2-D view so they are best analyzed in the 2-D split images (Figure 2, after Zemanek, et al., 1970). In Figure 3, nearly vertical fractures that strike about 180° are associated with low reflectivity values and large values of borehole radius. Other borehole parameters that can be extracted from image data, for example caliper information from the BHTV, may be represented as geophysical log profiles.

Intervals of the data may be selected from the 2-D unwrapped image, using the mouse much like selecting text in a Macintosh word processor program. The selected interval can then be viewed in a variety of projections. The cylindrical geometry of the data is best represented by polar cross sections of the data scans or isometric 3-D cylindrical projections (Figure 4). In the cylindrical projection, the radius of the cylinder is modulated by the borehole radius value at each pulse providing a true scale reconstructed image of the borehole wall. Three-dimensional wire frame cylindrical projections of the data show fine detail of the borehole wall not visible in conventional 2-D displays. The cylindrical

projection may be scrolled vertically to view the reconstructed "core like" image with depth or scrolled horizontally to rotate the image 360° about the vertical axis. The amplitude values can be used to color modulate the surface of the cylindrical projection for a composite image of the data (Figure 4, middle window). These views can also be interactively displayed as black on white to investigate only the topography (Figure 4, right window). The data displayed in Figure 4 were recorded over a cross-bedded interval in a well located in the Gulf Coast. A 3-D wire frame image with reflectivity values superimposed in color has become an important interpretative tool. As shown in Figure 4 there is more variability in the reflectivity image than in the corresponding travel time image indicating that the impedance contrast over this interval exceeds the small variations in the travel time due to the differential erosion of the interbedded sand and shale. There is an option in this view to exaggerate the surface of the cylinder to amplify small variation in the topography of the surface. The differential erosion between the sand and shale layers is evident in the black and white view of Figure 4 (right window).

Polar cross sections of the data scans can give an accurate bird's eye view of circumferential wellbore conditions and computed borehole radius values can modulate the radius of the cylinder to show fine detail of the wellbore wall.The polar projection also uses the travel time values to modulate the radius of the polar cross section. Scrolling the data in polar cross section allows a rapid view of borehole shape changes with depth (Figure 5, middle window). A compass plot around the polar scan is used to reference the data to geographic north. A graticule can be used in the polar plot for a more accurate assessment at the borehole dimensions. These alternative views of the data can be simultaneously displayed in other windows.

Additional views of any selected interval of data include a plot of the scans in Cartesian cross section showing azimuth versus borehole radius and a histogram view of the travel time data. These views are useful for evaluating borehole shape and noise contamination. Each view can be scrolled to inspect the data for changes with depth.

Data intervals can also be plotted as a cross plot of amplitude (x axis) versus distance (y axis) to look for anomalous relationships in the two variables that could indicate the presence of a particular borehole feature or the need to make a geometric correction to the data. There are expected relationships between reflectivity and travel time in the borehole, for example, low amplitude values and high travel time values within fracture zones, anomalous relationships such as high travel time and high amplitude isolated in a cross plot such as the upper plot in Figure 6 are the result of anomalies in the data. These plots can be used to interactively determine intervals of problematic data such as the off-center effects characteristic of the low travel time high amplitude cluster in Figure 6. After

correction for off-center effects the cross plot shows a normal distribution of data (Figure 6, lower plot).

Color or gray scale palettes are used to false color map the data to an image. Gray scale palettes can sometimes be a more intuitive interpretive tool using simple light to dark gray shades to indicate increasing values in the data. Data are color or gray scale mapped to either a linear palette where the data values are mapped to 16 different hues or to an enhanced palette which utilizes histogram equalization. Histogram equalization generates an image that assigns the available brightness levels or colors to equal numbers of samples and produces a display of higher color contrast which can accentuate features not visible in a linear scale. The same image over an 11 ft (36.9 m) section of a Gulf Coast well in Figure 7 shows the effects of histogram equalization. The left image has a linear color distribution and the right image has an equalized color map. Histogram equalization has been an extremely useful method to enhance borehole wall details.

Due to the variability in data, value ranges, and data quality, the linear or equalized color maps may not always provide the optimum display for interpretation in all cases. For this reason interactive palette manipulation was implemented which allows the palette hues to be interactively adjusted using a graphics mouse. This technique allows for expansion or reduction of the color contrast as needed for optimum enhancement.

Data thresholding is an additional palette manipulation. This technique was developed in order to examine gross scale features of the borehole reduced to black on white images. With thresholding the color palette is replaced by a sliding scale of the range of values in the data. A cutoff threshold value is interactively selected from this scale. Figure 8 shows an interval of the Cajon Pass well where breakouts and fine scale fractures are evident in both the reflectivity and borehole radius views. For reflectivity, the cutoff threshold marks the value below which all reflectivity pixels will be black and above which reflectivity pixels will be white. Similarly, a radius threshold can be used above which pixels will be black and below which they will be white. This view is useful for the correlation of BHTV logs with companion log data described below.

Low-pass filtering and subtractive smoothing (high-pass filtering) routines have been implemented as an aid in the detection of fine scale features. These filters are horizontal and 1-D. In subtractive smoothing the data are low-pass filtered to attenuate all of the high frequency features, such as edges and lines, then the smoothed image is subtracted from its original resulting in a difference image which has only edges and lines substantially remaining.

Standard Processing

The introduction of digital image data brought the possibility of correcting data for distortions caused by less than optimal recording geometry. Unfavorable logging conditions are a pervasive aspect of borehole image data acquisition. Instability of the borehole, washouts, fault zones, and the high pressures and temperatures at depth can lead to poor quality data. One objective for processing borehole image data is to identify these environmental or tool problems that distort the data and to provide the information required to make corrections to the data.

Analog data acquisition onto video tape is sensitive to human error as well as to poor borehole conditions. The missynchronization of recorder operation and winch operation can lead to missing or repeat log sections. When logging at sea ship's heave is seldom entirely mechanically compensated and data recorded at ocean drilling sites often show repetition of logged features. In addition, the tool may "stick" in the borehole for several rotations of the acoustic transducer then rapidly slip uphole creating a characteristic blocky image (Figure 9, left window).

For these reasons data need to be preprocess and edited prior to interpretation to avoid erroneous conclusions and the masking of subtle features. An interactive visual editing of the digital data has been implemented in the BHTV system to allow the user to delete data that should not be included in an interpretation. By selecting the unwanted interval with the mouse and using the standard Macintosh Edit Menu command "Cut" the selected scans are removed from the data file. Figure 9 shows the application of this interactive editing on data collected at Hole 504B in the East Pacific Rise. The blocky intervals in the left image of unedited data correspond to repeat scanlines due to ships heave; the right image of edited data reveals an interval of stress-induced wellbore breakouts that cannot be distinguished on the unedited image.

A fundamental effect of logging on the quality of BHTV image data is random noise. Whether it is electrical noise from the motor driving the rotation of the transducer or the interference from spurious voltage surges inscribed onto the videotape the result is anomalous spikes in the data. Scattering of energy due to the sampling geometry is another major source of noise. The optimum raypath geometry consists of a centralized tool in a circular borehole where each incident pulse has normal reflection to the tool. Non-normal incidence of a stray pulse from a rough surface can create complex raypaths and multiple reflections. These translate to anomalously high travel times and spurious reflectivity values. Noise spikes can interfere with data interpretation and they must be eliminated where automatic fitting or feature analysis routines are implemented.

Alternatively, if the spikes actually represent valid data, they may contain important information.

A median filter is used to mitigate this type of noise in the data. A median filter was selected among the myriad of smoothing operations in image processing because it is a smoothing in which the edges in an image are maintained. In median filtering a template is slid along the scans of data and the center value of the template is given the median value of all the values covered by the template. This type of filter is particularly good for removing impulse-like data because the pixels corresponding to noise spikes in their neighborhood are replaced by the most typical pixel in that neighborhood. A horizontal median template of any number of pixels can be used to pre-process BHTV data. A three point to median was determined to be the most appropriate because it provides sufficient filtering while having the advantage of being the fastest type of computational sort for large image files (Richards,1986).

In order to diagnose the degree of noise in a given data set the data scans may be examined in either polar cross section or Cartesian cross section to look for spikes. Symptomatic speckles in the unwrapped views also indicate noise contamination.

Geometric Corrections

A significant source of error in the interpretation of BHTV data can arise from the apparent location of borehole features from a non-centered tool which has the effect of "moving" features to incorrect positions on the borehole wall (Georgi, 1985). These effects can lead to errors in calculating orientations of planar features as well as incorrect azimuth measurements for features such as wellbore breakouts. Corrections to the travel time images for the effects of off center tools in circular boreholes are made either through geometric correction of the travel time data (Barton, 1988).

Off-center tools in elliptical boreholes present another, more complicated, geometric problem and the potential loss of a larger percentage of the returned reflection. This error is dependent upon the orientation of the ellipse and dip direction. If the long axis of the ellipse is coincident with the dip direction the dip is overestimated; if the long axis is perpendicular to the dip direction it is underestimated. (Georgi, 1985). A solution to this geometric problem using inversion was presented by Lysne (1986).

The borehole televiewer is designed to acquire data with the tool vertically positioned in a vertical borehole. Bowspring centralizers are positioned above and below the tool to stabilize it in the center of the borehole. Ideally the tool should be centrally located in a circular borehole. In reality, this optimum geometry is often not achieved. The possible raypaths for the BHTV pulse launched from the transducer are shown in Figure 10

(after Georgi, 1985). When the tool is significantly off-center in a circular drillhole vertical bands of missing data result from non-normal incidence of the pulse at the borehole wall and subsequent deflection of the returned signal away from the transducer.

To diagnose off-center effects the user can look for uneven vertical color banding in the unwrapped views or an off-center position in the polar cross section. A histogram of the travel time values will show a bimodal distribution if the tool is off-center and the Cartesian cross section will have a warped appearance instead of maintaining a horizontal line. The cross plot can also be used to diagnose off-center effects where anomalous data will occur as clusters off the main diagonal.

The polar, histogram and Cartesian views have been combined in an interactive correction window to facilitate the correction process. The upper left plot of Figure 11 displays the borehole radius in polar cross section, the lower plot in Cartesian cross section, and the upper right plot as a histogram in a single window for the user to evaluate potential off-center problems. The bimodal distribution of borehole radius, in yellow, and the curvature of the uncorrected Cartesian cross section indicate these data are from an off-centered tool in a circular borehole.

Geometric corrections for decentralized tools in circular boreholes are made using an algorithm which finds the true center of the borehole then calculates the corrected azimuth and radius for each reflected pulse. In the case of an off-center tool in a circular borehole the correction can be made by a relatively simple forward model. In an ideal circular borehole the point on the circumference with the minimum radial distance to the tool defines the tool position. Borehole features complicate this ideal scheme and, instead, an iterative search for the center is used to determine the true center. The minimum radius, r_{min}, initially defines the center of the borehole (Figure 12). Here d' is the recorded distance from the tool to the point P, d is the true distance from the center of the borehole to the point P, ϕ is the angle from the reference azimuth to the point P. The maximum radius, r_{max}, is taken as the diameter at the azimuth ϕ minus r_{min}. The distance the tool is offset from the true center, d_0, is simply $(r_{max} - r_{min})/2.0$. With this initial guess of the borehole center the radial distance, d, and angle to true center, θ, are computed for each pulse through:

$$d^2 = (d' - d_0 \cos \alpha)^2 + d_0 \sin^2\alpha \qquad (2)$$

and

$$\theta_0 = - (\phi + \pi/2) + \cos^{-1}(d_0 \sin \alpha) \qquad (3)$$

where $\alpha = \pi - \phi$ (see geometry in Figure 12).

The initial estimate for the tool position is accurate only for featureless circular boreholes. Where features are present the minimum radius may have no relationship to the true borehole center. To solve this problem the center of the borehole is iteratively determined until the routine converges to the true center. When the difference between the current iteration and the previous iteration, δd_0, is roughly zero the routine has converged. For most data sets convergence to the true center of the borehole occurs within 3 or 4 iterations. For extremely variable data, where adjacent travel time values vary more than 35%, stability in finding the true center is achieved by evaluating successive d_0 values. The smallest value of d_0 within a given number of iterations was found to provide the best estimate of the true borehole center. Once the borehole center and radial distances are calculated for each pulse the routine interpolates the amplitude values to their correct spatial position.

In the more complicated case of an off-center tool in an elliptical borehole a Marquardt inversion is used to determine the tool distance and azimuth from the borehole center (after Lysne, 1986). It was noted by Lysne (1986) that this inversion technique is unstable where the tool was off-center by less than 10% of the nominal borehole radius, in other words, as the tool approaches the center of an elliptical borehole the off-center direction becomes less unique. This was found to be the case when this algorithm was applied to field data where the tool was not sufficiently off axis in an elliptical borehole. This technique was found to successfully correct the data (Barton, 1988), however, field data recorded in an elliptical borehole where the tool was well off-axis was not available and synthetic data had to be generated to test this algorithm. The success of this algorithm applied to the synthetic data is shown in polar cross section in Figure 13 where the polar projection plotted in black is the synthetic data and the projection plotted in red is the corrected data and the crosshairs mark the center for both the original and corrected data. Note that this correction modifies both the azimuth and shape of the breakouts, features that are important to stress measurements.

APPLICATIONS OF BHTV IMAGE ANALYSIS

Perhaps the most significant potential benefit of digital BHTV data is to make accurate quantitative measurement of physical phenomena that are imaged by this logging tool. The measurements of planar features, bed boundaries, foliation and fractures are some of the primary targets for borehole image data analysis. The use of wellbore breakouts to measure in situ stress has made data recorded with the borehole televiewer an extremely valuable component in many investigations of crustal stresses.

Analysis of Fine Scale Features

Although wellbore breakouts, washouts, and key seating can be seen on most 2-D images they are best distinguished in polar section of BHTV data (Broding, 1981; Barton; 1988; Menger and Schepers, 1988). The detailed borehole shape available through polar cross sections of BHTV data and interactive measurement tools permit the rapid analysis of stress induced breakout orientation or the orientation of hydraulic fractures (Barton, 1988). Figure 14 is a conceptual drawing of the development of a breakout (see theoretical shapes in Zoback, et al., 1985) along with a polar cross section of data from the Cajon Pass well which demonstrates the picking technique. The greater travel time within the breakout defines the characteristic breakout shape. θ_b is the angle of breakout initiation with respect to S_{Hmax}. Several superimposed scans of travel time data (representing a vertical distance of several cm in the well) are plotted in polar cross section to allow measurement of breakout azimuth and minimum breakout width.

The minimum width of a breakout is a function of the initial failure of the borehole wall upon breakout formation and erosional effects on the initial shape of the breakout, such as fluid circulation or tool trips. Superimposing data scans before plotting was found to be preferable to averaging scans in order to preserve the minimum width of the breakout over the vertical interval. The data must be corrected for tool position and magnetic declination before plotting. The objectives of this analysis technique are to obtain precise breakout azimuths and the minimum breakout width and to utilize all of the recorded data. Figure 5 shows the systematic process of the data analysis where a 360^o unwrapped view of the data (left window) has been color tuned to enhance the breakouts in this interval. Polar cross sections of the borehole are plotted in the left window. The user visually picks the breakout widths using the graphics mouse to drag through the breakout angle. Where there are continuous reflections from the broken out sections, as in the example in Figure 14, the breakout widths are easily determined. The breakout width for each interval is picked interactively and stored in text window. The data window can be edited and miscellaneous notes entered regarding the data quality or other information as needed. The data window can be saved for further statistical analysis or for plotting of the depth distribution of breakouts. Several off-the-shelf Macintosh software packages are available for statistical reductions and graphics plotting.

In the data analysis, the two sides of a breakout are picked independently. The two radial lines in Figures 5 and 14 represent the picked angle of the breakout width, the breakout azimuth bisects this angle. Breakout azimuth should coincide with the direction of

least horizontal principal stress; breakout width is shown in the following discussion to be important for estimation of stress magnitude. Figure 15a is a typical histogram of the distribution of breakout azimuths and widths measured from data recorded in well EE-3 at the Fenton Geothermal site, New Mexico (Barton et al., 1988). 928 separate breakout azimuths and 644 breakout widths were measured in the analysis of the Fenton data where the mean direction is 119°, and the standard deviation 11° resulting in an S_{Hmax} direction of N30°E.

The occurrence of wellbore breakouts may be used to fully determine the in situ stress state. With knowledge of C_o, S_{hmin} and breakout width (Figure 15b) the magnitude of maximum horizontal principal stress can be estimated by the breakout analysis. A detailed description of the analysis of breakout data can be found in Barton et al. (1988). Using independently determined values for C_o and S_{hmin}, the analysis of breakout widths in the Fenton well constrains the value of maximum horizontal principal stress to be approximately S_v, as predicted from the occurrence of both strike-slip and extensional earthquakes in response to fluid injection at Fenton Hill (Fahler, et al. 1986). The Fenton well has been the site of extensive research and available information on the minimum horizontal principal stress and on rock strength made the site an excellent test of the calculation of stress magnitude using the angle of breakout initiation.

Detailed analyses of borehole shape using Televiewer data can provide well resolved orientations of the horizontal principal stresses. The magnitude of the maximum horizontal compressive stress can be constrained by these data. The analysis of breakout width may be a promising technique to estimate stress magnitude in drillholes where other techniques are not useful.

Fracture Analysis

The primary use of BHTV data since it became operational in geophysical logging has been the measurement of the orientation and distribution of planar features in a drillhole. As mentioned, planar features that intersect the borehole appear on the unwrapped 360° view as sinusoids (see Figure 2). These sinusoids are often discontinuous for fine scale fractures and they can show very complex patterns at points where several fractures intersect or where fractures are not perfectly planar. At least three fractures intersect at depth 5135.5 ft (1565.3 m) in the left window Figure 16. The circular features in the right window of Figure 16 are interpreted as fracture planes that enter and exit the borehole as a chord. The steeply dipping fracture at depth 149.2 m (489.5 ft) appears to merge with a shallow fracture above. It is important in these cases to use the various enhancement techniques discussed above to best resolve the trace of the fracture before

measuring its orientation. Because of the flexibility designed into the interactive analysis system different enhancement techniques can be explored until the optimum resolution of the fracture of interest is achieved before determining the fracture orientation.

The BHTV image of a fracture surface can be extremely irregular due in part to the true topography of the surface, the limits of the resolution of the transducer and to multiple reflections from within the fracture surfaces. Because the eye can often perform the best least-squares fit to a curve within a complex network of fractures an interactive routine has been implemented to measure the amplitude and phase of the sinusoid (Figure 16). The graphics mouse is used to drag an adjustable curve over the imaged fracture; up and down mouse movements controlling the amplitude of the sinusoid and left to right movements its phase. These measurements give the strike of the plane as 90^{o}-ϕ where ϕ is the minimum of the sinusoid and the dip angle, α, as $\tan^{-1}$ h/d where h is the peak to trough amplitude and d the borehole diameter. Interpreting fracture orientations using this interactive method reduces the possibility of errors from improperly fit sinusoids that can occur with other automatic methods in highly fractured intervals. It also aids in the detection of fracture planes not readily visible in the data. For example, in Figure 16 the trace of the steeply dipping fracture below the intersecting fractures at 5135.5 ft (1565.3 m) is not initially apparent; however placement of the flexible sinusoid reveals the fracture trace well below the intersection of the three fractures.

With the amplitude and phase of the sinusoid determined, a wire frame cylindrical projection of the BHTV data over the fracture interval is generated which is mathematically rotated into the plane of the fracture so that the fracture width can be measured perpendicular to the fracture plane (right side of Figure 17). This rotation is required to correct for apparent dip of the fracture. Measuring the width at a number of points around the wellbore where the aperture is smallest minimizes the increase of apparent aperture caused by spalling during drilling and localized erosion. Alteration zones that characteristically surround a fracture are susceptible to damage during drilling. The drill bit causes an initial destruction of the fracture zone at its intersection with the drillhole. This is followed by erosion from fluid flow, reamer tools and logging tool trips. This means that fracture aperture as preserved in the BHTV log is an upper bound to the true aperture of the fracture at some distance away from the borehole. The term "apparent fracture aperture" is used in this text to describe what is, in effect, an average of a number of "minimum width" measurements.

Once the fracture orientation and, if possible, the apparent aperture have been measured the measurement is stored in a text window for further data reduction. The text window (Figure 17) can be edited to add field notes or additional information as to the

quality of the log. The data recorded are depth, dip direction and dip and aperture (if measured). The ASCII data can be saved using the standard Macintosh Save command in the File menu and later plotted in stereographic projection or as a profile to investigate trends in the fractures with depth or trends controlled by fracture width.

Measurement of the dip direction of fractures vertical fractures that intersect a portion of the borehole as a chord (Figure 16, right window) is accomplished by selecting and recording the azimuth of each fracture intersection. The dip direction of this fracture is the midpoint of these two azimuths.

A comprehensive analysis of the natural fractures intersecting the Cajon Pass research well in Southern California is a good example of the application of the fracture analysis software to field data. The Cajon Pass Well has been drilled to investigate the low stress low heat flow paradox along a major plate boundary. The fracture study was completed in order to characterize the macroscopic structure of the crust over the depth interval 1840 to 3450 m (6036.7 to 11,318 ft) (Barton and Zoback, 1990).

Orientations of all macroscopic fractures, corrected for fracture dip are shown in Figure 18 in a lower hemisphere stereographic projection. On the left side the data are presented as poles to fracture planes and on the right side they are presented in a contour diagram of pole densities using spherical Gaussian statistics (after Kamb, 1959). The Kamb method of contouring pole densities calculates the number of standard deviations from a uniform distribution of points on the projection. The contour shading shown in the legend in Figure 18 represents the standard deviation from a random distribution. While there is clearly a random component of fracture orientations, a statistically significant concentration of fractures strikes north-south and dips to the West. The primary concentration of fractures strikes at an azimuth of 175° and dips 63° West. Also shown in Figure 18 is the N60°W local trend of the San Andreas Fault (SAF) and the average orientation of S_{Hmax} determined through the analysis of in-situ wellbore breakouts and hydraulic fractures (N59°E, Shamir and Zoback, 1990). Although the San Andreas Fault is the dominant tectonic feature at this site the majority of the macroscopic fractures in the Cajon Pass well are neither aligned with the San Andreas nor parallel to the direction of maximum horizontal stress as is often assumed (e.g. Engelder, 1982).

The fracture distribution in the Cajon Pass well does not decrease with depth. Figure 19 shows a fracture frequency profile over a subset of the fracture data measured. Aside from the interval from 1940 to 1960 m (6364.8 to 6430.4 ft) of stress-induced wellbore breakouts (Shamir et al., 1988), which contain only a few observable fractures, the total fracture population shows no trend in size or distribution with depth over the logged interval. These results are in contrast with a fracture analysis from an Illinois

drillhole where fracture density and hydraulic conductivity decrease with depth (Haimson and Doe, 1983). Fracture studies of ten wells located in the western Mojave Desert just west of the Cajon Pass well by Seeburger and Zoback (1982) found only a slight decrease of fracture density with depth for most wells studied. They found some wells to have a uniform fracture density distribution while others showed concentrations of fractures at various depths as is the case in the Cajon Pass well.

Where fractures are open along the extent of their intersection with the borehole, apparent fracture aperture could be measured. The double asterisks in the second profile of Figure 19 correspond to zones where the fracture width per meter is greater than 10 cm; the single asterisks to zones with fracture width between 5 and 10 cm. The remaining intervals have nominal apparent aperture per meter. In several intervals with a high frequency of fractures the cumulative width per meter is quite low. However, where the apparent aperture per meter is large there are usually a large number of fractures. Although mechanisms acting to close fractures would be expected to reduce the number of open fractures with increasing depth, the data do not show this trend.

Figure 19 also shows the fracture population correlated with lithology and sonic velocities. The Cajon Pass experiment has provided an ideal complementary data set to examine the acoustic waveform response to fluid-filled fractures. The complete BHTV log and the digital analysis of fracture geometry were used in conjunction with the full waveform sonic data to determine the response to fractures (Barton and Moos, 1988). Note that there is little apparent relationship between fracture density and sonic velocity. A much greater correlation exists between the velocities and the apparent apertures determined from the BHTV logs. The relationship between Stoneley wave amplitude and permeability has been demonstrated by a number of authors (Paillet, 1980; Burnes, et al, 1988). The amplitude of the Stoneley wave is particularly sensitive to the presence of hydraulically conductive fractures intersecting the borehole wall (Paillet and White, 1982; Rosenbaum, 1974), but it is also affected by variations in the borehole diameter and the seismic properties of the rock. The Stoneley arrivals in the sonic waveforms recorded in this interval of the Cajon Pass well (Figure 19) are an excellent example of this response.

Measurements of the orientation, distribution and apparent aperture of macroscopic fractures in the Cajon Pass well are extremely important to the interpretation of other geophysical and core data. Current research into the statistical distribution of fracture aperture, fracture orientation, and fracture spacings are providing insight into the mechanical character of the brittle crust at the Cajon Pass site (Barton and Zoback, 1990).

Correlation of BHTV "Log" Data

Log interpretation has long been the basis for discriminating changes in lithology, fluid content of pore space, structural horizons and general physical properties of rock both for industry exploration and scientific research. Geophysical logs that are generally recorded in a freshly drilled well include the caliper, natural gamma, spectral natural gamma (from which K, U, and Th concentrations can be determined), induction resistivity, neutron porosity, gamma-gamma density, and sonic travel-time. Correlation of these logs and extracted core provides ideal information for physical properties measurements with depth.

BHTV travel time data can be used to generate extremely fine scale "logs" of variations in downhole parameters such as pseudo 4-arm caliper emulation, cumulative cross sectional area and wellbore eccentricity. These profiles may be correlated with dipmeter, full waveform, resistivity, and other diagnostic logs to assess borehole stability and to define permeable zones or lithologic boundaries. The depth resolution of image data is generally much finer than the 0.5 ft depth resolution of geophysical logs, however, digital smoothing or decimation of image data to the scale of conventional logs provides excellent "ground truth" to the complex process of geophysical log analysis.

BHTV data provides information at about 1 cm (0.3 in) intervals whereas typical logging produces a data point for every 15 cm (6 in) of wellbore. For this reason, analog BHTV images are commonly photo-reduced to the scale of log data (5" = 100') before correlations can be made. As mentioned previously interpretation of an analog BHTV image usually involves overlays and tedious drafting. Digital data provides several advantages over analog data for this type of coarse scale data interpretation and correlation with standard logs. The first is the simplicity of scaling with a minimal loss of information. The second advantage is the ease of constructing an interpreted BHTV log. In a coarse scale analysis only the large scale features such as breakout intervals or through-going fractures are required for interpretation. The location of these features can be plotted through interactive thresholding of amplitude and borehole radius where black represents a feature and all other variations in the data have been suppressed into a white background (Figure 20, right profiles). Fractures may also be interactively picked and the interpreted sinusoids plotted. Figure 20 shows standard geophysical logs over the interval 9600 to 9800 ft (2926 m to 2987 m) recorded in the Cajon Pass Research well with the corresponding digitally interpreted section of BHTV data. Major features include the sinusoidal trace of fractures and wellbore breakouts which are represented by discontinuous black zones at 180^{o} azimuths and fractures.

The following preliminary correlation of the analog field data over this interval was made by F. Paillet (written communication, 1988). The continuous interval of wellbore breakouts below depth 9800 ft (2987 m) is evident on the caliper log (Figure 20, track 4, curve 1) and the elongation of the borehole is very pronounced in the x-y caliper log (Figure 20, track 1, curves 1 and 2). The fracture zone just below 9700 ft (2956.6 m) has caused a marked decrease in both the LLS and LLD resistivity curves (Figure 20, track 2, curves 1 and 2) however this zone has a minimal effect on the neutron porosity logs (Figure 20, track 4, curves 2 and 3). Severe breakouts at 9665 ft (2945.9 m) cause an anomaly in the caliper (Figure 20, track 4, curve 1) and density logs (Figure 20, track 3, curve 3). Between 9600 and 9650 ft (2926 and 2941 m) breakouts are interrupted by small fractures; breakouts often terminate at the intersection of a fracture.

It is interesting to compare the digital interpretation of BHTV logs with an "interpreted section" made from the black and white Polaroid field logs by a scientist who is very familiar with BHTV data and very experienced in log interpretation. In addition, this particular expert has artistic talents useful to this sort of data reduction. In Figure 20, the far right window is the manual interpretation of the interval 9400 to 9600 ft (2865 to 2926 m) in the Cajon Pass well, sketched by F. Paillet (written communication, 1988). Thick lines represent the interpreted trace of larger fractures visible in the analog records and thin lines the trace of smaller fractures. Breakouts are again represented by vertical black bands. Fractures located in the digital counterpart to the interpreted interval compares well with the manually picked fractures. Breakouts reduce with good precision and correlate very well with the manually interpreted section. The most logical use of the digital interpretation is to provide an easily generated, accurate base plot either for further computer based interpretation or manual interpretation. Scientists that lack substantial experience with interpreting BHTV data or general log interpretation (or artistic capabilities) can produce more reliable interpretations with the help of the digital BHTV system.

BHTV Generated "Logs"

Caliper tools usually have two to four mechanical arms that measure the borehole diameter with depth. The BHTV log can be thought of as having several hundred "arms" which provides data at a scale that is 15 times finer than the standard caliper log. In order to emulate the HDT Dipmeter tool, the horizontal and vertical resolution of the BHTV data must be made comparable to that of the HDT dipmeter pad. Performing a horizontal 15 point median filter is generally sufficient to mimic the HDT Dipmeter pad width. The maximum value in each scan of the filtered data then provides one radius and azimuth of the long axis caliper pair. The orthogonal values provide the short axis caliper pair. Averaging

successive caliper values with depth provides the correct vertical adjustment for comparison with the HDT dipmeter tool. Figure 21a represents the fit of the BHTV generated "four arm" caliper to a typical scan of BHTV data and 21b the fit over an interval of wellbore breakouts measured from the same well. Black represents the data scan and gray the measured four arm radii. Caliper information in this form can be easily correlated with other log data and with dipmeter data. As is the case with dipmeter data the caliper data can be used to discriminate between breakout zones, washout zones, zones of key seating and perfectly in-gauge zones (Plumb and Hickman, 1985). The long caliper arm measured in this way in many cases corresponds to the direction of minimum horizontal principal stress and in such a log provides a rapid method for breakout orientation analysis with depth. The left window in Figure 22 shows the image data for a 12 ft (3.7 m) interval of wellbore breakouts in the Auburn Geothermal Well, New York. The adjacent profile shows the emulation of the 4 arm dipmeter tool over this depth interval. The scatter plot indicates the orientation wellbore breakouts determined from this analysis.

There are a variety of causes for a non-circular borehole and wellbore breakouts may or may not coincide with the overall ellipticity of the borehole. For example, ellipticity can be drilling induced where the bit has tended to move up dip during drilling. The borehole wall may preferentially spall or washout in response to in situ stresses. A least-squares fit of an ellipse to the BHTV scans is used to measure the eccentricity of the borehole. The algorithm fits an ellipse to a field of points after each radius value is transformed to Cartesian x, y space from the polar r, θ pair by $x = r \cos \theta$, $y = r \sin \theta$. The angle of the ellipse is given by:

$$\phi = \frac{1}{2} \tan^{-1} \frac{\Sigma xy}{\Sigma x^2 - \Sigma y^2} \qquad (4)$$

A least-squares algorithm is used to determine the major, a, and minor, b, axes of the ellipse. From the equation of an ellipse:

$$b^2x^2 + a^2y^2 = a^2b^2 \qquad (5)$$

we have:

$$y^2 = b^2\left(1 - \frac{x^2}{a^2}\right) \qquad (6)$$

or

$$\hat{Y}_i = \left[b^2\left(1 - \frac{X_i^2}{a^2}\right)\right]^{1/2} \qquad (7)$$

where $\hat{Y}_i$ is the estimated value of Y_i at specified values of X_i.

We want to have $\sum_{i=1}^{n} Y_i^2 = (\hat{Y}_i - Y_i^2) = \text{minimum:}$

$$\sum_{i=1}^{n} Y_i^2 = b^2 n - \frac{b^2}{a^2} \sum_{i=1}^{n} X_i^2 \qquad (8)$$

Setting $b = b_0$ and $b_1 = b/a$ we have:

$$\sum_{i=1}^{n} Y_i^2 = b_0^2 n - b_1^2 \sum_{i=1}^{n} X_i^2 \qquad (9)$$

$$\sum_{i=1}^{n} X_i^2 Y_i^2 = b_0^2 n \sum_{i=1}^{n} X_i^2 - b_1^2 \sum_{i=1}^{n} X_i^4 \qquad (10)$$

Equations 9 and 10 are then inverted to determine the unknown values of b_1 and b_0. Generally only 20 equally spaced data points are required to accurately determine the shape of the ellipse. The percent eccentricity of the ellipse, defined as $\frac{a-b}{(a+b)/2}$, is calculated for each scan. Borehole televiewer data is capable of resolving borehole ellipticity in much finer detail than conventional caliper logs. Without some knowledge of borehole ellipticity the separation between caliper curves (C1 and C2 in standard HDT presentation) may be erroneously interpreted as wellbore breakouts.

Another profile computed with the BHTV travel time data is borehole the cross sectional area. The log of borehole cross sectional area is calculated by integrating adjacent triangles defined by the travel time values and the center of the borehole. Borehole irregularities, washouts or key seats for example, are indicated by large fluctuations in this log. A profile of cumulative cross sectional area with depth is also available. These logs are important for the determination of wellbore stability. A featureless borehole will have a smooth slope in its cumulative profile of cross sectional area whereas breaks in slope may indicate borehole failure.

The amplitudes of reflectivity values are used to generate a reflectivity log as an aid in the detection of lithologic and structural boundaries. Acoustic reflectivity of the borehole wall as measured by the BHTV tool has incorporated the effects of the impedance contrast from various rock types and the borehole fluid along with the effects of energy scattering from irregularities in the borehole wall. The true reflection amplitude is proportional to the

reflection coefficient at the borehole wall plus an unknown variation in amplitude due to scattering (the angle between the beam and the reflecting surface), thus no quantitative value of the reflectivity can be associated with a particular lithology. Because of these combined effects however, the BHTV image of the amplitude of the reflected energy often shows more detail than does the surface topography. This is particularly true for logged intervals of sedimentary rock where rock properties vary over small distances.

To determine the reflectivity value to represent a given depth interval a histogram of the amplitude values is computed for each scan. A single scan in the BHTV data has values that represent the reflectivity of unperturbed rock as well as reflectivity values associated with structural or erosional features (e.g. fractures, tool reamer marks). Interactive thresholding is used to determine the cutoff reflectivity value that best isolates the particular feature of interest. For example, to sample only the intact rock, a threshold determined cutoff reflectivity value is used above which histogram bins will be used to compute the mode value of the amplitude for each data scan as a single representative value. Figure 23 shows the results of this statistical approach to an interval containing the contact between a basement marble formation and an overlying sandstone unit at 5051 ft (1539.5 m) in the Auburn Well, New York. The marble has a very different reflectivity character that the overlying sediment and the contact can be more easily picked in the "log" plot than in the image itself.

Reflectivity logs can be used for correlation with companion log data. Sharp decreases in reflectivity track breakout zones exactly and the decrease has been found to be proportional to the width of the breakout (Zoback and Moos, 1988). Reflectivity logs prove to be quite useful for correlation with other log data to isolate borehole features such as breakouts and fractures. Using reflectivity logs generated from the analysis of BHTV data Zoback and Moos (1988) found that low reflectivity values correlate with breakout zones in the Moodus Research Well located in New York state. Reflectivity profiles used in conjunction with the BHTV caliper log are useful for discriminating between natural through going fractures and wellbore breakouts. A sharp low reflectivity response associated with a strong kick in the eccentricity log characterizes a natural fracture whereas low reflectivity values over a finite length of the borehole associated with a consistent azimuth of the major elliptical axis generally represents breakout zones.

SOFTWARE IMPLEMENTATION

As discussed previously, user interface consistency among application programs is an important factor in the ease of use of Macintosh computers. To help achieve the desired consistency in BHTVImage, the program was implemented using an Apple product called MacApp, in whose original development one of us played a part. MacApp is a so-called "object-oriented framework", i.e., a "generic" application that defines standard "objects" like windows and views. Any desired Macintosh application can be derived from MacApp by describing in program code only the differences between that application and the generic one. The resulting program achieves consistency with other Macintosh applications without special effort on the part of the programmer.

MacApp, as well as the bulk of the BHTV analysis program, is written in the object-oriented language Object Pascal. Object Pascal is an extension of the Pascal language that provides a record-like structure type called an "object type". One type of object can be defined as being a subtype of another type. If type "dog" is defined as a subtype of "mammal", it means that the characteristics of dogs are generally the same as those of mammals. Only differences need be specified. One must specify that dogs wag their tails and bark, but one need not specify that dogs breathe--that characteristic is inherited from mammals.

MacApp provides a type of object called a "document." A document is a file containing text, graphic, and/or image data. The definition of type document specifies attributes that every document must have, e.g., a file name. The definition also defines operations that can apply to any document, such as "opening" it for examination and possible change, "printing" it onto paper, and "saving" changes to the disk.

BHTVImage, in turn, defines an object type "BHTVDocument" that is a subtype of the standard MacApp document. A BHTVDocument is like the generic document except it sports additional attributes like well name and fluid velocity, and it defines additional operations such as the ability to convert a travel time measurement to a radius.

MacApp provides another type of object called a "view", used to display part or all of a document in a form desired by the user. BHTVImage also defines three major types of views: the unwrapped view, which displays false-color image data; the profile view, which can graph a profile of one parameter sampled at each depth in a range; and the plot view, which can graph data sampled at numerous places at each depth. BHTVImage further defines several types of plot views, e.g., the travel time histogram, the polar cross section, the Cartesian cross section, and the 3-D cylindrical projection. A cross section view

inherits the characteristics of a plot view and adds its own. A plot view *inherits* the characteristics of a generic view and adds its own.

The document and the view are the two most important object types defined by MacApp. The third most important object is called the "command". The generic command provides generic ways of dealing with doing the command, undoing it, and redoing it. If the command is issued by mouse action (like drawing a box in MacDraw), then the generic command also provides generic ways of tracking the movements of the mouse and giving the user an advance look at what will result when the mouse action terminates. In BHTVImage, subtypes of the generic command object are defined to support the following user actions, among others: changing a threshold value through a sliding scale; changing the hue of a palette color; cutting selected scans from the data file.

Certain BHTV analysis subroutines are written in the language C. The Macintosh Programmer's Workshop, a suite of software development tools, allows modules written in different languages (e.g., Pascal, C, Fortran, and Assembler) to be linked together into a single program and for procedure calls to be made between the modules.

CONCLUSIONS

The analysis of image data requires a high level of interactive manipulation by the analyst. Various features need to be observed in an optimal view in order to detect subtle features and the analyst must be able to make decisions as the analysis proceeds. To meet these goals for the image analysis of borehole televiewer data we have taken advantage of the interactive user interface of the Apple, Inc. Macintosh II computer. In addition, in order to conform to the Macintosh user interface standards we used an Apple, Inc. product called MacApp; a developer's tool that provides easy programming access to the windows, menus, and dialog boxes of the Macintosh user interface. The program design defines a set of tools specific to borehole cylindrical geometry and to the particular features that are imaged by and can be quantified by BHTV data (e.g. fractures, wellbore breakouts). The program also provides a base for experimentation with new techniques to improve data quality, develop new measurement techniques and to explore unusual features encountered in a particular data set.

BHTVImage has been used as the primary analysis tool for BHTV data recorded in the Cajon Pass scientific research well in southern California and is also being used at the KTB ultradeep well site in Germany for the analysis of wellbore breakouts and the evaluation of wellbore stability.

Although the software is specific to BHTV data the analysis tools extend to other types of image data, for example the Schlumberger, Inc., Formation Microscanner (FMS). The human interface approach, however, extends beyond image analysis programs. Geophysicists often encounter data that is voluminous and complex. They require the freedom to pursue various paths of reasoning and curiosity in order to make scientific discoveries without the burden of extensive computer programming at each turn in the path. One of the ways to achieve this freedom is to develop software tools that permit interaction with the data and minimize interaction with the computer. Our current work includes the development of similar analysis tools for the analysis of FMS image data and standard geophysical logs.

ACKNOWLEDGMENTS

The authors would like to thank Apple Computer, Inc. for their cooperation in the development of BHTVImage. This work was supported in part by the Continental Lithosphere Program of the National Science Foundation through DOSECC, by the Kontinentales Tiefbohrprogramm of the Federal Republic of Germany, and by the contributors to the Stanford Rock Physics and borehole Geophysics Project.

REFERENCES

Barton, C.A. and Zoback, M.D., 1990. Self-similar distribution and properties of macroscopic fractures at depth in crystalline rock in the Cajon Pass scientific drillhole, Journ. Geophy. Res., in press.

Barton , C.A., 1988, Development of in situ stress measurement techniques for deep drillholes, Ph.D. Thesis, Stanford University.

Barton, C.A., Zoback, M.D. and Burns, K.L., 1988, In situ stress orientation and magnitude at the Fenton Geothermal site, New Mexico, determined from wellbore breakouts, Geophy., Res. Let, 15, 467-470.

Barton, C.A. and Moos D., 1988, Analysis of macroscopic fractures in the Cajon Pass Scientific Drillhole over the interval 1829 - 2115 meters, Geophy. Res. Let., 15, 9, 1013-1016.

Broding, R. A., 1982. Volumetric scanning well logging: The Log Analyst, 23, 1, 14-19.

Burnes, D.R., Cheng, C.H., Schmitt, D.P. and Toksoz, M.N. 1988. Permeability estimation from full waveform acoustic logging data, The Log Analyst, 29, 112-122.

Engelder, T., 1982. Is there a genetic relationship between selected regional joints and contemporary stress within the lithosphere of North America?, Tectonophysics, 1, 161-177.

Faraguna, J.K., Chace, D.M. and Schmidt, M.G., 1989. An improved borehole televiewer system — image acquisition analysis and integration: S.P.W.L.A. Annual Logging Symp., 30th, Denver, CO., Trans, Paper UU.

Fehler, M., House, L., and Kaieda, H., 1986, Seismic monitoring of hydraulic fracturing, 27th U.S. Symposium on Rock Mechanics, Univ. of Alabama, 606-613.

Georgi, D. T., 1985, Geometrical aspects of borehole televiewer images. SPWLA Logging Symposium Transactions, Paper 1-C.

Haimson, B. C. and Doe, T.W., 1983, State of stress, permeability and fractures in the Precambrian granite of northern Illinois, Journ. Geophy. Res., 88, 7355-7371.

Hinz, K. and Schepers, R., 1985, SABIS - The digital version of the borehole televiewer, Eighth European Formation Evaluation Symposium.

Kamb, W.B., Ice petrofabric observations from Blue Glacier, Washington, in relation to theory and experiment, J. Geophy. Res., 64, 1891-1910, 1959.

Lysne, P., 1986, Determination of borehole shape by inversion of televiewer data, The Log Analyst, 26, 64-71.

Paillet, F. L., 1980, Acoustic propagation in the vicinity of fractures which intersect a fluid filled borehole, SPWLA, 21st Ann. Log. Symp., Paper D.

Paillet, F. L. and White J. E., 1982, Acoustic modes of propagation in the borehole and their relationship to rock properties: Geophysics, 47, 8, 1215-1228.

Pasternack, E.S. and and Goodwill, W.P., 1983. Applications of digitial borehole televiewer logging: S.P.W.L.A. Annual Logging Symposeum, 25th, Calgary, Canada, Trans., Paper C.

Plumb, R.A. and Hickman, S.H., 1985, Stress induced borehole elongation: A comparison between the four-arm dipmeter and the borehole televiewer in the Auburn Geothermal well, Journ. Geoph. Res., 90, B7, 5513-5521.

Rambow, F.H.K., 1984. The borehole televiewer — some field examples: S.P.W.L.A. Annual/ Logging Symp, 25th, New Orleans, La., Trans., paper C.

Richards, J.A., Remote sensing digital image analysis, Springer-Verlag, New York, 1986.

Rosenbaum, J.H., 1974, Synthetic microseismograms: logging in porous formations, Geophysics, 39,14-32.

Seeberger, D.A. and Zoback, M.D. 1982, The distribution of natural fractures and joints at depth in crystalline rock, Journ. Geoph. Res., 87, 5517-5534, 1982.

Shamir, G. and Zoback, M.D., 1990, In situ stress orientation near the San Andreas fault: Preliminary results to 2.1 km depth from the Cajon Pass Scientific Drillhole, Journ. Geophy. Res, in press.

Taylor, T.J., 1983. Interpretation and application of borehole televiewer surveys: S.P. W.L.A. Annual Logging Symp., 24th, Calgary, Canada, Transactions, Paper QQ.

Wiley, R. 1980. Borehole televiewer — revisited: S.P.W.L.A. Annual Logging Symp, 21st, Lafayette, La., Trans., Paper HH.

Wong, S.A., Startzman, R.A., and Kuo, T-B, 1989. Enhancing borehole image data on a high-resolution PC: Soc. Pet. Eng, SPE 19124, 37-48.

Zemanek, J., Glenn, E.E., Norton, L.J. and Caldwell, R.L., 1970, Formation evaluation by inspection with the borehole televiewer. Geophysics, 35, 254-269.

Zoback, M.D., Moos, D., Mastin, L., Anderson, R.N., 1985, Wellbore breakouts and in situ stress, J. Geophys. Res., 90, 5523-5530.

Zoback, M.D. and Moos, D.,1988, In situ stress, natural fracture and sonic measurements in the Moodus, Connecticut scientific research well, report prepared for Woodword-Clyde Consultants, Wayne, N.J.

Table I

Data Attribute	Definition
Well Name	Well identification used as title for graphics output
Well Location	Well location used as title for graphics output
Log Date	Date BHTV data were recorded
Mag Dec	Magnetic declination at site in degrees east of north
Marker	Azimuth correction for data collected in marker mode
Deviation	Borehole deviation in degrees
Max Depth	Bottom depth of digitized interval
Min Depth	Top depth of digitized interval
Tool Spec	Calibration adjustment
Tool Units	Units of the calibration adjustment
Fluid Vel	Velocity of the borehole fluid during logging
Vel Units	Units of the fluid velocity
Ddelay	Time delay for initiation of digitization in μs
Tool Offset	Transit time from the transducer to its housing in μs
Samprt	Sample rate in samples/μs
Window	Sampling window length in μs
Samples	Number of samples digitized for each pulse
Max TT	Maximum recorded travel time
Max AMP	Maximum recorded amplitude of the reflected pulse
Min TT	Minimum recorded travel time
Min AMP	Minimum recorded amplitude of the reflected pulse
Cutoff TT	Array of histogram equalization bins for travel time
Cutoff AMP	Array of histogram equalization bins for amplitude
Width	Number of pulses per scan
Height	Total number of scans (full revolutions) in the data file

FIGURE CAPTIANS

Fig. 1. (a) Schematic diagram of the acoustic mechanism of the borehole televiewer. (b) Analog wave train of the televiewer signal.

Fig. 2. Intersection of a plane with a cylinder and the effective sinusoidal curve on the 2-D unwrapped cylindrical surface (from Zemanek, et al., 1970).

Fig. 3. Standard unwrapped 360° images of the borehole wall. Vertical axis is depth, horizontal axis is azimuth, and color represents the amplitude of the reflected pulse (left window) or the borehole radius (right window).

Fig. 4. Highlighting in 2-D view (left window) over a cross bedded interval of BHTV data recorded in a Gulf Coast well indicates user selection of the image data for rendering 3-D projections. 3-D projection where surface color represents the amplitude value (middle window) and 3-D projection in black and white (right window) where differences in weathering of the beds is apparent.

Fig. 5. The right window is an unwrapped view of borehole radius over a 14 ft interval of breakouts in the Cajon Pass well. The left window shows data scans in polar cross section and the interactive analysis of breakout azimuth and width for this data.

Fig. 6. Top window is a cross plot of the reflectivity values (x-axis) versus traveltime values (y-axis) over an interval in the Cajon Pass well where the BHTV tool was off-center in the borehole. The bottom window is the cross plot over the same interval after the data have been corrected for off-center effects.

Fig. 7. An example of the effects of histogram equalization. The left display shows the standard linear color distribution and the right panel the equalized color distribution. Note that the details of the cross bedding are enhanced at depth 7380.5 ft using the equalized color scale.

Fig. 8. Right window is the amplitude of the reflected energy and the left window the borehole radius where cutoff threshold levels have been used to suppress all data except borehole features.

Fig. 9. Right window shows unedited BHTV data recorded in HOLE 504B located in the East Pacific Rise, left window shows the results of visual editing where breakouts are now visible in the data centered at azimuths 100° and 280° between depths 6,406 and 6,401 ft.

Fig. 10. The possible raypaths for the BHTV pulse for circular and elliptical boreholes with centralized and off-centered tools (after Georgi, 1985).

Fig. 11. Workstation screen showing the interactive data correction of borehole geometric effects. Upper left polar plot shows original data scan and corrected scan of data. Histograms of the original travel time data (yellow) and the corrected data are shown in the upper right plot. The lower plot represents the original data and the corrected data in cartesian coordinates where the x axis is azimuth and the y axis is radius.

Fig. 12. Geometry of the correction of BHTV data for the effects of an off-centered tool in a circular borehole.

Fig. 13. Polar cross sections are sample scans of the synthetic data (black) and data corrected for the effects of an off-center tool in an elliptical borehole (gray). The cross hairs mark the center position for each scan.

Fig. 14. Schematic representation of the breakout process showing the angle of breakout initiation ϕ_b. Also shown is BHTV data over a breakout interval where polar cross sections delineate the breakout shape.The radial lines indicate the picks of breakout width. Breakout azimuth is the bisector of this angle.

Fig. 15. (a) Histogram of breakout azimuths over a 262 m interval in the EE-3 well of the Fenton Geothermal Field. (b) Histogram of breakout widths over the same 262 m interval.

Fig. 16. Left window shows intersecting fractures at depth 5135.5 ft in the Auburn Geothermal well, New York. White curve represents the interactive fit to a steeply dipping fracture. Right window is an example of data recorded over a complex fracture zone where fractures are not perfectly planar in a well located near Anza, California.

Fig. 17. Interactive fit of a flexible sinusoid to a shallow dipping fracture at depth 3321 m in the Cajon Pass research well is shown in the left window. In the right window is the 3-D cylindrical image of the fracture plane.

Fig. 18. (a) Lower hemisphere equal area projection of poles to fracture planes over the interval 1829 to 3454 m in the Cajon Pass reserach well. (b) Kamb contours of the poles to fracture planes over the same interval. Also shown is the orientations of the San Andreas Fault (SAF) and the principal stress directions determined from wellbore breakout and hydraulic fracturing experiments in the well.

Fig. 19. Lithology, fracture density, apparent aperture, sonic velocities and filtered sonic waveforms over the interval 1829 to 2115 m in the Cajon Pass research well.

Fig. 20. Standard Schlumberger logs over the interval 9600 to 9800 ft in the Cajon Pass research well correlated with BHTV data recorded over the same interval. The BHTV data have been both digitally and manually interpreted.

Fig. 21. (a) Black represents the data scan and gray the "four arm" caliper measurement for a typical scan of data. (b) Black represents the data scan and gray the "four arm" caliper measurement over an interval of wellbore breakouts. (c) Black represents the data scan and gray the fit of an ellipse to a typical scan of data. The major axis of the ellipse is shown for reference. (d) Black represents the BHTV data scan and gray the fit of an ellipse over an interval where breakouts are evident.

Fig. 22. Caliper analysis over a 30 ft interval of wellbore breakouts in the Auburn Geothermal well, New York.

Fig. 23. Reflectivity log over the contact between the basement marble formation and the Potsdam sandstone from data recorded in the Auburn Geothermal Well, New York.

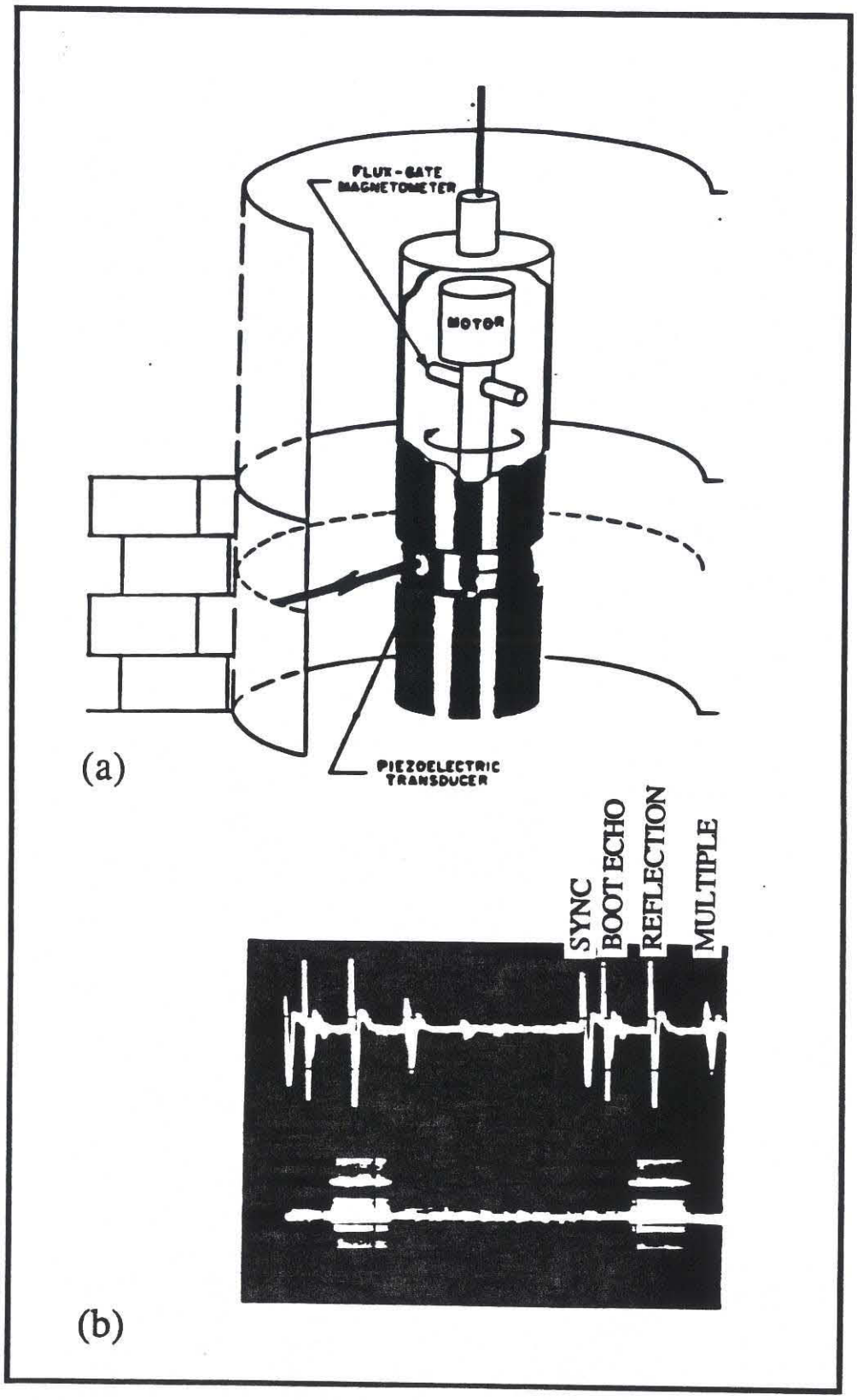
FLUX-GATE MAGNETOMETER
MOTOR
PIEZOELECTRIC TRANSDUCER
(a)
SYNC
BOOT ECHO
REFLECTION
MULTIPLE
(b)

Figure 1

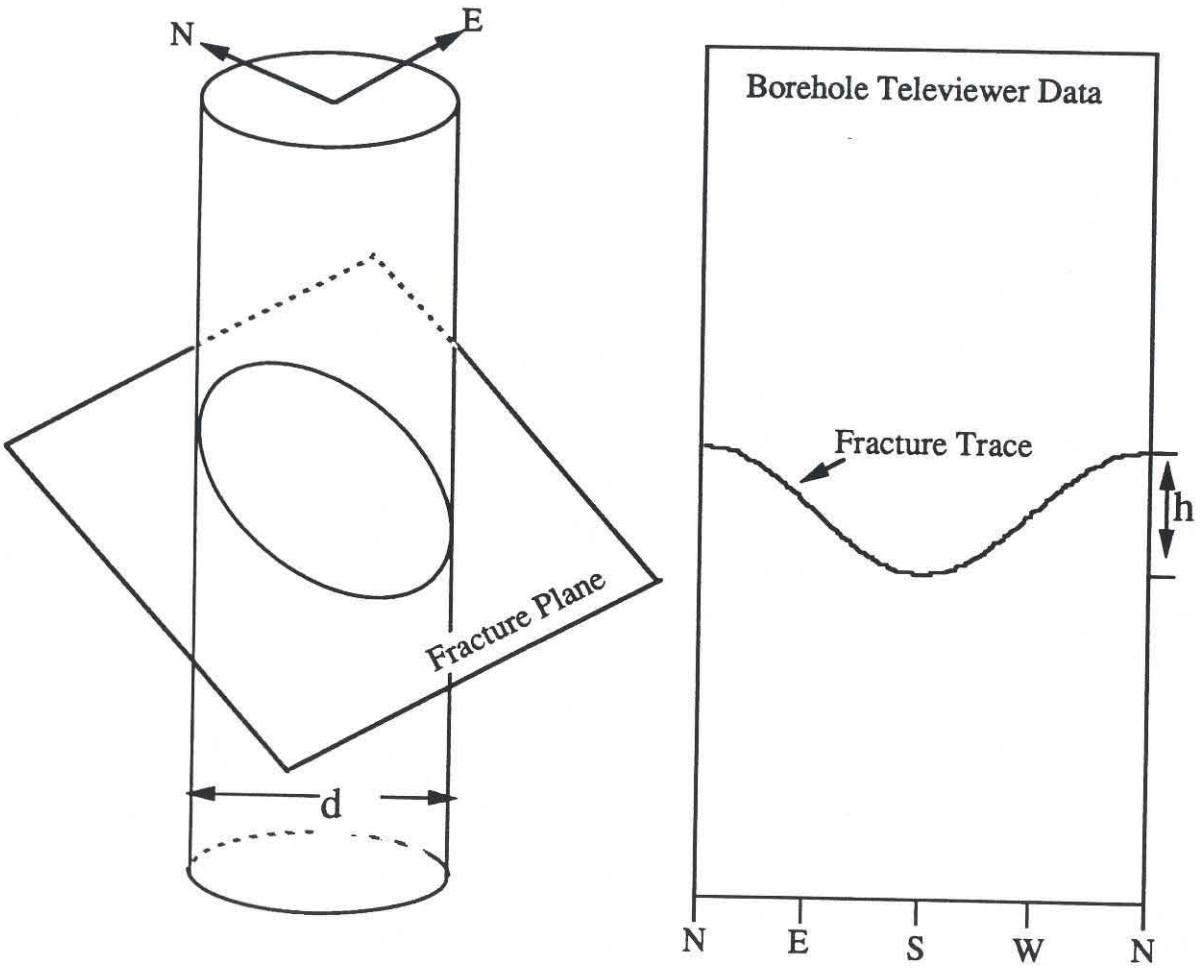
N
E
Fracture Plane
d
Borehole Televiewer Data
Fracture Trace
h
N
E
S
W
N

Figure 2

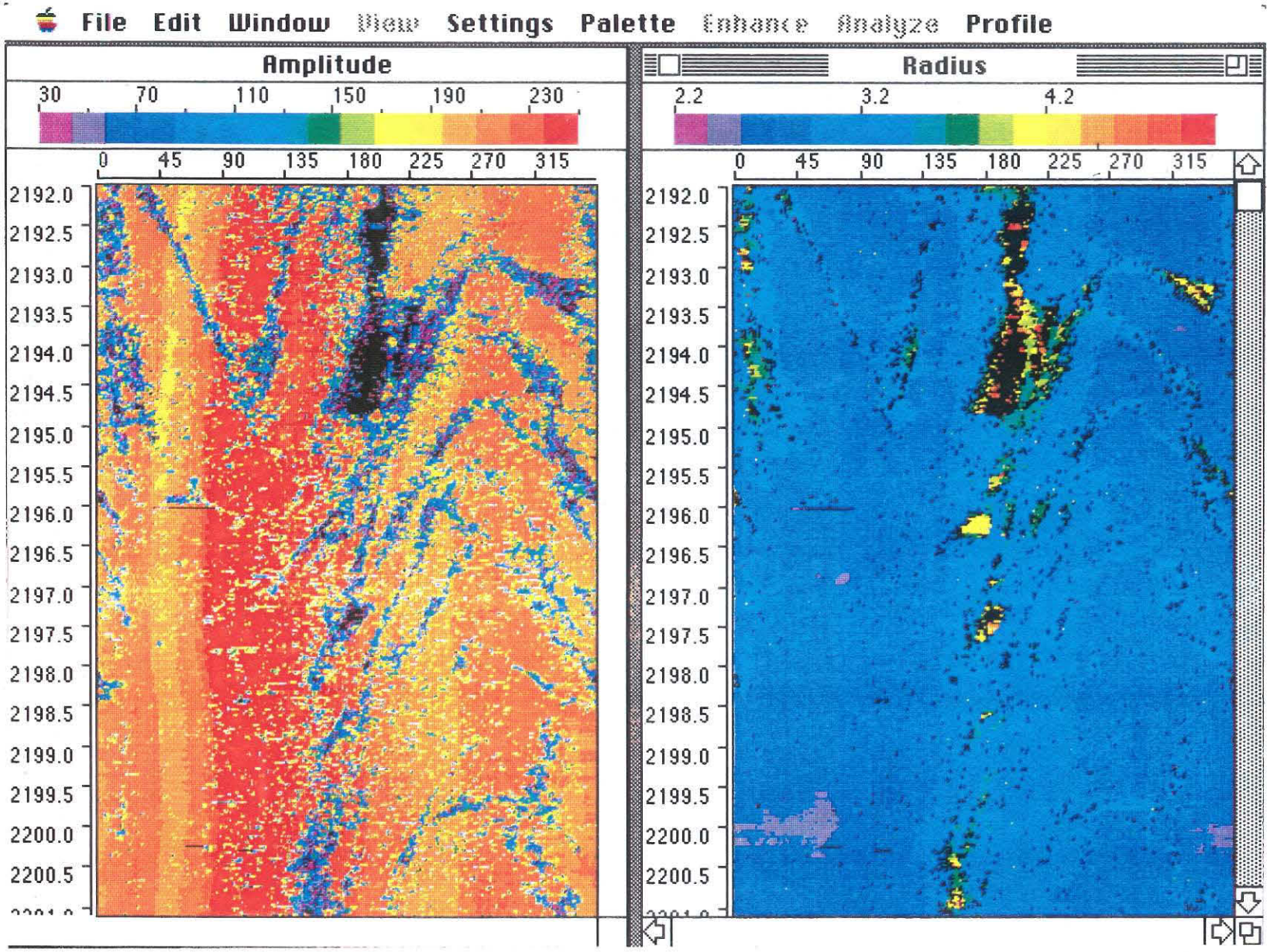
File Edit Window View Settings Palette Enhance Analyze Profile
Amplitude
30 70 110 150 190 230
0 45 90 135 180 225 270 315
2192.0 2192.5 2193.0 2193.5 2194.0 2194.5 2195.0 2195.5 2196.0 2196.5 2197.0 2197.5 2198.0 2198.5 2199.0 2199.5 2200.0 2200.5
Radius
2.2 3.2 4.2
0 45 90 135 180 225 270 315
2192.0 2192.5 2193.0 2193.5 2194.0 2194.5 2195.0 2195.5 2196.0 2196.5 2197.0 2197.5 2198.0 2198.5 2199.0 2199.5 2200.0 2200.5

Figure 3

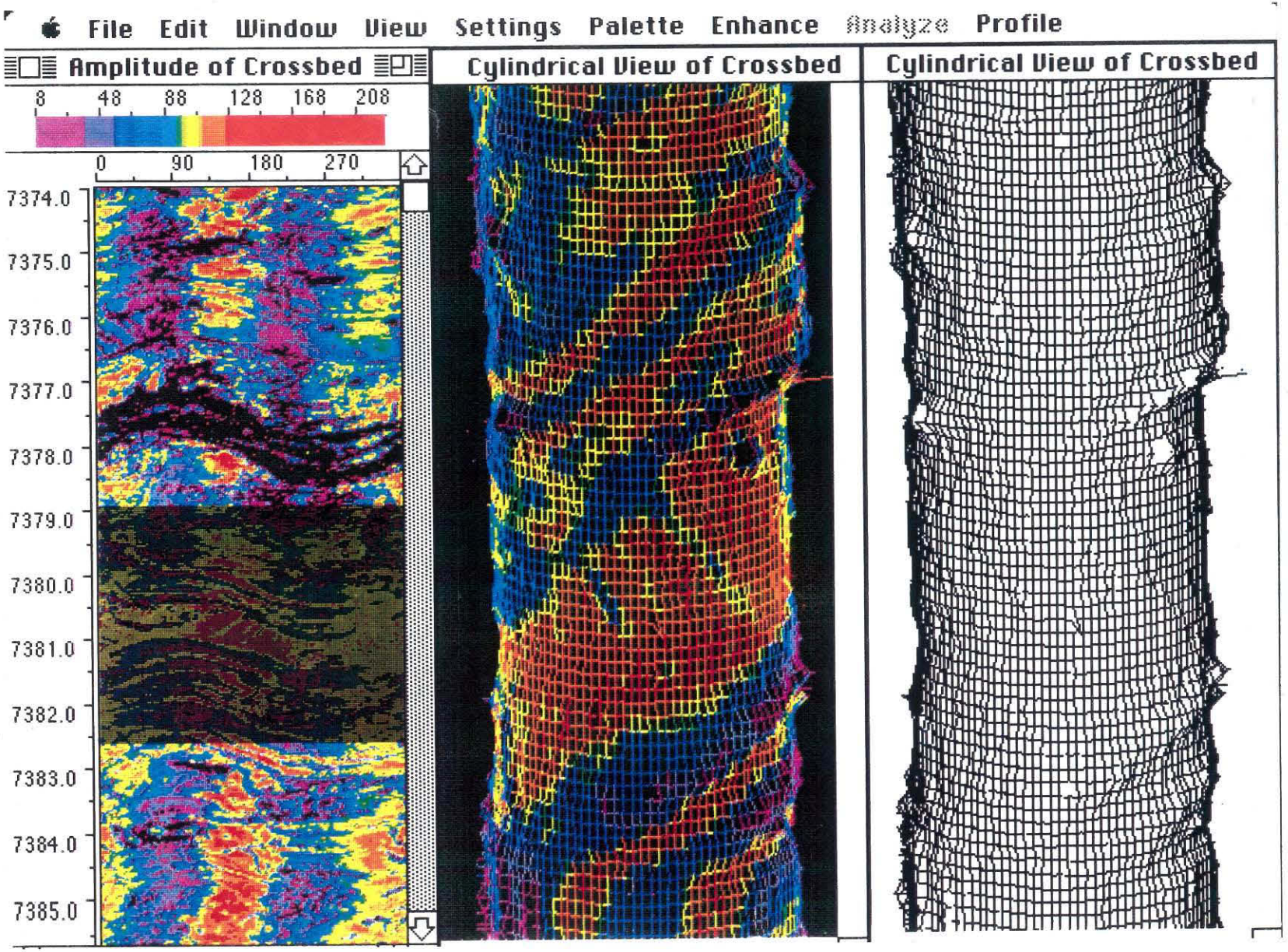
File Edit Window View Settings Palette Enhance Analyze Profile
Amplitude of Crossbed
8 48 88 128 168 208
0 90 180 270
7374.0
7375.0
7376.0
7377.0
7378.0
7379.0
7380.0
7381.0
7382.0
7383.0
7384.0
7385.0
Cylindrical View of Crossbed
Cylindrical View of Crossbed

Figure 4

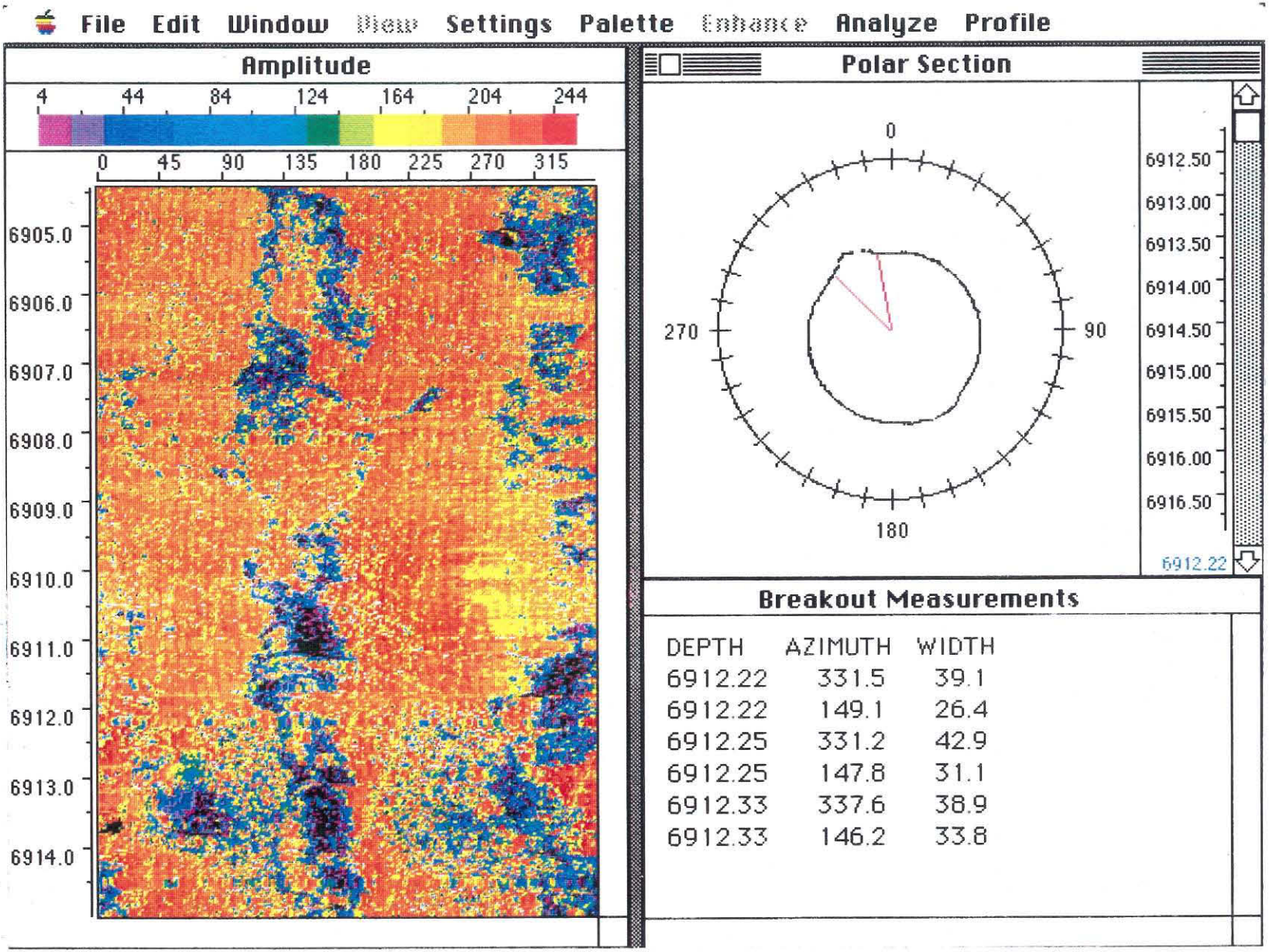
File Edit Window View Settings Palette Enhance Analyze Profile
Amplitude
4 44 84 124 164 204 244
0 45 90 135 180 225 270 315
6905.0
6906.0
6907.0
6908.0
6909.0
6910.0
6911.0
6912.0
6913.0
6914.0
Polar Section
0
90
180
270
6912.50
6913.00
6913.50
6914.00
6914.50
6915.00
6915.50
6916.00
6916.50
6912.22
Breakout Measurements
DEPTH AZIMUTH WIDTH
6912.22 331.5 39.1
6912.22 149.1 26.4
6912.25 331.2 42.9
6912.25 147.8 31.1
6912.33 337.6 38.9
6912.33 146.2 33.8

Figure 5

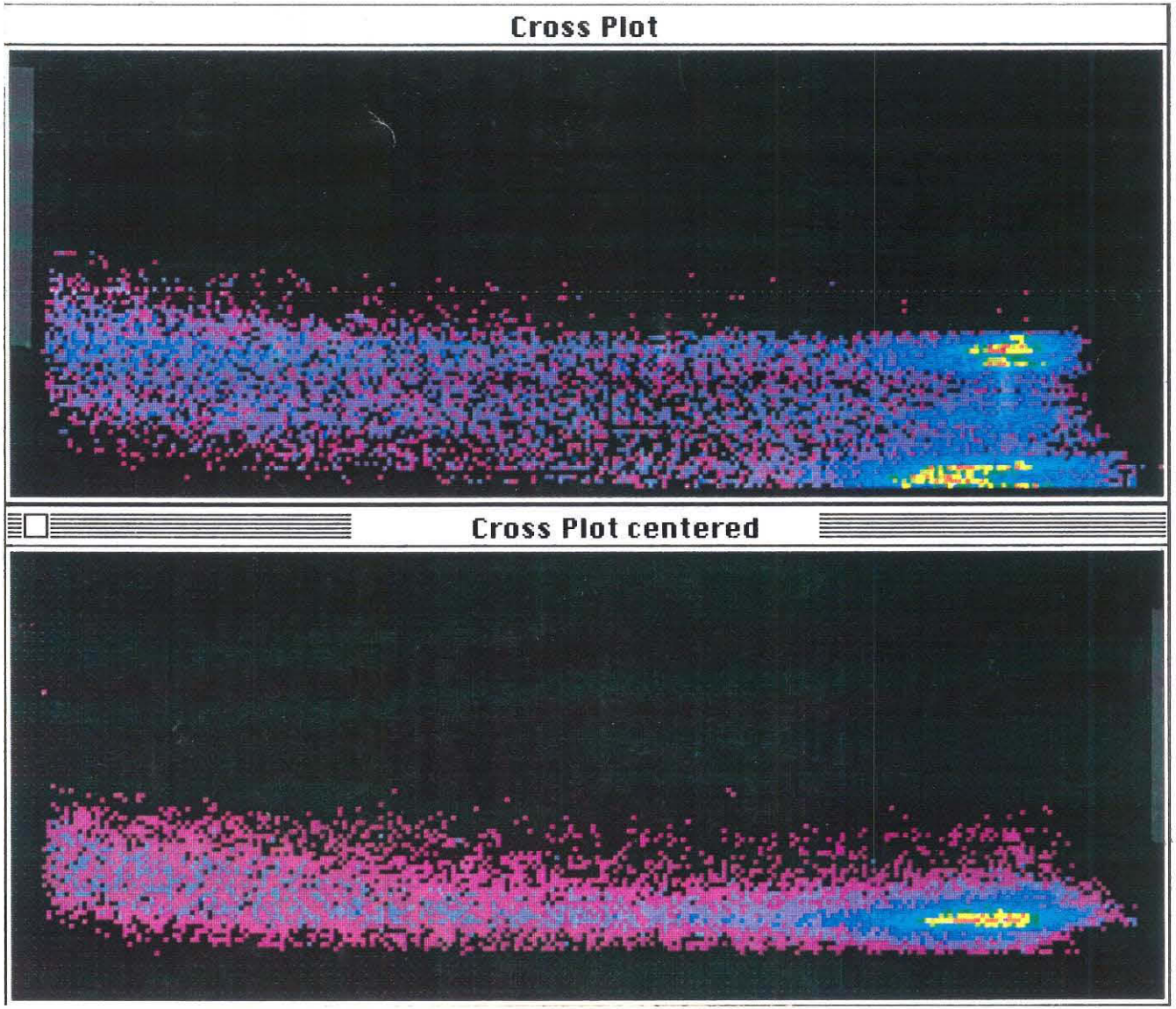

Figure 6

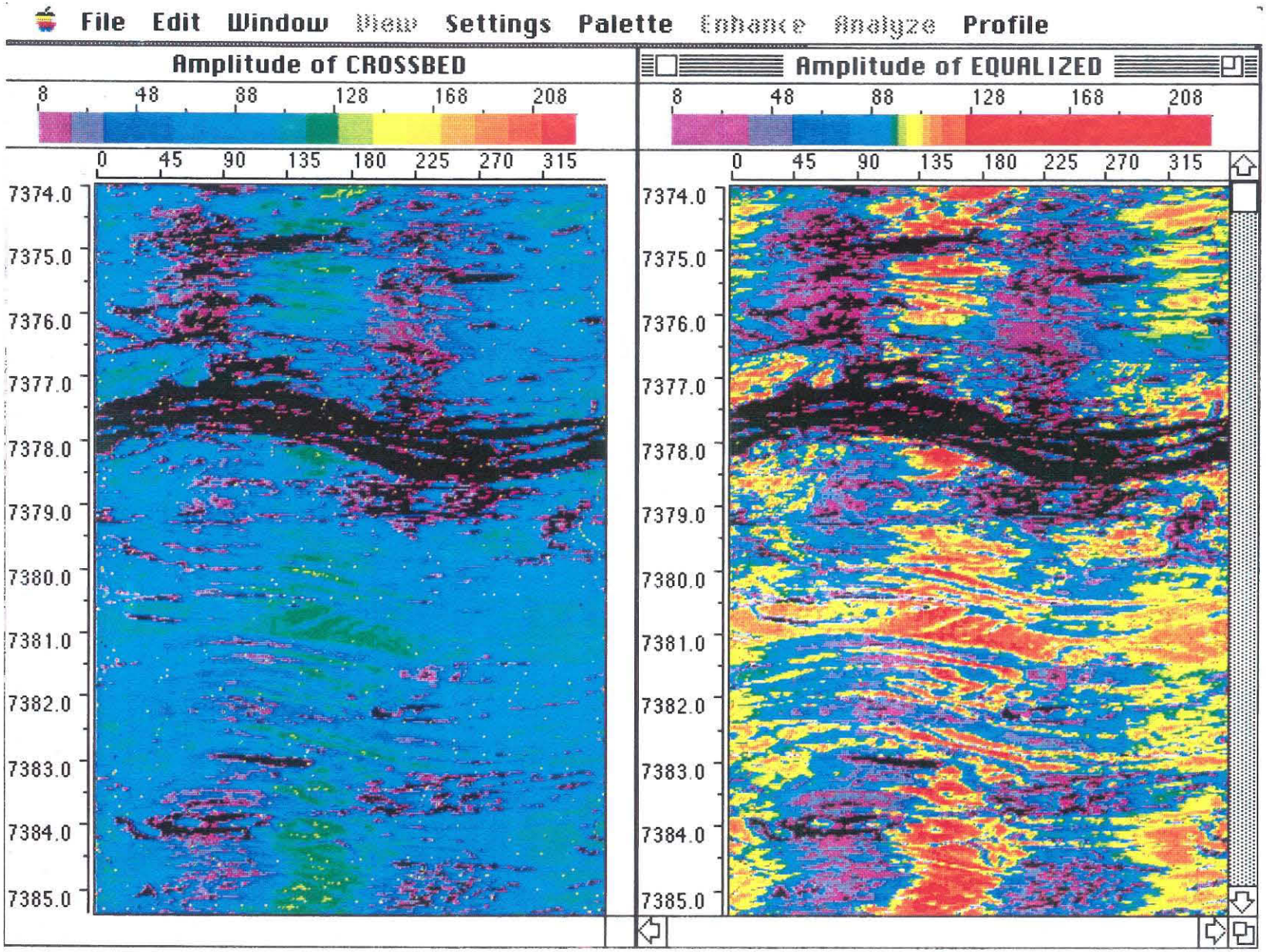
File Edit Window View Settings Palette Enhance Analyze Profile
Amplitude of CROSSBED
8 48 88 128 168 208
0 45 90 135 180 225 270 315
7374.0 7375.0 7376.0 7377.0 7378.0 7379.0 7380.0 7381.0 7382.0 7383.0 7384.0 7385.0
Amplitude of EQUALIZED
8 48 88 128 168 208
0 45 90 135 180 225 270 315
7374.0 7375.0 7376.0 7377.0 7378.0 7379.0 7380.0 7381.0 7382.0 7383.0 7384.0 7385.0

Figure 7

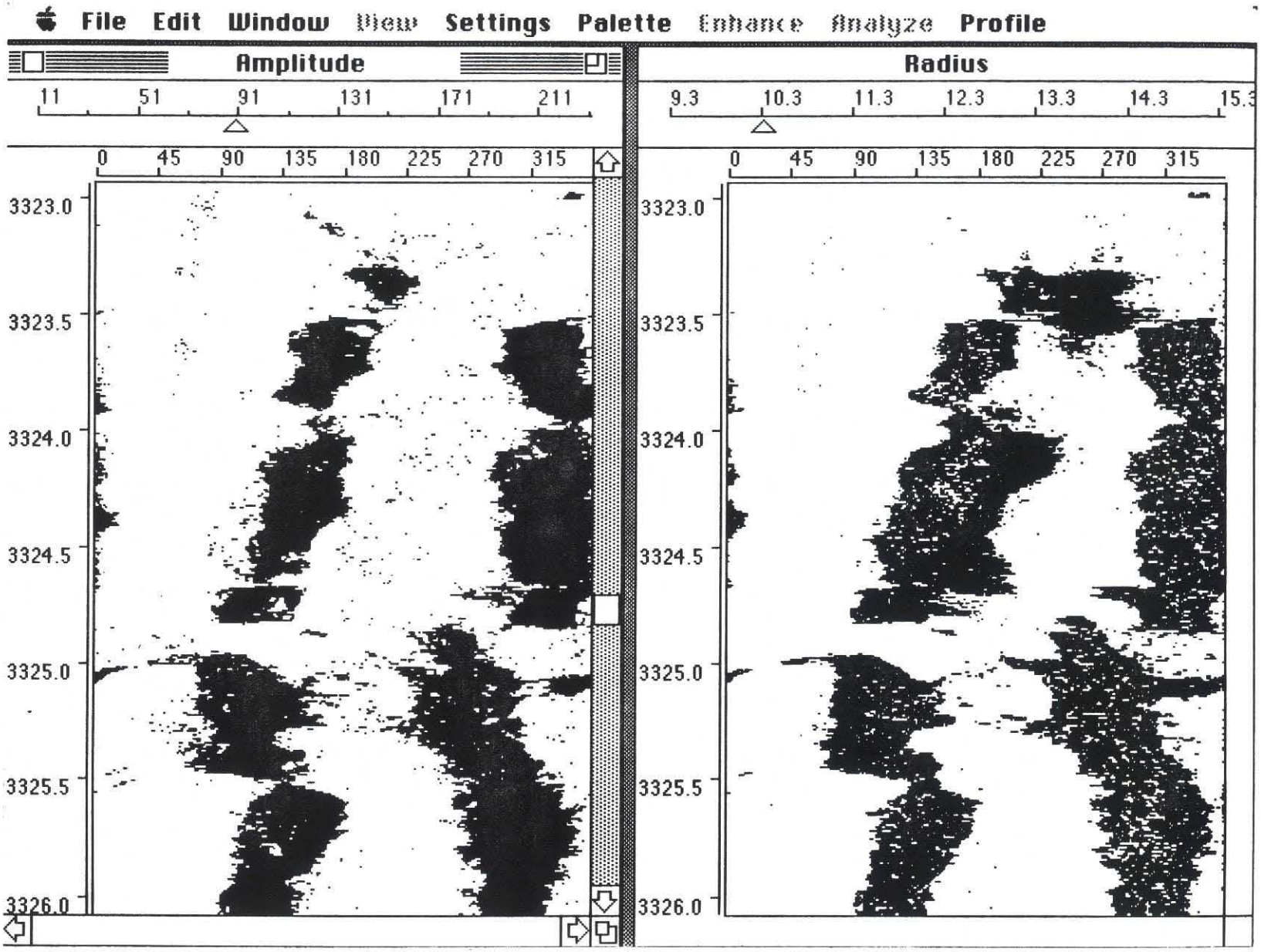
File Edit Window View Settings Palette Enhance Analyze Profile
Amplitude
11 51 91 131 171 211
0 45 90 135 180 225 270 315
3323.0
3323.5
3324.0
3324.5
3325.0
3325.5
3326.0
Radius
9.3 10.3 11.3 12.3 13.3 14.3 15.3
0 45 90 135 180 225 270 315
3323.0
3323.5
3324.0
3324.5
3325.0
3325.5
3326.0

Figure 8

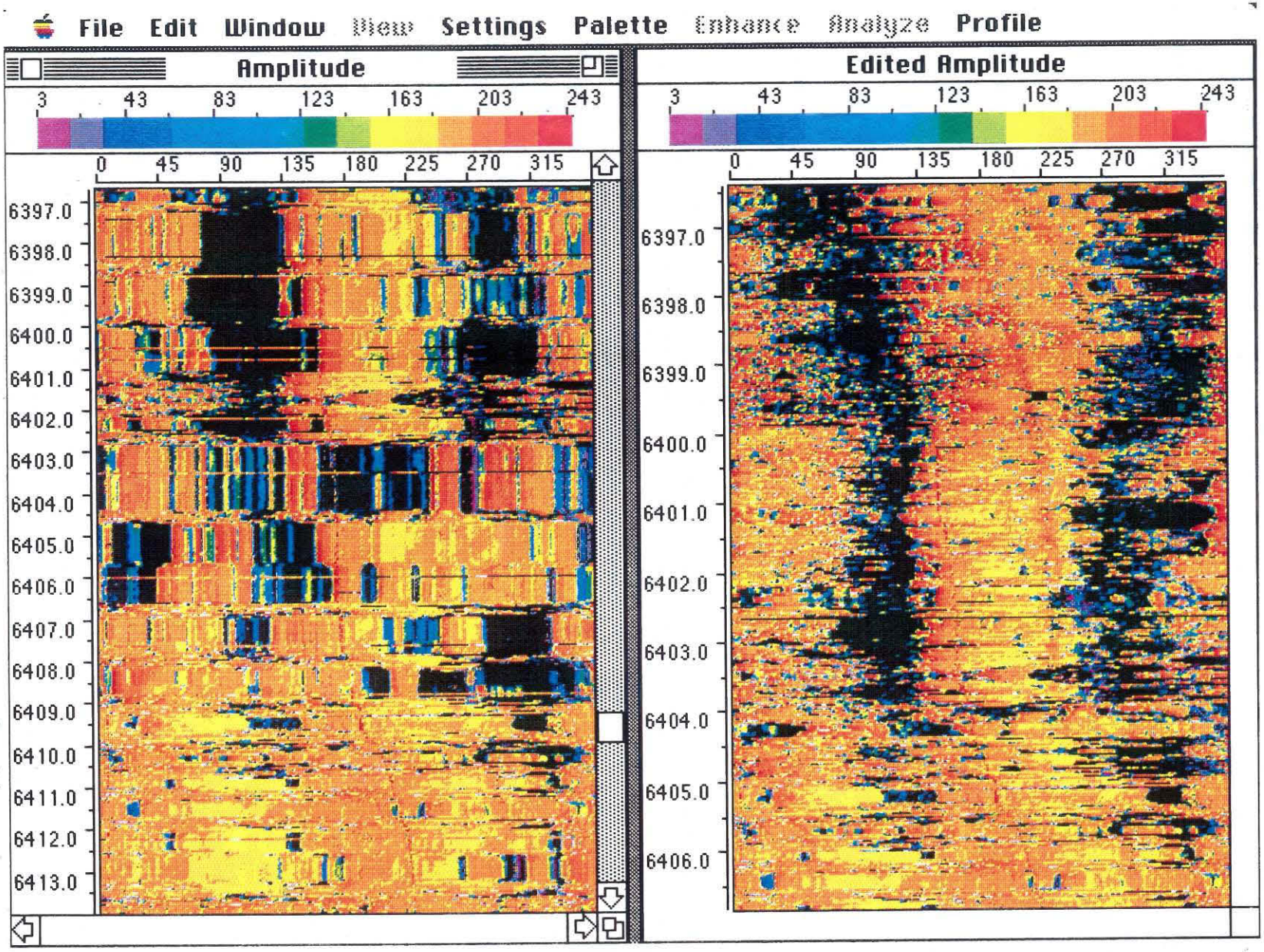
File Edit Window View Settings Palette Enhance Analyze Profile
Amplitude
3 43 83 123 163 203 243
0 45 90 135 180 225 270 315
6397.0 6398.0 6399.0 6400.0 6401.0 6402.0 6403.0 6404.0 6405.0 6406.0 6407.0 6408.0 6409.0 6410.0 6411.0 6412.0 6413.0
Edited Amplitude
3 43 83 123 163 203 243
0 45 90 135 180 225 270 315
6397.0 6398.0 6399.0 6400.0 6401.0 6402.0 6403.0 6404.0 6405.0 6406.0

Figure 9

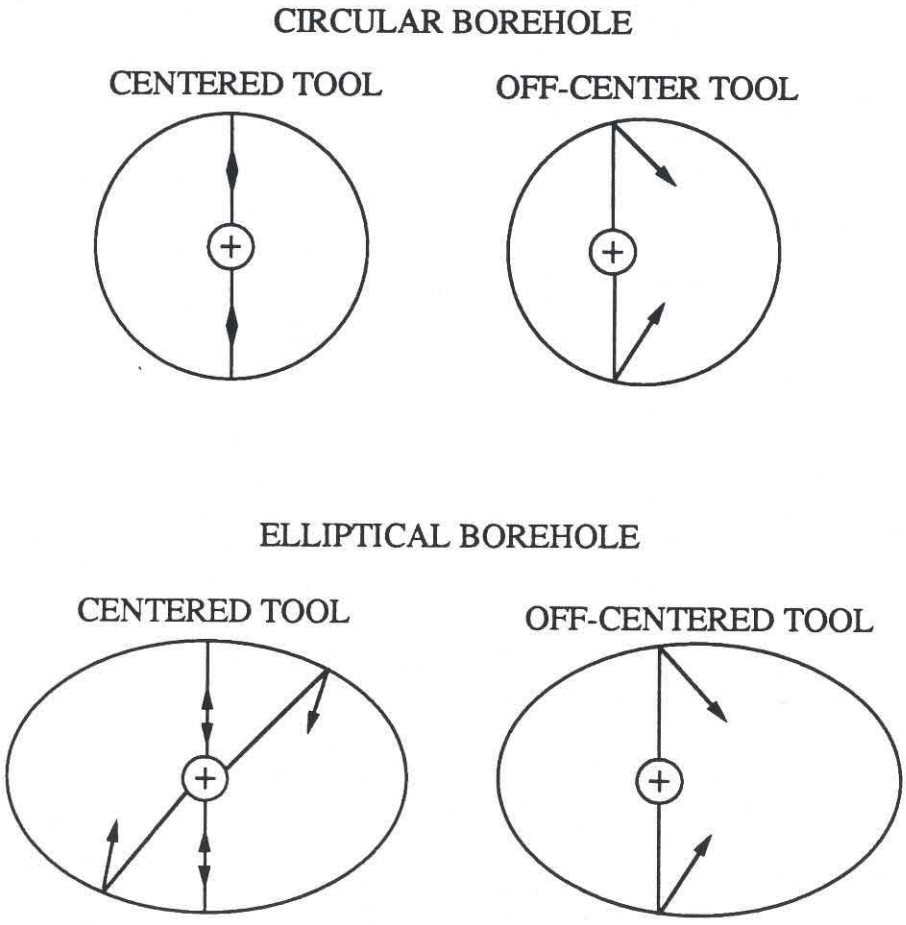
CIRCULAR BOREHOLE
CENTERED TOOL
OFF-CENTER TOOL
ELLIPTICAL BOREHOLE
CENTERED TOOL
OFF-CENTERED TOOL

Figure 10

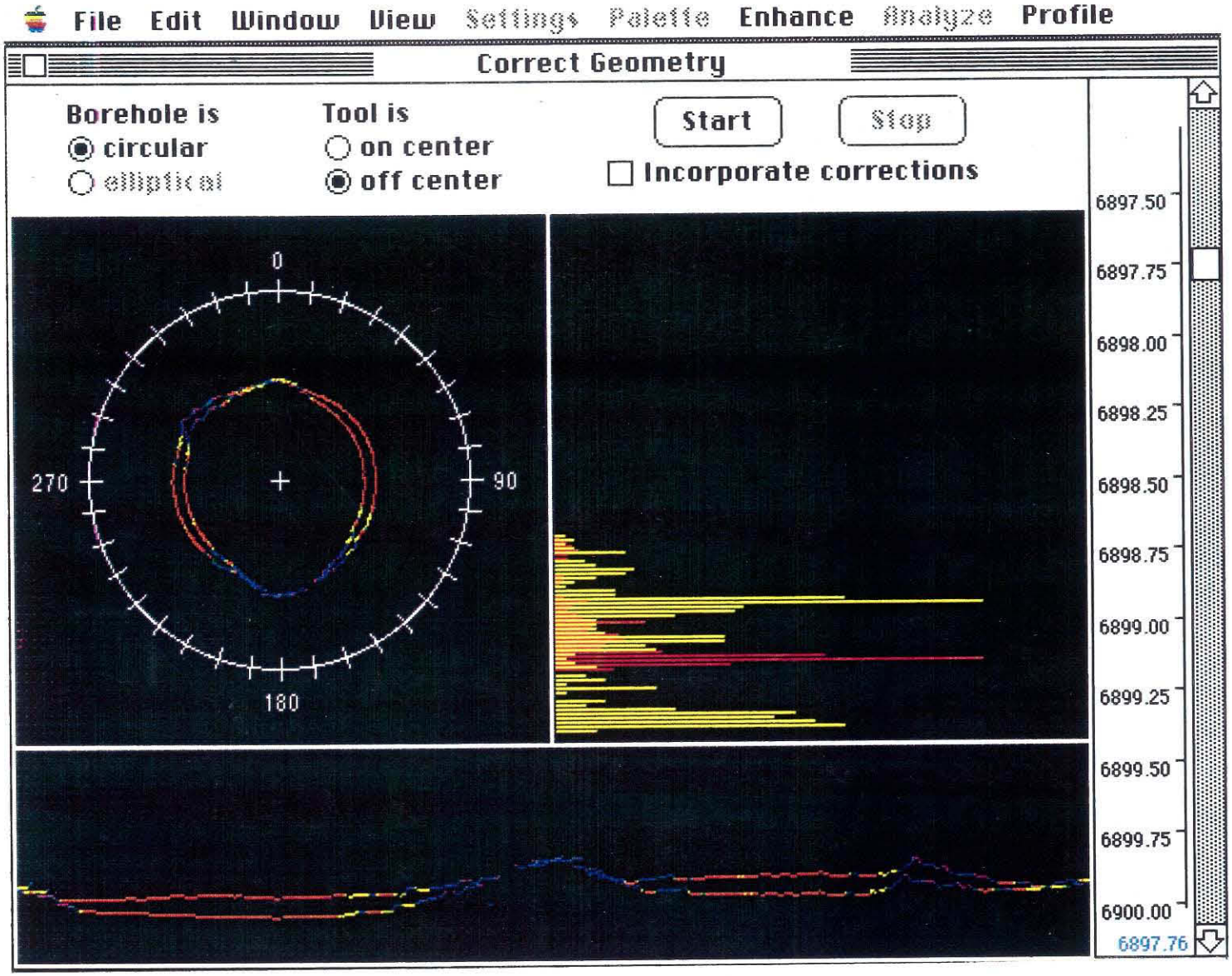
File Edit Window View Settings Palette Enhance Analyze Profile
Correct Geometry
Borehole is
circular
elliptical
Tool is
on center
off center
Start
Stop
Incorporate corrections
0
90
180
270
6897.50
6897.75
6898.00
6898.25
6898.50
6898.75
6899.00
6899.25
6899.50
6899.75
6900.00
6897.76

Figure 11

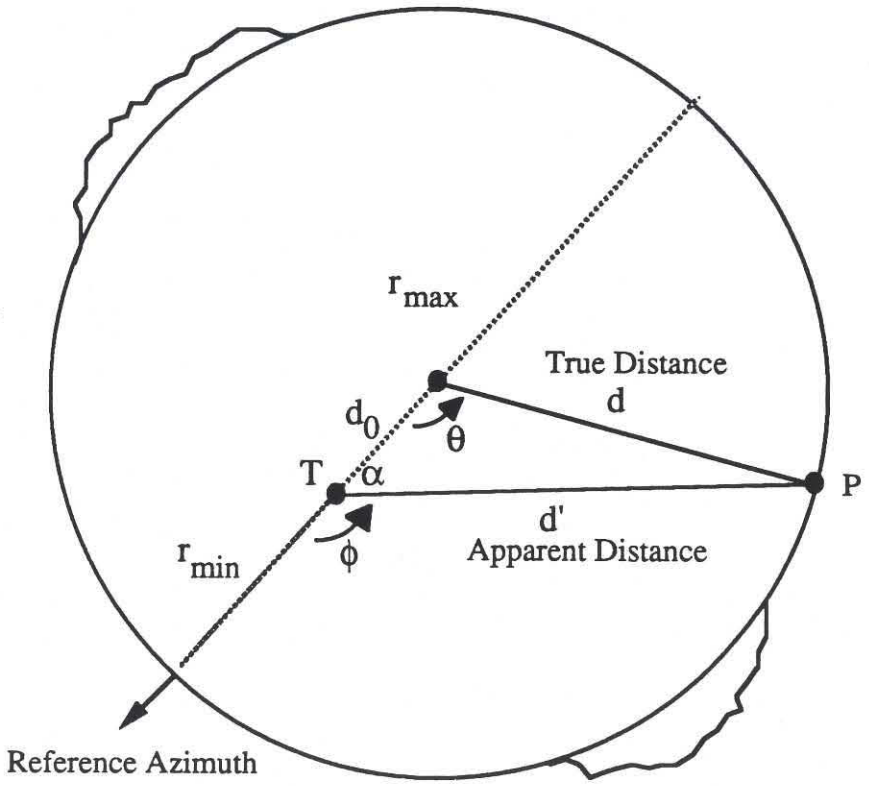
r max
True Distance
d
d0
θ
T
α
P
d'
Apparent Distance
r min
ϕ
Reference Azimuth

Figure 12

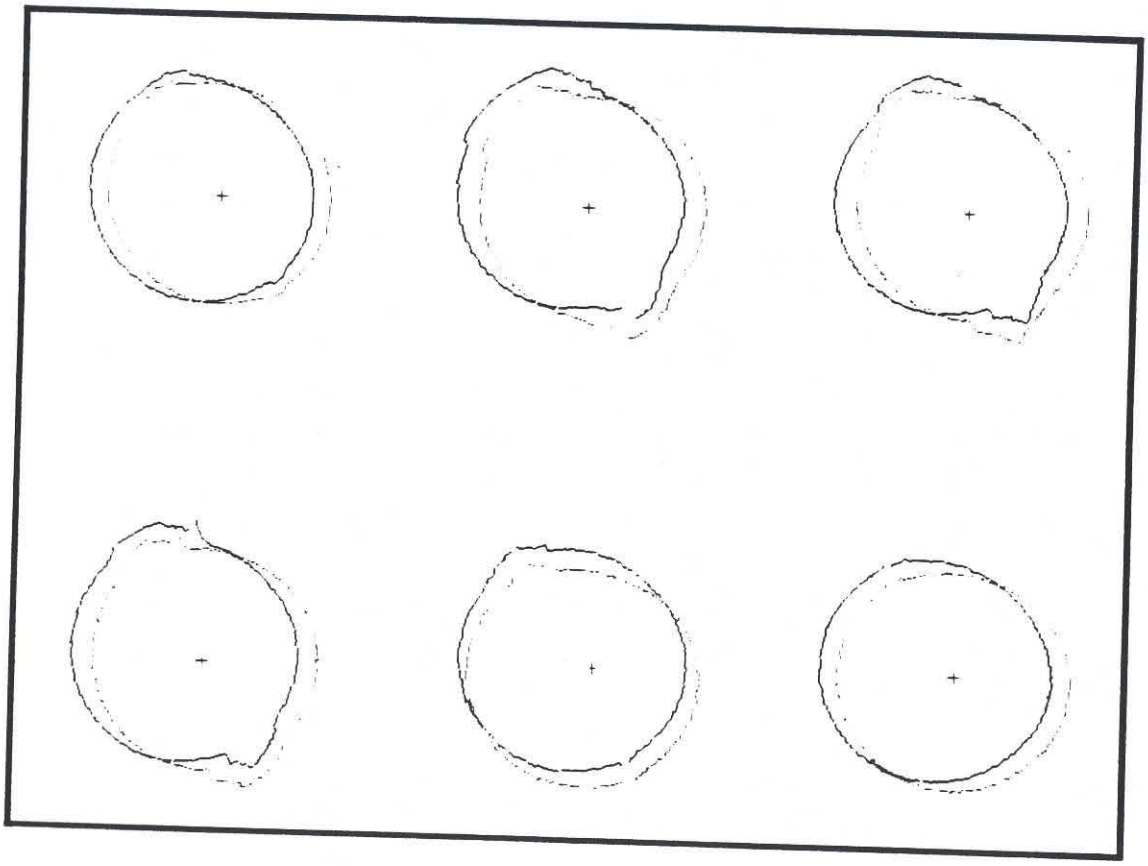

Figure 13

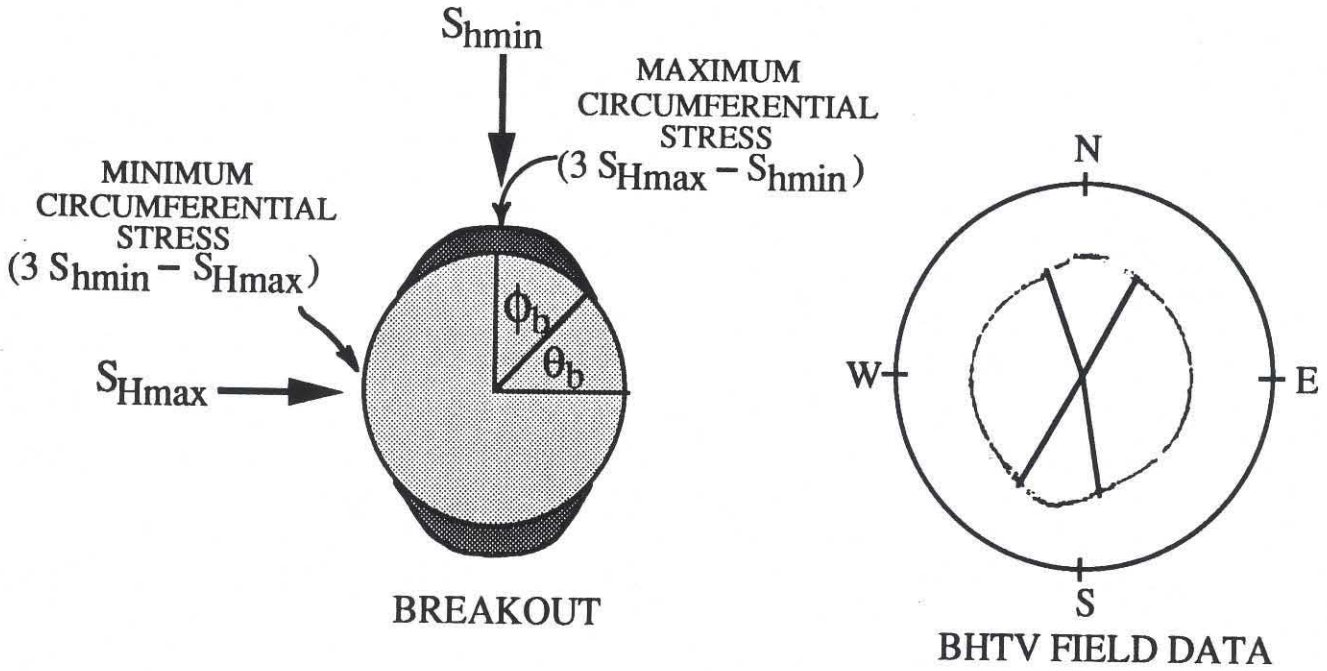
S_{hmin}
MAXIMUM CIRCUMFERENTIAL STRESS
$(3\ S_{Hmax} - S_{hmin})$
MINIMUM CIRCUMFERENTIAL STRESS
$(3\ S_{hmin} - S_{Hmax})$
S_{Hmax}
ϕ_b
θ_b
BREAKOUT
N
W
E
S
BHTV FIELD DATA

Figure 14

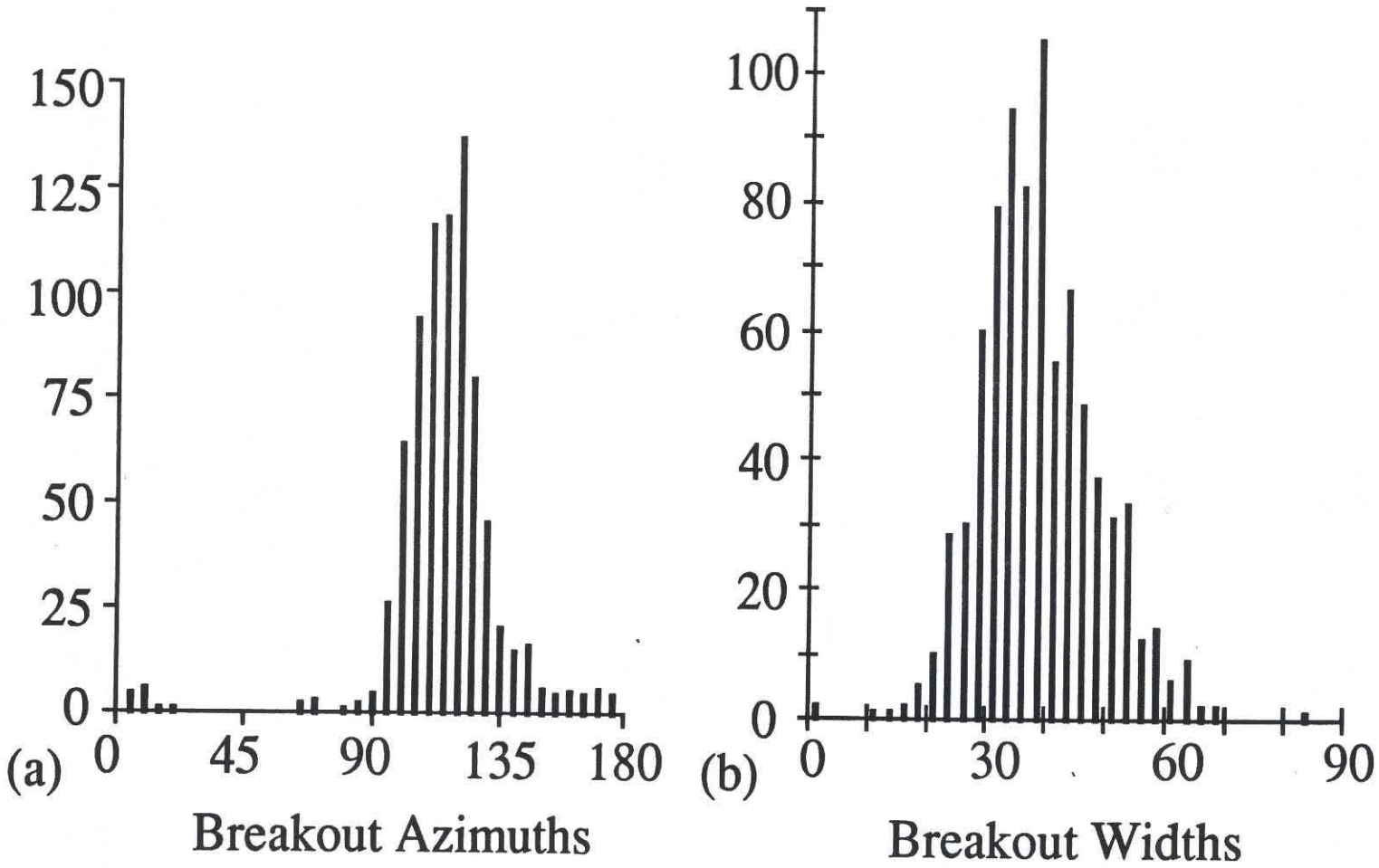
150
125
100
75
50
25
0
0
45
90
135
180
(a)
Breakout Azimuths
100
80
60
40
20
0
0
30
60
90
(b)
Breakout Widths

Figure 15

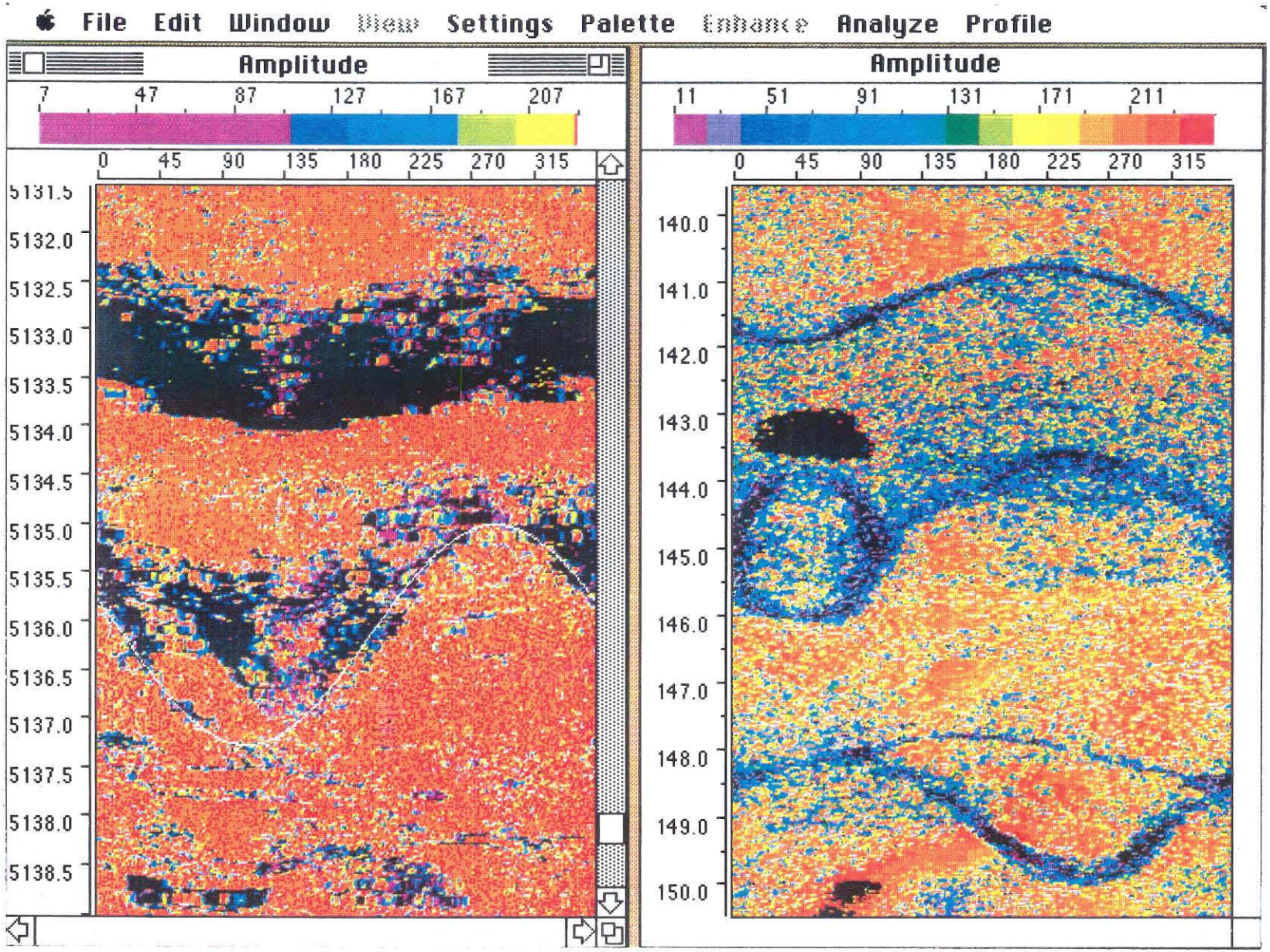
File Edit Window View Settings Palette Enhance Analyze Profile
Amplitude
7 47 87 127 167 207
0 45 90 135 180 225 270 315
5131.5
5132.0
5132.5
5133.0
5133.5
5134.0
5134.5
5135.0
5135.5
5136.0
5136.5
5137.0
5137.5
5138.0
5138.5
Amplitude
11 51 91 131 171 211
0 45 90 135 180 225 270 315
140.0
141.0
142.0
143.0
144.0
145.0
146.0
147.0
148.0
149.0
150.0

Figure 16

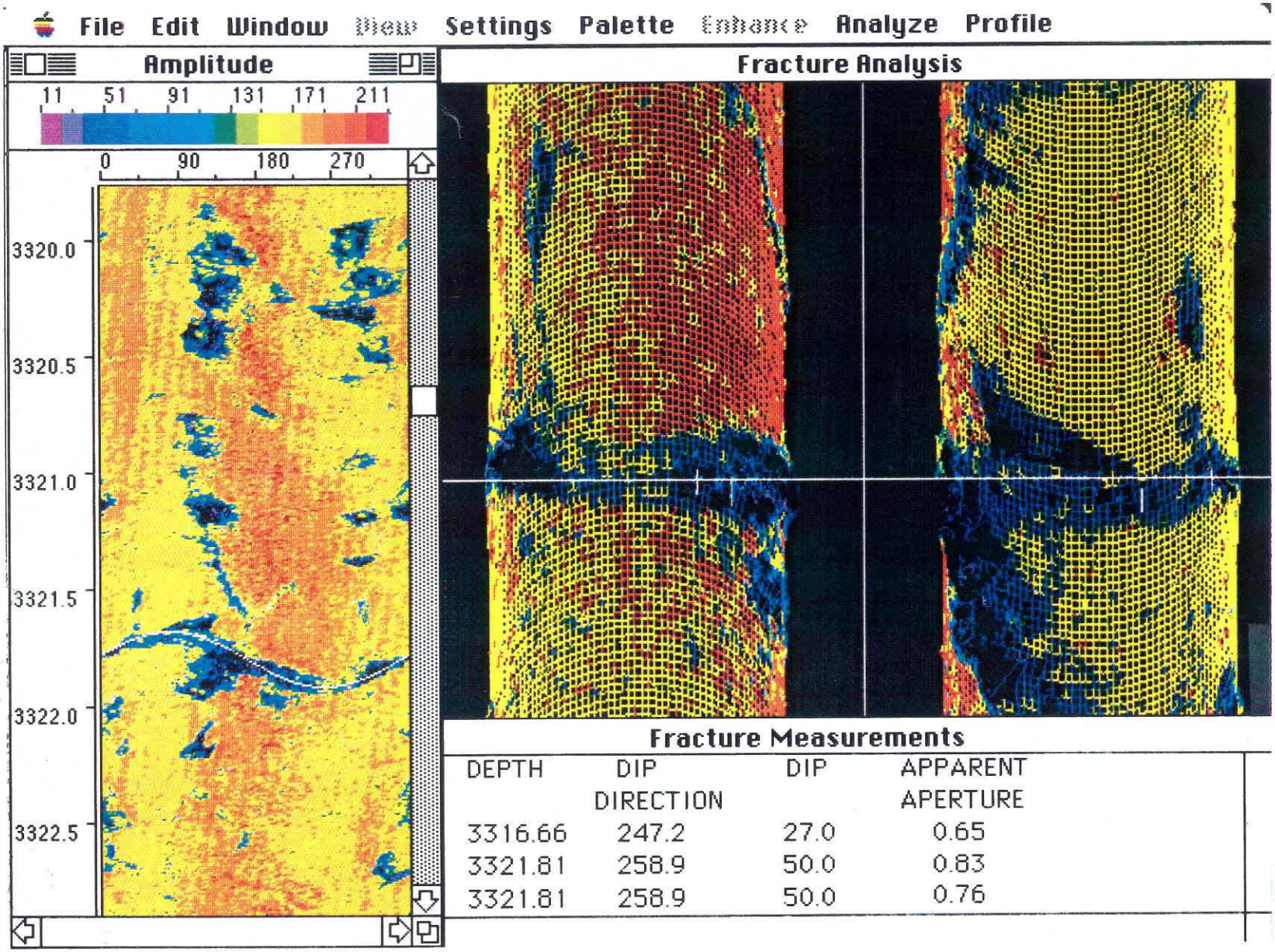
File Edit Window View Settings Palette Enhance Analyze Profile
Amplitude
11 51 91 131 171 211
0 90 180 270
3320.0
3320.5
3321.0
3321.5
3322.0
3322.5
Fracture Analysis
Fracture Measurements
DEPTH DIP DIRECTION DIP APPARENT APERTURE
3316.66 247.2 27.0 0.65
3321.81 258.9 50.0 0.83
3321.81 258.9 50.0 0.76

Figure 17

JOURNAL OF GEOPHYSICAL RESEARCH, VOL. 95, NO. B6, PAGES 9305–9325, JUNE 10, 1990

Utilization of Observations of Well Bore Failure to Constrain the Orientation and Magnitude of Crustal Stresses: Application to Continental, Deep Sea Drilling Project, and Ocean Drilling Program Boreholes

DANIEL MOOS AND MARK D. ZOBACK

Department of Geophysics, Stanford University, Stanford, California

The conditions necessary for compressive and tensile failure of well bores drilled into crystalline rock can be adequately represented by simple elastic failure criteria, and analysis of well bore failure can provide constraints on the magnitudes of in situ stresses if the strength of the rock is known. When applied to several boreholes drilled into continental crust where there is relatively complete knowledge of stress magnitudes, these criteria enable us to predict the depth at which compressive failure of the well bores is observed. In oceanic crust, breakouts have been observed at depths below 700 m below sea floor in Deep Sea Drilling Project (DSDP) hole 504B, drilled into 5.9 Ma crust south of the Costa Rica Rift, and near the bottom of DSDP hole 395A, drilled into 7.3 Ma crust west of the Mid–Atlantic Ridge. In both cases the azimuth of maximum horizontal compressive stress is roughly perpendicular to the ridge axis. As the unconfined compressive strengths of basalt samples from DSDP hole 504B are generally above 200 MPa (Bauer and Handin, 1985), the existence of breakouts in DSDP holes 395A and 504B requires a highly compressional stress state, where $S_{hmin} \sim S_v$ and $S_{Hmax} \geq 100$ MPa at about 500 m subbasement. These results are consistent with the state of stress inferred from compressional (strike-slip and reverse faulting) earthquake focal mechanisms in young oceanic crust. As ridge push forces are relatively small in young oceanic crust, we concur with previous suggestions that the high horizontal compressive stresses result from the thermoelastic effects of a convectively cooled upper crustal layer overlying a conductively cooling lithosphere.

INTRODUCTION

Determination of the magnitude and orientation of in situ stress in the continents and oceans is important to understand lithospheric deformation and to evaluate models of a wide variety of plate tectonic processes. While many aspects of crustal deformation and plate tectonics can be adequately addressed from a kinematic perspective, data on the forces acting within plates are needed to provide constraints on the physical processes causing and resisting plate motion and deformation.

Compilations of stress orientation and relative magnitude data have become increasingly more complete over the past 10 years, and tectonic stress orientation can be reliably mapped in many parts of the world. In total, over 3400 reliable indicators of tectonic stress are now available to define global patterns of intraplate stress [*Zoback et al.*, 1989]. The remarkable improvement in the quantity and distribution of in situ stress orientation data makes it possible to utilize such data to interpret tectonic processes in a number of important ways. However, there are still some very large data gaps in the stress maps, and there is almost a complete absence of stress magnitude data from depths greater than about 1 km [e.g., *Rummel*, 1986]. The lack of data on stress orientation and magnitude is especially severe in the oceans. While earthquake focal plane mechanisms help constrain the orientations and relative magnitudes of oceanic crustal stresses [e.g., *Okal et al.*, 1980; *Okal*, 1984; *Bergman and Solomon*, 1984; *Wiens and Stein*, 1984; *Bergman*, 1986], intraplate events are rare, no direct measure of stress magnitude is obtained, and measurements of stress direction from a single earthquake focal mechanism are complicated by the fact that the earthquakes often occur on preexisting faults [*McKenzie*, 1969; *Raleigh et al.*, 1972]. *Newmark et al.* [1984] and *Morin et al.* [this issue] determined stress directions in oceanic crust from analysis of well bore breakouts. In this paper we expand on these two studies and consider the more general problem of utilization of well bore failure for evaluating stress magnitudes, with the potential for studying the state of stress throughout the ocean basins.

In general, borehole failure can occur as a result of either compressive or tensile stress concentrations around the well bore. Compressive stress failures at the azimuth of the least principal horizontal in situ stress (where the compressive stress concentration is greatest) are termed stress-induced well bore breakouts [*Bell and Gough*, 1979, 1983; *Gough and Bell*, 1981; *Cox*, 1983; *Zoback et al.*, 1985] and have proven to be a reliable measure of stress orientation on land in many areas [*Bell and Gough*, 1979; *Zoback and Zoback*, 1980; *Plumb and Cox*, 1987; *Zoback et al.*, 1987; *Mount and Suppe*, 1987; *Zoback et al.*, 1989]. In this paper we show the range of conditions under which breakouts occur in both continental and oceanic boreholes and the manner in which information about stress magnitude can be obtained from the breakouts. Tensile failures around the well bore form at the azimuth of the greatest principal horizontal in situ stress (where the stress concentration around the well is least compressive). Tensile fractures may form adjacent to the well bore because of the localized stress concentration, and thermally induced tensile stresses due to cooling of the borehole wall by circulation of relatively cold drilling fluids also promote tensile failure. In these cases the fractures cannot propagate significant distances away from the well

Paper number 90JB00495
0148-0227/90/90JB-00495$05.00

bore unless the well bore fluid pressure exceeds the least principal in situ stress [cf. *Stock et al.*, 1985]. As is the case for well bore breakouts, observations of tensile failure of the well bore provide information about both stress orientation and magnitude. Our overall goal is to illustrate the simple fact that the presence (or absence) of compressive and/or tensile failure at the well bore can provide useful information about the magnitudes of in situ stresses.

Frictional Strength of the Crust

As suggested by *Sibson* [1974] and *Brace and Kohlstedt* [1980], we assume that the ratio of the maximum to minimum effective stress cannot exceed that required to cause motion on preexisting faults that are optimally oriented to the principal stress field. We also assume that principal stresses (S_1, S_2, and S_3) in the upper few kilometers of the Earth's crust generally act in the vertical direction, corresponding to the weight of the overburden (S_v) and in two orthogonal horizontal directions (S_{hmin} and S_{Hmax}, corresponding to the least and greatest horizontal principal stresses). The validity of this assumption is borne out by the very small number of intraplate crustal earthquake focal mechanisms in which neither the P nor the T axis is observed to be within 10°–15° of horizontal or vertical [e.g., *Zoback et al.*, 1989]. If these assumptions are correct, the limiting stress ratio can be written [after *Jaeger and Cook*, 1979] as

$$(S_1 - P_0)/(S_3 - P_0) = [(1 + \mu^2)^{1/2} + \mu]^2 \qquad (1)$$

where μ is the coefficient of friction of the preexisting plane of weakness and P_0 is the pore pressure. Thus the stress can range from lithostatic (in the absence of tectonic forces, [*McGarr*, 1988]) to the limit defined by (1).

A large number of in situ stress measurements in seismically active areas have shown this to be generally correct [*McGarr*, 1980; *Brace and Kohlstedt*, 1980; *Zoback and Healy*, 1984]. As we are applying these results to the upper part of the crystalline crust, we assume that pore pressure is approximately hydrostatic, which is borne out from a number of drilling experiments in both continental crystalline crust [*Kozlovsky*, 1984; *Rummel*, 1986; *Coyle and Zoback*, 1988] and oceanic crust [*Anderson and Zoback*, 1982; Hickman et al., 1984*a*; *Shipboard Scientific Party*, 1985].

Figure 1 illustrates the range of allowable values for horizontal principal stresses in the earth's crust for normal-, reverse-, and strike-slip-faulting environments using (1) and *Anderson*'s [1951] theory of faulting. For reference the figure is shown for a depth of 5 km in continental crust (average density of 2600 kg/m^3 and $\mu = 0.8$) and for a depth of 1 km into basalt in 4 km of water for the oceanic crust (rock density of 2800 kg/m^3 and $\mu = 0.8$). We choose these depths for illustration simply because they are within the depth range of scientific boreholes within the continents and oceans. By definition, the fact that $S_{\text{hmin}} \leq S_{\text{Hmax}}$ requires all stress states to be above the line of unit slope in Figure 1. The vertical and horizontal lines corresponding to S_v separate the fields of normal (NF), strike slip (SS), and reverse (RF) faulting as defined by Anderson. The vertical line constraining the lowest value of S_{hmin} is the failure bound for normal faulting (i.e., (1) with $S_1 = S_v$ and $S_3 = S_{\text{hmin}}$). The horizontal line constraining the greatest allowable value of $S_{H\text{max}}$ is the failure bound for reverse faulting (i.e., (1) with $S_1 = S_{\text{Hmax}}$ and $S_3 = S_v$). The inclined line is the limit of the allowable stress states for strike-slip faulting (i.e., (1) with $S_1 = S_{\text{Hmax}}$ and $S_3 = S_{\text{hmin}}$). In cases of incipient fault activity (a case that may be true of much of the upper crust) the expected stress state is found along one of these three limiting lines, depending on the style of faulting. It is clear in Figure 1 that principal stress magnitudes are appreciably lower in the oceanic crust than in the continental crust for the depths chosen. This has an important impact on the likelihood of well bore failure at the depths reached by drilling within the oceans. For reference to several specific cases the circles shown in Figure 1 correspond to simultaneous strike-slip and normal faulting, where $S_v = S_{\text{Hmax}} = S_1$ and $S_{\text{hmin}} = S_3$.

Stresses Around a Borehole

In the following discussion we continue to assume that the vertical stress is a principal stress, and we further assume that the well bore is drilled in the vertical direction and that the rock behaves elastically. We will present equations describing the magnitudes of the vertical, radial, and circumferential elastic stresses as a function of azimuth at the well bore; of the principal stresses; of fluid pressure differences between the well bore and the surrounding rock; and of the effects of temperature changes induced by the drilling fluid. These equations can be generalized for arbitrary stress and borehole orientations [e.g., *Fairhurst*, 1968; *Mastin*, 1988].

For a cylindrical hole in a homogeneous, isotropic elastic plate subjected to effective minimum and maximum far-field principal stresses (S^*_{hmin} and S^*_{Hmax}), the effective radial (σ_{rr}), circumferential ($\sigma_{\theta\theta}$), and tangential shear ($\tau_{r\theta}$) stresses described by *Kirsch* [1898] reduce at the borehole wall to

$$\begin{aligned}
\sigma_{rr} &= \Delta P \\
\sigma_{\theta\theta} &= S^*_{\text{Hmax}} + S^*_{\text{hmin}} - 2(S^*_{\text{Hmax}} - S^*_{\text{hmin}}) \cos 2\theta - \Delta P \\
\sigma_{zz} &= S^*_v - 2\nu(S^*_{\text{Hmax}} - S^*_{\text{hmin}}) \cos 2\theta \\
\tau_{r\theta} &= 0 \\
\tau_{zr} &= 0 \\
\tau_{z\theta} &= 0
\end{aligned} \qquad (2)$$

where ΔP is the difference between the well bore fluid pressure and the pore pressure in the rock, σ_{zz} is from *Fairhurst* [1968], and ν is the static Poisson's ratio. Theta (θ) is measured from the azimuth of the maximum horizontal stress. The circumferential stress is greatest at the azimuth of S^*_{hmin} and smallest at the azimuth of S^*_{Hmax}. Figure 2 shows the variation in $\sigma_{\theta\theta}$, the circumferential stress, and σ_{zz}, the vertical stress, as a function of azimuth at the well bore for the stress states indicated by the circles in Figure 1. It is important to note the wide range of circumferential stresses for this stress state. For the case at 5 km depth in the continents, $\sigma_{\theta\theta}$ varies from a point on the borehole at the azimuth of S^*_{hmin} where the circumferential stress is quite compressive ($3S^*_{\text{Hmax}} - S^*_{\text{hmin}} \approx 220$ MPa) to a point where, for the case shown, the well bore is in tension ($3S^*_{\text{hmin}} - S^*_{\text{Hmax}} \approx -25$ MPa) at the azimuth of S^*_{Hmax}. For the oceanic crust at 1 km below sea floor, $\sigma_{\theta\theta}$ ranges from about 50 MPa to −5 MPa. The vertical stress has the same θ dependence as the circumferential stress. However, the range in vertical stress in crystalline rock is considerably less than the far-

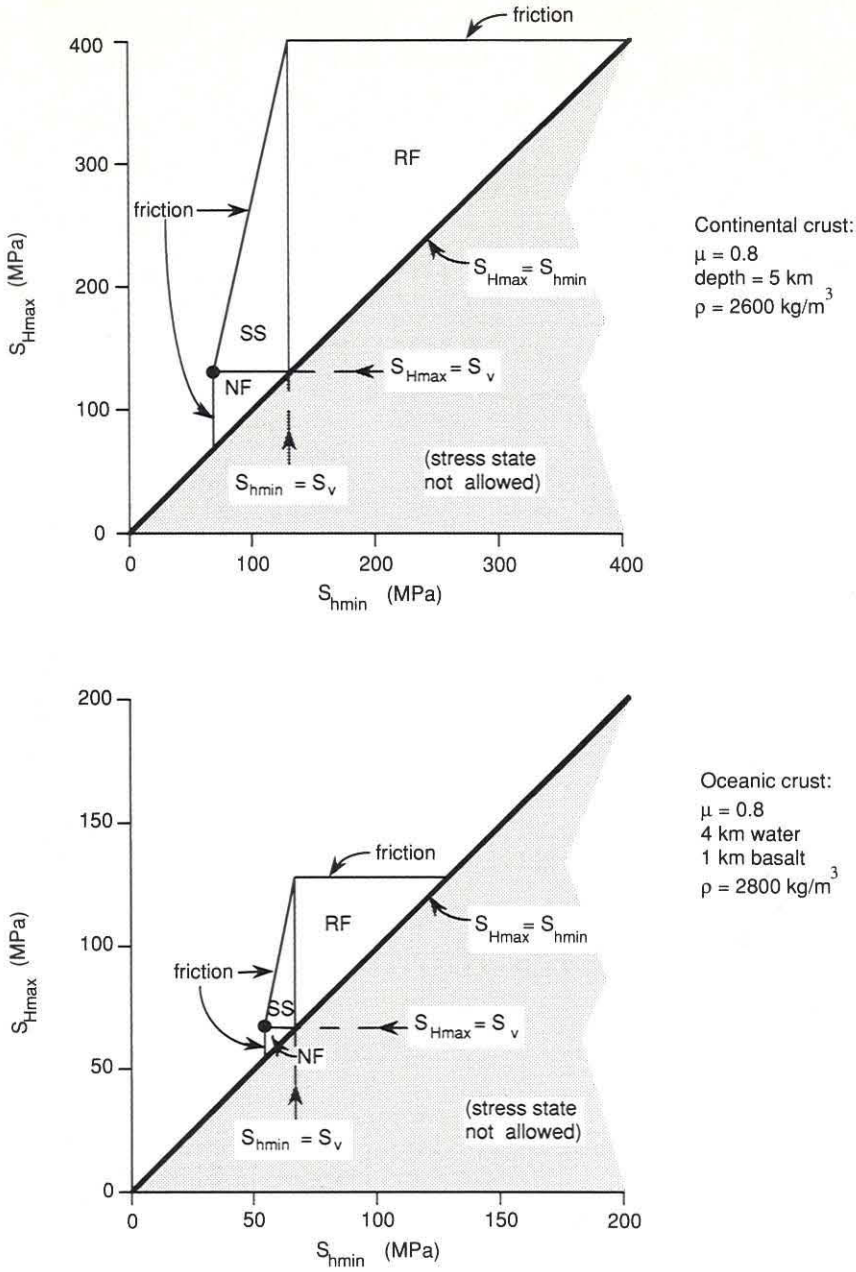

Fig. 1. Allowable stress conditions based on the frictional strength of favorably oriented fault planes, assuming $\mu = 0.8$, for continental crust at 5 km depth and for oceanic crust at 1 km below seafloor. (Note the different scales.) S_v is calculated from the weight of overburden, and pore pressure is assumed to be hydrostatic. The stress state is constrained to lie inside the polygon, because $S_{H\max} \geq S_{h\min}$, by definition, and the ratio $(S_1 - P_0)/(S_3 - P_0)$ is bounded by friction (equation (1)). For reverse faulting, $S_1 = S_{\mathrm{Hmax}}$ and $S_3 = S_v$, defining a maximum bound on S_{Hmax}. For normal faulting, $S_1 = S_v$ and $S_3 = S_{\mathrm{hmin}}$, defining a minimum bound on S_{hmin}. For strike-slip faulting, friction bounds the ratio $(S_{H\max} - P_0)/(S_{\mathrm{hmin}} - P_0)$. The circle represents in each case the stress state $S_{\mathrm{Hmax}} = S_v$, with S_{hmin} constrained by the frictional strength of normal or strike-slip faults.

field stress difference for static Poisson's ratios <0.25 [e.g., *Carmichael*, 1982].

Effect of Temperature Changes on Borehole Stresses

Additional stresses are applied to the rock at the borehole wall if the well bore fluid is at a significantly different temperature than the rock. These stresses can be compressive or tensile depending on whether the temperature of the fluid is higher or lower, respectively, than the ambient temperature. The effect of temperature is time-dependent, in the sense that the longer the rock is in contact with the well bore fluid, the further away from the hole the temperature perturbation will propagate. *Coussy* [1990] presents a complete treatment of the problem for a Biot coupled thermoporoelastic material, which requires for its solution detailed knowledge of rock properties such as permeability. However, if one assumes that the material is impermeable with no thermoelastic coupling, simpler integral equations can be written for the magnitudes of $\sigma_{\theta\theta}$ and σ_{rr} as a function of

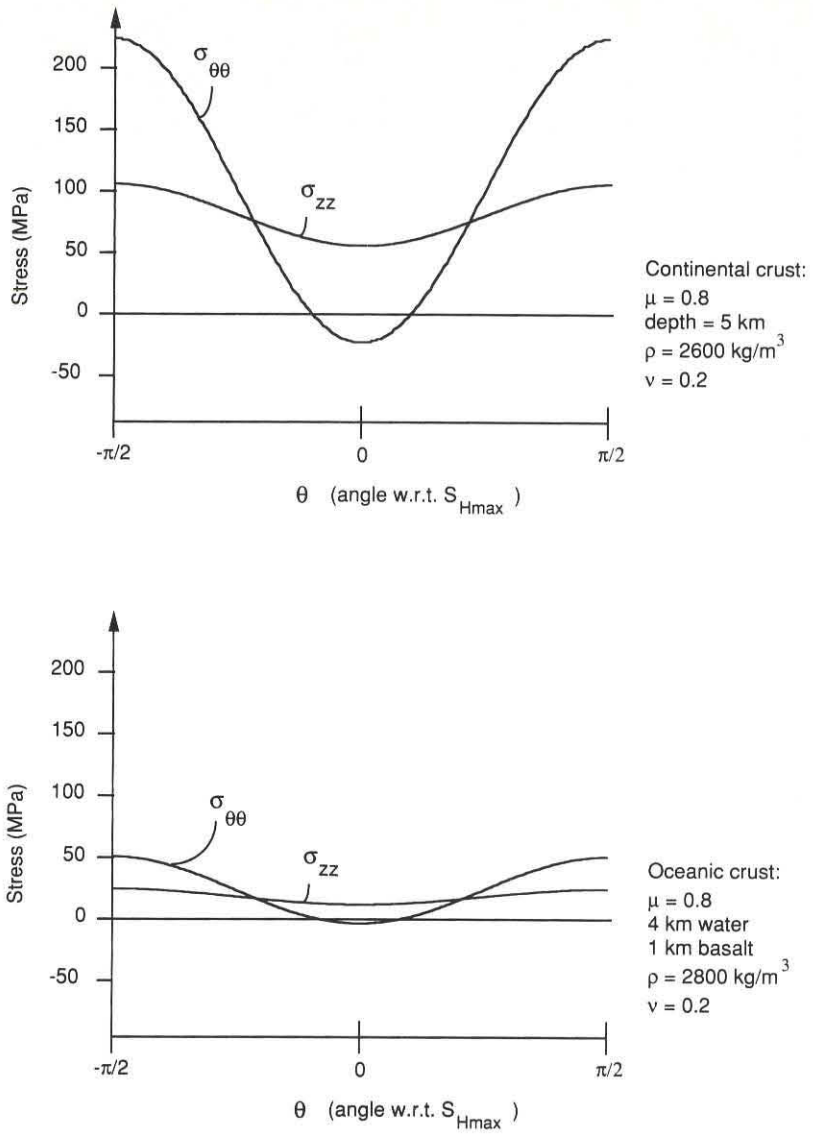

Fig. 2. The distribution of circumferential and vertical stresses around a well bore for the stress states defined by the circles in Figure 1. Note that for these strike-slip-faulting cases the well bore wall is in tension because of the circumferential stress concentration at the azimuth of S_{Hmax}.

radial position r and time t (see, for example, *Stephens and Voight* [1982]). Although the exact solution for the temperature distribution near a constant-temperature well bore is a series expansion [*Ritchie and Sakakura*, 1956], solutions which approximate the temperature using the first two terms of the expansion give sufficiently accurate results close to the hole, and the stresses become

$$\sigma_{\theta\theta} = [\alpha E \Delta T/(1-\nu)]\{[1/(2\rho) - \tfrac{1}{2} - \ln \rho]I_0^{-1} - [\tfrac{1}{2} + 1/(2\rho)]\}$$

$$\sigma_{rr} = [\alpha E \Delta T/(1-\nu)]\{[-1/(2\rho) + \tfrac{1}{2} - \ln \rho]I_0^{-1} - [\tfrac{1}{2} - 1/(2\rho)]\} \quad (3)$$

where

$$I_0^{-1} = \frac{1}{2\pi i}\int_{-\infty}^{0^+} \frac{e^{(4\tau/\sigma^2)z}}{z \ln z}\, dz$$

Here α is the coefficient of thermal expansion; E is the static Young's modulus; ΔT is the temperature difference between the well bore fluid and the rock surrounding the borehole; ν is the static Poisson's ratio; $\sigma = e^{\gamma}$; γ is Euler's constant; ρ is radial position normalized by the well bore radius R; and the parameter $\tau = \kappa t/R^2$ is the Fourier number. Here κ is the thermal diffusivity, and t is the time during which the well bore fluid temperature is perturbed.

If the well bore fluid is colder than the rock, the thermally induced stresses are extensional. This will generally be true where drilling fluids exit the pipe, particularly in Ocean Drilling Program (ODP) and Deep Sea Drilling Project (DSDP) drill holes, as in situ temperatures are generally higher than the temperature of the drilling fluid. However, drilling fluids returning to the surface from greater depths may be somewhat warmer than the undisturbed temperature of the rock and thus may induce compressional thermal stresses. For the purposes of this paper we will consider only the case of the effect of cooling the rock at the drill bit.

Equation (3) is plotted in Figure 3 for various values of time, assuming a 15-cm borehole radius and a coefficient of

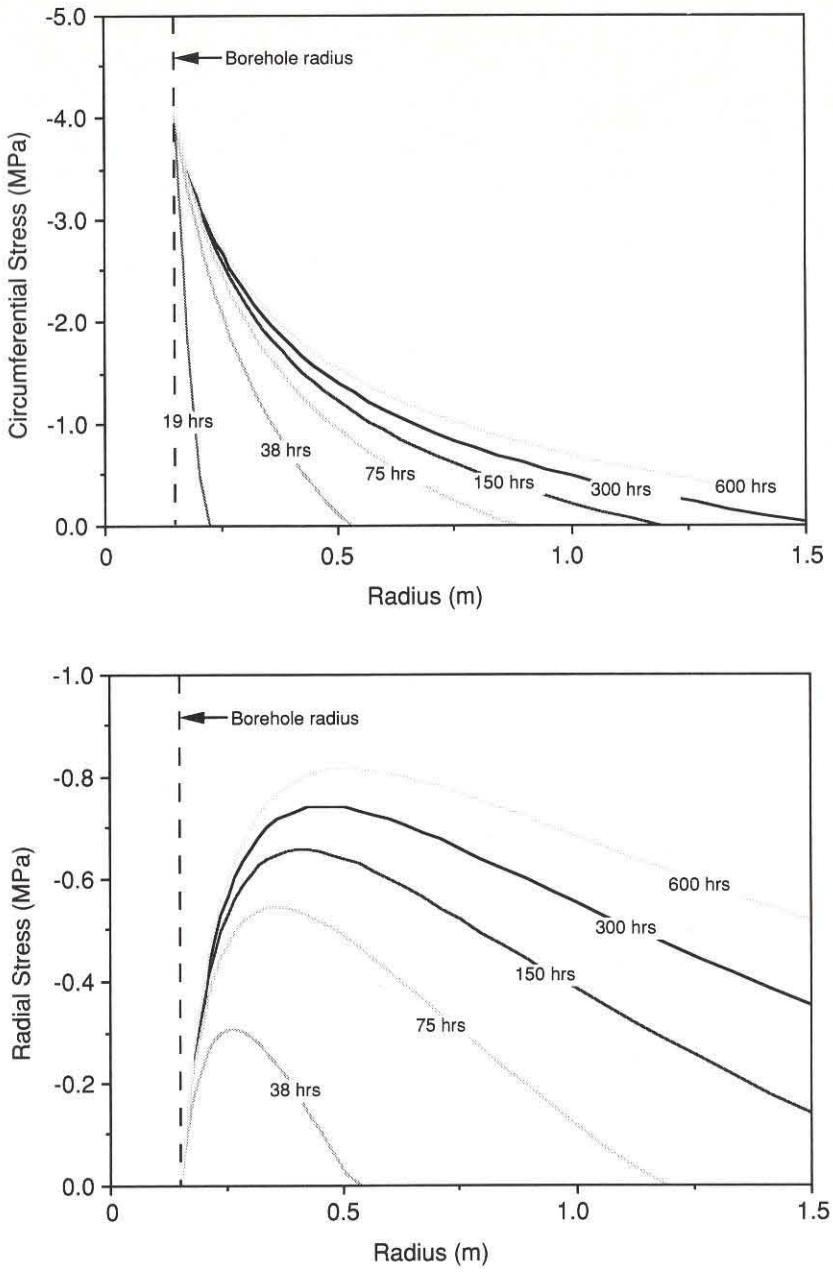

Fig. 3. Radial and circumferential stresses generated by a decrease in well bore fluid temperature of 10°C as a function of time, for a 15-cm-radius borehole drilled through basalt. Plotted as a function of radial distance from the center of the borehole, the lines correspond to pumping times of 19, 38, 75, 150, 300, and 600 hours. After 19 hours the radial stress perturbation is imperceptible at the scale of this plot. As the pumping time increases, the stress perturbations move away from the borehole wall.

thermal expansion of 5.4×10^{-6} °C^{-1} (values appropriate for DSDP and ODP boreholes penetrating oceanic crustal basalts). For these values and a thermal diffusivity $\kappa = 10^{-6}$ m^2/s the curves illustrate the effect of maintaining a 10°C temperature reduction within the well bore for 19, 38, 75, 150, 300, and 600 hours (from less than 1 day to 25 days). For this case, well bore cooling applies 4.1 MPa of circumferential tension at the borehole wall. The thermally applied stress decreases rapidly with radial distance, and after 19 hours of circulation is confined to less than 1 borehole radius. As circulation time increases, the stress anomaly progresses further away from the well bore but even after several weeks of cooling is insignificant beyond about 10 borehole radii (1.5 m). The thermally induced radial stress is zero at the well bore, attains a most tensile value a short distance away from the hole, and decreases at greater distances. The peak of the radial stress anomaly migrates away from the well bore as circulation is maintained for longer times, but as in the case of the circumferential stress, the effect is still confined to within a few borehole radii. Times shorter than 19 hours are not accurately modeled by the simplified (3) above but have a similar form.

WELL BORE FAILURE

In this section we consider the role of tectonic stress, applied fluid pressure and well bore temperature changes in

terms of the stresses required to cause compressive and tensile failure.

Conditions for Breakout Formation

As first suggested by *Gough and Bell* [1981] and *Bell and Gough* [1983], breakouts are spalled regions centered on the azimuth of the least horizontal far-field stress and are formed by compressive shear failure due to the large difference between the radial stress and the circumferential stress at that point. *Zoback et al.* [1985] extended this model to account for the shape of the breakout region, using a modified Mohr-Coulomb criterion for shear failure. They showed that breakout shapes are generally consistent with those predicted by the Mohr-Coulomb theory and proposed that information about the shape of breakouts could allow estimates of the horizontal stress ratio. This technique was successfully applied by *Barton et al.* [1988]. It is not our intent in this paper, however, to utilize breakout shape information to constrain the stresses.

In the simple elastic Mohr-Coulomb analysis, compressive failure will occur at the well bore wall due to differences between the circumferential and the radial stress when the stress concentration exceeds C, the strength of the rock, i.e.,

$$\sigma_{\theta\theta} = S_{\mathrm{Hmax}} + S_{\mathrm{hmin}} - 2(S_{\mathrm{Hmax}} - S_{\mathrm{hmin}}) \cos 2\theta - 2P_0 \geq C \tag{4a}$$

for failure due to differences between circumferential and radial stresses, and

$$\sigma_{zz} = S_v - 2\nu(S_{\mathrm{Hmax}} - S_{\mathrm{hmin}}) \cos 2\theta - P_0 \geq C \tag{4b}$$

for failure due to differences between the vertical stress and the radial stress. Because $\sigma_{rr} \sim 0$ (when $\Delta P \sim 0$) and $\sigma_{\theta\theta}$ and σ_{zz} are both nonzero, the stress state around the well bore is polyaxial. In general, rock is stronger under polyaxial conditions than under uniaxial conditions, and as described by *Wiebols and Cook* [1968], the appropriate rock strength when one principal stress is zero is between the uniaxial strength (where $\sigma_2 = 0$) and the biaxial plane strength (where $\sigma_2 = \sigma_1$). Wiebols and Cook relate the biaxial plane strength to the uniaxial strength C_0 through the formula $C_b = C_0(1.0 + 0.6\mu_f)$, where μ_f is the coefficient of sliding friction on microcracks. For reasonable values of μ_f (~0.6 [*Byerlee*, 1978]), $C_b = 1.36C_0$. Therefore the strength of interest for well bore failure lies within the range $C_0 \leq C \leq 1.36C_0$. In the remainder of the paper we will assume that this range of values is appropriate for the study of breakouts.

Zheng et al. [1989] present a different model for breakout formation by extensional cracking (spalling) parallel to the well bore. As their spalling process requires some microcrack sliding to initiate the tensile cracks, the stresses necessary to initiate breakouts in their model are those required to promote sliding on favorably oriented microcracks. Thus the far-field stress magnitudes are similar to those necessary to cause compressive shear failure in the model of *Zoback et al.* [1985] using the *Wiebols and Cook* [1968] failure criterion. Laboratory results [*Mastin*, 1984; *Haimson and Herrick*, 1986, 1989] show that breakout formation generally occurs at stresses consistent with the Mohr-Coulomb criterion for shear failure as modified to include the effect of the intermediate stress, and although *Haimson and Herrick* [1989] observed features within breakouts that mimic spalling, the stress state for which the breakouts formed was similar to that of the *Zoback et al.* [1985] model. *Vardoulakis et al.* [1988] suggest an alternative failure criterion, based on a rigid plastic pressure sensitive dilatant rheology, and a bifurcation analysis to define failure development. This results both in a modification of the stress concentration at the well bore and a more complicated failure criterion. Unfortunately, this analysis has not yet been developed for unequal stresses acting perpendicular to the well bore and cannot be utilized for interpretation of field observations.

We now consider the in situ stress conditions under which (1) breakouts do not occur, (2) breakouts occur only near the azimuth of S^*_{hmin}, and (3) breakouts occur everywhere around the well bore. The boundaries between these three "fields" in horizontal stress space are determined by the strength of the rock and the differences between the far-field total stresses. In general, it is not necessary to evaluate the conditions for compressive failure due to the vertical stress, as in the region of the well bore the maximum circumferential stress ($3S_{\mathrm{Hmax}} - S_{\mathrm{hmin}} - 2P_0$) is generally greater than the maximum vertical stress ($S_v + 2\nu(S_{\mathrm{Hmax}} - S_{\mathrm{hmin}}) - P_0$), for reasonable values of the static Poisson's ratio (≤ 0.25), except in the case of normal faulting where the two horizontal stresses are approximately equal ($S_v \gg S_{\mathrm{Hmax}} \approx S_{\mathrm{hmin}}$). For the present we assume that $\Delta P = \Delta T = 0$, but from the discussions above one can see that it is straightforward to vary these parameters and incorporate their effects.

In Figure 4 the fields in which breakouts do and do not occur are shown for an assumed rock strength $C = 200$ MPa for the same depths and conditions as Figure 1. As discussed below, $C \approx 200$ MPa is somewhat high for many crystalline rocks but comparable to the strength of basalt. The allowable stress states defined by the frictional strength of the crust that are shown in Figure 1 are also shown in Figure 4. The breakout fields in the figure are defined using (4*a*) by $S_{\mathrm{Hmax}} \geq \frac{1}{3}(C + S_{\mathrm{hmin}} + 2P_0)$, for failure only at the azimuth of S_{hmin}, and $S_{\mathrm{hmin}} \geq \frac{1}{3}(C + S_{\mathrm{Hmax}} + 2P_0)$, for failure occurring everywhere around the hole. For a strength of 200 MPa it is clear that at a depth of 5 km on land, breakouts are to be expected under nearly all stress conditions except those of normal faulting, and in a highly compressive tectonic stress state, breakouts would be expected to occur nearly everywhere around the well bore. Conversely, at a depth of 1 km in the ocean crust, breakouts would only occur at relatively high values of S_{Hmax} and a large horizontal stress difference, a reverse/strike-slip stress regime.

Breakouts have been found in many wells drilled on land, and the frequency of breakouts (and the likelihood that breakouts would be encountered) in a given well increases with depth. This can be understood by simply considering limits on the horizontal stresses in reverse-, strike-slip-, and normal-faulting regimes (where the values of S_1 and S_3 are limited by (1) and the coefficient of friction μ) and the criteria for breakout formation due to the circumferential stress concentration (Equation (4)). The relationship between the rock strength and the minimum depth of breakout occurrence from these equations is illustrated in Figure 5. In this figure the vertical stress S_v is equal to the weight of overburden, pore pressure is hydrostatic, and well bore fluid pressure is equal to the pore pressure. The value of the intermediate stress is conveniently defined in terms of a

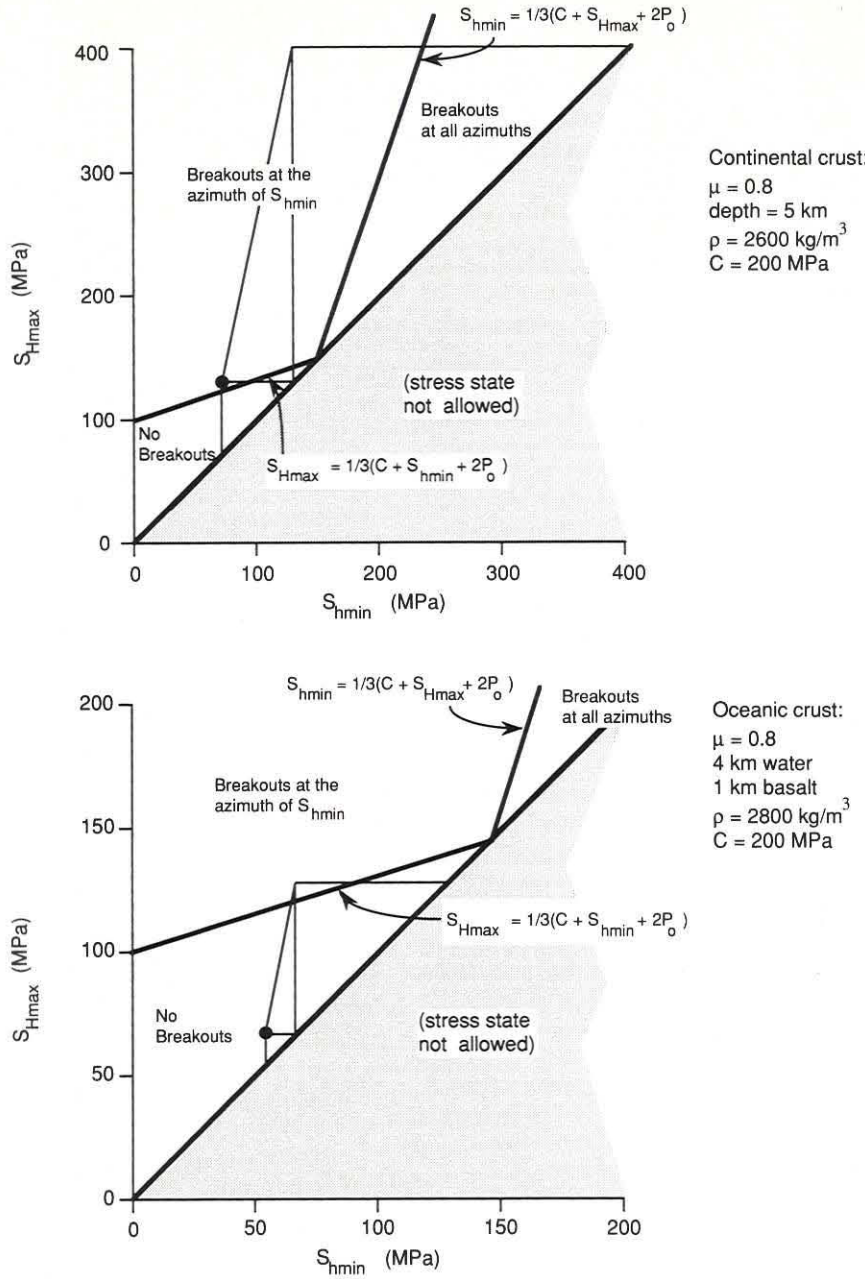

Fig. 4. Schematic illustration of the type of compressive well bore failure (breakout) possible for stress conditions as defined in Figure 1, for a rock strength of 200 MPa. As in Figure 1, the stress state must lie within the bounds imposed by friction and the definition that $S_{Hmax} \geq S_{hmin}$. Note that at 5 km depth in the continents, breakouts will occur for any stress state except a low-stress strike-slip one, whereas at 1 km into oceanic crust, breakouts will only occur if the horizontal stresses are quite high.

parameter ϕ, where $\phi = (S_2 - S_3)/(S_1 - S_3)$ [*Angelier*, 1979]. The figure shows, for the stress states defined by the respective faulting regimes and the value of ϕ, the depth at which breakouts would form for a given strength. As seen in this figure, breakouts develop at much shallower depths in a reverse-faulting regime than in a normal-faulting regime, for a given rock strength. For example, for a rock strength of 200 MPa and $\phi = 0.5$, breakouts would occur below a depth of approximately 1.2 km in a reverse-faulting environment, but in a normal-faulting environment they are not expected until depths of more than 9 km.

Figure 6 presents an analysis similar to Figure 5 for the oceanic crust assuming a water depth of 4 km. In this case, breakout formation occurs roughly at the same depth below the seafloor as below the ground surface on the continents, for the same tectonic stress and rock strength. Unfortunately, wells penetrating more than a few hundred meters of the oceanic crust are extremely rare, and breakouts would be expected only if the level of compressive stress was quite high and the rocks were anomalously weak.

Borehole Televiewer Observations of Well Bore Breakouts

The borehole televiewer (BHTV) is an acoustic logging device which scans the interior wall of a borehole, as first

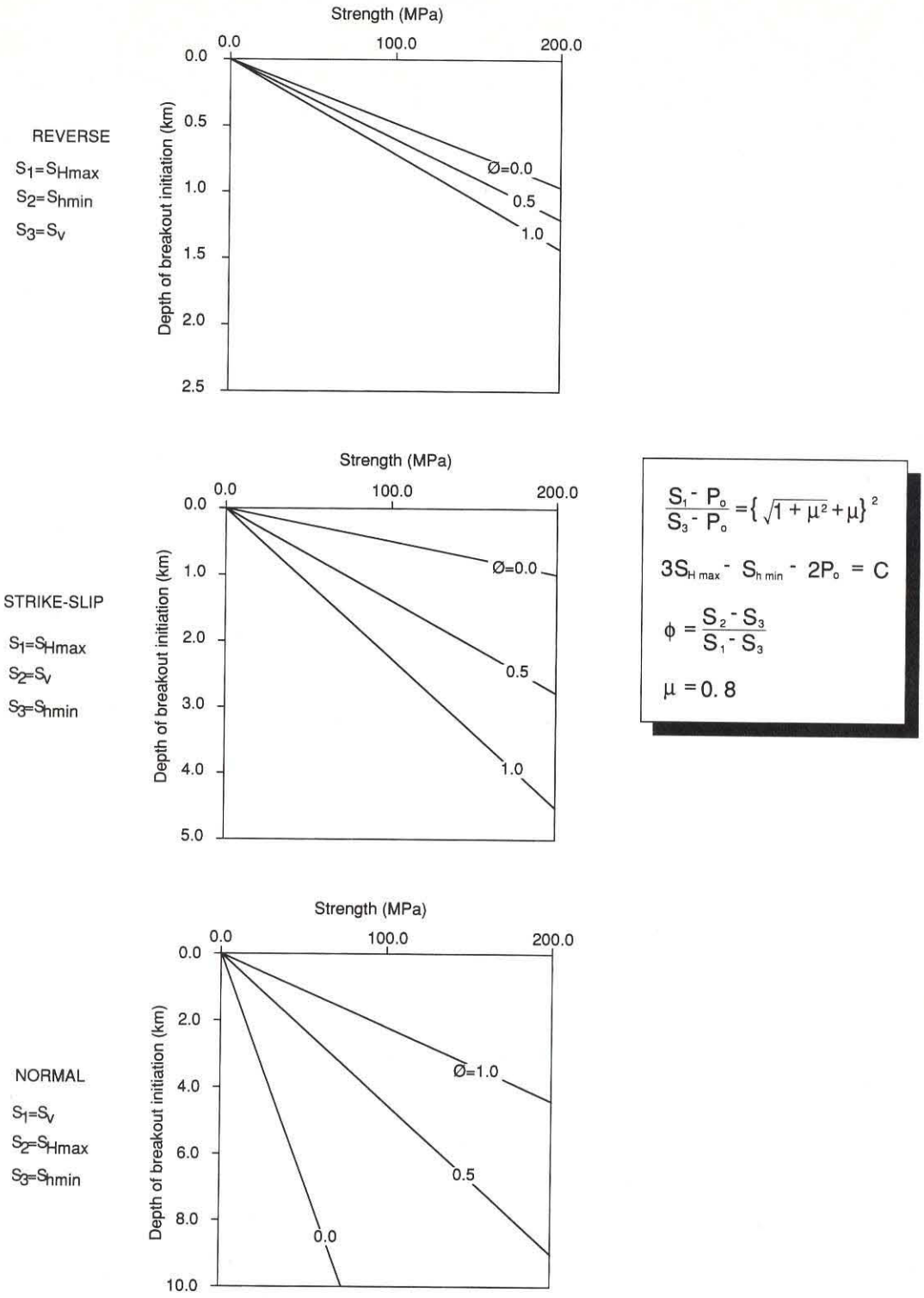

Fig. 5. Minimum depth of breakout formation due to the circumferential stress concentration around a well drilled into continental crust, plotted as a function of rock strength. For each stress state the stresses are at the limit constrained by a coefficient of friction $\mu = 0.8$ on favorably oriented fault planes.

described by *Zemanek et al.* [1970], to produce a magnetically oriented image of the reflectivity of the borehole wall as a function of depth and azimuth in the hole. *Zoback et al.* [1985] demonstrated that breakouts could be imaged with the BHTV and produced the first detailed study of breakout cross sections. Since that time, considerable improvement has been made in the analysis of borehole televiewer data [*Barton*, 1988], and travel times determined from digitized data are now used to determine borehole shape [e.g., *Shamir et al.*, 1988; *Morin et al.*, this issue].

Plate 1*a* shows breakouts imaged with the BHTV in the Cajon Pass research well [*Shamir et al.*, 1988]. The images

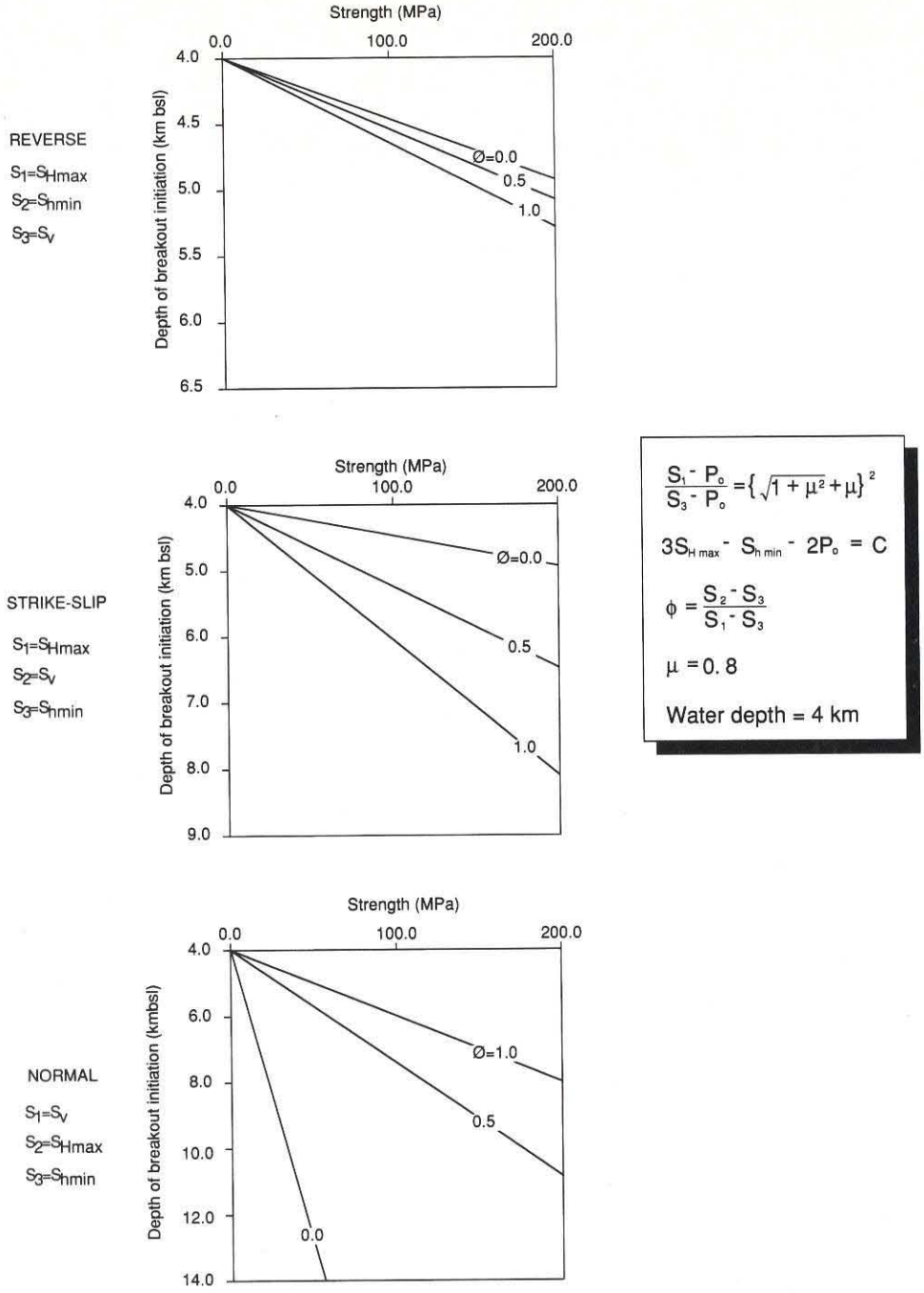

Fig. 6. Minimum depth of breakout formation in kilometers below sea level due to the circumferential stress concentration around a well drilled into oceanic crust overlain by 4 km of water, plotted as a function of rock strength. For each stress state the stresses are at the limit constrained by a coefficient of friction $\mu = 0.8$ on favorably oriented fault planes.

on the left are borehole radius as a function of depth and azimuth. On the right, cross sections of the borehole are shown at various depths. Each cross section involves superposition of three transducer scans (spanning approximately 10 cm vertically). The breakouts appear in cross section as smooth enlargements on opposite sides of the borehole. The amplitude of the reflected signal is lower within the breakout, due to the rougher surface and the fact that the reflection within the breakout is scattered away from the transducer because of nonnormal incidence of the acoustic pulse. As a result, one finds that often a reflection is returned only from the back of the breakout. In the images on the left side of the figure the breakouts appear as irregular vertical bands spanning several meters along the borehole.

Conditions for Tensile Failure

The conditions for tensile failure have been discussed extensively in the context of hydraulic fracturing. In typical

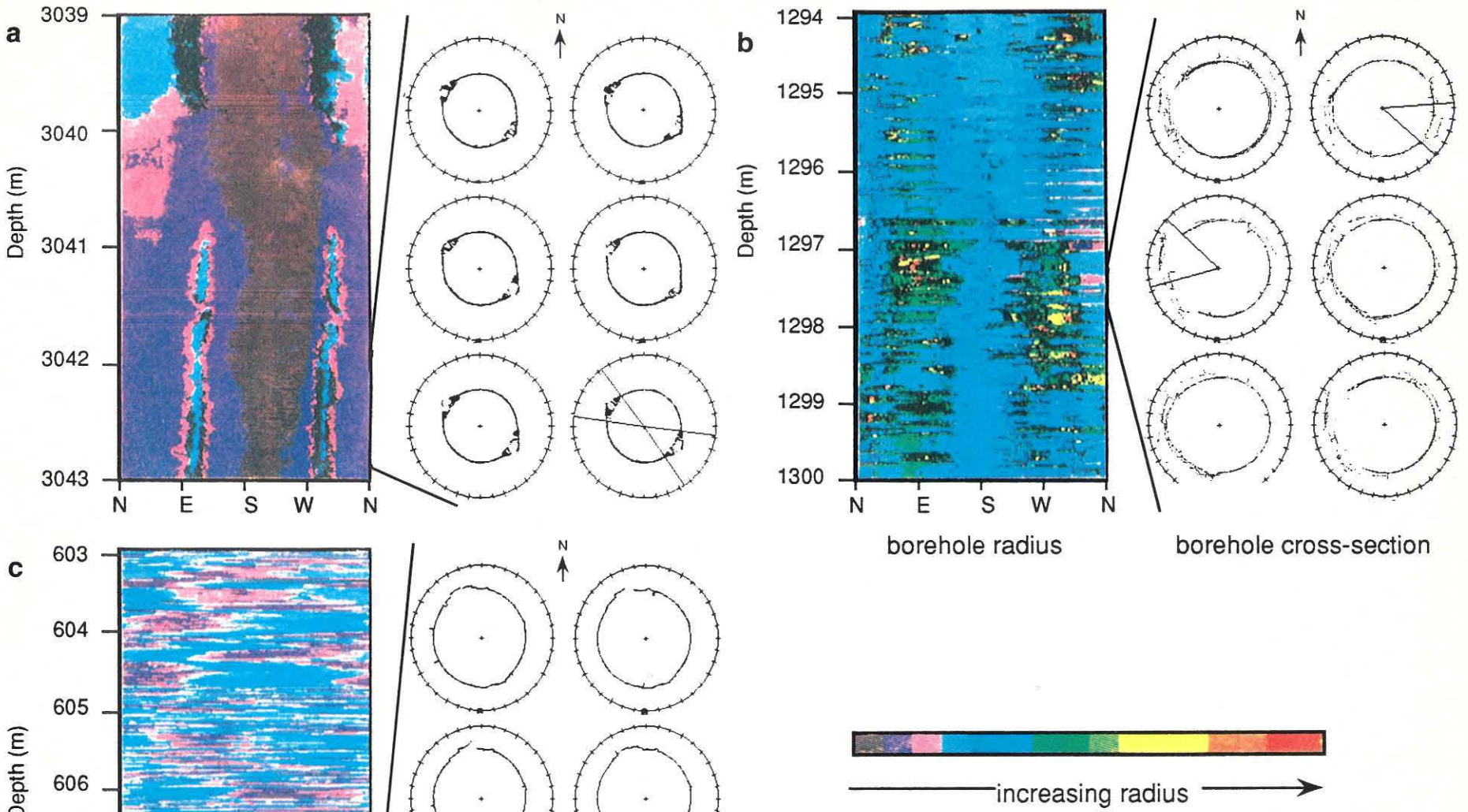

Plate 1. (*a*) Observations of well bore breakouts at 3 km depth in the granitic rocks penetrated by the Cajon Pass well (data from *Shamir et al.* [1988]). On the left is an oriented, false color image of the well bore radius as a function of azimuth. The difference in radius between light blue and deep purple is about 0.6 cm in an ~8.5-cm-radius borehole. The cross sections on the right have somewhat enhanced borehole relief, to show the characteristic broad, flat-bottomed shape of the breakouts. These are typical of well bore breakouts observed by the borehole televiewer in crystalline rock. (*b*) Observations of well bore failure at 1.3 km below seafloor in sheeted dikes in DSDP hole 504B (data courtesy of R. Morin) are shown. The difference in radius denoted by the color change from blue where the hole is not enlarged to yellow within the breakouts is 1.4 cm. (*c*) Borehole televiewer data recorded during DSDP leg 78B in hole 395A, showing very small (incipient) breakouts at a depth of 603 mbsf, are illustrated.

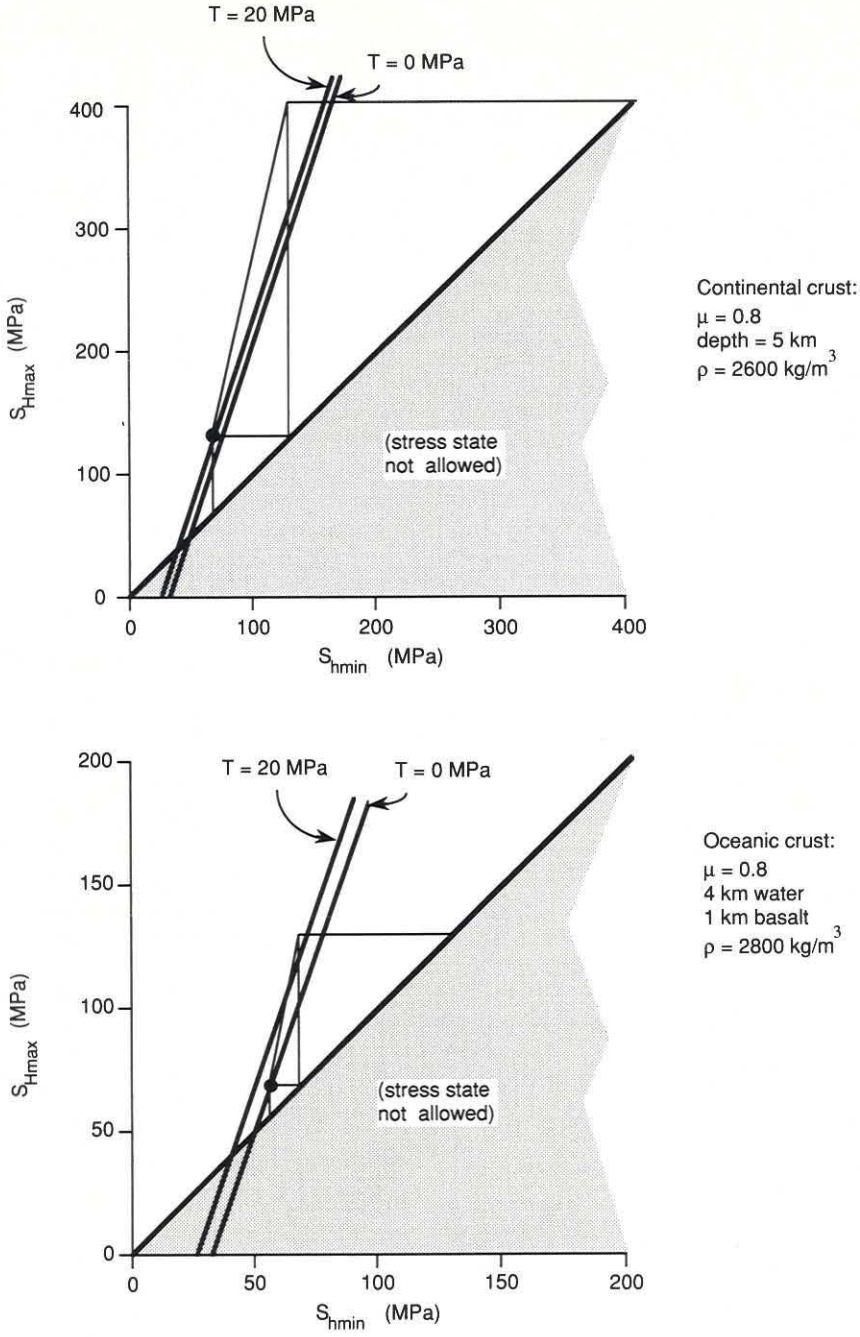

Fig. 7. Stress conditions necessary to cause tensile fracturing at the azimuth of S_{Hmax}, for the stress conditions defined in Figure 1. The lines illustrate the stress values necessary to cause tensile failure for the given values of tensile strength, if the well bore fluid pressure is equal to the ambient pore pressure (i.e., $S_{\mathrm{Hmax}} = 3S_{\mathrm{hmin}} - 2P_0 + T$). Tensile failure can occur under normal drilling conditions where the lines intersect the polygon constraining the stress state. For example, the stress state indicated by the circle will cause tensile failure if the tensile strength is zero, as shown also in Figure 2.

hydraulic fracturing operations, increasing the fluid pressure in the well bore induces tensile failure in a vertical well bore at the azimuth of the greatest far-field horizontal principal stress. Hydraulic fractures will be produced when the pressure in the well bore exceeds the sum of the tensile strength and the circumferential stress concentration. Written in terms of the total stresses and the pore pressure, this condition [after *Hubbert and Willis*, 1957] is

$$P_b = 3S_{\mathrm{hmin}} - S_{\mathrm{Hmax}} - P_0 + T \tag{5}$$

where P_b is termed the breakdown pressure and T is the tensile strength.

Under certain tectonic stress conditions, however, tensile failure occurs during drilling simply because of the pressure of the fluid column in the borehole resulting in "drilling-induced" hydrofracs. At the Nevada Test Site (NTS), where

TABLE 1. Relationship Between Observed and Predicted Breakout Depths

Well Name	C_0, MPa	C, MPa	Measured ϕ	Stress Regime	Depth of Breakout Initiation, km	Predicted Depth of Initiation, km	Predicted Range of ϕ
Moodus	>105*	>105–143	0.5	R	~1.1	0.90–1.22	>0.25
NTS	15–120†	15–163	0.35–0.6	N	~1.1	0.50–5.45	>0.3
Cajon Pass	100–150*	100–204	1.0	N/SS	~2.7	2.30–4.47	>0.9
Fenton Hill	124–176‡	124–240	1.0	N/SS	2.9	2.88–5.58	>0.85

*C_0 inferred from tensile strengths measured using the Brazilian test and the relationship between tensile and uniaxial compressive strength $C_0 \sim (8\text{–}12)T_0$.
†*Price and Bauer* [1985].
‡T. Dey (personal communication, 1987) [after *Barton et al.*, 1988].

the ambient pore pressure is appreciably subhydrostatic, the water used to fill the well bore during drilling frequently caused hydraulic fractures to occur [*Stock et al.*, 1985].

Figure 7 illustrates the range of stresses that could lead to tensile failure at the well bore, if the well bore fluid pressure is equal to the ambient pore pressure. Tensile failure can occur for a given value of tensile strength if the stress state lies to the left of the indicated line. Drilling-induced hydrofracturing can occur whenever the horizontal stress ratio is close to the limit constrained by the strength of strike-slip faults (i.e., where the ratio of the effective principal horizontal stresses is about 3). In some cases, as a consequence of the excess pumping pressure required to lift cuttings, the pressure at the bottom of a well during drilling can exceed the pressure due to the static fluid column by as much as 10 MPa. This is equivalent to reducing the "effective" tensile strength and would shift the lines of constant tensile strength to the right, making tensile failure more likely. Nevertheless, it is clear that the presence of drilling-induced hydraulic fractures would still constrain the possible stress state to be close to that associated with incipient strike-slip faulting.

Tensile failure at the well bore can also be induced by the thermal stresses associated with well bore cooling. *Allison and Nielson* [1988] observed features in four-arm caliper (dipmeter) logs in geothermal wells which may be due to tensile fractures developed because of well bore cooling. Similarly, tensile fractures were produced during drilling in geothermal fields in France and are suggested to have formed in the KTB (German deep drilling project) pilot hole (L. Mastin, written communication, 1989). The effect of thermal stresses is equivalent to that of the excess well bore pressure. Cooling the well would induce tensile thermal stresses, lower the apparent tensile strength, and promote tensile failure. Depending on the magnitude of the thermal stress, this could lead to failure within the oceanic crust even if the rock is fairly strong.

Thus although the presence of tensile cracks requires a large ratio of effective horizontal stresses and a strike-slip-faulting regime, it does not generally differentiate between cases in which $S_v \approx S_{\mathrm{Hmax}}$ (strike-slip and normal faulting) and $S_v \approx S_{\mathrm{hmin}}$ (strike-slip and reverse faulting). Distinguishing between these cases requires observations related to compressive failure (breakouts).

Application to Continental Crust

Over the past 5 years a number of wells have been studied in sufficient detail that data are available on the magnitude of in situ stresses, distribution of well bore breakouts, and compressive strength of the rock. This makes it possible either to utilize all of the data that are available from these wells to test the overall validity of the analysis, or to utilize only a portion of the available data in an attempt to place constraints on stress magnitudes simulating the general approach that we are suggesting for cases in which relatively complete information from a given well is not available.

Table 1 summarizes the key information from several wells in which the state of stress was found to be consistent with that predicted from the frictional strength of well-oriented faults (that is, in accordance with (1)) and for which information is available on the distribution of well bore breakouts and rock strength. Note that these four cases involve normal, normal/strike-slip, and reverse-faulting environments. Relatively continuous breakouts were observed in each case from the shallowest depth to the total drilled depth.

Utilizing (4*a*) and the information on strength and stress magnitudes in Table 1, we can calculate the range of depths below which "relatively continuous" breakouts would be expected in each well. The term relatively continuous refers to the fact that we want to consider failure of the well bore at representative stresses and rock strength values, not isolated and discontinuous breakouts that might be observed only in selected sections of the well bore where locally the rock might be unusually weak. We compare the observed depth below which breakouts are relatively continuous with the calculated depths. In each case the depth below which relatively continuous breakouts were observed is within the range predicted by the calculation. However, one must keep in mind the fact that the strength values are poorly constrained by laboratory measurements, particularly where unconfined compressive strength is calculated, rather than measured directly. In fact, the largest range of predicted depth (at NTS) is the one for which the largest range of strengths were assumed. The NTS wells were drilled into imbricated tuffs, for which the strengths depended on the degree of imbrication, which varied greatly from unit to unit. In general, breakouts were only observed in the weaker units, consistent with the known stress state. Aside from this case the depth of initiation observed is close to the lowest calculated value, suggesting that the appropriate strength is closer to C_0 than to C_b.

Alternatively, one can use the depth of breakout initiation to constrain the stress state. Table 1 shows the range of ϕ values predicted on the basis of the breakout distribution if the vertical stress and one limiting stress are known. In all cases the vertical stress was measured, and the stress magnitudes are at failure equilibrium; therefore (1) is valid for these data. The comparison between the calculated range of ϕ and the measured values illustrates our ability to predict one of the three principal stresses simply from knowledge of

TABLE 2. Physical Properties of Oceanic Basalts

Parameter	Value
Tensile strength T	23–34 MPa
Unconfined compressive strength C_0	170–224 MPa
Poisson's ratio ν	0.17–0.25
Young's modulus E	50–70 GPa
Thermal expansion coefficient α	$5.4 \pm 1 \times 10^{-6}$ °C^{-1}
Thermal diffusivity κ	1×10^{-6} m^2/s

the depth range of compressive well bore failure and of the other two stresses. In each case the predicted range includes the known value of ϕ. The power of the method lies in its ability to restrict ϕ and hence to place one bound (either a lower or an upper bound) on the intermediate stress. For example, for Moodus, where ϕ was measured to be 0.5, the analysis constrains ϕ to lie above 0.25. For NTS, where ϕ is between 0.35 and 0.6, the analysis requires ϕ to be greater than 0.3. At Cajon Pass and Fenton Hill, where ϕ is close to 1, the analysis also predicts very large values for this ratio.

All of these results are limited by our knowledge of the appropriate value of rock strength. The large range of values for ϕ result from the large range of possible values for C. These uncertainties will persist until laboratory strengths can be determined for rock from within these wells both in intervals which contain breakouts and in those which do not.

Application to Oceanic Crust

Although a large number of boreholes have been drilled into oceanic basement during the DSDP and ODP, only a small number of these have been logged with the borehole televiewer, and none have been tested by hydraulic fracturing. As described above, the presence of breakouts allows the determination of the orientation of the principal horizontal stresses and places a lower bound on the stress difference, whereas the absence of breakouts provides an upper bound on the stress difference. If tensile cracks are present, a further constraint can be placed on the ratio of the effective principal horizontal stresses.

We make the following assumptions in this analysis. First, we can reasonably assume that the in situ pore fluid pressures are close to hydrostatic. In fact, measured pore pressures in hole 504B [*Anderson and Zoback*, 1982], hole 395A [*Hickman et al.*, 1984*a*], and hole 597C [*Shipboard Scientific Party*, 1985] indicate that pore pressures are within 1 MPa (2.5%) of hydrostatic. We also assume that S_v is a principal stress and is equal to the weight of the overlying rock and seawater.

To place constraints on the stresses necessary for well bore failure, we need to know the properties of the basalts. Table 2 shows typical values for the parameters necessary for these calculations [*Clark*, 1966; *Carmichael*, 1982]. With the exception of one anomalously low-strength sample, *Bauer and Handin*'s [1985] measurements of E and C_0 of basalts from DSDP hole 504B lie within the range presented in this table.

There is considerable scatter in these data, particularly for the tensile and unconfined compressive shear strengths. The constraints presented below should therefore be considered in light of this fact and will have to serve until better information concerning the strength of specific oceanic basalts is available. For the purpose of this paper we will use the following (average) values of the properties tabulated above: $T = 28.5$ MPa, $C_0 = 200$ MPa, $\nu = 0.2$, $E = 60$ GPa, $\alpha = 5.4 \times 10^{-6}$ °C^{-1}, and $\kappa = 1 \times 10^{-6}$ m^2/s.

DSDP Holes 504B and 501

Hole 504B was drilled over a succession of DSDP and ODP legs to a total depth of 1562 m below seafloor (mbsf) in 3460 m of water and penetrates over 1200 m of 5.9-Ma oceanic crust south of the Costa Rica Rift (Figure 8). Pillows and minor flows were encountered in the uppermost 571.5 m of basement, below which was a 209-m transition zone followed by sheeted dikes and massive units [*Becker et al.*, 1989].

In hole 504B, *Newmark et al.* [1984] observed stress-induced well bore breakouts in the section of the hole drilled on legs 69 and 70. *Morin et al.* [this issue] digitized both the televiewer data from the leg 83 log and from a log recorded during leg 111. The digitized data cover a depth range from 440 mbsf to 1525 mbsf. The uppermost 170 m of basement could not be studied, as no data were recorded on tape during the log of this interval on leg 83. *Morin et al.* [this issue] identify a bimodal distribution of hole enlargements throughout the interval from about 700 mbsf to total depth and attribute the predominant azimuth of enlargement (117.5° ± 20°) to compressive failure (breakouts) and the secondary mode (about 27°) to tensile failure. The breakouts become nearly continuous below about 1.2 km below seafloor. The maximum compression direction inferred from these data (N27.5°E) agrees with the P axes of focal plane mechanisms of nearby earthquakes [*Bergman*, 1986].

Plate 1*b* presents a short section of digitized televiewer data from leg 111. The leg 111 data contain clearly imaged well bore enlargements, over the interval 1294–1300 mbsf, within the intrusive section of sheeted dikes. Hole enlargements occur at 90° and 270° here, within the range of scatter of the measurements presented by *Morin et al.* [this issue]. Although the breakouts are not as regular or as well imaged in data from hole 504B as they are in holes such as Cajon Pass (Plate 1*a*), the fact that enlargements occur on both sides of the hole, and at a generally consistent azimuth, suggests that they are stress-induced.

DSDP hole 501 was drilled 400 m west of hole 504B through 264 m of sediments and penetrated 73 m of basement. Core recovery was moderate and indicated a mixed assemblage of pillows and massive units. Televiewer data were recorded in the uppermost 25 m of basement only, but data were recorded in almost the entire sedimentary section [*Zoback and Anderson*, 1982]. We analyzed these data in detail and found no breakouts, either in the sedimentary section or in the basement interval.

The presence of breakouts within the depths penetrated by hole 504B demonstrates that high horizontal stresses must exist at a relatively shallow depth of less than 1 km into young oceanic crust. To illustrate this, we present in Figure 9 schematic plots of two possible stress states at sites 501 and 504. In these figures we calculate S_v from the weight of the overlying rock and seawater. In Figure 9*a* we assume that the stress regime is extensional, with $S_1 = S_v = S_{\mathrm{Hmax}}$, and allow S_{hmin} to range between that value and the value limited by a coefficient of friction $\mu = 0.8$. In Figure 9*b* we assume the stress regime is compressional, with $S_3 = S_v = S_{\mathrm{hmin}}$, and allow S_{Hmax} to range between that value and the

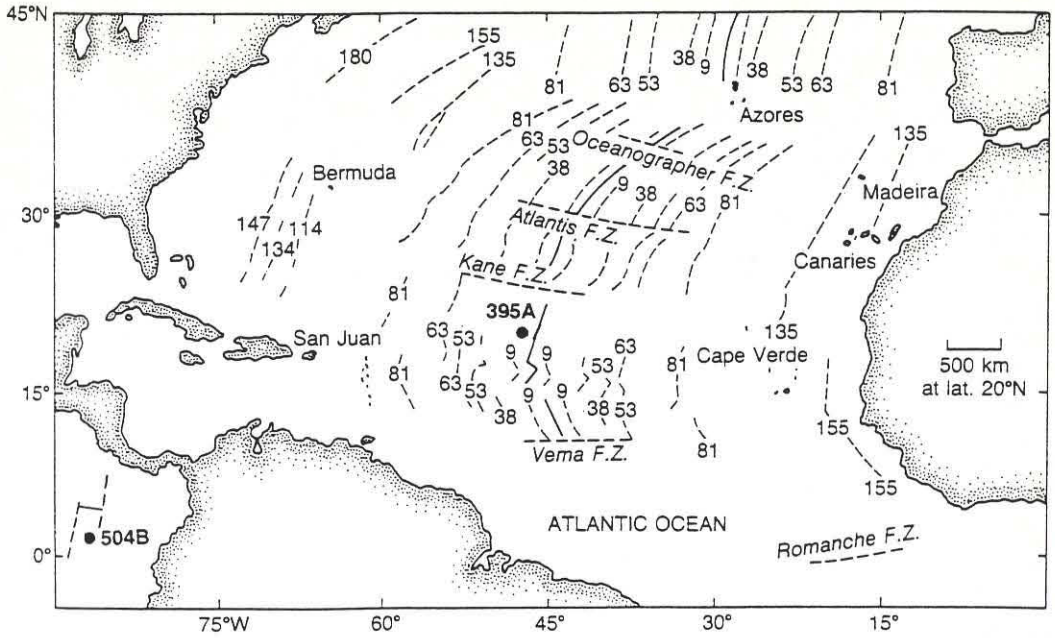

Fig. 8. Map [after *Hyndman and Salisbury*, 1984] showing the locations of DSDP hole 504B and of DSDP hole 395A. Hole 501 is within the area covered by the circle at site 504. The orientations of nearby spreading centers and transforms are also shown.

value limited by a coefficient of friction $\mu = 0.8$. In each case, setting one horizontal stress equal to S_v is equivalent to the most favorable stress state for the formation of breakouts. Lines are shown illustrating the value of rock strength (C) below which breakouts would occur for a given value of the unknown principal stress. It is evident in Figure 9*a* that breakouts cannot occur in an extensional stress environment at the depths penetrated by DSDP hole 504B unless the rock strengths were less than 75 MPa. This is a factor of 3 smaller than the average value of C_0 of more than 200 MPa measured by *Bauer and Handin* [1985]. We see in Figure 9*b*, however, that for a rock strength of between 200 and 272 MPa ($C_0 \leq C \leq 1.36C_0$), nearly continuous breakouts would be expected to occur at depths of about 1 km below seafloor, but only if the maximum horizontal stress was at the limit imposed by the strength of reverse faults and $\phi = 1$ (or $S_{\text{hmin}} = S_v = S_3$).

As illustrated in Figure 9, *Morin et al.* [this issue] report relatively continuous breakouts in hole 504B below about 1.2 km below seafloor. Therefore S_{Hmax} must be quite high (close to the limit constrained by the frictional strength of the crust), and S_{hmin} must be equal to S_v. Short intervals with breakouts which occur above that depth can be explained simply by localized sections of the hole with lower than average compressive strength. *Morin et al.* [this issue] also report the presence of tensile failure in DSDP hole 504B. We can develop a similar set of criteria for tensile failure, to constrain the ratio of the horizontal stresses. However, in this instance the thermal stress and therefore the temperature difference due to pumping cold fluid into the well bore must be known.

Calculating the thermal effect of circulation is quite difficult as pumping rate, rotation rate, fluid viscosity, and the temperature profile outside the pipe all influence the heat transfer among the drilling fluid, the fluid outside the pipe, and the rock surrounding the hole. Furthermore, although drilling fluids exiting the bit may cool the bottom of the hole, returning fluids may warm shallower sections. However, estimates of the minimum temperature perturbation can be obtained from temperature logs run shortly after circulation ceased. Temperatures within hole 504B were recorded a number of times, either shortly after drilling or after the well bore had equilibrated during legs 69, 70, 83, 92, and 111 [*Becker et al.*, 1989]. On the basis of the results of these measurements, drilling and circulating within hole 504B resulted in a minimum of 40°C cooling of the bottom of the well bore. During each circulation phase, shallower sections of the hole may have been warmed somewhat. As suggested by *Morin et al.* [this issue], temperatures were most strongly perturbed at the points where the fluid exited the pipe and for the periods during which the hole was deliberately cooled prior to logging. On the basis of 40°C cooling, the rock properties in Table 2, and (3), the minimum additional circumferential tensile stress applied during circulation within hole 504B is 16.4 MPa. Figures 10*a* and 10*b* are similar to Figures 9*a* and 9*b* and illustrate the stress conditions necessary to cause tensile failure at the borehole wall if well bore fluid pressure is equal to the in situ pore fluid pressure. The additional stresses generated by well bore cooling can be considered simply by reducing the tensile strength by the magnitude of the tensile thermal stress. In other words, a tensile strength of 20 MPa and a tensile thermal stress of 20 MPa are equivalent to a zero effective tensile strength. For the assumed average tensile strength of 28.5 MPa and a 40°C decrease in well bore temperature, the effective tensile strength is 12.1 MPa. For this strength and the reverse/strike-slip stress regime required for breakouts, tensile failure could occur at almost any depth below the top of basement. Thus the stress state required to produce breakouts would also produce tensile failure by well bore cooling, and it is therefore not surprising that such features were observed by *Morin et al.* [this issue].

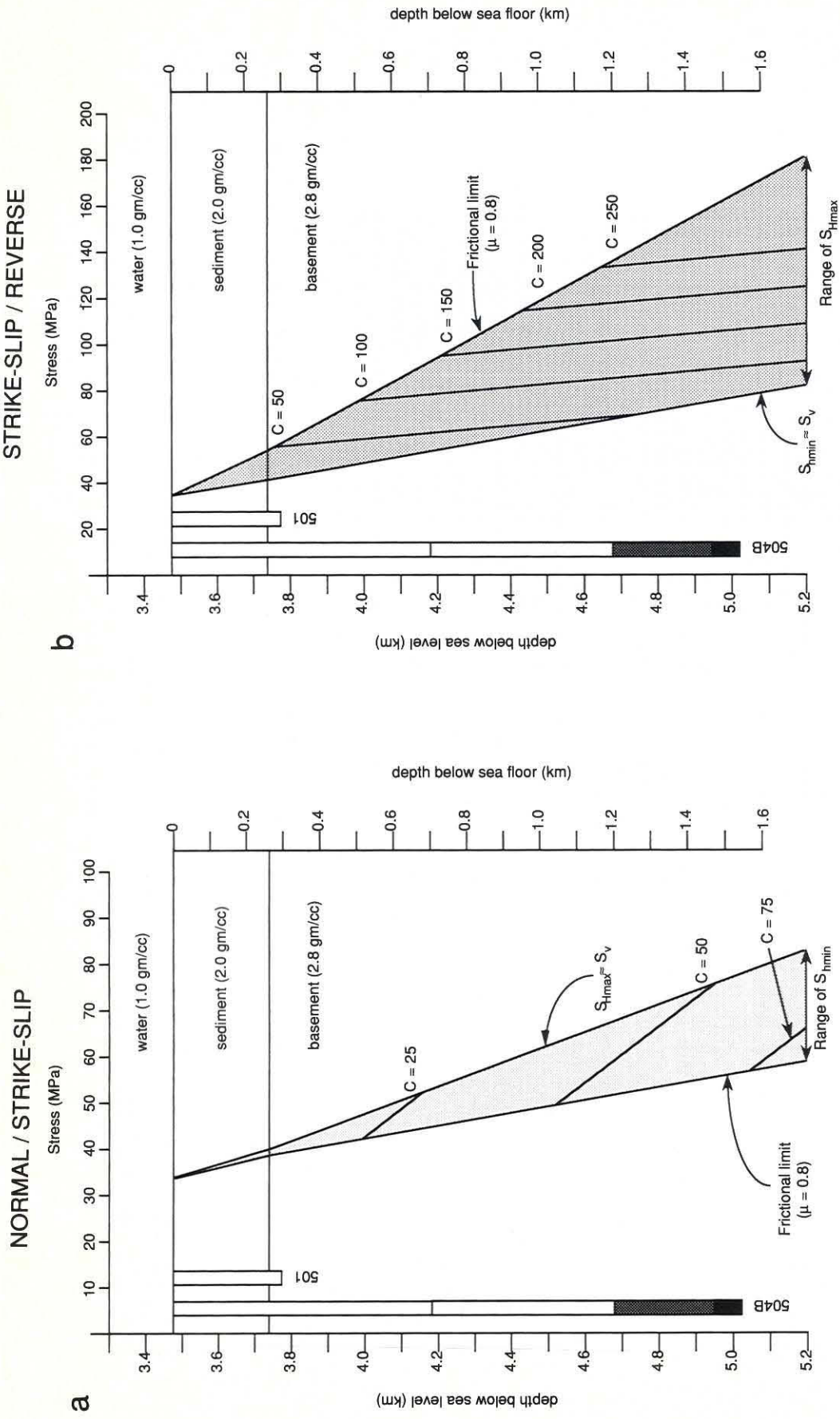

Fig. 9. Schematic illustration of possible stress conditions at DSDP sites 504 and 501. Also shown is the incidence of breakouts in holes 504B [*Morin et al.*, this issue] and 501. No breakouts were observed in 501, and breakouts were intermittent in 504B below about 700 mbsf, common below about 1.2 km below seafloor, and nearly continuous below about 1.5 km below seafloor. (*a*) A normal/strike-slip environment, with $S_{Hmax} = S_v = S_1$, $S_{hmin} = S_3$, is shown. S_{hmin} can range from equal to S_{Hmax} to a minimum value controlled by friction (equation (1)). The lines are $S_{Hmax} = \frac{1}{3}(S_{hmin} + P_0 + C)$, for the values of C shown. (*b*) A strike-slip/reverse environment, with $S_{hmin} = S_v = S_3$, $S_{Hmax} = S_1$, is also illustrated. S_{Hmax} can range from equal to S_{hmin} to a maximum value controlled by friction (equation (1)). The lines are $S_{hmin} = 3S_{Hmax} - C - 2P_0$ for the values of C shown. In each case, breakouts will form only if the rock strength C is below the contoured values. For strengths of 200–270 MPa, typical of samples from hole 504B [*Bauer and Handin*, 1985], breakouts would not be expected in a normal/strike-slip environment at any depth penetrated by hole 504B. The observations of breakouts are, however, consistent with a reverse-faulting regime with S_{Hmax} close to the limit imposed by a coefficient of friction $\mu = 0.8$.

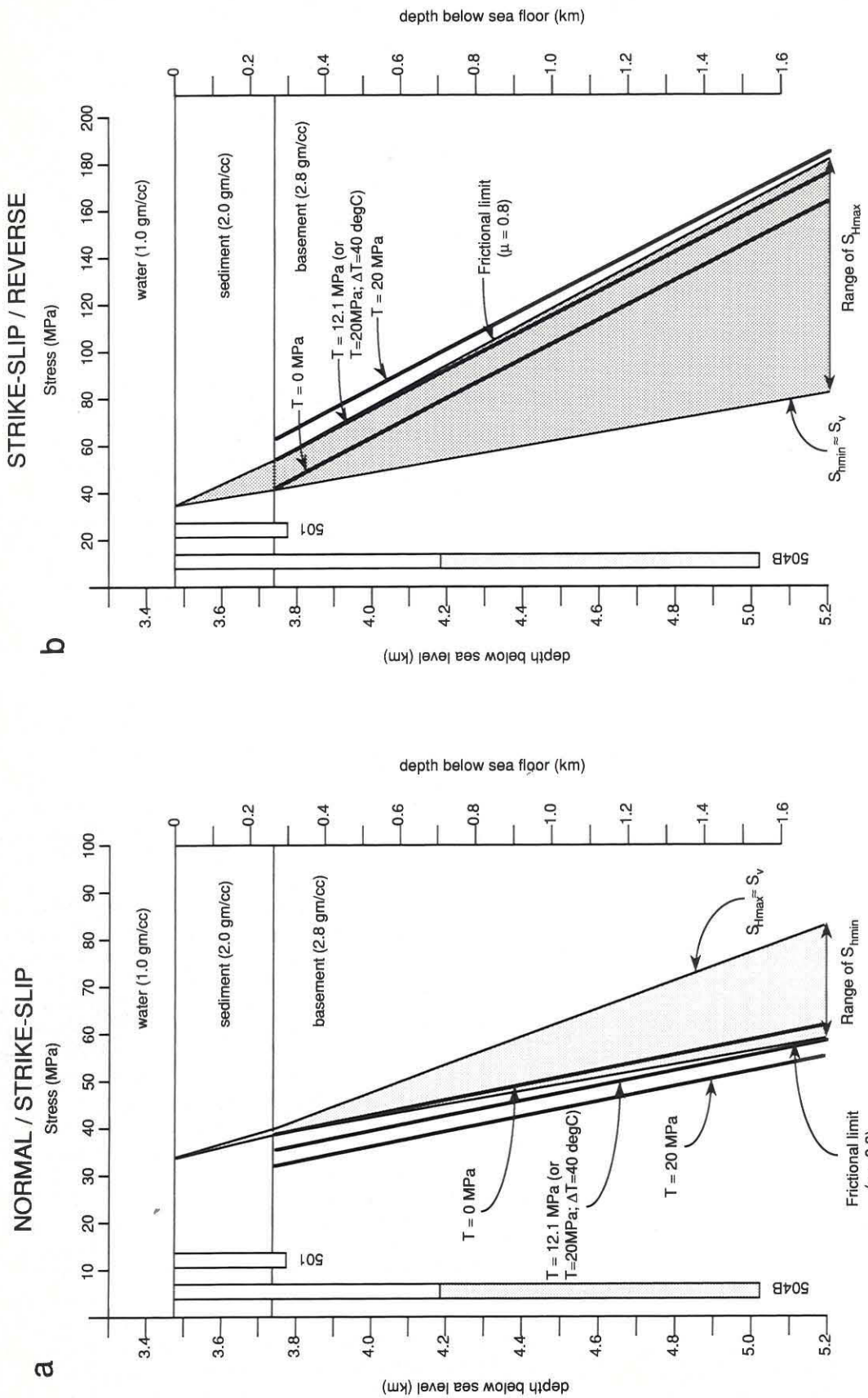

Fig. 10. Schematic illustration of possible stress conditions at DSDP sites 504 and 501. The stress states are as described in the caption Figure 9. Also shown is the depth range over which tensile failure was observed in hole 504B [*Morin et al.*, this issue]. (*a*) The maximum values of S_{hmin} for which tensile failure would occur at a given depth if the tensile strength of the rock is below the indicated values and the stress regime is transitional between normal and strike-slip faulting. (*b*) The minimum values of S_{Hmax} for which tensile failure would occur at a given depth if the tensile strength of the rock is below the indicated values and the stress regime is transitional between reverse and strike-slip faulting. In both cases it is assumed that the fluid pressure in the well bore is equal to the pore pressure in the rock and that the fluid temperature is equal to the ambient temperature. The intermediate value of tensile strength is the effective tensile strength computed assuming a 40°C decrease in well bore temperature during fluid circulation and a tensile strength of 28.5 MPa. Note that the presence of tensile cracks is only somewhat more likely for a reverse-faulting regime, but that in either a reverse- or normal-faulting regime the maximum horizontal stress difference (strike-slip equilibrium) is required.

DSDP HOLE 395A

DSDP site 395 is situated on the edge of a small sediment pond near the center of magnetic anomaly 4, at 22°45'N latitude, in 7.4 Ma crust between the Kane and the Vema fracture zones (Figure 8). Hole 395A was drilled to a total depth of 664 m below seafloor in 4493 m of water, through 93 m of sediments and 571 m of pillow basalts. A borehole televiewer log was obtained during DSDP leg 78B in the interval from 112 mbsf to 609 mbsf [*Hickman et al.*, 1984*b*]. Well bore enlargements satisfying the criteria for breakouts (that is, that enlargements were observed on both sides of the hole over a series of successive scans) were observed only near the bottom of the hole. No indications of well bore failure in tension were observed within hole 395A.

Plate 1*c* shows an example of the breakout data within DSDP hole 395A. Although the breakouts are impossible to resolve in the panel on the left, the well bore cross sections on the right clearly reveal shallow, poorly developed well bore enlargements oriented at approximately N20°W and S20°E. These indicate a maximum compressive stress N70°E, about 60° to the trend of the mid-Atlantic Ridge. The fact that the breakouts are very small and occur only intermittently suggests that the stresses are barely large enough to cause failure, and then only for anomalously weak rock.

Figure 11 shows possible stress regimes at site 395, along with lines for breakout formation as a function of maximum stress for various values of rock strength. As in the case of hole 504B, no breakouts would be expected in an extensional regime (Figure 11*a*) unless the rock is extraordinarily weak. Furthermore, Figure 11*b* illustrates that for a rock strength of 200 MPa, breakouts would not be expected even near the bottom of the hole, regardless of the state of stress. The well bore enlargements seen near the bottom of the hole could only occur by compressive shear failure if the rock strength in that short interval is about 150 MPa and if S_{Hmax} was at the limiting stress for reverse faulting and $S_{\mathrm{hmin}} = S_v$. These results are quite similar to those obtained at site 504, and together they suggest that in relatively young crust in both the Atlantic and the Pacific Oceans, very large compressive stresses are at a large angle to the ridge axes.

An attempted hydraulic fracturing experiment in this hole [*Hickman et al.*, 1984*a*] was unsuccessful after attaining an excess well bore fluid pressure of 15.2 MPa. The experiment was conducted with the packer set at a depth of 582 mbsf, in competent rock near the bottom of the hole. Using the values for tensile strength from Table 2 (23–34 MPa), the fact that breakdown did not occur is not surprising. Even if the state of stress implied by the breakouts near the bottom of the hole is correct, the expected breakdown pressure would be over 50 MPa. Temperature profiles recorded during leg 78B [*Becker et al.*, 1984] and during ODP leg 109 [*Shipboard Scientific Party*, 1988*b*] indicate that temperatures were essentially isothermal to 250 mbsf. Extrapolating a conductive gradient to total depth indicates a maximum thermal "shock" of less than 5°C, and thus the maximum applied circumferential tensile stress at the borehole wall due to this flow is about 7 MPa, much too small to substantially aid development of tensile cracks.

DSDP HOLE 597C

Site 597 is located at latitude 18°14'S, longitude 129°46'W, and is the westernmost site of an east-west transect of the southeast Pacific conducted during DSDP leg 92. DSDP hole 597C, drilled into 28.5-Ma crust (water depth 4160 m) generated at the Mendoza Rise, penetrated 52.5 m of sediments and 91 m of oceanic basalts; the hole has a reentry cone and therefore can be reoccupied and deepened in the future. Recovery was almost 54% and consisted largely of massive basalts [*Shipboard Scientific Party*, 1985]. Two complete BHTV logs were made in the hole within the basement interval. *Newmark et al.* [1984] reported the presence of intermittent breakouts throughout the total depth of the hole, from which a maximum horizontal compressive stress direction of N110°E ± 25° was determined. The presence of breakouts at such shallow depths is quite unusual, on the basis of both our experience and the theories presented above, and therefore we reanalyzed the data to confirm their presence.

No evidence of breakouts was found. Although the water depth and sediment thickness are slightly different at site 597 than those at sites 395 or 504, a figure similar to Figures 9 or 11 would reveal that breakouts could not develop at the depths penetrated by hole 597C (to 140 mbsf) even in a highly compressive stress regime, unless rock strength is extremely low. For a compressive strength of 200–270 MPa this borehole would have to be drilled an additional 600 m before breakouts might be expected. On the basis of these considerations, measurements of stress orientation from well bore enlargements in hole 597C should be treated with caution.

DISCUSSION OF SITES 504B AND 395A

Summarizing the results of previous work and of the above analyses, breakouts were observed in DSDP hole 504B and in the bottom of DSDP hole 395A, and no breakouts were observed at shallow depths in DSDP hole 501 or in DSDP hole 597C. Tensile failure within hole 504B could have occurred only with the addition of large tensile stresses generated by well bore cooling. The orientation of maximum compression inferred from the breakouts in holes 504B and 395A is roughly perpendicular to nearby ridge axes and in the case of hole 504B is parallel to that inferred from nearby earthquake focal mechanisms, as pointed out by *Morin et al.* [this issue]. In order for breakouts to occur at the depths penetrated by these wells, the stress state must be $S_{\mathrm{hmin}} \approx S_v \ll S_{\mathrm{Hmax}}$; S_{Hmax} must be large enough to cause reverse faulting on planes with a coefficient of friction $\mu = 0.8$.

The presence of thermally induced tensile fractures in hole 504B, and their absence in hole 395A, can be related to differences in the temperature profiles within the two holes. Heat flow at site 504 is about 200 mW/m^2 [e.g., *Langseth et al.*, 1988; *Becker et al.*, 1989], and the temperature gradient in hole 504B is also quite high. In contrast, heat flow in the sediments at site 395 is of the order of 37 mW/m^2, less than one fifth that at site 504 [*Hussong et al.*, 1979]. The undisturbed temperature gradient within basement at site 395 is similarly quite low, a consequence of strong lateral convection within shallow basement [e.g., *Becker et al.*, 1984; *Kopietz et al.*, 1990]. Thus temperatures increase much more slowly with depth within hole 395A, and the likelihood of large thermal stresses generated by fluid circulation at equivalent depths in 395A is therefore much smaller than in 504B.

Figure 12*a*, which gives an overview of earthquake focal

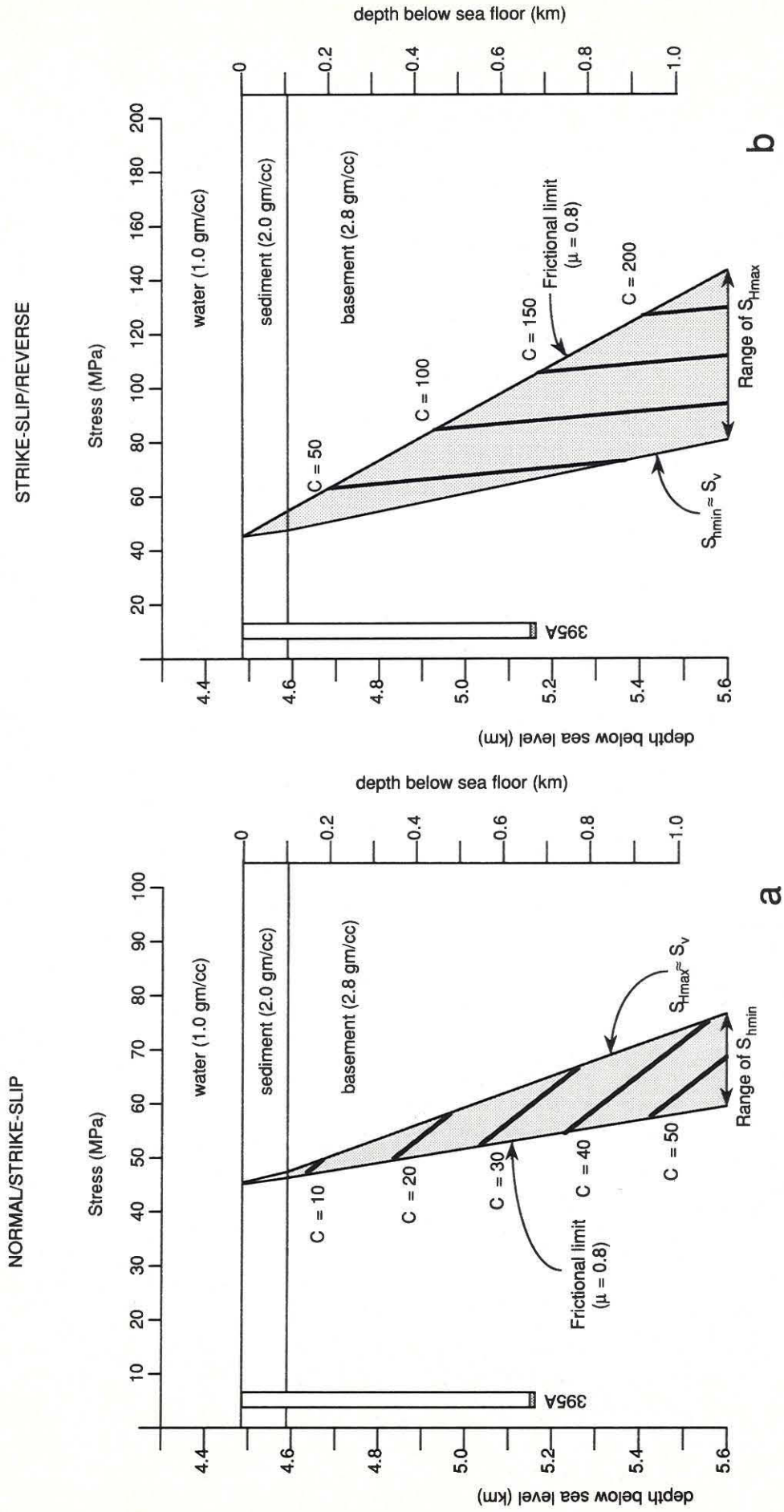

Fig. 11. Schematic illustration of possible stress states at DSDP site 395, if stresses are controlled by the frictional strength of well-oriented fault planes. The figure is similar to Figure 9 but for the conditions in hole 395A. Note that for breakouts to occur at 0.6 km below seafloor within DSDP hole 395A the compressive strength of the rock must be less than 150 MPa, and the stress regime must be as illustrated in Figure 11*b*.

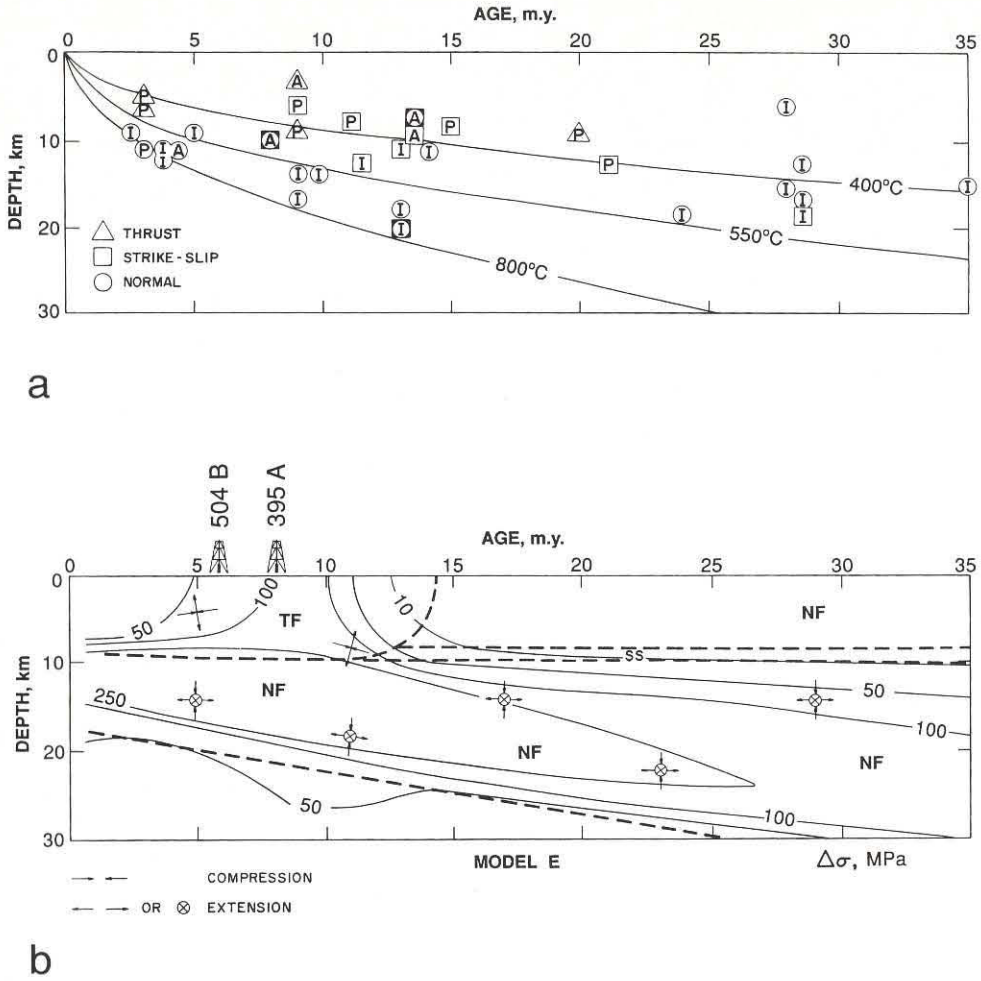

Fig. 12. (*a*) Focal mechanism and centroid depth relative to the seafloor as a function of lithospheric age for 32 near-ridge earthquakes from *Bratt et al.* [1985], after *Bergman and Solomon* [1984]. Mixed-faulting earthquakes are indicated by superimposed symbols, and the ocean in which each earthquake occurs is indicated by A (Atlantic), P (Pacific), and I (Indian Ocean). (*b*) Model E of *Bratt et al.* [1985] illustrates the effect of a 10-km-thick cooled layer with an elastic blocking temperature of 550°C, overlying a conductively cooling half-space, and a time constant for stress relaxation of 10 Ma. The age of the crust at sites 395 and 504 is shown.

mechanisms within oceanic lighosphere as a function of crustal age as tabulated by *Bergman and Solomon* [1984], reveals that reverse faulting predominates at shallow depths in young crust and that at greater depths and as the crust ages, strike-slip and normal faulting become more common. *Bratt et al.* [1985] have proposed that this state of stress is generated by thermoelastic effects in a plate consisting of a convectively cooled lid over a conductively cooling half-space, as illustrated in Figure 12*b*. The differential stresses generated by thermoelastic effects can exceed 100 Mpa at shallow depth, for crustal ages similar to those of sites 395 and 504. Ridge push forces cannot explain this stress distribution, as the horizontal stress generated by ridge push is zero at the ridge crest and increases with crustal age [e.g., *Bott and Kuzsnir*, 1984]. Although various models for stress relief and the depth of hydrothermal cooling lead to differences in the age to which shallow compressional stresses persist, thrust faulting predominates to ages older than 5 Ma in every case examined by *Bratt et al.* [1985], and the maximum deviatoric compression is horizontal and perpendicular to the ridge axis. In *Bratt et al.*'s [1985] model, stress relief is a function of time. This is quite different than the model used here, where the frictional strength of suitably oriented faults controls the maximum stress difference. However, if we combine the thermoelastic stress model of *Bratt et al.* [1985] with the frictional constraint on stress magnitudes, then in young oceanic lithosphere a thrust-faulting regime should predominate at shallow depths with S_{Hmax} maintained at a value constrained by strength and the (fixed) magnitude of the vertical stress, as in (1), and S_{hmin} approximately equal to S_v (there is no thermoelastic contribution to the horizontal stress parallel to the ridge axis), as required by the presence of breakouts within holes 504B and 395A.

As the crust ages, however, the model of *Bratt et al.* [1985] predicts that the importance of thermoelastic stress on the total lithospheric stress decreases. At an age of approximately 10–15 Ma, thermoelastic stresses are less important than the accumulated ridge push, and although the superposition of the two effects causes compressional stress normal to the ridge axis at all ages, the magnitude of the deviatoric compression is less than 50 MPa to ages of more than 35 Ma. Two implications arise from this observation. First, earthquakes and stress measurements within oceanic lithosphere

younger than 15 Ma probably do not record plate-driving stress, and second, it is unlikely that in situ stresses in older oceanic lithosphere are large enough to allow their orientation to be established by observing well bore failure at depths less than 1 km below the seafloor. This second conclusion may be invalidated by the presence of additional stress sources such as midplate swells, seamounts, or bending stresses related to subduction. Unfortunately, these stresses would also obscure those related to plate-driving forces.

CONCLUSIONS

We have presented here a simple model describing the conditions necessary for compressive and tensile failure of well bores in response to far-field stresses and well bore temperature variations generated by circulation of drilling fluids to depth. Using a simple elastic model for the stress concentration around a borehole, we find that the presence or absence of breakouts allows reasonable constraints to be placed on the magnitude of the horizontal principal stresses. Comparisons of the model predictions and the measured stresses in boreholes drilled on land show that in most cases the relatively simple failure criterion enables us to predict the depths at which breakouts are actually observed. The single largest uncertainty lies in the large variation of strength in these rocks and the lack of precise values to use in this analysis.

The presence of breakouts in DSDP holes 504B and 395A requires very high horizontal compression in young (5.9 and 7.3 Ma, respectively) crust, with $S_{\mathrm{Hmax}} \gg S_{\mathrm{hmin}} = S_v$. S_{Hmax} is within 30° of the spreading direction in both cases and reaches a value of more than 100 MPa at depths less than 0.5 km subbasement. Our conclusion that the stress magnitudes must be large enough to cause reverse faulting on planes with a coefficient of friction $\mu = 0.8$ is consistent with the observation of reverse and strike-slip earthquake focal mechanisms within young oceanic crust.

Thermally induced stresses due to well bore cooling by drill fluid circulation can play a large role in the generation of tensile failure at the azimuth of S_{Hmax}, as seen in DSDP hole 504B. This is especially true where heat flow and the geothermal gradient are both quite high, either in young oceanic crust or in geothermal regimes on the continents, but is less important in the case of DSDP hole 395A, where the temperature increase with depth is more modest. The occurrence of thermally induced tensile cracks in hole 504B is consistent with the strike-slip/reverse-faulting regime indicated by the breakout analysis. These thermally generated tensile cracks do not propagate away from the well bore unless the well bore fluid pressure exceeds the minimum far-field principal stress, which is unlikely unless the formation is severely underpressured.

The compressive crustal stresses required by observations of breakouts in DSDP holes 504B and 395A are due to thermoelastic effects of plate cooling and are not associated with plate-driving forces. Measurements of stresses from observations of well bore failure in crust older than 25 Ma, where stresses are dominated by the forces which drive the plates, require boreholes with significant penetration below the seafloor. This is a consequence of the high strength of oceanic basalts and the fact that the horizontal stresses are limited by the vertical stress and the strength of the crust.

Acknowledgments. The authors benefited in the preparation of this paper from discussions with a number of people, including Stephen Hickman, Lev Vernik, Oona Scotti, and Gadi Shamir. Larry Mastin and Karl Fuchs informally reviewed the paper, and we appreciate their comments. We also thank Roger Morin and Robin Newmark for permission to use their data in this work and Colleen Barton, who designed and programmed the borehole televiewer digitization and analysis system. The paper benefited substantially from thoughtful and insightful reviews by Bezalel Haimson and Randall Richardson. The research was supported by the National Science Foundation under contract OCE-8907922.

REFERENCES

Allison, M. L., and D. L. Nielson, Stress in active geothermal systems, Advances in Geothermal Reservoir Technology, *Tech. Rep. ESL-88027-JP*, Lawrence Berkeley Lab., Berkeley, Calif., 1988.

Anderson, E. M., *The Dynamics of Faulting and Dike Formation With Applications in Britain*, 2nd ed., Oliver and Boyd, Edinburgh, 1951.

Anderson, R. N., and M. D. Zoback, Permeability, underpressures and convection in the oceanic crust near the Costa Rica Rift, eastern equatorial Pacific, *J. Geophys. Res.*, *87*, 2860–2868, 1982.

Angelier, J., Determination of the mean principal directions of stresses for a given fault population, *Tectonophysics*, *56*, T17–T26, 1979.

Barton, C. A., Development of in-situ stress measurement techniques for deep drillholes, Ph.D. thesis, 192 pp., Stanford Univ., Stanford, Calif., 1988.

Barton, C. A., M. D. Zoback, and K. L. Burns, In-situ stress orientation and magnitude at the Fenton Hill geothermal site, New Mexico, determined from wellbore breakouts, *Geophys. Res. Lett.*, *15*, 467–470, 1988.

Bauer, S. J., and J. Handin, Mechanical properties of basalt cores from Deep Sea Drilling Project hole 504B, *Initial Rep. Deep Sea Drill. Proj.*, *83*, 371–378, 1985.

Becker, K., M. G. Langseth, and R. D. Hyndman, Temperature measurements in hole 395A, leg 78B, *Initial Rep. Deep Sea Drill. Proj.*, *78B*, 689–698, 1984.

Becker, K., et al., Drilling deep into the oceanic crust at hole 504B, Costa Rica Rift, *Rev. Geophys.*, *27*, 79–102, 1989.

Bell, J. S., and D. I. Gough, Northeast-southwest compressive stress in Alberta: Evidence from oil wells, *Earth Planet. Sci. Lett.*, *45*, 475–482, 1979.

Bell, J. S., and D. I. Gough, The use of borehole breakouts in the study of crustal stress, in *Hydraulic Fracturing Stress Measurements*, edited by M. D. Zoback and B. C. Haimson, pp. 201–209, National Academy Press, Washington, D. C., 1983.

Bergman, E. A., Intraplate earthquakes and the state of stress in oceanic lithosphere, *Tectonophysics*, *132*, 1–35, 1986.

Bergman, E. A., and S. C. Solomon, Source mechanisms of earthquakes near mid-ocean ridges from body wave inversion: Implications for the early evolution of oceanic lithosphere, *J. Geophys. Res.*, *89*, 11,415–11,441, 1984.

Bott, M. H. P., and N. J. Kuzsnir, The origin of tectonic stress in the lithosphere, *Tectonophysics*, *105*, 1–13, 1984.

Brace, W. F., and D. L. Kohlstedt, Limits on lithospheric stress imposed by laboratory experiments, *J. Geophys. Res.*, *85*, 6248–6252, 1980.

Bratt, S. R., E. A. Bergman, and S. C. Solomon, Thermoelastic stress: How important as a cause of earthquakes in young oceanic lithosphere? *J. Geophys. Res.*, *90*, 10,249–10,260, 1985.

Byerlee, J. D., Friction of rock, *Pure Appl. Geophys.*, *116*, 615–626, 1978.

Carmichael, R. S., *Handbook of Physical Properties of Rocks*, vol. II, 345 pp., CRC Press, Boca Raton, Fla., 1982.

Clark, S. P., Handbook of Physical Constants, *Mem. Geol. Soc. Am.*, *97*, 587 pp., 1966.

Coussy, O., Thermoporoelastic response of a borehole, *Int. J. Rock Mech. Min. Sci.*, in press, 1990.

Cox, J. W., Long axis orientation in elongated boreholes and its correlation with rock stress data, *Trans. SPWLA Annu. Logging Symp.*, *24th*, 1983.

Coyle, B. J., and M. D. Zoback, In situ permeability and fluid pressure measurements at ~2 km depth in the Cajon Pass research well., *Geophys. Res. Lett.*, *15*, 1029–1032, 1988.

Fairhurst, C., Methods of determining in situ rock stresses at great depths, *Tech. Rep. TRI-68*, Mo. River Div. Corps of Eng., Omaha, Nebr., 1968.

Gough, D. I., and J. S. Bell, Stress orientations from oil well fractures in Alberta and Texas, *Can. J. Earth Sci.*, *18*, 1358–1370, 1981.

Haimson, B. C., and C. G. Herrick, Borehole breakouts—A new tool for estimating in situ stress?, paper presented at the International Symposium on Rock Stress and Rock Stress Measurements, Luleå Univ. of Technol., Stockholm, Sweden, 1986.

Haimson, B. C., and C. G. Herrick, Borehole breakouts and in situ stress, in *Proceedings of the 12th Annual Energy-Sources Technology Conference and Exhibition*, pp. 17–22, American Society of Mechanical Engineers, New York, 1989.

Hickman, S. H., M. G. Langseth, and J. F. Svitek, In situ permeability and pore-pressure measurements near the mid-Atlantic Ridge, Deep Sea Drilling Project hole 395A, *Initial Rep. Deep Sea Drill. Proj.*, *78B*, 699–708, 1984*a*.

Hickman, S. H., J. F. Svitek, and M. G. Langseth, Borehole televiewer log of hole 395A, *Initial Rep. Deep Sea Drill. Proj.*, *78B*, 709–715, 1984*b*.

Hubbert, M. K., and D. G. Willis, Mechanics of hydraulic fracturing, *J. Pet. Technol.*, *9*, 153–168, 1957.

Hussong, D. M., P. B. Fryer, J. D. Tuthill, and L. K. Wipperman, The geological and geophysical setting near site 395, North Atlantic, *Initial Rep. Deep Sea Drill. Proj.*, *45*, 23–38, 1979.

Hyndman, R. D., and M. H. Salisbury, The physical nature of young upper oceanic crust on the mid-Atlantic Ridge, Deep Sea Drilling Project hole 395A, *Initial Rep. Deep Sea Drill. Proj.*, *78B*, 839–848, 1984.

Jaeger, J. C., and N. G. W. Cook, *Fundamentals of Rock Mechanics*, 3rd ed., 593 pp., Chapman and Hall, New York, 1979.

Kirsch, G., Die Theorie der Elastizitat und die Bedurfnisse der Festigkeitslehre, *VDI Z.*, *42*, 797–807, 1898.

Kopietz, J., K. Becker, and Y. Hamano, Temperature measurements at site 395, ODP leg 109, in *Proceedings of ODP, Scientific Results*, vol. 106/109, edited by R. Detrick, pp. 197–203, Ocean Drilling Program, College Station, Tex., 1990.

Kozlovski, Y. A., *The Superdeep Well of the Kola Peninsula*, 558 pp., Springer-Verlag, New York, 1984.

Langseth, M. G., M. J. Mottl, M. Hobart, and A. Fisher, The distribution of geothermal and geochemical gradients near site 501/504: Implications for hydrothermal circulation in the oceanic crust, in *Proceedings of ODP, Initial Reports, Part A*, vol. 111, pp. 23–32, Ocean Drilling Program, College Station, Tex., 1988.

Mastin, L. G., The development of borehole breakouts in sandstone, M.S. thesis, Stanford Univ., Stanford, Calif., 1984.

Mastin, L. G., Effect of borehole deviation on breakout orientations, *J. Geophys. Res.*, *93*, 9187–9195, 1988.

McGarr, A., Some constraints on levels of shear stress in the crust from observations and theory, *J. Geophys. Res.*, *85*, 6231–6238, 1980.

McGarr, A., On the state of lithospheric stress in the absence of applied tectonic forces, *J. Geophys. Res.*, *93*, 13,609–13,617, 1988.

McKenzie, D. P., The relation between fault plane solutions for earthquakes and the directions of the principal stresses, *Bull. Seismol. Soc. Am.*, *59*, 591–601, 1969.

Morin, R. H., R. L. Newmark, C. A. Barton, and R. N. Anderson, State of lithospheric stress and borehole stability at Deep Sea Drilling Project site 504B, eastern equatorial Pacific, *J. Geophys. Res.*, this issue.

Mount, V. S., and J. Suppe, State of stress near the San Andreas Fault: Implications for wrench tectonics, *Geology*, *15*, 1143–1146, 1987.

Newmark, R. L., M. D. Zoback, and R. N. Anderson, Orientation of in situ stresses in the oceanic crust, *Nature*, *311*, 424–428, 1984.

Okal, E. A., Intraplate seismicity of the southern part of the Pacific Plate, *J. Geophys. Res.*, *89*, 10,053–10,071, 1984.

Okal, E. A., J. Talandier, K. A. Sverdrup, and T. H. Jordan, Seismicity and tectonic stress in the south-central Pacific, *J. Geophys. Res.*, *85*, 6479–6495, 1980.

Plumb, R. A., and J. W. Cox, Stress directions in eastern North America determined to 4.5 km from borehole elongation measurements, *J. Geophys. Res.*, *92*, 4805–4816, 1987.

Price, R. H., and S. J. Bauer, Analysis of the elastic and strength properties of Yucca Mountain tuff, Nevada, *Proc. U.S. Symp. Rock. Mech.*, *26th*, 89–96, 1985.

Raleigh, C. B., J. H. Healy, and J. D. Bredehoeft, Faulting and crustal stress at Rangeley, Colorado, in *Flow and Fracture of Rocks*, *Geophys. Monogr. Ser.*, vol. 16, edited by H. C. Heard et al., pp. 275–284, AGU, Washington D. C., 1972.

Ritchie, R. H., and A. Y. Sakakura, Asymptotic expansions of solutions of the heat conduction equation in internally bounded cylindrical geometry, *J. Appl. Phys.*, *27*, 1453–1459, 1956.

Rummel, F., Stresses and tectonics of the upper continental crust—A review, in *Proceedings of the International Symposium on Rock Stress and Rock Stress Measurements, Stockholm, 1986 September 1–3*, Centek Publishers, Luleå, Sweden, 1986.

Shamir, G., M. D. Zoback, and C. A. Barton, In situ stress orientation near the San Andreas fault: Preliminary results to 2.1 km depth from the Cajon Pass scientific drillhole, *Geophys. Res. Lett.*, *15*, 989–992, 1988.

Shipboard Scientific Party, Site 597, *Initial Rep. Deep Sea Drill. Proj.*, *92*, 25–97, 1985.

Shipboard Scientific Party, Site 504, in *Proceedings of ODP, Initial Reports, Part A*, vol. 111, edited K. Becker et al., pp. 35–252, Ocean Drilling Program, College Station, Tex., 1988*a*.

Shipboard Scientific Party, Site 395, in *Proceedings of ODP, Initial Reports, Part A*, vol. 106/109, edited by R. B. Detrick et al., pp. 175–202, Ocean Drilling Program, College Station, Tex., 1988*b*.

Sibson, R. H., Frictional constraints on thrust, wrench and normal faults, *Nature*, *249*, 542–544, 1974.

Stephens, G., and B. Voight, Hydraulic fracturing theory for conditions of thermal stress, *Int. J. Rock Mech. Min. Sci.*, *19*, 279–284, 1982.

Stock, J. M., J. H. Healy, S. H. Hickman, and M. D. Zoback, Hydraulic fracturing stress measurements at Yucca Mountain, Nevada, and the relationship to the regional stress field, *J. Geophys. Res.*, *90*, 8691–8706, 1985.

Vardoulakis, I., J. Sulem, and A. Guenot, Borehole instabilities as bifurcation phenomena, *Int. J. Rock. Mech. Min. Geomech. Abstr.*, *25*, 159–170, 1988.

Wiebols, G. A., and N. G. W. Cook, An energy criterion for the strength of rock in polyaxial compression, *Int. J. Rock Mech. Min. Sci.*, *5*, 529–549, 1968.

Wiens, D. A., and S. Stein, Intraplate seismicity and stress in young oceanic lithosphere, *J. Geophys. Res.*, *89*, 11,442–11,464, 1984.

Zemanek, J., E. E. Glenn, Jr., J. J. Norton, and R. L. Caldwell, Formation evaluation by inspection with the borehole televiewer, *Geophysics*, *35*, 254–269, 1970.

Zheng, Z., J. Kemeny, and N. G. W. Cook, Analysis of borehole breakouts, *J. Geophys. Res.*, *94*, 7171–7182, 1989.

Zoback, M. D., and R. N. Anderson, Ultrasonic borehole televiewer investigation of oceanic crustal layer 2A, Costa Rica Rift, *Nature*, *295*, 375–379, 1982.

Zoback, M. D., and J. H. Healy, Friction, faulting and in situ stress, *Ann. Geophys.*, *2*, 689–698, 1984.

Zoback, M. L., and M. D. Zoback, State of stress in the conterminous United States, *J. Geophys. Res.*, *85*, 6113–6156, 1980.

Zoback, M. D., D. Moos, L. Mastin, and R. N. Anderson, Well bore breakouts and in situ stress, *J. Geophys. Res.*, *90*, 5523–5530, 1985.

Zoback, M. D., et al., New evidence on the state of stress of the San Andreas fault system, *Science*, *238*, 1105–1111, 1987.

Zoback, M. L., et al., Global patterns of intraplate stress: A status report on the world stress map project of the International Lithosphere Program, *Nature*, *341*, 291–298, 1989.

D. Moos and M. D. Zoback, Department of Geophysics, Stanford University, Stanford, CA 94305.

(Received July 28, 1989;
revised February 20, 1990;
accepted January 29, 1990.)

Appendix VI - Quality Assurance Documentation

This section includes photostatic copies of all of the field and digitization checklists completed during the collection and analysis of the data included in this report. With the exception of the lack of a post-log calibration for NONAME-1, all of the standard procedures were carried out in the course of this work. The final (post-log) calibration of the hi-temperature televiewer in INEL-1 was completed successfully, according to field notes, and the results apparently agreed with the pre-log calibration. However, no photograph of this calibration was found. We therefore have operated in the body of this report under the assumption that this calibration was not obtained. During the second phase log of INEL-1 no checklist sheets were available, and so photocopies of the field notebook are provided instead.

Appendix VI - Quality Assurance Documentation

This section includes photostatic copies of all of the field and digitization checklists completed during the collection and analysis of the data included in this report. With the exception of the lack of a post-log calibration for NONAME-1, all of the standard procedures were carried out in the course of this work. The final (post-log) calibration of the hi-temperature televiewer in INEL-1 was completed successfully, according to field notes, and the results apparently agreed with the pre-log calibration. However, no photograph of this calibration was found. We therefore have operated in the body of this report under the assumption that this calibration was not obtained. During the second phase log of INEL-1 no checklist sheets were available, and so photocopies of the field notebook are provided instead.

Borehole televiewer field check list

Date: 5/15/90
Time: 1230
Observer: MOOS/TAVARES
Well Name : USGS-17
INEL

Cable:

cable length 22,000'
number of conductors 7
resistance (ohms):

	1	2	3	4	5	6	7	armor
1	230	x	x	x	x	x	x	
2	∞	235	x	x	x	x	x	
3	∞	∞	240	x	x	x	x	
4	∞	∞	∞	240	x	x	x	
5	∞	∞	∞	∞	255	x	x	
6	∞	∞	∞	∞	∞	240	x	
7	∞	∞	∞	∞	∞	∞	240	0

Equipment

tool small.
surface panel number _____.
monitor _____. scope _____.

Pre-log calibration at 5/15 1545 (date/time)
Run in hole at 1550 (date/time)
Water level at 1600 (date/time)
Casing at — (date/time)
Total depth at 1605 (date/time)
Log start at 1630 (date/time)
Log end at 1703 (date/time)
Post-log calibration at 1710 (date/time)

Borehole televiewer field check list

Date: 5/15/90
Time: 15:45
Observer: Moos/Tavares
Well Name : USGS-17

pre-log calibration:

Time since turn-on ~ 20 minutes

Test in Al Tank, Fluid is Water.

Magnetic North is _____ degrees azimuth.

Magnetic East is _____ degrees azimuth.

Magnetic South is _____ degrees azimuth.

Magnetic West is _____ degrees azimuth.

place photograph here:

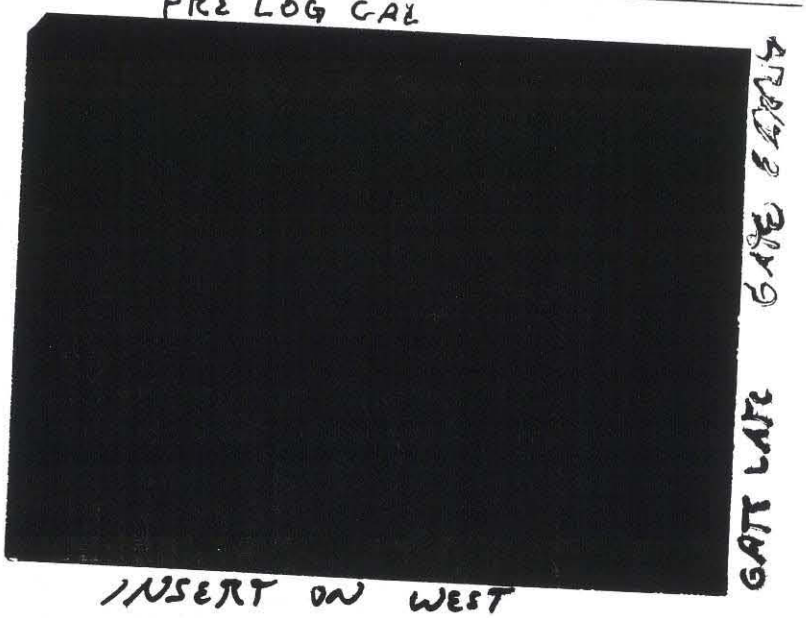

Annotations:

Borehole televiewer field check list

Date: 5/15/90
Time: 17:10
Observer: Mock/Tavares
Well Name : USGS-17

post-log calibration:

Time since turn-on 1:45.

Test in Aluminum tank. Fluid is Clear Water.

Magnetic North is _____ degrees azimuth.

Magnetic East is _____ degrees azimuth.

Magnetic South is _____ degrees azimuth.

Magnetic West is _____ degrees azimuth.

place photograph here:

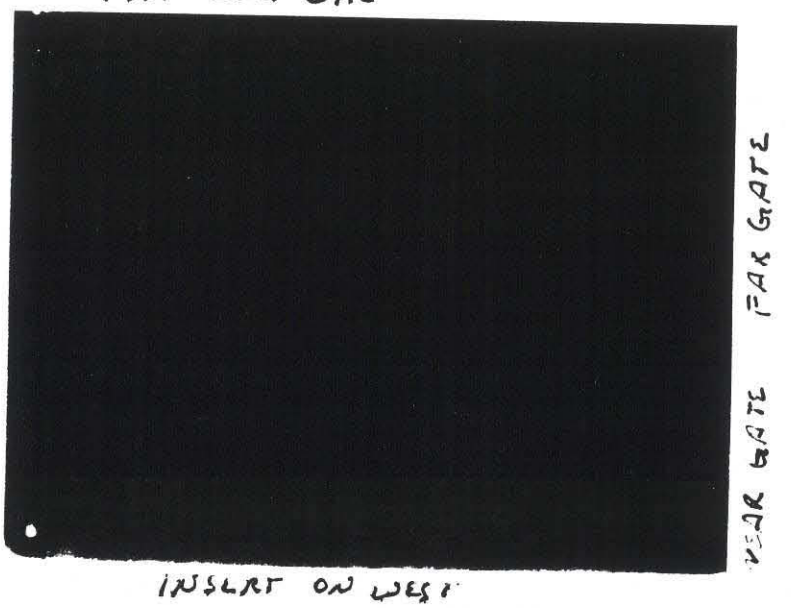

Annotations:

Borehole televiewer field check list

Date: 5/15/90
Time:
Observer: MOOS/TAVARES
Well Name : USGS-17
INEL

CABLE DEPTHS TO TIE POINTS

DRILLER'S DEPTHS	TIE POINT	MECHANICAL COUNTER	ELECTRONIC COUNTER
Reference Top Casing ∅	GROUND LEVEL (top of casing	699940	∅
400?	WATER LEVEL	700332	392
20'	CASING	?	?
600	TOTAL DEPTH	700510 ~~568~~	568
?	OTHER(specify)		
	water knockout		~~392~~ 390.5
∅	OTHER(specify) re-zero	699939	-3.1
	OTHER(specify)		

Borehole televiewer field check list

Date: 5/16/90
Time: _____
Observer: MOOS/TAVARES
Well Name : USGS-7

Cable:

INEL

cable length 22,000'
number of conductors 7
resistance (ohms):

See 5/15/90 INEL

	1	2	3	4	5	6	armor
1		x	x	x	x	x	
2			x	x	x	x	
3				x	x	x	
4					x	x	
5						x	
6							
7							

Equipment

tool small.
surface panel number New.
monitor _____. scope _____.

Pre-log calibration at 1300 5/16 (date/time)
Run in hole at 1320 (date/time)
Water level at 1325 (date/time)
Casing at 1330 (date/time)
Total depth at 1335 (date/time)
Log start at 1345 (date/time)
Log end at 1420 (date/time)
Post-log calibration at 1440 (date/time)

Borehole televiewer field check list

Date: 5/16/90
Time: 1300
Observer: MOOS/TAVARES
Well Name : USGS-7

pre-log calibration:

Time since turn-on ~10 minutes.

Test in Aluminum tank. Fluid is Clear Water.

Magnetic North is _____ degrees azimuth.

Magnetic East is _____ degrees azimuth.

Magnetic South is _____ degrees azimuth.

Magnetic West is _____ degrees azimuth.

place photograph here:

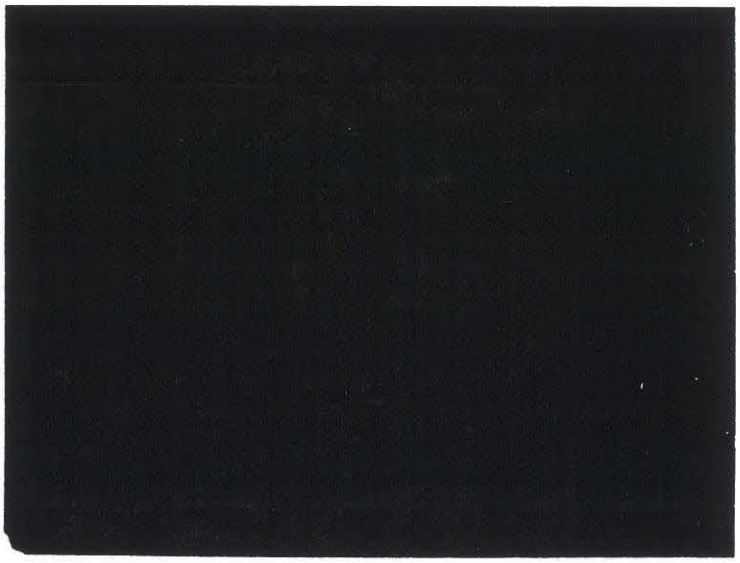

Compass
Mark
Far
Both

Isolate Near

Annotations:

Sleave on West

Oriented using old compass (NOT Brunton)

Borehole televiewer field check list

Date: 5/16/90
Time: 1440
Observer: MOOS/TAVARES
Well Name : USGS-7

post
~~pre~~-log calibration:

Time since turn-on 1:50.

Test in ALUMINUM TANK. Fluid is WATER.

Magnetic North is _____ degrees azimuth.

Magnetic East is _____ degrees azimuth.

Magnetic South is _____ degrees azimuth.

Magnetic West is _____ degrees azimuth.

place photograph here:

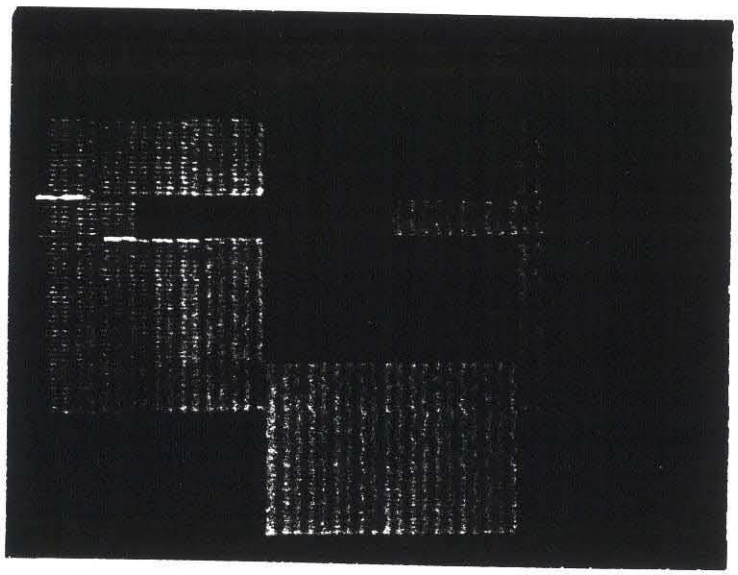

Annotations:

Compass
Mark
Far Gate
Both
Near Gate

4

Gain higher than pre-log

Borehole televiewer field check list

Date:_____
Time:_____
Observer:_____
Well Name : USGS- 7

CABLE DEPTHS TO TIE POINTS

DRILLER'S DEPTHS	TIE POINT	MECHANICAL COUNTER	ELECTRONIC COUNTER
	GROUND LEVEL	699935	0
390 +	WATER LEVEL		207
760'	CASING (6" diameter)		740 ± ?
~~1200'~~ 940'	TOTAL DEPTH 5 1/2" holesize		
J. ⇒ 895'	OTHER(specify) hole bottom (silt layer)	700827	894
1200'	OTHER(specify) 3 1/2" rathole		
	OTHER(specify)	699933	99918.0

Borehole televiewer field check list

Date: 5/16/90
Time: _____
Observer: MOOS/TAVARES
Well Name : NONAME #1

Cable:

cable length 22,000'
number of conductors 7
resistance (ohms):

See 5/15

	1	2	3	4	5	6	armor
1		x	x	x	x	x	
2			x	x	x	x	
3				x	x	x	
4					x	x	
5						x	
6							
7							

Equipment

tool small.
surface panel number New.
monitor _____. scope _____.

Pre-log calibration at 1635 (date/time)
Run in hole at 1646 (date/time)
Water level at 1650 (date/time)
Casing at 1651 (date/time)
Total depth at 1655 (date/time)
Log start at " (date/time)
Log end at 1750 (date/time)
Post-log calibration at 1755 * (date/time)

* No recal- Compass not triggering

Borehole televiewer field check list

Date: 5/16/90
Time: 16:35
Observer: Moos/Tavares
Well Name : Vorame #1

pre-log calibration:

Time since turn-on 10 minutes.

Test in Al Tank. Fluid is Water.

Magnetic North is _____ degrees azimuth.

Magnetic East is _____ degrees azimuth.

Magnetic South is _____ degrees azimuth.

Magnetic West is _____ degrees azimuth.

place photograph here:

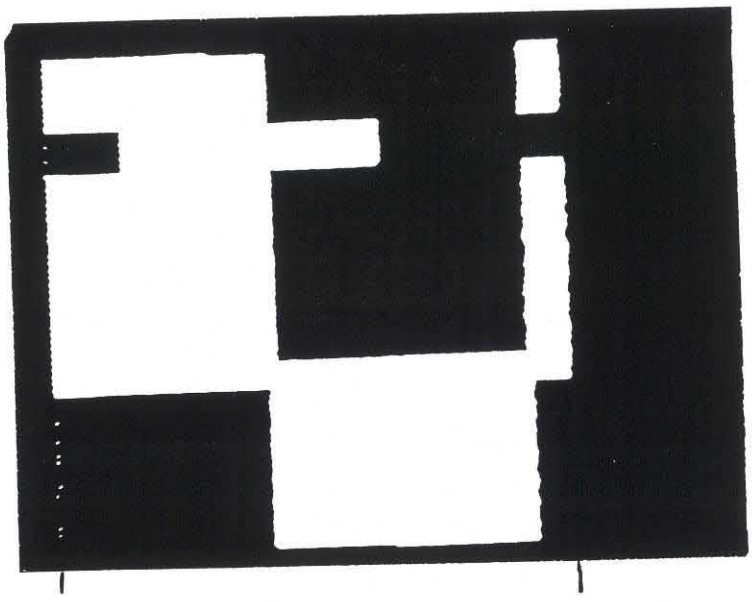

Annotations:

Sleeve on west
Orientation of field affected by trucks...

Borehole televiewer field check list

Date: 5/19/90
Time: 1500
Observer: MOORE / TAVARES
Well Name : WELL - 1

pre-log calibration:

Time since turn-on ~ 30 minutes.

Test in Aluminum tank. Fluid is Water.

Magnetic North is _____ degrees azimuth.

Magnetic East is _____ degrees azimuth.

Magnetic South is _____ degrees azimuth.

Magnetic West is _____ degrees azimuth.

place photograph here:

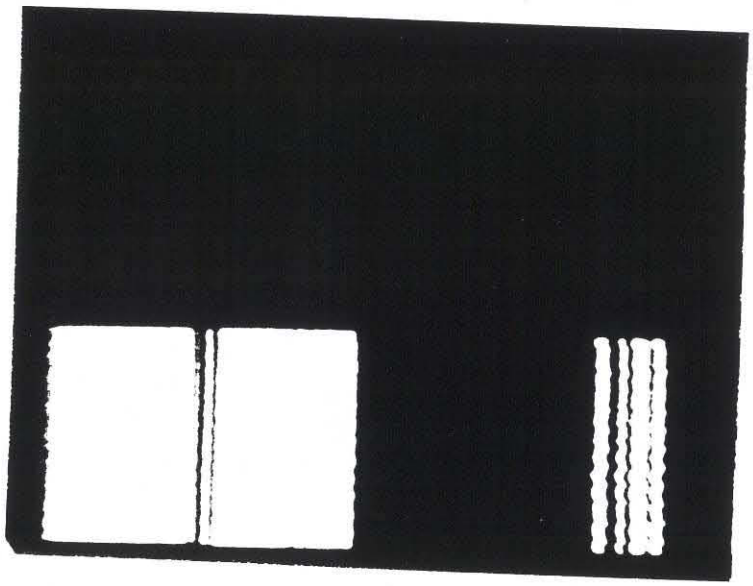

Annotations:

Gate Late
Sleeve West
Absorbin rod East Hi-F (short focus)

Borehole televiewer field check list

Date:_____
Time:_____
Observer:_____
Well Name : NONAME #1

CABLE DEPTHS TO TIE POINTS

DRILLER'S DEPTHS	TIE POINT	MECHANICAL COUNTER	ELECTRONIC COUNTER
	1 1/2' ABOVE GROUND LEVEL	699935	0
?	WATER LEVEL		204
270'/271.5'	CASING 12 3/4 casing		272
548'/549.5'	TOTAL DEPTH 12" hole		549
	OTHER(specify)		
	OTHER(specify)		
	OTHER(specify)		

Borehole televiewer field check list

Date: 5/19/90
Time: 1100
Observer: MOOS/JAVARES
Well Name : INEL-1

Cable:

cable length 21,800
number of conductors 7
resistance (ohms):

	1	2	3	4	5	6	7 armor	armor
1	220	x	x	x	x	x	∞	∞
2	∞	220	x	x	x	x	∞	∞
3	∞	∞	225	x	x	x	∞	∞
4	∞	∞	∞	220	x	x	∞	∞
5	∞	∞	∞	∞	240	x	∞	∞
6	∞	∞	∞	∞	∞	220	∞	∞
7	∞	∞	∞	∞	∞	∞	200	∞
ARMOR	—	—	—	—	—	—	—	0

Equipment

tool Hi Temp
surface panel number Old
monitor _____ scope _____
1st pass 2nd pass

Pre-log calibration at 3:00 pm (date/time)
Run in hole at 3:45 pm (date/time) 17:50
Water level at _____ (date/time)
Casing at 4:35 (date/time) ← 1850 hrs
Total depth at _____ (date/time) 1910 hrs (dinner time)
Log start at _____ (date/time)
Log end at _____ (date/time)
Post-log calibration at _____ (date/time)

Borehole televiewer field check list

Date: 5.19.90

Time: _____

Observer: _____

Well Name : INEL 1

CABLE DEPTHS TO TIE POINTS

DRILLER'S DEPTHS	TIE POINT	MECHANICAL COUNTER	ELECTRONIC COUNTER	
Ø	13 5/8 GROUND LEVEL (TOP OF CASING ~6' ABOVE GL	700008 70000	Ø -9999.5	
	WATER LEVEL	700369	302.5 in 297 out	
3282	TOP OF LINER 9 7/8 CASING		3282 in 3275 out	3275*
6796	TOP OF OPEN HOLE ~~TOTAL DEPTH~~	706790	6782	6785* 6783**
10,333	OTHER(specify) TOP OF 7 7/8 HOLE	710243*	10243*	10230* Rattan
6796	~~OTHER(specify)~~ TOP OF OPEN HOLE OUT	699993	99993	
10,000	OTHER(specify) Marker 12' open hole			

* 2nd run in hole

** 3rd run in hole

Borehole televiewer field check list

Date: 5/20/90
Time: 14:20
Observer: MWD/TAVARES
Well Name : INEL-1

Cable:

POST GEOTHERMAL CABLE CHECK
PRE small BHTV run

cable length 21,800
number of conductors 7
resistance (ohms):

	1	2	3	4	5	6	7 ~~armor~~
1	230	x	x	x	x	x	
2	∞	230	x	x	x	x	
3		∞	230	x	x	x	
4			∞	230	x	x	
5				∞	240	x	
6					∞	230	
7						∞	200
armor							

Equipment

tool Small
surface panel number old
monitor _____. scope _____.

Tool on 2:30

Pre-log calibration at 2:45 (date/time)
Run in hole at 2:50 (date/time)
Water level at 307' 2:58 (date/time)
Casing at 3:10 (liner) (date/time)
Total depth at 9300' (date/time)
Log start at _____ (date/time)
Log end at _____ (date/time)
Post-log calibration at _____ (date/time)

Borehole televiewer field check list

Date: 5·20·90

Time: _____

Observer: _____

Well Name : INEL 1

CABLE DEPTHS TO TIE POINTS

DRILLER'S DEPTHS	Hole Size	TIE POINT	MECHANICAL COUNTER	ELECTRONIC COUNTER IN	OUT
ϕ	13 3/8"	GROUND LEVEL	[illegible]	0	
		WATER LEVEL	700300	303'	
3282	9 3/8"	CASING Liner		3274.5	3275
6796	9 3/8"	Bottom Liner TOTAL DEPTH		6784	6783
10333	12"	OTHER(specify) TD			9300 10236
		OTHER(specify)			
		OTHER(specify)			

444 6/5/90 Time Event

3:45 pm AT INEL 1 - Setting up
Check out Large tool, new surface panel

'Ring out' Cable

								1/TTTT
1	260	∞	∞	∞	∞	∞	∞	∞
1 2		260	∞	∞	∞	∞	∞	∞
1 2 3			260	∞	∞	∞	∞	∞
1 2 3 4				260	∞	∞	∞	∞
1 2 3 4 5					280	∞	∞	∞
1 2 3 4 5 6						260	∞	∞
1 2 3 4 5 6 7							235	∞
								10

4:00 pm Calibration & testing the tool at surface
7:30 pm Shutting down calibration

6/6/90 Tape length 90 min x 5'/min = 450' = 1250(')of tape
5.5'/min = 495.0'
500'/Tape

(0-904)
Tape 1 10,240 - 10,000 + calibration pre
Tape 2 10,000 - 9,500 (0 - 1260)
3 9500 - 9000
4 9000 - 8500 (0 - 1212)
5 8500 - 8000
6 8000 - 7500
7 7500 - 7000 (0 - 1420)
8 7000 - 6785 + calibration post

Borehole televiewer field check list

Date: 6/6/90
Time: 0900
Observer: TAVARES/JOHNSON
Well Name : INEL-1

pre-log calibration:

Time since turn-on 1:00 hr.

Test in Al cal Tank. Fluid is Water.

Magnetic North is — degrees azimuth.

Magnetic East is — degrees azimuth.

Magnetic South is — degrees azimuth.

Magnetic West is degrees azimuth.

place photograph here:

Photographs on following page

Annotations:

WEST

6/6/90 Cont

Time	Event
8:00 Am	At site checking tool calibration
	Got orientation by photographing scope
	with TV signal on channel 1
	Blanking on channel 2
	~~XI Pulse~~ on channel 3 (trigger)
	took polaroid of these signals for
	sleeve in tank and for phenolic rod
	in tank. Phenolic rod in tank used as
	calibration for check:
	HF-1 compass
	HF-2 ✓
	HF-3 ✓
	LF-1 ✓
	LF-2 ✓
	Mark mode not working
11:30 Am	RIH
11:35	Zero Reset does not work on computer EDC1
11:42	0' 699990' ~~0'~~ GL
11:50	304' 303' WL
	3275 TL
	6784 BL
	10236 TD
12:05 pm	0' 699992.5' 0' GL
12:08	303.7' 700296. 303 WL
12:18	3270.5' 703263.0 3275 TL
12:32	6780 706772. 6784 BL
12:55	10236 TD
12:57	10240 710233 10240 5.8'/min
1:00 pm	Tool LF #4

6/6/90 Cont

Time	Event
1:50 pm	10,000 (709992.5) 10,244 - 10,000' TAPE 1 (0 - 904')

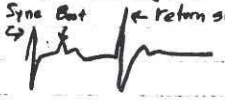

clear water 24.6 μs = 1" round trip

190 - 220 Maybe 16-18 μs/round trip inch

heavy salt 14 μs/round trip inch

base mud

?? → 2:10 10,000 709992.5 Re logging N pulse doubling

3:50 9500 Logging 5.8'/min

Gain → 4:00 9480 LF transducer Gain 3

Change → 4:10 9500 HF Gain 4

4:55 pm 9250 Taking pictures

5:50 9000' Tape 4

7:50 8500' 708492.5' Tape 5 Elevate boom to center tool with approx. 1 ft rise - note Δ 0

9:50 8000' 707992.5' Logging 5.8'/min

11:30 7500' 7492.5' " "

6/7/90 1:10 am 7000' " "

1:50 Am 6780' BL See photo for depth verif.

2:20 Am 3277. Smallest 3270' TL & etc

3270 Next largest

3267. ± largest

2:45 Am 295.5 303.7 WL ?

2:50 99990.1 699982.5' GL

3:30 Post run calibration complete HF #4, Compass

Borehole Televiewer Field Check List: DIGITAL DATA ACQUISITION
SUMMARY SHEET

Date: 7/13/90
Time: 10:00 AM
Operator : C. BARTON

Well Name INEL-1
Well Location INEL IDAHO
Log Date 5/17/90 5/19/90 5/20/90 6/6/90 6/7/90
Magnetic Declination (east of North) 16°
Max Depth 10243
Min Depth 6780
Depth Units FEET
Sweep setting 3.9
Trigger 7.5
Gate width 5.8
Blanking 3.1
T.V. gain FULL
Gate position 7.9
Borehole gain HF
Digitization Delay 150
Digitization Window 100
Tool Specification 0.97
Fluid Velocity 1490
Marker 0
Borehole Deviation OK

Borehole Televiewer Field Check List: DIGITAL DATA ACQUISITION
SUMMARY SHEET

Date: 7/12/90
Time: 3:00 PM
Operator : D. Moos

Well Name USGS-17
Well Location INEL IDAHO
Log Date 5/15/90
Magnetic Declination (east of North) 16°
Max Depth 567
Min Depth 390
Depth Units FEET
Sweep setting 6.4
Trigger 5.2
Gate width 8.5
Blanking 1.5
T.V. gain FULL
Gate position 5.6
Borehole gain HF
Digitization Delay 120
Digitization Window 400
Tool Specification 0.83
Fluid Velocity 1500
Marker 30
Borehole Deviation OK

Borehole Televiewer Field Check List: DIGITAL DATA ACQUISITION
SUMMARY SHEET

Date: 7/9/90
Time: 12:00 PM
Operator : C BARTON

Well Name USGS 7
Well Location INEL IDAHO
Log Date 5/16/90
Magnetic Declination (east of North) 16
Max Depth 895
Min Depth 750
Depth Units FEET
Sweep setting 7.2
Trigger 5.0
Gate width 8.8
Blanking 13.5
T.V. gain ROLL
Gate position 6.8
Borehole gain HF
Digitization Delay 90
Digitization Window 100
Tool Specification 0.83
Fluid Velocity 1500
Marker 30
Borehole Deviation OK

Borehole Televiewer Field Check List: DIGITAL DATA ACQUISITION
SUMMARY SHEET

Date: 7/9/90
Time: 9.00 AM
Operator : C. BARTON

Well Name NONAME
Well Location INEL IDAHO
Log Date 5/16/90
Magnetic Declination (east of North) 16
Max Depth 589
Min Depth 265
Depth Units FEET
Sweep setting 7.9
Trigger 4.9
Gate width 8.2
Blanking 13.8
T.V. gain FULL
Gate position 7.5
Borehole gain HF
Digitization Delay 150
Digitization Window 150
Tool Specification 0.83
Fluid Velocity 1500 M/S
Marker 35
Borehole Deviation UK

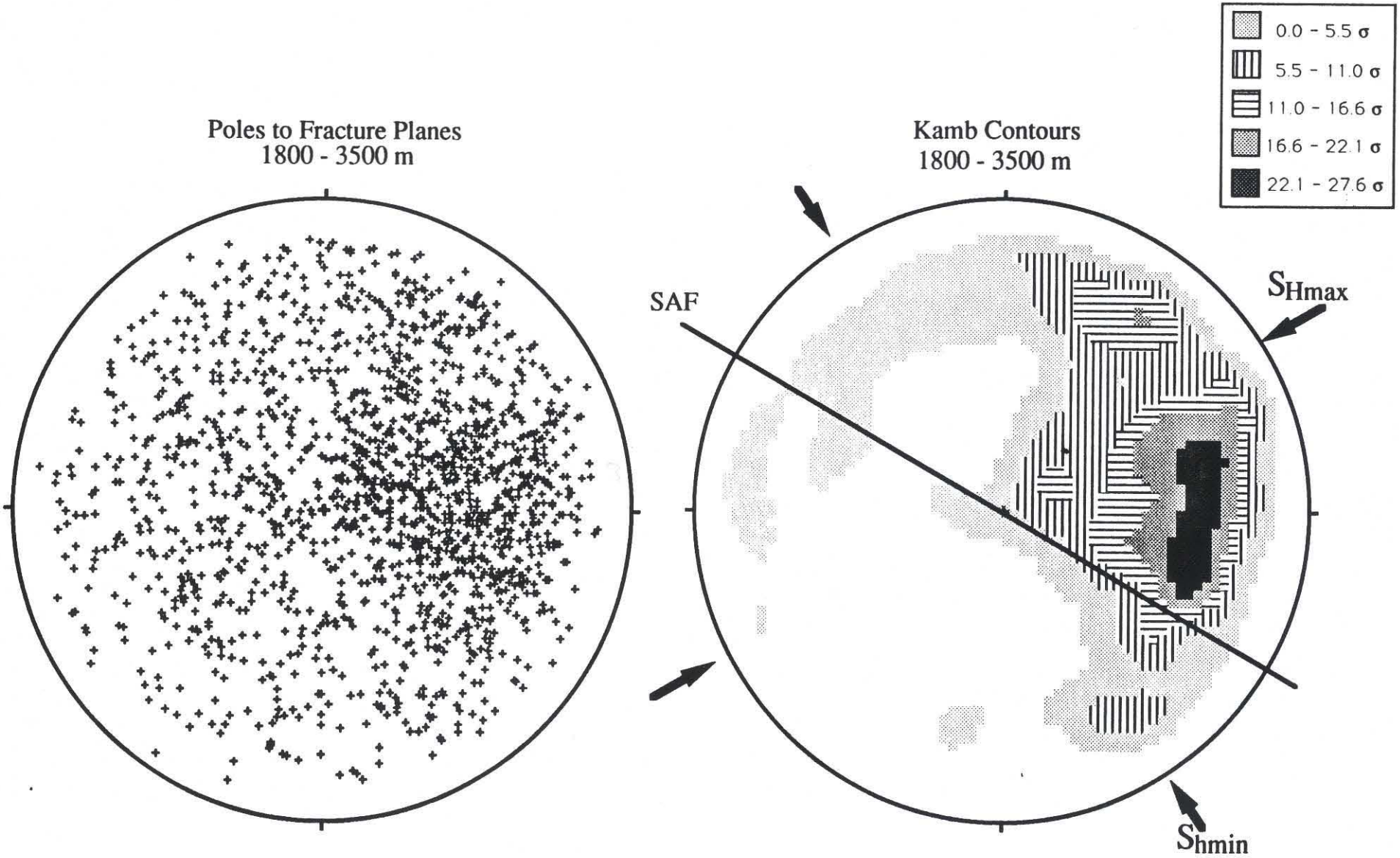
Poles to Fracture Planes
1800 - 3500 m
Kamb Contours
1800 - 3500 m
0.0 - 5.5 σ
5.5 - 11.0 σ
11.0 - 16.6 σ
16.6 - 22.1 σ
22.1 - 27.6 σ
SAF
SHmax
Shmin

Figure 18

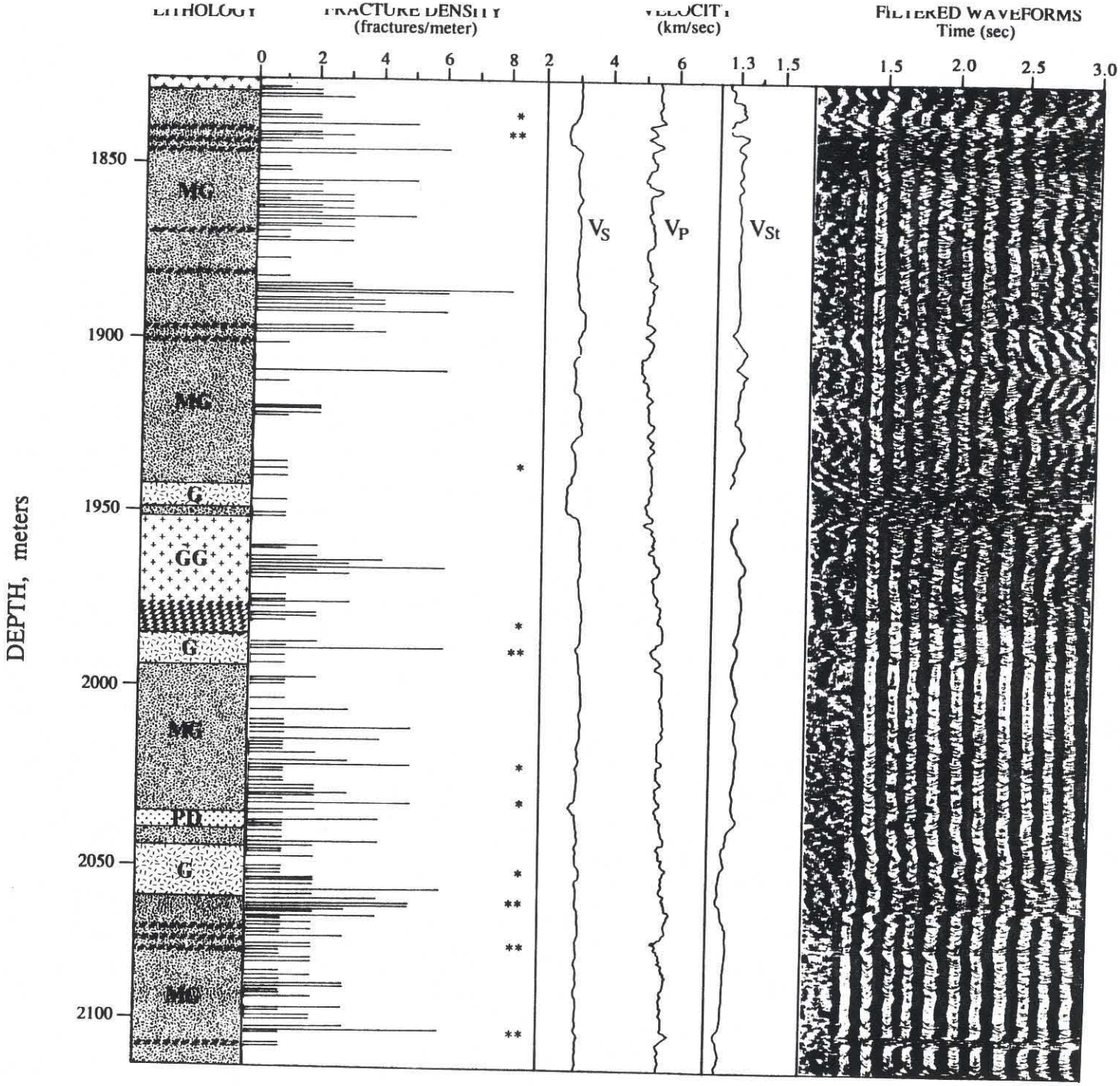
LITHOLOGY
FRACTURE DENSITY
(fractures/meter)
VELOCITY
(km/sec)
FILTERED WAVEFORMS
Time (sec)
0
2
4
6
8
2
4
6
1.3
1.5
1.5
2.0
2.5
3.0
DEPTH, meters
1850
1900
1950
2000
2050
2100
MG
G
GG
PD
V_S
V_P
V_{St}

Figure 19

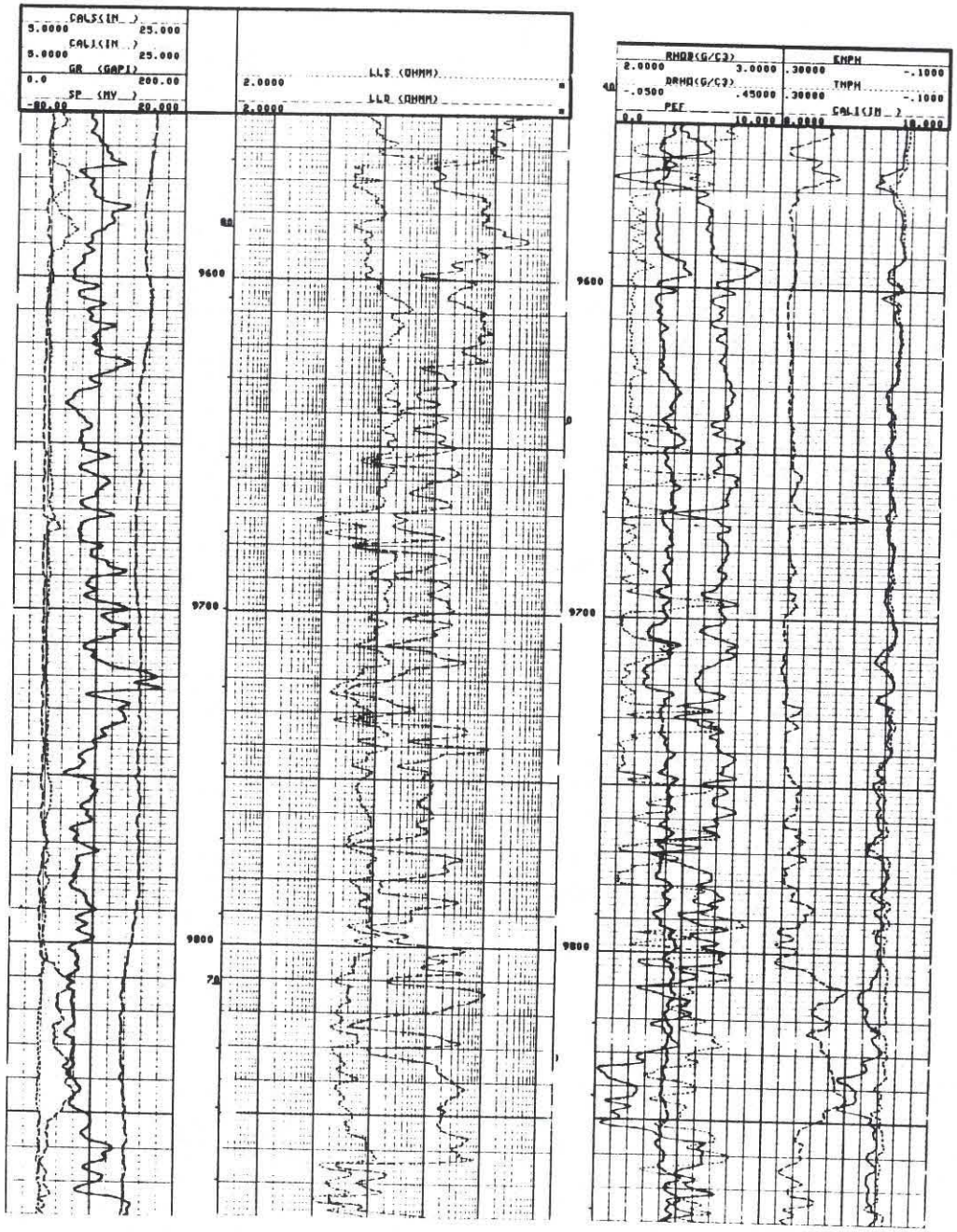

BHTV INTERPRETED SECTION

DIGITAL MANUAL

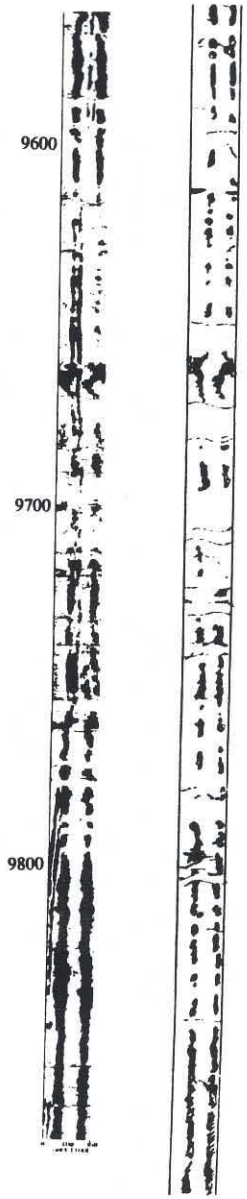

Figure 20

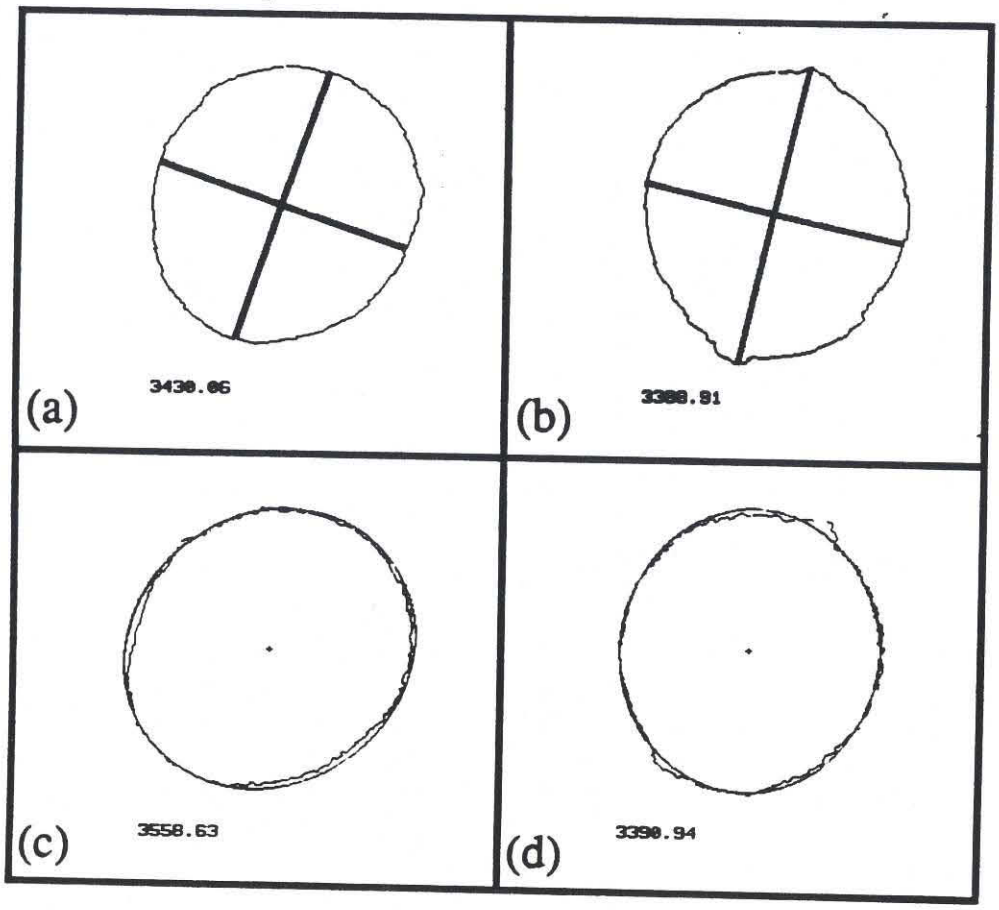

Figure 21

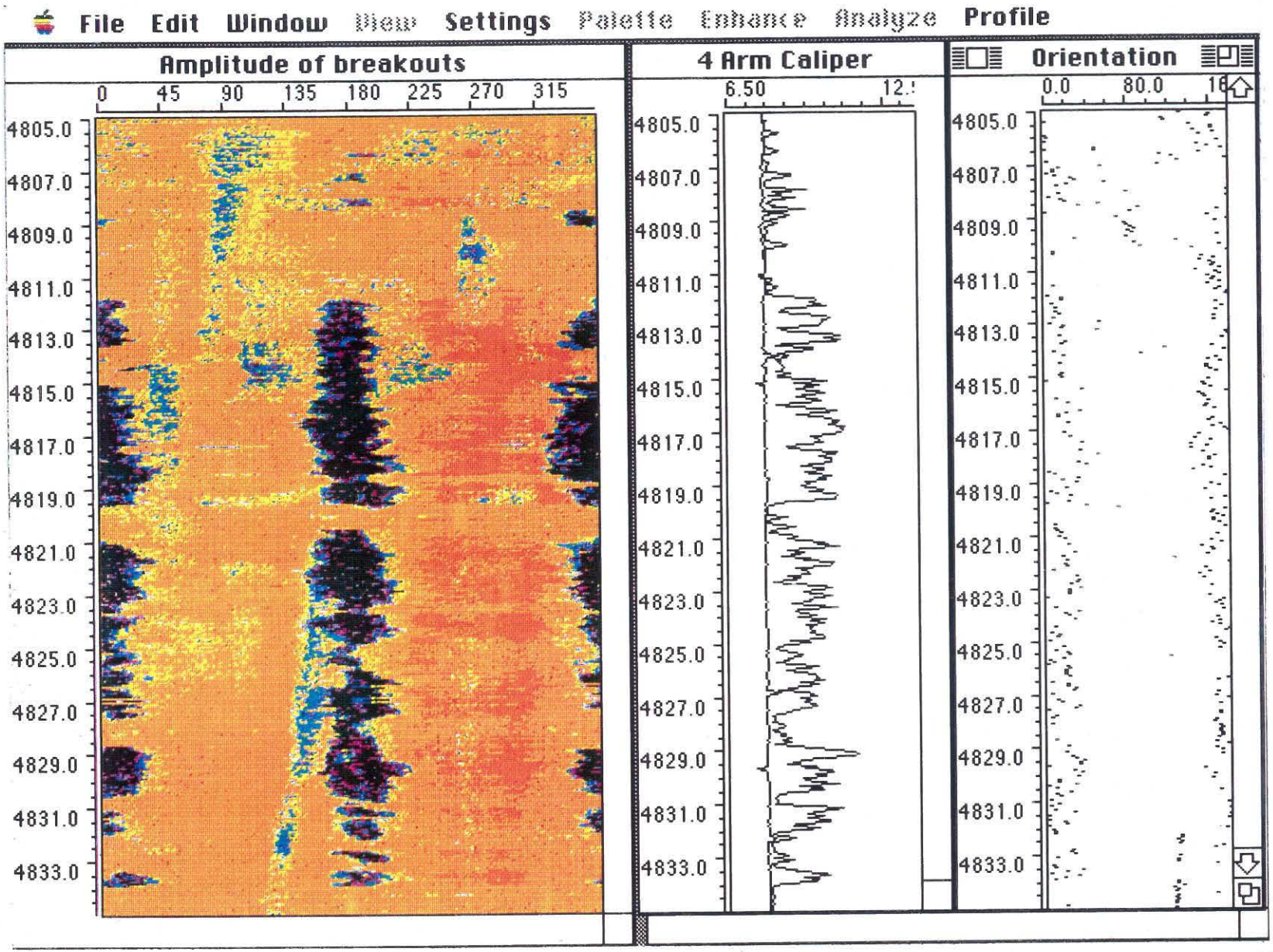
File Edit Window View Settings Palette Enhance Analyze Profile
Amplitude of breakouts
0 45 90 135 180 225 270 315
4805.0 4807.0 4809.0 4811.0 4813.0 4815.0 4817.0 4819.0 4821.0 4823.0 4825.0 4827.0 4829.0 4831.0 4833.0
4 Arm Caliper
6.50
4805.0 4807.0 4809.0 4811.0 4813.0 4815.0 4817.0 4819.0 4821.0 4823.0 4825.0 4827.0 4829.0 4831.0 4833.0
Orientation
0.0 80.0
4805.0 4807.0 4809.0 4811.0 4813.0 4815.0 4817.0 4819.0 4821.0 4823.0 4825.0 4827.0 4829.0 4831.0 4833.0

Figure 22

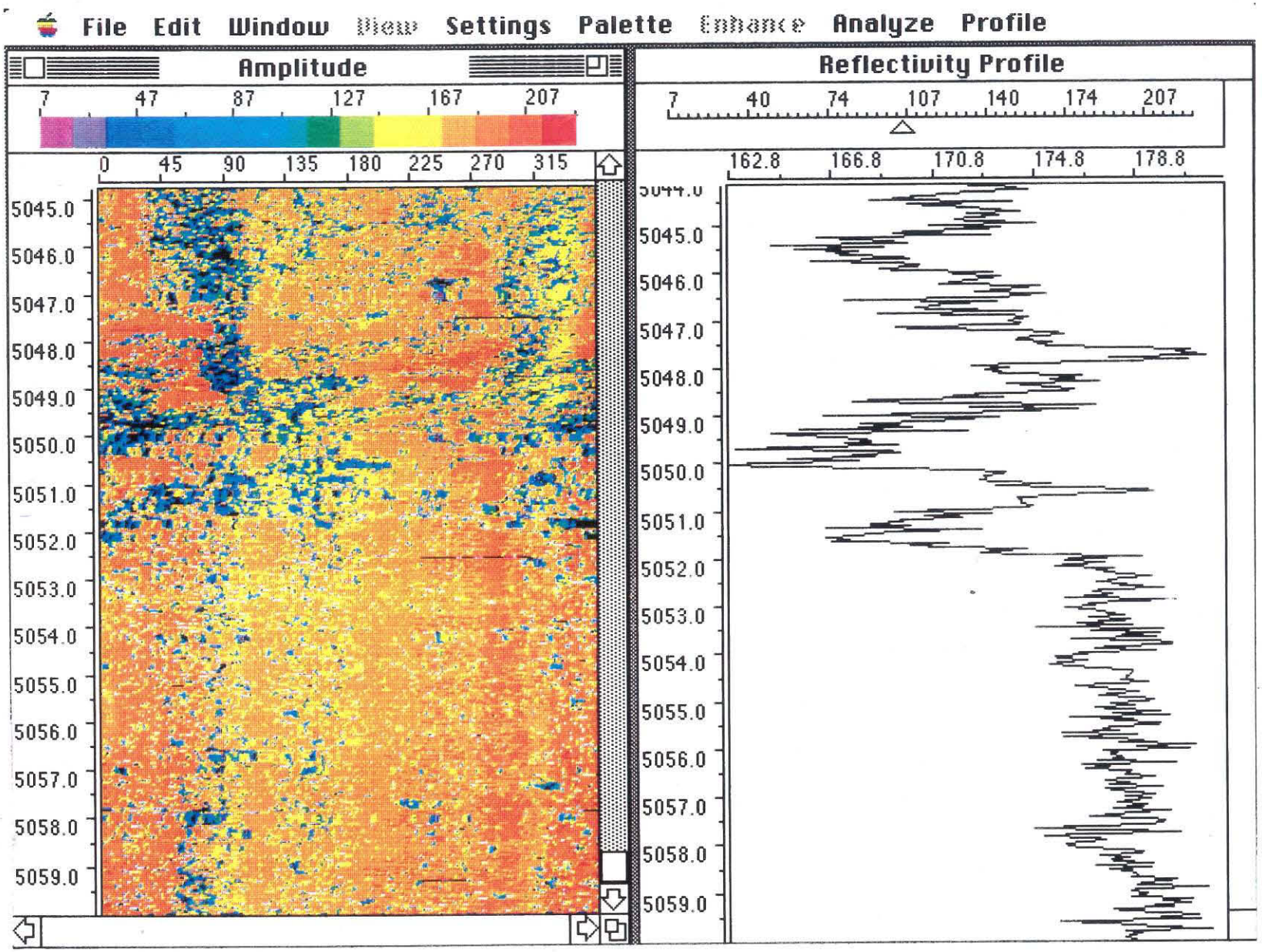
File Edit Window View Settings Palette Enhance Analyze Profile
Amplitude
7 47 87 127 167 207
0 45 90 135 180 225 270 315
5045.0 5046.0 5047.0 5048.0 5049.0 5050.0 5051.0 5052.0 5053.0 5054.0 5055.0 5056.0 5057.0 5058.0 5059.0
Reflectivity Profile
7 40 74 107 140 174 207
162.8 166.8 170.8 174.8 178.8
5045.0 5046.0 5047.0 5048.0 5049.0 5050.0 5051.0 5052.0 5053.0 5054.0 5055.0 5056.0 5057.0 5058.0 5059.0

Figure 23

Appendix V - Moos and Zoback stress estimation paper

The paper included here as Appendix V was published in the July 1990 *Journal of Geophysical Research*, and describes the methodology used to estimate stress magnitudes from the presence or absence of wellbore breakouts and drilling-induced hydraulic fractures.

EGG-NPR-10631
September 1990

INFORMAL REPORT

IN-SITU STRESS AND NATURAL FRACTURING AT THE INEL SITE, IDAHO

EGG-NPR-10631
September 1990

IN-SITU STRESS AND NATURAL FRACTURING AT THE INEL SITE, IDAHO

by

Danial Moos and Colleen A. Barton
Rock and Borehole Geophysics Project
Department of Geophysics
Stanford University
Stanford, California

Prepared for U.S. Department of Energy
Office of New Production Reactors
Under DOE Idaho Field Office
Contract No. DE-AC07-76ID01570

INFORMAL REPORT NUMBER → EGG-NPR-10631
September 1990

In-situ Stress and Natural Fracturing at the INEL Site, Idaho

A Report to
EG&G Idaho, Inc.

Daniel Moos
Colleen A. Barton

Rock and Borehole Geophysics Project
Department of Geophysics
Stanford University

September 10, 1990

Executive summary

It has long been noted that, although Basin-Range extension is active on both sides of the Eastern Snake River Plain (ESRP), only micro-earthquakes have been detected beneath the plain itself. To help understand this observation, borehole televiewer (BHTV) logs were recorded in four wells previously drilled at the Idaho National Engineering Laboratory, with the principal goal of detecting stress-induced wellbore breakouts to help constrain the magnitudes and determine the orientations of the horizontal principal stresses. These data also provide a detailed look at fracturing and lithostratigraphy within the volcanic rocks of the ESRP.

Wells USGS-17, USGS-7, and NONAME-1 were drilled to relatively shallow depths (less than 1000') and penetrate only the uppermost basaltic flows. These wells were logged over the intervals 390-567 feet, 757-890 feet, and 265-549 feet, respectively. The INEL-1 well, drilled to a total depth of 10,333 feet, was logged over the interval 6780 to 10,243 feet, within the underlying silicic volcanics. Analog BHTV data recorded during logging were digitized and interactively processed utilizing specially developed software which provides an integrated environment for analyzing borehole shape and features.

Analyses of the depth distribution and orientation of fractures intersecting USGS-17, USGS-7, and NONAME-1 provide a detailed picture of flow stratigraphy within the basalts. Although there are some interesting differences between the data from each of these wells, a characteristic lithostratigraphy within each flow unit emerges. At the base of each flow is a narrow zone of rubbly material, which grades into a massive interior cut by near-vertical fractures, possibly columnar joints. Near the top is a narrow zone a few meters thick of shallow dipping fractures. This pattern of fractures detected in the basalts penetrated by the shallow wells is most likely due to thermal stresses generated during cooling. Individual flows identified on the bases of this characteristic pattern have thicknesses on the order of 85 feet. However, it was not possible to positively match specific flow units between wells.

The positions, orientations and apparent apertures of macroscopic fractures intersecting the INEL-1 well within the interval 6780 to 10,243 ft were determined to study their distribution and to investigate their effect on the physical properties of the silicic volcanics. The majority of fractures encountered in the well strike ENE-WSW and dip steeply NNW. Most are sealed, providing evidence of past hydrothermal flow at this site. Fracture frequency does not systematically decrease with depth in the study interval. These steeply dipping fractures are interpreted as relict structures related to caldera collapse, and thus were not formed in the present-day stress field. Furthermore, they

strike in the direction of the least horizontal stress inferred from earthquake focal mechanisms outside of the plain. However, until we have direct knowledge of the orientations and magnitudes of the principal horizontal stresses, we cannot determine their potential for re-activation.

In addition to these fractures, numerous more shallow-dipping fractures were found. These tend to cluster within specific depth intervals. This pattern is similar to that found in the extrusive basalts, suggesting that the cyclic repetition of high density fracturing with intervening zones of moderate to low fracture density may be a consequence of processes occurring during deposition and cooling of the silicic volcanics.

No breakouts were found in the logged interval within the INEL-1 well. This requires a normal faulting stress regime beneath the ESRP based on the analysis of the stresses necessary to cause breakouts. However, until precise measurements of the strengths of these rocks are made we cannot discriminate between a hydrostatic (i.e. $S_{hmin} \approx S_{Hmax} \approx S_v$) and an incipient faulting (i.e. both S_{hmin} and $S_{Hmax} << S_v$) environment. Thus we cannot determine based on breakout analysis whether the lack of earthquakes greater than $M_S = 3$ within the SRP is due to low stress differences at depth, or to the greater strength of crustal rocks.

We suggest that hydraulic fracturing stress measurements be made in the INEL-1 well to measure the magnitudes of the horizontal stresses. The BHTV logs obtained in this study could be used to select unfractured intervals for those tests.

Table of Contents

Introduction

This report presents the results of analyses of borehole televiewer (BHTV) data recorded in four wells drilled on the Idaho National Engineering Laboratory plant site in the Eastern Snake River Plain (ESRP) near Idaho Falls, Idaho. The data was collected in holes USGS-7, USGS-17, NONAME-1, and INEL-1, all of which had been drilled previously for other purposes. The locations of the holes are shown in Figure 1.

The report is written in two sections. The main section briefly describes the geology and tectonics of the ESRP, to place the measurements in the proper context. We then briefly describe the technique of logging with the BHTV, outline the measurement sequence, and present the principal results. Finally, we suggest additional work which would help to quantify the conclusions, and propose some measurements which are a logical adjunct to the BHTV data acquisition and which would resolve the principal question posed by the study, that is, what is the state of stress at depth beneath the ESRP, and what are the consequences for seismic hazard to structures. The second section is a series of appendices which present the primary data, and include detailed chronologies of the data acquisition, reprints of previously published reports that describe the methods in detail, and documentation of the calibrations, data acquisition procedures and analysis methods used in this study.

The primary purpose of recording BHTV data in the four study wells was to determine the state of stress beneath the Eastern portion of the SRP. Although data was acquired in four wells, only data from the deepest of these, INEL-1 (drilled to a depth of 10,333'), could be used for this purpose. In this study we relied on the anticipated presence of stress-induced wellbore breakouts to provide information about the orientations and magnitudes of the in situ stresses beneath the ESRP. Breakouts (Bell and Gough, 1979) are wellbore enlargements oriented in the direction of the least horizontal principal stress, due to compressive shear failure of the wellbore where the circumferential stress concentration is greatest (e.g., Zoback et al., 1985). Recent work indicates that the presence (or absence) of wellbore breakouts can also provide estimates of the horizontal stress magnitudes (see Appendix V; Moos and Zoback, 1990). For example, breakouts are much more likely in a highly compressive (reverse-faulting) environment than in an extensional (normal faulting) one. Previous experience in a wide variety of stress regimes and regions had suggested that, at the depth reached by the INEL-1 well in particular, stress-induced wellbore failure is common (Stock et al., 1985; Hickman et al., 1985; Plumb and Cox, 1987; Moos et al., 1988).

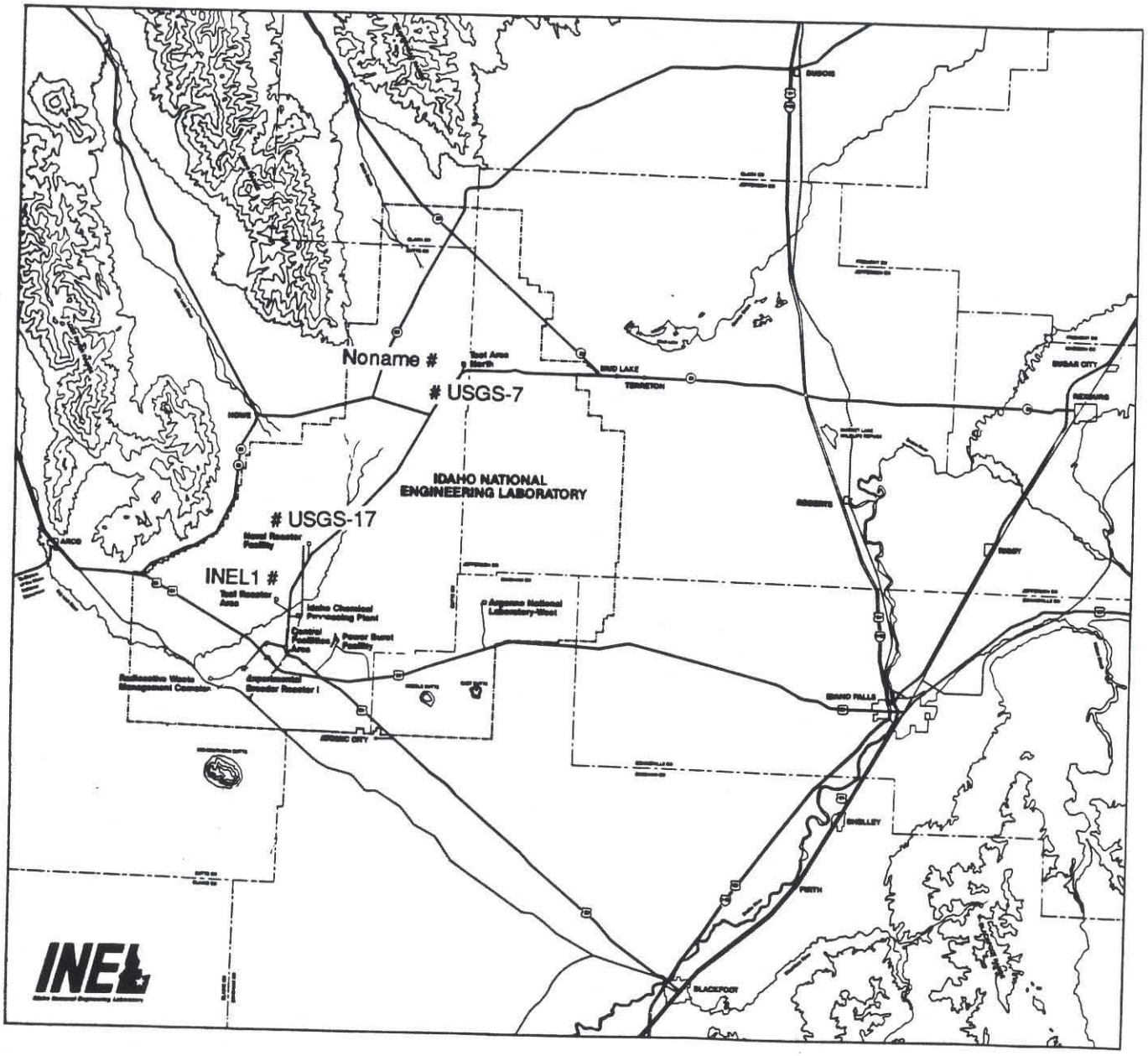

Figure 1: Location of the INEL plant site and positions of the wells used in this study.

A secondary objective of logging all four wells with the BHTV was to determine the orientations and characteristics of fractures and other discontinuities intersecting the wellbores. Fractures are particularly important in crystalline rock in determining the hydrologic, mechanical and seismic properties of the rock mass. In an otherwise competent material fractures provide permeable pathways, and if fluid filled may result in detectable seismic anisotropy. Furthermore, in active tectonic environments earthquakes typically occur on planes of weakness preferentially aligned with the principal stress directions. If fractures are found to have a strong preferred orientation which is aligned with the present-day stress field, then these fractures are potentially seismically active. In instances in which fracture orientations are not related in any obvious way to the present stress field, they record a history of cooling and/or paleo-tectonic activity which can reveal much about the history of a given region.

Geologic Setting

The Idaho National Engineering Laboratory is sited on the Eastern Snake River Plain (ESRP) just west of Idaho Falls, ID (Figure 1). The Snake River Plane cuts a concave Northward arc across the northern Basin and Range physiographic province, the trace of a hotspot whose present position is marked by the Yellowstone caldera (e.g., Morgan, 1972). In the ESRP, initial silicic volcanism has since given way to extensive extrusion of basalts which now overlie the silicic volcanics. This volcanism is still active; flows within the Craters of the Moon National Monument a few miles West of the INEL are less than 100 years old.

Information regarding the composition of the materials that underlie the ESRP has generally been obtained from interpretations of surface geophysical investigations. Analyses of cores and cuttings obtained during drilling of the INEL-1 well provide one of the few direct observations of the subsurface (Prestwich and Bowman, et al., 1980). Based on these analyses, more than 2000 feet of basalts have been extruded onto the ESRP. Sands and gravels are interlayered with these basalts. The underlying silicic volcanics extend to the total depth of more than 3.1 km. These include more than 5500 feet of welded tuffs, with minor amounts of cinders and tuffaceous interbeds. Dense, recrystallized hydrothermally altered rhyodacite ash-flows were found in the well below about 8000 feet. Below this depth the rock becomes increasingly dacitic; at 9460 feet an abrupt change to dacites was inferred from an increase in logged density. At greater depths, basaltic intrusions comprise as much as 25% of the present 40 km thick crust, based on interpretations of seismic refraction data (e.g., Sparlin, et al, 1982).

Basin and Range tectonic activity characterizes the regions on both sides of the ESRP, as characterized by the 1983 Borah Peak earthquake immediately to the North of the INEL. Although significant activity appears to be concentrated within a parabolic arc with its head beneath Yellowstone National Park, no earthquakes larger than $M_S = 3$ have been detected in the period since 1961 beneath the plain itself (Figure 2, after Anders et al., 1989). However, feeder vents for the extrusive basalts are aligned in a north-northwest direction, suggesting that the plain is extending in the same direction as the surrounding province. A number of ideas have been proposed to explain the lack of seismic activity beneath the plain. These include that the plain is undergoing ductile deformation, a consequence of elevated subsurface temperatures (e.g., Furlong, 1979), or alternatively that the basalts are simply too strong to fail (Anders et al., 1989). A recent alternative explanation proposed by Thompson et al. (in press) is that magmatic overpressure accompanying intrusion of dikes applies a large enough lateral stress to raise the least horizontal compression above the value necessary to allow normal faulting. Resolving between these competing explanations requires measurements of the stress state beneath the ESRP.

Unfortunately, there is a pronounced lack of information regarding the in situ stress state in the immediate region of the INEL plant. This is a consequence largely of the lack of seismicity. Figure 2 shows the locations of earthquakes larger than $M_S = 3$ in the region surrounding the ESRP. Figure 3 shows the stress data for a larger region surrounding the plain. This figure was compiled from the World Stress Data Base and includes data through 1989. Three earthquakes in northern Nevada indicate a roughly NE-SW direction of principal horizontal compression in the Basin and Range and a normal faulting environment. A series of earthquakes near the Idaho/Utah border suggests a similar magnitude and orientation of the principal stress field immediately to the SE of the plain. Immediately to the North of the SRP, maximum compression trends NW-SE, as illustrated by the stress directions inferred from the 1983 Borah Peak normal faulting event (indicated by a solid triangle). Not surprisingly, focal plane solutions surrounding the ESRP (Figure 3) yield maximum compression directions paralleling the trends of the latest Quaternary surface (normal) faults on which they presumably occurred (Figure 2). These point slightly towards the Yellowstone hot-spot, rather than being exactly perpendicular to the axis of the plain, a consequence of their origin along the "wake" of the hotspot trace.

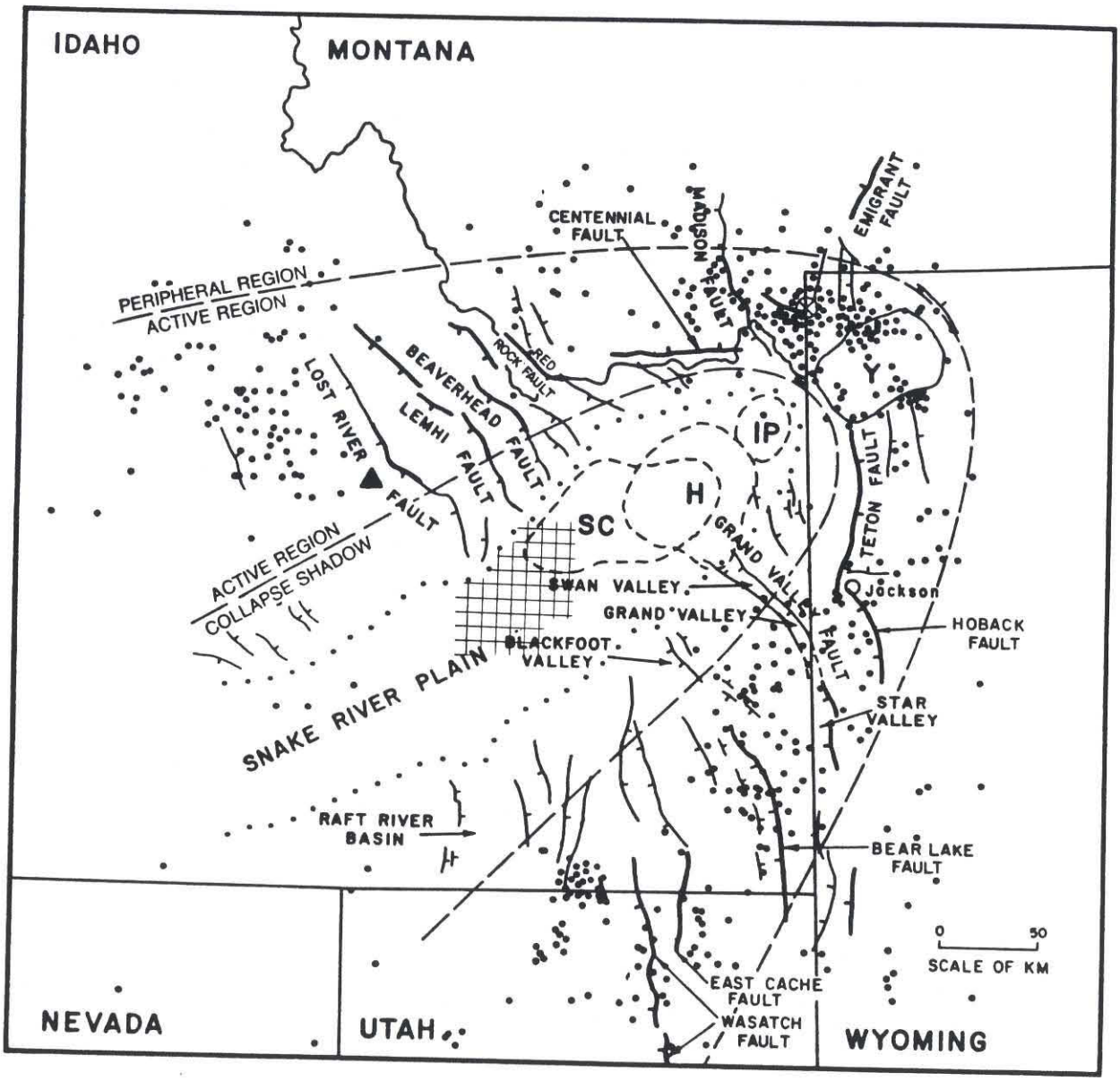

Figure 2: Distribution of earthquakes greater than $M_S = 3$ in the region of the eastern Snake River Plain, after Anders et al., 1989. The triangle shows the location of the 1983 Borah Peak earthquake, and the boundary of the INEL is marked.

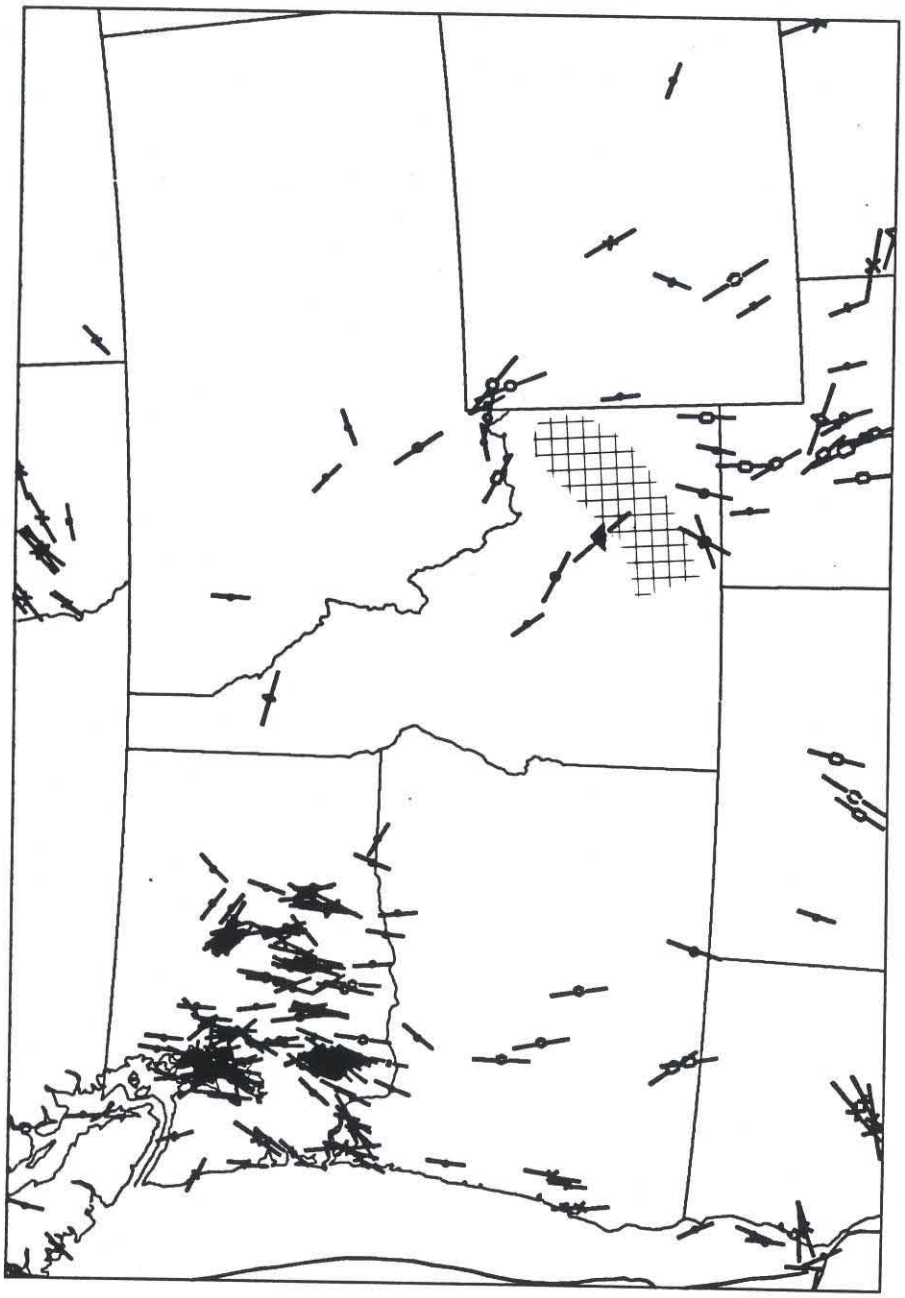

Figure 3: Stress data for the region surrounding the SRP, compiled from the 1989 World Stress Database (Zoback, et al., 1989). The triangle shows the location of the 1983 Borah Peak earthquake, and the boundary of the Snake River Plain is marked.

Description of the wells used in this study

Four wells were reoccupied for BHTV log data acquisition. Table I shows the depths, hole sizes and logged intervals in each of these wells. Three of these (USGS-17, USGS-7, and NONAME-1) penetrate to shallow depths in the basalts. Figures 4, 5 and 6 are well summaries for the shallow wells. The fourth (INEL-1) reached a total depth during drilling of 10,333 feet, and bottomed in silicic volcanics (Figure 7). Data in this hole was collected only in the open-hole interval below 9 5/8" casing. Thus only the silicic volcanics were logged in INEL-1 during the course of this study.

The intervals logged in these wells were constrained by the depth of the water table or of casing, and the total depth of the well. In each case we lowered the logging sonde until it was resting on the bottom of the well. The distance between the transducer measurement point and the end of the tool is about 4 feet. Therefore, the present total well depth can be found by adding 4 feet to the tabulated bottom of the logged interval. As the acoustic pulse generated by the transducer must propagate through the wellbore fluid to be reflected from the borehole wall, we can determine water table very precisely from the depth at which the signal return is lost. In each case the water table was measured a number of times; the numbers presented in Table I are the averages of these observations.

Table I: Well descriptions and summary of the intervals logged in the course of this study:

Well Name	Water Table (BHTV, ft)	Casing Depth (Driller's, ft)	Total Depth (Driller's, ft)	Interval Logged (open-hole, ft)	Hole size (in)
USGS-7	207	760	940	757-890	5.5
USGS-17	392	≈30	600	390-567	18
NONAME-1	204	272*	549*	265-549	12.25
INEL-1	303††	6796†	10,333†	10,243-6780	12.25

*inferred from BHTV log results

†referenced to Kelly Bushing, 20 feet above ground level

††from depths logged running into the well only

We briefly summarize the geological information available for each drillhole in the sections describing the televiewer data acquired in each. These descriptions were obtained from copies of well geometry figures and lithologic summaries provided by R. P. Smith (EG&G) prior to the start of logging.

Well Summary: USGS-7

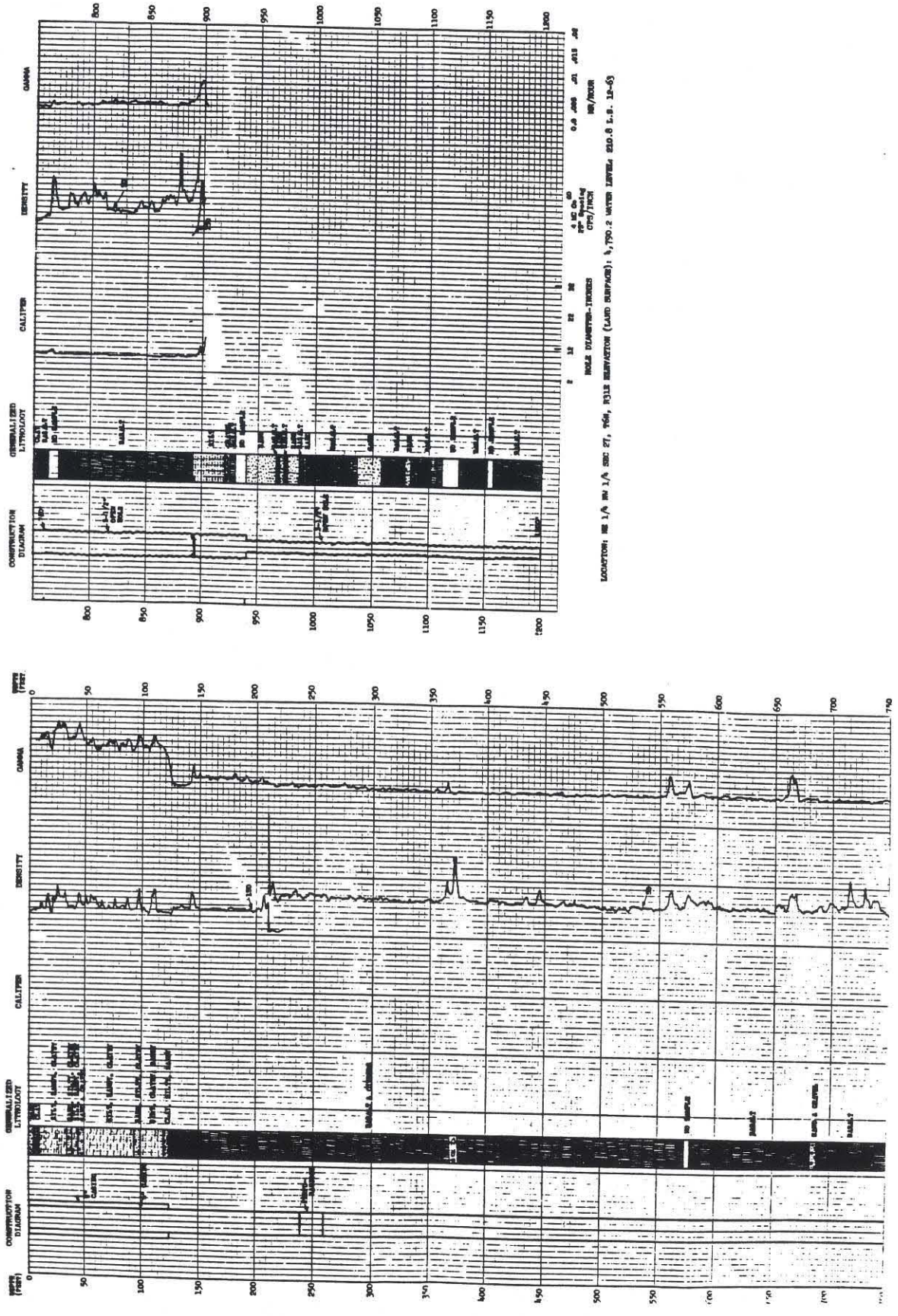

Figure 4: Construction diagram for well USGS-7

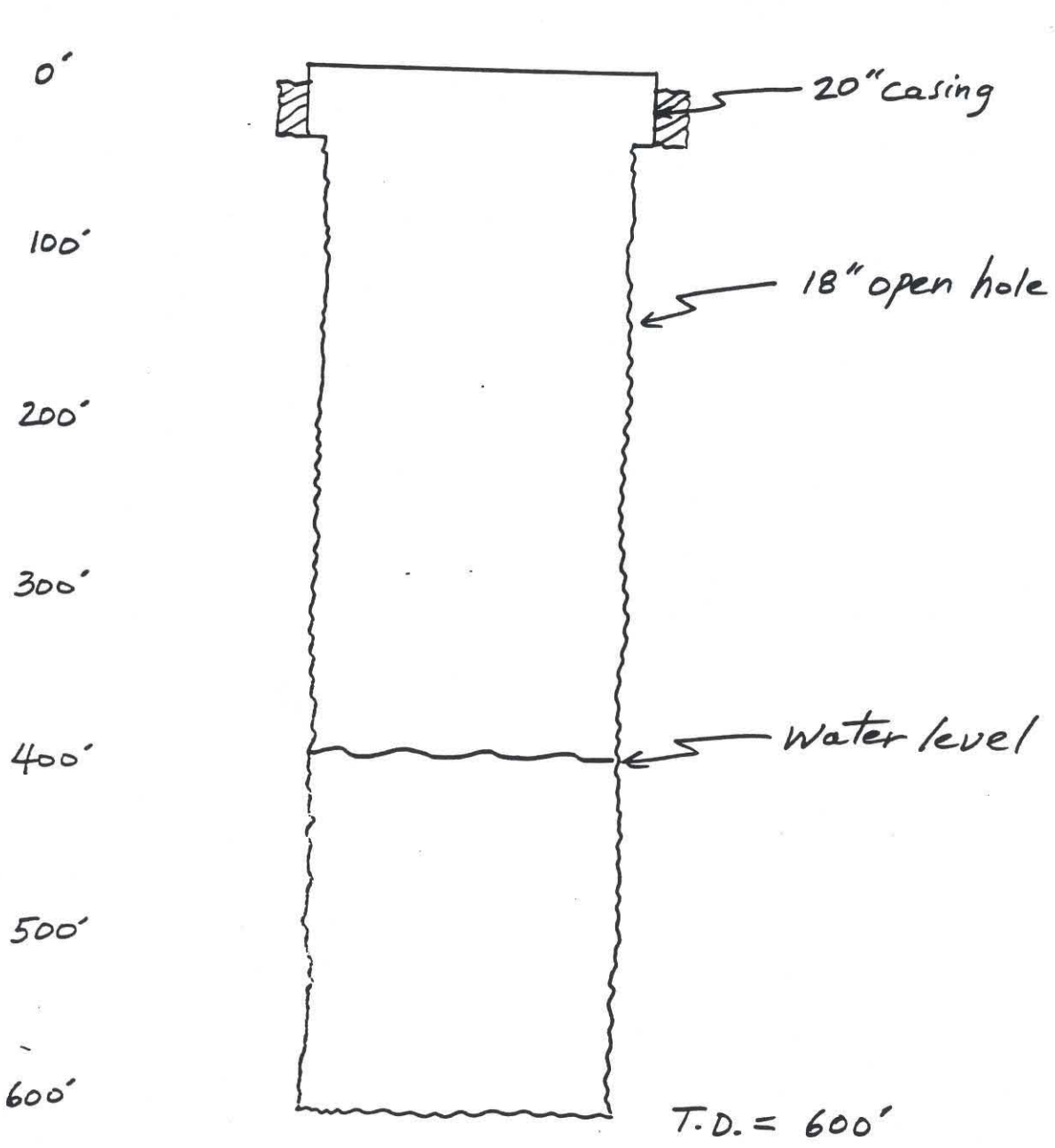

Figure 5: Construction diagram for well USGS-17

Well Summary: Noname

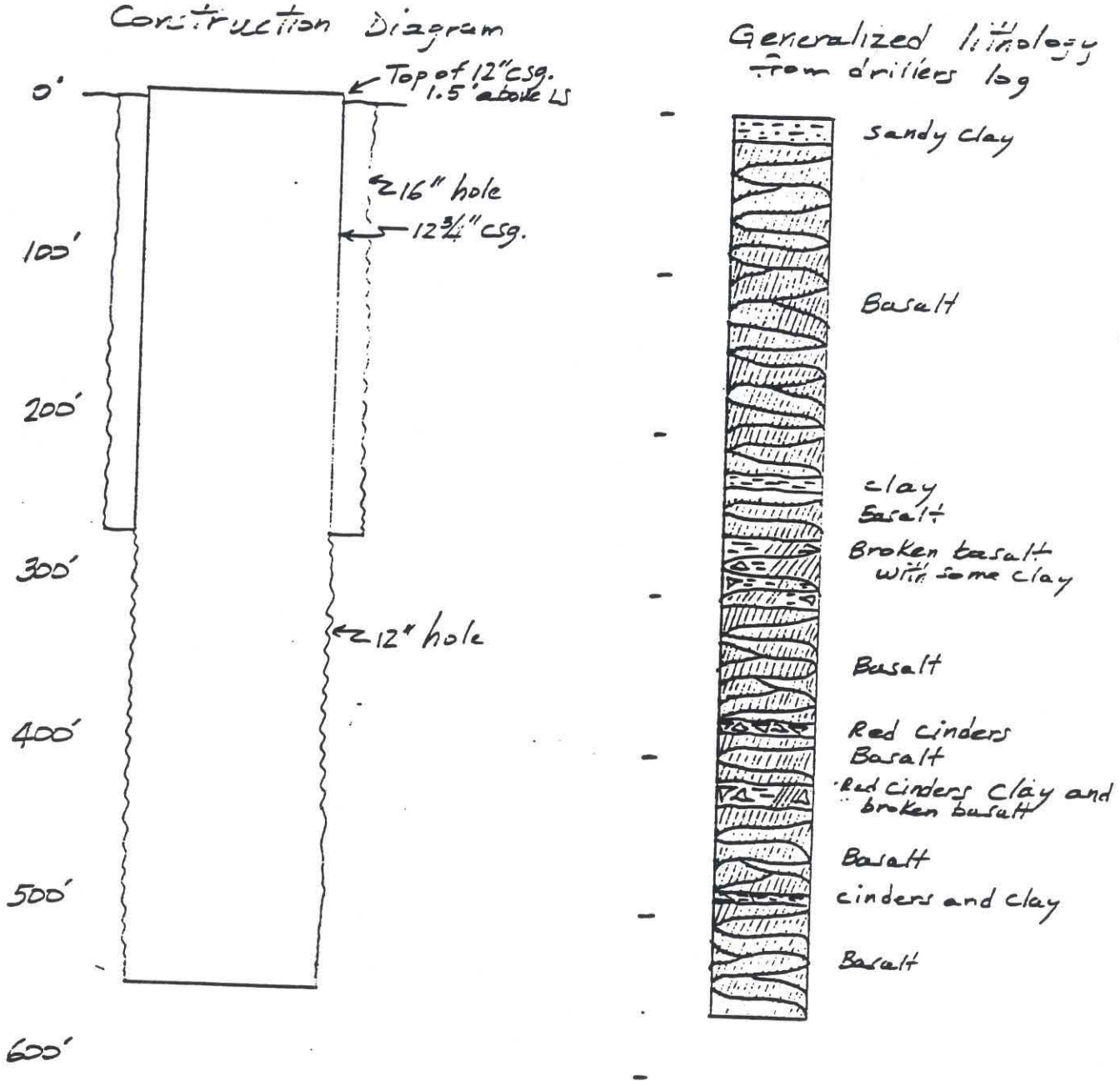

Figure 6: Construction diagram for well NONAME-1

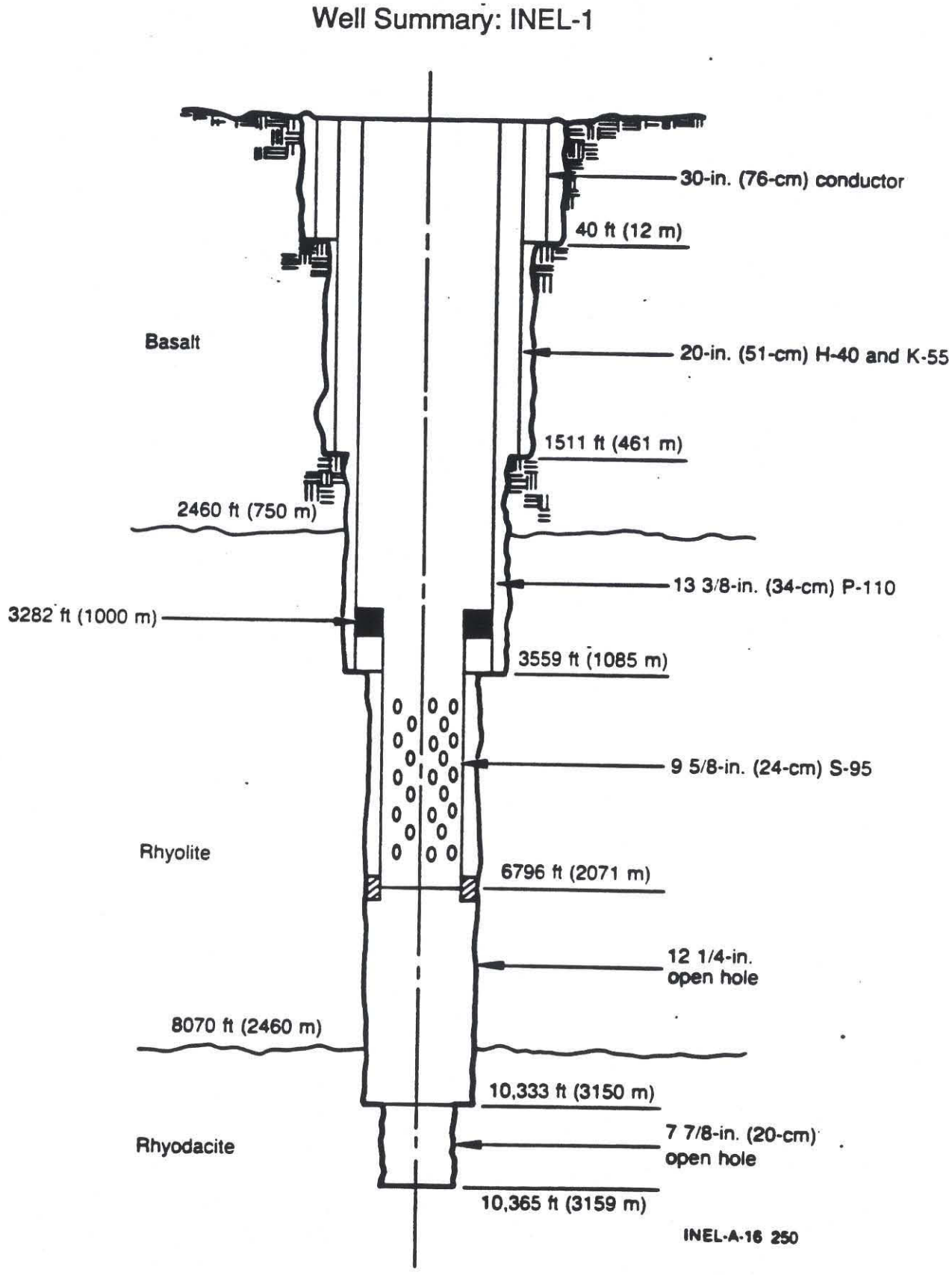

Figure 7: Construction diagram for well INEL-1

Previously Recorded Televiewer Data

The USGS Denver Water Resources Group collected BHTV data at INEL-1 during and shortly after the completion of drilling operations. Their depths are all referenced to the Kelly Bushing, 20' above ground level. Unfortunately, the USGS logs do not provide complete coverage of the INEL-1 hole. Furthermore, the data is available only as photographic copies of polaroids taken during logging, and thus is not appropriate for quantitative analysis. The depth intervals for which this data is available are 7100-7250, 7300-7380, 7420-7500, 7580-7780, 7980-8030, 8540-8600, 8900-9060, 9680-9800, and 10045-10200 feet.

These logs clearly show the effects of eccentering of the televiewer sonde as dark stripes running vertically along the images (Georgi, 1985). However, large numbers of sub-vertical fractures striking within 20° of EW can be seen in the images. No stress-induced breakouts were observed in these early logs.

A completely new set of borehole televiewer data was collected in this study for several reasons. First, the original logs are incomplete. Second, the quality of the new generation BHTV is superior to that available in 1981, through use of better centralizers and a newly designed, focussed transducer assembly. Furthermore, wellbore breakouts are often detectable in digitized data where they are invisible in the analog photographs. Also, there is some evidence elsewhere (for example, in the Kola well; L. Vernik, pers. comm.) that breakouts develop in time, and thus it was suspected that the 9-year interval between the early logs and the present date may have allowed new breakouts to occur. Finally, the BHTV data can be used to select intervals for later hydraulic fracturing stress measurements, and can be compared to televiewer logs made after successful tests to image the resultant hydrofracs.

DATA ACQUISITION

The borehole televiewer is an ultrasonic well-logging tool useful for imaging lithostratigraphic features and for measuring the orientation and distribution of fractures as well as the orientation and width of stress-induced wellbore breakouts. The analog televiewer, originally designed by Mobil Oil, Inc. (Zemanek et al., 1970), contains a rotating transducer that emits an acoustic pulse at the rate of 1800 times a second (See Figure 1, Appendix IV). The 1.4 Mhz transducer is mounted on a shaft which rotates at three revolutions per second. The logging sonde is centered in the wellbore using bowsprings, and is drawn upwards at a speed of 2.5 cm/s. Thus the reflection point describes a helical path as the tool moves up the wellbore, with repeat samples at each

azimuth obtained approximately every 0.8 cm. A fluxgate magnetometer within the tool fires at each crossing of magnetic north, making it possible to orient the data. The raw data displayed as a function of azimuth and depth in the hole presents a N-E-S-W-N unwrapped section of the amplitude of the reflected pulse in the borehole. A schematic of the tool and a sample of the data recorded during logging is presented in Figure 8.

Borehole televiewer data were collected in USGS-17, USGS-7, NONAME-1 and INEL-1 in late May and early June of 1990. Appendix I summarizes the data acquisition sequence, and the depth intervals for which data were acquired in each well are presented in Table I. Two different logging sondes were used to acquire the data. A 1 3/4" diameter sonde designed for use in small holes was used in USGS-17, USGS-7, and NONAME-1. Excellent data was recorded in USGS-7 and NONAME-1, but as described below the 18" hole size of USGS-17 was too large to adequately center the tool. Regardless, the piezoelectric source is powerful enough to return reflections even in this hole, provided the pulse strikes the borehole at normal incidence. Thus we were still able to extract useful information from the digitized and processed data. Data was recorded in INEL-1 using a 3 5/8" diameter, newly designed, high temperature televiewer. As this was our first use of this new tool, a number of electronic and mechanical failures plagued the recording effort. Even though we spent one week at the manufacturer prior to logging at the INEL, recording a complete log in that hole required a visit to the site by a technician from the manufacturing company. A detailed discussion of the procedures we used to verify the correct operation of this tool is presented in Appendix II.

The raw televiewer data recorded in the field on videotape were digitized at Stanford prior to analysis. This process is described in detail by Barton (1988) and in Appendix IV of this report. In post logging digitization the recorded BHTV signal is examined within a specified window to determine the peak amplitude and its associated travel time (Barton, 1988). Figure 1b of Appendix IV is an oscilloscope image of the playback of the analog wave train recorded on videotape for each pulse firing of the BHTV tool. The signal below the BHTV wave train represents the Mhz frequency clock used to discretely sample the windowed borehole wall reflection. The peak amplitude and associated travel time are measured for each pulse firing, for later display as false-color images of reflection amplitude and wellbore radius.

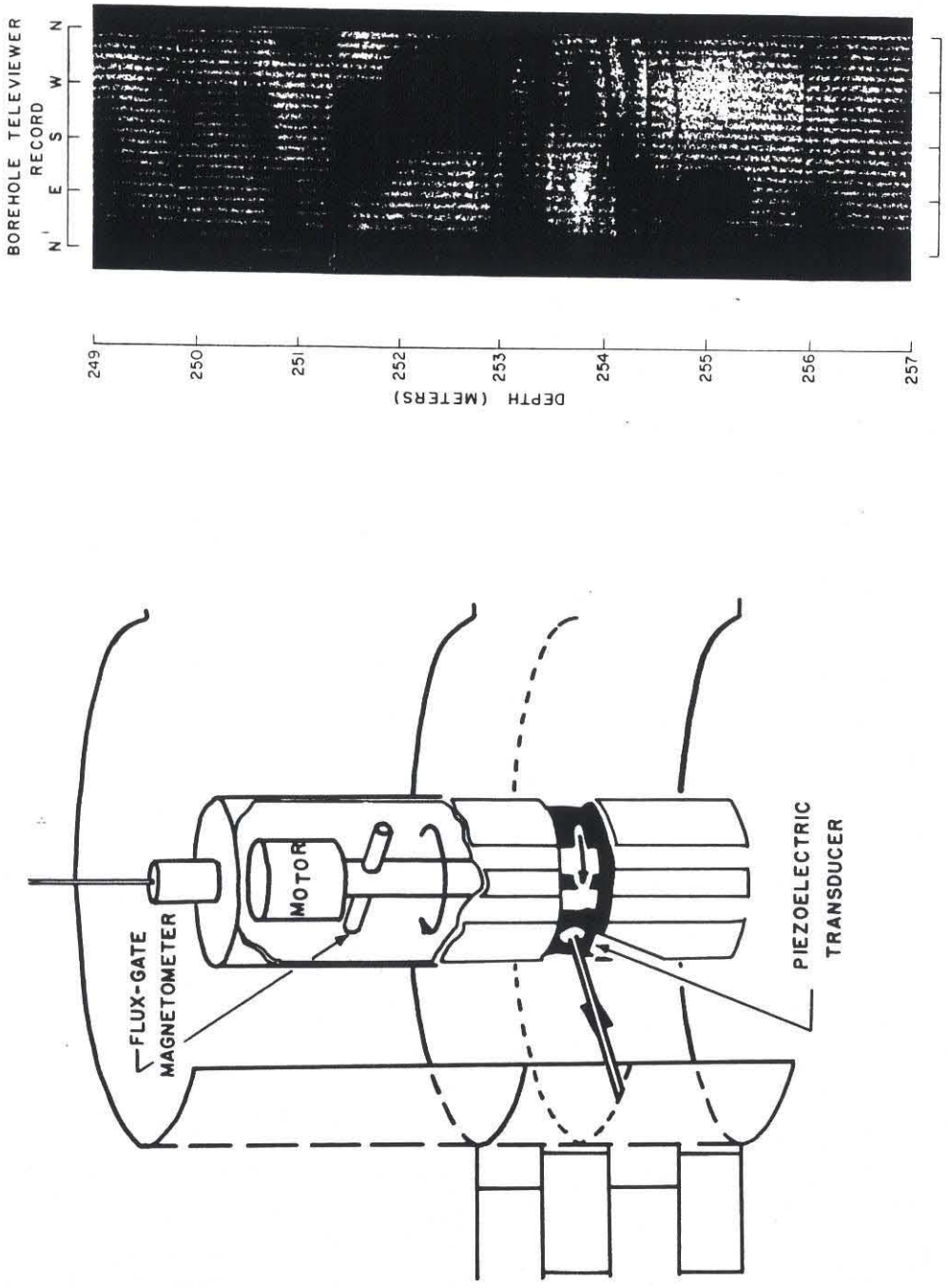

Figure 8: Schematic of the operation of the borehole televiewer, showing a sample Polaroid image recorded during logging.

The digital data are preprocessed before display. Preprocessing involves visual editing of the data for unwanted scans, median filtering to remove noise, and removal of the effects of off-centered tools. The data are shifted to correct for the magnetic declination at the logging site or of any other azimuthal data shift, and the amplitude and travel time values are scaled to the range 0 to 256. The editing and preprocessing procedures followed for the digital data recorded in INEL-1 and the three shallow wells of this study are described in detail in Appendix IV.

Conversion of travel time to true borehole radius requires prior calibration of the BHTV, as each tool is slightly different. These calibrations are carried out prior to and following each logging run, as described in Appendix II. Correct hole size determination requires knowing the speed of sound in the fluid in the wellbore, and thus these calibrations are generally carried out using samples of the mud in the hole. All four wellbores logged at the INEL were filled with clear water, so we simply used tap water for this study. The calculations required to convert travel time to borehole radius are thoroughly discussed in Appendix IV.

Stresses Beneath the ESRP

The data from the INEL-1 well was studied in detail to determine if stress-induced spalling of the wellbore (wellbore breakouts) had occurred. Appendix V describes the process of formation of breakouts, and outlines a methodology whereby the magnitudes of the horizontal stresses can be determined from the depth at which they begin to become common in a given well or region. These developments are briefly summarized below.

The process of drilling a wellbore into the earth's crust results in the concentration of stresses at the borehole wall. The equation relating the principal far-field horizontal stresses (S_{Hmax} and S_{hmin}) to the resulting circumferential stress ($\sigma_{\theta\theta}$) at the wellbore were derived by Kirsch (1898), and can be generalized to include wellbore fluid pressure (P_{mud}) different from the pore pressure (P_p):

$$\sigma_{\theta\theta}(\theta)=S_{Hmax} + S_{hmin} -2(S_{Hmax} -S_{hmin})\cos 2\theta - P_p - P_{mud} \qquad (1)$$

The maximum circumferential stress is attained at the azimuth of the minimum far-field horizontal stress ($\theta=90^o$), and the minimum circumferential stress is attained at the azimuth of the far-field maximum stress ($\theta=0^o$). The assumptions implicit in this equation are that the borehole is drilled in a vertical direction, that the vertical stress is a principal stress, and that the effective stress law is valid.

In general, wellbore failure can occur as a result of either compressive or tensile stress concentrations around the borehole, and, as described by Moos and Zoback (1990), observations of wellbore failure can provide information about the magnitudes of the in situ stresses.

Compressive stress failures at the azimuth of the least principal horizontal in situ stress (where the compressive stress concentration is greatest) are termed stress-induced wellbore breakouts (Bell and Gough, 1979) and have proven to be a reliable measure of stress orientation on land in many areas (see summary by Zoback et al., 1989). Breakouts have been identified both in uncomputed dipmeter logs (e.g., Bell and Gough, 1979) and in borehole televiewer logs (e.g., Zoback et al., 1985). Where both logs are run in the same hole, similar results have been obtained (e.g., Plumb and Hickman, 1985).

Wellbore breakouts occur by compressive shear failure wherever $\sigma_{\theta\theta}$ exceeds the strength of the rock, C (e.g., Zoback et al., 1985). If the two horizontal stresses are different, failure will occur at the azimuth of Shmin, where:

$$\sigma_{\theta\theta}^{max} = 3S_{Hmax} - S_{hmin} - P_p - P_{mud} \geq C \qquad (2)$$

From this equation and knowledge of the appropriate rock strength, C, constraints can be placed on the magnitudes of S_{Hmax} and S_{hmin}.

Tensile failures around the wellbore form at the azimuth of the greatest principal horizontal in situ stress (where the stress concentration around the well is least compressive). The hydraulic fracturing stress measurement technique takes advantage of this effect (Hubbert and Willis, 1957). However, tensile fractures may form adjacent to the wellbore simply as a consequence of drilling the hole. As is the case for wellbore breakouts, observations of tensile failure at the wellbore provide information about both stress orientation and magnitude.

Tensile fractures will occur whenever the minimum value of circumferential stress at the azimuth of SHmax is less than the tensile strength of the rock, T:

$$\sigma_{\theta\theta}^{min} = 3S_{hmin} - S_{Hmax} - P_p - P_{mud} < -T \qquad (3)$$

Thermally-induced tensile stresses due to cooling of the borehole wall by circulation of relatively cold drilling fluids can also promote tensile failure while drilling (Allison and Nielson, 1988; Morin et al., 1990). In these cases the fractures cannot propagate significant distances away from the wellbore unless the wellbore fluid pressure exceeds the least principal in situ stress (c.f., Stock et al., 1985; Moos and Zoback, 1990). Thus in

some cases tensile fractures can be formed at the wellbore but will not be observed during drilling because they are not associated with pronounced fluid loss. These can sometimes be observed by scanning logs such as the borehole televiewer or the formation microscanner.

As described above, the stress regime within the Basin and Range surrounding the ESRP is an extensional one. Thus breakouts were not expected to occur until a significant depth below ground level. It was still surprising, however, that no breakouts were detected in the INEL-1 well to its total depth of more than 3.1 km. Figure 9 illustrates the range of horizontal stresses allowed by the frictional strength of the crust for a depth in the INEL-1 well of 2.5 km. Superimposed on the figure are lines which subdivide the stress fields based on the presence or absence of breakouts, if the strength of the rocks is 100 MPa. Two strength criteria are illustrated. The first is the biaxial strength criterion employed by Moos and Zoback (1990). The second is the criterion suggested by Vernik and Zoback (submitted) to apply to rocks at depths below which microcracks are entirely closed and permeability and porosity approach zero.

Resolving the question of which of these two criteria is appropriate for the case at INEL-1 requires the determination of the so-called Biot coefficient, α, in the effective stress equation:

$$P_{eff} = P_c - \alpha P_p \qquad (5)$$

If $\alpha = 1$ the effective stress law applies, the fluid pressure in the wellbore offsets the rock pore pressure, Eqn's. 1-3 are appropriate to describe the wellbore stress concentration, and the rock strength for the case in which $P_{mud} = P_p$ is the biaxial strength (at the wellbore wall $S_1 = \sigma_{\theta\theta}$, $S_2 = S_v$; $S_3 = 0$). If $\alpha = 0$, the wellbore fluid pressure, P_{mud}, acts as a boundary condition on the wellbore, Eqn's. 1-3 must be modified to treat the total stresses, and the appropriate strength is approximately 1/2 the ultimate strength for the polyaxial stress case, C_p (at the wellbore wall $S_1 = \sigma_{\theta\theta}$, $S_2 = S_v$; $S_3 = P_{mud}$). This value ($\approx 0.5C_p$) is the point at which dilatent microcracks begin to develop, which for the wellbore case will lead immediately to failure and the formation of breakouts. The failure criterion then becomes (after Vernik and Zoback):

$$\sigma_{\theta\theta}^{max} = 3S_{Hmax} - S_{hmin} - P_{mud} \geq C_{ef} \; (\approx 0.5C_p) \qquad (6)$$

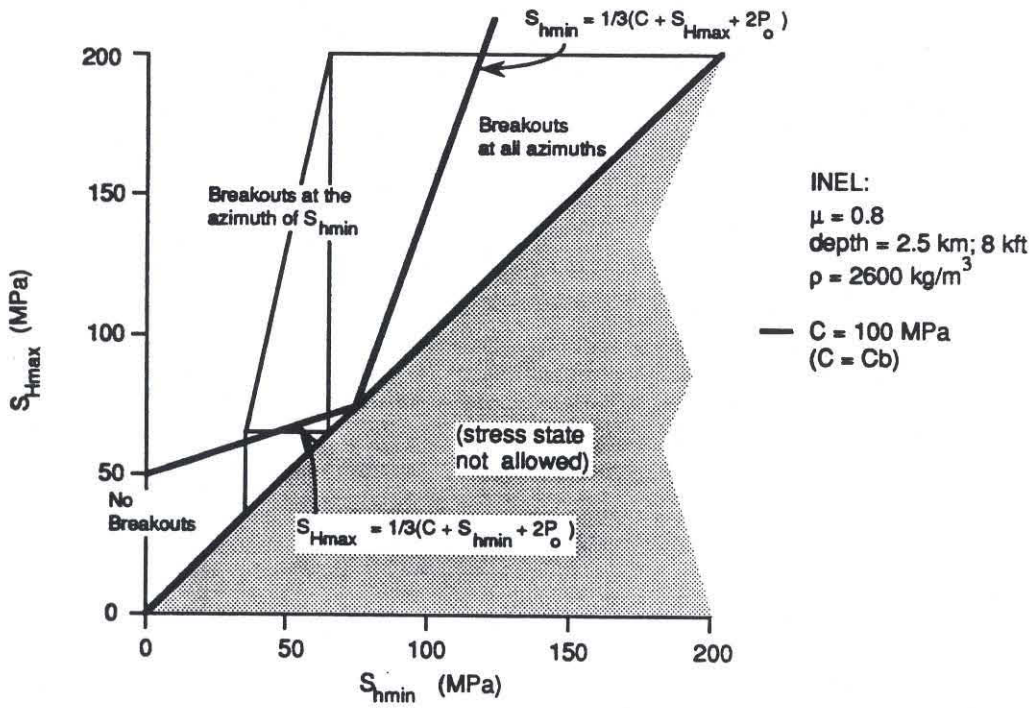

ASSUMING EFFECTIVE STRESS GOVERNS FAILURE
(Moos and Zoback, 1990)

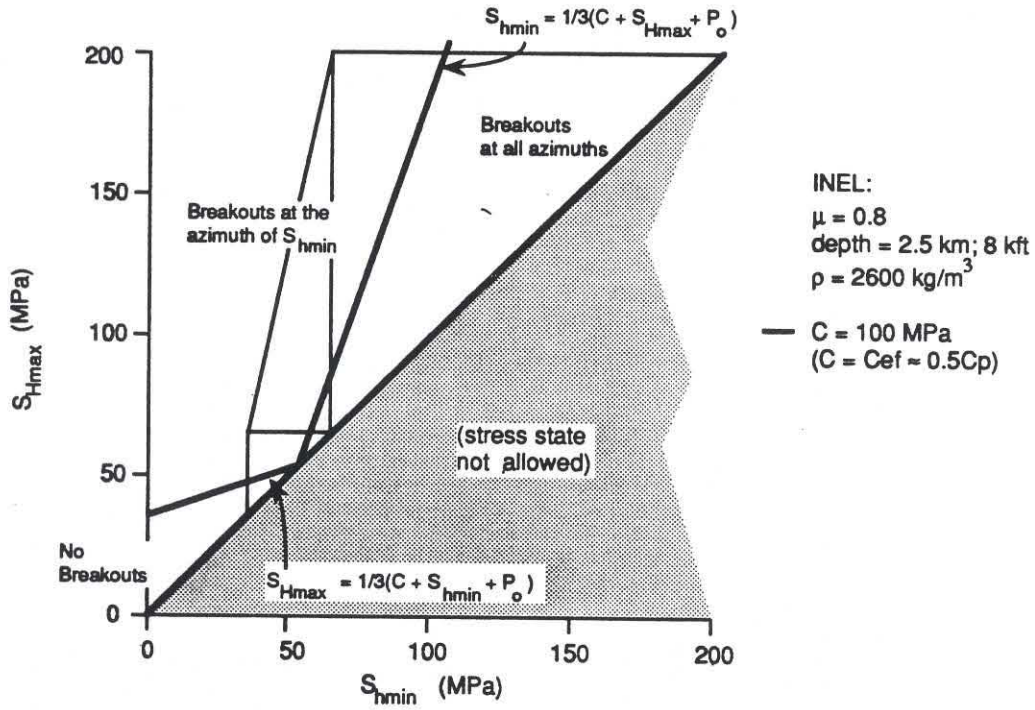

ASSUMING TOTAL STRESS GOVERNS FAILURE
(Vernik and Zoback, submitted)

Figure 9: Frictional constraints on the horizontal principal stresses appropriate for the INEL site, along with the fields within which breakouts are or are not expected. The upper figure illustrates the range of stresses at 2.5 km depth that would be expected to cause or not to cause breakouts, if the effective stress law applies. The lower figure is the same, but assumes that the effective stress law does not apply.

As a first estimate of the value of α, the ratio Vp/Vs provides a useful discriminator. Low values of this ratio are typical of rock with few microcracks, and indicate that the appropriate value is $\alpha = 0$. Higher values result from the presence of microcracks which enhance the porosity and permeability of the rock and lead to values of α closer to 1. Unfortunately, no measurements of V_p/V_s at the wellbore are available for the INEL-1 well. However, values of $\alpha \approx 0$ are associated with resistivities (which are sharply lower in the presence of microcracks) above 10,000 ohm-m. Examination of resistivity logs recorded in the INEL-1 well, therefore, should allow determination of which method should be used to estimate stress magnitudes.

As lithologies are variable within the INEL-1 well, it is reasonable to expect that rock strengths are also. A wide variety of values for welded tuffs are reported. For illustration, therefore, we choose strengths of 100 MPa, within the range reported for crystalline rocks. For strengths close to these, the absence of breakouts requires a normal faulting stress regime. Large horizontal stress differences are unlikely. However, more precise strength values are required to discriminate between a between a hydrostatic (i.e. $S_{hmin} \approx S_{Hmax} \approx S_v$) and an incipient faulting (i.e. both S_{hmin} and $S_{Hmax} << S_v$) stress regime.

As there are no breakouts within the depths penetrated by the INEL-1 well, we next asked the question of whether the drillers reported anything that might suggest that hydraulic fractures were created in the wellbore during drilling. As described by Moos and Zoback (1990) and others, the likelihood of tensile failure in a wellbore increases if cold drilling fluids are juxtaposed against warmer rocks, as the cooling of the wellbore which results causes the generation of circumferential tension. The preponderance of vertical fractures in the INEL-1 well, and their strong preferred orientation, is characteristic of drilling induced hydraulic fracturing observed elsewhere (for example, Stock et al., 1985).

However, there was no evidence of lost circulation within the depths logged by the BHTV. Furthermore, all the available evidence suggests that the fractures we saw in the INEL-1 data are old. Thus we conclude that the horizontal stresses were not sufficiently different to cause hydraulic fracturing. This places a lower bound on the horizontal stress difference, as it requires that strike-slip faults cannot be active in the current stress regime.

Thus the results of borehole televiewer logging in the INEL-1 well, although they require low (normal faulting) horizontal stresses and only a modest horizontal stress difference, do not resolve the issue of either the orientation of the horizontal principal stresses, or their precise magnitudes.

Fracturing in INEL-1

High quality borehole televiewer (BHTV) data were available from the INEL-1 drillhole for detailed analysis over the interval 6780 to 10,243 ft. The analog BHTV logs indicated that the data were generally of very good quality. In the following discussion we present the results for the data from INEL-1. The analog data were digitized and interactively processed prior to analysis using the techniques summarized above and described in more detail in Appendix IV.

While our study provides detailed data of fracture distribution at only a single location, it provides 3505 feet of continuous sampling in the silicic volcanics. The strike, dip and apparent aperture of 2568 natural fractures encountered over the depth range studied are reported below. The large number of fractures provides a representative sample of fracturing at the INEL site and presents an opportunity to examine their statistical distribution.

Measurement of Fracture Orientation and Apparent Aperture

Fracture orientations and apparent apertures were measured throughout the 3505 feet of hole logged in INEL-1. An example of the measurement of fracture orientation and apparent aperture for data typical of the INEL-1 BHTV log is presented in Figure 10. The left window of Figure 10 shows the fit of a sinusoid to the trace of a steeply dipping fracture at 9725 ft and the right window the interactive measurement of fracture aperture. A detailed description of the measurement technique is given in Appendix IV.

All fractures with apertures in the range from 0.2 in to 20 in were detected and measured. Many fractures with smaller apertures were also detected but their widths could not be accurately measured. Shear zones more than 20 in wide cause such disruption of wellbore conditions that the apparent fracture aperture cannot be measured with the televiewer. In total, 2568 macroscopic fracture orientations were analyzed from the INEL-1 image data. Of the 2568 fractures studied 2273 apertures were measured.

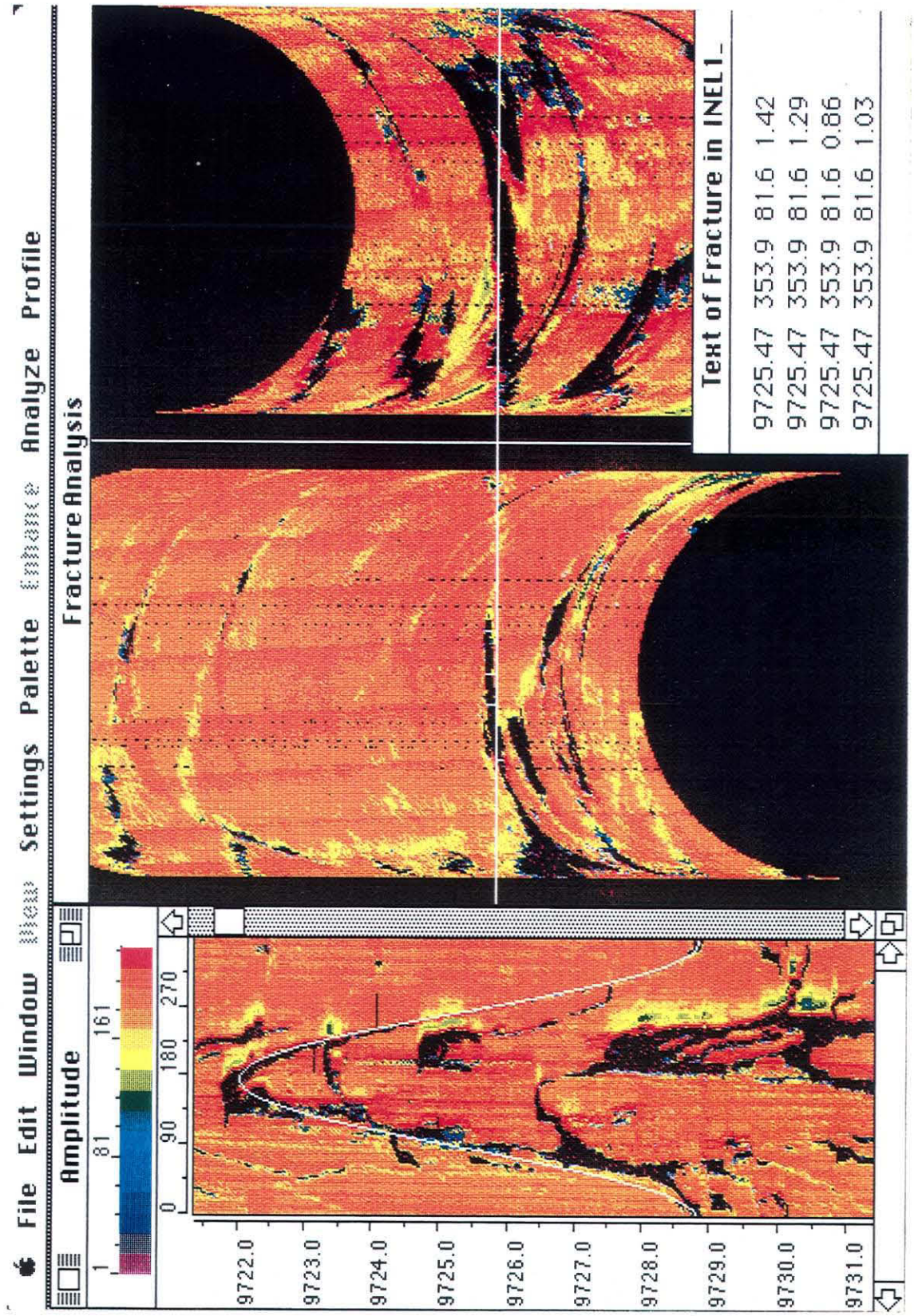

Figure 10: Interactive workstation screen showing the measurement of fracture orientation and apparent aperture for data typical of the INEL-1. The left window shows the fit of a sinusoid to the trace of a steeply dipping fracture at 9725 ft and the right window the interactive measurement of fracture aperture.

The BHTV reflectivity image data indicate that a different, often lower, reflectivity material infills the majority of fractures in the well. Figure 11 is an example of the acoustic character of the infill found in most fractures measured in the INEL-1 well. The fracture between 8505.5 and 8508.5 ft is only defined at its peak and trough. Little of this fracture trace can be discriminated in the corresponding travel time section. Toward the bottom of this interval between 8513.5 and 8514.5 a fracture is clearly filled with a material of lower reflectivity. Again, this fracture causes only minor changes in the borehole radius. The enlarged fracture from 8515 to 8516 ft appears to be partially infilled and substantially eroded. The most convincing evidence that these fractures are sealed is that in most cases it is only possible to distinctly discriminate the peak and trough of a fracture where the mechanical erosion of these steep features is the greatest. The remaining segments of the sealed fractures can be seen only by careful examination of the enhanced reflectivity image data.

The character of fractures shown in Figure 11 is typical for much of the logged section of INEL-1. Thus, most of fractures imaged by the BHTV in this study appear to be sealed, probably with calcite. The large number of fractures and the extent of their infilling and connectivity provides evidence for the past movement of groundwater.

Fracture Distribution

Plotted in Figure 12 is the fracture frequency per foot over the interval 6780 to 10,245 feet. The fracture distribution tends to be clustered with intermittent high fracture densities (c.f. 7725 ft; 8340 ft; 9525 ft; 10,200 ft). Several zones of intense fracturing are indicated by the hashed lines. Many of these correlate with a high measured fracture density, although over some highly fractured intervals the BHTV signal is reduced resulting in the inability to discriminate fractures. Data on apparent fracture aperture is shown in Figure 12 as the cumulative amount of fracture aperture (in inches) per 1 foot of depth. Comparing this profile to that of fracture density, several intervals with a high frequency of fractures correspond to a low cumulative width per foot. However, where the apparent aperture per foot is large there are usually a large number of fractures. Although mechanisms acting to close fractures would be expected to reduce the number of open fractures with increasing depth, the data do not show this trend.

There appears to be a cyclic repetition of high density fracturing followed by moderate to low fracture density throughout the logged interval (c.f. 7725 - 8325 ft; 9525 - 10,100 ft). These apparent cycles may be associated with repeated deposition of the volcanics and with the associated compositional changes.

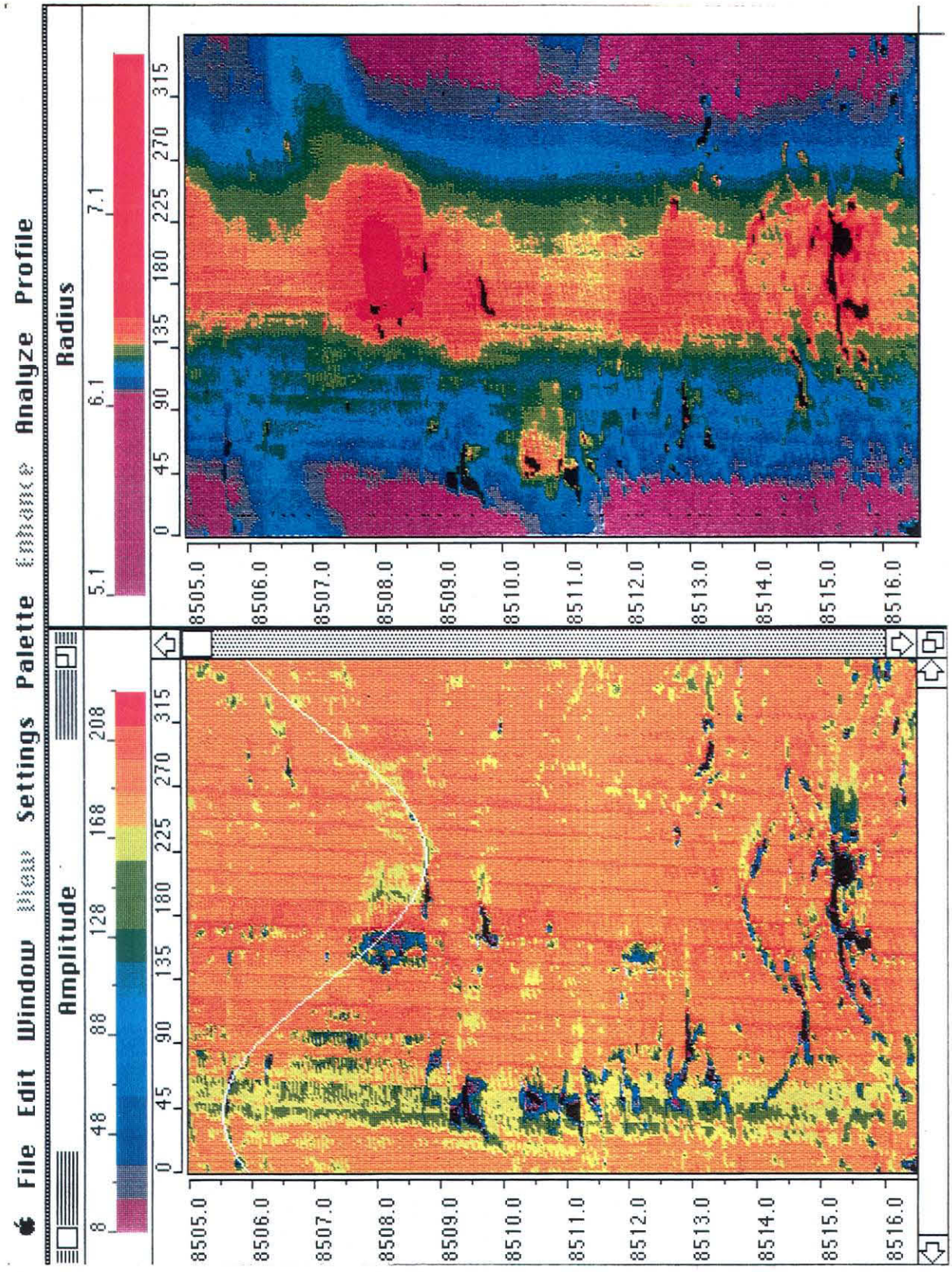

Figure 11: An example of the acoustic character of the infilling material found in most fractures measured in the INEL-1 well. Left window of the amplitude of the reflected energy indicates the fracture trace visible at its peak and trough while the wellbore radius image (right window) shows little of the fracture trace.

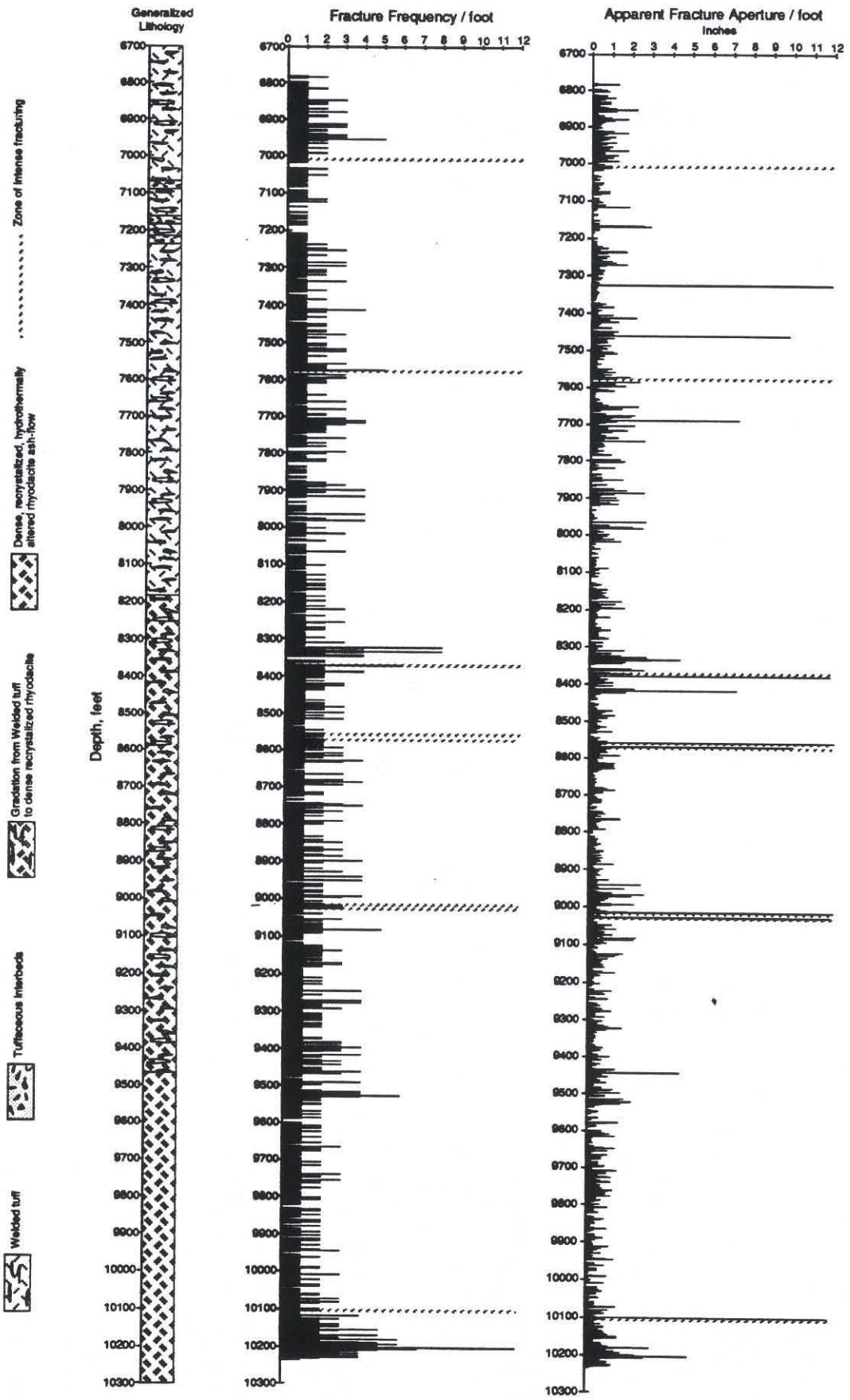

Figure 12: Generalized lithology, fracture frequency and apparent aperture per foot over the interval 6780 to 10,245 feet. in well INEL-1

Fracture Orientation

Orientations of all of the macroscopic fractures detected in the INEL-1 well are shown in Figure 13 in a lower hemisphere stereographic projection. On the left side the data are presented as poles to fracture planes and on the right side they are presented as a contour diagram of pole densities. A step function method was used to contour pole densities. The contour shading shown in the legend in Figure 13 represents the percentage of points that fall within the area of the point counting circle.

While there is clearly a random component of fracture orientations, a statistically significant concentration of fractures strikes East-southeast and dips steeply to the Northwest. The primary concentration of fractures strike at an azimuth of 155° and dip 78° Northwest. A secondary significant population is comprised of subhorizontal fractures dipping from 5° to 30°.

The strike of fracture planes for 500 foot depth intervals within the INEL-1 well is presented in Figure 14. This includes all fractures, regardless of their dip angle. Aside from the interval between 7500 and 8500 ft, where the azimuth of the predominant fracture strike is 250°, the predominant fracture strike azimuth in the INEL-1 well is 265°. There is no clear relationship between fracture strike (Figure 14) and either lithology or fracture frequency (Figure 12).

A summary of fracture orientation with depth is presented in Figure 15 as a tadpole plot. The dip of the fracture is plotted along the x-axis, and the dip direction of each fracture is indicated by the compass angle along which the tail of the tadpole points. The size of the tadpole sphere represents the aperture of the fracture. Open spheres indicate a fracture too small to accurately measure apparent aperture. There is a predominance of steeply dipping fractures throughout the logged interval. There is also a significant number shallow dipping fractures. This representation of the data shows larger fractures have steeper dip than smaller fractures and that it is the majority of large macroscopic fracture that comprise the overall ENE trend that dips North-northwest. Although data are compressed in this representation the cyclic repetition of fracturing is again clear.

The large number of near-vertical fractures, and their strong preferred orientations, suggest a common origin for these features. One likely explanation is that the INEL-1 well penetrated a zone of intense fracturing related to the collapse of a caldera within the silicic volcanics. The fact that these fractures are largely filled supports this inference. This is perhaps the first direct evidence for the existence of collapse structures buried beneath the flow basalts mantling the plain. Although the lack of breakouts in the INEL-1 well suggests that the magnitude of horizontal stresses is low, we cannot determine the potential for re-activation of these fractures (or of others penetrated by the INEL-1 well) until we

Figure 13: Lower hemisphere stereographic projection of the orientations of all of the macroscopic fractures detected in well INEL-1.

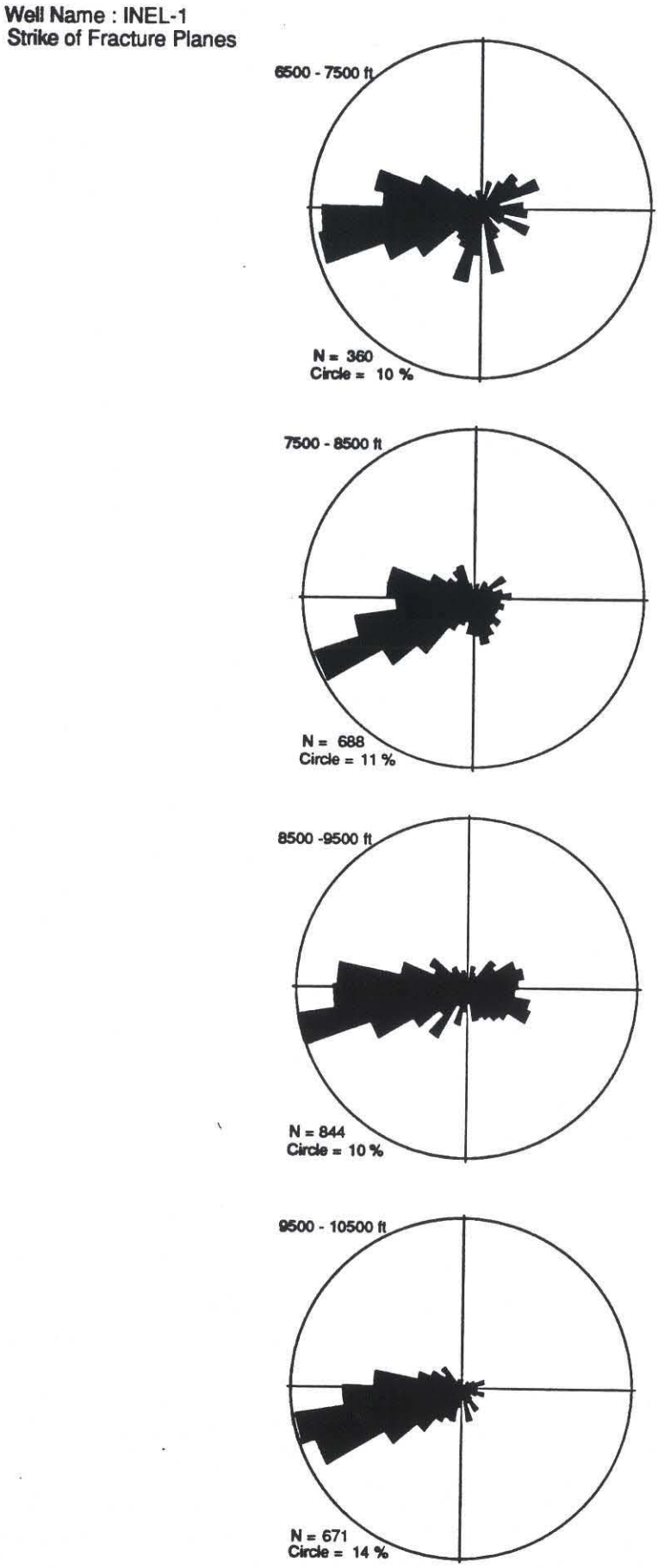

Figure 14: The strike of fracture planes for 500 foot depth intervals within the INEL-1 well.

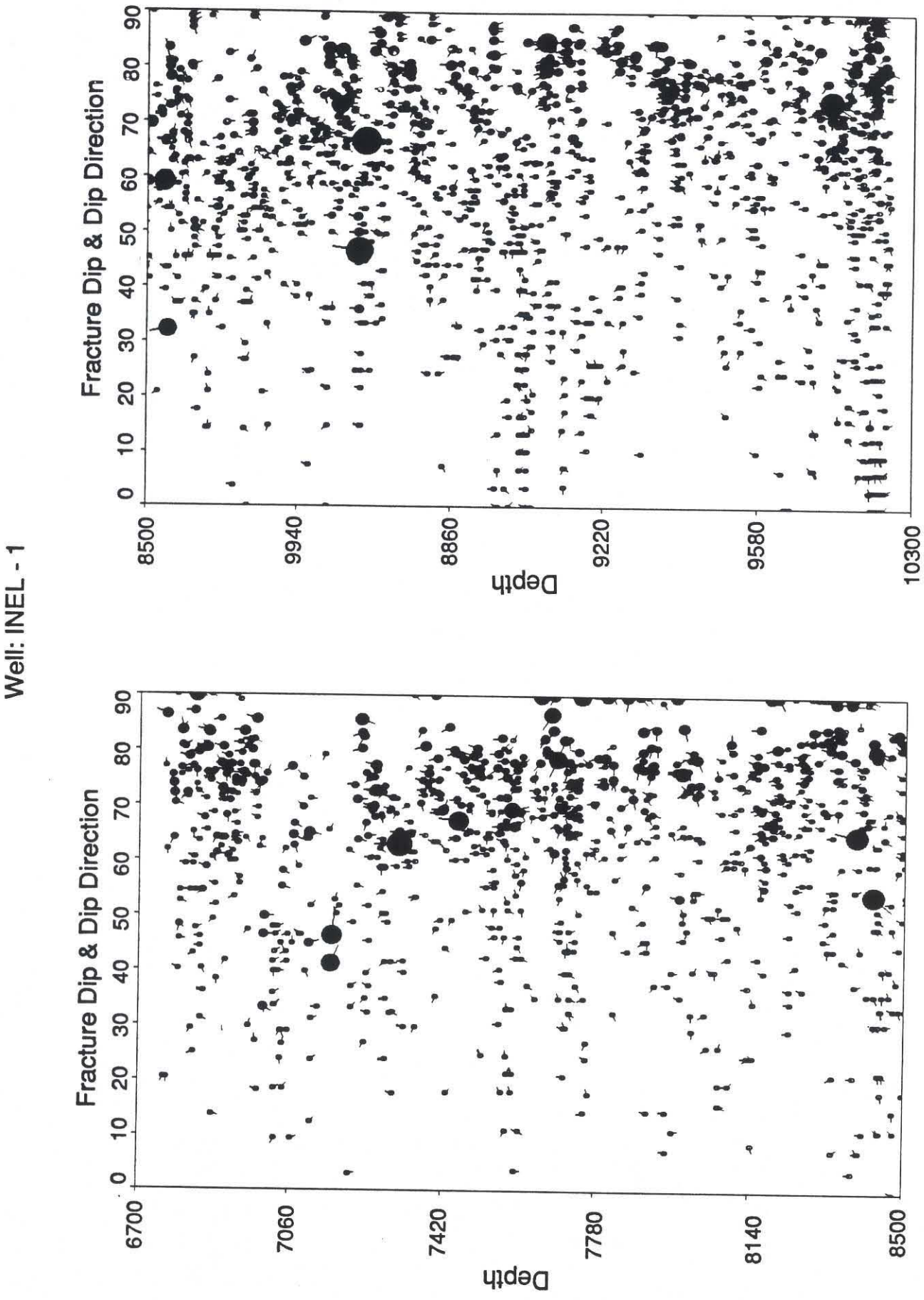

Figure 15: Tadpole plot of fracture orientation with depth for well INEL-1. Fracture dip is plotted along the x-axis, and the dip direction of each fracture is indicated by the compass angle of the tadpole tail.

have direct knowledge of the orientations and magnitudes of the principal horizontal stresses. However, for these fractures to be reactivated as normal faults the least horizontal stress beneath the plain would have to be oriented perpendicular to its axis.

Fractures and Lithology

Figure 12 includes a sketch of the major lithologic units (based on a report by Prestwich and Bowman, et al., 1980) provided at the scale of the fracture density profile. The generalized lithology over the interval of recorded BHTV data in the INEL-1 drillhole consists of an upper unit of welded tuffs with interbeds of reworked tuffaceous sands, non-welded ash-flow tuff, and air-fall ash. Below approximately 9000 ft there is a gradual change to dacite. Although fracture density does not have a strong correlation with lithology at this very generalized scale this does not rule out a possibility of better correlation and lithologic control of fracturing at a smaller scale.

In order to investigate the relationship between fracturing and lithology we subdivided the interval at the logged top of the dacites, picked at 9460 ft (Prestwich and Bowman, et al., 1980), and present the orientations of fractures above and below this boundary in stereographic projection. Figure 16a represents those fractures above the lithologic boundary, and 16b those fractures below this boundary. A population of shallow dipping fractures appears in the data from below 9460 ft (Figure 16b) that is not well developed above that depth (Figure 16a). However, from the tadpole plot of Figure 15 it is clear that these shallow dipping fractures are also found above the dacite, and that the significance of this cluster in the data from below the dacite is a statistical fluke due to the shorter depth interval. High densities of sub-horizontal fractures are found at 8450, 9400 and 10,200 ft.

Physical Properties and Fracturing

Prestwich and Bowman, et al. (1980) present only a brief summary of the geophysical logs recorded in the INEL-1 well over the depth interval of this study. Although we do not have access to the log data itself, it is worth while to compare their description of the log responses to the BHTV data we discuss here. Unfortunately, comparison of geophysical log anomalies with fracturing is often quite difficult, as variations in lithology or vein fill material, foliation, grain size, degree of alteration, or geologic contacts can produce variations in geophysical log measurements that are not related to the presence of fractures but could resemble those that are (Paillet, 1985; 1988).

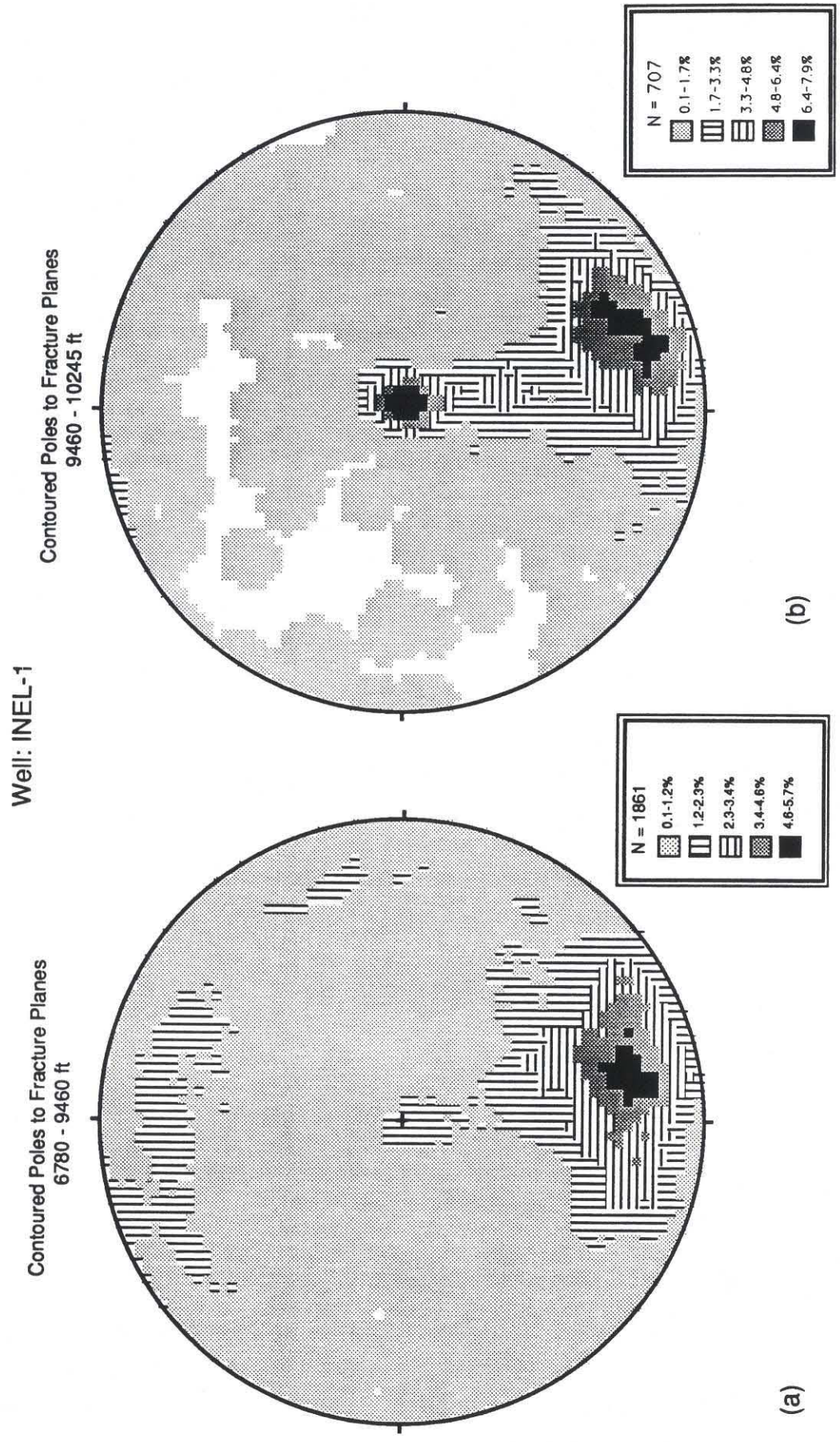

Figure 16: (a) Lower hemisphere stereographic projection of measured fractures above the lithologic boundary at 9460 ft in well INEL-1 and (b) measured fractures below this boundary.

The most valuable logs to augment fracture data are temperature, resistivity, sonic, neutron porosity and natural gamma. The following paragraph briefly summarizes the usefulness of each of these logs to the interpretation of the fracture data.

Both compressional and shear sonic velocities often decrease markedly at fractured horizons, with an accompanied increase in V_p/V_s, which is an expected result of the decrease in stiffness associated with fracturing (Moos and Zoback, 1983). Sonic data is extremely useful in the characterization of fracturing when used in conjunction with borehole image data as it generally provides information about which fractures persist away from the borehole. Gamma values often increase at depths of greater fracture frequency. The comparison of BHTV identified fractures to gamma anomalies is significant in that the BHTV often detects open fractures while the gamma tool is most sensitive to the potassium content of infilling clay minerals and to the presence of uranium which is often concentrated in fractures due to hydrothermal activity. Thus the presence or absence of a gamma increase reveals much about the nature of the infilling material. Neutron porosity logs, which measure the concentration of atomic hydrogen, should not be very sensitive to fractures as the associated porosity increase is small; however, the roughness of the borehole at the intersection of a fracture may cause a porosity anomaly (Paillet, 1988). High porosity values in basalts are probably due to hydration of the basalts around fractures and the associated borehole enlargement and not representative of true fracture porosity. It is not possible to discriminate between neutron porosity anomalies associated with true fracture porosity and those caused by infill or alteration however these logs usually present a good empirical relationship between anomalies and the location of fractures. Electrical logging can usually locate natural fractures in a wellbore because alteration minerals associated with fractures provide exchange cations for the conduction of current even if the adjacent intact rock may be resistive. The association between the electrical response and fracture permeability remains qualitative due to the similarity between the electrical response due to clay alteration around fractures and that due to brine infilled fractures (see Paillet, 1985; Pezard, 1988; Pezard et al., 1990; and references therein). Anomalies detected in temperature logs associated with fractures provide evidence for fluid flow into or out of the well, giving an anomalous change in thermal gradient. Thus temperature logging is perhaps the most reliable survey technique to assess hydrogeologic properties.

Although the log data from INEL-1 have not yet been made available to perform an in depth analysis of the relationship between physical properties measurements and fracturing the following relationship between fracturing and log response was noted.

The interbedded zone of porous and dense rock from 7070 to 7231 ft detected in the geophysical logs (sonic, neutron and resistivity) is a zone of low to moderate fracture frequency but with isolated large aperture fractures. The anomaly at 7110 feet marks a 15 foot wide fracture zone visible in the BHTV image data. This depth correlated exactly with the depth of a recorded temperature anomaly. The BHTV image data at another temperature anomaly near 7285 ft reveals a number of open fractures. Although several large steeply dipping fractures occur at a lower depth (7500 ft) these fractures appear to be at least partially filled. Temperature anomalies between 9600 and 9750 ft are associated with a depth interval where the majority of fractures are in fact open in contrast to the obviously sealed fractures previously discussed.

Changes in the sonic and neutron signature at 8081 ft correspond to a region of low fracture frequency and cumulative aperture. The BHTV data is in general agreement with the geophysical log data which indicate few open fractures for geothermal production. As mentioned previously, there is strong evidence of past hydrothermal flow inferred from the extent to which the fractures are sealed.

Analysis of fracturing in USGS-17, USGS-7, and NONAME-1

Wells USGS-17, USGS-7, and NONAME-1 were all drilled to shallow depths (less than 1000') and encountered basalt flows, rubble, and intercallated sediments. Borehole televiewer data were obtained in these wells primarily to study the fracturing and lithostratigraphy of the basalt section. The results provide an opportunity to study in a localized area changes in the character of individual flow units. The well geometry and the intervals logged in each well are presented in Table I, and the detailed operational procedures are described in the Appendices I and II. The procedures used to analyze these data are identical to those used for the data from INEL-1, with the exception that fracture apertures were not determined.

USGS-7

USGS-7 was drilled to a depth of 940 feet using a 5 1/2" drill-bit (Fig. 4). The hole was logged with the 1 3/4" televiewer over the interval from its present total depth of 895' and the bottom of 6" casing at 760' (driller's depth). The loss of the hole below that depth is most likely due to wellbore collapse within a silt sequence in the interval 885 to 940 feet (Fig. 4). The geologic section interpreted from cuttings and geophysical logs in this hole indicates a thick sequence of undifferentiated basalts within the entire logged interval. The BHTV results, however, present a quite different picture.

The amplitude of the reflected signal and the wellbore radius calculated from the calibrated travel-times are presented as false-color images in Appendix III. Examination of these images reveals a characteristic lithostratigraphy within the logged section. The intervals from 890 to 857 feet and 802 to 773 feet are characterized by chaotic, partially missing reflections, either due to a large number of intersecting fractures or a brecciated or blocky fabric. In the interval 857 to 802 feet, a thick interval of massive basalt is cut by a series of near-vertical fractures. Near the top of this interval, a series of sub-horizontal fractures occur with spacings of a few feet. The interval above 773 feet seems to repeat this sequence, but the top of the interval, where the sub-horizontal fractures presumably occurred, is now behind casing.

The orientations of fractures intersecting the wellbore were picked interactively from the image data. In this exercise we attempted to extract fracture planes from the chaotic images presented in the intervals 890 to 857 and 802 to 773 feet. Figures 17 to 19 display the results. In Figure 17 fracture frequency is plotted as a function of depth. Concentrations of fractures occur in the chaotic zones (the intervals 890 to 857 and 802 to 773 feet). It is not at all clear that these are fractures, but by treating them as such we can gain a more quantitative idea of the degree of "brecciation". Figure 18 shows a tadpole plot of fracture orientations as a function of depth. With the exception of the chaotic zones, the majority of the fractures are steeply dipping (more than 60 degrees), and most of the fractures in the massive interval 857 to 815 feet dip more than 80 degrees.

Plots of fracture orientations (Figure 19) reveal three clusters of fractures, striking NS, about N30°E, and S50°E. These all dip more than 60°, and in the case of the N30°E set are nearly vertical. Furthermore, these fractures are concentrated in the centers of the massive basalts. This, combined with the fact that the strike directions of these sets are approximately 120° apart, suggests that these are columnar joints formed by cooling of the thick basalt flows.

In this context, the origins of the other characteristic layers in the image can be inferred to be due to processes occurring during emplacement and cooling. The chaotic zones may correspond to the rubbly base of the flows, while the discrete sub-horizontal fractures are typical of fractures found below flow tops. The same characteristic patterns can also be found in NONAME-1.

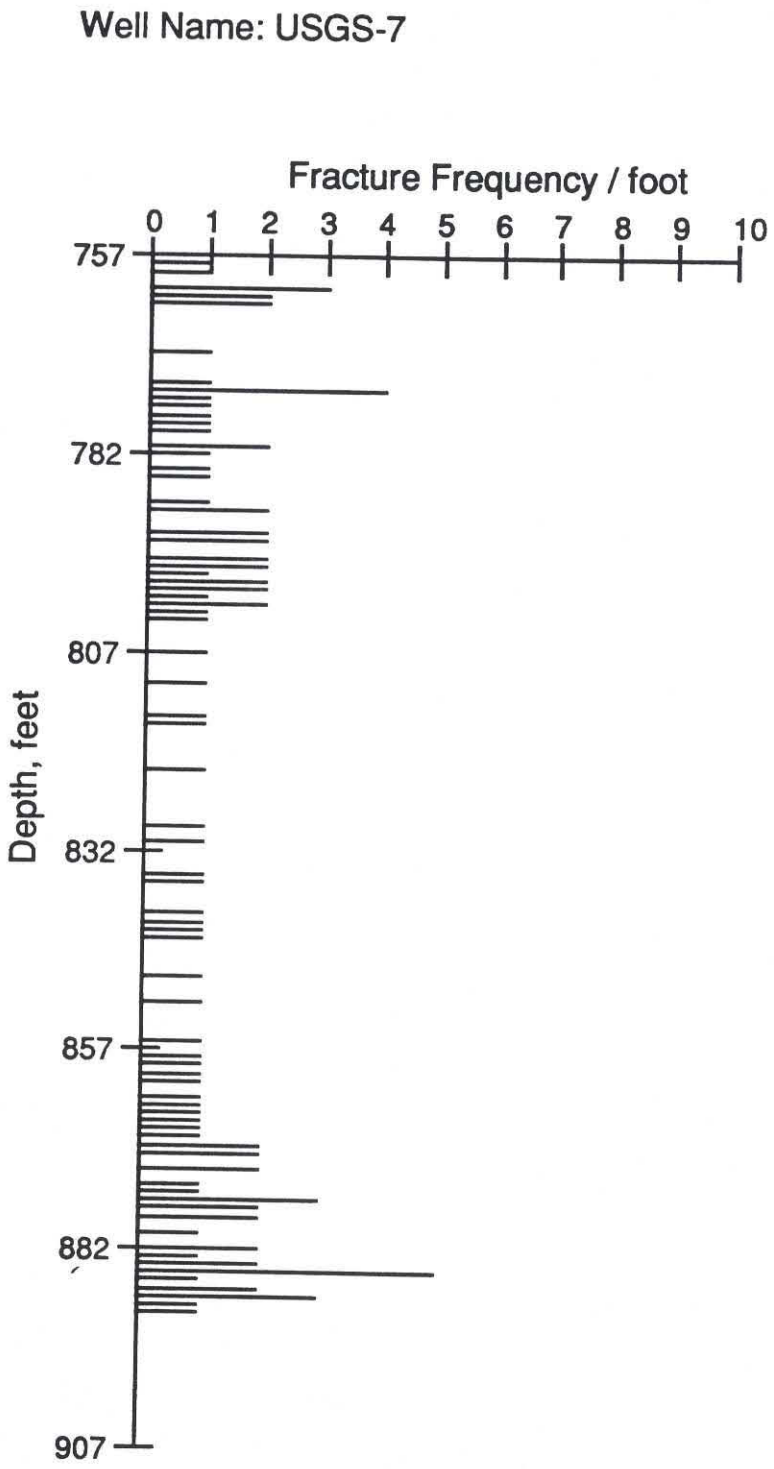

Figure 17: Fracture frequency plotted as a function of depth for well USGS-7.

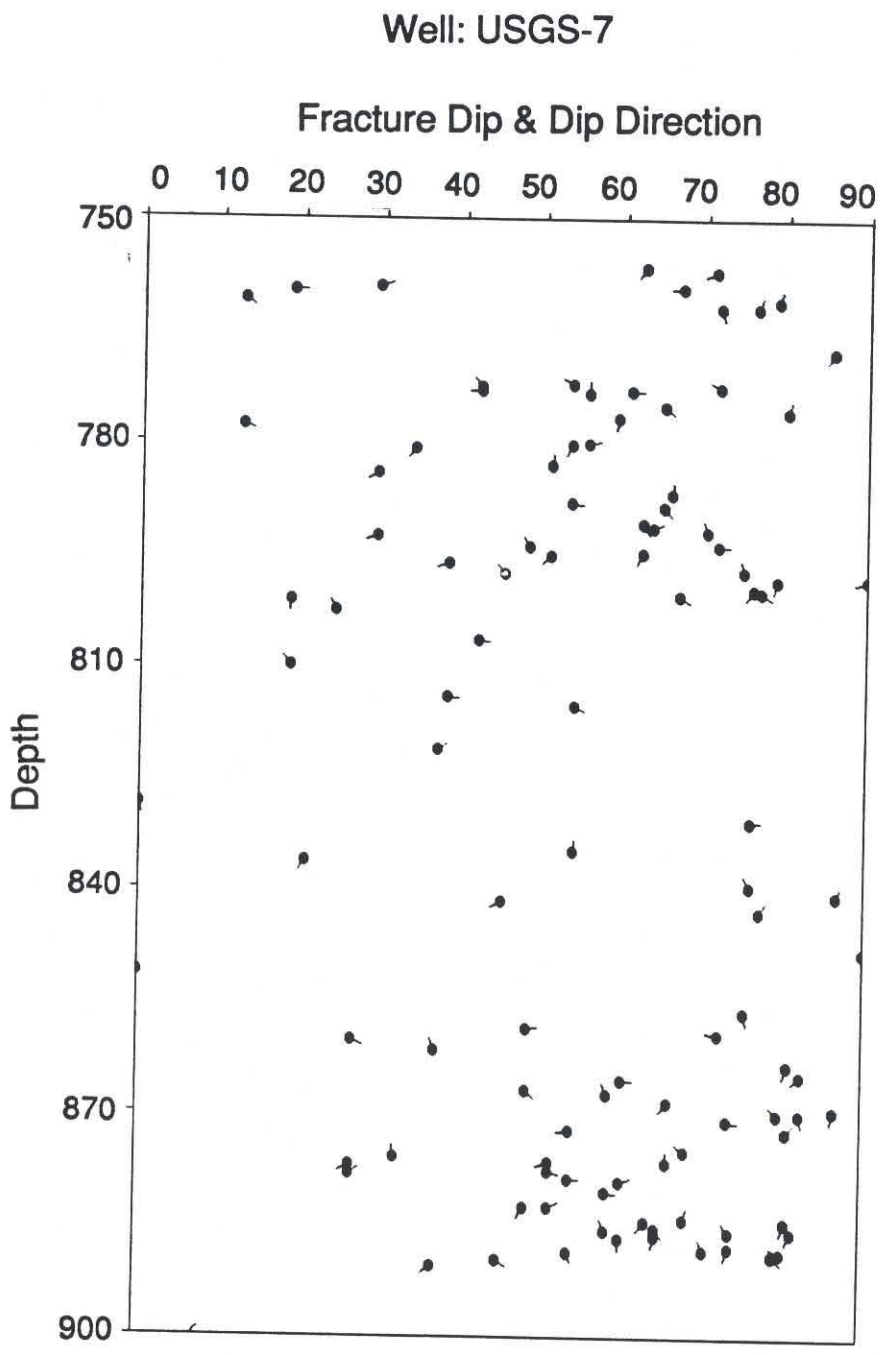

Figure 18: Tadpole plot of fracture orientation with depth for well USGS-7. Fracture dip is plotted along the x-axis, and the dip direction of each fracture is indicated by the compass angle of the tadpole tail. Tadpole plot of fracture orientations as a function of depth.

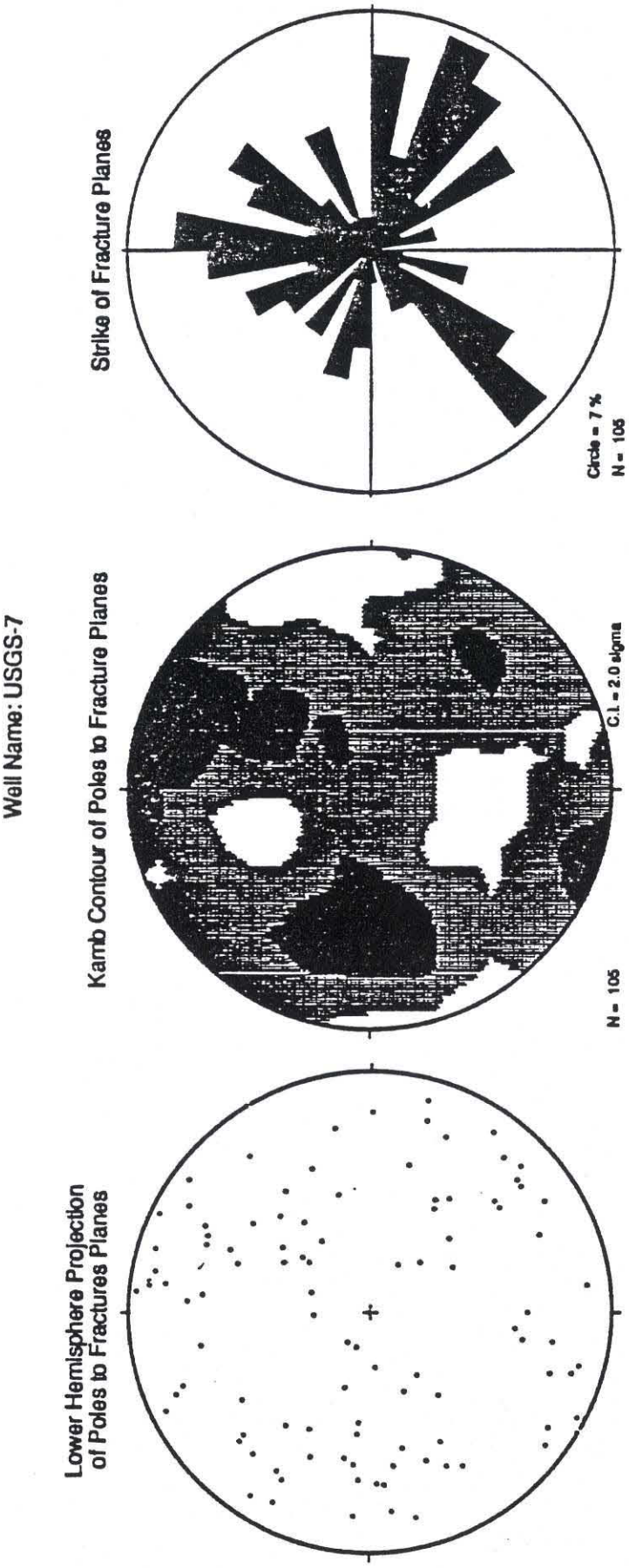

Figure 19: Lower hemisphere stereographic projections of poles to fracture planes, contoured poles to planes and strike of all fractures measured in well USGS-7.

NONAME-1

The NONAME-1 well was drilled using a 12" bit to a total depth of approximately 550 feet. The well geology interpreted from the driller's log is displayed in Figure 5. The interval is comprised primarily of basalts, with broken basalts, red cinders, and/or clay in the intervals 272-300', 380-385', 415-425', and 495-490' (depths approximate). Again, analyses of the BHTV data allowed these intervals to be related to structural features of the basalts.

The interval from 549' to 265' was logged in this well, again with the 1 3/4" (slim-hole) televiewer. The results in NONAME-1 are the best of those recorded in the basalts. Appendix III includes false-color images of the reflected amplitude and wellbore radius determined from the digitized data. In these images the intervals 549-543', 522-518', 494-492', 437-440', 424-428', 381-378', 317-325', and 287-291' contain subhorizontal fractures or enlarged sections of hole. Some of these correspond to the intervals of broken basalts, red cinders, or clay noted in the driller's logs. Some of these were not noted, however. Massive basalts with only a few near-vertical fractures are found in the intervals between these zones.

The positions and orientations of fractures picked interactively from the image data are presented in Figures 20 to 22. Figure 20, which shows fracture frequency plotted as a function of depth, reveals that fractures are not evenly distributed in this well, as inspection of the images suggests. The zones of densest fracturing have generally shallowly dipping fractures (less than 40°, Fig 21). However, some of these (for example, the interval 317-325') also contain fractures which dip more steeply (50 to 70 degrees).

In contrast to the results at USGS-7, the preponderance of fractures detected in NONAME-1 are sub-horizontal. These fractures contribute to a cluster with an approximate N50°W strike and dip between 10° and 30° NE (Figure 22). The rose diagram reveals two secondary maxima, one striking about 20°N of East and the other about 30°S of East. These have intermediate dips (between 40° and 70°).

However, as in the case of USGS-7, several vertical fractures were detected. These subtend chords in the well, rather than diameters (for example, at 490') and have a variety of strikes. Although most of these strike roughly E-W, two strike NS, and three strike approximately S30°E. Furthermore, as is the case at USGS-7, these fractures are found near the centers of otherwise massive intervals. Thus, although these do not reveal the strong pattern suggestive of columnar joints found in the data from USGS-7, we prefer this explanation of their origin in this well also.

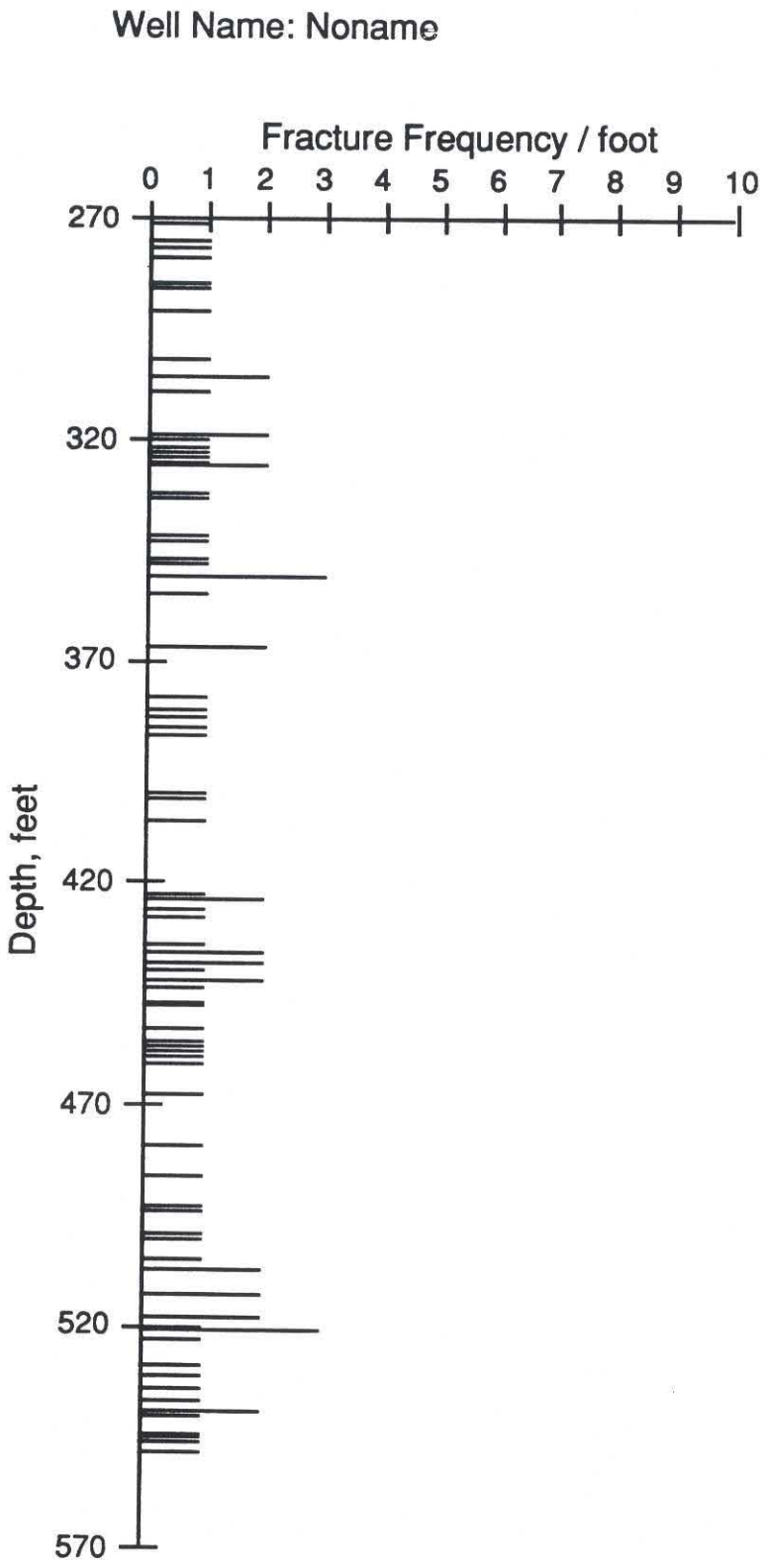

Figure 20: Fracture frequency plotted as a function of depth for well NONAME-1.

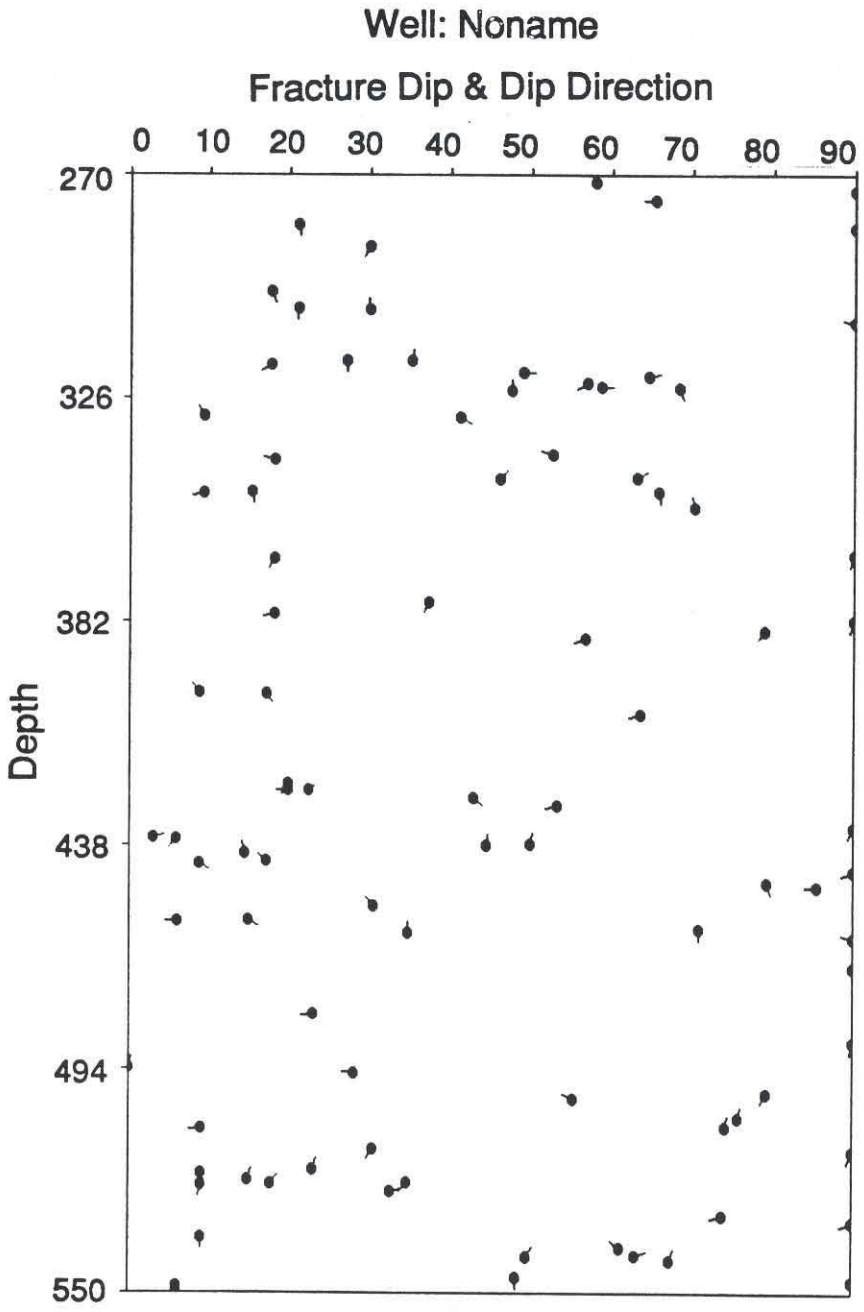

Figure 21: Tadpole plot of fracture orientation with depth for well NONAME-1. Fracture dip is plotted along the x-axis, and the dip direction of each fracture is indicated by the compass angle of the tadpole tail.Tadpole plot of fracture orientations as a function of depth.

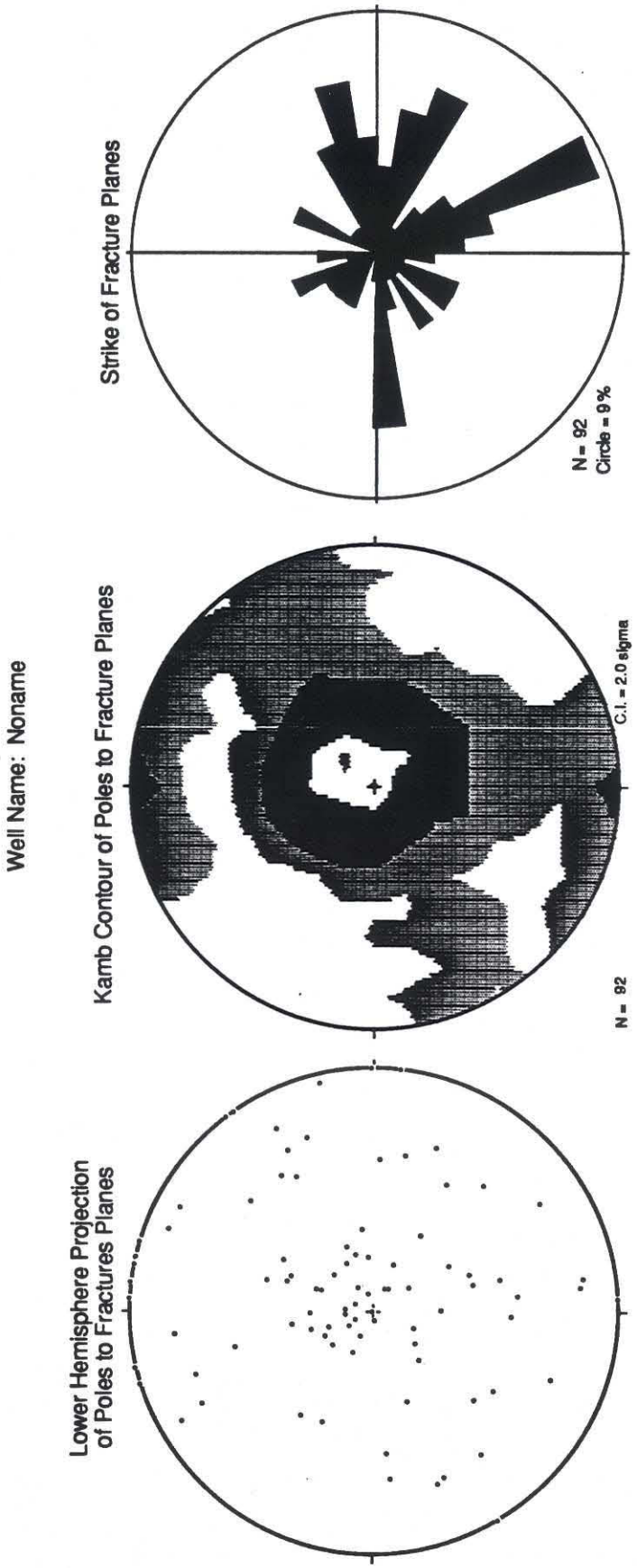

Figure 22: Lower hemisphere stereographic projections of poles to fracture planes, contoured poles to planes and strike of all fractures measured in well NONAME-1.

USGS-17

The USGS-17 well was drilled using an 18" bit to a total depth of 600 feet (Figure 6). No data is available for this well regarding the lithostratigraphy of the penetrated section. However, based on the results from the other wells, the interval penetrated presumably consists of interlayered basalt flows and more chaotic or brecciated intervals.

USGS-17 was logged with the 1 3/4" (slim-hole) televiewer over the interval between its present depth of 567 feet and the static water table at 390 feet. The data were digitized and are displayed as false-color images of wellbore radius and reflected amplitude in Appendix III. Because of the large diameter of the wellbore, the televiewer sonde could not be adequately centered in the hole. This resulted in incomplete azimuthal coverage of the hole, as can be seen in the false-color images (see Georgi, 1985 for a description of the effects of eccentering on BHTV images). Consequently, fractures are more difficult to detect in these data than in data from the other three wells. However, the orientations of those fractures that could be detected were picked interactively (as described above for INEL-1) and the results are presented in Figures 23 through 25.

Figure 23 presents a plot of detected fracture frequency versus depth in USGS-17. In general, fractures are detectable only intermittently across the 275' depth interval logged. Most of the fractures dip steeply to the South, (more than 80°) and strike essentially E-W, as can be seen in the tadpole plot (Figure 24) and the stereonets and rose diagrams (Figure 25). This apparent strong preferred orientation may result from the fact that the fractures are most easily imaged in their up- and down-dip directions, and that the data returned from this well is primarily in a band of azimuths centered roughly on North and South. Thus any steeply dipping fractures with dip azimuths more than 20 degrees from a N-S line are less likely to be detected. A small subsidiary maximum strikes approximately S50°E and dips about 40°SW.

The remaining few fractures are sub-horizontal. Most of these occur within the interval 470 to 480 feet, although single shallow-dipping features are also detected at about 400' and near the total depth of 565' (Figure 24); the bottom of the logged interval is characterized by a broad subhorizontal band of missing data (Appendix III). If these sub-horizontal features are interpreted as fracturing near flow tops (in the case of the feature detected at 400') and/or as inter-flow materials (in the case of the intervals 470-480 and 565-567'), as analysis of the much better data from USGS-7 and NONAME-1 implies, then it suggests that the interval 565 to 480 feet may be a complete section of a single basalt flow, and the top of the logged interval may be near the top of the overlying flow. The fact that the logging sonde could not penetrate to total depth in the well may be a consequence of hole collapse within the weaker materials at the base of the lower flow.

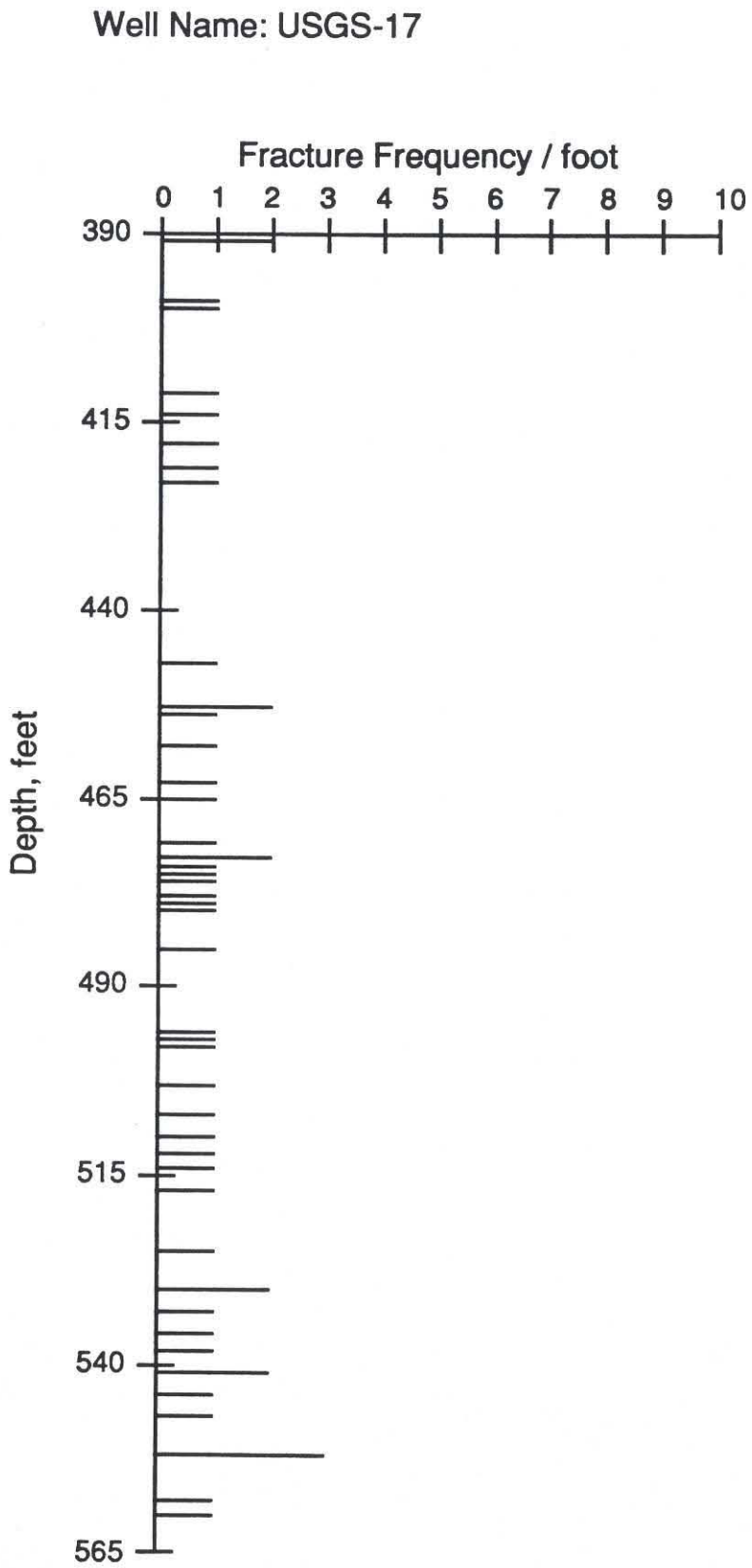

Figure 23: Fracture frequency plotted as a function of depth for well USGS-17.

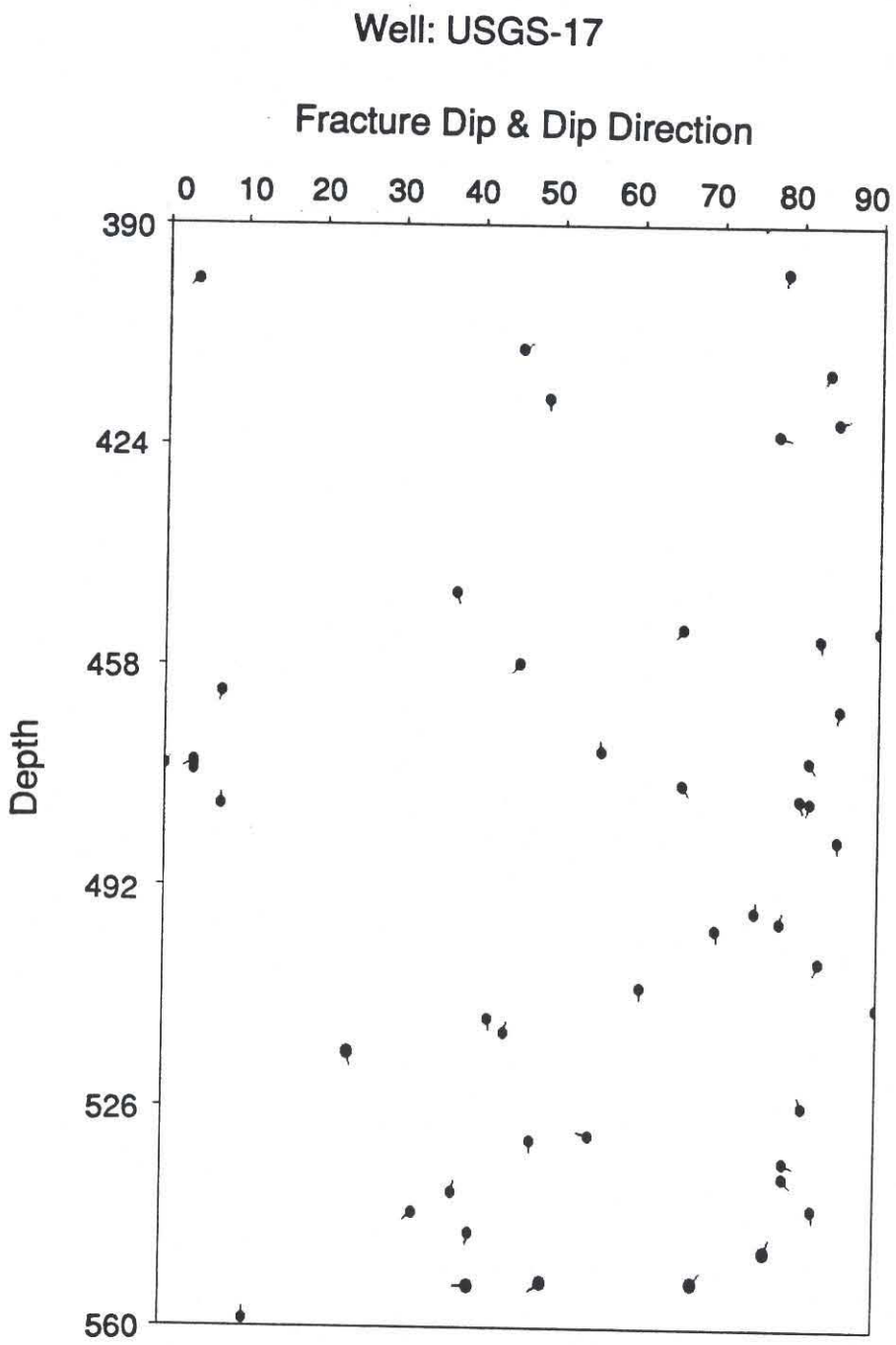

Figure 24: Tadpole plot of fracture orientation with depth for well USGS-17. Fracture dip is plotted along the x-axis, and the dip direction of each fracture is indicated by the compass angle of the tadpole tail.Tadpole plot of fracture orientations as a function of depth.

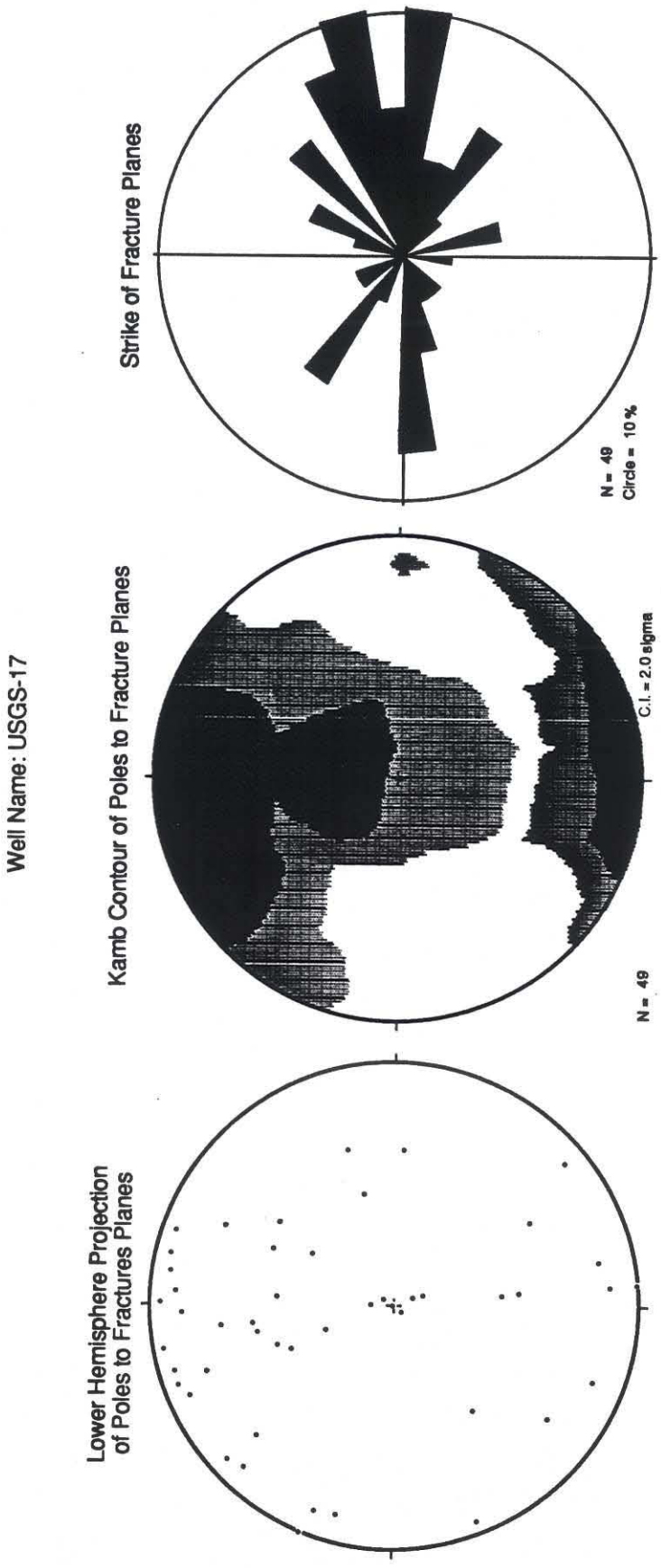

Figure 25: Lower hemisphere stereographic projections of poles to fracture planes, contoured poles to planes and strike of all fractures measured in well USGS-17.

The approximately 85' thickness of the intervals between sub-horizontal features may correspond to a characteristic thickness for the flow units. The steeper fractures detected at intervals throughout the well would then be, as in the other wells, columnar joints within the massive flow interiors.

Summary of results for the basalts

No wellbore breakouts were detected in wells USGS-17, USGS-7, and NONAME-1. This can be ascribed to the shallow depths of these wells, and the fact that they were drilled through basalts, which are quite strong and thus unlikely to fail in compression at the shallow depths studied.

The logs in the three holes drilled into basalts reveal a characteristic pattern of fracturing, related to emplacement and cooling of the basalts. This pattern was also noted by Paillet and Kim (1987) for televiewer data recorded in basalts on the Columbia River Plateau. At the base of each flow is a narrow zone of rubbly material, which grades into a massive interior cut by near-vertical fractures, possibly columnar joints. Near the top is a narrow zone a few meters thick of shallow dipping fractures. Based on this pattern in two of the wells the average flow thickness is slightly less than 100 m. Although this overall pattern is apparent in each of the wells studied, differences between the wells will need to be studied in more detail before possible inter-well interpretations can be made.

Recommendations for Related Studies

The results borehole televiewer logging in INEL-1, USGS-7, USGS-17, and NONAME-1 provide a detailed look at the lithostratigraphy and fracturing within the basalts and underlying silicic volcanics beneath the Eastern Snake River Plane. However, the primary purpose of obtaining BHTV data, to determine the orientations and constrain the magnitudes of the crustal stresses, requires the collection of some additional data and more complete analysis of the data already in hand.

Systematic comparison of these results to geophysical well logs (particularly temperature, resistivity, sonic waveform, and natural gamma) could reveal additional valuable information about the fractures, filling, permeability, and lithostratigraphy of the silicic volcanics. Furthermore, such analysis is required to determine the appropriate equations to use to describe the wellbore stress concentration and related failure.

Strength measurements on cores from the INEL-1 well are necessary to apply the techniques of Moos and Zoback (1990) to the determination of stress magnitudes from the

lack of breakouts. Although the absence of breakouts in INEL-1 to 3.1 km requires that both horizontal stresses be less than the vertical stress, it does not distinguish between an incipient normal faulting environment (ie $S_h << S_v$) and a more nearly hydrostatic one (ie $S_h \approx S_v$). It is therefore necessary to obtain a more detailed knowledge of the range of uniaxial compressive strengths appropriate for the rocks penetrated by the INEL-1 well, coupled with careful analysis of the logs to infer the Biot α.

Finally, to determine quantitatively the magnitudes of the horizontal stresses, there is no substitute for hydraulic fracturing stress measurements. The BHTV data acquired as part of the work described herein can be used to select unfractured intervals for testing. In this (normal-faulting) environment it should be relatively easy to hydrofrac the rock to total depth. Furthermore, standard analyses (e.g. Hickman and Zoback, 1983) should suffice to provide determinations of S_{hmin}, as this stress is the least principal stress. The temperature at total depth in INEL-1 of $\approx 150^{o}C$ should not be a factor, as hydraulic fracturing stress measurements have been made at similar temperatures elsewhere (for example, in the Cajon Pass Scientific Drillhole, Healy and Zoback, 1988).

References Cited

Allison, M.L. and D.L. Nielson, Stress in active geothermal systems, in *Advances in Geothermal Reservoir Technology,* Lawrence Berkeley Lab - ESL-88027-JP, 1988.

Anders, M.H., J.W. Geissman, L.A. Piety, and J.T. Sullivan, Parabolic distribution of circumeastern Snake River Plain seismicity and latest Quaternary faulting: Migratory pattern and association with the Yellowstone hotspot, *J. Geophys. Res., 94*, 1589-1621, 1989.

Barton, C.A., *Development of in-situ stress measurement techniques for deep drillholes*, PhD. Thesis, Stanford University, 192 pp, 1988.

Bell, J. S. and D.I. Gough, Northeast-southwest compressive stress in Alberta: Evidence from oil wells, *Earth Planet. Sci. Lett.*, 45, 475-482, 1979.

Furlong, K.P., An analytic stress model applied to the Snake River Plain (Northern Basin and Range Province, USA), *Tectonophysics, 58*, T11-15, 1979.

Georgi, D.T., Geometrical aspects of borehole televiewer images, *Trans. 26th Ann. SPWLA Logging Symposium*, 1-C, 1985.

Healy, J.H. and M.D. Zoback, Hydraulic fracturing in situ stress measurements to 2.1 km depth at Cajon Pass, California, *Geophys. Res. Lett., 15(9)*, 1005-1008, 1988.

Hickman, S.H., and M.D. Zoback, The interpretation of hydraulic fracturing pressure-time data for in situ stress determination, in *Proceedings of the Workshop on Hydraulic Fracturing Stress Measurements*, U.S. National Committee on Rock Mechanics, Washington, D.C., 11 pp., 1983.

Hubbert, M.K., and D.G. Willis, Mechanics of hydraulic fracturing, *J. Petrol. Tech., 9*, 153-168, 1957.

Kirsch, G., Die Theorie der Elastizitat und die Bedurfnisse der Festigkeitslehre, VDI Z, 42, 707, 1898.

Moos, D., and M.D. Zoback; In situ studies of velocity in fractured crystalline rocks; *J. Geophys. Res., 88*; p. 2345-2358, 1983.

Moos, D., M.D. Zoback, F. Paillet, and C. Barton, Stress orientation and magnitude from wellbore breakouts in the Moodus Research Borehole -- comparison with regional data, (abs), *EOS, Trans. AGU (69)*, p. 492, 1988.

Moos, D., and M.D. Zoback, Utilization of observations of wellbore failure to constrain the orientation and magnitude of crustal stresses: Application to continental, DSDP and ODP borehole, *J. Geophys. Res., 95*, 9305-9325, 1990.

Morgan, J.W., Deep mantle convection plume and plate motions, *Am. Assoc. Pet. Geol. Bull., 56*, 203-312, 1972.

Morin, R.H., R.L. Newmark, C.A. Barton, and R.N. Anderson, State of lithospheric stress and borehole stability at DSDP Site 504B, eastern equatorial Pacific, *J. Geophys, Res., 95*, 9293-9303, 1990.

Paillet, F.L., Problems in fractured-reservoir evaluation and possible routes to their solution, *The Log Analyst, 26*, 6, 26-41, 1985.

Paillet, F.L., and K. Kim, Character and distribution of borehole breakouts and their relationship to in situ stresses in deep Columbia River basalts, *J. Geophys. Res., 92*, 6223-6234, 1987.

Paillet, F. L., Fracture characterization and fracture-permeability estimation at the underground research laboratory on southwestern Manitoba, Canada, U.S.G.S., *Water Resources Investigations Report, 88-4009*, 1988.

Pezard, P.A., R.N. Anderson, J.J. Howard, and S.M. Luthi, Electrical properties of mid ocean ridge basalt and implications for the structure of the upper oceanic crust in Hole 504B, *J. Geophys. Res., 95, B6*, 9237 - 9264, 1990.

Pezard, P.A., Fracture distribution and basement structure from measurements of electrical resistivity in the basement of the Cajon Pass scientific drillhole, California, *Geophys. Res. Lett., 15*, 9, 1021 - 1024, 1988.

Plumb, R.A., and S.A. Hickman, Stress-induced wellbore elongation: A comparison between the four-arm dipmeter and the borehole televiewer in the Auburn Geothermal Well, *J. Geophys. Res., 90*, 5513-5521, 1985.

Plumb, R. A. and J.W. Cox, Stress directions in eastern North America determined to 4.5 km from borehole elongation measurements, *J. Geophys. Res., 92*, 4805-4816, 1987.

Prestwich, S.M., and Bowman, J.A., et al., Completion and testing report: INEL geothermal exploratory well one (INEL-1), U.S. Dep't. of Energy, Report #IDO-10096, 1980.

Sparlin, M.A., L.W. Braile, and R.B. Smith, Crustal structure of the eastern Snake River Plain from ray tracve modeling of seismic refraction data, *J. Geophys. Res., 87*, 2619-2633, 1982.

Stock, J.M., J.H. Healy, S.H. Hickman, and M.D. Zoback, Hydraulic fracturing stress measurements at Yucca Mountain, Nevada, and the relationship to the regional stress field, *J. Geophys. Res., 90*, 8691-8706, 1985.

Thompson, G.A., Parsons, T., and Smith, R.B., Examples of magma overpressure suppressing normal faulting and inhibiting seismicity: Snake River Plain, Idaho,

Yucca Mountain, Nevada, and Mono Craters, California, (abs) *EOS, Trans. AGU*, in press.

Vernik, L. and M.D. Zoback, Estimation of maximum horizontal principal stress magnitude from stress-induced wellbore breakouts in the Cajon Pass Scientific Research Borehole, submitted to *J. Geophys. Res.*

Zemanek, J., E.E. Glenn, Jr., J.J. Norton, and R.L. Caldwell, Formation evaluation by inspection with the borehole televiewer, *Geophys. 35*, 254-269, 1970.

Zoback, M.D., D. Moos, L. Mastin and R.N. Anderson, Wellbore breakouts and in situ stress, *J. Geophys. Res.*, 90, 5523-5530, 1985.

Zoback, M. L., M.D. Zoback, J. Adams, M. Assumpção, S. Bell, E.A. Bergman, P. Blümling, N.R. Brereton, D. Denham, J. Ding, K. Fuchs, N. Gay, S. Gregersen, H.K. Gupta, A. Gvishiani, K. Jacob, R. Klein, P. Knoll, M. Magee, J.L. Mercier, B.C. Müller, C. Paquin, J. Rajendran, O. Stephansson, G. Suarez, M. Suter, A. Udias, Z.H. Xu, and M. Zhizhin, Global patterns of intraplate stress: A status report on the world stress map project of the International Lithosphere Program, *Nature*, 341, 291-298, 1989.

Appendix I - Field Chronology

Operations at the INEL were carried out in two separate phases. The first phase occupied the period between May 14 and May 21. During that time span holes USGS-17, USGS-7 and NONAME-1 were logged with the 1 3/4" televiewer tool, and the lowermost portion of INEL-1 (from 10243 to 9250 feet) was logged with the 3 3/8" geothermal tool. Operations terminated after repeated attempts to log INEL-1 with both the 1 3/4" tool and the 3 3/8" geothermal tool failed to recover a complete log of the hole. The second phase of operations commenced June 3 with the arrival on-site of an engineer from M&W Instruments (the manufacturer of the televiewers) to effect repairs on the 3 3/8" geothermal tool, and ended June 8 with the successful recovery of a complete log of INEL-1.

Tables A-1-I and A-1-II are chronologies of field operations at the INEL site for phases one and two, respectively. Table A-1-III summarizes the data collected in each of the holes during the course of operations. All of this data was digitized for analysis. As described elsewhere in this report, the final log from INEL-1 was a composite of the phase one and two logs. Otherwise, each data set was recorded in a single pass. Furthermore, with the exception of the data from NONAME-1 and INEL-1, both pre- and post-logging calibrations were obtained.

Appendix II presents the color renderings of the calibrations used to correct the data for magnetic declination and for the offset between apparent magnetic North determined by the tool and its true azimuth. Appendix III presents the final color figures showing borehole radius and reflected amplitude as a function of depth and azimuth in USGS-17, USGS-7, NONAME-1 and INEL-1. These displays have been corrected for declination and for the offset between apparent magnetic North determined by the tool and its true azimuth. The field data sheets and the post-logging digitization data sheets are included in Appendix VI.

TABLE A-1-I: INEL Phase I operations – May 14 to May 21

May 14 - truck and personnel arrive Idaho Falls (1900 hrs)
May 15 - arrive INEL plant, obtain badges, BHTV log of USGS-17
logging truck and boom truck on site at USGS 17 1040 hrs
Rig up
Attempt operation with geothermal BHTV 1200 - 1500 hrs
Record pre-log calibration
Log USGS 17 with small BHTV 1500 - 1750 hrs
Record post-log calibration
May 16 - BHTV logs of USGS-7 and NONAME-1
move to USGS 7 site and rig up 0930 - 1230 hrs
Record pre-log calibration
log USGS 7 with 1 3/4" BHTV 1230 - 1430 hrs
(while on site at USGS 7 review quality assurance)
Record post-log calibration
rig down; move to Noname 1; rig up 1430 - 1645 hrs
Record pre-log calibration
log Noname 1 with 1 3/4" BHTV 1645 - 1800 hrs
Post-log calibration failed
move equipment to INEL 1 1800 - 1900 hrs
May 17 - set up on INEL 1 - attempt log with 1 3/4" BHTV
run pig into well - hung up at top of liner 1015 - 1100 hrs
rehead cable 1130 - 1600 hrs
RIH with small BHTV: Compass failed while running in hole;
we ran to TD to test operations at high temperature
and successfully logged 300 feet at 10'/minute,
but without compass orientations . 1735 - 2200 hrs
Problems with the tool were traced to a flooded cable head.
May 18 - repair and testing of equipment 0900 - 1715 hrs
rehead cable
inspect and repair minor connector damage in the 3 3/8" geothermal tool
confirm tool operations.
May 19 - Log lower portion of INEL-1 with 3 3/8" geothermal tool
RIH with geothermal tool - tool sticking just below casing 1230 hrs
POOH
move upper centralizers to relaxed position 1640 hrs
RIH to TD. @ TD 1910 hrs
Log 10,234 to 9,250' - At 9400' we encountered problems with the tool
Tried adding a DC power supply without success
left tool in casing at 6000' 0100 hrs, May 20
May 20 - Attempt to continue logging INEL-1
added DC power supply borrowed from the EG&G shop
RIH to 9300' - tool failed in same mode 1245 hrs ->
POOH w/ geothermal tool 1315 hrs
RIH with small BHTV 1450 ->
tool failed in compass mode just below liner (as before)
Pulled small tool out of the hole 1640 hrs
May 21 - Shut down operations: return crane, move truck to staging area, fly home

TABLE A-1-II: INEL Phase II Operations – June 3 to June 8

June 3 - Stanford crew arrives Idaho Falls 1800 hrs
June 4 - refuel truck, technician arrives from M&W Instruments
work on 3 3/8" geothermal tool at EG&G office 0730 - 1800 hrs
June 5 - complete tool repair
return to INEL site and prepare for logging 0730 - 2130 hrs
June 6 - successful pre-log calibration.
record log of INEL-1 0630 ->
June 7 - log continues - attempted post-log calibration failed 0500 hrs
rigged down
returned to EG&G to work on tool again 1100 - 1800 hrs
June 8 - return to Stanford

TABLE A-1-III: Data recovered in each well:

Well Name	Date	Depth Interval, ft	Logging Tool	Comments
USGS-17	May 15	567-390	1 3/4"	pre- and post-log cal
USGS-7	May 16	895-850	1 3/4"	pre-log cal &
USGS-7	May 16	895-750	1 3/4"	post-log cal (higher gain settings - tool never left the hole)
NONAME-1	May 16	550-265	1 3/4"	pre-log cal only
INEL-1	May 17	10133-9800	1 3/4"	no orientations
INEL-1	May 19	10243-9250	3 1/8"	pre-log cal only tool failed at 9250' - log orientations identical to USGS log
INEL-1	May 20	none	1 3/4"	compass orientation failed, ending attempt
INEL-1	June 6-7	10243-6780	3 1/8"	pre-log cal only complete log - but orientations invalid below 9946'

Appendix II - Tool Calibration

As part of standard field procedures with the borehole televiewer, a calibration of the compass orientation and of the conversion of travel-time to radius is made both prior to and after completion of a logging operation. In the case of operations at INEL, pre- and post-log calibrations were obtained at USGS-7 and USGS-17. A pre-log calibration only was obtained at NONAME-1. A pre-log calibration only was obtained for both Phase I and Phase II logging runs in INEL-1. The lack of a post-log calibration for INEL-1 and NONAME-1 is not deemed to be critical, as in each instance in which pre- and post-log calibrations were obtained, the calibrations agree to within a few degrees and a fraction of an inch radius.

The details and figures illustrating the results of these calibrations are discussed in this section.

In the case of USGS-7, USGS-17, and NONAME-1, the logs we obtained are the only data available with which the orientations of features within the boreholes can be determined. Thus there is no independent data to compare to our results. Consequently, the tool calibrations are necessary to validate the orientations we obtained. In the case of the INEL-1 well, a previous borehole televiewer log was recorded by the U.S. Geological Survey. Thus we can compare our orientations to those obtained independently by the USGS. As it turns out, this exercise is critical in selecting the data to analyze in the INEL-1 well, as described in more detail below.

Field Calibrations

This section describes the compass and radius calibrations we obtained in the field for each of the logging runs at the Idaho National Engineering Laboratory. These calibrations are designed to verify tool operation and are run as standard operating procedures both before and after logging in each hole. In general, orientations and radius corrections do not change over the course of a field survey. Copies of the checklists completed in the field for each logging run are provided in Appendix VI, Quality Assurance Documentation.

Instrument calibrations are obtained by placing the televiewer tool in an aluminum tank with 1/2"-thick walls, of interior diameter 6.5". Four aluminum bars are placed at 90° intervals around the tank, and an interior sleeve of 1/2"-thick aluminum is placed in one half of the tank. The entire tank is placed as far away as possible from sources of magnetic fields, and oriented wrt magnetic North. The tank is typically buried to prevent its tipping over, and the tool is placed into a hole in its center. The top of the tool is also centered, by means of an aluminum ring. A schematic drawing of the orientation device is shown below.

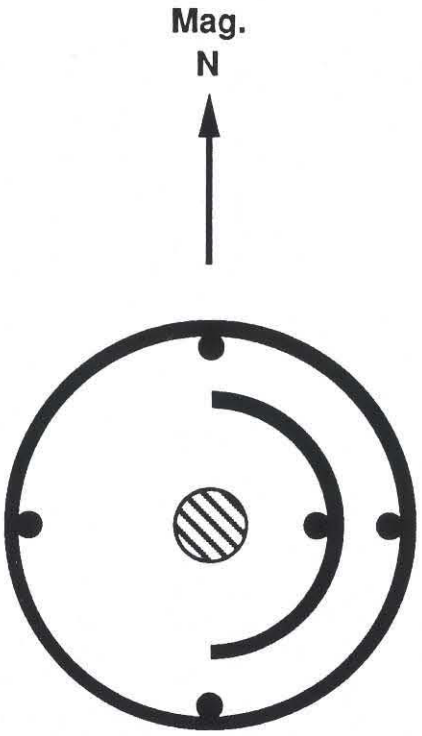

Fig A-II-1: Schematic drawing of the calibration tank used to verify the operation of the magnetic orientation device of the borehole televiewer.

Once the tool is in the orientation tank power is applied and the tool is allowed to warm up for a short time. The pre-log orientation calibration is obtained by recording the signal for approximately one minute. The procedure for calibrating the 1 3/4" tool is as follows: First the tool is placed in magnetic orientation mode, and a short section of data is recorded on videotape and on film. To assist in rapid interpretation of the photographic image the signal is first gated to display only reflections from the insert (early times) and then to display both the reflections from the outer and inner section, and finally to display only sections from the outer wall. The tool is then switched to "mark" mode and then back to "compass" mode, to verify that both modes are working. This procedure had to be modified for the large tool due to its use of focussed transducers, which do not produce a clear image for radii smaller than the focussing point, by inserting into the tank an absorbing rod at a known orientation.

After completion of the pre-log calibration, the tool is removed from the tank and run into the hole, with power applied to the tool the entire time. While running into the hole gain settings are adjusted to obtain an optimal image, and thus a post-calibration log is required. This log also allows us to assess possible drift due to changes in temperature of the tool electronics. The post-log calibration procedure is identical to the pre-log procedure. To assure the best assessment of the tool operation, power is applied to the tool from the start of the pre-log calibration to the end of the post-log calibration.

USGS-17

A successful log was obtained in USGS-17 using the 1 3/4" (slimhole) borehole televiewer. Pre and post log calibrations were obtained and are presented along with the field data sheets in Appendix VI. As can be seen from the images, the orientation correction did not change during the course of the log, and the azimuth correction determined from the post-log calibration was applied to the data prior to display and analysis. Figure A-II-2) shows a color rendering of the corrected (azimuthally and for radius conversion) calibration image. On this figure and in the final data a further correction for the magnetic declination at the site was also made.

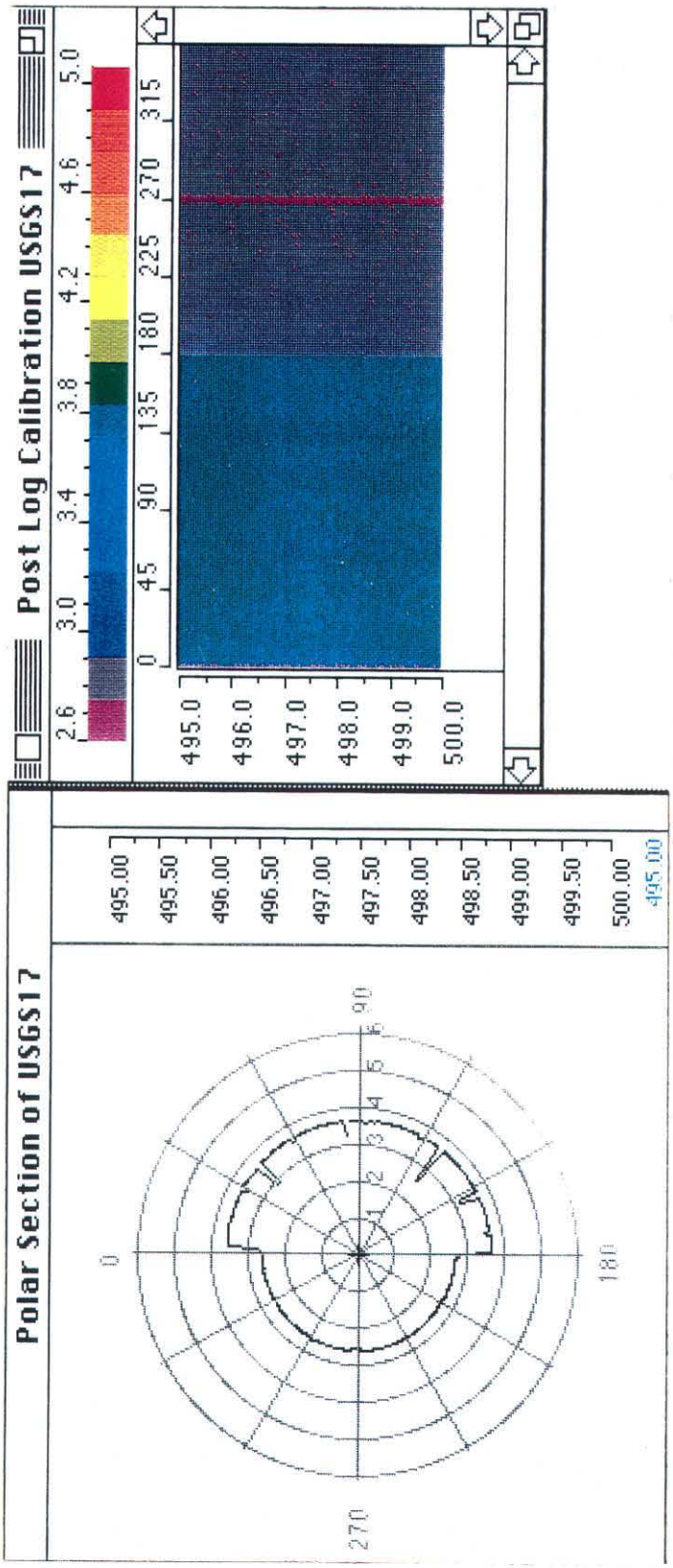

Figure: A-II-2: Polar projection (left window) and unwrapped view of the post log calibration recorded for well USGS-17.

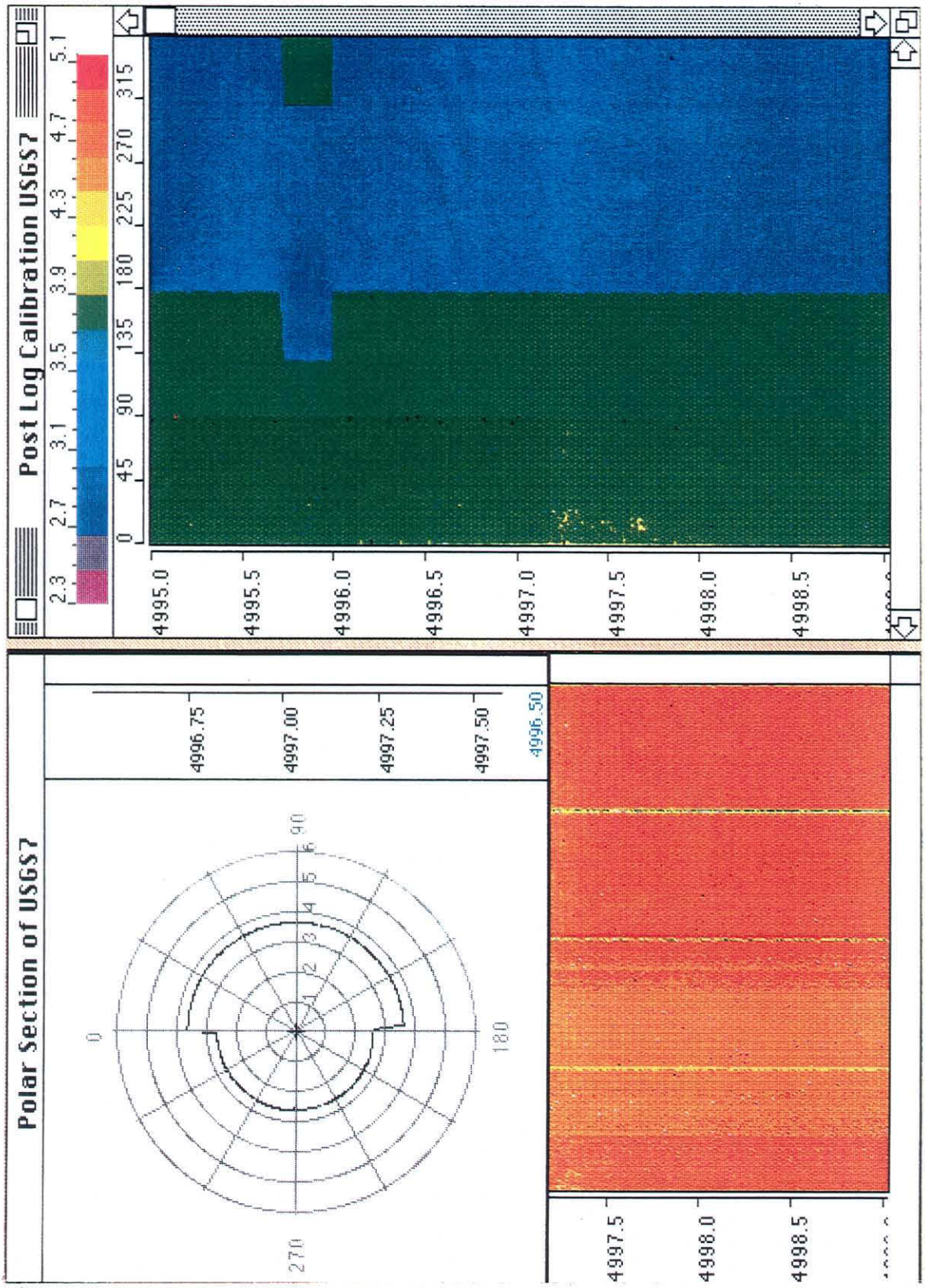

Figure A-II-3: Polar projection (left window) and unwrapped view of the post log calibration recorded for well USGS-7.

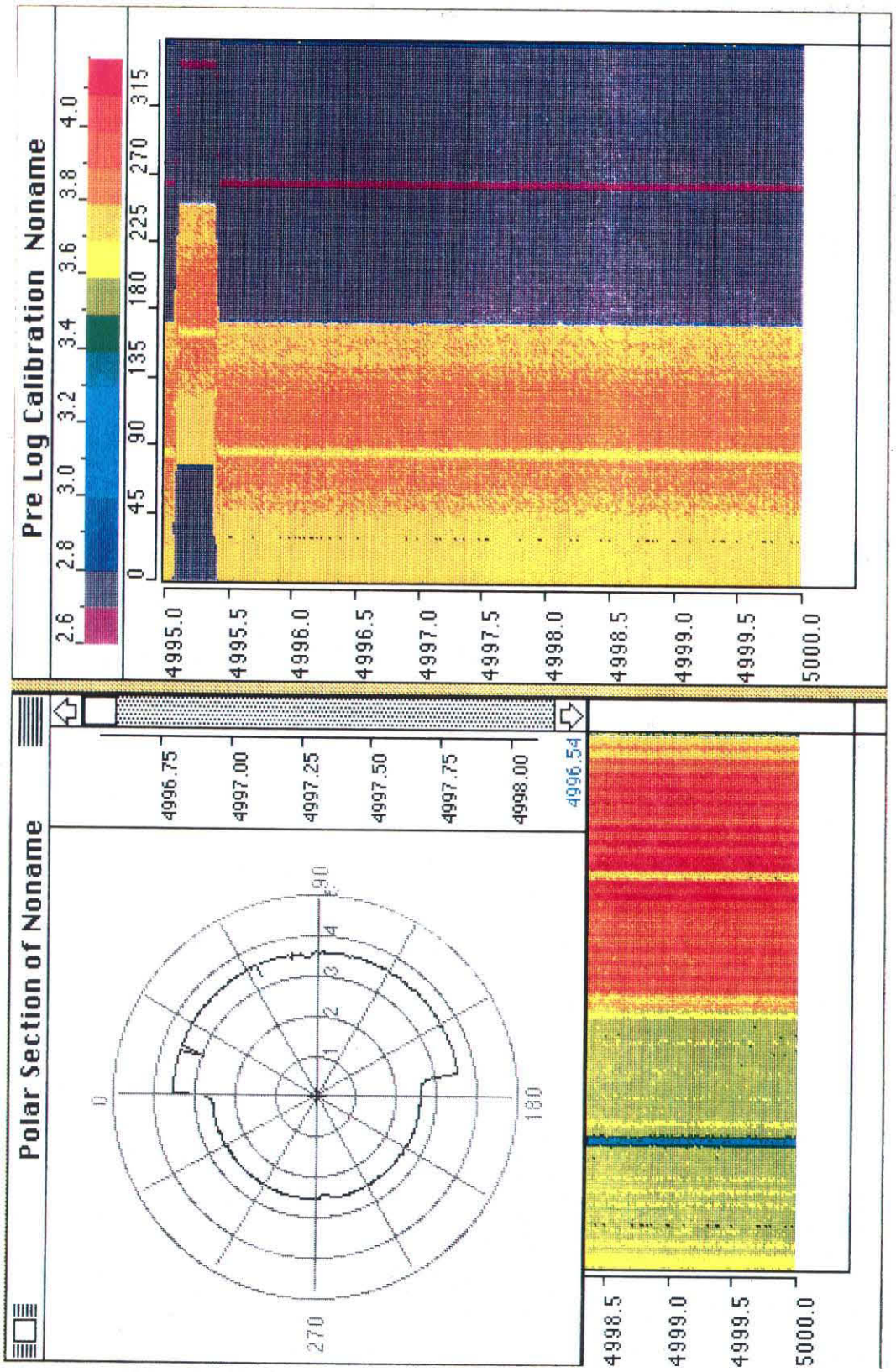

Figure A-II-4: Polar projection (left window) and unwrapped view of the post log calibration recorded for well NONAME-1.

USGS-7

A successful log was obtained in USGS-7 using the 1 3/4" (slimhole) borehole televiewer. Pre and post log calibrations were obtained and are presented along with the field data sheets in Appendix VI. As can be seen from the images, the orientation correction did not change during the course of the log, and the azimuth correction determined from the post-log calibration was applied to the data prior to display and analysis. Figure A-II-3 shows a color rendering of the corrected (azimuthally and for radius conversion) calibration image. On this figure and on the final data a further correction for the magnetic declination at the site was also made.

NONAME-1

A successful log was obtained in NONAME-1 using the 1 3/4" (slimhole) borehole televiewer. No post log calibration was obtained in this well, however, due to the failure of the compass after completion of the log. The symptom of that failure was the complete loss of an orienting signal, rather than its progressive deterioration. Thus we are confident that the log was obtained with the correct compass orientation. Furthermore, the lack of drift for the pre- and post- log calibrations at the previous two wells suggests that no drift is associated with the azimuth data obtained here. The pre-log calibration is presented along with the field data sheets in Appendix VI. The azimuth correction determined from this pre-log calibration was applied to the data prior to display and analysis. Figure A-II-4 shows a color rendering of the corrected (azimuthally and for radius conversion) calibration image. On this figure and on the final data a further correction for the magnetic declination at the site was also made.

Orientation Verification - INEL-1

The 3 3/8" geothermal tool was used to obtain the borehole televiewer data at INEL-1. Calibrations for this tool were difficult to obtain, and in fact no post-log calibrations were obtained for either the Phase I or Phase II logs of the hole. Fortunately, a previously recorded log (by the U.S. Geological Survey) provided images of the hole which overlapped a substantial portion of the open-hole interval. Checks of the orientations of these images vs. the new logs provided an additional test of the orientation data, as described below.

Pass I: 10243 - 9250 feet.

The pre-log calibration of the near-focus transducer (the one used to record the data) is presented in Appendix VI along with the field data sheets. In this calibration an absorbing rod was attached to the tool at magnetic East, and the window was gated on the far reflection from the East side of the tank. The insert was placed on the West side of the tank for this test. The edge of the inner sleeve was located by the tool at $\approx 180^{o}$, and the rod was located $\approx 90^{o}$, indicating that no orientation correction was necessary for this tool, except to correct for the magnetic declination at the site. Attempts to digitize the calibration for analysis interactively were unsuccessful. Thus the radius calibration was made within the 9 7/8" o.d. liner, which is presumed based on a wall thickness of 1/4" to have an i.d. of 9 3/8". The velocity of sound in the fluid was assumed to be 1494 m/s..

Pass II: 10243 - 6780 feet.

Pre-log calibration of the orientation was made for the phase two log in INEL-1 in the aluminum tank with a phenolic rod placed at magnetic West. The gain was varied as described in the figure (Appendix VI). Magnetic West was determined to be aligned correctly for the tool, and thus no static correction was applied to the data, except to correct for magnetic declination at the site. Attempts to digitize the calibration for analysis interactively were unsuccessful. Thus the radius calibration was made within the 9 7/8" o.d. liner, which is presumed based on a wall thickness of 1/4" to have an i.d. of 9 3/8". The velocity of sound in the fluid was assumed to be 1494 m/s.

Comparison of Phase I, Phase II, and USGS logs of INEL-1:

Because of the lack of post-log calibrations for the data recorded at INEL-1, we compared the orientations of data recorded in the well during three different logging runs (the earlier USGS log, and our Phase I and Phase II logs). If all three logs agreed then we

could assume that the pre-log calibration suggesting that there was no error in compass orientation was reliable. If only two of the three logs agreed then we could assume that the third log was in error, and attempt to trace the source of that error. The results of this comparison indicated that three orientations agree to within measurement error within the interval 9946 to 9250 feet, but the Phase II log orientations differed from the other two logs in the interval below 9946 feet. Accompanying this difference are abrupt changes in orientation over short intervals in the Phase II log, that were revealed in the travel-time images from that data set. We studied the voice-over comments recorded during the Phase II log and traced a problem in that log to a level of DC power delivered to the tool that may have been too low to operate the magnetic orienting device. The DC level was increased at a depth of 9946 feet, the point above which the logs agreed.

In the course of this analysis we discovered that our depth reference at ground level resulted in a systematic 20' discrepancy between the depths in the USGS log and those in our two surveys. The USGS depths were uniformly deeper than those we recorded for the identical intervals. This is most likely due to the reference depth of the USGS log at a rig floor 20' above the ground level. All depths we report in this document are those we recorded.

The results for the tie points we selected are tabulated in Table A-II-1. At some of those depths we also provide figures, as noted in the table.

Table A-II-1: Tie points for orientation checks in INEL-1*:

Description	Phase I		Phase II	USGS	
	depth	azimuth	azimuth	depth	azimuth
	7130	-	190	7150	185-190
	7572	-	314	7592	330
	7995	-	129	8015	130
	8949	-	128	8973	128
(see Figure A-II-5)	9513	130	122	no data	
	9520	340	340	no data	
fracture					
(see Figure A-II-6)	9714	110-130	110-130	9738	110-124
	9730	90	90	9752	94
(see Figure A-II-7)	9942	130	130	no data	
	9949	120	257	no data	
	9955	180	296	no data	
(see Figure A-II-8)	9975	302	118	no data	
hourglass					
(see Figure A-II-9)	10032	148	342	10053	148

*all azimuths w.r.t. magnetic North

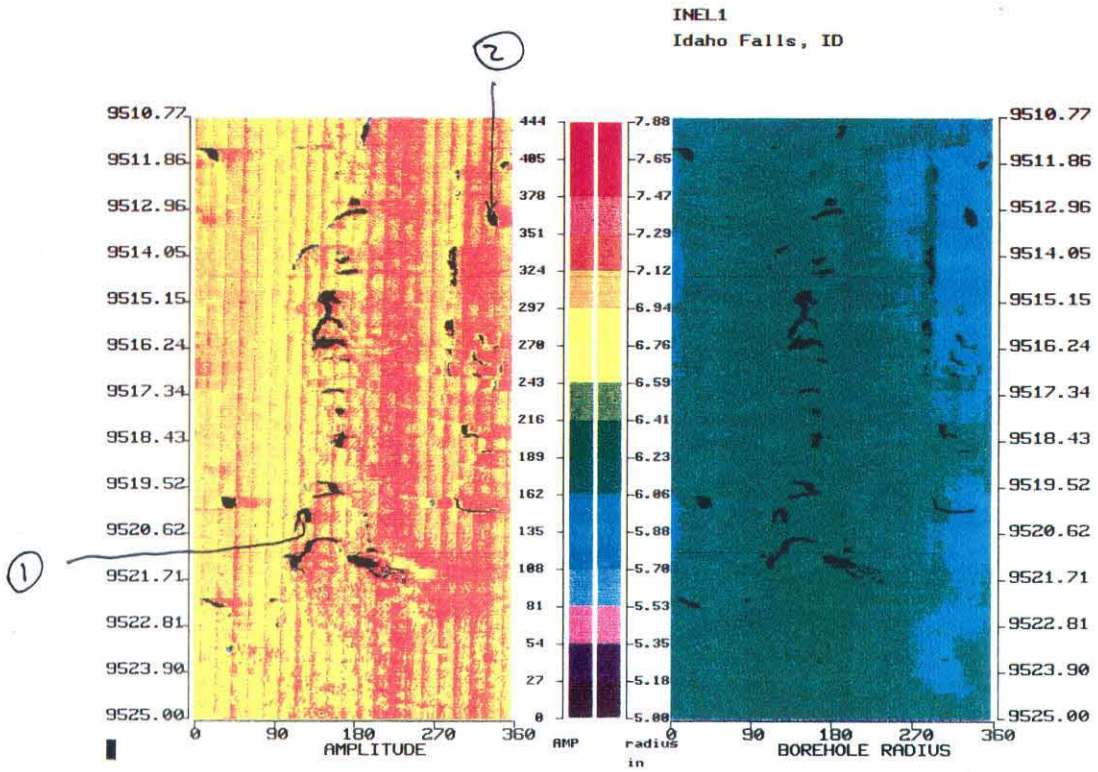

AZIMUTH CALIBRATION

① @ 9520'

azimuth phase 2 122°

azimuth phase 1 ~~285°~~ 130°

② @ 9513'

azimuth phase 2 340°

azimuth phase 1 340°

Figure A-II-5: Comparisons of the phase one and phase two azimuths of features observed in the INEL-1 well at depths of 9513 and 9520 feet. No data is available at this depth from the USGS log.

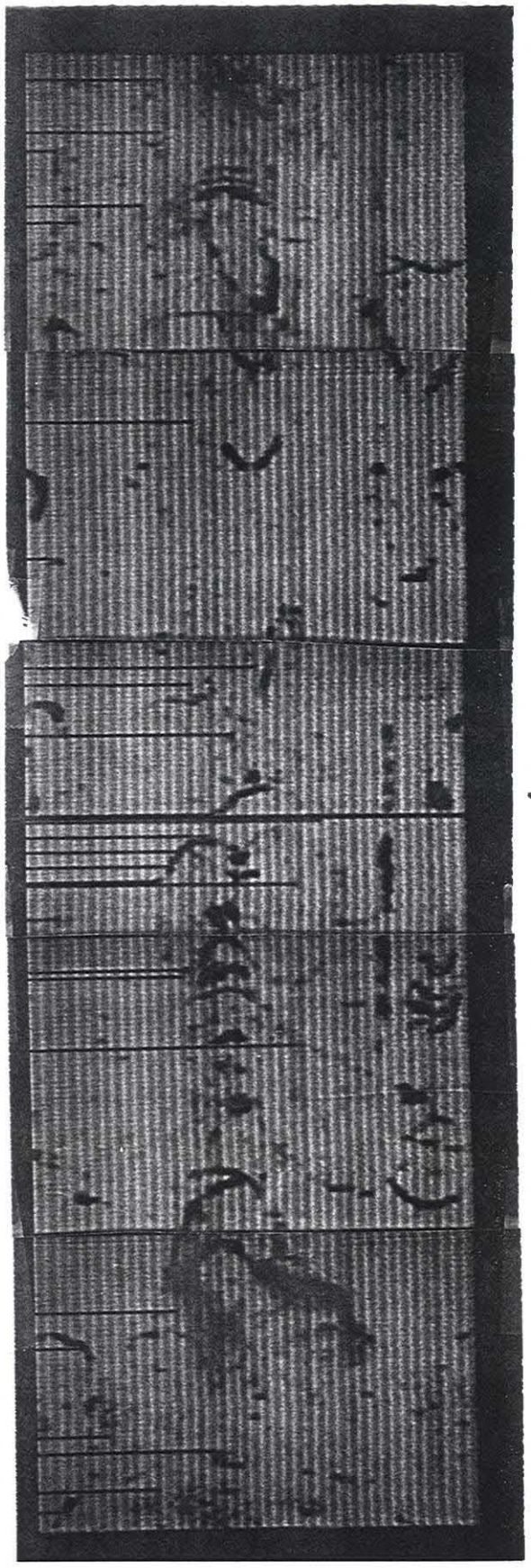
9500
2
1
9525

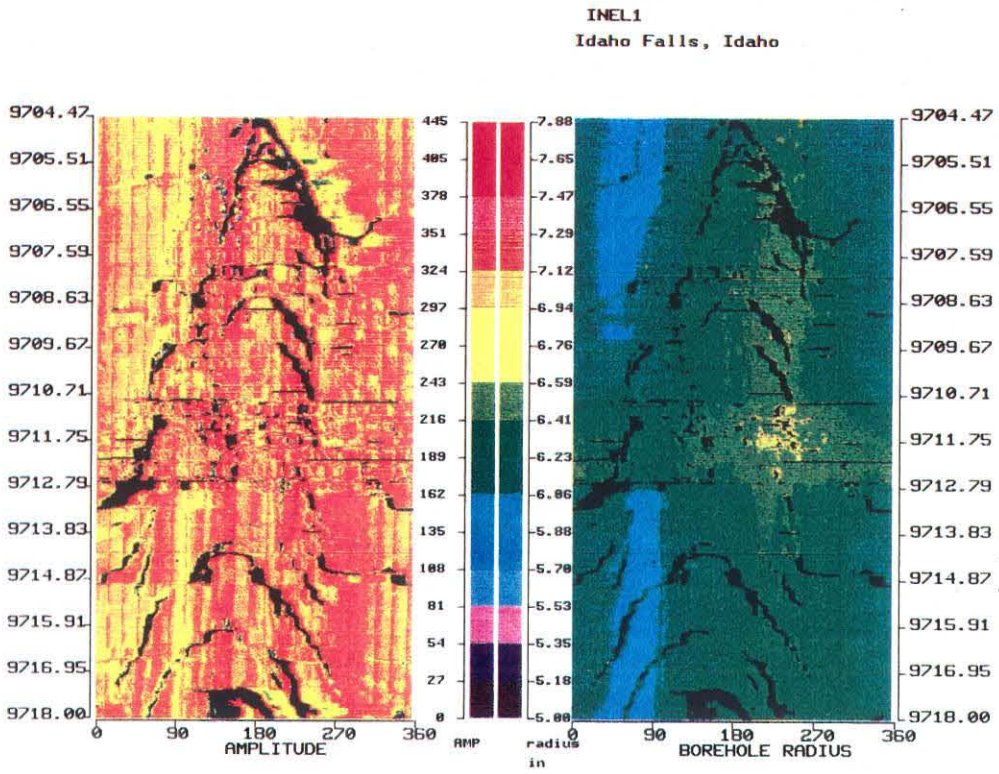

] fracture ~110° - 130°

ORIENTATION COMPARISON

AT DEPTH:

Paillet: 9718'

Pass 1: 9718'

Pass 2: (corrected to Pass 1 depths)
9715'

Figure A-II-6: Comparisons between the azimuths of features observed in the phase one, phase two and USGS logs of the INEL-1 well at depths of 9714 and 9730 feet.

Idaho Falls, Idaho INEL #1
June 21, 1980
10045 - 10095

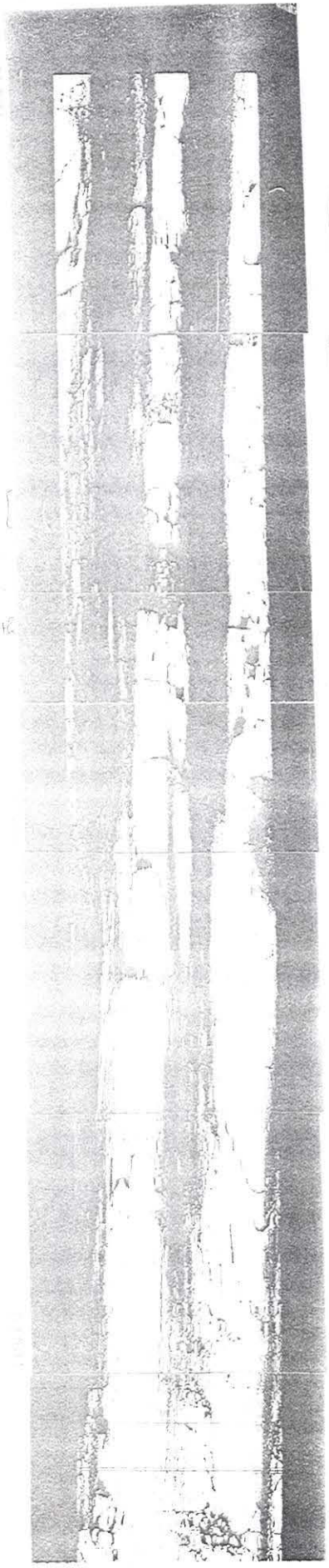

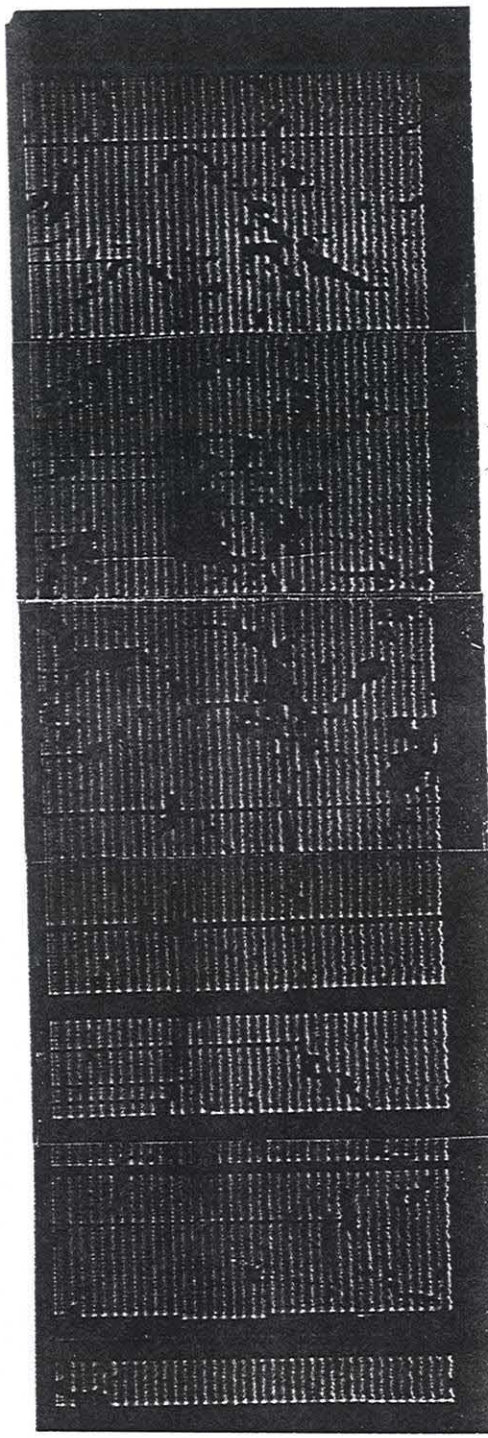

INEL-1 PASS 1
PHOTOGRAPH

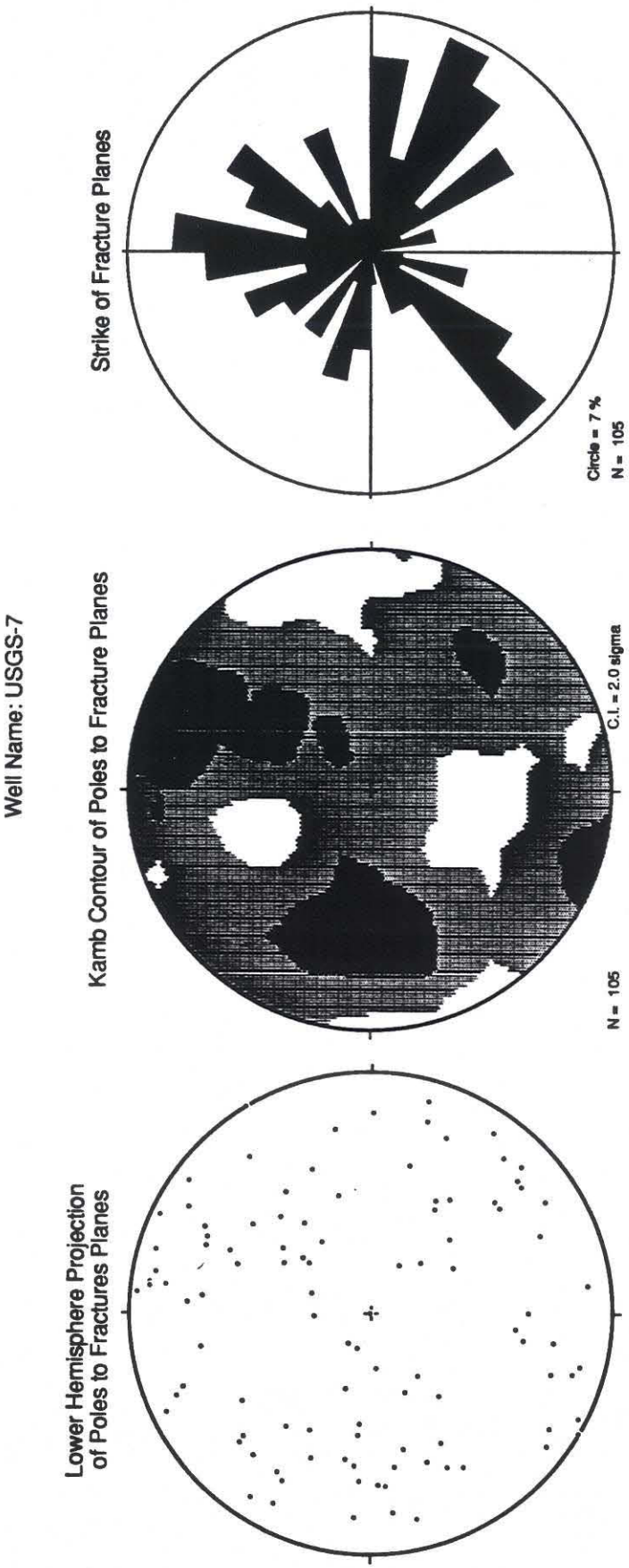

Figure 19: Lower hemisphere stereographic projections of poles to fracture planes, contoured poles to planes and strike of all fractures measured in well USGS-7.

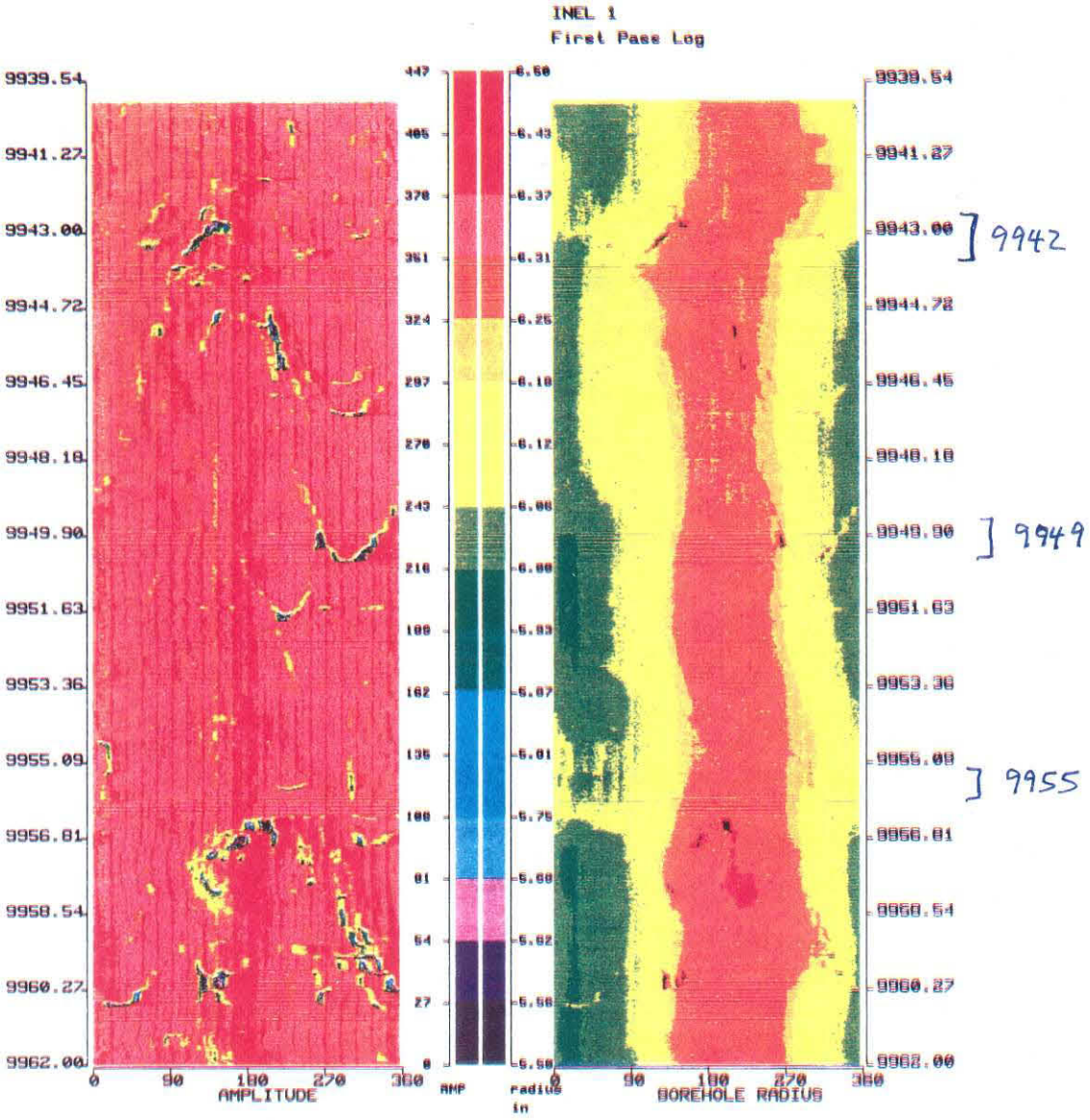

Figure A-II-7: Comparisons of the phase one and phase two azimuths of features observed in the INEL-1 well at depths of 9942 (where the azimuths agree), and 9949 and 9955 feet, where a different amount of offset in the azimuths is observed. No data is available at this depth from the USGS log.

INEL#1
Idaho Falls, Idaho

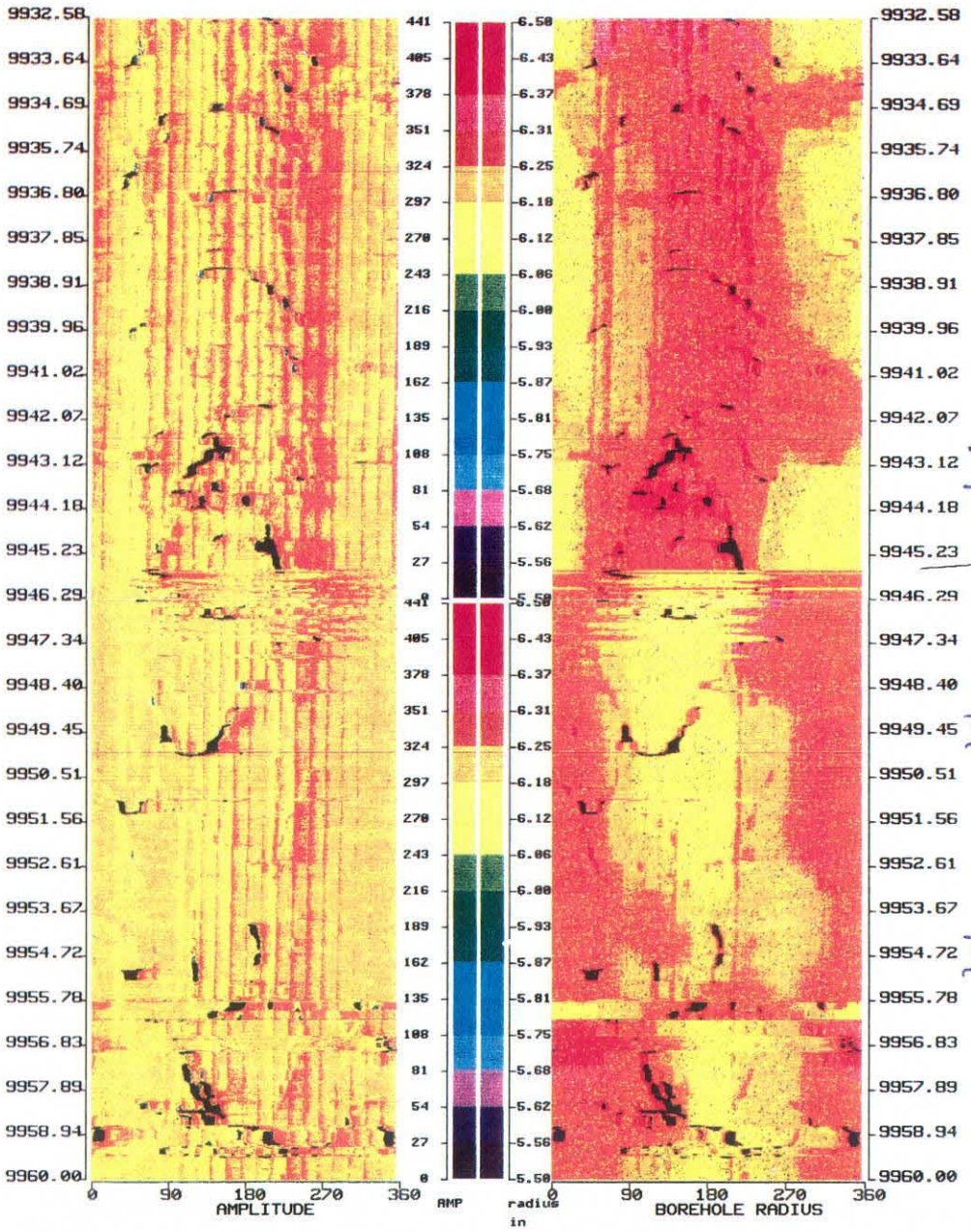

] 9942

orientation jump

(adjusted borehole DC during recording)

] 9949

radius ~6.25

] 9955

= orientation jump

= orientation jump

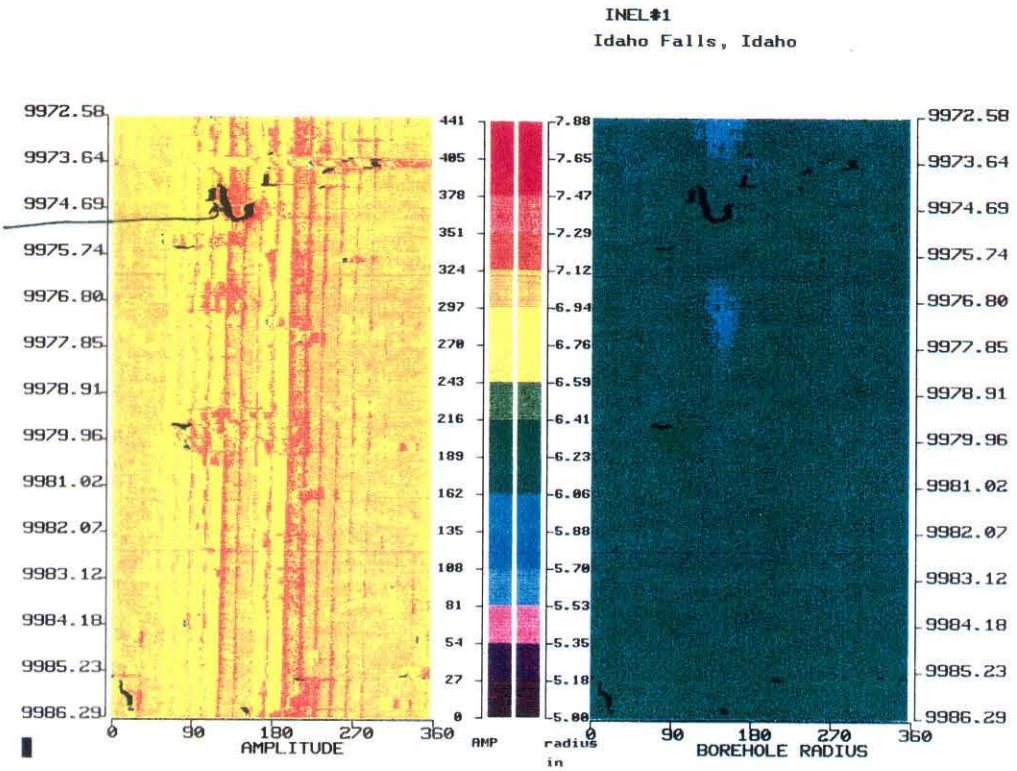

turn in center of ntical black

118°

ORIENTATION CHECK:

digitized pass 2 118°

photos pass 1 302°

@ 9974.5 subtract 176° from digitized to match

Pass 1

Figure A-II-8: Comparison of the phase one and phase two azimuths of features observed in the INEL-1 well at a depth of 9975 feet, where the orientations do not agree. No data is available at this depth from the USGS log.

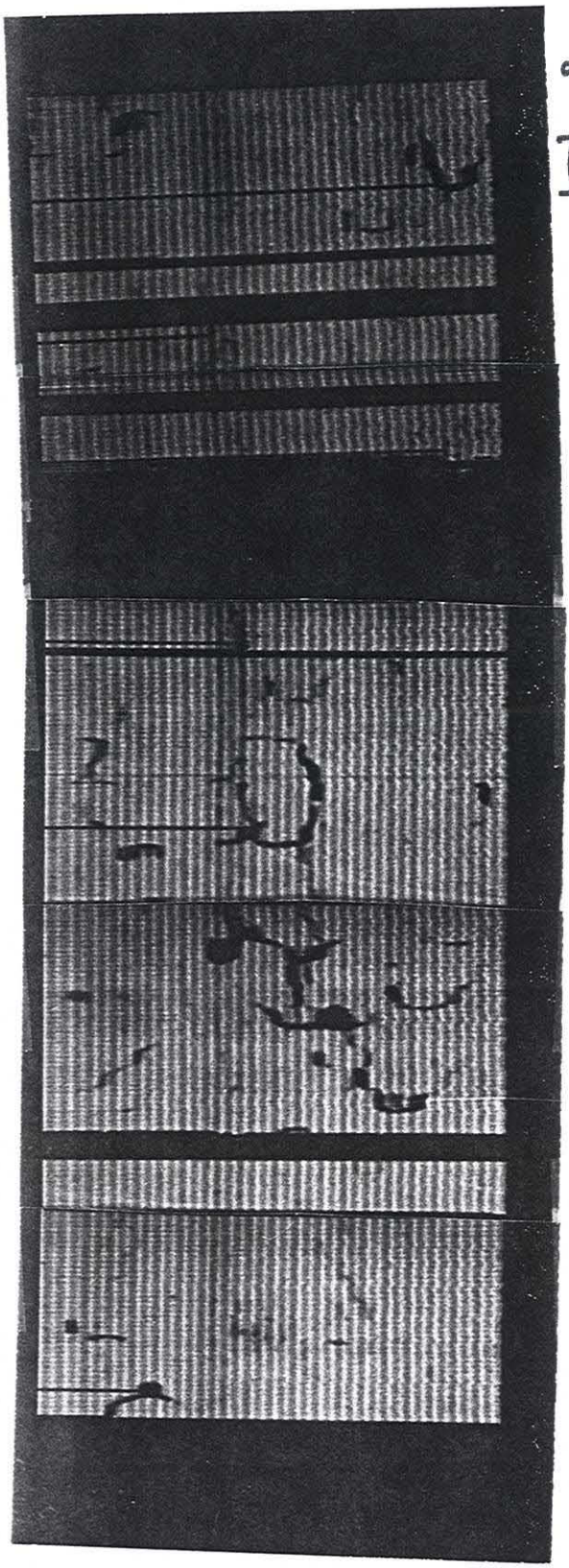
9975
10,000

Digitized data Pass 2

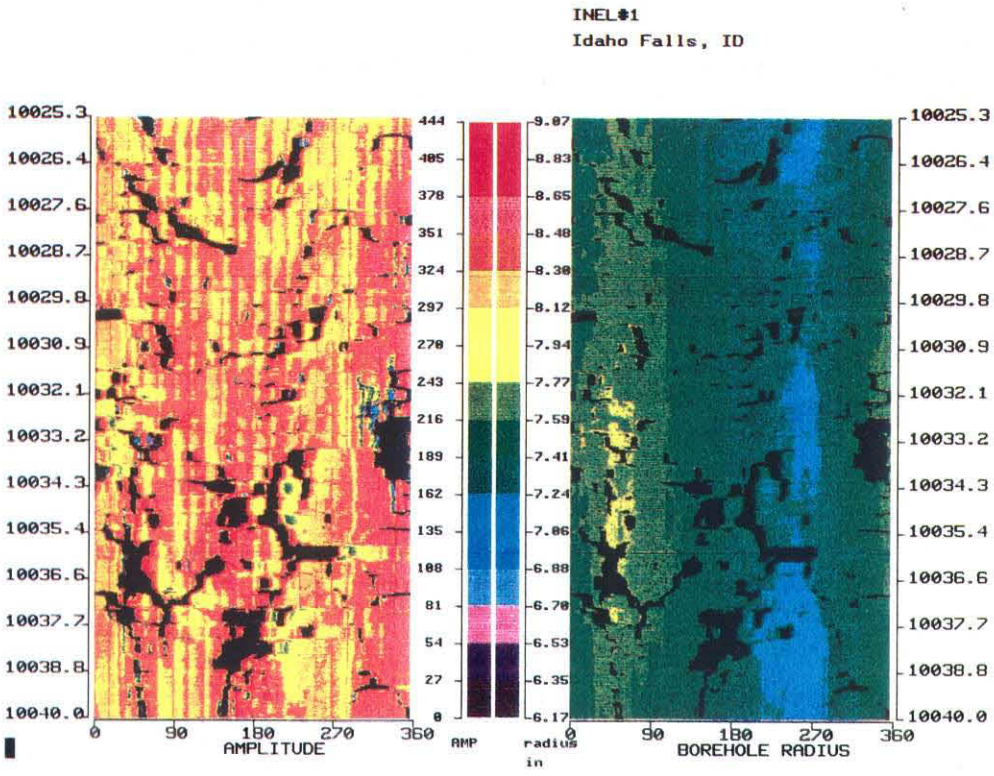

] "hourglass" @ 342°

ORIENTATION COMPARISON AT DEPTH:

Paillet	Pass 1	Pass 2
148°	148°	342°

(subtract 194° from pass two to equal other logs)

Paillet: 10,053'

Pass 1: 10,032'

Pass 2: (corrected to pass 1 depths) no photos @ this depth during the log

Figure A-II-9: Comparison of the phase one, phase two, and USGS azimuths of features observed in the INEL-1 well at a depth of 10,032 feet. Note that the orientations of the USGS and phase one logs are the same, whereas that of the phase two log is different.

acoustic televiewer log
Idaho Falls, Idaho EXEL #1
June 21, 1980
9730 - 9780

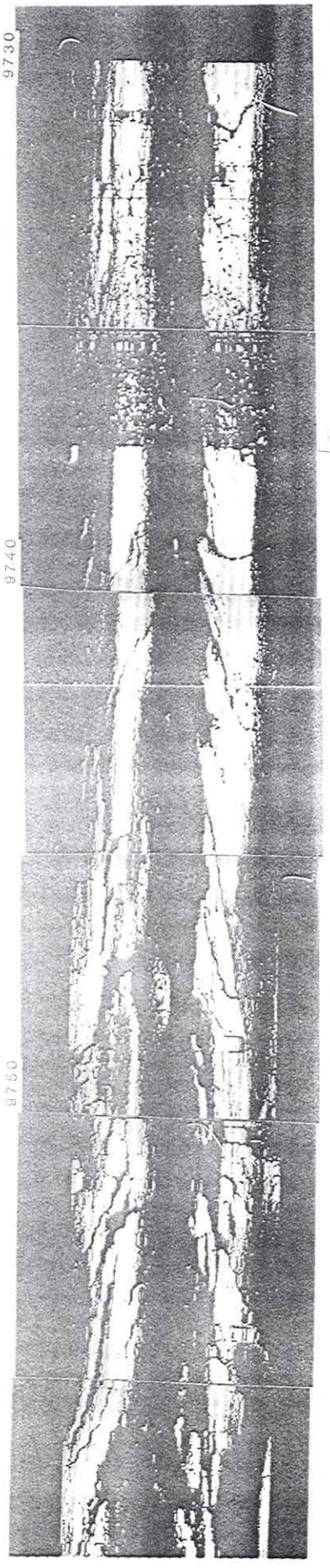

9737

depth tie

9716.5

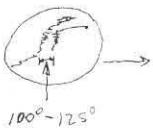

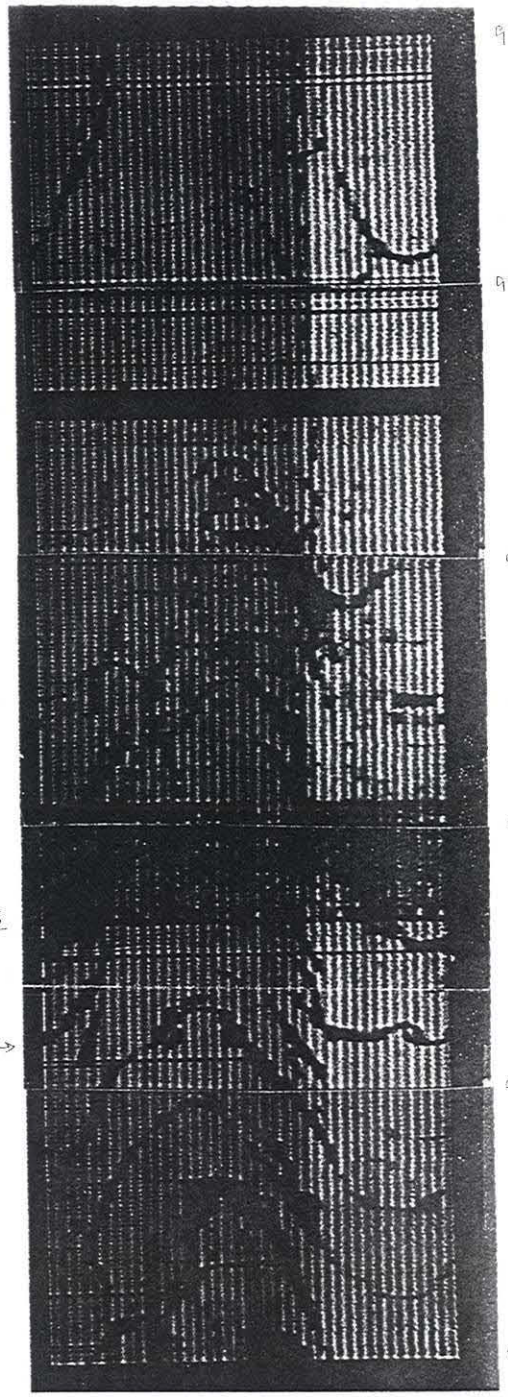

Appendix III - Color Images

BHTV image data from USGS-7, USGS-17 and Noname was shipped to R. Smith on July 15, 1990. Image data from INEL-1 was shipped to R. Smith on August 8, 1990.

Appendix IV - Barton et al., BHTV analysis paper

The paper included here as Appendix IV is in press (Springer-Verlag). It describes in detail the algorithms used to digitize, calibrate, and filter the televiewer data prior to analysis. Also described are the algorithms used to analyze the data, and the interactive front end which simplifies the analysis.

INTERACTIVE IMAGE ANALYSIS OF BOREHOLE TELEVIEWER DATA

by

Colleen A. Barton, Lawrence G. Tesler

and Mark D. Zoback

ABSTRACT

This chapter describes an interactive graphics system designed for borehole televiewer (BHTV) image analysis. The software provides one of the first comprehensive tools for borehole image data analysis available to exploration and research scientists on a low cost and easy-to-use personal computer, the Apple Macintosh II.

The program, called BHTVImage, provides an integrated environment for analyzing borehole shape and features. Images of BHTV data are displayed in false color on a graphics screen and are manipulated with a mouse pointing device. A variety of two and three-dimensional displays of borehole radius and acoustic reflectivity are used to display the data. Tens of meters of borehole wall can be rapidly viewed by scrolling through the data within a graphics window. Interactive measuring tools are provided to quickly measure and record wellbore features. The values of the scales, units, and grid intervals can be modified interactively during program execution. Gross scale features can be easily extracted from the images through interactive thresholding to produce a scaled comparison with complementary log data such as resistivity or sonic recordings. Alternatively, full resolution images can be analyzed to investigate the fine details of fractures or cross-bedding intersecting the well.

One of the reasons Macintosh applications are easy to use is that there is remarkable human interface consistency among applications. To help meet that standard of consistency, the BHTV analysis software was implemented using an Apple product called MacApp. MacApp is an "object-oriented framework", i.e., a "generic" application that defines standard "objects" like windows and views. Any desired Macintosh application can be derived from MacApp by describing in code only the differences between that application and the generic one. The resulting program achieves consistency with other Macintosh applications without special effort on the part of the programmer. MacApp, as well as the bulk of the BHTV analysis program, is written in the object-oriented language Object Pascal. Certain BHTV analysis subroutines are written in the language C.

The software discussed has provided the primary analysis tool for the BHTV image data recorded in the Cajon Pass and KTB research wells. The Cajon Pass Well, located in Southern California near the San Andreas fault, was drilled to investigate the paradox of low stress, low heat flow measurements along an active plate boundary. The KTB deep

drilling project located in the Oberpfalz zone of West Germany was undertaken to evaluate an ancient continental suture. The accurate determination of borehole shape and the characterization of wellbore breakouts and fractures with depth have been essential to understanding fault mechanics and tectonic stresses and to the interpretation of geophysical and core data from these and many other wells.

INTRODUCTION

The borehole televiewer is an ultrasonic well-logging tool useful for imaging lithostratigraphic features and for measuring the orientation and distribution of fractures as well as the orientation and width of stress-induced wellbore breakouts. The analog Televiewer, originally designed by Mobil Oil, Inc. (Zemanek et al., 1970), contains a rotating transducer that emits an acoustic pulse at the rate of 1800 times a second. Figure 1 is a schematic diagram of the acoustic mechanism of the Televiewer tool. The 1.4 Mhz transducer rotates at three revolutions per second and moves vertically up the borehole at a speed of 2.5 cm/s. The transducer diameter is about 1.27 cm (0.5 in) however the emitted sound is focused to a narrow beam of about 3^{o} due to the high frequency. A fluxgate magnetometer within the tool fires at each crossing of magnetic north, making it possible to orient the data.

Prior to the 1980's and the emergence of downhole digital imaging tools, borehole wall images were limited to analog photographs. Image analysis was a static, tedious process. With the inception of the microprocessor, digital images of the borehole wall have become the standard data presentation format.

Image photographs are still routinely collected in standard field operation of the analog BHTV tools. The analog televiewer tool transmits ultrasonic seismograms through a standard wireline logging cable which are recorded on videotape. The analog data are channeled into a three-axis oscilloscope where the horizontal sweep represents the scan of the rotating transducer around the borehole, the vertical sweep represents the rise of the tool in the borehole and the intensity is modulated by the reflected energy from the borehole wall. The oscilloscope then produces an unwrapped 360^{o} gray scale image of about 1.52 m (5 ft) of the borehole wall. The BHTV "log" is constructed from Polaroid photographs taken of successive oscilloscope screens as the tool progresses uphole during field logging. Each 3x5 photograph is then assembled into a composite log. The analog "north pulse" is recorded on one of the two audio channels of the video recorder. Depth is also analog analog on the remaining audio track of the video recorder.

The analog Televiewer tool has not undergone any major design changes since it was first introduced to geophysical logging in 1970. Interpretation of the photographic log has been limited to estimations of gross structure from the reflected image. The primary use of Televiewer data had been to determine the orientation of fractures in granitic rocks, analyses which involved tedious and inaccurate measurements. No capability existed in the analog data to correct the measured orientations of planar features for the effects of off-center tools or elliptical boreholes, conditions which can lead to substantial measurement error. With the rising use of wellbore breakouts to determine in situ stress, televiewer data has become increasingly important.

Digital televiewers have recently been designed that contain downhole processors to reduce the received signal to a peak amplitude and associated travel time before digital transmission (Heinz and Schepers, 1985; Schlumberger, Inc.). In digital tools, the horizontal resolution of the data is generally reduced by about one half of that of the analog tools. However, precision is gained by eliminating noise problems such as analog signal degradation in the cable. The marker pulse at magnetic north and depth readings are encoded automatically in the data recorded by the digital tools. The tilt of the tool is monitored by two inclinometers and an accelerometer provides continuous data on tool speed. Although the resolution is completely dependent upon hole size and logging speed, the Televiewer typically will provide horizontal resolution of a few millimeters and a one centimeter vertical resolution in a 30.5 cm (12 in) borehole.

Uphole data processing schemes for analog borehole image data have been operational since the early 1980's. Early post logging processing of the images was accomplished by fiber optics recording hardware (Wiley, 1980; Broding, 1982). At the outset of the development of uphole digitization systems specialized equipment was built; today inexpensive off the shelf data acquisition boards are available for workstations and most personal computers. In post logging digitization the recorded BHTV signal is examined within a specified window to determine the peak amplitude and its associated travel time. The determination can be performed by efficient software algorithms (Barton, 1988) or electronically measured by edge detection hardware (Pasternack and Goodwill, 1983; Taylor, 1983; Rambow, 1984; Wong et al., 1989; Faraguna et al., 1989). The time required to capture and record each pair of values is generally within 0.5 microseconds.

Digitization of standard analog data results in dual measurement of acoustic reflectivity of the borehole wall and the ultrasonic travel time of the imaging pulse at a spatial resolution well above conventional logging tools. The software and techniques described herein to analyze and interpret BHTV data are applicable to any digital televiewer

data set whether obtained directly from a digital tool or derived by analog-to-digital conversion from an analog wave train (Figure 1b).

Advantages of Digital Interactive BHTV Data Analysis

Digitizing and digital processing of the analog Televiewer data has opened a new dimension in the interpretation of BHTV data, most significantly, the precise measurement and display of the travel time of the reflected pulse. Assuming a known mud velocity along the raypath for the source and reflected pulses, the two-way travel time can be converted to distance to give the detailed topography of the borehole wall. Another advantage of digital data is that it can be enhanced and corrected for geometric effects. Borehole features can be displayed in a way that best suits the type of feature under investigation. For example, wellbore breakouts are best represented in polar cross section. Finally, it is possible to make systematic quantitative measurements quickly and accurately.

BHTVImage utilizes various two- and three-dimensional displays of the borehole radius and acoustic reflectivity to facilitate data analysis. It allows the user to make quantitative measurements of borehole features such as breakouts, fracture orientation and apparent aperture, and lithologic features. The analysis software has been implemented on a Macintosh II personal computer. The program provides an integrated environment for analyzing borehole shape and features where images of BHTV data are displayed in false color on a graphics screen and are manipulated by graphics mouse and keyboard commands.

The primary advantages to interactive data analysis are that it gives the geophysicist the ability to (1) interactively manipulate the data to obtain an optimal view of a particular feature, (2) look at the same data interval simultaneously from a variety of perspectives and (3) make decisions as the analysis proceeds.

Menu driven commands and analysis operations provide an ease of use factor to the software. Tens of meters of borehole wall image can be rapidly viewed by scrolling through the data within a graphics window. Images can be enlarged to the full resolution of the screen and scrolled to search for fine features. Alternatively, larger sections of the well can be displayed at the scale of standard logs. Interactive measurement tools are provided to quickly measure wellbore features. The values of the scales, units, and grid intervals can be modified interactively during program execution. Menu-operated window management provides easy access to the various views the user is interpreting.

BHTV File Format

A common aspect to all borehole image data is the physical size of the data set and the associated difficulties in managing the volume of data generated. The voluminous size of image data controls the configuration of the computer hardware and impacts software design along every step of the acquisition, display, enhancement and analysis process. Computer speed and memory capacity are rapidly increasing, however, these constraints remain a significant consideration in the design of an image processing system. Data compression is a widely used and widely researched topic in computer science. Compression and decompression algorithms exist for computer systems common to oil industry, research and government facilities. They are at present too costly in computational time to be useful in interactive image analysis.

The data input consists of header information followed by arrays of amplitude and travel time values. Careful thought is required in header format design given the extreme variability in image data and the fact that other scientists may use the data. For example, image enhancement involves filtering and other processing that results in permanent transformation of the data. It is important to keep a history of the transformations that a particular image data set has undergone to preserve the ability to interpret the data. In header format design it is beneficial to consider extensibility, that is, the flexibility to extend the header at a later time it to include more, fewer or different header parameters. Table I summarizes header specifications used in this system. The header parameters can be inspected by choosing a menu command which presents a dialog box, a display of the current settings of the header parameters. These parameters can be edited as necessary to adjust the data to the proper depths, compass azimuth, etc.

In the uphole digitization scheme developed at Stanford the returned reflection is windowed and discretely sampled (Figure 1b). The peak amplitude and associated travel time are measured for each pulse firing. The conversion of travel time to true borehole radius is completely dependent on the BHTV tool and transducer frequency used to record the data. The mud fluid velocity in the borehole, V_f, the correct radius of the televiewer tool, T_r, must also be known. The transit time between the transducer and the outside of the window housing the transducer, T_{off}, must be known for the particular tool and transducer frequency used to record the data. For example, T_{off} is 16 μs for the large diameter high frequency Simplec Inc. televiewer and 9.81 μs for the Schlumberger Inc. high frequency large diameter tool. Conversion of the travel time data to borehole radius is then:

$$R = \frac{((S*T_i*W/N) + D - T_{off})}{2} * V_f + T_r \qquad (1)$$

where T_i is the two-way travel time, S the sample rate in samples/μs, D is the digitizing delay time in μs, W the digitization window length in μs and N the number of samples digitized per pulse. To assure accuracy in the conversion of travel time to radius for each logging run a calibration adjustment can be added to equation (1). The calibration constant is obtained from a calibration test of the tool in a specially designed tank before each logging run. A calibration tank requires at least two different radius values, for example, a smaller radius from 0° to 180° circumference and a larger radius from 180° to 360°. The measured travel time values measured at known radius values can be used to compute the calibration constant and the fluid velocity. Data recorded in this tank may also be used to calibrate the compass azimuth of the transducer with respect to magnetic north.

Conversion to the format for BHTVImage includes resampling of variable scan length data to a fixed length, shifting the data to correct for the magnetic declination at the logging site or any other azimuthal data shift, and scaling of the amplitude and travel time values to the range 0 to 256 expected by the program. An essential consideration during data acquisition is the threshold detection level imposed during data acquisition. When no reflection is detected above the noise threshold that particular pulse must be flagged within the data set to signify that no energy returned to the transducer. These values of missing data are important elements of the BHTV data format.

HUMAN INTERFACE DESIGN

Experience with a predecessor to BHTVImage on a different computer had shown that the utility and appeal of the program would be quite limited unless the user could interact freely with an image, i.e., display it alone or alongside other images, scroll through it to study its features, decide whether to correct for geometric distortion and do so if desired, decide whether to enhance the image in one or more ways and do so if desired, choose views that seem at the time to be useful, and make measurements of any desired features in any order at all. Achievement of these goals required a highly interactive graphical user interface.

Another goal we chose was to make the BHTVImage software accessible to other researchers. Two factors were important to achieve this goal: affordability and ease of use. The Macintosh II computer met all the above criteria as well as technical requirements such

as sufficient memory capacity to hold multi-megabyte images and a high-fidelity color display.

One of the reasons Macintosh applications are easy to use is that there is remarkable human interface consistency among applications. After a user has learned one or two applications, the knowledge he or she has gained about how to interact with them can be generalized to other applications. Studies have shown this to result in reduced learning time. To accrue the advantages of consistency, BHTVImage was designed to follow Apple's user interface guidelines wherever feasible.

The Macintosh user interface is based on a number of principles. One is modelessness. A mode is a state of an interactive system that affects the meaning of user actions. If the user takes an action in one mode thinking the system is in another mode, undesired effects can result. As a result, the Macintosh guidelines discourage modes, and insist that when modes are unavoidable, the current mode be inescapably obvious to the user. If BHTVImage, for example, had been designed so that the user specified a filter command and then the borehole section to filter, then between the first and second specification, the system would have been in a mode expecting the section to be specified. Instead, in analogy with other Macintosh applications, BHTVImage was designed so that the user first specifies ("selects") a borehole section and then any operation on it—or several sequential operations, or none. Between the selection and the operation, there is no mode. The user may scroll or move the window, run other Macintosh applications, peruse the menus in search of a desired command, select a different section of the borehole for the operation, or even change one's mind and never specify the operation.

Another principle of the Macintosh user interface is that everything the user must think about should be visible. When we added the ability to measure a fracture or breakout, our first thought was to write the measurement data directly to a text file. However, if we had done so, the user would not have been able to see the measurements until after the file was saved and another program was run to examine it. Instead, we decided to display the measurements in a text window immediately after they were made. In addition to providing the desired visibility, we discovered the additional benefit that the measurements could be edited using a standard text window editor to delete a mistaken measurement or for other useful purposes.

One other principle of the Macintosh user interface is that applications should be tested on typical users, revised in response to difficulties they encounter, retested, revised again, etc., until the ease of use level meets expectations. In the case of BHTVImage, one target user (an author of this paper) was involved in the detailed design and implementation of the program. Thus, it was not surprising that all of the twenty-odd geophysicists who

have tried it thus far—some with no help but a ten-page preliminary manual--have reported extreme satisfaction with the user interface.

Key components of the Macintosh user interface, and their expression in BHTVImage (discussed below), include:

Macintosh	BHTVImage
Windows:	Amplitude window, borehole radius window, correction window, etc.
Views:	Unwrapped view, polar cross-section view, cylindrical projection, etc.
Selections:	Selection of text, of one fracture, or of all data between two depths
Menus:	File, Edit, Windows, Views, Settings, Palette, Analyze, and Profile
Dialogs:	Dialogs to provide control over the display of scales, filter options, etc.
Keyboard shortcuts:	
	The escape key to record a fracture, command-X to remove a section
Palettes:	Palette of 16 hues, gray scale or black and white

OVERVIEW OF PROGRAM USAGE: A Scenario of the Analysis of BHTV Data

Open a Data File

The standard representation of borehole image data has been a 2-D unwrapped 360° view of borehole azimuth versus depth. The interpretation of borehole image data involves the display of different borehole features in an optimal geometry so that they can be viewed and most accurately measured. Planar features that intersect the borehole appear as sinusoids on the 2-D view so they are best analyzed in the 2-D split images (Figure 2, after Zemanek, et al., 1970). In Figure 3, nearly vertical fractures that strike about 180° are associated with low reflectivity values and large values of borehole radius. Other borehole parameters that can be extracted from image data, for example caliper information from the BHTV, may be represented as geophysical log profiles.

Intervals of the data may be selected from the 2-D unwrapped image, using the mouse much like selecting text in a Macintosh word processor program. The selected interval can then be viewed in a variety of projections. The cylindrical geometry of the data is best represented by polar cross sections of the data scans or isometric 3-D cylindrical projections (Figure 4). In the cylindrical projection, the radius of the cylinder is modulated by the borehole radius value at each pulse providing a true scale reconstructed image of the borehole wall. Three-dimensional wire frame cylindrical projections of the data show fine detail of the borehole wall not visible in conventional 2-D displays. The cylindrical

projection may be scrolled vertically to view the reconstructed "core like" image with depth or scrolled horizontally to rotate the image 360° about the vertical axis. The amplitude values can be used to color modulate the surface of the cylindrical projection for a composite image of the data (Figure 4, middle window). These views can also be interactively displayed as black on white to investigate only the topography (Figure 4, right window). The data displayed in Figure 4 were recorded over a cross-bedded interval in a well located in the Gulf Coast. A 3-D wire frame image with reflectivity values superimposed in color has become an important interpretative tool. As shown in Figure 4 there is more variability in the reflectivity image than in the corresponding travel time image indicating that the impedance contrast over this interval exceeds the small variations in the travel time due to the differential erosion of the interbedded sand and shale. There is an option in this view to exaggerate the surface of the cylinder to amplify small variation in the topography of the surface. The differential erosion between the sand and shale layers is evident in the black and white view of Figure 4 (right window).

Polar cross sections of the data scans can give an accurate bird's eye view of circumferential wellbore conditions and computed borehole radius values can modulate the radius of the cylinder to show fine detail of the wellbore wall.The polar projection also uses the travel time values to modulate the radius of the polar cross section. Scrolling the data in polar cross section allows a rapid view of borehole shape changes with depth (Figure 5, middle window). A compass plot around the polar scan is used to reference the data to geographic north. A graticule can be used in the polar plot for a more accurate assessment at the borehole dimensions. These alternative views of the data can be simultaneously displayed in other windows.

Additional views of any selected interval of data include a plot of the scans in Cartesian cross section showing azimuth versus borehole radius and a histogram view of the travel time data. These views are useful for evaluating borehole shape and noise contamination. Each view can be scrolled to inspect the data for changes with depth.

Data intervals can also be plotted as a cross plot of amplitude (x axis) versus distance (y axis) to look for anomalous relationships in the two variables that could indicate the presence of a particular borehole feature or the need to make a geometric correction to the data. There are expected relationships between reflectivity and travel time in the borehole, for example, low amplitude values and high travel time values within fracture zones, anomalous relationships such as high travel time and high amplitude isolated in a cross plot such as the upper plot in Figure 6 are the result of anomalies in the data. These plots can be used to interactively determine intervals of problematic data such as the off-center effects characteristic of the low travel time high amplitude cluster in Figure 6. After

correction for off-center effects the cross plot shows a normal distribution of data (Figure 6, lower plot).

Color or gray scale palettes are used to false color map the data to an image. Gray scale palettes can sometimes be a more intuitive interpretive tool using simple light to dark gray shades to indicate increasing values in the data. Data are color or gray scale mapped to either a linear palette where the data values are mapped to 16 different hues or to an enhanced palette which utilizes histogram equalization. Histogram equalization generates an image that assigns the available brightness levels or colors to equal numbers of samples and produces a display of higher color contrast which can accentuate features not visible in a linear scale. The same image over an 11 ft (36.9 m) section of a Gulf Coast well in Figure 7 shows the effects of histogram equalization. The left image has a linear color distribution and the right image has an equalized color map. Histogram equalization has been an extremely useful method to enhance borehole wall details.

Due to the variability in data, value ranges, and data quality, the linear or equalized color maps may not always provide the optimum display for interpretation in all cases. For this reason interactive palette manipulation was implemented which allows the palette hues to be interactively adjusted using a graphics mouse. This technique allows for expansion or reduction of the color contrast as needed for optimum enhancement.

Data thresholding is an additional palette manipulation. This technique was developed in order to examine gross scale features of the borehole reduced to black on white images. With thresholding the color palette is replaced by a sliding scale of the range of values in the data. A cutoff threshold value is interactively selected from this scale. Figure 8 shows an interval of the Cajon Pass well where breakouts and fine scale fractures are evident in both the reflectivity and borehole radius views. For reflectivity, the cutoff threshold marks the value below which all reflectivity pixels will be black and above which reflectivity pixels will be white. Similarly, a radius threshold can be used above which pixels will be black and below which they will be white. This view is useful for the correlation of BHTV logs with companion log data described below.

Low-pass filtering and subtractive smoothing (high-pass filtering) routines have been implemented as an aid in the detection of fine scale features. These filters are horizontal and 1-D. In subtractive smoothing the data are low-pass filtered to attenuate all of the high frequency features, such as edges and lines, then the smoothed image is subtracted from its original resulting in a difference image which has only edges and lines substantially remaining.

Standard Processing

The introduction of digital image data brought the possibility of correcting data for distortions caused by less than optimal recording geometry. Unfavorable logging conditions are a pervasive aspect of borehole image data acquisition. Instability of the borehole, washouts, fault zones, and the high pressures and temperatures at depth can lead to poor quality data. One objective for processing borehole image data is to identify these environmental or tool problems that distort the data and to provide the information required to make corrections to the data.

Analog data acquisition onto video tape is sensitive to human error as well as to poor borehole conditions. The missynchronization of recorder operation and winch operation can lead to missing or repeat log sections. When logging at sea ship's heave is seldom entirely mechanically compensated and data recorded at ocean drilling sites often show repetition of logged features. In addition, the tool may "stick" in the borehole for several rotations of the acoustic transducer then rapidly slip uphole creating a characteristic blocky image (Figure 9, left window).

For these reasons data need to be preprocess and edited prior to interpretation to avoid erroneous conclusions and the masking of subtle features. An interactive visual editing of the digital data has been implemented in the BHTV system to allow the user to delete data that should not be included in an interpretation. By selecting the unwanted interval with the mouse and using the standard Macintosh Edit Menu command "Cut" the selected scans are removed from the data file. Figure 9 shows the application of this interactive editing on data collected at Hole 504B in the East Pacific Rise. The blocky intervals in the left image of unedited data correspond to repeat scanlines due to ships heave; the right image of edited data reveals an interval of stress-induced wellbore breakouts that cannot be distinguished on the unedited image.

A fundamental effect of logging on the quality of BHTV image data is random noise. Whether it is electrical noise from the motor driving the rotation of the transducer or the interference from spurious voltage surges inscribed onto the videotape the result is anomalous spikes in the data. Scattering of energy due to the sampling geometry is another major source of noise. The optimum raypath geometry consists of a centralized tool in a circular borehole where each incident pulse has normal reflection to the tool. Non-normal incidence of a stray pulse from a rough surface can create complex raypaths and multiple reflections. These translate to anomalously high travel times and spurious reflectivity values. Noise spikes can interfere with data interpretation and they must be eliminated where automatic fitting or feature analysis routines are implemented.

Alternatively, if the spikes actually represent valid data, they may contain important information.

A median filter is used to mitigate this type of noise in the data. A median filter was selected among the myriad of smoothing operations in image processing because it is a smoothing in which the edges in an image are maintained. In median filtering a template is slid along the scans of data and the center value of the template is given the median value of all the values covered by the template. This type of filter is particularly good for removing impulse-like data because the pixels corresponding to noise spikes in their neighborhood are replaced by the most typical pixel in that neighborhood. A horizontal median template of any number of pixels can be used to pre-process BHTV data. A three point to median was determined to be the most appropriate because it provides sufficient filtering while having the advantage of being the fastest type of computational sort for large image files (Richards,1986).

In order to diagnose the degree of noise in a given data set the data scans may be examined in either polar cross section or Cartesian cross section to look for spikes. Symptomatic speckles in the unwrapped views also indicate noise contamination.

Geometric Corrections

A significant source of error in the interpretation of BHTV data can arise from the apparent location of borehole features from a non-centered tool which has the effect of "moving" features to incorrect positions on the borehole wall (Georgi, 1985). These effects can lead to errors in calculating orientations of planar features as well as incorrect azimuth measurements for features such as wellbore breakouts. Corrections to the travel time images for the effects of off center tools in circular boreholes are made either through geometric correction of the travel time data (Barton, 1988).

Off-center tools in elliptical boreholes present another, more complicated, geometric problem and the potential loss of a larger percentage of the returned reflection. This error is dependent upon the orientation of the ellipse and dip direction. If the long axis of the ellipse is coincident with the dip direction the dip is overestimated; if the long axis is perpendicular to the dip direction it is underestimated. (Georgi, 1985). A solution to this geometric problem using inversion was presented by Lysne (1986).

The borehole televiewer is designed to acquire data with the tool vertically positioned in a vertical borehole. Bowspring centralizers are positioned above and below the tool to stabilize it in the center of the borehole. Ideally the tool should be centrally located in a circular borehole. In reality, this optimum geometry is often not achieved. The possible raypaths for the BHTV pulse launched from the transducer are shown in Figure 10

(after Georgi, 1985). When the tool is significantly off-center in a circular drillhole vertical bands of missing data result from non-normal incidence of the pulse at the borehole wall and subsequent deflection of the returned signal away from the transducer.

To diagnose off-center effects the user can look for uneven vertical color banding in the unwrapped views or an off-center position in the polar cross section. A histogram of the travel time values will show a bimodal distribution if the tool is off-center and the Cartesian cross section will have a warped appearance instead of maintaining a horizontal line. The cross plot can also be used to diagnose off-center effects where anomalous data will occur as clusters off the main diagonal.

The polar, histogram and Cartesian views have been combined in an interactive correction window to facilitate the correction process. The upper left plot of Figure 11 displays the borehole radius in polar cross section, the lower plot in Cartesian cross section, and the upper right plot as a histogram in a single window for the user to evaluate potential off-center problems. The bimodal distribution of borehole radius, in yellow, and the curvature of the uncorrected Cartesian cross section indicate these data are from an off-centered tool in a circular borehole.

Geometric corrections for decentralized tools in circular boreholes are made using an algorithm which finds the true center of the borehole then calculates the corrected azimuth and radius for each reflected pulse. In the case of an off-center tool in a circular borehole the correction can be made by a relatively simple forward model. In an ideal circular borehole the point on the circumference with the minimum radial distance to the tool defines the tool position. Borehole features complicate this ideal scheme and, instead, an iterative search for the center is used to determine the true center. The minimum radius, r_{min}, initially defines the center of the borehole (Figure 12). Here d' is the recorded distance from the tool to the point P, d is the true distance from the center of the borehole to the point P, ϕ is the angle from the reference azimuth to the point P. The maximum radius, r_{max}, is taken as the diameter at the azimuth ϕ minus r_{min}. The distance the tool is offset from the true center, d_0, is simply $(r_{max} - r_{min})/2.0$. With this initial guess of the borehole center the radial distance, d, and angle to true center, θ, are computed for each pulse through:

$$d^2 = (d' - d_0 \cos \alpha)^2 + d_0 \sin^2\alpha \qquad (2)$$

and

$$\theta_0 = - (\phi + \pi/2) + \cos^{-1}(d_0 \sin \alpha) \qquad (3)$$

where $\alpha = \pi - \phi$ (see geometry in Figure 12).

The initial estimate for the tool position is accurate only for featureless circular boreholes. Where features are present the minimum radius may have no relationship to the true borehole center. To solve this problem the center of the borehole is iteratively determined until the routine converges to the true center. When the difference between the current iteration and the previous iteration, δd_0, is roughly zero the routine has converged. For most data sets convergence to the true center of the borehole occurs within 3 or 4 iterations. For extremely variable data, where adjacent travel time values vary more than 35%, stability in finding the true center is achieved by evaluating successive d_0 values. The smallest value of d_0 within a given number of iterations was found to provide the best estimate of the true borehole center. Once the borehole center and radial distances are calculated for each pulse the routine interpolates the amplitude values to their correct spatial position.

In the more complicated case of an off-center tool in an elliptical borehole a Marquardt inversion is used to determine the tool distance and azimuth from the borehole center (after Lysne, 1986). It was noted by Lysne (1986) that this inversion technique is unstable where the tool was off-center by less than 10% of the nominal borehole radius, in other words, as the tool approaches the center of an elliptical borehole the off-center direction becomes less unique. This was found to be the case when this algorithm was applied to field data where the tool was not sufficiently off axis in an elliptical borehole. This technique was found to successfully correct the data (Barton, 1988), however, field data recorded in an elliptical borehole where the tool was well off-axis was not available and synthetic data had to be generated to test this algorithm. The success of this algorithm applied to the synthetic data is shown in polar cross section in Figure 13 where the polar projection plotted in black is the synthetic data and the projection plotted in red is the corrected data and the crosshairs mark the center for both the original and corrected data. Note that this correction modifies both the azimuth and shape of the breakouts, features that are important to stress measurements.

APPLICATIONS OF BHTV IMAGE ANALYSIS

Perhaps the most significant potential benefit of digital BHTV data is to make accurate quantitative measurement of physical phenomena that are imaged by this logging tool. The measurements of planar features, bed boundaries, foliation and fractures are some of the primary targets for borehole image data analysis. The use of wellbore breakouts to measure in situ stress has made data recorded with the borehole televiewer an extremely valuable component in many investigations of crustal stresses.

Analysis of Fine Scale Features

Although wellbore breakouts, washouts, and key seating can be seen on most 2-D images they are best distinguished in polar section of BHTV data (Broding, 1981; Barton; 1988; Menger and Schepers, 1988). The detailed borehole shape available through polar cross sections of BHTV data and interactive measurement tools permit the rapid analysis of stress induced breakout orientation or the orientation of hydraulic fractures (Barton, 1988). Figure 14 is a conceptual drawing of the development of a breakout (see theoretical shapes in Zoback, et al., 1985) along with a polar cross section of data from the Cajon Pass well which demonstrates the picking technique. The greater travel time within the breakout defines the characteristic breakout shape. θ_b is the angle of breakout initiation with respect to S_{Hmax}. Several superimposed scans of travel time data (representing a vertical distance of several cm in the well) are plotted in polar cross section to allow measurement of breakout azimuth and minimum breakout width.

The minimum width of a breakout is a function of the initial failure of the borehole wall upon breakout formation and erosional effects on the initial shape of the breakout, such as fluid circulation or tool trips. Superimposing data scans before plotting was found to be preferable to averaging scans in order to preserve the minimum width of the breakout over the vertical interval. The data must be corrected for tool position and magnetic declination before plotting. The objectives of this analysis technique are to obtain precise breakout azimuths and the minimum breakout width and to utilize all of the recorded data. Figure 5 shows the systematic process of the data analysis where a 360^o unwrapped view of the data (left window) has been color tuned to enhance the breakouts in this interval. Polar cross sections of the borehole are plotted in the left window. The user visually picks the breakout widths using the graphics mouse to drag through the breakout angle. Where there are continuous reflections from the broken out sections, as in the example in Figure 14, the breakout widths are easily determined. The breakout width for each interval is picked interactively and stored in text window. The data window can be edited and miscellaneous notes entered regarding the data quality or other information as needed. The data window can be saved for further statistical analysis or for plotting of the depth distribution of breakouts. Several off-the-shelf Macintosh software packages are available for statistical reductions and graphics plotting.

In the data analysis, the two sides of a breakout are picked independently. The two radial lines in Figures 5 and 14 represent the picked angle of the breakout width, the breakout azimuth bisects this angle. Breakout azimuth should coincide with the direction of

least horizontal principal stress; breakout width is shown in the following discussion to be important for estimation of stress magnitude. Figure 15a is a typical histogram of the distribution of breakout azimuths and widths measured from data recorded in well EE-3 at the Fenton Geothermal site, New Mexico (Barton et al., 1988). 928 separate breakout azimuths and 644 breakout widths were measured in the analysis of the Fenton data where the mean direction is 119°, and the standard deviation 11° resulting in an S_{Hmax} direction of N30°E.

The occurrence of wellbore breakouts may be used to fully determine the in situ stress state. With knowledge of C_o, S_{hmin} and breakout width (Figure 15b) the magnitude of maximum horizontal principal stress can be estimated by the breakout analysis. A detailed description of the analysis of breakout data can be found in Barton et al. (1988). Using independently determined values for C_o and S_{hmin}, the analysis of breakout widths in the Fenton well constrains the value of maximum horizontal principal stress to be approximately S_v, as predicted from the occurrence of both strike-slip and extensional earthquakes in response to fluid injection at Fenton Hill (Fahler, et al. 1986). The Fenton well has been the site of extensive research and available information on the minimum horizontal principal stress and on rock strength made the site an excellent test of the calculation of stress magnitude using the angle of breakout initiation.

Detailed analyses of borehole shape using Televiewer data can provide well resolved orientations of the horizontal principal stresses. The magnitude of the maximum horizontal compressive stress can be constrained by these data. The analysis of breakout width may be a promising technique to estimate stress magnitude in drillholes where other techniques are not useful.

Fracture Analysis

The primary use of BHTV data since it became operational in geophysical logging has been the measurement of the orientation and distribution of planar features in a drillhole. As mentioned, planar features that intersect the borehole appear on the unwrapped 360° view as sinusoids (see Figure 2). These sinusoids are often discontinuous for fine scale fractures and they can show very complex patterns at points where several fractures intersect or where fractures are not perfectly planar. At least three fractures intersect at depth 5135.5 ft (1565.3 m) in the left window Figure 16. The circular features in the right window of Figure 16 are interpreted as fracture planes that enter and exit the borehole as a chord. The steeply dipping fracture at depth 149.2 m (489.5 ft) appears to merge with a shallow fracture above. It is important in these cases to use the various enhancement techniques discussed above to best resolve the trace of the fracture before

measuring its orientation. Because of the flexibility designed into the interactive analysis system different enhancement techniques can be explored until the optimum resolution of the fracture of interest is achieved before determining the fracture orientation.

The BHTV image of a fracture surface can be extremely irregular due in part to the true topography of the surface, the limits of the resolution of the transducer and to multiple reflections from within the fracture surfaces. Because the eye can often perform the best least-squares fit to a curve within a complex network of fractures an interactive routine has been implemented to measure the amplitude and phase of the sinusoid (Figure 16). The graphics mouse is used to drag an adjustable curve over the imaged fracture; up and down mouse movements controlling the amplitude of the sinusoid and left to right movements its phase. These measurements give the strike of the plane as 90^{o}-ϕ where ϕ is the minimum of the sinusoid and the dip angle, α, as $\tan^{-1}$ h/d where h is the peak to trough amplitude and d the borehole diameter. Interpreting fracture orientations using this interactive method reduces the possibility of errors from improperly fit sinusoids that can occur with other automatic methods in highly fractured intervals. It also aids in the detection of fracture planes not readily visible in the data. For example, in Figure 16 the trace of the steeply dipping fracture below the intersecting fractures at 5135.5 ft (1565.3 m) is not initially apparent; however placement of the flexible sinusoid reveals the fracture trace well below the intersection of the three fractures.

With the amplitude and phase of the sinusoid determined, a wire frame cylindrical projection of the BHTV data over the fracture interval is generated which is mathematically rotated into the plane of the fracture so that the fracture width can be measured perpendicular to the fracture plane (right side of Figure 17). This rotation is required to correct for apparent dip of the fracture. Measuring the width at a number of points around the wellbore where the aperture is smallest minimizes the increase of apparent aperture caused by spalling during drilling and localized erosion. Alteration zones that characteristically surround a fracture are susceptible to damage during drilling. The drill bit causes an initial destruction of the fracture zone at its intersection with the drillhole. This is followed by erosion from fluid flow, reamer tools and logging tool trips. This means that fracture aperture as preserved in the BHTV log is an upper bound to the true aperture of the fracture at some distance away from the borehole. The term "apparent fracture aperture" is used in this text to describe what is, in effect, an average of a number of "minimum width" measurements.

Once the fracture orientation and, if possible, the apparent aperture have been measured the measurement is stored in a text window for further data reduction. The text window (Figure 17) can be edited to add field notes or additional information as to the

quality of the log. The data recorded are depth, dip direction and dip and aperture (if measured). The ASCII data can be saved using the standard Macintosh Save command in the File menu and later plotted in stereographic projection or as a profile to investigate trends in the fractures with depth or trends controlled by fracture width.

Measurement of the dip direction of fractures vertical fractures that intersect a portion of the borehole as a chord (Figure 16, right window) is accomplished by selecting and recording the azimuth of each fracture intersection. The dip direction of this fracture is the midpoint of these two azimuths.

A comprehensive analysis of the natural fractures intersecting the Cajon Pass research well in Southern California is a good example of the application of the fracture analysis software to field data. The Cajon Pass Well has been drilled to investigate the low stress low heat flow paradox along a major plate boundary. The fracture study was completed in order to characterize the macroscopic structure of the crust over the depth interval 1840 to 3450 m (6036.7 to 11,318 ft) (Barton and Zoback, 1990).

Orientations of all macroscopic fractures, corrected for fracture dip are shown in Figure 18 in a lower hemisphere stereographic projection. On the left side the data are presented as poles to fracture planes and on the right side they are presented in a contour diagram of pole densities using spherical Gaussian statistics (after Kamb, 1959). The Kamb method of contouring pole densities calculates the number of standard deviations from a uniform distribution of points on the projection. The contour shading shown in the legend in Figure 18 represents the standard deviation from a random distribution. While there is clearly a random component of fracture orientations, a statistically significant concentration of fractures strikes north-south and dips to the West. The primary concentration of fractures strikes at an azimuth of 175° and dips 63° West. Also shown in Figure 18 is the N60°W local trend of the San Andreas Fault (SAF) and the average orientation of S_{Hmax} determined through the analysis of in-situ wellbore breakouts and hydraulic fractures (N59°E, Shamir and Zoback, 1990). Although the San Andreas Fault is the dominant tectonic feature at this site the majority of the macroscopic fractures in the Cajon Pass well are neither aligned with the San Andreas nor parallel to the direction of maximum horizontal stress as is often assumed (e.g. Engelder, 1982).

The fracture distribution in the Cajon Pass well does not decrease with depth. Figure 19 shows a fracture frequency profile over a subset of the fracture data measured. Aside from the interval from 1940 to 1960 m (6364.8 to 6430.4 ft) of stress-induced wellbore breakouts (Shamir et al., 1988), which contain only a few observable fractures, the total fracture population shows no trend in size or distribution with depth over the logged interval. These results are in contrast with a fracture analysis from an Illinois

drillhole where fracture density and hydraulic conductivity decrease with depth (Haimson and Doe, 1983). Fracture studies of ten wells located in the western Mojave Desert just west of the Cajon Pass well by Seeburger and Zoback (1982) found only a slight decrease of fracture density with depth for most wells studied. They found some wells to have a uniform fracture density distribution while others showed concentrations of fractures at various depths as is the case in the Cajon Pass well.

Where fractures are open along the extent of their intersection with the borehole, apparent fracture aperture could be measured. The double asterisks in the second profile of Figure 19 correspond to zones where the fracture width per meter is greater than 10 cm; the single asterisks to zones with fracture width between 5 and 10 cm. The remaining intervals have nominal apparent aperture per meter. In several intervals with a high frequency of fractures the cumulative width per meter is quite low. However, where the apparent aperture per meter is large there are usually a large number of fractures. Although mechanisms acting to close fractures would be expected to reduce the number of open fractures with increasing depth, the data do not show this trend.

Figure 19 also shows the fracture population correlated with lithology and sonic velocities. The Cajon Pass experiment has provided an ideal complementary data set to examine the acoustic waveform response to fluid-filled fractures. The complete BHTV log and the digital analysis of fracture geometry were used in conjunction with the full waveform sonic data to determine the response to fractures (Barton and Moos, 1988). Note that there is little apparent relationship between fracture density and sonic velocity. A much greater correlation exists between the velocities and the apparent apertures determined from the BHTV logs. The relationship between Stoneley wave amplitude and permeability has been demonstrated by a number of authors (Paillet, 1980; Burnes, et al, 1988). The amplitude of the Stoneley wave is particularly sensitive to the presence of hydraulically conductive fractures intersecting the borehole wall (Paillet and White, 1982; Rosenbaum, 1974), but it is also affected by variations in the borehole diameter and the seismic properties of the rock. The Stoneley arrivals in the sonic waveforms recorded in this interval of the Cajon Pass well (Figure 19) are an excellent example of this response.

Measurements of the orientation, distribution and apparent aperture of macroscopic fractures in the Cajon Pass well are extremely important to the interpretation of other geophysical and core data. Current research into the statistical distribution of fracture aperture, fracture orientation, and fracture spacings are providing insight into the mechanical character of the brittle crust at the Cajon Pass site (Barton and Zoback, 1990).

Correlation of BHTV "Log" Data

Log interpretation has long been the basis for discriminating changes in lithology, fluid content of pore space, structural horizons and general physical properties of rock both for industry exploration and scientific research. Geophysical logs that are generally recorded in a freshly drilled well include the caliper, natural gamma, spectral natural gamma (from which K, U, and Th concentrations can be determined), induction resistivity, neutron porosity, gamma-gamma density, and sonic travel-time. Correlation of these logs and extracted core provides ideal information for physical properties measurements with depth.

BHTV travel time data can be used to generate extremely fine scale "logs" of variations in downhole parameters such as pseudo 4-arm caliper emulation, cumulative cross sectional area and wellbore eccentricity. These profiles may be correlated with dipmeter, full waveform, resistivity, and other diagnostic logs to assess borehole stability and to define permeable zones or lithologic boundaries. The depth resolution of image data is generally much finer than the 0.5 ft depth resolution of geophysical logs, however, digital smoothing or decimation of image data to the scale of conventional logs provides excellent "ground truth" to the complex process of geophysical log analysis.

BHTV data provides information at about 1 cm (0.3 in) intervals whereas typical logging produces a data point for every 15 cm (6 in) of wellbore. For this reason, analog BHTV images are commonly photo-reduced to the scale of log data (5" = 100') before correlations can be made. As mentioned previously interpretation of an analog BHTV image usually involves overlays and tedious drafting. Digital data provides several advantages over analog data for this type of coarse scale data interpretation and correlation with standard logs. The first is the simplicity of scaling with a minimal loss of information. The second advantage is the ease of constructing an interpreted BHTV log. In a coarse scale analysis only the large scale features such as breakout intervals or through-going fractures are required for interpretation. The location of these features can be plotted through interactive thresholding of amplitude and borehole radius where black represents a feature and all other variations in the data have been suppressed into a white background (Figure 20, right profiles). Fractures may also be interactively picked and the interpreted sinusoids plotted. Figure 20 shows standard geophysical logs over the interval 9600 to 9800 ft (2926 m to 2987 m) recorded in the Cajon Pass Research well with the corresponding digitally interpreted section of BHTV data. Major features include the sinusoidal trace of fractures and wellbore breakouts which are represented by discontinuous black zones at 180^{o} azimuths and fractures.

The following preliminary correlation of the analog field data over this interval was made by F. Paillet (written communication, 1988). The continuous interval of wellbore breakouts below depth 9800 ft (2987 m) is evident on the caliper log (Figure 20, track 4, curve 1) and the elongation of the borehole is very pronounced in the x-y caliper log (Figure 20, track 1, curves 1 and 2). The fracture zone just below 9700 ft (2956.6 m) has caused a marked decrease in both the LLS and LLD resistivity curves (Figure 20, track 2, curves 1 and 2) however this zone has a minimal effect on the neutron porosity logs (Figure 20, track 4, curves 2 and 3). Severe breakouts at 9665 ft (2945.9 m) cause an anomaly in the caliper (Figure 20, track 4, curve 1) and density logs (Figure 20, track 3, curve 3). Between 9600 and 9650 ft (2926 and 2941 m) breakouts are interrupted by small fractures; breakouts often terminate at the intersection of a fracture.

It is interesting to compare the digital interpretation of BHTV logs with an "interpreted section" made from the black and white Polaroid field logs by a scientist who is very familiar with BHTV data and very experienced in log interpretation. In addition, this particular expert has artistic talents useful to this sort of data reduction. In Figure 20, the far right window is the manual interpretation of the interval 9400 to 9600 ft (2865 to 2926 m) in the Cajon Pass well, sketched by F. Paillet (written communication, 1988). Thick lines represent the interpreted trace of larger fractures visible in the analog records and thin lines the trace of smaller fractures. Breakouts are again represented by vertical black bands. Fractures located in the digital counterpart to the interpreted interval compares well with the manually picked fractures. Breakouts reduce with good precision and correlate very well with the manually interpreted section. The most logical use of the digital interpretation is to provide an easily generated, accurate base plot either for further computer based interpretation or manual interpretation. Scientists that lack substantial experience with interpreting BHTV data or general log interpretation (or artistic capabilities) can produce more reliable interpretations with the help of the digital BHTV system.

BHTV Generated "Logs"

Caliper tools usually have two to four mechanical arms that measure the borehole diameter with depth. The BHTV log can be thought of as having several hundred "arms" which provides data at a scale that is 15 times finer than the standard caliper log. In order to emulate the HDT Dipmeter tool, the horizontal and vertical resolution of the BHTV data must be made comparable to that of the HDT dipmeter pad. Performing a horizontal 15 point median filter is generally sufficient to mimic the HDT Dipmeter pad width. The maximum value in each scan of the filtered data then provides one radius and azimuth of the long axis caliper pair. The orthogonal values provide the short axis caliper pair. Averaging

successive caliper values with depth provides the correct vertical adjustment for comparison with the HDT dipmeter tool. Figure 21a represents the fit of the BHTV generated "four arm" caliper to a typical scan of BHTV data and 21b the fit over an interval of wellbore breakouts measured from the same well. Black represents the data scan and gray the measured four arm radii. Caliper information in this form can be easily correlated with other log data and with dipmeter data. As is the case with dipmeter data the caliper data can be used to discriminate between breakout zones, washout zones, zones of key seating and perfectly in-gauge zones (Plumb and Hickman, 1985). The long caliper arm measured in this way in many cases corresponds to the direction of minimum horizontal principal stress and in such a log provides a rapid method for breakout orientation analysis with depth. The left window in Figure 22 shows the image data for a 12 ft (3.7 m) interval of wellbore breakouts in the Auburn Geothermal Well, New York. The adjacent profile shows the emulation of the 4 arm dipmeter tool over this depth interval. The scatter plot indicates the orientation wellbore breakouts determined from this analysis.

There are a variety of causes for a non-circular borehole and wellbore breakouts may or may not coincide with the overall ellipticity of the borehole. For example, ellipticity can be drilling induced where the bit has tended to move up dip during drilling. The borehole wall may preferentially spall or washout in response to in situ stresses. A least-squares fit of an ellipse to the BHTV scans is used to measure the eccentricity of the borehole. The algorithm fits an ellipse to a field of points after each radius value is transformed to Cartesian x, y space from the polar r, θ pair by $x = r \cos \theta$, $y = r \sin \theta$. The angle of the ellipse is given by:

$$\phi = \frac{1}{2} \tan^{-1} \frac{\Sigma xy}{\Sigma x^2 - \Sigma y^2} \qquad (4)$$

A least-squares algorithm is used to determine the major, a, and minor, b, axes of the ellipse. From the equation of an ellipse:

$$b^2x^2 + a^2y^2 = a^2b^2 \qquad (5)$$

we have:

$$y^2 = b^2\left(1 - \frac{x^2}{a^2}\right) \qquad (6)$$

or

$$\hat{Y}_i = \left[b^2\left(1 - \frac{X_i^2}{a^2}\right)\right]^{1/2} \qquad (7)$$

where $\hat{Y}_i$ is the estimated value of Y_i at specified values of X_i.

We want to have $\sum_{i=1}^{n} Y_i^2 = (\hat{Y}_i - Y_i^2) = \text{minimum:}$

$$\sum_{i=1}^{n} Y_i^2 = b^2 n - \frac{b^2}{a^2} \sum_{i=1}^{n} X_i^2 \qquad (8)$$

Setting $b = b_0$ and $b_1 = b/a$ we have:

$$\sum_{i=1}^{n} Y_i^2 = b_0^2 n - b_1^2 \sum_{i=1}^{n} X_i^2 \qquad (9)$$

$$\sum_{i=1}^{n} X_i^2 Y_i^2 = b_0^2 n \sum_{i=1}^{n} X_i^2 - b_1^2 \sum_{i=1}^{n} X_i^4 \qquad (10)$$

Equations 9 and 10 are then inverted to determine the unknown values of b_1 and b_0. Generally only 20 equally spaced data points are required to accurately determine the shape of the ellipse. The percent eccentricity of the ellipse, defined as $\frac{a-b}{(a+b)/2}$, is calculated for each scan. Borehole televiewer data is capable of resolving borehole ellipticity in much finer detail than conventional caliper logs. Without some knowledge of borehole ellipticity the separation between caliper curves (C1 and C2 in standard HDT presentation) may be erroneously interpreted as wellbore breakouts.

Another profile computed with the BHTV travel time data is borehole the cross sectional area. The log of borehole cross sectional area is calculated by integrating adjacent triangles defined by the travel time values and the center of the borehole. Borehole irregularities, washouts or key seats for example, are indicated by large fluctuations in this log. A profile of cumulative cross sectional area with depth is also available. These logs are important for the determination of wellbore stability. A featureless borehole will have a smooth slope in its cumulative profile of cross sectional area whereas breaks in slope may indicate borehole failure.

The amplitudes of reflectivity values are used to generate a reflectivity log as an aid in the detection of lithologic and structural boundaries. Acoustic reflectivity of the borehole wall as measured by the BHTV tool has incorporated the effects of the impedance contrast from various rock types and the borehole fluid along with the effects of energy scattering from irregularities in the borehole wall. The true reflection amplitude is proportional to the

reflection coefficient at the borehole wall plus an unknown variation in amplitude due to scattering (the angle between the beam and the reflecting surface), thus no quantitative value of the reflectivity can be associated with a particular lithology. Because of these combined effects however, the BHTV image of the amplitude of the reflected energy often shows more detail than does the surface topography. This is particularly true for logged intervals of sedimentary rock where rock properties vary over small distances.

To determine the reflectivity value to represent a given depth interval a histogram of the amplitude values is computed for each scan. A single scan in the BHTV data has values that represent the reflectivity of unperturbed rock as well as reflectivity values associated with structural or erosional features (e.g. fractures, tool reamer marks). Interactive thresholding is used to determine the cutoff reflectivity value that best isolates the particular feature of interest. For example, to sample only the intact rock, a threshold determined cutoff reflectivity value is used above which histogram bins will be used to compute the mode value of the amplitude for each data scan as a single representative value. Figure 23 shows the results of this statistical approach to an interval containing the contact between a basement marble formation and an overlying sandstone unit at 5051 ft (1539.5 m) in the Auburn Well, New York. The marble has a very different reflectivity character that the overlying sediment and the contact can be more easily picked in the "log" plot than in the image itself.

Reflectivity logs can be used for correlation with companion log data. Sharp decreases in reflectivity track breakout zones exactly and the decrease has been found to be proportional to the width of the breakout (Zoback and Moos, 1988). Reflectivity logs prove to be quite useful for correlation with other log data to isolate borehole features such as breakouts and fractures. Using reflectivity logs generated from the analysis of BHTV data Zoback and Moos (1988) found that low reflectivity values correlate with breakout zones in the Moodus Research Well located in New York state. Reflectivity profiles used in conjunction with the BHTV caliper log are useful for discriminating between natural through going fractures and wellbore breakouts. A sharp low reflectivity response associated with a strong kick in the eccentricity log characterizes a natural fracture whereas low reflectivity values over a finite length of the borehole associated with a consistent azimuth of the major elliptical axis generally represents breakout zones.

SOFTWARE IMPLEMENTATION

As discussed previously, user interface consistency among application programs is an important factor in the ease of use of Macintosh computers. To help achieve the desired consistency in BHTVImage, the program was implemented using an Apple product called MacApp, in whose original development one of us played a part. MacApp is a so-called "object-oriented framework", i.e., a "generic" application that defines standard "objects" like windows and views. Any desired Macintosh application can be derived from MacApp by describing in program code only the differences between that application and the generic one. The resulting program achieves consistency with other Macintosh applications without special effort on the part of the programmer.

MacApp, as well as the bulk of the BHTV analysis program, is written in the object-oriented language Object Pascal. Object Pascal is an extension of the Pascal language that provides a record-like structure type called an "object type". One type of object can be defined as being a subtype of another type. If type "dog" is defined as a subtype of "mammal", it means that the characteristics of dogs are generally the same as those of mammals. Only differences need be specified. One must specify that dogs wag their tails and bark, but one need not specify that dogs breathe--that characteristic is inherited from mammals.

MacApp provides a type of object called a "document." A document is a file containing text, graphic, and/or image data. The definition of type document specifies attributes that every document must have, e.g., a file name. The definition also defines operations that can apply to any document, such as "opening" it for examination and possible change, "printing" it onto paper, and "saving" changes to the disk.

BHTVImage, in turn, defines an object type "BHTVDocument" that is a subtype of the standard MacApp document. A BHTVDocument is like the generic document except it sports additional attributes like well name and fluid velocity, and it defines additional operations such as the ability to convert a travel time measurement to a radius.

MacApp provides another type of object called a "view", used to display part or all of a document in a form desired by the user. BHTVImage also defines three major types of views: the unwrapped view, which displays false-color image data; the profile view, which can graph a profile of one parameter sampled at each depth in a range; and the plot view, which can graph data sampled at numerous places at each depth. BHTVImage further defines several types of plot views, e.g., the travel time histogram, the polar cross section, the Cartesian cross section, and the 3-D cylindrical projection. A cross section view

inherits the characteristics of a plot view and adds its own. A plot view *inherits* the characteristics of a generic view and adds its own.

The document and the view are the two most important object types defined by MacApp. The third most important object is called the "command". The generic command provides generic ways of dealing with doing the command, undoing it, and redoing it. If the command is issued by mouse action (like drawing a box in MacDraw), then the generic command also provides generic ways of tracking the movements of the mouse and giving the user an advance look at what will result when the mouse action terminates. In BHTVImage, subtypes of the generic command object are defined to support the following user actions, among others: changing a threshold value through a sliding scale; changing the hue of a palette color; cutting selected scans from the data file.

Certain BHTV analysis subroutines are written in the language C. The Macintosh Programmer's Workshop, a suite of software development tools, allows modules written in different languages (e.g., Pascal, C, Fortran, and Assembler) to be linked together into a single program and for procedure calls to be made between the modules.

CONCLUSIONS

The analysis of image data requires a high level of interactive manipulation by the analyst. Various features need to be observed in an optimal view in order to detect subtle features and the analyst must be able to make decisions as the analysis proceeds. To meet these goals for the image analysis of borehole televiewer data we have taken advantage of the interactive user interface of the Apple, Inc. Macintosh II computer. In addition, in order to conform to the Macintosh user interface standards we used an Apple, Inc. product called MacApp; a developer's tool that provides easy programming access to the windows, menus, and dialog boxes of the Macintosh user interface. The program design defines a set of tools specific to borehole cylindrical geometry and to the particular features that are imaged by and can be quantified by BHTV data (e.g. fractures, wellbore breakouts). The program also provides a base for experimentation with new techniques to improve data quality, develop new measurement techniques and to explore unusual features encountered in a particular data set.

BHTVImage has been used as the primary analysis tool for BHTV data recorded in the Cajon Pass scientific research well in southern California and is also being used at the KTB ultradeep well site in Germany for the analysis of wellbore breakouts and the evaluation of wellbore stability.

Although the software is specific to BHTV data the analysis tools extend to other types of image data, for example the Schlumberger, Inc., Formation Microscanner (FMS). The human interface approach, however, extends beyond image analysis programs. Geophysicists often encounter data that is voluminous and complex. They require the freedom to pursue various paths of reasoning and curiosity in order to make scientific discoveries without the burden of extensive computer programming at each turn in the path. One of the ways to achieve this freedom is to develop software tools that permit interaction with the data and minimize interaction with the computer. Our current work includes the development of similar analysis tools for the analysis of FMS image data and standard geophysical logs.

ACKNOWLEDGMENTS

The authors would like to thank Apple Computer, Inc. for their cooperation in the development of BHTVImage. This work was supported in part by the Continental Lithosphere Program of the National Science Foundation through DOSECC, by the Kontinentales Tiefbohrprogramm of the Federal Republic of Germany, and by the contributors to the Stanford Rock Physics and borehole Geophysics Project.

REFERENCES

Barton, C.A. and Zoback, M.D., 1990. Self-similar distribution and properties of macroscopic fractures at depth in crystalline rock in the Cajon Pass scientific drillhole, Journ. Geophy. Res., in press.

Barton , C.A., 1988, Development of in situ stress measurement techniques for deep drillholes, Ph.D. Thesis, Stanford University.

Barton, C.A., Zoback, M.D. and Burns, K.L., 1988, In situ stress orientation and magnitude at the Fenton Geothermal site, New Mexico, determined from wellbore breakouts, Geophy., Res. Let, 15, 467-470.

Barton, C.A. and Moos D., 1988, Analysis of macroscopic fractures in the Cajon Pass Scientific Drillhole over the interval 1829 - 2115 meters, Geophy. Res. Let., 15, 9, 1013-1016.

Broding, R. A., 1982. Volumetric scanning well logging: The Log Analyst, 23, 1, 14-19.

Burnes, D.R., Cheng, C.H., Schmitt, D.P. and Toksoz, M.N. 1988. Permeability estimation from full waveform acoustic logging data, The Log Analyst, 29, 112-122.

Engelder, T., 1982. Is there a genetic relationship between selected regional joints and contemporary stress within the lithosphere of North America?, Tectonophysics, 1, 161-177.

Faraguna, J.K., Chace, D.M. and Schmidt, M.G., 1989. An improved borehole televiewer system — image acquisition analysis and integration: S.P.W.L.A. Annual Logging Symp., 30th, Denver, CO., Trans, Paper UU.

Fehler, M., House, L., and Kaieda, H., 1986, Seismic monitoring of hydraulic fracturing, 27th U.S. Symposium on Rock Mechanics, Univ. of Alabama, 606-613.

Georgi, D. T., 1985, Geometrical aspects of borehole televiewer images. SPWLA Logging Symposium Transactions, Paper 1-C.

Haimson, B. C. and Doe, T.W., 1983, State of stress, permeability and fractures in the Precambrian granite of northern Illinois, Journ. Geophy. Res., 88, 7355-7371.

Hinz, K. and Schepers, R., 1985, SABIS - The digital version of the borehole televiewer, Eighth European Formation Evaluation Symposium.

Kamb, W.B., Ice petrofabric observations from Blue Glacier, Washington, in relation to theory and experiment, J. Geophy. Res., 64, 1891-1910, 1959.

Lysne, P., 1986, Determination of borehole shape by inversion of televiewer data, The Log Analyst, 26, 64-71.

Paillet, F. L., 1980, Acoustic propagation in the vicinity of fractures which intersect a fluid filled borehole, SPWLA, 21st Ann. Log. Symp., Paper D.

Paillet, F. L. and White J. E., 1982, Acoustic modes of propagation in the borehole and their relationship to rock properties: Geophysics, 47, 8, 1215-1228.

Pasternack, E.S. and and Goodwill, W.P., 1983. Applications of digitial borehole televiewer logging: S.P.W.L.A. Annual Logging Symposeum, 25th, Calgary, Canada, Trans., Paper C.

Plumb, R.A. and Hickman, S.H., 1985, Stress induced borehole elongation: A comparison between the four-arm dipmeter and the borehole televiewer in the Auburn Geothermal well, Journ. Geoph. Res., 90, B7, 5513-5521.

Rambow, F.H.K., 1984. The borehole televiewer — some field examples: S.P.W.L.A. Annual/ Logging Symp, 25th, New Orleans, La., Trans., paper C.

Richards, J.A., Remote sensing digital image analysis, Springer-Verlag, New York, 1986.

Rosenbaum, J.H., 1974, Synthetic microseismograms: logging in porous formations, Geophysics, 39,14-32.

Seeberger, D.A. and Zoback, M.D. 1982, The distribution of natural fractures and joints at depth in crystalline rock, Journ. Geoph. Res., 87, 5517-5534, 1982.

Shamir, G. and Zoback, M.D., 1990, In situ stress orientation near the San Andreas fault: Preliminary results to 2.1 km depth from the Cajon Pass Scientific Drillhole, Journ. Geophy. Res, in press.

Taylor, T.J., 1983. Interpretation and application of borehole televiewer surveys: S.P. W.L.A. Annual Logging Symp., 24th, Calgary, Canada, Transactions, Paper QQ.

Wiley, R. 1980. Borehole televiewer — revisited: S.P.W.L.A. Annual Logging Symp, 21st, Lafayette, La., Trans., Paper HH.

Wong, S.A., Startzman, R.A., and Kuo, T-B, 1989. Enhancing borehole image data on a high-resolution PC: Soc. Pet. Eng, SPE 19124, 37-48.

Zemanek, J., Glenn, E.E., Norton, L.J. and Caldwell, R.L., 1970, Formation evaluation by inspection with the borehole televiewer. Geophysics, 35, 254-269.

Zoback, M.D., Moos, D., Mastin, L., Anderson, R.N., 1985, Wellbore breakouts and in situ stress, J. Geophys. Res., 90, 5523-5530.

Zoback, M.D. and Moos, D.,1988, In situ stress, natural fracture and sonic measurements in the Moodus, Connecticut scientific research well, report prepared for Woodword-Clyde Consultants, Wayne, N.J.

Table I

Data Attribute	Definition
Well Name	Well identification used as title for graphics output
Well Location	Well location used as title for graphics output
Log Date	Date BHTV data were recorded
Mag Dec	Magnetic declination at site in degrees east of north
Marker	Azimuth correction for data collected in marker mode
Deviation	Borehole deviation in degrees
Max Depth	Bottom depth of digitized interval
Min Depth	Top depth of digitized interval
Tool Spec	Calibration adjustment
Tool Units	Units of the calibration adjustment
Fluid Vel	Velocity of the borehole fluid during logging
Vel Units	Units of the fluid velocity
Ddelay	Time delay for initiation of digitization in μs
Tool Offset	Transit time from the transducer to its housing in μs
Samprt	Sample rate in samples/μs
Window	Sampling window length in μs
Samples	Number of samples digitized for each pulse
Max TT	Maximum recorded travel time
Max AMP	Maximum recorded amplitude of the reflected pulse
Min TT	Minimum recorded travel time
Min AMP	Minimum recorded amplitude of the reflected pulse
Cutoff TT	Array of histogram equalization bins for travel time
Cutoff AMP	Array of histogram equalization bins for amplitude
Width	Number of pulses per scan
Height	Total number of scans (full revolutions) in the data file

FIGURE CAPTIANS

Fig. 1. (a) Schematic diagram of the acoustic mechanism of the borehole televiewer. (b) Analog wave train of the televiewer signal.

Fig. 2. Intersection of a plane with a cylinder and the effective sinusoidal curve on the 2-D unwrapped cylindrical surface (from Zemanek, et al., 1970).

Fig. 3. Standard unwrapped 360° images of the borehole wall. Vertical axis is depth, horizontal axis is azimuth, and color represents the amplitude of the reflected pulse (left window) or the borehole radius (right window).

Fig. 4. Highlighting in 2-D view (left window) over a cross bedded interval of BHTV data recorded in a Gulf Coast well indicates user selection of the image data for rendering 3-D projections. 3-D projection where surface color represents the amplitude value (middle window) and 3-D projection in black and white (right window) where differences in weathering of the beds is apparent.

Fig. 5. The right window is an unwrapped view of borehole radius over a 14 ft interval of breakouts in the Cajon Pass well. The left window shows data scans in polar cross section and the interactive analysis of breakout azimuth and width for this data.

Fig. 6. Top window is a cross plot of the reflectivity values (x-axis) versus traveltime values (y-axis) over an interval in the Cajon Pass well where the BHTV tool was off-center in the borehole. The bottom window is the cross plot over the same interval after the data have been corrected for off-center effects.

Fig. 7. An example of the effects of histogram equalization. The left display shows the standard linear color distribution and the right panel the equalized color distribution. Note that the details of the cross bedding are enhanced at depth 7380.5 ft using the equalized color scale.

Fig. 8. Right window is the amplitude of the reflected energy and the left window the borehole radius where cutoff threshold levels have been used to suppress all data except borehole features.

Fig. 9. Right window shows unedited BHTV data recorded in HOLE 504B located in the East Pacific Rise, left window shows the results of visual editing where breakouts are now visible in the data centered at azimuths 100° and 280° between depths 6,406 and 6,401 ft.

Fig. 10. The possible raypaths for the BHTV pulse for circular and elliptical boreholes with centralized and off-centered tools (after Georgi, 1985).

Fig. 11. Workstation screen showing the interactive data correction of borehole geometric effects. Upper left polar plot shows original data scan and corrected scan of data. Histograms of the original travel time data (yellow) and the corrected data are shown in the upper right plot. The lower plot represents the original data and the corrected data in cartesian coordinates where the x axis is azimuth and the y axis is radius.

Fig. 12. Geometry of the correction of BHTV data for the effects of an off-centered tool in a circular borehole.

Fig. 13. Polar cross sections are sample scans of the synthetic data (black) and data corrected for the effects of an off-center tool in an elliptical borehole (gray). The cross hairs mark the center position for each scan.

Fig. 14. Schematic representation of the breakout process showing the angle of breakout initiation ϕ_b. Also shown is BHTV data over a breakout interval where polar cross sections delineate the breakout shape.The radial lines indicate the picks of breakout width. Breakout azimuth is the bisector of this angle.

Fig. 15. (a) Histogram of breakout azimuths over a 262 m interval in the EE-3 well of the Fenton Geothermal Field. (b) Histogram of breakout widths over the same 262 m interval.

Fig. 16. Left window shows intersecting fractures at depth 5135.5 ft in the Auburn Geothermal well, New York. White curve represents the interactive fit to a steeply dipping fracture. Right window is an example of data recorded over a complex fracture zone where fractures are not perfectly planar in a well located near Anza, California.

Fig. 17. Interactive fit of a flexible sinusoid to a shallow dipping fracture at depth 3321 m in the Cajon Pass research well is shown in the left window. In the right window is the 3-D cylindrical image of the fracture plane.

Fig. 18. (a) Lower hemisphere equal area projection of poles to fracture planes over the interval 1829 to 3454 m in the Cajon Pass reserach well. (b) Kamb contours of the poles to fracture planes over the same interval. Also shown is the orientations of the San Andreas Fault (SAF) and the principal stress directions determined from wellbore breakout and hydraulic fracturing experiments in the well.

Fig. 19. Lithology, fracture density, apparent aperture, sonic velocities and filtered sonic waveforms over the interval 1829 to 2115 m in the Cajon Pass research well.

Fig. 20. Standard Schlumberger logs over the interval 9600 to 9800 ft in the Cajon Pass research well correlated with BHTV data recorded over the same interval. The BHTV data have been both digitally and manually interpreted.

Fig. 21. (a) Black represents the data scan and gray the "four arm" caliper measurement for a typical scan of data. (b) Black represents the data scan and gray the "four arm" caliper measurement over an interval of wellbore breakouts. (c) Black represents the data scan and gray the fit of an ellipse to a typical scan of data. The major axis of the ellipse is shown for reference. (d) Black represents the BHTV data scan and gray the fit of an ellipse over an interval where breakouts are evident.

Fig. 22. Caliper analysis over a 30 ft interval of wellbore breakouts in the Auburn Geothermal well, New York.

Fig. 23. Reflectivity log over the contact between the basement marble formation and the Potsdam sandstone from data recorded in the Auburn Geothermal Well, New York.

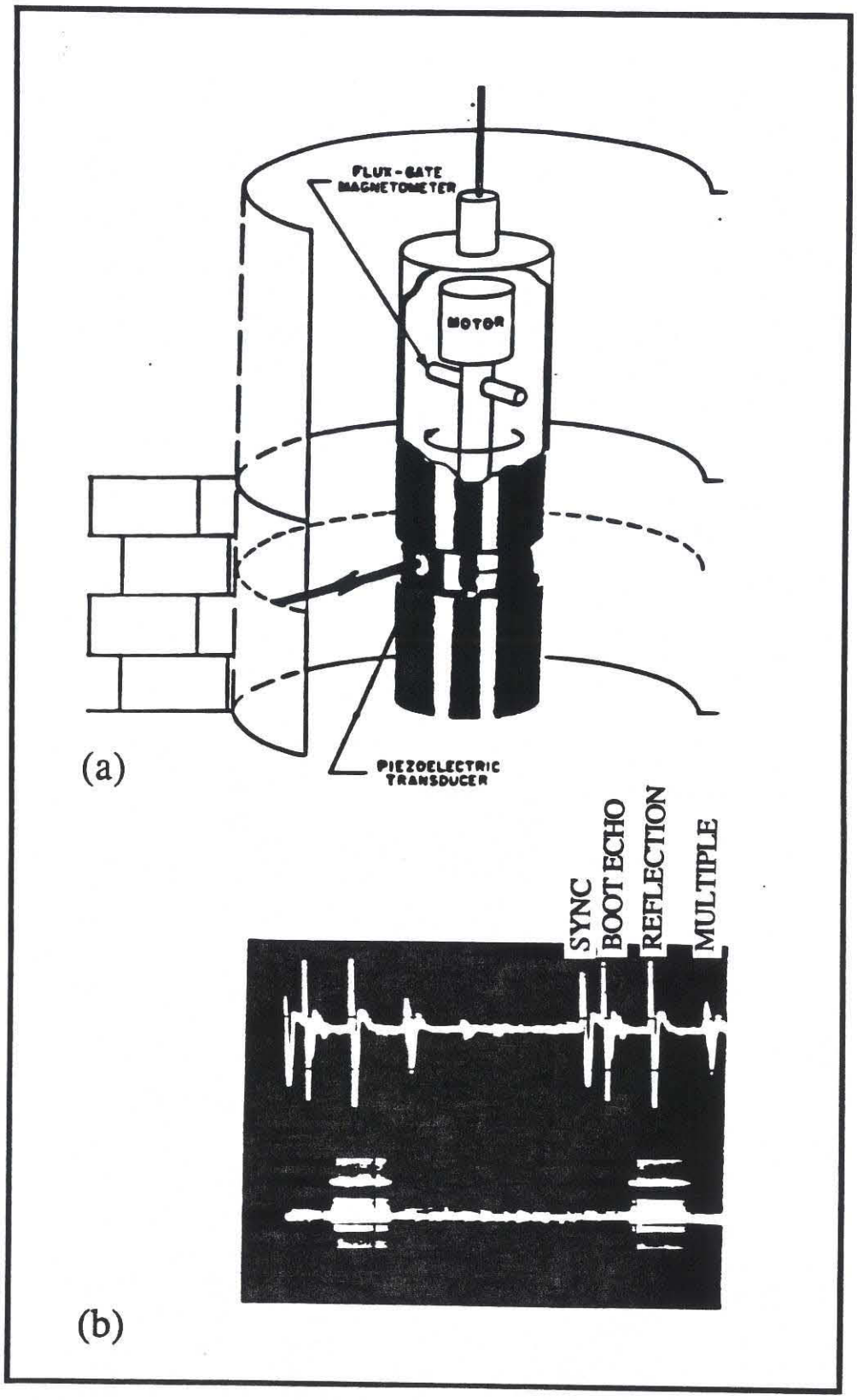
FLUX-GATE MAGNETOMETER
MOTOR
PIEZOELECTRIC TRANSDUCER
(a)
SYNC
BOOT ECHO
REFLECTION
MULTIPLE
(b)

Figure 1

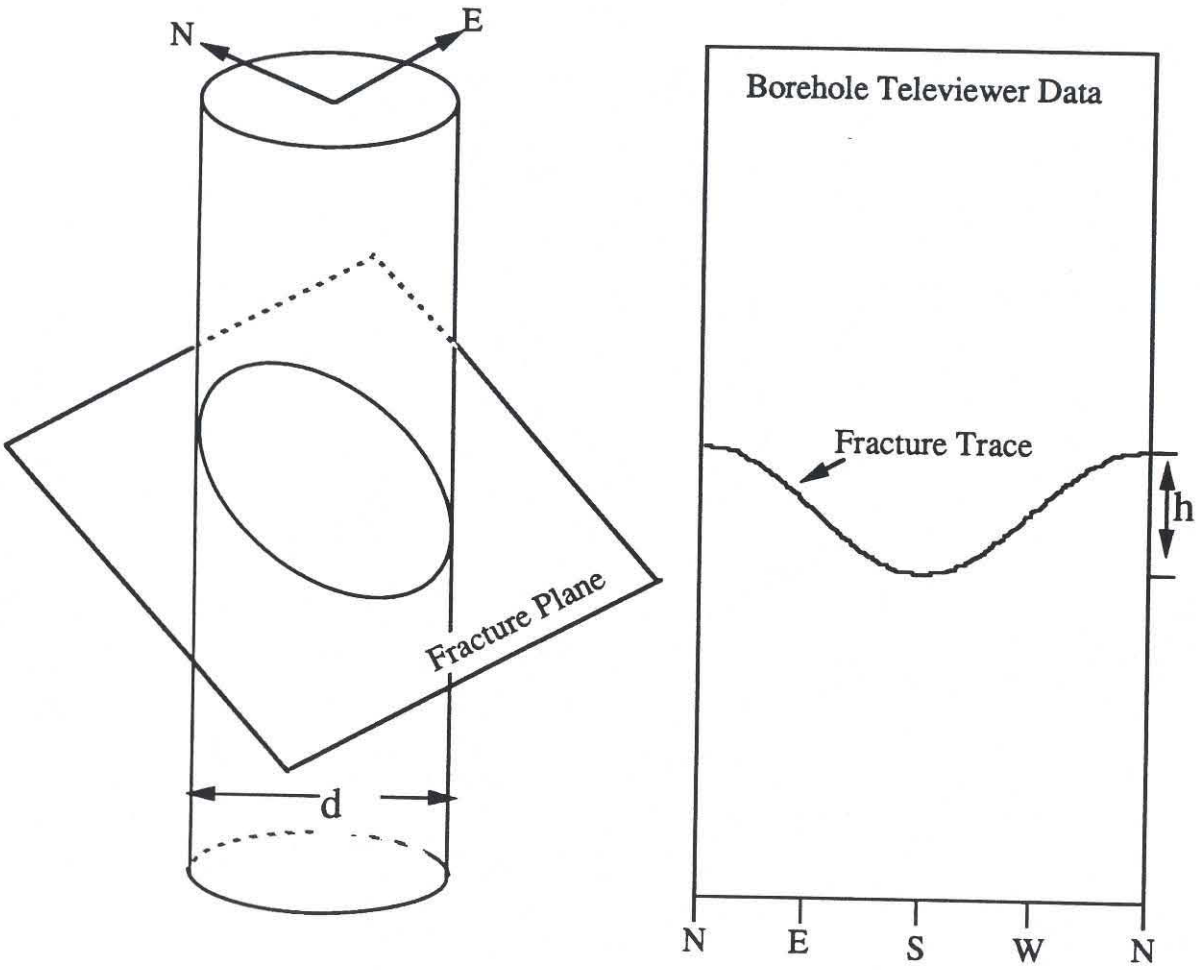
N
E
Fracture Plane
d
Borehole Televiewer Data
Fracture Trace
h
N
E
S
W
N

Figure 2

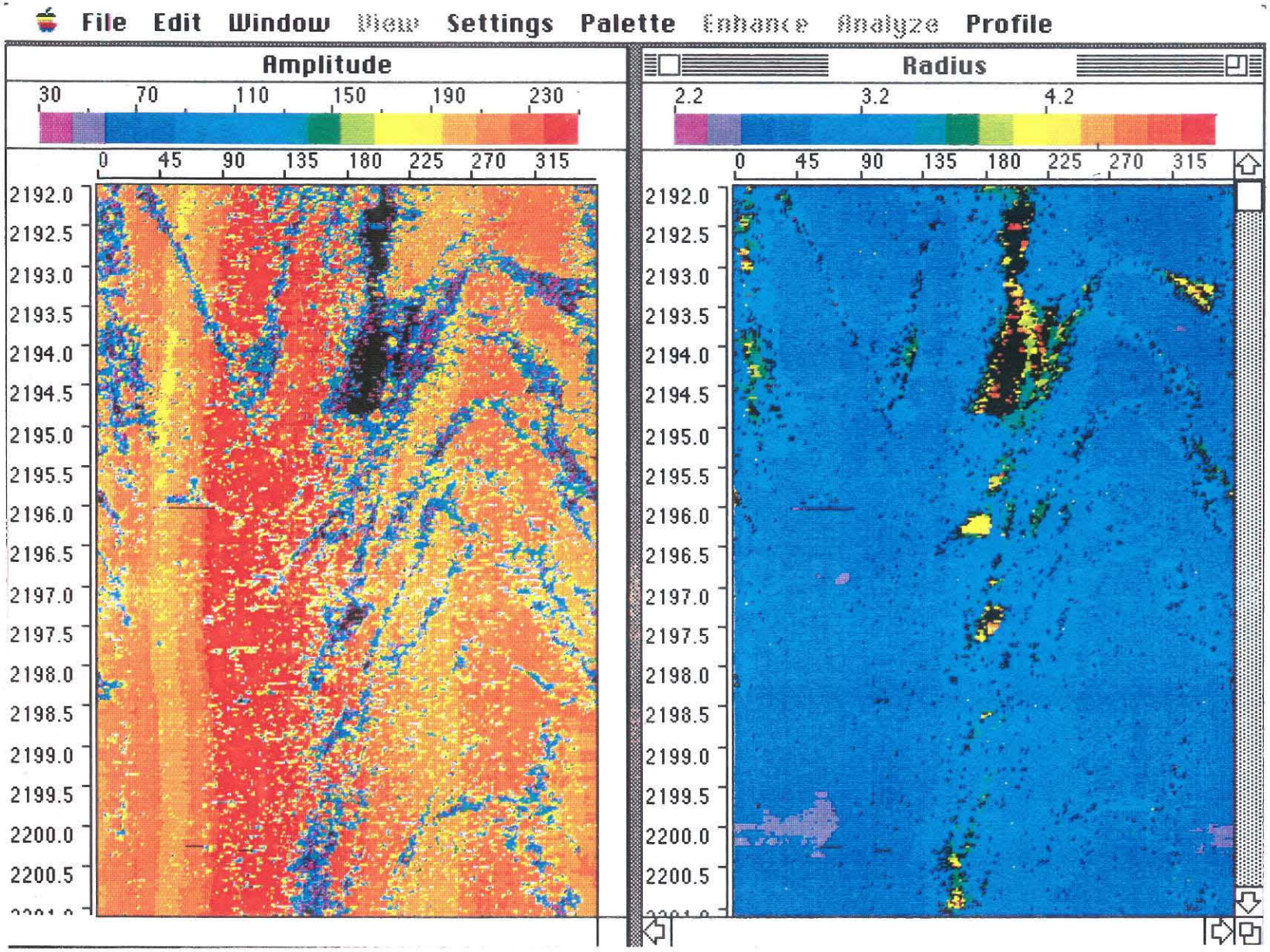
File Edit Window View Settings Palette Enhance Analyze Profile
Amplitude
30 70 110 150 190 230
0 45 90 135 180 225 270 315
2192.0 2192.5 2193.0 2193.5 2194.0 2194.5 2195.0 2195.5 2196.0 2196.5 2197.0 2197.5 2198.0 2198.5 2199.0 2199.5 2200.0 2200.5
Radius
2.2 3.2 4.2
0 45 90 135 180 225 270 315
2192.0 2192.5 2193.0 2193.5 2194.0 2194.5 2195.0 2195.5 2196.0 2196.5 2197.0 2197.5 2198.0 2198.5 2199.0 2199.5 2200.0 2200.5

Figure 3

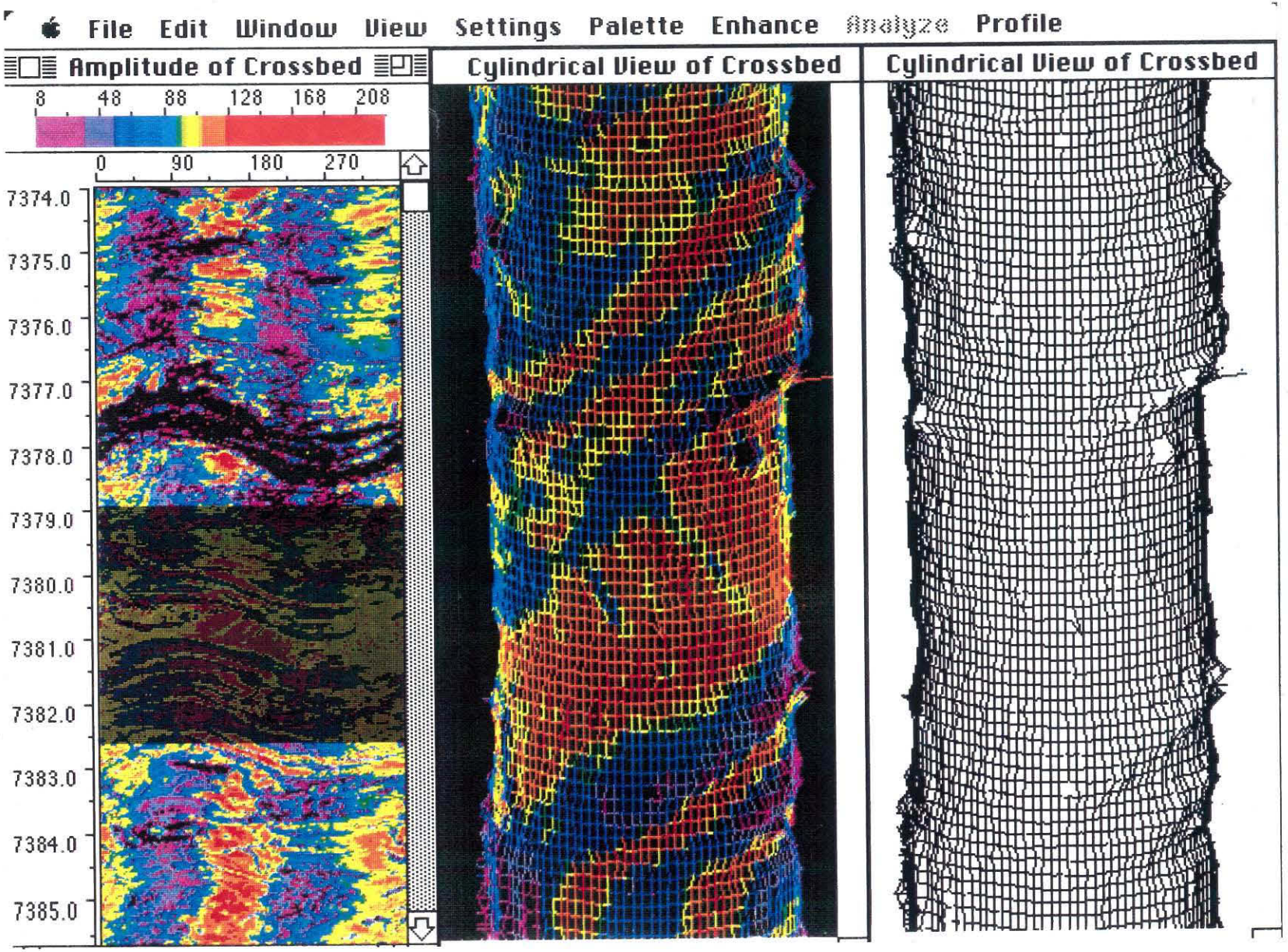
File Edit Window View Settings Palette Enhance Analyze Profile
Amplitude of Crossbed
8 48 88 128 168 208
0 90 180 270
7374.0
7375.0
7376.0
7377.0
7378.0
7379.0
7380.0
7381.0
7382.0
7383.0
7384.0
7385.0
Cylindrical View of Crossbed
Cylindrical View of Crossbed

Figure 4

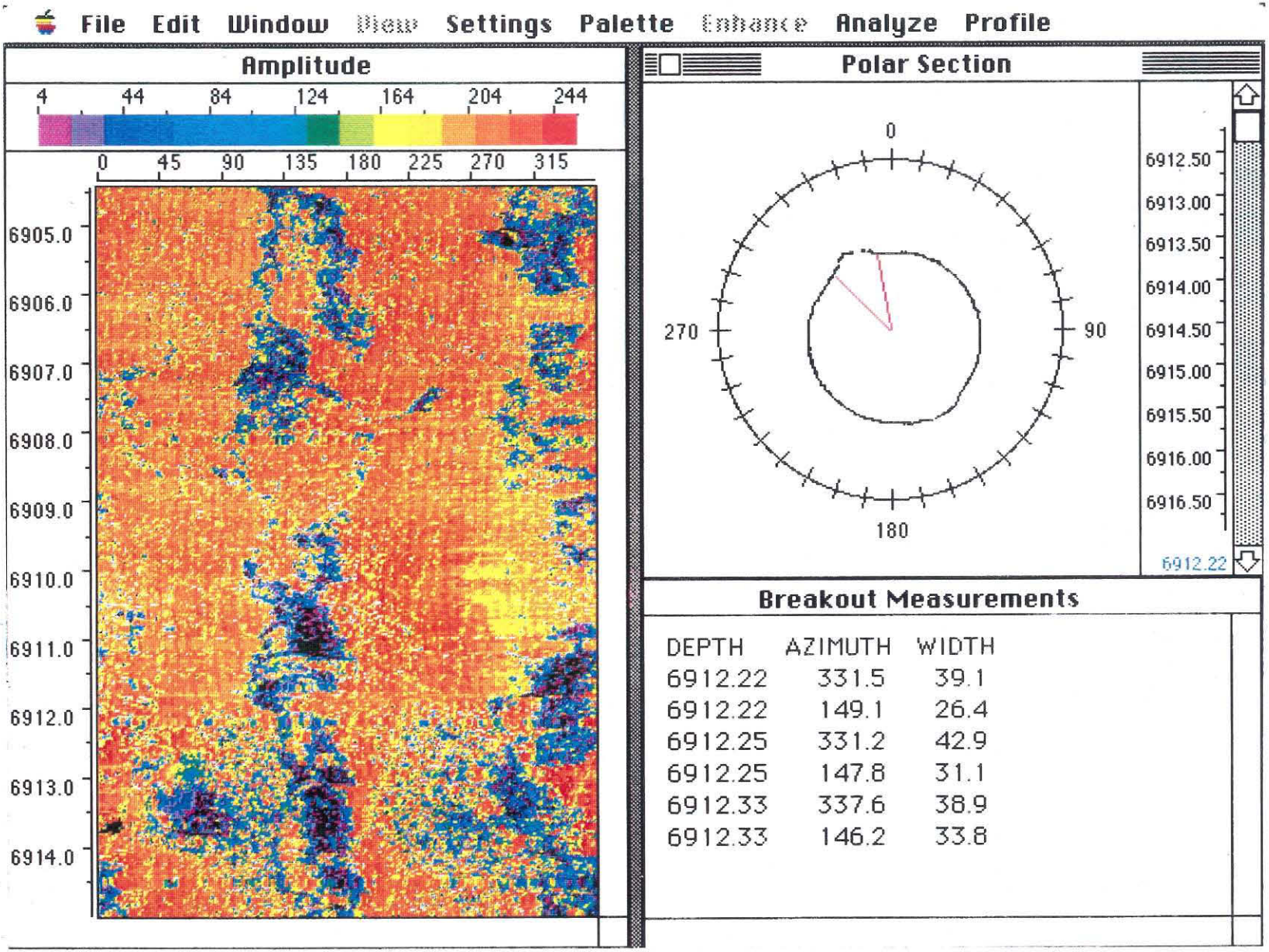
File Edit Window View Settings Palette Enhance Analyze Profile
Amplitude
4 44 84 124 164 204 244
0 45 90 135 180 225 270 315
6905.0
6906.0
6907.0
6908.0
6909.0
6910.0
6911.0
6912.0
6913.0
6914.0
Polar Section
0
90
180
270
6912.50
6913.00
6913.50
6914.00
6914.50
6915.00
6915.50
6916.00
6916.50
6912.22
Breakout Measurements
DEPTH AZIMUTH WIDTH
6912.22 331.5 39.1
6912.22 149.1 26.4
6912.25 331.2 42.9
6912.25 147.8 31.1
6912.33 337.6 38.9
6912.33 146.2 33.8

Figure 5

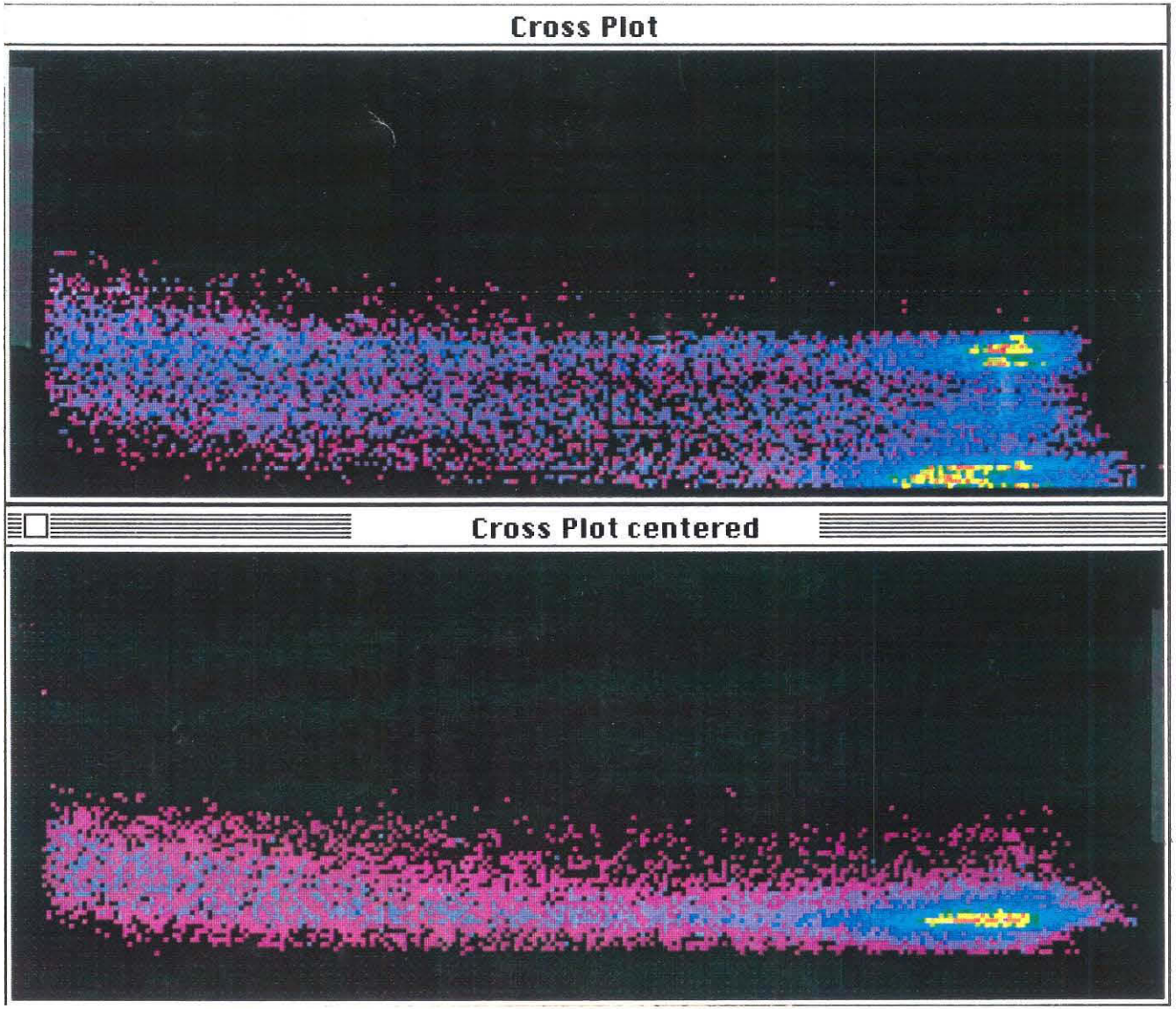

Figure 6

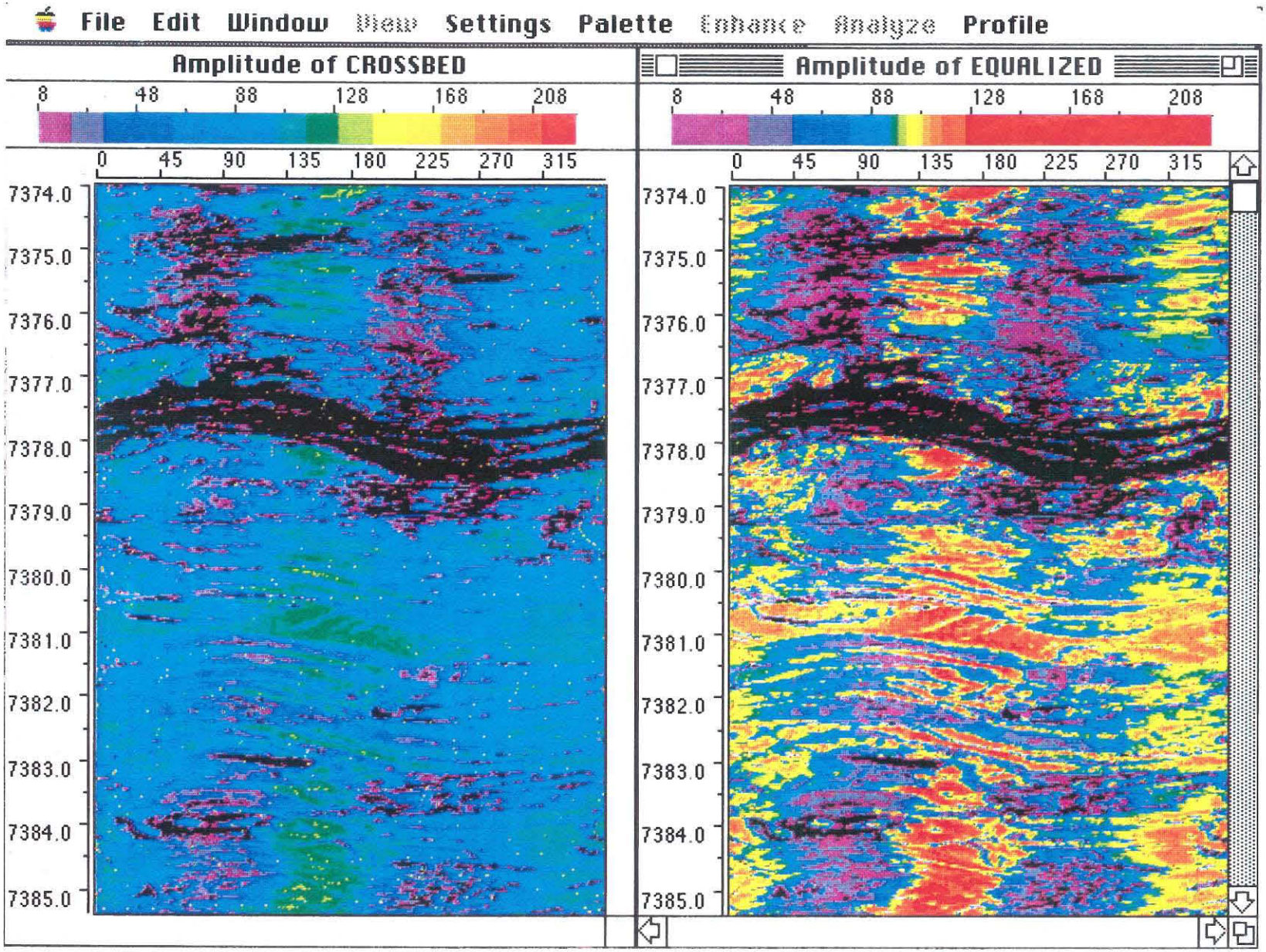
File Edit Window View Settings Palette Enhance Analyze Profile
Amplitude of CROSSBED
8 48 88 128 168 208
0 45 90 135 180 225 270 315
7374.0 7375.0 7376.0 7377.0 7378.0 7379.0 7380.0 7381.0 7382.0 7383.0 7384.0 7385.0
Amplitude of EQUALIZED
8 48 88 128 168 208
0 45 90 135 180 225 270 315
7374.0 7375.0 7376.0 7377.0 7378.0 7379.0 7380.0 7381.0 7382.0 7383.0 7384.0 7385.0

Figure 7

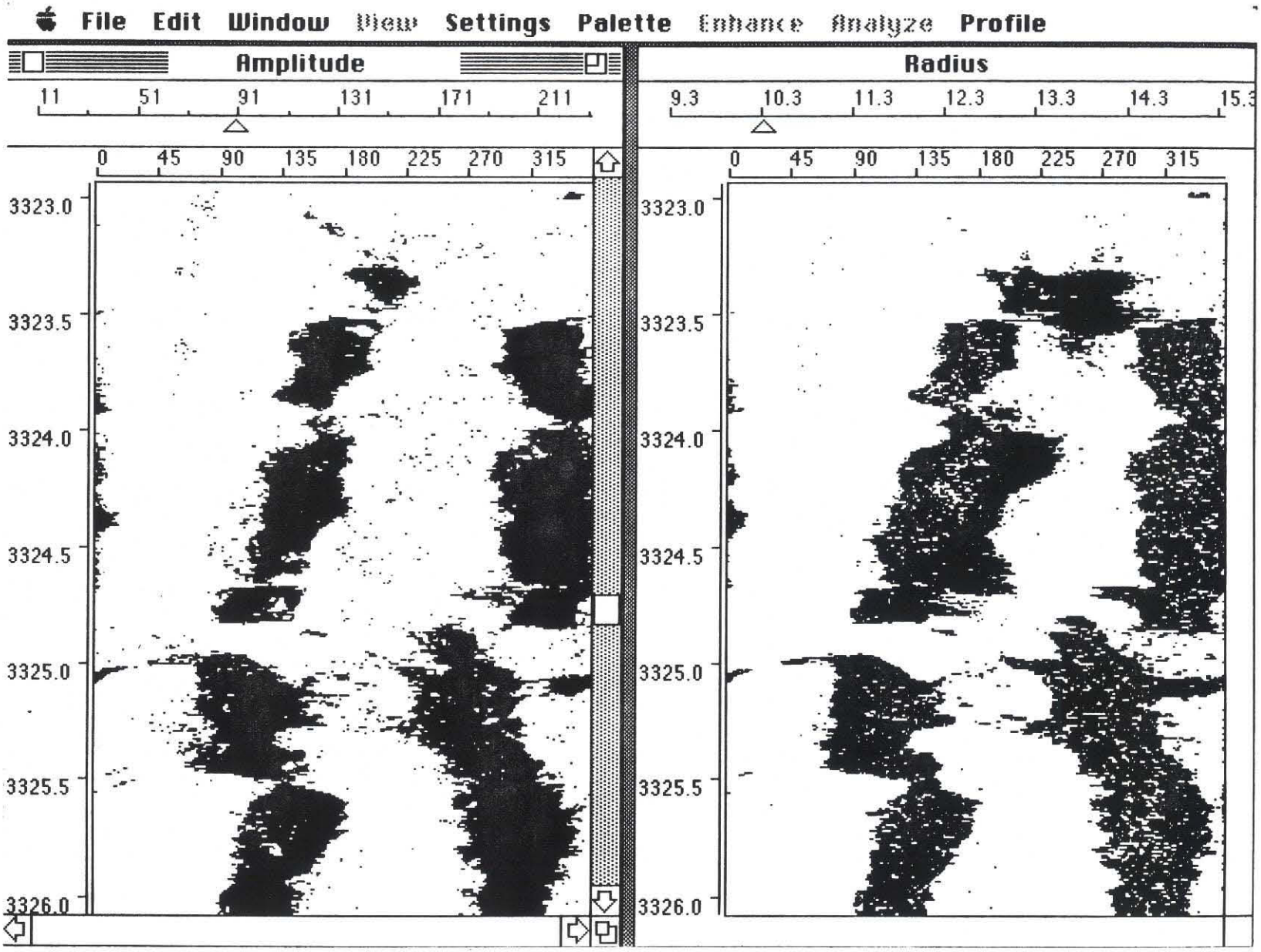
File Edit Window View Settings Palette Enhance Analyze Profile
Amplitude
11 51 91 131 171 211
0 45 90 135 180 225 270 315
3323.0
3323.5
3324.0
3324.5
3325.0
3325.5
3326.0
Radius
9.3 10.3 11.3 12.3 13.3 14.3 15.3
0 45 90 135 180 225 270 315
3323.0
3323.5
3324.0
3324.5
3325.0
3325.5
3326.0

Figure 8

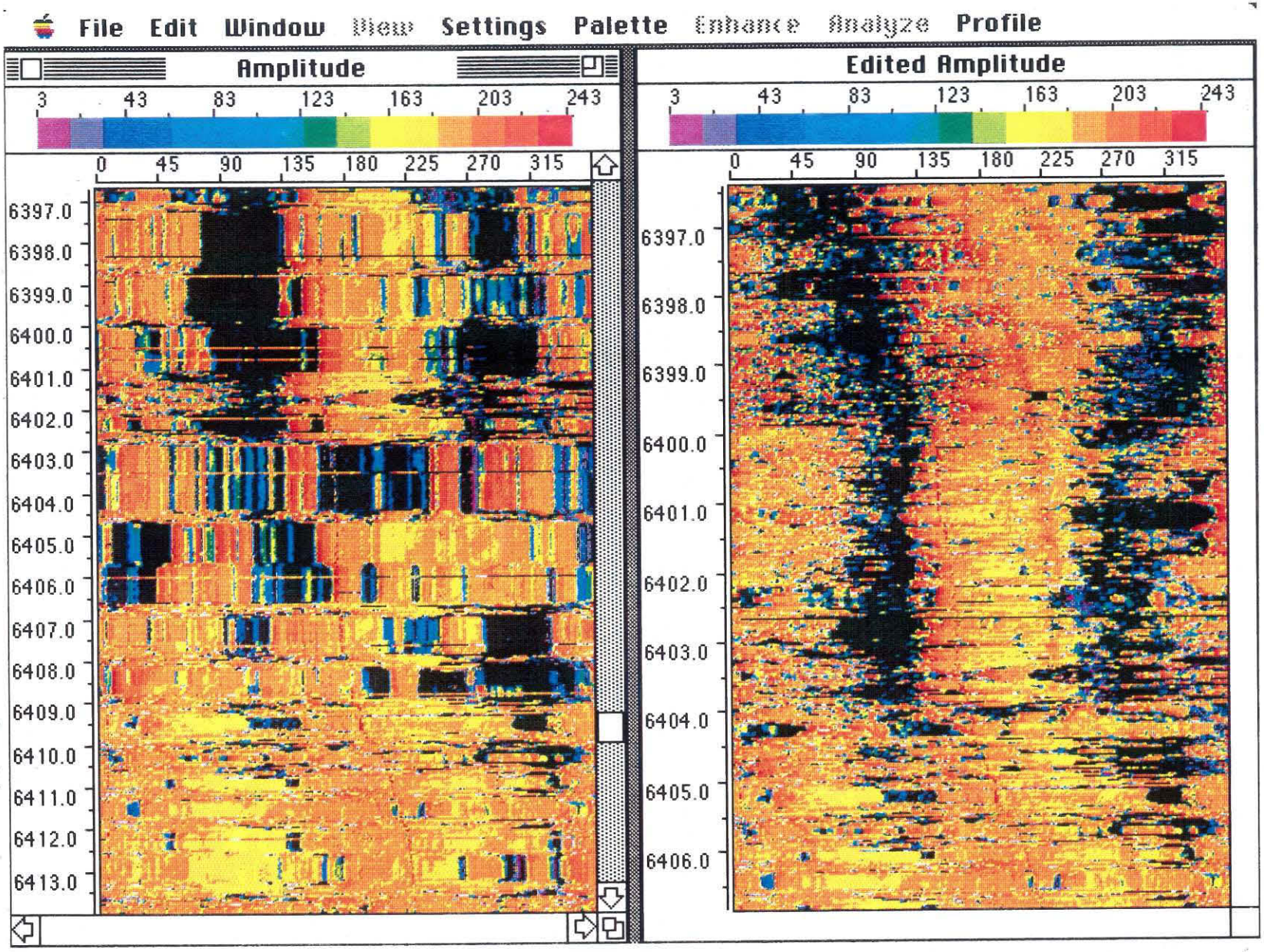
File Edit Window View Settings Palette Enhance Analyze Profile
Amplitude
3 43 83 123 163 203 243
0 45 90 135 180 225 270 315
6397.0 6398.0 6399.0 6400.0 6401.0 6402.0 6403.0 6404.0 6405.0 6406.0 6407.0 6408.0 6409.0 6410.0 6411.0 6412.0 6413.0
Edited Amplitude
3 43 83 123 163 203 243
0 45 90 135 180 225 270 315
6397.0 6398.0 6399.0 6400.0 6401.0 6402.0 6403.0 6404.0 6405.0 6406.0

Figure 9

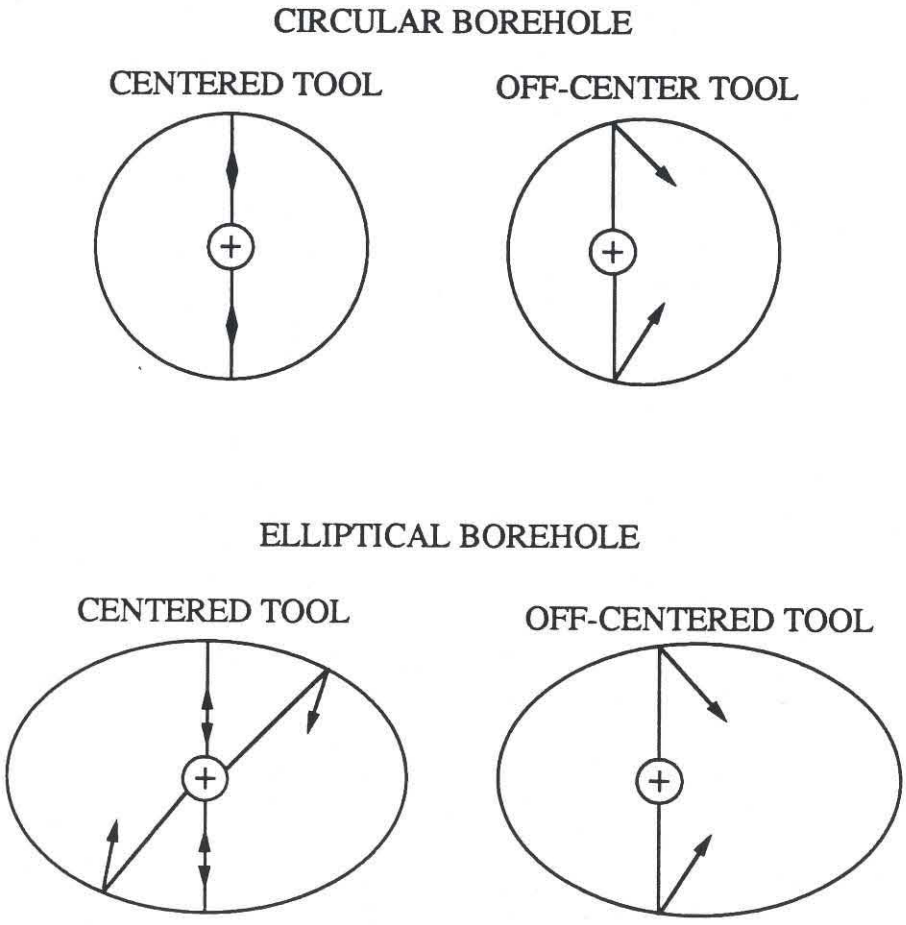
CIRCULAR BOREHOLE
CENTERED TOOL
OFF-CENTER TOOL
ELLIPTICAL BOREHOLE
CENTERED TOOL
OFF-CENTERED TOOL

Figure 10

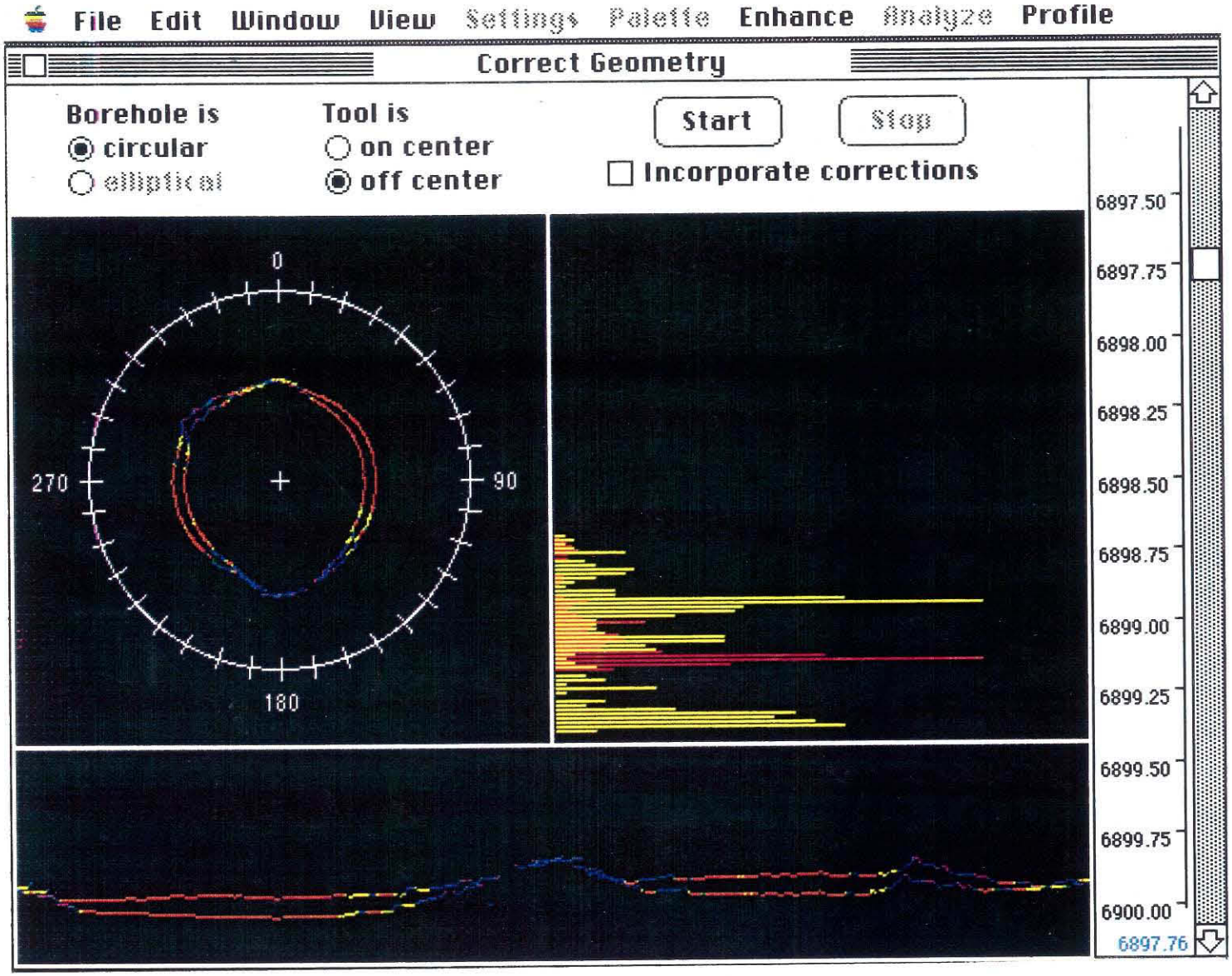
File Edit Window View Settings Palette Enhance Analyze Profile
Correct Geometry
Borehole is
circular
elliptical
Tool is
on center
off center
Start
Stop
Incorporate corrections
0
90
180
270
6897.50
6897.75
6898.00
6898.25
6898.50
6898.75
6899.00
6899.25
6899.50
6899.75
6900.00
6897.76

Figure 11

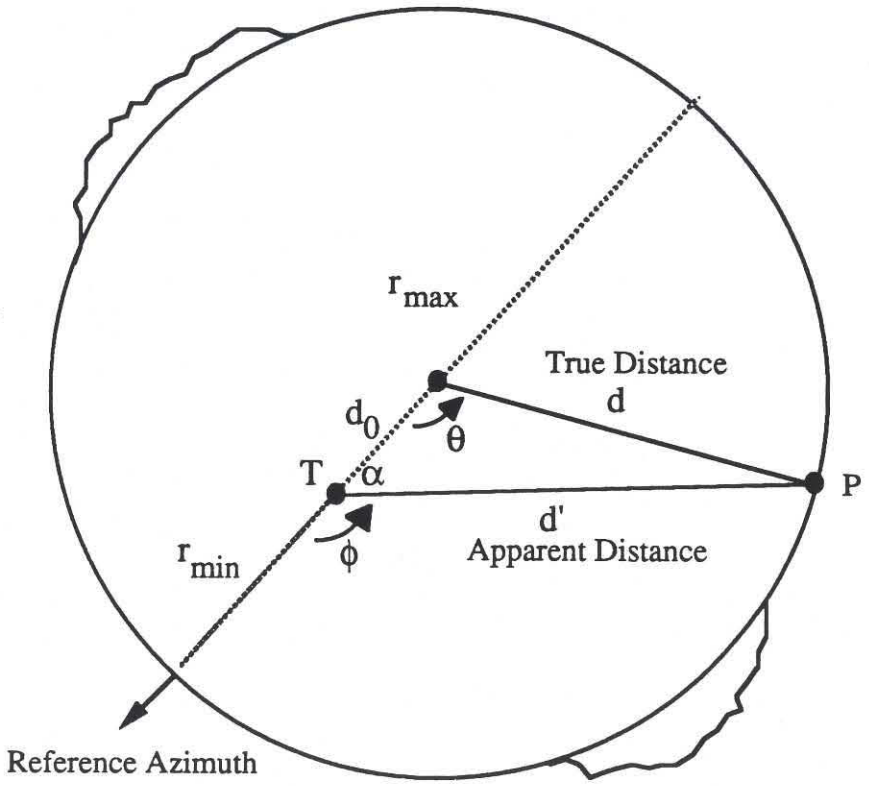
r max
True Distance
d
d0
θ
T
α
P
d'
Apparent Distance
r min
ϕ
Reference Azimuth

Figure 12

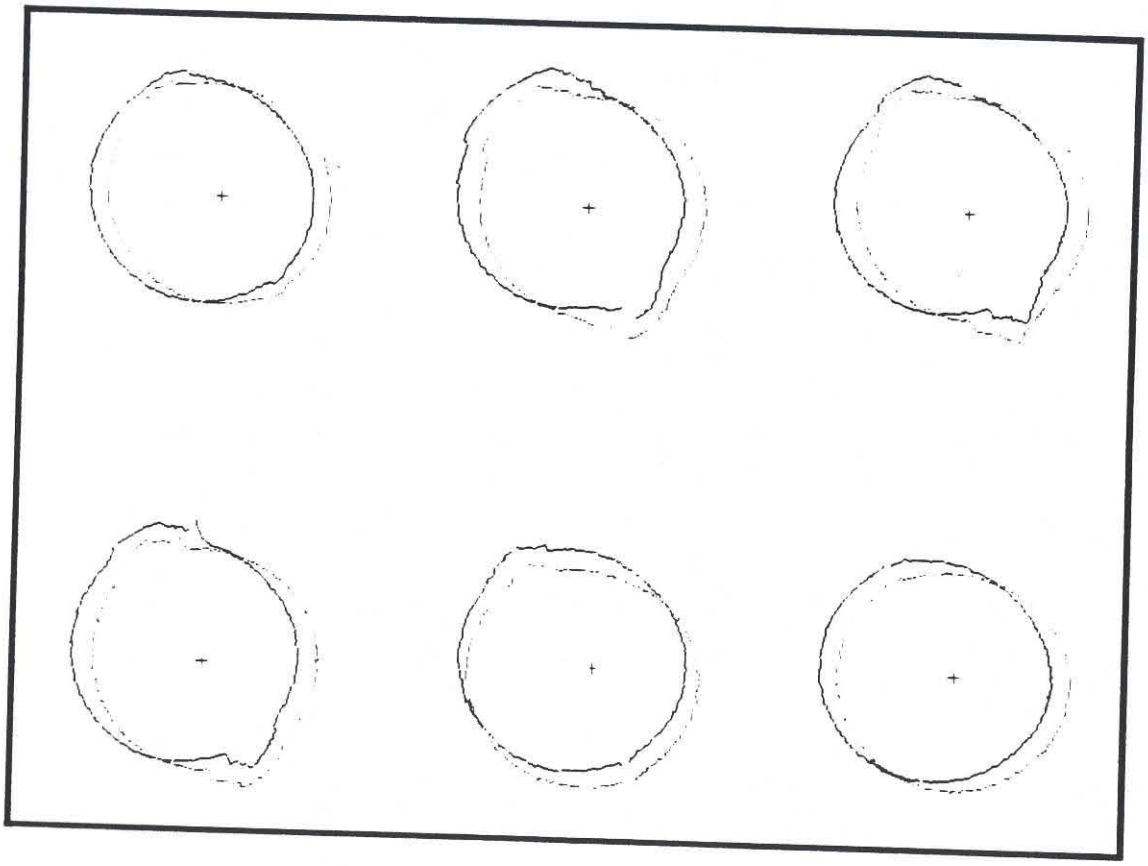

Figure 13

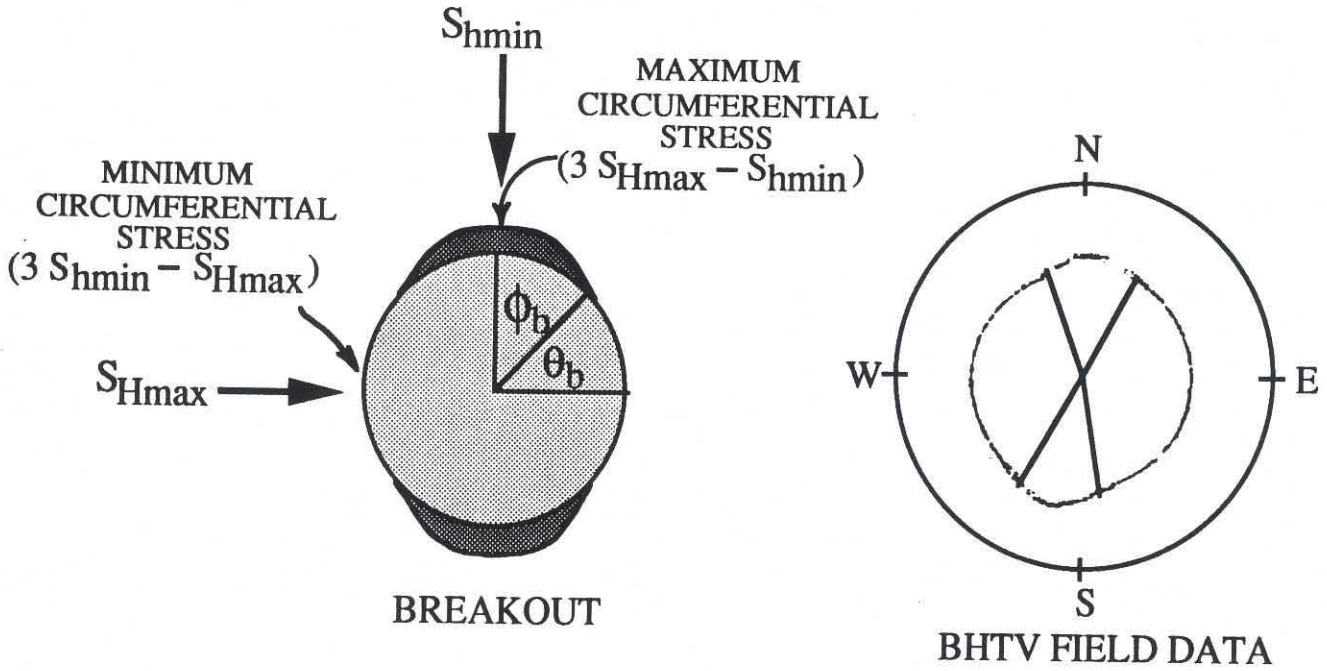
S_{hmin}
MAXIMUM CIRCUMFERENTIAL STRESS
$(3\ S_{Hmax} - S_{hmin})$
MINIMUM CIRCUMFERENTIAL STRESS
$(3\ S_{hmin} - S_{Hmax})$
S_{Hmax}
ϕ_b
θ_b
BREAKOUT
N
W
E
S
BHTV FIELD DATA

Figure 14

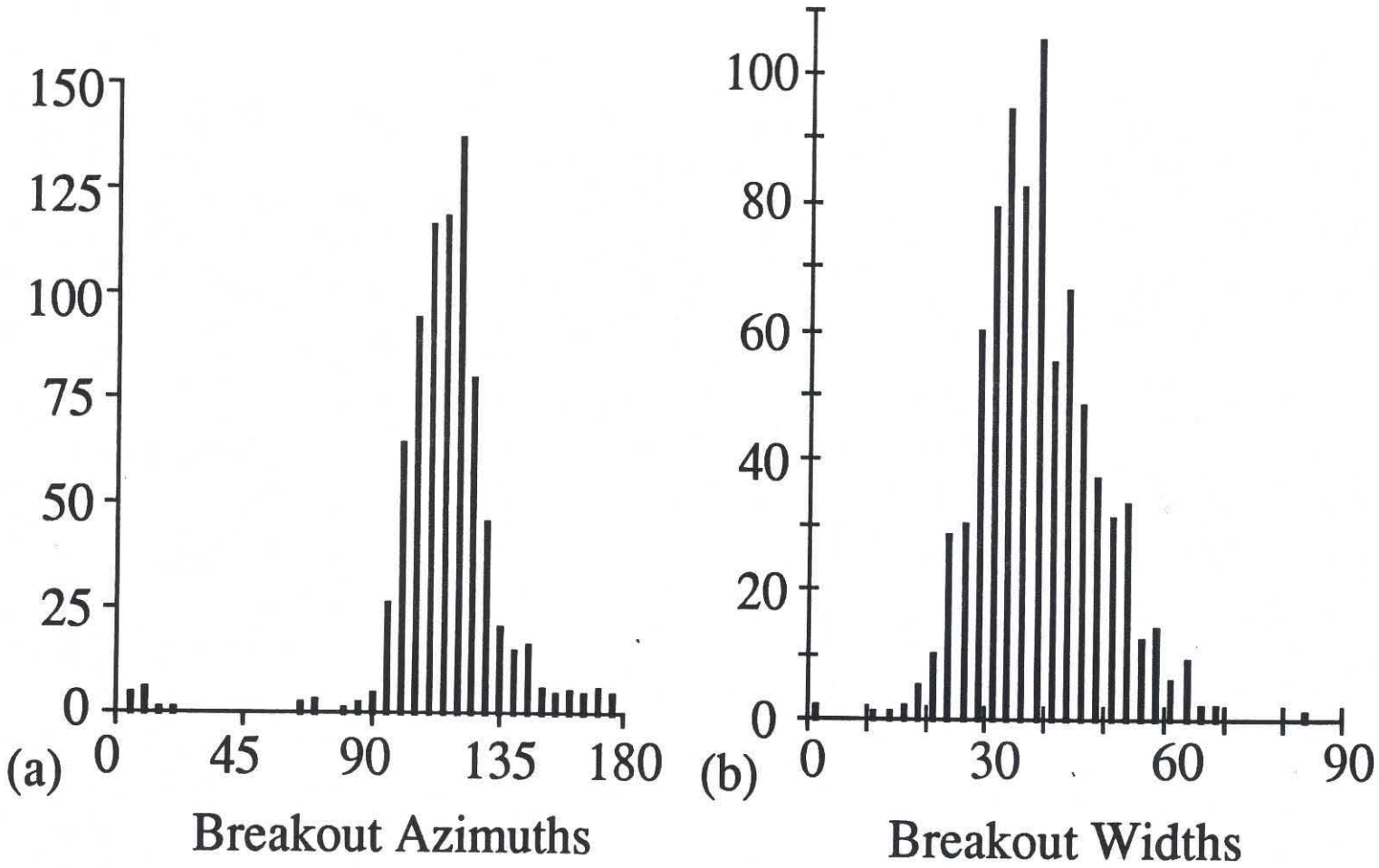
150
125
100
75
50
25
0
0
45
90
135
180
(a)
Breakout Azimuths
100
80
60
40
20
0
0
30
60
90
(b)
Breakout Widths

Figure 15

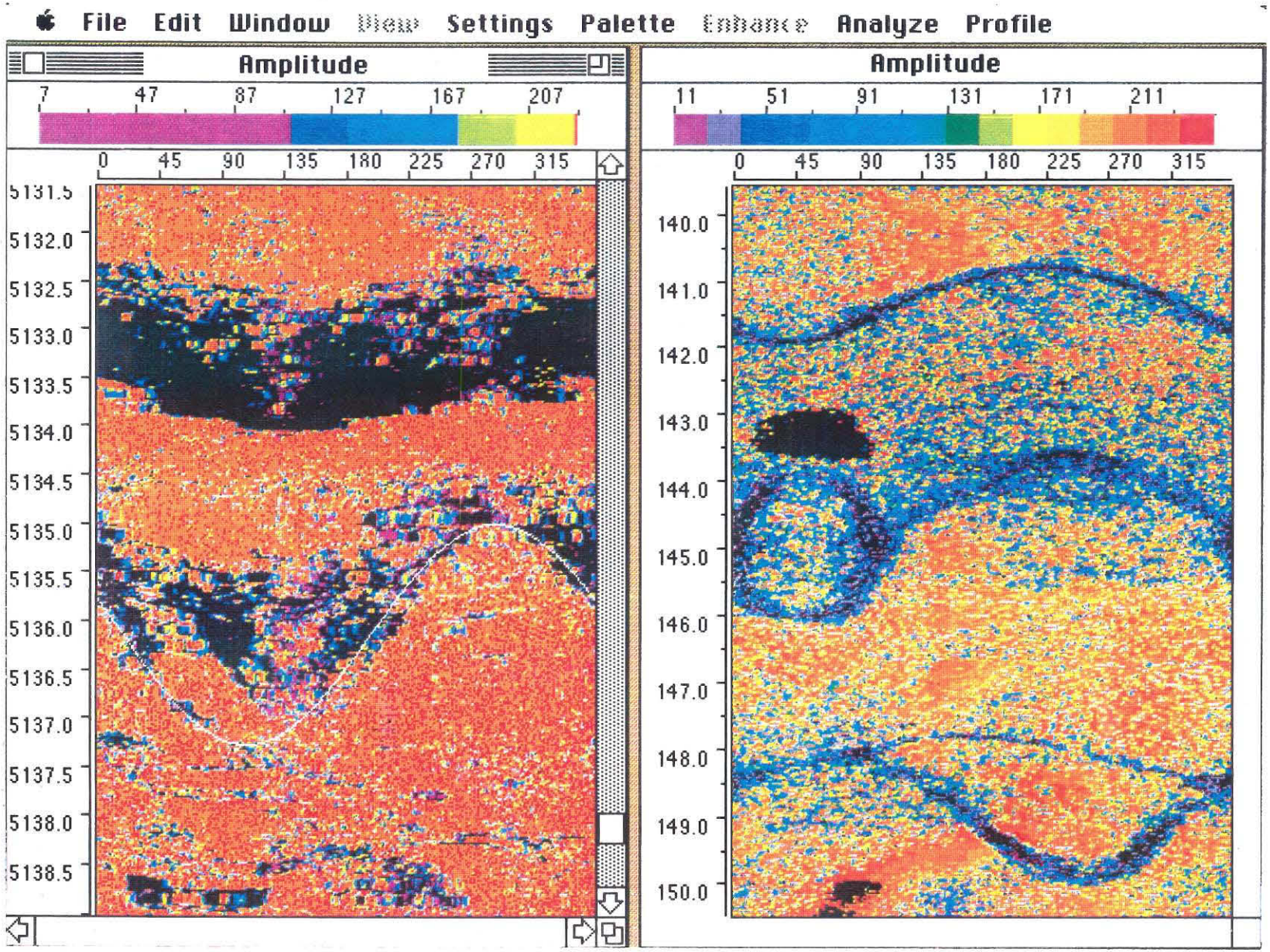
File Edit Window View Settings Palette Enhance Analyze Profile
Amplitude
7 47 87 127 167 207
0 45 90 135 180 225 270 315
5131.5
5132.0
5132.5
5133.0
5133.5
5134.0
5134.5
5135.0
5135.5
5136.0
5136.5
5137.0
5137.5
5138.0
5138.5
Amplitude
11 51 91 131 171 211
0 45 90 135 180 225 270 315
140.0
141.0
142.0
143.0
144.0
145.0
146.0
147.0
148.0
149.0
150.0

Figure 16

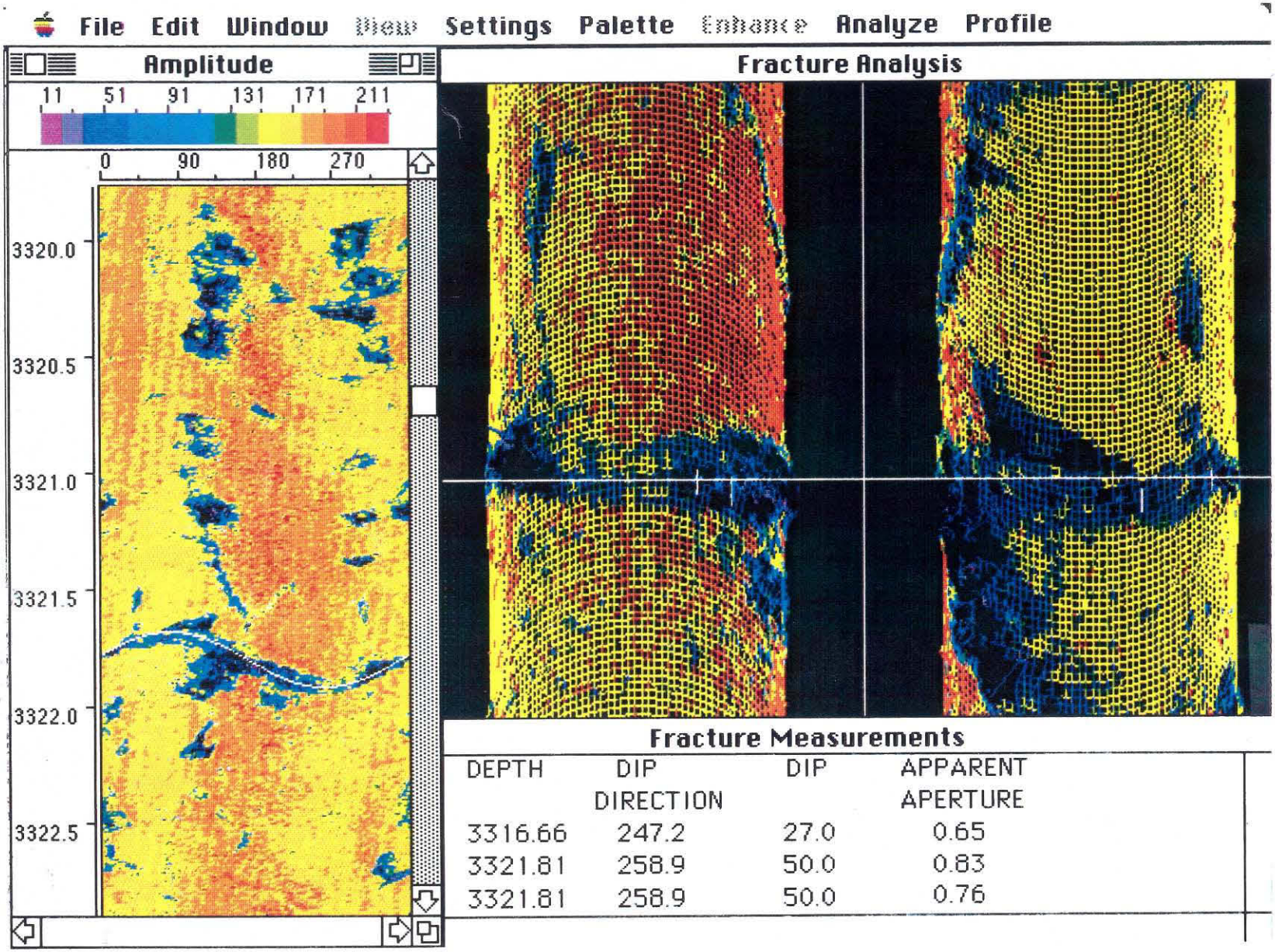
File Edit Window View Settings Palette Enhance Analyze Profile
Amplitude
11 51 91 131 171 211
0 90 180 270
3320.0
3320.5
3321.0
3321.5
3322.0
3322.5
Fracture Analysis
Fracture Measurements
DEPTH DIP DIRECTION DIP APPARENT APERTURE
3316.66 247.2 27.0 0.65
3321.81 258.9 50.0 0.83
3321.81 258.9 50.0 0.76

Figure 17

JOURNAL OF GEOPHYSICAL RESEARCH, VOL. 95, NO. B6, PAGES 9305–9325, JUNE 10, 1990

Utilization of Observations of Well Bore Failure to Constrain the Orientation and Magnitude of Crustal Stresses: Application to Continental, Deep Sea Drilling Project, and Ocean Drilling Program Boreholes

DANIEL MOOS AND MARK D. ZOBACK

Department of Geophysics, Stanford University, Stanford, California

The conditions necessary for compressive and tensile failure of well bores drilled into crystalline rock can be adequately represented by simple elastic failure criteria, and analysis of well bore failure can provide constraints on the magnitudes of in situ stresses if the strength of the rock is known. When applied to several boreholes drilled into continental crust where there is relatively complete knowledge of stress magnitudes, these criteria enable us to predict the depth at which compressive failure of the well bores is observed. In oceanic crust, breakouts have been observed at depths below 700 m below sea floor in Deep Sea Drilling Project (DSDP) hole 504B, drilled into 5.9 Ma crust south of the Costa Rica Rift, and near the bottom of DSDP hole 395A, drilled into 7.3 Ma crust west of the Mid–Atlantic Ridge. In both cases the azimuth of maximum horizontal compressive stress is roughly perpendicular to the ridge axis. As the unconfined compressive strengths of basalt samples from DSDP hole 504B are generally above 200 MPa (Bauer and Handin, 1985), the existence of breakouts in DSDP holes 395A and 504B requires a highly compressional stress state, where $S_{hmin} \sim S_v$ and $S_{Hmax} \geq 100$ MPa at about 500 m subbasement. These results are consistent with the state of stress inferred from compressional (strike-slip and reverse faulting) earthquake focal mechanisms in young oceanic crust. As ridge push forces are relatively small in young oceanic crust, we concur with previous suggestions that the high horizontal compressive stresses result from the thermoelastic effects of a convectively cooled upper crustal layer overlying a conductively cooling lithosphere.

INTRODUCTION

Determination of the magnitude and orientation of in situ stress in the continents and oceans is important to understand lithospheric deformation and to evaluate models of a wide variety of plate tectonic processes. While many aspects of crustal deformation and plate tectonics can be adequately addressed from a kinematic perspective, data on the forces acting within plates are needed to provide constraints on the physical processes causing and resisting plate motion and deformation.

Compilations of stress orientation and relative magnitude data have become increasingly more complete over the past 10 years, and tectonic stress orientation can be reliably mapped in many parts of the world. In total, over 3400 reliable indicators of tectonic stress are now available to define global patterns of intraplate stress [*Zoback et al.*, 1989]. The remarkable improvement in the quantity and distribution of in situ stress orientation data makes it possible to utilize such data to interpret tectonic processes in a number of important ways. However, there are still some very large data gaps in the stress maps, and there is almost a complete absence of stress magnitude data from depths greater than about 1 km [e.g., *Rummel*, 1986]. The lack of data on stress orientation and magnitude is especially severe in the oceans. While earthquake focal plane mechanisms help constrain the orientations and relative magnitudes of oceanic crustal stresses [e.g., *Okal et al.*, 1980; *Okal*, 1984; *Bergman and Solomon*, 1984; *Wiens and Stein*, 1984; *Bergman*, 1986], intraplate events are rare, no direct measure of stress magnitude is obtained, and measurements of stress direction from a single earthquake focal mechanism are complicated by the fact that the earthquakes often occur on preexisting faults [*McKenzie*, 1969; *Raleigh et al.*, 1972]. *Newmark et al.* [1984] and *Morin et al.* [this issue] determined stress directions in oceanic crust from analysis of well bore breakouts. In this paper we expand on these two studies and consider the more general problem of utilization of well bore failure for evaluating stress magnitudes, with the potential for studying the state of stress throughout the ocean basins.

In general, borehole failure can occur as a result of either compressive or tensile stress concentrations around the well bore. Compressive stress failures at the azimuth of the least principal horizontal in situ stress (where the compressive stress concentration is greatest) are termed stress-induced well bore breakouts [*Bell and Gough*, 1979, 1983; *Gough and Bell*, 1981; *Cox*, 1983; *Zoback et al.*, 1985] and have proven to be a reliable measure of stress orientation on land in many areas [*Bell and Gough*, 1979; *Zoback and Zoback*, 1980; *Plumb and Cox*, 1987; *Zoback et al.*, 1987; *Mount and Suppe*, 1987; *Zoback et al.*, 1989]. In this paper we show the range of conditions under which breakouts occur in both continental and oceanic boreholes and the manner in which information about stress magnitude can be obtained from the breakouts. Tensile failures around the well bore form at the azimuth of the greatest principal horizontal in situ stress (where the stress concentration around the well is least compressive). Tensile fractures may form adjacent to the well bore because of the localized stress concentration, and thermally induced tensile stresses due to cooling of the borehole wall by circulation of relatively cold drilling fluids also promote tensile failure. In these cases the fractures cannot propagate significant distances away from the well

Paper number 90JB00495
0148-0227/90/90JB-00495$05.00

bore unless the well bore fluid pressure exceeds the least principal in situ stress [cf. *Stock et al.*, 1985]. As is the case for well bore breakouts, observations of tensile failure of the well bore provide information about both stress orientation and magnitude. Our overall goal is to illustrate the simple fact that the presence (or absence) of compressive and/or tensile failure at the well bore can provide useful information about the magnitudes of in situ stresses.

Frictional Strength of the Crust

As suggested by *Sibson* [1974] and *Brace and Kohlstedt* [1980], we assume that the ratio of the maximum to minimum effective stress cannot exceed that required to cause motion on preexisting faults that are optimally oriented to the principal stress field. We also assume that principal stresses (S_1, S_2, and S_3) in the upper few kilometers of the Earth's crust generally act in the vertical direction, corresponding to the weight of the overburden (S_v) and in two orthogonal horizontal directions (S_{hmin} and S_{Hmax}, corresponding to the least and greatest horizontal principal stresses). The validity of this assumption is borne out by the very small number of intraplate crustal earthquake focal mechanisms in which neither the P nor the T axis is observed to be within 10°–15° of horizontal or vertical [e.g., *Zoback et al.*, 1989]. If these assumptions are correct, the limiting stress ratio can be written [after *Jaeger and Cook*, 1979] as

$$(S_1 - P_0)/(S_3 - P_0) = [(1 + \mu^2)^{1/2} + \mu]^2 \qquad (1)$$

where μ is the coefficient of friction of the preexisting plane of weakness and P_0 is the pore pressure. Thus the stress can range from lithostatic (in the absence of tectonic forces, [*McGarr*, 1988]) to the limit defined by (1).

A large number of in situ stress measurements in seismically active areas have shown this to be generally correct [*McGarr*, 1980; *Brace and Kohlstedt*, 1980; *Zoback and Healy*, 1984]. As we are applying these results to the upper part of the crystalline crust, we assume that pore pressure is approximately hydrostatic, which is borne out from a number of drilling experiments in both continental crystalline crust [*Kozlovsky*, 1984; *Rummel*, 1986; *Coyle and Zoback*, 1988] and oceanic crust [*Anderson and Zoback*, 1982; Hickman et al., 1984*a*; *Shipboard Scientific Party*, 1985].

Figure 1 illustrates the range of allowable values for horizontal principal stresses in the earth's crust for normal-, reverse-, and strike-slip-faulting environments using (1) and *Anderson*'s [1951] theory of faulting. For reference the figure is shown for a depth of 5 km in continental crust (average density of 2600 kg/m^3 and $\mu = 0.8$) and for a depth of 1 km into basalt in 4 km of water for the oceanic crust (rock density of 2800 kg/m^3 and $\mu = 0.8$). We choose these depths for illustration simply because they are within the depth range of scientific boreholes within the continents and oceans. By definition, the fact that $S_{\text{hmin}} \leq S_{\text{Hmax}}$ requires all stress states to be above the line of unit slope in Figure 1. The vertical and horizontal lines corresponding to S_v separate the fields of normal (NF), strike slip (SS), and reverse (RF) faulting as defined by Anderson. The vertical line constraining the lowest value of S_{hmin} is the failure bound for normal faulting (i.e., (1) with $S_1 = S_v$ and $S_3 = S_{\text{hmin}}$). The horizontal line constraining the greatest allowable value of $S_{H\text{max}}$ is the failure bound for reverse faulting (i.e., (1) with $S_1 = S_{\text{Hmax}}$ and $S_3 = S_v$). The inclined line is the limit of the allowable stress states for strike-slip faulting (i.e., (1) with $S_1 = S_{\text{Hmax}}$ and $S_3 = S_{\text{hmin}}$). In cases of incipient fault activity (a case that may be true of much of the upper crust) the expected stress state is found along one of these three limiting lines, depending on the style of faulting. It is clear in Figure 1 that principal stress magnitudes are appreciably lower in the oceanic crust than in the continental crust for the depths chosen. This has an important impact on the likelihood of well bore failure at the depths reached by drilling within the oceans. For reference to several specific cases the circles shown in Figure 1 correspond to simultaneous strike-slip and normal faulting, where $S_v = S_{\text{Hmax}} = S_1$ and $S_{\text{hmin}} = S_3$.

Stresses Around a Borehole

In the following discussion we continue to assume that the vertical stress is a principal stress, and we further assume that the well bore is drilled in the vertical direction and that the rock behaves elastically. We will present equations describing the magnitudes of the vertical, radial, and circumferential elastic stresses as a function of azimuth at the well bore; of the principal stresses; of fluid pressure differences between the well bore and the surrounding rock; and of the effects of temperature changes induced by the drilling fluid. These equations can be generalized for arbitrary stress and borehole orientations [e.g., *Fairhurst*, 1968; *Mastin*, 1988].

For a cylindrical hole in a homogeneous, isotropic elastic plate subjected to effective minimum and maximum far-field principal stresses (S^*_{hmin} and S^*_{Hmax}), the effective radial (σ_{rr}), circumferential ($\sigma_{\theta\theta}$), and tangential shear ($\tau_{r\theta}$) stresses described by *Kirsch* [1898] reduce at the borehole wall to

$$\begin{aligned}
\sigma_{rr} &= \Delta P \\
\sigma_{\theta\theta} &= S^*_{\text{Hmax}} + S^*_{\text{hmin}} - 2(S^*_{\text{Hmax}} - S^*_{\text{hmin}}) \cos 2\theta - \Delta P \\
\sigma_{zz} &= S^*_v - 2\nu(S^*_{\text{Hmax}} - S^*_{\text{hmin}}) \cos 2\theta \\
\tau_{r\theta} &= 0 \\
\tau_{zr} &= 0 \\
\tau_{z\theta} &= 0
\end{aligned} \qquad (2)$$

where ΔP is the difference between the well bore fluid pressure and the pore pressure in the rock, σ_{zz} is from *Fairhurst* [1968], and ν is the static Poisson's ratio. Theta (θ) is measured from the azimuth of the maximum horizontal stress. The circumferential stress is greatest at the azimuth of S^*_{hmin} and smallest at the azimuth of S^*_{Hmax}. Figure 2 shows the variation in $\sigma_{\theta\theta}$, the circumferential stress, and σ_{zz}, the vertical stress, as a function of azimuth at the well bore for the stress states indicated by the circles in Figure 1. It is important to note the wide range of circumferential stresses for this stress state. For the case at 5 km depth in the continents, $\sigma_{\theta\theta}$ varies from a point on the borehole at the azimuth of S^*_{hmin} where the circumferential stress is quite compressive ($3S^*_{\text{Hmax}} - S^*_{\text{hmin}} \approx 220$ MPa) to a point where, for the case shown, the well bore is in tension ($3S^*_{\text{hmin}} - S^*_{\text{Hmax}} \approx -25$ MPa) at the azimuth of S^*_{Hmax}. For the oceanic crust at 1 km below sea floor, $\sigma_{\theta\theta}$ ranges from about 50 MPa to −5 MPa. The vertical stress has the same θ dependence as the circumferential stress. However, the range in vertical stress in crystalline rock is considerably less than the far-

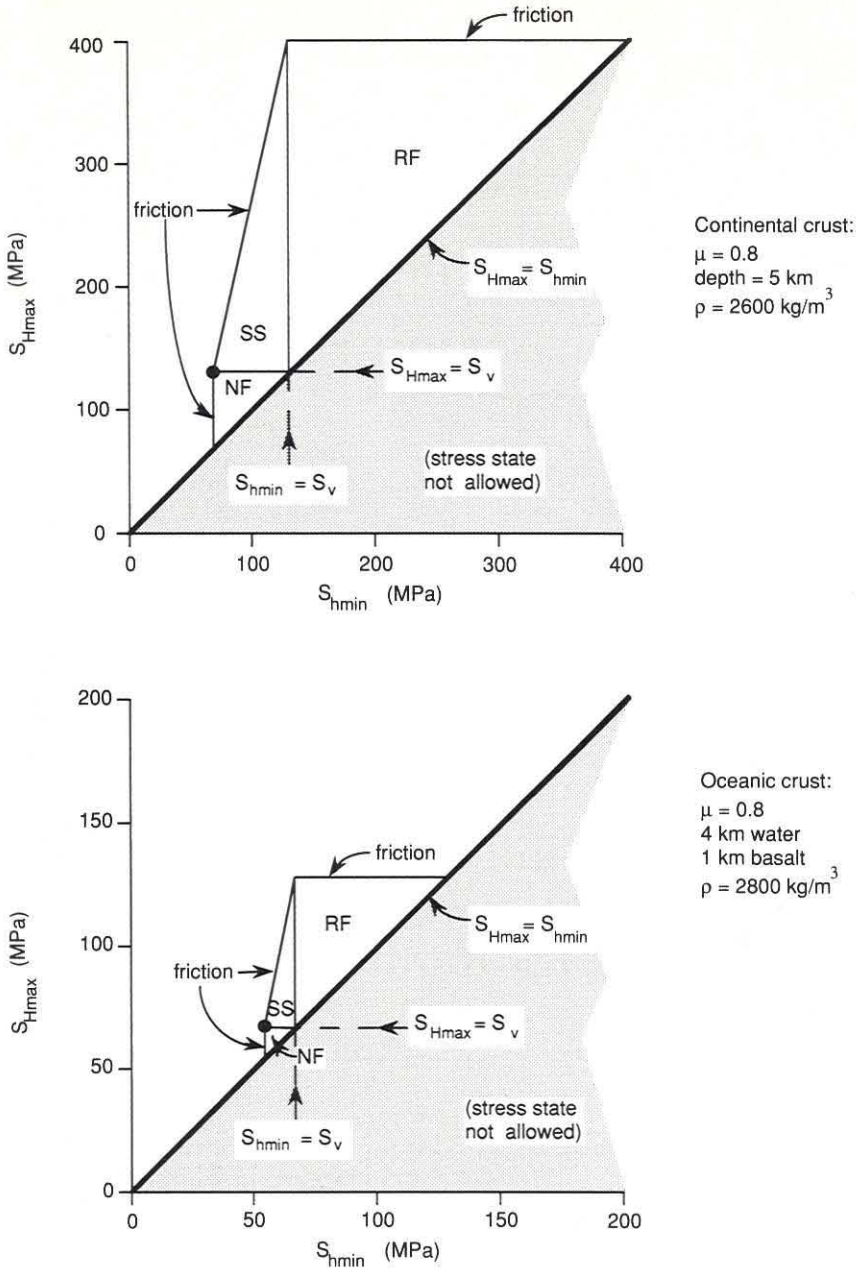

Fig. 1. Allowable stress conditions based on the frictional strength of favorably oriented fault planes, assuming $\mu = 0.8$, for continental crust at 5 km depth and for oceanic crust at 1 km below seafloor. (Note the different scales.) S_v is calculated from the weight of overburden, and pore pressure is assumed to be hydrostatic. The stress state is constrained to lie inside the polygon, because $S_{H\max} \geq S_{h\min}$, by definition, and the ratio $(S_1 - P_0)/(S_3 - P_0)$ is bounded by friction (equation (1)). For reverse faulting, $S_1 = S_{\mathrm{Hmax}}$ and $S_3 = S_v$, defining a maximum bound on S_{Hmax}. For normal faulting, $S_1 = S_v$ and $S_3 = S_{\mathrm{hmin}}$, defining a minimum bound on S_{hmin}. For strike-slip faulting, friction bounds the ratio $(S_{H\max} - P_0)/(S_{\mathrm{hmin}} - P_0)$. The circle represents in each case the stress state $S_{\mathrm{Hmax}} = S_v$, with S_{hmin} constrained by the frictional strength of normal or strike-slip faults.

field stress difference for static Poisson's ratios <0.25 [e.g., *Carmichael*, 1982].

Effect of Temperature Changes on Borehole Stresses

Additional stresses are applied to the rock at the borehole wall if the well bore fluid is at a significantly different temperature than the rock. These stresses can be compressive or tensile depending on whether the temperature of the fluid is higher or lower, respectively, than the ambient temperature. The effect of temperature is time-dependent, in the sense that the longer the rock is in contact with the well bore fluid, the further away from the hole the temperature perturbation will propagate. *Coussy* [1990] presents a complete treatment of the problem for a Biot coupled thermoporoelastic material, which requires for its solution detailed knowledge of rock properties such as permeability. However, if one assumes that the material is impermeable with no thermoelastic coupling, simpler integral equations can be written for the magnitudes of $\sigma_{\theta\theta}$ and σ_{rr} as a function of

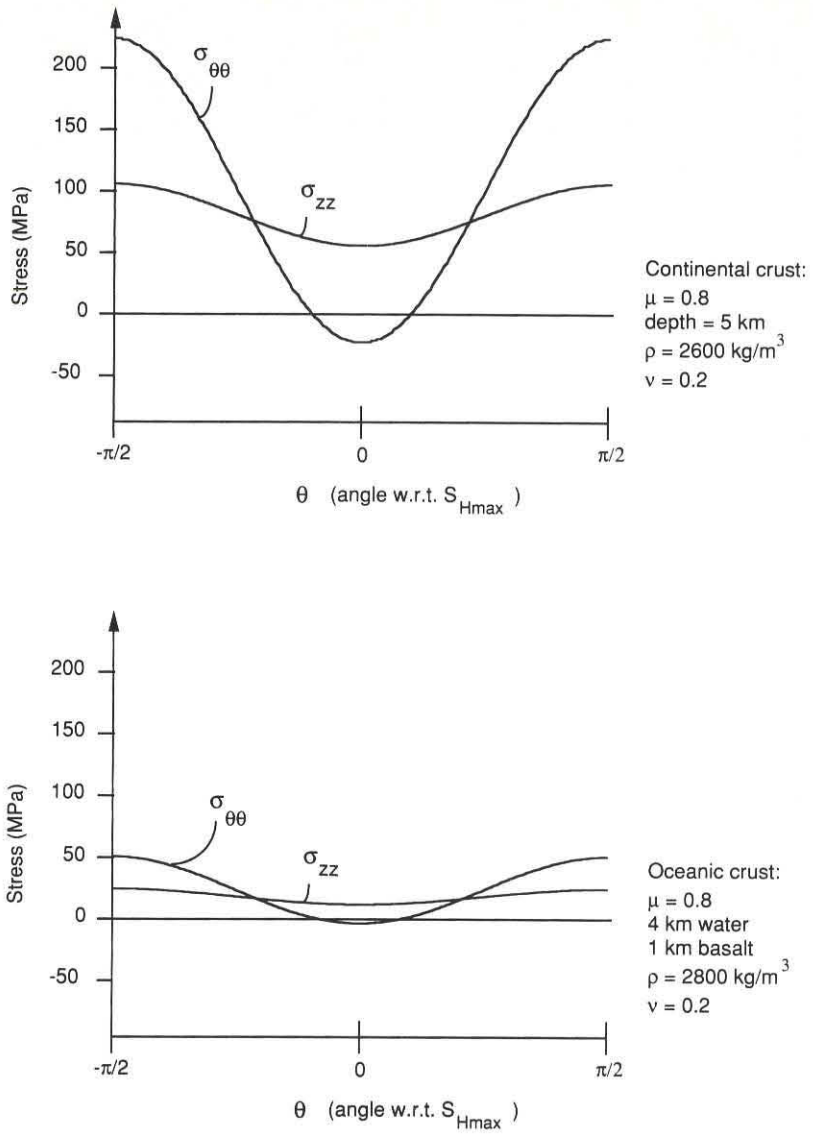

Fig. 2. The distribution of circumferential and vertical stresses around a well bore for the stress states defined by the circles in Figure 1. Note that for these strike-slip-faulting cases the well bore wall is in tension because of the circumferential stress concentration at the azimuth of S_{Hmax}.

radial position r and time t (see, for example, *Stephens and Voight* [1982]). Although the exact solution for the temperature distribution near a constant-temperature well bore is a series expansion [*Ritchie and Sakakura*, 1956], solutions which approximate the temperature using the first two terms of the expansion give sufficiently accurate results close to the hole, and the stresses become

$$\sigma_{\theta\theta} = [\alpha E \Delta T/(1-\nu)]\{[1/(2\rho) - \tfrac{1}{2} - \ln \rho]I_0^{-1} - [\tfrac{1}{2} + 1/(2\rho)]\}$$

$$\sigma_{rr} = [\alpha E \Delta T/(1-\nu)]\{[-1/(2\rho) + \tfrac{1}{2} - \ln \rho]I_0^{-1} - [\tfrac{1}{2} - 1/(2\rho)]\} \quad (3)$$

where

$$I_0^{-1} = \frac{1}{2\pi i}\int_{-\infty}^{0^+} \frac{e^{(4\tau/\sigma^2)z}}{z \ln z}\, dz$$

Here α is the coefficient of thermal expansion; E is the static Young's modulus; ΔT is the temperature difference between the well bore fluid and the rock surrounding the borehole; ν is the static Poisson's ratio; $\sigma = e^{\gamma}$; γ is Euler's constant; ρ is radial position normalized by the well bore radius R; and the parameter $\tau = \kappa t/R^2$ is the Fourier number. Here κ is the thermal diffusivity, and t is the time during which the well bore fluid temperature is perturbed.

If the well bore fluid is colder than the rock, the thermally induced stresses are extensional. This will generally be true where drilling fluids exit the pipe, particularly in Ocean Drilling Program (ODP) and Deep Sea Drilling Project (DSDP) drill holes, as in situ temperatures are generally higher than the temperature of the drilling fluid. However, drilling fluids returning to the surface from greater depths may be somewhat warmer than the undisturbed temperature of the rock and thus may induce compressional thermal stresses. For the purposes of this paper we will consider only the case of the effect of cooling the rock at the drill bit.

Equation (3) is plotted in Figure 3 for various values of time, assuming a 15-cm borehole radius and a coefficient of

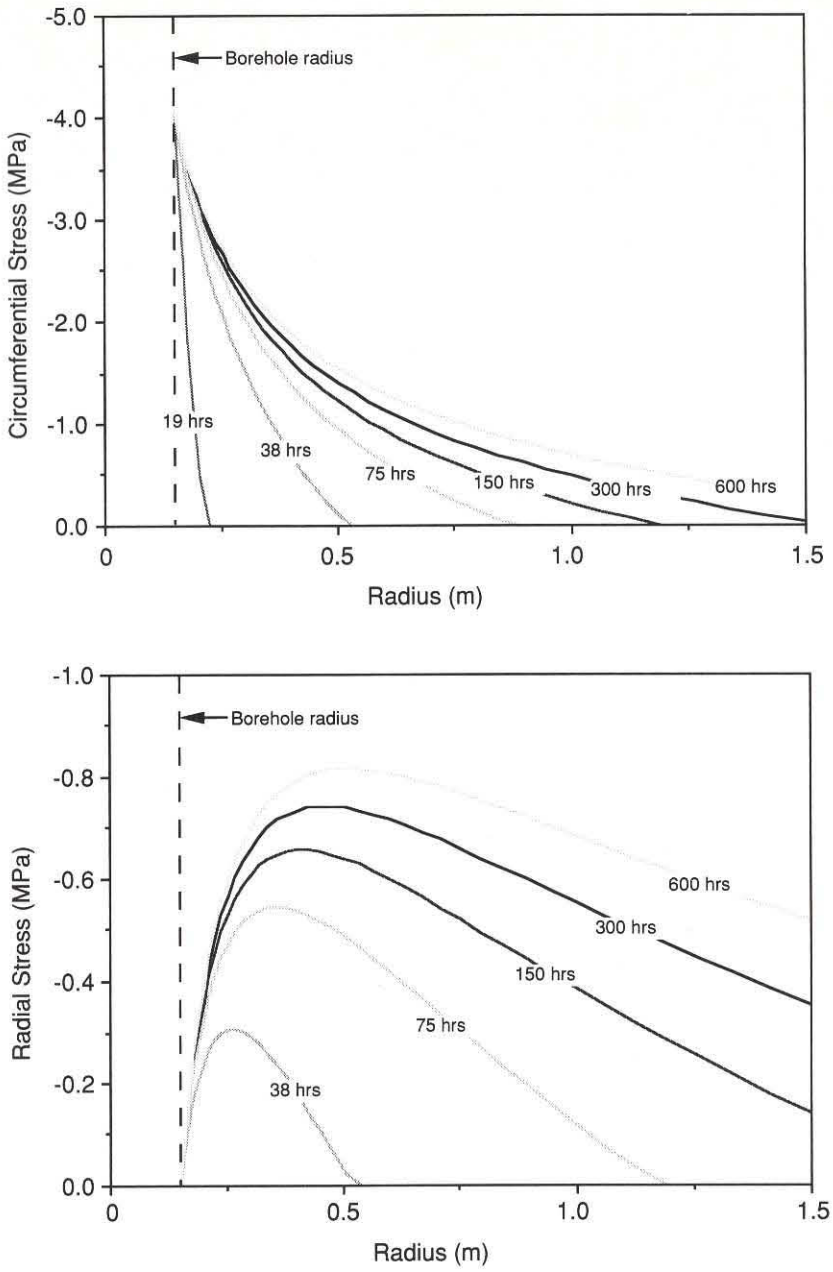

Fig. 3. Radial and circumferential stresses generated by a decrease in well bore fluid temperature of 10°C as a function of time, for a 15-cm-radius borehole drilled through basalt. Plotted as a function of radial distance from the center of the borehole, the lines correspond to pumping times of 19, 38, 75, 150, 300, and 600 hours. After 19 hours the radial stress perturbation is imperceptible at the scale of this plot. As the pumping time increases, the stress perturbations move away from the borehole wall.

thermal expansion of 5.4×10^{-6} °C^{-1} (values appropriate for DSDP and ODP boreholes penetrating oceanic crustal basalts). For these values and a thermal diffusivity $\kappa = 10^{-6}$ m^2/s the curves illustrate the effect of maintaining a 10°C temperature reduction within the well bore for 19, 38, 75, 150, 300, and 600 hours (from less than 1 day to 25 days). For this case, well bore cooling applies 4.1 MPa of circumferential tension at the borehole wall. The thermally applied stress decreases rapidly with radial distance, and after 19 hours of circulation is confined to less than 1 borehole radius. As circulation time increases, the stress anomaly progresses further away from the well bore but even after several weeks of cooling is insignificant beyond about 10 borehole radii (1.5 m). The thermally induced radial stress is zero at the well bore, attains a most tensile value a short distance away from the hole, and decreases at greater distances. The peak of the radial stress anomaly migrates away from the well bore as circulation is maintained for longer times, but as in the case of the circumferential stress, the effect is still confined to within a few borehole radii. Times shorter than 19 hours are not accurately modeled by the simplified (3) above but have a similar form.

WELL BORE FAILURE

In this section we consider the role of tectonic stress, applied fluid pressure and well bore temperature changes in

terms of the stresses required to cause compressive and tensile failure.

Conditions for Breakout Formation

As first suggested by *Gough and Bell* [1981] and *Bell and Gough* [1983], breakouts are spalled regions centered on the azimuth of the least horizontal far-field stress and are formed by compressive shear failure due to the large difference between the radial stress and the circumferential stress at that point. *Zoback et al.* [1985] extended this model to account for the shape of the breakout region, using a modified Mohr-Coulomb criterion for shear failure. They showed that breakout shapes are generally consistent with those predicted by the Mohr-Coulomb theory and proposed that information about the shape of breakouts could allow estimates of the horizontal stress ratio. This technique was successfully applied by *Barton et al.* [1988]. It is not our intent in this paper, however, to utilize breakout shape information to constrain the stresses.

In the simple elastic Mohr-Coulomb analysis, compressive failure will occur at the well bore wall due to differences between the circumferential and the radial stress when the stress concentration exceeds C, the strength of the rock, i.e.,

$$\sigma_{\theta\theta} = S_{\mathrm{Hmax}} + S_{\mathrm{hmin}} - 2(S_{\mathrm{Hmax}} - S_{\mathrm{hmin}}) \cos 2\theta - 2P_0 \geq C \tag{4a}$$

for failure due to differences between circumferential and radial stresses, and

$$\sigma_{zz} = S_v - 2\nu(S_{\mathrm{Hmax}} - S_{\mathrm{hmin}}) \cos 2\theta - P_0 \geq C \tag{4b}$$

for failure due to differences between the vertical stress and the radial stress. Because $\sigma_{rr} \sim 0$ (when $\Delta P \sim 0$) and $\sigma_{\theta\theta}$ and σ_{zz} are both nonzero, the stress state around the well bore is polyaxial. In general, rock is stronger under polyaxial conditions than under uniaxial conditions, and as described by *Wiebols and Cook* [1968], the appropriate rock strength when one principal stress is zero is between the uniaxial strength (where $\sigma_2 = 0$) and the biaxial plane strength (where $\sigma_2 = \sigma_1$). Wiebols and Cook relate the biaxial plane strength to the uniaxial strength C_0 through the formula $C_b = C_0(1.0 + 0.6\mu_f)$, where μ_f is the coefficient of sliding friction on microcracks. For reasonable values of μ_f (~0.6 [*Byerlee*, 1978]), $C_b = 1.36C_0$. Therefore the strength of interest for well bore failure lies within the range $C_0 \leq C \leq 1.36C_0$. In the remainder of the paper we will assume that this range of values is appropriate for the study of breakouts.

Zheng et al. [1989] present a different model for breakout formation by extensional cracking (spalling) parallel to the well bore. As their spalling process requires some microcrack sliding to initiate the tensile cracks, the stresses necessary to initiate breakouts in their model are those required to promote sliding on favorably oriented microcracks. Thus the far-field stress magnitudes are similar to those necessary to cause compressive shear failure in the model of *Zoback et al.* [1985] using the *Wiebols and Cook* [1968] failure criterion. Laboratory results [*Mastin*, 1984; *Haimson and Herrick*, 1986, 1989] show that breakout formation generally occurs at stresses consistent with the Mohr-Coulomb criterion for shear failure as modified to include the effect of the intermediate stress, and although *Haimson and Herrick* [1989] observed features within breakouts that mimic spalling, the stress state for which the breakouts formed was similar to that of the *Zoback et al.* [1985] model. *Vardoulakis et al.* [1988] suggest an alternative failure criterion, based on a rigid plastic pressure sensitive dilatant rheology, and a bifurcation analysis to define failure development. This results both in a modification of the stress concentration at the well bore and a more complicated failure criterion. Unfortunately, this analysis has not yet been developed for unequal stresses acting perpendicular to the well bore and cannot be utilized for interpretation of field observations.

We now consider the in situ stress conditions under which (1) breakouts do not occur, (2) breakouts occur only near the azimuth of S^*_{hmin}, and (3) breakouts occur everywhere around the well bore. The boundaries between these three "fields" in horizontal stress space are determined by the strength of the rock and the differences between the far-field total stresses. In general, it is not necessary to evaluate the conditions for compressive failure due to the vertical stress, as in the region of the well bore the maximum circumferential stress ($3S_{\mathrm{Hmax}} - S_{\mathrm{hmin}} - 2P_0$) is generally greater than the maximum vertical stress ($S_v + 2\nu(S_{\mathrm{Hmax}} - S_{\mathrm{hmin}}) - P_0$), for reasonable values of the static Poisson's ratio (≤ 0.25), except in the case of normal faulting where the two horizontal stresses are approximately equal ($S_v \gg S_{\mathrm{Hmax}} \approx S_{\mathrm{hmin}}$). For the present we assume that $\Delta P = \Delta T = 0$, but from the discussions above one can see that it is straightforward to vary these parameters and incorporate their effects.

In Figure 4 the fields in which breakouts do and do not occur are shown for an assumed rock strength $C = 200$ MPa for the same depths and conditions as Figure 1. As discussed below, $C \approx 200$ MPa is somewhat high for many crystalline rocks but comparable to the strength of basalt. The allowable stress states defined by the frictional strength of the crust that are shown in Figure 1 are also shown in Figure 4. The breakout fields in the figure are defined using (4*a*) by $S_{\mathrm{Hmax}} \geq \frac{1}{3}(C + S_{\mathrm{hmin}} + 2P_0)$, for failure only at the azimuth of S_{hmin}, and $S_{\mathrm{hmin}} \geq \frac{1}{3}(C + S_{\mathrm{Hmax}} + 2P_0)$, for failure occurring everywhere around the hole. For a strength of 200 MPa it is clear that at a depth of 5 km on land, breakouts are to be expected under nearly all stress conditions except those of normal faulting, and in a highly compressive tectonic stress state, breakouts would be expected to occur nearly everywhere around the well bore. Conversely, at a depth of 1 km in the ocean crust, breakouts would only occur at relatively high values of S_{Hmax} and a large horizontal stress difference, a reverse/strike-slip stress regime.

Breakouts have been found in many wells drilled on land, and the frequency of breakouts (and the likelihood that breakouts would be encountered) in a given well increases with depth. This can be understood by simply considering limits on the horizontal stresses in reverse-, strike-slip-, and normal-faulting regimes (where the values of S_1 and S_3 are limited by (1) and the coefficient of friction μ) and the criteria for breakout formation due to the circumferential stress concentration (Equation (4)). The relationship between the rock strength and the minimum depth of breakout occurrence from these equations is illustrated in Figure 5. In this figure the vertical stress S_v is equal to the weight of overburden, pore pressure is hydrostatic, and well bore fluid pressure is equal to the pore pressure. The value of the intermediate stress is conveniently defined in terms of a

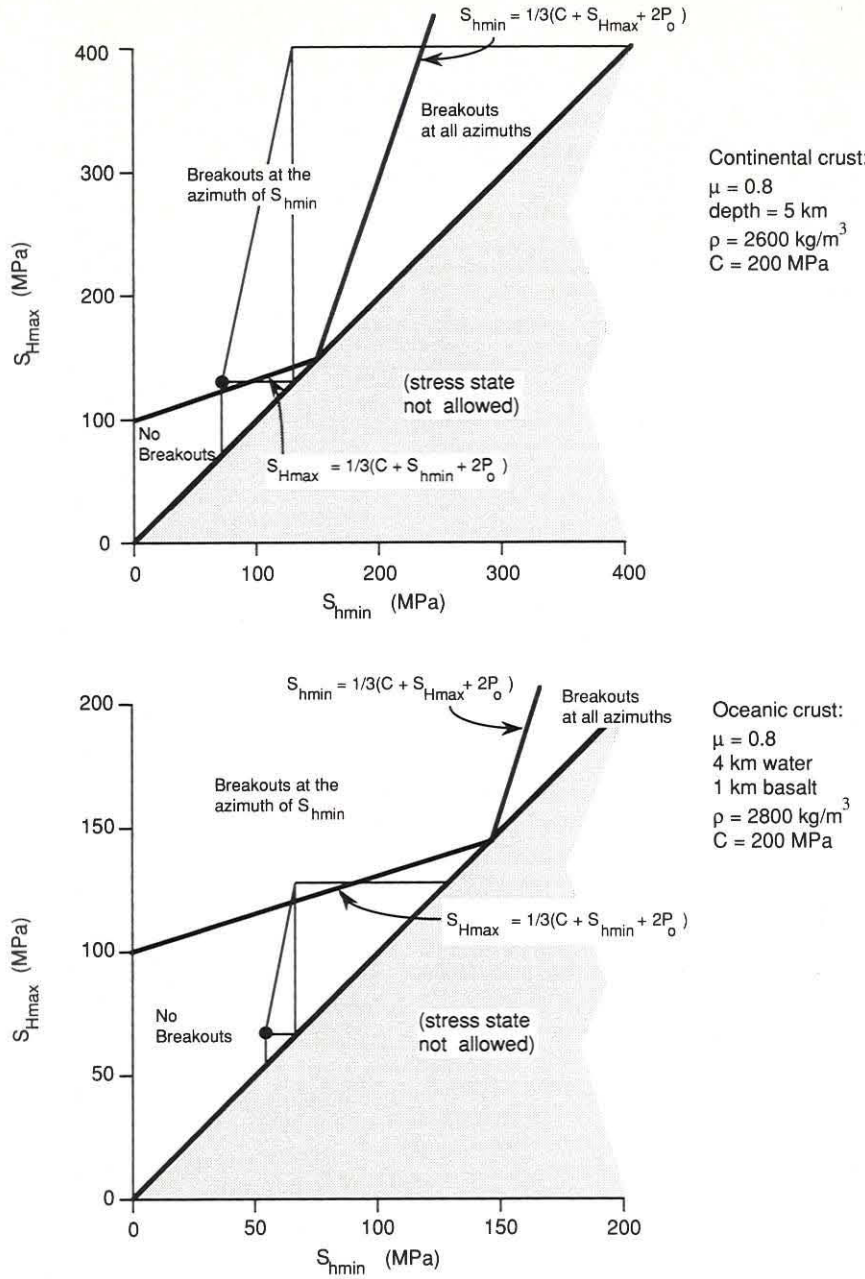

Fig. 4. Schematic illustration of the type of compressive well bore failure (breakout) possible for stress conditions as defined in Figure 1, for a rock strength of 200 MPa. As in Figure 1, the stress state must lie within the bounds imposed by friction and the definition that $S_{Hmax} \geq S_{hmin}$. Note that at 5 km depth in the continents, breakouts will occur for any stress state except a low-stress strike-slip one, whereas at 1 km into oceanic crust, breakouts will only occur if the horizontal stresses are quite high.

parameter ϕ, where $\phi = (S_2 - S_3)/(S_1 - S_3)$ [*Angelier*, 1979]. The figure shows, for the stress states defined by the respective faulting regimes and the value of ϕ, the depth at which breakouts would form for a given strength. As seen in this figure, breakouts develop at much shallower depths in a reverse-faulting regime than in a normal-faulting regime, for a given rock strength. For example, for a rock strength of 200 MPa and $\phi = 0.5$, breakouts would occur below a depth of approximately 1.2 km in a reverse-faulting environment, but in a normal-faulting environment they are not expected until depths of more than 9 km.

Figure 6 presents an analysis similar to Figure 5 for the oceanic crust assuming a water depth of 4 km. In this case, breakout formation occurs roughly at the same depth below the seafloor as below the ground surface on the continents, for the same tectonic stress and rock strength. Unfortunately, wells penetrating more than a few hundred meters of the oceanic crust are extremely rare, and breakouts would be expected only if the level of compressive stress was quite high and the rocks were anomalously weak.

Borehole Televiewer Observations of Well Bore Breakouts

The borehole televiewer (BHTV) is an acoustic logging device which scans the interior wall of a borehole, as first

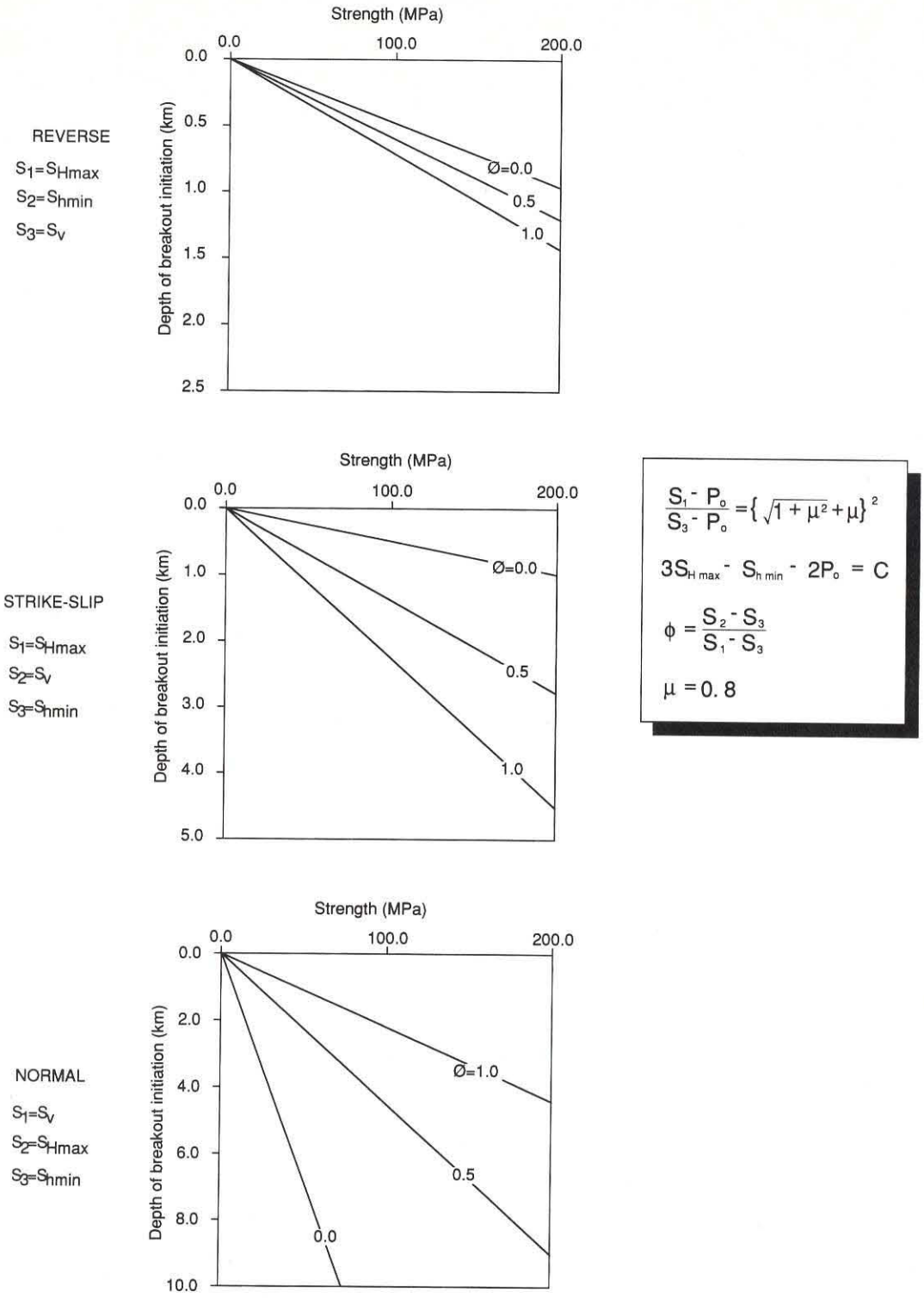

Fig. 5. Minimum depth of breakout formation due to the circumferential stress concentration around a well drilled into continental crust, plotted as a function of rock strength. For each stress state the stresses are at the limit constrained by a coefficient of friction $\mu = 0.8$ on favorably oriented fault planes.

described by *Zemanek et al.* [1970], to produce a magnetically oriented image of the reflectivity of the borehole wall as a function of depth and azimuth in the hole. *Zoback et al.* [1985] demonstrated that breakouts could be imaged with the BHTV and produced the first detailed study of breakout cross sections. Since that time, considerable improvement has been made in the analysis of borehole televiewer data [*Barton*, 1988], and travel times determined from digitized data are now used to determine borehole shape [e.g., *Shamir et al.*, 1988; *Morin et al.*, this issue].

Plate 1*a* shows breakouts imaged with the BHTV in the Cajon Pass research well [*Shamir et al.*, 1988]. The images

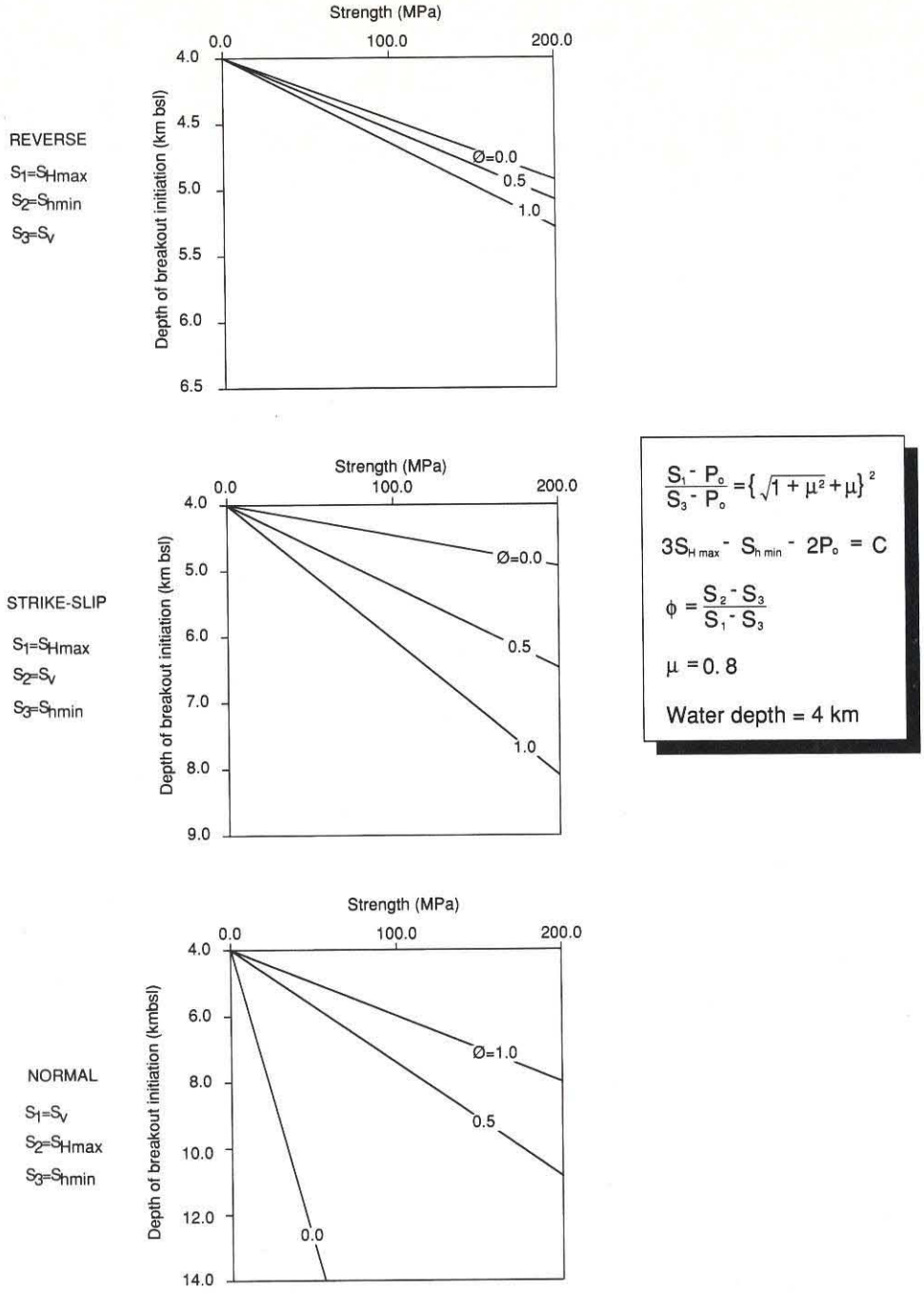

Fig. 6. Minimum depth of breakout formation in kilometers below sea level due to the circumferential stress concentration around a well drilled into oceanic crust overlain by 4 km of water, plotted as a function of rock strength. For each stress state the stresses are at the limit constrained by a coefficient of friction $\mu = 0.8$ on favorably oriented fault planes.

on the left are borehole radius as a function of depth and azimuth. On the right, cross sections of the borehole are shown at various depths. Each cross section involves superposition of three transducer scans (spanning approximately 10 cm vertically). The breakouts appear in cross section as smooth enlargements on opposite sides of the borehole. The amplitude of the reflected signal is lower within the breakout, due to the rougher surface and the fact that the reflection within the breakout is scattered away from the transducer because of nonnormal incidence of the acoustic pulse. As a result, one finds that often a reflection is returned only from the back of the breakout. In the images on the left side of the figure the breakouts appear as irregular vertical bands spanning several meters along the borehole.

Conditions for Tensile Failure

The conditions for tensile failure have been discussed extensively in the context of hydraulic fracturing. In typical

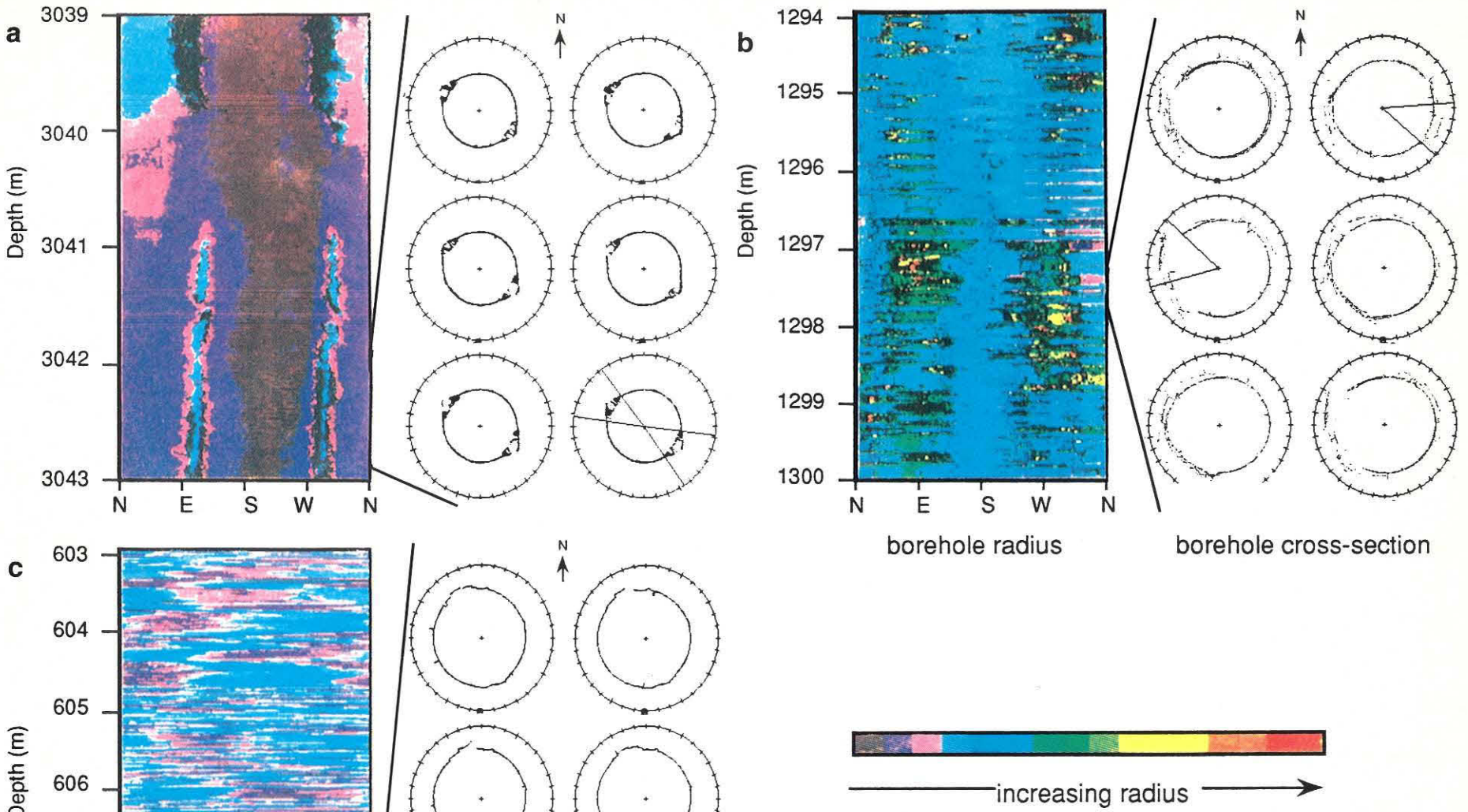

Plate 1. (*a*) Observations of well bore breakouts at 3 km depth in the granitic rocks penetrated by the Cajon Pass well (data from *Shamir et al.* [1988]). On the left is an oriented, false color image of the well bore radius as a function of azimuth. The difference in radius between light blue and deep purple is about 0.6 cm in an ~8.5-cm-radius borehole. The cross sections on the right have somewhat enhanced borehole relief, to show the characteristic broad, flat-bottomed shape of the breakouts. These are typical of well bore breakouts observed by the borehole televiewer in crystalline rock. (*b*) Observations of well bore failure at 1.3 km below seafloor in sheeted dikes in DSDP hole 504B (data courtesy of R. Morin) are shown. The difference in radius denoted by the color change from blue where the hole is not enlarged to yellow within the breakouts is 1.4 cm. (*c*) Borehole televiewer data recorded during DSDP leg 78B in hole 395A, showing very small (incipient) breakouts at a depth of 603 mbsf, are illustrated.

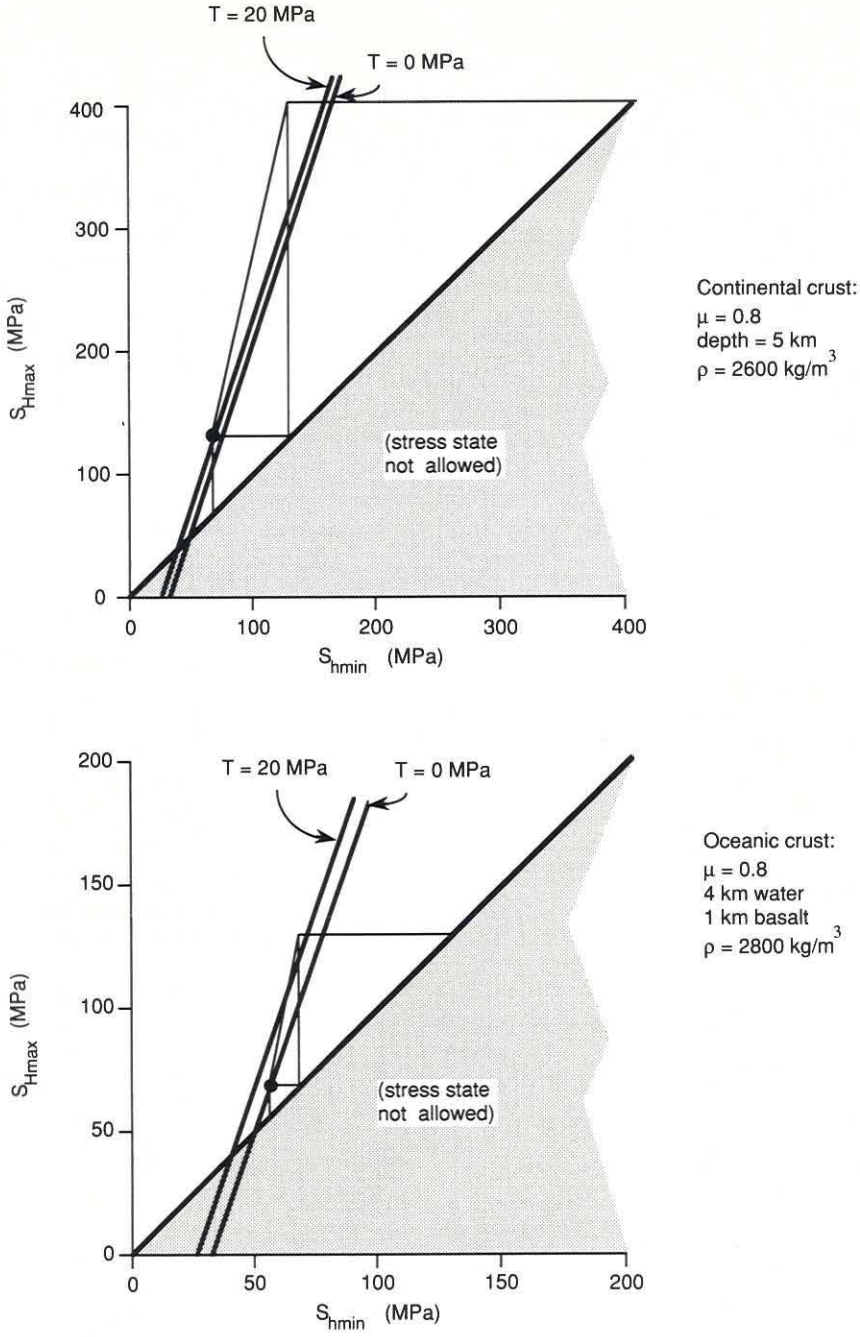

Fig. 7. Stress conditions necessary to cause tensile fracturing at the azimuth of S_{Hmax}, for the stress conditions defined in Figure 1. The lines illustrate the stress values necessary to cause tensile failure for the given values of tensile strength, if the well bore fluid pressure is equal to the ambient pore pressure (i.e., $S_{\mathrm{Hmax}} = 3S_{\mathrm{hmin}} - 2P_0 + T$). Tensile failure can occur under normal drilling conditions where the lines intersect the polygon constraining the stress state. For example, the stress state indicated by the circle will cause tensile failure if the tensile strength is zero, as shown also in Figure 2.

hydraulic fracturing operations, increasing the fluid pressure in the well bore induces tensile failure in a vertical well bore at the azimuth of the greatest far-field horizontal principal stress. Hydraulic fractures will be produced when the pressure in the well bore exceeds the sum of the tensile strength and the circumferential stress concentration. Written in terms of the total stresses and the pore pressure, this condition [after *Hubbert and Willis*, 1957] is

$$P_b = 3S_{\mathrm{hmin}} - S_{\mathrm{Hmax}} - P_0 + T \tag{5}$$

where P_b is termed the breakdown pressure and T is the tensile strength.

Under certain tectonic stress conditions, however, tensile failure occurs during drilling simply because of the pressure of the fluid column in the borehole resulting in "drilling-induced" hydrofracs. At the Nevada Test Site (NTS), where

TABLE 1. Relationship Between Observed and Predicted Breakout Depths

Well Name	C_0, MPa	C, MPa	Measured ϕ	Stress Regime	Depth of Breakout Initiation, km	Predicted Depth of Initiation, km	Predicted Range of ϕ
Moodus	>105*	>105–143	0.5	R	~1.1	0.90–1.22	>0.25
NTS	15–120†	15–163	0.35–0.6	N	~1.1	0.50–5.45	>0.3
Cajon Pass	100–150*	100–204	1.0	N/SS	~2.7	2.30–4.47	>0.9
Fenton Hill	124–176‡	124–240	1.0	N/SS	2.9	2.88–5.58	>0.85

*C_0 inferred from tensile strengths measured using the Brazilian test and the relationship between tensile and uniaxial compressive strength $C_0 \sim (8\text{–}12)T_0$.
†*Price and Bauer* [1985].
‡T. Dey (personal communication, 1987) [after *Barton et al.*, 1988].

the ambient pore pressure is appreciably subhydrostatic, the water used to fill the well bore during drilling frequently caused hydraulic fractures to occur [*Stock et al.*, 1985].

Figure 7 illustrates the range of stresses that could lead to tensile failure at the well bore, if the well bore fluid pressure is equal to the ambient pore pressure. Tensile failure can occur for a given value of tensile strength if the stress state lies to the left of the indicated line. Drilling-induced hydrofracturing can occur whenever the horizontal stress ratio is close to the limit constrained by the strength of strike-slip faults (i.e., where the ratio of the effective principal horizontal stresses is about 3). In some cases, as a consequence of the excess pumping pressure required to lift cuttings, the pressure at the bottom of a well during drilling can exceed the pressure due to the static fluid column by as much as 10 MPa. This is equivalent to reducing the "effective" tensile strength and would shift the lines of constant tensile strength to the right, making tensile failure more likely. Nevertheless, it is clear that the presence of drilling-induced hydraulic fractures would still constrain the possible stress state to be close to that associated with incipient strike-slip faulting.

Tensile failure at the well bore can also be induced by the thermal stresses associated with well bore cooling. *Allison and Nielson* [1988] observed features in four-arm caliper (dipmeter) logs in geothermal wells which may be due to tensile fractures developed because of well bore cooling. Similarly, tensile fractures were produced during drilling in geothermal fields in France and are suggested to have formed in the KTB (German deep drilling project) pilot hole (L. Mastin, written communication, 1989). The effect of thermal stresses is equivalent to that of the excess well bore pressure. Cooling the well would induce tensile thermal stresses, lower the apparent tensile strength, and promote tensile failure. Depending on the magnitude of the thermal stress, this could lead to failure within the oceanic crust even if the rock is fairly strong.

Thus although the presence of tensile cracks requires a large ratio of effective horizontal stresses and a strike-slip-faulting regime, it does not generally differentiate between cases in which $S_v \approx S_{\mathrm{Hmax}}$ (strike-slip and normal faulting) and $S_v \approx S_{\mathrm{hmin}}$ (strike-slip and reverse faulting). Distinguishing between these cases requires observations related to compressive failure (breakouts).

Application to Continental Crust

Over the past 5 years a number of wells have been studied in sufficient detail that data are available on the magnitude of in situ stresses, distribution of well bore breakouts, and compressive strength of the rock. This makes it possible either to utilize all of the data that are available from these wells to test the overall validity of the analysis, or to utilize only a portion of the available data in an attempt to place constraints on stress magnitudes simulating the general approach that we are suggesting for cases in which relatively complete information from a given well is not available.

Table 1 summarizes the key information from several wells in which the state of stress was found to be consistent with that predicted from the frictional strength of well-oriented faults (that is, in accordance with (1)) and for which information is available on the distribution of well bore breakouts and rock strength. Note that these four cases involve normal, normal/strike-slip, and reverse-faulting environments. Relatively continuous breakouts were observed in each case from the shallowest depth to the total drilled depth.

Utilizing (4*a*) and the information on strength and stress magnitudes in Table 1, we can calculate the range of depths below which "relatively continuous" breakouts would be expected in each well. The term relatively continuous refers to the fact that we want to consider failure of the well bore at representative stresses and rock strength values, not isolated and discontinuous breakouts that might be observed only in selected sections of the well bore where locally the rock might be unusually weak. We compare the observed depth below which breakouts are relatively continuous with the calculated depths. In each case the depth below which relatively continuous breakouts were observed is within the range predicted by the calculation. However, one must keep in mind the fact that the strength values are poorly constrained by laboratory measurements, particularly where unconfined compressive strength is calculated, rather than measured directly. In fact, the largest range of predicted depth (at NTS) is the one for which the largest range of strengths were assumed. The NTS wells were drilled into imbricated tuffs, for which the strengths depended on the degree of imbrication, which varied greatly from unit to unit. In general, breakouts were only observed in the weaker units, consistent with the known stress state. Aside from this case the depth of initiation observed is close to the lowest calculated value, suggesting that the appropriate strength is closer to C_0 than to C_b.

Alternatively, one can use the depth of breakout initiation to constrain the stress state. Table 1 shows the range of ϕ values predicted on the basis of the breakout distribution if the vertical stress and one limiting stress are known. In all cases the vertical stress was measured, and the stress magnitudes are at failure equilibrium; therefore (1) is valid for these data. The comparison between the calculated range of ϕ and the measured values illustrates our ability to predict one of the three principal stresses simply from knowledge of

TABLE 2. Physical Properties of Oceanic Basalts

Parameter	Value
Tensile strength T	23–34 MPa
Unconfined compressive strength C_0	170–224 MPa
Poisson's ratio ν	0.17–0.25
Young's modulus E	50–70 GPa
Thermal expansion coefficient α	$5.4 \pm 1 \times 10^{-6}$ °C^{-1}
Thermal diffusivity κ	1×10^{-6} m^2/s

the depth range of compressive well bore failure and of the other two stresses. In each case the predicted range includes the known value of ϕ. The power of the method lies in its ability to restrict ϕ and hence to place one bound (either a lower or an upper bound) on the intermediate stress. For example, for Moodus, where ϕ was measured to be 0.5, the analysis constrains ϕ to lie above 0.25. For NTS, where ϕ is between 0.35 and 0.6, the analysis requires ϕ to be greater than 0.3. At Cajon Pass and Fenton Hill, where ϕ is close to 1, the analysis also predicts very large values for this ratio.

All of these results are limited by our knowledge of the appropriate value of rock strength. The large range of values for ϕ result from the large range of possible values for C. These uncertainties will persist until laboratory strengths can be determined for rock from within these wells both in intervals which contain breakouts and in those which do not.

Application to Oceanic Crust

Although a large number of boreholes have been drilled into oceanic basement during the DSDP and ODP, only a small number of these have been logged with the borehole televiewer, and none have been tested by hydraulic fracturing. As described above, the presence of breakouts allows the determination of the orientation of the principal horizontal stresses and places a lower bound on the stress difference, whereas the absence of breakouts provides an upper bound on the stress difference. If tensile cracks are present, a further constraint can be placed on the ratio of the effective principal horizontal stresses.

We make the following assumptions in this analysis. First, we can reasonably assume that the in situ pore fluid pressures are close to hydrostatic. In fact, measured pore pressures in hole 504B [*Anderson and Zoback*, 1982], hole 395A [*Hickman et al.*, 1984*a*], and hole 597C [*Shipboard Scientific Party*, 1985] indicate that pore pressures are within 1 MPa (2.5%) of hydrostatic. We also assume that S_v is a principal stress and is equal to the weight of the overlying rock and seawater.

To place constraints on the stresses necessary for well bore failure, we need to know the properties of the basalts. Table 2 shows typical values for the parameters necessary for these calculations [*Clark*, 1966; *Carmichael*, 1982]. With the exception of one anomalously low-strength sample, *Bauer and Handin*'s [1985] measurements of E and C_0 of basalts from DSDP hole 504B lie within the range presented in this table.

There is considerable scatter in these data, particularly for the tensile and unconfined compressive shear strengths. The constraints presented below should therefore be considered in light of this fact and will have to serve until better information concerning the strength of specific oceanic basalts is available. For the purpose of this paper we will use the following (average) values of the properties tabulated above: $T = 28.5$ MPa, $C_0 = 200$ MPa, $\nu = 0.2$, $E = 60$ GPa, $\alpha = 5.4 \times 10^{-6}$ °C^{-1}, and $\kappa = 1 \times 10^{-6}$ m^2/s.

DSDP Holes 504B and 501

Hole 504B was drilled over a succession of DSDP and ODP legs to a total depth of 1562 m below seafloor (mbsf) in 3460 m of water and penetrates over 1200 m of 5.9-Ma oceanic crust south of the Costa Rica Rift (Figure 8). Pillows and minor flows were encountered in the uppermost 571.5 m of basement, below which was a 209-m transition zone followed by sheeted dikes and massive units [*Becker et al.*, 1989].

In hole 504B, *Newmark et al.* [1984] observed stress-induced well bore breakouts in the section of the hole drilled on legs 69 and 70. *Morin et al.* [this issue] digitized both the televiewer data from the leg 83 log and from a log recorded during leg 111. The digitized data cover a depth range from 440 mbsf to 1525 mbsf. The uppermost 170 m of basement could not be studied, as no data were recorded on tape during the log of this interval on leg 83. *Morin et al.* [this issue] identify a bimodal distribution of hole enlargements throughout the interval from about 700 mbsf to total depth and attribute the predominant azimuth of enlargement (117.5° ± 20°) to compressive failure (breakouts) and the secondary mode (about 27°) to tensile failure. The breakouts become nearly continuous below about 1.2 km below seafloor. The maximum compression direction inferred from these data (N27.5°E) agrees with the P axes of focal plane mechanisms of nearby earthquakes [*Bergman*, 1986].

Plate 1*b* presents a short section of digitized televiewer data from leg 111. The leg 111 data contain clearly imaged well bore enlargements, over the interval 1294–1300 mbsf, within the intrusive section of sheeted dikes. Hole enlargements occur at 90° and 270° here, within the range of scatter of the measurements presented by *Morin et al.* [this issue]. Although the breakouts are not as regular or as well imaged in data from hole 504B as they are in holes such as Cajon Pass (Plate 1*a*), the fact that enlargements occur on both sides of the hole, and at a generally consistent azimuth, suggests that they are stress-induced.

DSDP hole 501 was drilled 400 m west of hole 504B through 264 m of sediments and penetrated 73 m of basement. Core recovery was moderate and indicated a mixed assemblage of pillows and massive units. Televiewer data were recorded in the uppermost 25 m of basement only, but data were recorded in almost the entire sedimentary section [*Zoback and Anderson*, 1982]. We analyzed these data in detail and found no breakouts, either in the sedimentary section or in the basement interval.

The presence of breakouts within the depths penetrated by hole 504B demonstrates that high horizontal stresses must exist at a relatively shallow depth of less than 1 km into young oceanic crust. To illustrate this, we present in Figure 9 schematic plots of two possible stress states at sites 501 and 504. In these figures we calculate S_v from the weight of the overlying rock and seawater. In Figure 9*a* we assume that the stress regime is extensional, with $S_1 = S_v = S_{\mathrm{Hmax}}$, and allow S_{hmin} to range between that value and the value limited by a coefficient of friction $\mu = 0.8$. In Figure 9*b* we assume the stress regime is compressional, with $S_3 = S_v = S_{\mathrm{hmin}}$, and allow S_{Hmax} to range between that value and the

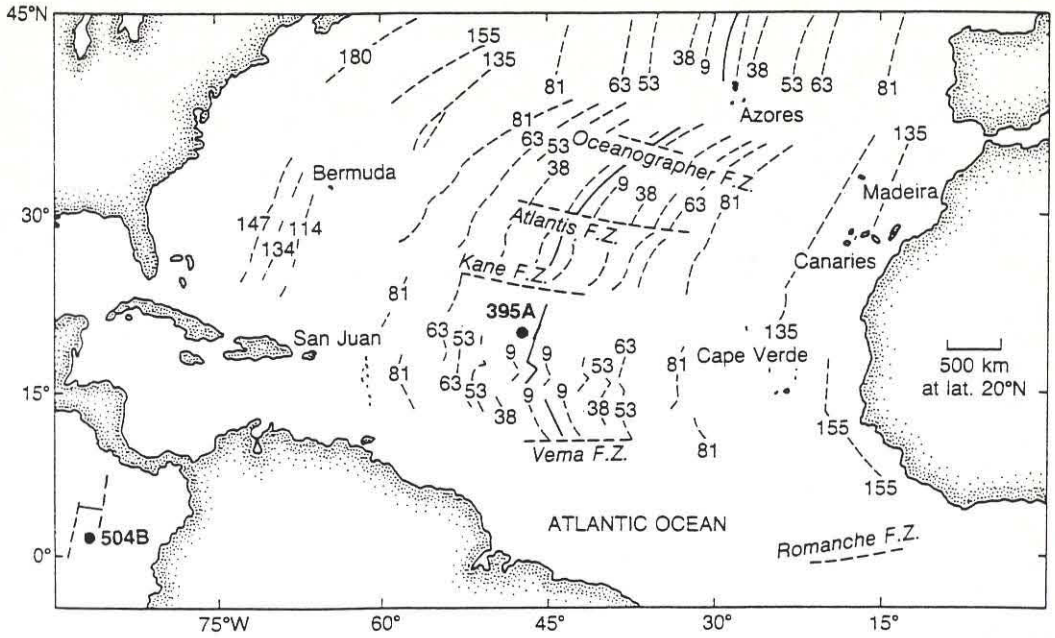

Fig. 8. Map [after *Hyndman and Salisbury*, 1984] showing the locations of DSDP hole 504B and of DSDP hole 395A. Hole 501 is within the area covered by the circle at site 504. The orientations of nearby spreading centers and transforms are also shown.

value limited by a coefficient of friction $\mu = 0.8$. In each case, setting one horizontal stress equal to S_v is equivalent to the most favorable stress state for the formation of breakouts. Lines are shown illustrating the value of rock strength (C) below which breakouts would occur for a given value of the unknown principal stress. It is evident in Figure 9*a* that breakouts cannot occur in an extensional stress environment at the depths penetrated by DSDP hole 504B unless the rock strengths were less than 75 MPa. This is a factor of 3 smaller than the average value of C_0 of more than 200 MPa measured by *Bauer and Handin* [1985]. We see in Figure 9*b*, however, that for a rock strength of between 200 and 272 MPa ($C_0 \leq C \leq 1.36C_0$), nearly continuous breakouts would be expected to occur at depths of about 1 km below seafloor, but only if the maximum horizontal stress was at the limit imposed by the strength of reverse faults and $\phi = 1$ (or $S_{\text{hmin}} = S_v = S_3$).

As illustrated in Figure 9, *Morin et al.* [this issue] report relatively continuous breakouts in hole 504B below about 1.2 km below seafloor. Therefore S_{Hmax} must be quite high (close to the limit constrained by the frictional strength of the crust), and S_{hmin} must be equal to S_v. Short intervals with breakouts which occur above that depth can be explained simply by localized sections of the hole with lower than average compressive strength. *Morin et al.* [this issue] also report the presence of tensile failure in DSDP hole 504B. We can develop a similar set of criteria for tensile failure, to constrain the ratio of the horizontal stresses. However, in this instance the thermal stress and therefore the temperature difference due to pumping cold fluid into the well bore must be known.

Calculating the thermal effect of circulation is quite difficult as pumping rate, rotation rate, fluid viscosity, and the temperature profile outside the pipe all influence the heat transfer among the drilling fluid, the fluid outside the pipe, and the rock surrounding the hole. Furthermore, although drilling fluids exiting the bit may cool the bottom of the hole, returning fluids may warm shallower sections. However, estimates of the minimum temperature perturbation can be obtained from temperature logs run shortly after circulation ceased. Temperatures within hole 504B were recorded a number of times, either shortly after drilling or after the well bore had equilibrated during legs 69, 70, 83, 92, and 111 [*Becker et al.*, 1989]. On the basis of the results of these measurements, drilling and circulating within hole 504B resulted in a minimum of 40°C cooling of the bottom of the well bore. During each circulation phase, shallower sections of the hole may have been warmed somewhat. As suggested by *Morin et al.* [this issue], temperatures were most strongly perturbed at the points where the fluid exited the pipe and for the periods during which the hole was deliberately cooled prior to logging. On the basis of 40°C cooling, the rock properties in Table 2, and (3), the minimum additional circumferential tensile stress applied during circulation within hole 504B is 16.4 MPa. Figures 10*a* and 10*b* are similar to Figures 9*a* and 9*b* and illustrate the stress conditions necessary to cause tensile failure at the borehole wall if well bore fluid pressure is equal to the in situ pore fluid pressure. The additional stresses generated by well bore cooling can be considered simply by reducing the tensile strength by the magnitude of the tensile thermal stress. In other words, a tensile strength of 20 MPa and a tensile thermal stress of 20 MPa are equivalent to a zero effective tensile strength. For the assumed average tensile strength of 28.5 MPa and a 40°C decrease in well bore temperature, the effective tensile strength is 12.1 MPa. For this strength and the reverse/strike-slip stress regime required for breakouts, tensile failure could occur at almost any depth below the top of basement. Thus the stress state required to produce breakouts would also produce tensile failure by well bore cooling, and it is therefore not surprising that such features were observed by *Morin et al.* [this issue].

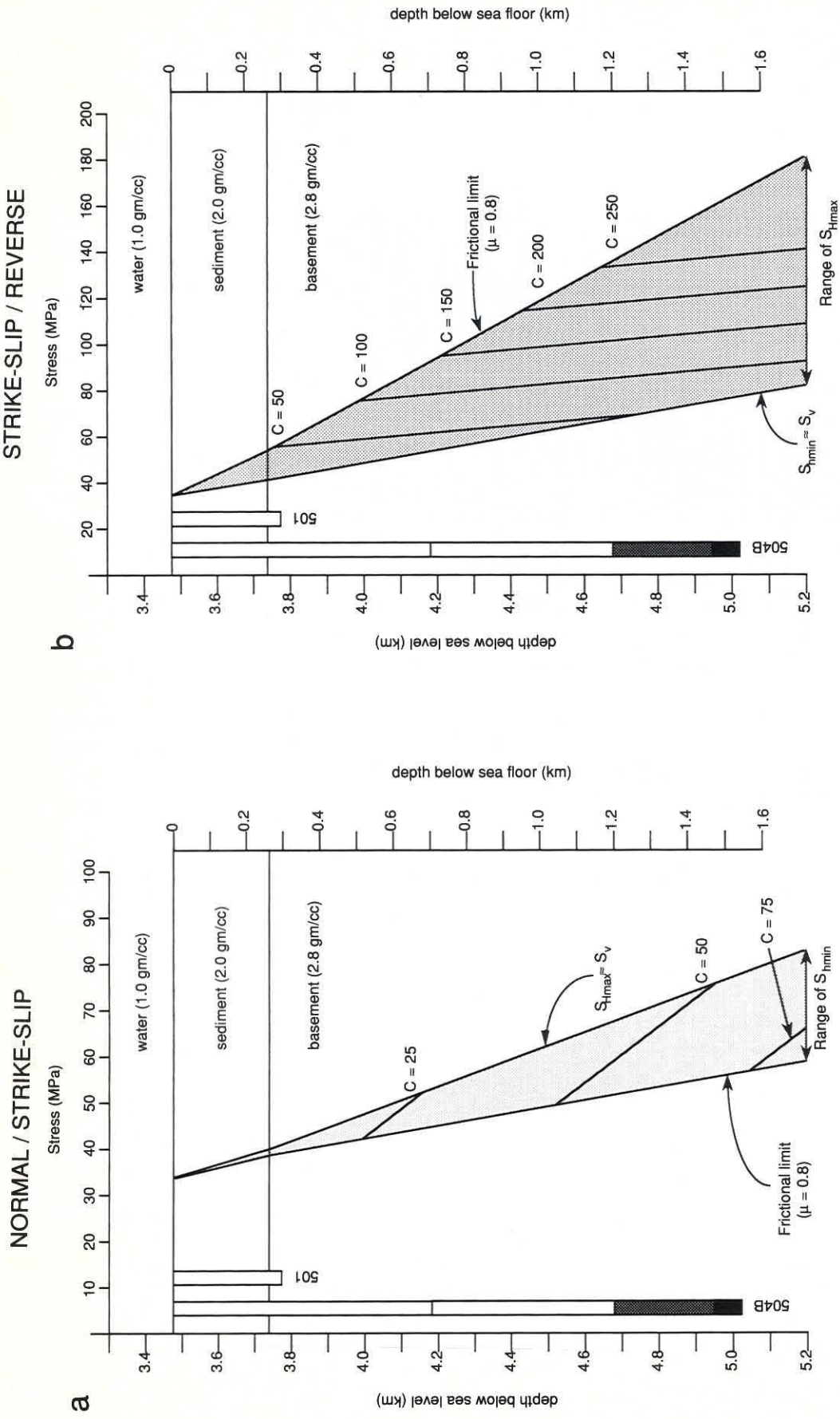

Fig. 9. Schematic illustration of possible stress conditions at DSDP sites 504 and 501. Also shown is the incidence of breakouts in holes 504B [*Morin et al.*, this issue] and 501. No breakouts were observed in 501, and breakouts were intermittent in 504B below about 700 mbsf, common below about 1.2 km below seafloor, and nearly continuous below about 1.5 km below seafloor. (*a*) A normal/strike-slip environment, with $S_{Hmax} = S_v = S_1$, $S_{hmin} = S_3$, is shown. S_{hmin} can range from equal to S_{Hmax} to a minimum value controlled by friction (equation (1)). The lines are $S_{Hmax} = \frac{1}{3}(S_{hmin} + P_0 + C)$, for the values of C shown. (*b*) A strike-slip/reverse environment, with $S_{hmin} = S_v = S_3$, $S_{Hmax} = S_1$, is also illustrated. S_{Hmax} can range from equal to S_{hmin} to a maximum value controlled by friction (equation (1)). The lines are $S_{hmin} = 3S_{Hmax} - C - 2P_0$ for the values of C shown. In each case, breakouts will form only if the rock strength C is below the contoured values. For strengths of 200–270 MPa, typical of samples from hole 504B [*Bauer and Handin*, 1985], breakouts would not be expected in a normal/strike-slip environment at any depth penetrated by hole 504B. The observations of breakouts are, however, consistent with a reverse-faulting regime with S_{Hmax} close to the limit imposed by a coefficient of friction $\mu = 0.8$.

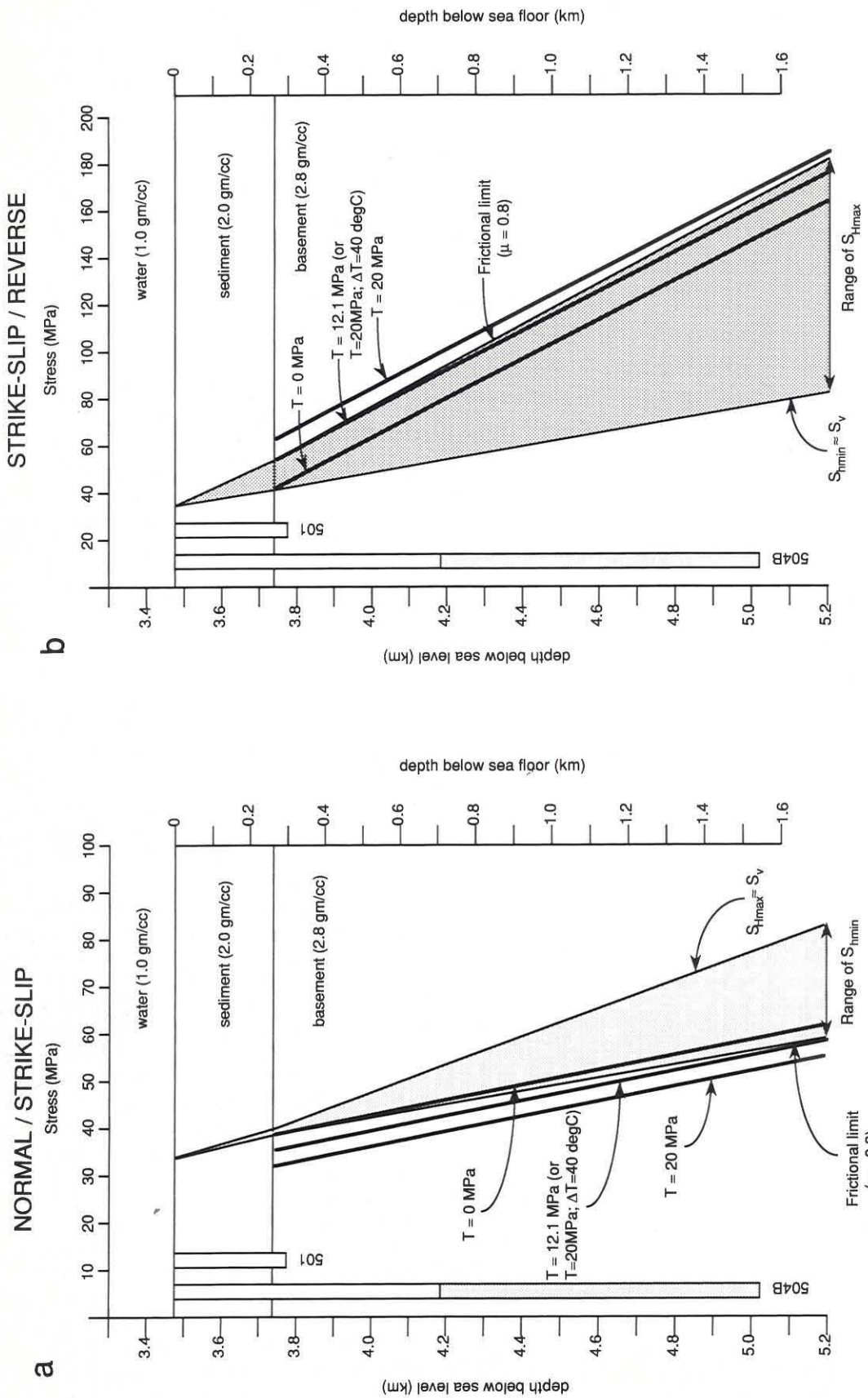

Fig. 10. Schematic illustration of possible stress conditions at DSDP sites 504 and 501. The stress states are as described in the caption Figure 9. Also shown is the depth range over which tensile failure was observed in hole 504B [*Morin et al.*, this issue]. (*a*) The maximum values of S_{hmin} for which tensile failure would occur at a given depth if the tensile strength of the rock is below the indicated values and the stress regime is transitional between normal and strike-slip faulting. (*b*) The minimum values of S_{Hmax} for which tensile failure would occur at a given depth if the tensile strength of the rock is below the indicated values and the stress regime is transitional between reverse and strike-slip faulting. In both cases it is assumed that the fluid pressure in the well bore is equal to the pore pressure in the rock and that the fluid temperature is equal to the ambient temperature. The intermediate value of tensile strength is the effective tensile strength computed assuming a 40°C decrease in well bore temperature during fluid circulation and a tensile strength of 28.5 MPa. Note that the presence of tensile cracks is only somewhat more likely for a reverse-faulting regime, but that in either a reverse- or normal-faulting regime the maximum horizontal stress difference (strike-slip equilibrium) is required.

DSDP HOLE 395A

DSDP site 395 is situated on the edge of a small sediment pond near the center of magnetic anomaly 4, at 22°45'N latitude, in 7.4 Ma crust between the Kane and the Vema fracture zones (Figure 8). Hole 395A was drilled to a total depth of 664 m below seafloor in 4493 m of water, through 93 m of sediments and 571 m of pillow basalts. A borehole televiewer log was obtained during DSDP leg 78B in the interval from 112 mbsf to 609 mbsf [*Hickman et al.*, 1984*b*]. Well bore enlargements satisfying the criteria for breakouts (that is, that enlargements were observed on both sides of the hole over a series of successive scans) were observed only near the bottom of the hole. No indications of well bore failure in tension were observed within hole 395A.

Plate 1*c* shows an example of the breakout data within DSDP hole 395A. Although the breakouts are impossible to resolve in the panel on the left, the well bore cross sections on the right clearly reveal shallow, poorly developed well bore enlargements oriented at approximately N20°W and S20°E. These indicate a maximum compressive stress N70°E, about 60° to the trend of the mid-Atlantic Ridge. The fact that the breakouts are very small and occur only intermittently suggests that the stresses are barely large enough to cause failure, and then only for anomalously weak rock.

Figure 11 shows possible stress regimes at site 395, along with lines for breakout formation as a function of maximum stress for various values of rock strength. As in the case of hole 504B, no breakouts would be expected in an extensional regime (Figure 11*a*) unless the rock is extraordinarily weak. Furthermore, Figure 11*b* illustrates that for a rock strength of 200 MPa, breakouts would not be expected even near the bottom of the hole, regardless of the state of stress. The well bore enlargements seen near the bottom of the hole could only occur by compressive shear failure if the rock strength in that short interval is about 150 MPa and if S_{Hmax} was at the limiting stress for reverse faulting and $S_{\mathrm{hmin}} = S_v$. These results are quite similar to those obtained at site 504, and together they suggest that in relatively young crust in both the Atlantic and the Pacific Oceans, very large compressive stresses are at a large angle to the ridge axes.

An attempted hydraulic fracturing experiment in this hole [*Hickman et al.*, 1984*a*] was unsuccessful after attaining an excess well bore fluid pressure of 15.2 MPa. The experiment was conducted with the packer set at a depth of 582 mbsf, in competent rock near the bottom of the hole. Using the values for tensile strength from Table 2 (23–34 MPa), the fact that breakdown did not occur is not surprising. Even if the state of stress implied by the breakouts near the bottom of the hole is correct, the expected breakdown pressure would be over 50 MPa. Temperature profiles recorded during leg 78B [*Becker et al.*, 1984] and during ODP leg 109 [*Shipboard Scientific Party*, 1988*b*] indicate that temperatures were essentially isothermal to 250 mbsf. Extrapolating a conductive gradient to total depth indicates a maximum thermal "shock" of less than 5°C, and thus the maximum applied circumferential tensile stress at the borehole wall due to this flow is about 7 MPa, much too small to substantially aid development of tensile cracks.

DSDP HOLE 597C

Site 597 is located at latitude 18°14'S, longitude 129°46'W, and is the westernmost site of an east-west transect of the southeast Pacific conducted during DSDP leg 92. DSDP hole 597C, drilled into 28.5-Ma crust (water depth 4160 m) generated at the Mendoza Rise, penetrated 52.5 m of sediments and 91 m of oceanic basalts; the hole has a reentry cone and therefore can be reoccupied and deepened in the future. Recovery was almost 54% and consisted largely of massive basalts [*Shipboard Scientific Party*, 1985]. Two complete BHTV logs were made in the hole within the basement interval. *Newmark et al.* [1984] reported the presence of intermittent breakouts throughout the total depth of the hole, from which a maximum horizontal compressive stress direction of N110°E ± 25° was determined. The presence of breakouts at such shallow depths is quite unusual, on the basis of both our experience and the theories presented above, and therefore we reanalyzed the data to confirm their presence.

No evidence of breakouts was found. Although the water depth and sediment thickness are slightly different at site 597 than those at sites 395 or 504, a figure similar to Figures 9 or 11 would reveal that breakouts could not develop at the depths penetrated by hole 597C (to 140 mbsf) even in a highly compressive stress regime, unless rock strength is extremely low. For a compressive strength of 200–270 MPa this borehole would have to be drilled an additional 600 m before breakouts might be expected. On the basis of these considerations, measurements of stress orientation from well bore enlargements in hole 597C should be treated with caution.

DISCUSSION OF SITES 504B AND 395A

Summarizing the results of previous work and of the above analyses, breakouts were observed in DSDP hole 504B and in the bottom of DSDP hole 395A, and no breakouts were observed at shallow depths in DSDP hole 501 or in DSDP hole 597C. Tensile failure within hole 504B could have occurred only with the addition of large tensile stresses generated by well bore cooling. The orientation of maximum compression inferred from the breakouts in holes 504B and 395A is roughly perpendicular to nearby ridge axes and in the case of hole 504B is parallel to that inferred from nearby earthquake focal mechanisms, as pointed out by *Morin et al.* [this issue]. In order for breakouts to occur at the depths penetrated by these wells, the stress state must be $S_{\mathrm{hmin}} \approx S_v \ll S_{\mathrm{Hmax}}$; S_{Hmax} must be large enough to cause reverse faulting on planes with a coefficient of friction $\mu = 0.8$.

The presence of thermally induced tensile fractures in hole 504B, and their absence in hole 395A, can be related to differences in the temperature profiles within the two holes. Heat flow at site 504 is about 200 mW/m^2 [e.g., *Langseth et al.*, 1988; *Becker et al.*, 1989], and the temperature gradient in hole 504B is also quite high. In contrast, heat flow in the sediments at site 395 is of the order of 37 mW/m^2, less than one fifth that at site 504 [*Hussong et al.*, 1979]. The undisturbed temperature gradient within basement at site 395 is similarly quite low, a consequence of strong lateral convection within shallow basement [e.g., *Becker et al.*, 1984; *Kopietz et al.*, 1990]. Thus temperatures increase much more slowly with depth within hole 395A, and the likelihood of large thermal stresses generated by fluid circulation at equivalent depths in 395A is therefore much smaller than in 504B.

Figure 12*a*, which gives an overview of earthquake focal

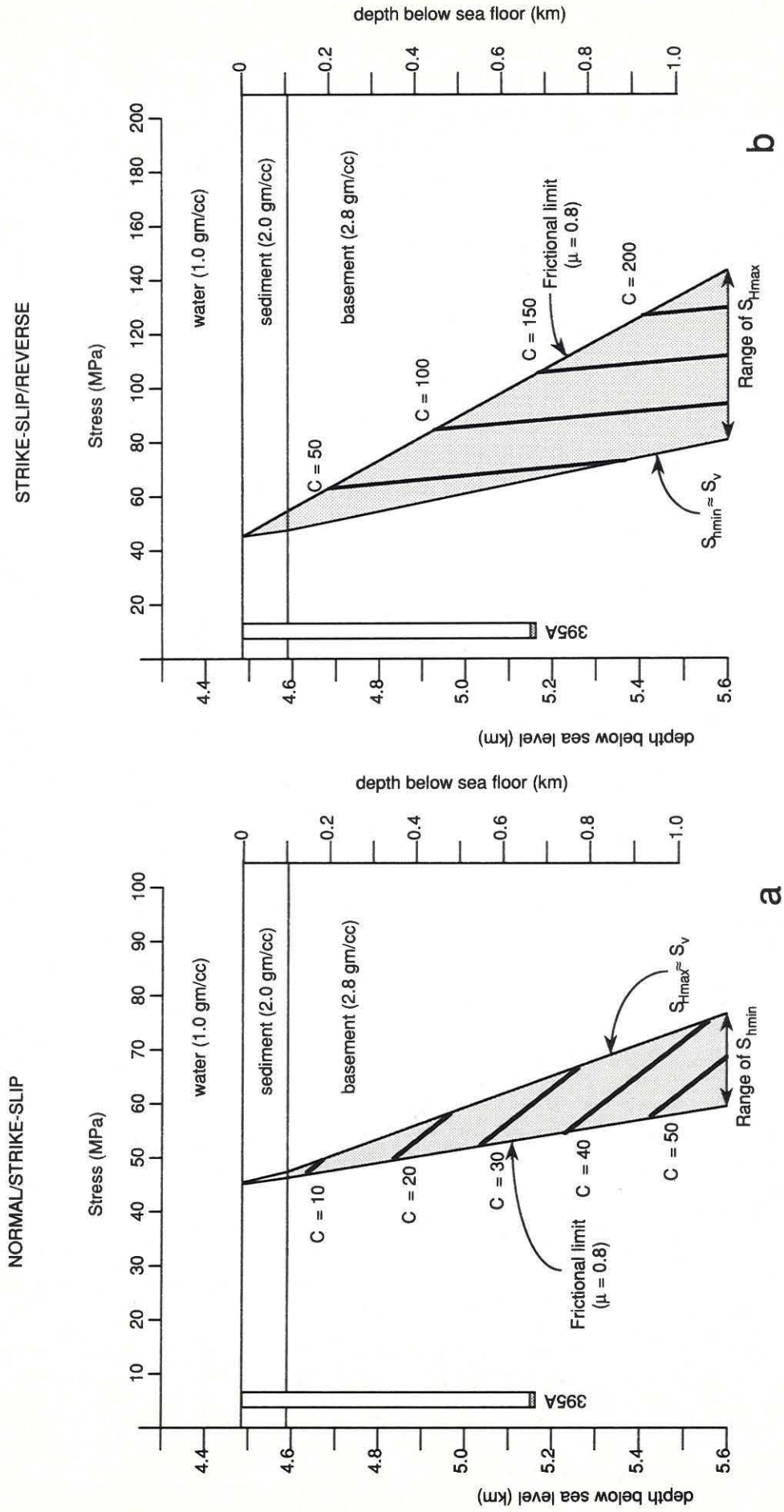

Fig. 11. Schematic illustration of possible stress states at DSDP site 395, if stresses are controlled by the frictional strength of well-oriented fault planes. The figure is similar to Figure 9 but for the conditions in hole 395A. Note that for breakouts to occur at 0.6 km below seafloor within DSDP hole 395A the compressive strength of the rock must be less than 150 MPa, and the stress regime must be as illustrated in Figure 11*b*.

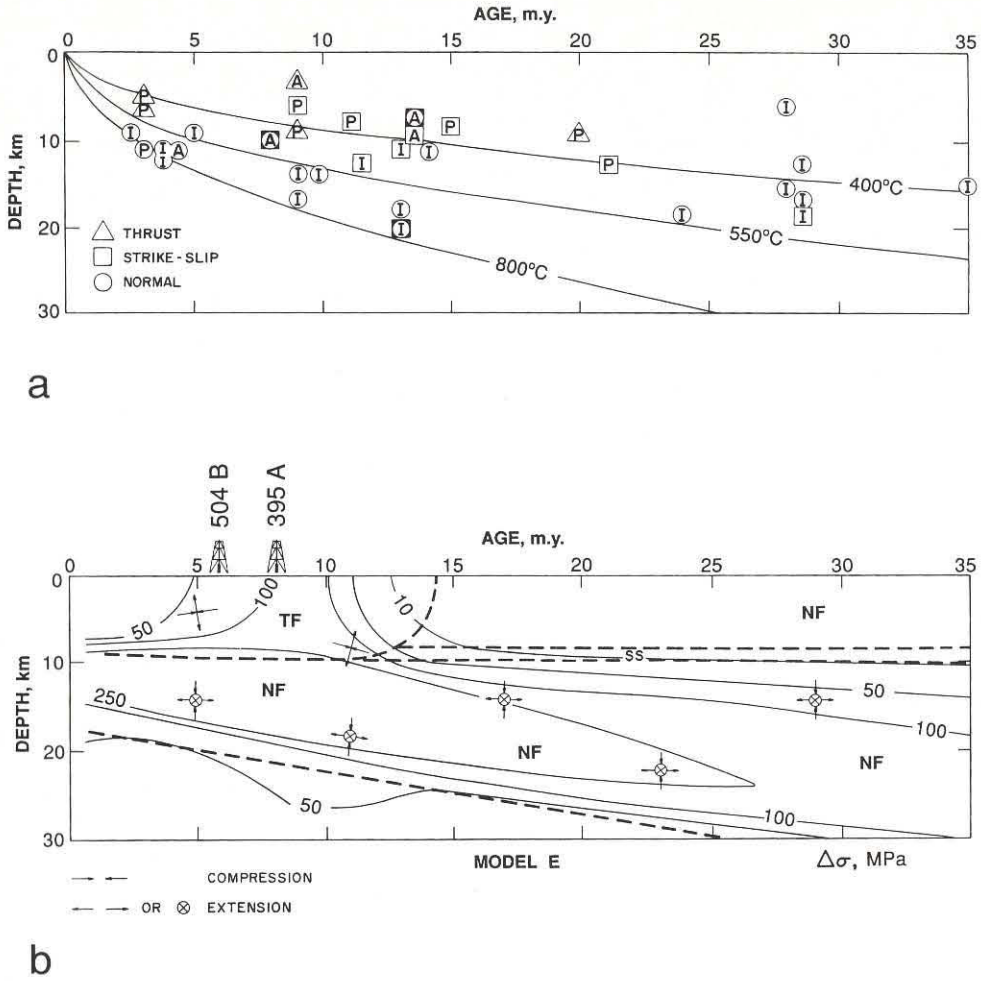

Fig. 12. (*a*) Focal mechanism and centroid depth relative to the seafloor as a function of lithospheric age for 32 near-ridge earthquakes from *Bratt et al.* [1985], after *Bergman and Solomon* [1984]. Mixed-faulting earthquakes are indicated by superimposed symbols, and the ocean in which each earthquake occurs is indicated by A (Atlantic), P (Pacific), and I (Indian Ocean). (*b*) Model E of *Bratt et al.* [1985] illustrates the effect of a 10-km-thick cooled layer with an elastic blocking temperature of 550°C, overlying a conductively cooling half-space, and a time constant for stress relaxation of 10 Ma. The age of the crust at sites 395 and 504 is shown.

mechanisms within oceanic lighosphere as a function of crustal age as tabulated by *Bergman and Solomon* [1984], reveals that reverse faulting predominates at shallow depths in young crust and that at greater depths and as the crust ages, strike-slip and normal faulting become more common. *Bratt et al.* [1985] have proposed that this state of stress is generated by thermoelastic effects in a plate consisting of a convectively cooled lid over a conductively cooling half-space, as illustrated in Figure 12*b*. The differential stresses generated by thermoelastic effects can exceed 100 Mpa at shallow depth, for crustal ages similar to those of sites 395 and 504. Ridge push forces cannot explain this stress distribution, as the horizontal stress generated by ridge push is zero at the ridge crest and increases with crustal age [e.g., *Bott and Kuzsnir*, 1984]. Although various models for stress relief and the depth of hydrothermal cooling lead to differences in the age to which shallow compressional stresses persist, thrust faulting predominates to ages older than 5 Ma in every case examined by *Bratt et al.* [1985], and the maximum deviatoric compression is horizontal and perpendicular to the ridge axis. In *Bratt et al.*'s [1985] model, stress relief is a function of time. This is quite different than the model used here, where the frictional strength of suitably oriented faults controls the maximum stress difference. However, if we combine the thermoelastic stress model of *Bratt et al.* [1985] with the frictional constraint on stress magnitudes, then in young oceanic lithosphere a thrust-faulting regime should predominate at shallow depths with S_{Hmax} maintained at a value constrained by strength and the (fixed) magnitude of the vertical stress, as in (1), and S_{hmin} approximately equal to S_v (there is no thermoelastic contribution to the horizontal stress parallel to the ridge axis), as required by the presence of breakouts within holes 504B and 395A.

As the crust ages, however, the model of *Bratt et al.* [1985] predicts that the importance of thermoelastic stress on the total lithospheric stress decreases. At an age of approximately 10–15 Ma, thermoelastic stresses are less important than the accumulated ridge push, and although the superposition of the two effects causes compressional stress normal to the ridge axis at all ages, the magnitude of the deviatoric compression is less than 50 MPa to ages of more than 35 Ma. Two implications arise from this observation. First, earthquakes and stress measurements within oceanic lithosphere

younger than 15 Ma probably do not record plate-driving stress, and second, it is unlikely that in situ stresses in older oceanic lithosphere are large enough to allow their orientation to be established by observing well bore failure at depths less than 1 km below the seafloor. This second conclusion may be invalidated by the presence of additional stress sources such as midplate swells, seamounts, or bending stresses related to subduction. Unfortunately, these stresses would also obscure those related to plate-driving forces.

CONCLUSIONS

We have presented here a simple model describing the conditions necessary for compressive and tensile failure of well bores in response to far-field stresses and well bore temperature variations generated by circulation of drilling fluids to depth. Using a simple elastic model for the stress concentration around a borehole, we find that the presence or absence of breakouts allows reasonable constraints to be placed on the magnitude of the horizontal principal stresses. Comparisons of the model predictions and the measured stresses in boreholes drilled on land show that in most cases the relatively simple failure criterion enables us to predict the depths at which breakouts are actually observed. The single largest uncertainty lies in the large variation of strength in these rocks and the lack of precise values to use in this analysis.

The presence of breakouts in DSDP holes 504B and 395A requires very high horizontal compression in young (5.9 and 7.3 Ma, respectively) crust, with $S_{\mathrm{Hmax}} \gg S_{\mathrm{hmin}} = S_v$. S_{Hmax} is within 30° of the spreading direction in both cases and reaches a value of more than 100 MPa at depths less than 0.5 km subbasement. Our conclusion that the stress magnitudes must be large enough to cause reverse faulting on planes with a coefficient of friction $\mu = 0.8$ is consistent with the observation of reverse and strike-slip earthquake focal mechanisms within young oceanic crust.

Thermally induced stresses due to well bore cooling by drill fluid circulation can play a large role in the generation of tensile failure at the azimuth of S_{Hmax}, as seen in DSDP hole 504B. This is especially true where heat flow and the geothermal gradient are both quite high, either in young oceanic crust or in geothermal regimes on the continents, but is less important in the case of DSDP hole 395A, where the temperature increase with depth is more modest. The occurrence of thermally induced tensile cracks in hole 504B is consistent with the strike-slip/reverse-faulting regime indicated by the breakout analysis. These thermally generated tensile cracks do not propagate away from the well bore unless the well bore fluid pressure exceeds the minimum far-field principal stress, which is unlikely unless the formation is severely underpressured.

The compressive crustal stresses required by observations of breakouts in DSDP holes 504B and 395A are due to thermoelastic effects of plate cooling and are not associated with plate-driving forces. Measurements of stresses from observations of well bore failure in crust older than 25 Ma, where stresses are dominated by the forces which drive the plates, require boreholes with significant penetration below the seafloor. This is a consequence of the high strength of oceanic basalts and the fact that the horizontal stresses are limited by the vertical stress and the strength of the crust.

Acknowledgments. The authors benefited in the preparation of this paper from discussions with a number of people, including Stephen Hickman, Lev Vernik, Oona Scotti, and Gadi Shamir. Larry Mastin and Karl Fuchs informally reviewed the paper, and we appreciate their comments. We also thank Roger Morin and Robin Newmark for permission to use their data in this work and Colleen Barton, who designed and programmed the borehole televiewer digitization and analysis system. The paper benefited substantially from thoughtful and insightful reviews by Bezalel Haimson and Randall Richardson. The research was supported by the National Science Foundation under contract OCE-8907922.

REFERENCES

Allison, M. L., and D. L. Nielson, Stress in active geothermal systems, Advances in Geothermal Reservoir Technology, *Tech. Rep. ESL-88027-JP*, Lawrence Berkeley Lab., Berkeley, Calif., 1988.

Anderson, E. M., *The Dynamics of Faulting and Dike Formation With Applications in Britain*, 2nd ed., Oliver and Boyd, Edinburgh, 1951.

Anderson, R. N., and M. D. Zoback, Permeability, underpressures and convection in the oceanic crust near the Costa Rica Rift, eastern equatorial Pacific, *J. Geophys. Res.*, *87*, 2860–2868, 1982.

Angelier, J., Determination of the mean principal directions of stresses for a given fault population, *Tectonophysics*, *56*, T17–T26, 1979.

Barton, C. A., Development of in-situ stress measurement techniques for deep drillholes, Ph.D. thesis, 192 pp., Stanford Univ., Stanford, Calif., 1988.

Barton, C. A., M. D. Zoback, and K. L. Burns, In-situ stress orientation and magnitude at the Fenton Hill geothermal site, New Mexico, determined from wellbore breakouts, *Geophys. Res. Lett.*, *15*, 467–470, 1988.

Bauer, S. J., and J. Handin, Mechanical properties of basalt cores from Deep Sea Drilling Project hole 504B, *Initial Rep. Deep Sea Drill. Proj.*, *83*, 371–378, 1985.

Becker, K., M. G. Langseth, and R. D. Hyndman, Temperature measurements in hole 395A, leg 78B, *Initial Rep. Deep Sea Drill. Proj.*, *78B*, 689–698, 1984.

Becker, K., et al., Drilling deep into the oceanic crust at hole 504B, Costa Rica Rift, *Rev. Geophys.*, *27*, 79–102, 1989.

Bell, J. S., and D. I. Gough, Northeast-southwest compressive stress in Alberta: Evidence from oil wells, *Earth Planet. Sci. Lett.*, *45*, 475–482, 1979.

Bell, J. S., and D. I. Gough, The use of borehole breakouts in the study of crustal stress, in *Hydraulic Fracturing Stress Measurements*, edited by M. D. Zoback and B. C. Haimson, pp. 201–209, National Academy Press, Washington, D. C., 1983.

Bergman, E. A., Intraplate earthquakes and the state of stress in oceanic lithosphere, *Tectonophysics*, *132*, 1–35, 1986.

Bergman, E. A., and S. C. Solomon, Source mechanisms of earthquakes near mid-ocean ridges from body wave inversion: Implications for the early evolution of oceanic lithosphere, *J. Geophys. Res.*, *89*, 11,415–11,441, 1984.

Bott, M. H. P., and N. J. Kuzsnir, The origin of tectonic stress in the lithosphere, *Tectonophysics*, *105*, 1–13, 1984.

Brace, W. F., and D. L. Kohlstedt, Limits on lithospheric stress imposed by laboratory experiments, *J. Geophys. Res.*, *85*, 6248–6252, 1980.

Bratt, S. R., E. A. Bergman, and S. C. Solomon, Thermoelastic stress: How important as a cause of earthquakes in young oceanic lithosphere? *J. Geophys. Res.*, *90*, 10,249–10,260, 1985.

Byerlee, J. D., Friction of rock, *Pure Appl. Geophys.*, *116*, 615–626, 1978.

Carmichael, R. S., *Handbook of Physical Properties of Rocks*, vol. II, 345 pp., CRC Press, Boca Raton, Fla., 1982.

Clark, S. P., Handbook of Physical Constants, *Mem. Geol. Soc. Am.*, *97*, 587 pp., 1966.

Coussy, O., Thermoporoelastic response of a borehole, *Int. J. Rock Mech. Min. Sci.*, in press, 1990.

Cox, J. W., Long axis orientation in elongated boreholes and its correlation with rock stress data, *Trans. SPWLA Annu. Logging Symp.*, *24th*, 1983.

Coyle, B. J., and M. D. Zoback, In situ permeability and fluid pressure measurements at ~2 km depth in the Cajon Pass research well., *Geophys. Res. Lett.*, *15*, 1029–1032, 1988.

Fairhurst, C., Methods of determining in situ rock stresses at great depths, *Tech. Rep. TRI-68*, Mo. River Div. Corps of Eng., Omaha, Nebr., 1968.

Gough, D. I., and J. S. Bell, Stress orientations from oil well fractures in Alberta and Texas, *Can. J. Earth Sci.*, *18*, 1358–1370, 1981.

Haimson, B. C., and C. G. Herrick, Borehole breakouts—A new tool for estimating in situ stress?, paper presented at the International Symposium on Rock Stress and Rock Stress Measurements, Luleå Univ. of Technol., Stockholm, Sweden, 1986.

Haimson, B. C., and C. G. Herrick, Borehole breakouts and in situ stress, in *Proceedings of the 12th Annual Energy-Sources Technology Conference and Exhibition*, pp. 17–22, American Society of Mechanical Engineers, New York, 1989.

Hickman, S. H., M. G. Langseth, and J. F. Svitek, In situ permeability and pore-pressure measurements near the mid-Atlantic Ridge, Deep Sea Drilling Project hole 395A, *Initial Rep. Deep Sea Drill. Proj.*, *78B*, 699–708, 1984*a*.

Hickman, S. H., J. F. Svitek, and M. G. Langseth, Borehole televiewer log of hole 395A, *Initial Rep. Deep Sea Drill. Proj.*, *78B*, 709–715, 1984*b*.

Hubbert, M. K., and D. G. Willis, Mechanics of hydraulic fracturing, *J. Pet. Technol.*, *9*, 153–168, 1957.

Hussong, D. M., P. B. Fryer, J. D. Tuthill, and L. K. Wipperman, The geological and geophysical setting near site 395, North Atlantic, *Initial Rep. Deep Sea Drill. Proj.*, *45*, 23–38, 1979.

Hyndman, R. D., and M. H. Salisbury, The physical nature of young upper oceanic crust on the mid-Atlantic Ridge, Deep Sea Drilling Project hole 395A, *Initial Rep. Deep Sea Drill. Proj.*, *78B*, 839–848, 1984.

Jaeger, J. C., and N. G. W. Cook, *Fundamentals of Rock Mechanics*, 3rd ed., 593 pp., Chapman and Hall, New York, 1979.

Kirsch, G., Die Theorie der Elastizitat und die Bedurfnisse der Festigkeitslehre, *VDI Z.*, *42*, 797–807, 1898.

Kopietz, J., K. Becker, and Y. Hamano, Temperature measurements at site 395, ODP leg 109, in *Proceedings of ODP, Scientific Results*, vol. 106/109, edited by R. Detrick, pp. 197–203, Ocean Drilling Program, College Station, Tex., 1990.

Kozlovski, Y. A., *The Superdeep Well of the Kola Peninsula*, 558 pp., Springer-Verlag, New York, 1984.

Langseth, M. G., M. J. Mottl, M. Hobart, and A. Fisher, The distribution of geothermal and geochemical gradients near site 501/504: Implications for hydrothermal circulation in the oceanic crust, in *Proceedings of ODP, Initial Reports, Part A*, vol. 111, pp. 23–32, Ocean Drilling Program, College Station, Tex., 1988.

Mastin, L. G., The development of borehole breakouts in sandstone, M.S. thesis, Stanford Univ., Stanford, Calif., 1984.

Mastin, L. G., Effect of borehole deviation on breakout orientations, *J. Geophys. Res.*, *93*, 9187–9195, 1988.

McGarr, A., Some constraints on levels of shear stress in the crust from observations and theory, *J. Geophys. Res.*, *85*, 6231–6238, 1980.

McGarr, A., On the state of lithospheric stress in the absence of applied tectonic forces, *J. Geophys. Res.*, *93*, 13,609–13,617, 1988.

McKenzie, D. P., The relation between fault plane solutions for earthquakes and the directions of the principal stresses, *Bull. Seismol. Soc. Am.*, *59*, 591–601, 1969.

Morin, R. H., R. L. Newmark, C. A. Barton, and R. N. Anderson, State of lithospheric stress and borehole stability at Deep Sea Drilling Project site 504B, eastern equatorial Pacific, *J. Geophys. Res.*, this issue.

Mount, V. S., and J. Suppe, State of stress near the San Andreas Fault: Implications for wrench tectonics, *Geology*, *15*, 1143–1146, 1987.

Newmark, R. L., M. D. Zoback, and R. N. Anderson, Orientation of in situ stresses in the oceanic crust, *Nature*, *311*, 424–428, 1984.

Okal, E. A., Intraplate seismicity of the southern part of the Pacific Plate, *J. Geophys. Res.*, *89*, 10,053–10,071, 1984.

Okal, E. A., J. Talandier, K. A. Sverdrup, and T. H. Jordan, Seismicity and tectonic stress in the south-central Pacific, *J. Geophys. Res.*, *85*, 6479–6495, 1980.

Plumb, R. A., and J. W. Cox, Stress directions in eastern North America determined to 4.5 km from borehole elongation measurements, *J. Geophys. Res.*, *92*, 4805–4816, 1987.

Price, R. H., and S. J. Bauer, Analysis of the elastic and strength properties of Yucca Mountain tuff, Nevada, *Proc. U.S. Symp. Rock. Mech.*, *26th*, 89–96, 1985.

Raleigh, C. B., J. H. Healy, and J. D. Bredehoeft, Faulting and crustal stress at Rangeley, Colorado, in *Flow and Fracture of Rocks*, *Geophys. Monogr. Ser.*, vol. 16, edited by H. C. Heard et al., pp. 275–284, AGU, Washington D. C., 1972.

Ritchie, R. H., and A. Y. Sakakura, Asymptotic expansions of solutions of the heat conduction equation in internally bounded cylindrical geometry, *J. Appl. Phys.*, *27*, 1453–1459, 1956.

Rummel, F., Stresses and tectonics of the upper continental crust—A review, in *Proceedings of the International Symposium on Rock Stress and Rock Stress Measurements, Stockholm, 1986 September 1–3*, Centek Publishers, Luleå, Sweden, 1986.

Shamir, G., M. D. Zoback, and C. A. Barton, In situ stress orientation near the San Andreas fault: Preliminary results to 2.1 km depth from the Cajon Pass scientific drillhole, *Geophys. Res. Lett.*, *15*, 989–992, 1988.

Shipboard Scientific Party, Site 597, *Initial Rep. Deep Sea Drill. Proj.*, *92*, 25–97, 1985.

Shipboard Scientific Party, Site 504, in *Proceedings of ODP, Initial Reports, Part A*, vol. 111, edited K. Becker et al., pp. 35–252, Ocean Drilling Program, College Station, Tex., 1988*a*.

Shipboard Scientific Party, Site 395, in *Proceedings of ODP, Initial Reports, Part A*, vol. 106/109, edited by R. B. Detrick et al., pp. 175–202, Ocean Drilling Program, College Station, Tex., 1988*b*.

Sibson, R. H., Frictional constraints on thrust, wrench and normal faults, *Nature*, *249*, 542–544, 1974.

Stephens, G., and B. Voight, Hydraulic fracturing theory for conditions of thermal stress, *Int. J. Rock Mech. Min. Sci.*, *19*, 279–284, 1982.

Stock, J. M., J. H. Healy, S. H. Hickman, and M. D. Zoback, Hydraulic fracturing stress measurements at Yucca Mountain, Nevada, and the relationship to the regional stress field, *J. Geophys. Res.*, *90*, 8691–8706, 1985.

Vardoulakis, I., J. Sulem, and A. Guenot, Borehole instabilities as bifurcation phenomena, *Int. J. Rock. Mech. Min. Geomech. Abstr.*, *25*, 159–170, 1988.

Wiebols, G. A., and N. G. W. Cook, An energy criterion for the strength of rock in polyaxial compression, *Int. J. Rock Mech. Min. Sci.*, *5*, 529–549, 1968.

Wiens, D. A., and S. Stein, Intraplate seismicity and stress in young oceanic lithosphere, *J. Geophys. Res.*, *89*, 11,442–11,464, 1984.

Zemanek, J., E. E. Glenn, Jr., J. J. Norton, and R. L. Caldwell, Formation evaluation by inspection with the borehole televiewer, *Geophysics*, *35*, 254–269, 1970.

Zheng, Z., J. Kemeny, and N. G. W. Cook, Analysis of borehole breakouts, *J. Geophys. Res.*, *94*, 7171–7182, 1989.

Zoback, M. D., and R. N. Anderson, Ultrasonic borehole televiewer investigation of oceanic crustal layer 2A, Costa Rica Rift, *Nature*, *295*, 375–379, 1982.

Zoback, M. D., and J. H. Healy, Friction, faulting and in situ stress, *Ann. Geophys.*, *2*, 689–698, 1984.

Zoback, M. L., and M. D. Zoback, State of stress in the conterminous United States, *J. Geophys. Res.*, *85*, 6113–6156, 1980.

Zoback, M. D., D. Moos, L. Mastin, and R. N. Anderson, Well bore breakouts and in situ stress, *J. Geophys. Res.*, *90*, 5523–5530, 1985.

Zoback, M. D., et al., New evidence on the state of stress of the San Andreas fault system, *Science*, *238*, 1105–1111, 1987.

Zoback, M. L., et al., Global patterns of intraplate stress: A status report on the world stress map project of the International Lithosphere Program, *Nature*, *341*, 291–298, 1989.

D. Moos and M. D. Zoback, Department of Geophysics, Stanford University, Stanford, CA 94305.

(Received July 28, 1989;
revised February 20, 1990;
accepted January 29, 1990.)

Appendix VI - Quality Assurance Documentation

This section includes photostatic copies of all of the field and digitization checklists completed during the collection and analysis of the data included in this report. With the exception of the lack of a post-log calibration for NONAME-1, all of the standard procedures were carried out in the course of this work. The final (post-log) calibration of the hi-temperature televiewer in INEL-1 was completed successfully, according to field notes, and the results apparently agreed with the pre-log calibration. However, no photograph of this calibration was found. We therefore have operated in the body of this report under the assumption that this calibration was not obtained. During the second phase log of INEL-1 no checklist sheets were available, and so photocopies of the field notebook are provided instead.

Appendix VI - Quality Assurance Documentation

This section includes photostatic copies of all of the field and digitization checklists completed during the collection and analysis of the data included in this report. With the exception of the lack of a post-log calibration for NONAME-1, all of the standard procedures were carried out in the course of this work. The final (post-log) calibration of the hi-temperature televiewer in INEL-1 was completed successfully, according to field notes, and the results apparently agreed with the pre-log calibration. However, no photograph of this calibration was found. We therefore have operated in the body of this report under the assumption that this calibration was not obtained. During the second phase log of INEL-1 no checklist sheets were available, and so photocopies of the field notebook are provided instead.

Borehole televiewer field check list

Date: 5/15/90
Time: 1230
Observer: MOOS/TAVARES
Well Name : USGS-17
INEL

Cable:

cable length 22,000'
number of conductors 7
resistance (ohms):

	1	2	3	4	5	6	7	armor
1	230	x	x	x	x	x	x	
2	∞	235	x	x	x	x	x	
3	∞	∞	240	x	x	x	x	
4	∞	∞	∞	240	x	x	x	
5	∞	∞	∞	∞	255	x	x	
6	∞	∞	∞	∞	∞	240	x	
7	∞	∞	∞	∞	∞	∞	240	0

Equipment

tool small.
surface panel number _____.
monitor _____. scope _____.

Pre-log calibration at 5/15 1545 (date/time)
Run in hole at 1550 (date/time)
Water level at 1600 (date/time)
Casing at — (date/time)
Total depth at 1605 (date/time)
Log start at 1630 (date/time)
Log end at 1703 (date/time)
Post-log calibration at 1710 (date/time)

Borehole televiewer field check list

Date: 5/15/90
Time: 15:45
Observer: Moos/Tavares
Well Name : USGS-17

pre-log calibration:

Time since turn-on ~ 20 minutes

Test in Al Tank, Fluid is Water.

Magnetic North is _____ degrees azimuth.

Magnetic East is _____ degrees azimuth.

Magnetic South is _____ degrees azimuth.

Magnetic West is _____ degrees azimuth.

place photograph here:

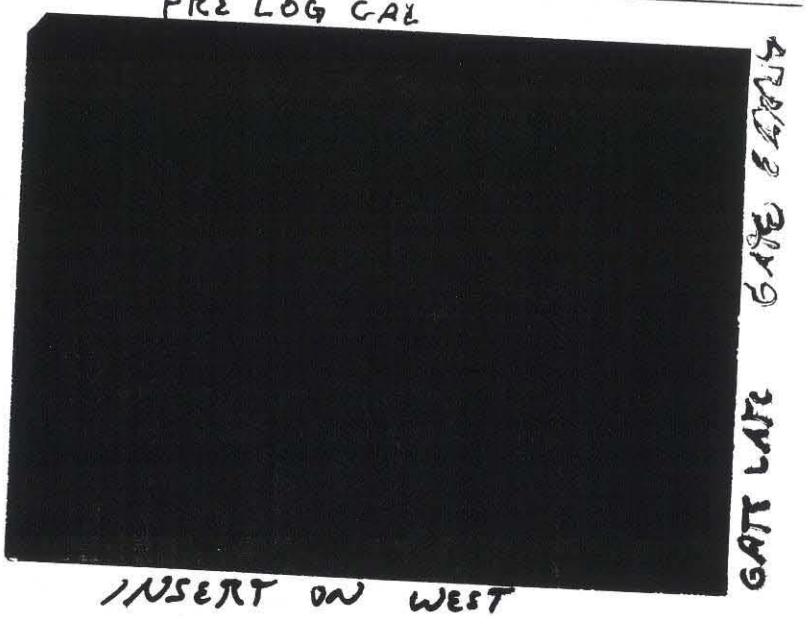

Annotations:

Borehole televiewer field check list

Date: 5/15/90
Time: 17:10
Observer: Mock/Tavares
Well Name : USGS-17

post-log calibration:

Time since turn-on 1:45.

Test in Aluminum tank. Fluid is Clear Water.

Magnetic North is _____ degrees azimuth.

Magnetic East is _____ degrees azimuth.

Magnetic South is _____ degrees azimuth.

Magnetic West is _____ degrees azimuth.

place photograph here:

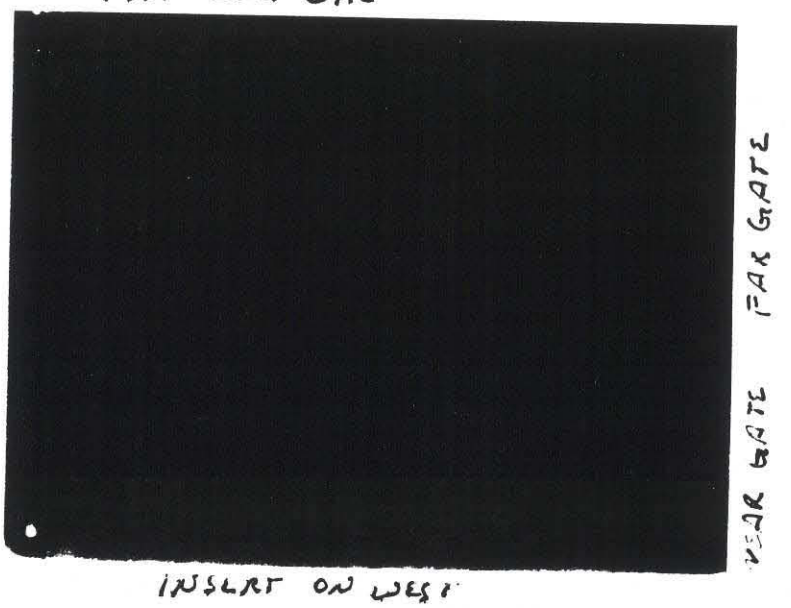

Annotations:

Borehole televiewer field check list

Date: 5/15/90
Time:
Observer: MOOS/TAVARES
Well Name : USGS-17
INEL

CABLE DEPTHS TO TIE POINTS

DRILLER'S DEPTHS	TIE POINT	MECHANICAL COUNTER	ELECTRONIC COUNTER
Reference Top Casing ∅	GROUND LEVEL (top of casing	699940	∅
400?	WATER LEVEL	700332	392
20'	CASING	?	?
600	TOTAL DEPTH	700510 ~~568~~	568
?	OTHER(specify)		
	water knockout		~~392~~ 390.5
∅	OTHER(specify) re-zero	699939	-3.1
	OTHER(specify)		

Borehole televiewer field check list

Date: 5/16/90
Time: _____
Observer: MOOS/TAVARES
Well Name : USGS-7

Cable:

INEL

cable length 22,000'
number of conductors 7
resistance (ohms):

See 5/15/90 INEL

	1	2	3	4	5	6	armor
1		x	x	x	x	x	
2			x	x	x	x	
3				x	x	x	
4					x	x	
5						x	
6							
7							

Equipment

tool small.
surface panel number New.
monitor _____. scope _____.

Pre-log calibration at 1300 5/16 (date/time)
Run in hole at 1320 (date/time)
Water level at 1325 (date/time)
Casing at 1330 (date/time)
Total depth at 1335 (date/time)
Log start at 1345 (date/time)
Log end at 1420 (date/time)
Post-log calibration at 1440 (date/time)

Borehole televiewer field check list

Date: 5/16/90
Time: 1300
Observer: MOOS/TAVARES
Well Name : USGS-7

pre-log calibration:

Time since turn-on ~10 minutes.

Test in Aluminum tank. Fluid is Clear Water.

Magnetic North is _____ degrees azimuth.

Magnetic East is _____ degrees azimuth.

Magnetic South is _____ degrees azimuth.

Magnetic West is _____ degrees azimuth.

place photograph here:

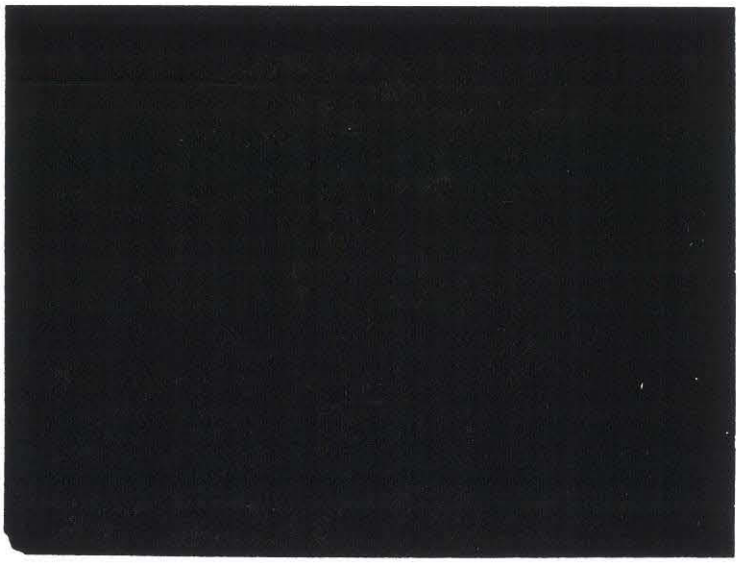

Compass
Mark
Far
Both

Isolate Near

Annotations:

Sleave on West

Oriented using old compass (NOT Brunton)

Borehole televiewer field check list

Date: 5/16/90
Time: 1440
Observer: MOOS/TAVARES
Well Name : USGS-7

post
~~pre~~-log calibration:

Time since turn-on 1:50.

Test in ALUMINUM TANK. Fluid is WATER.

Magnetic North is _____ degrees azimuth.

Magnetic East is _____ degrees azimuth.

Magnetic South is _____ degrees azimuth.

Magnetic West is _____ degrees azimuth.

place photograph here:

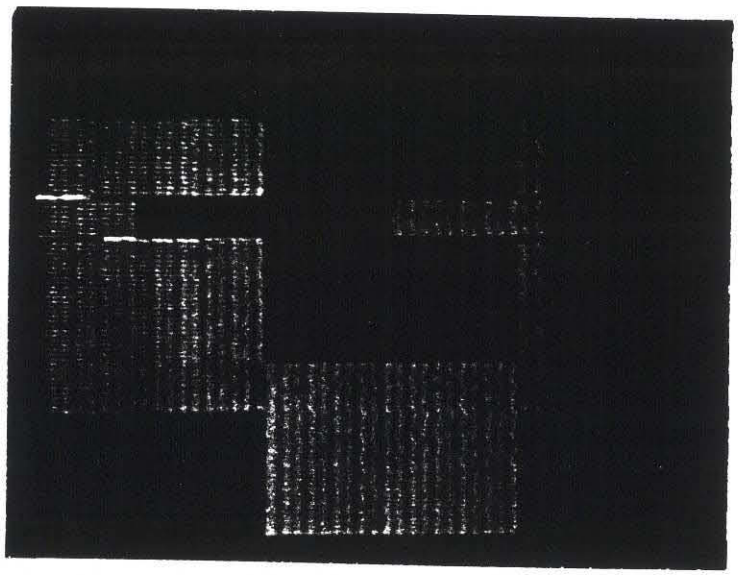

Annotations:

Compass
Mark
Far Gate
Both
Near Gate

4

Gain higher than pre-log

Borehole televiewer field check list

Date:_____
Time:_____
Observer:_____
Well Name : USGS- 7

CABLE DEPTHS TO TIE POINTS

DRILLER'S DEPTHS	TIE POINT	MECHANICAL COUNTER	ELECTRONIC COUNTER
	GROUND LEVEL	699935	0
390 +	WATER LEVEL		207
760'	CASING (6" diameter)		740 ± ?
~~1200'~~ 940'	TOTAL DEPTH 5 1/2" holesize		
J. ⇒ 895'	OTHER(specify) hole bottom (silt layer)	700827	894
1200'	OTHER(specify) 3 1/2" rathole		
	OTHER(specify)	699933	99918.0

Borehole televiewer field check list

Date: 5/16/90
Time: _____
Observer: MOOS/TAVARES
Well Name : NONAME #1

Cable:

cable length 22,000'
number of conductors 7
resistance (ohms):

See 5/15

	1	2	3	4	5	6	armor
1		x	x	x	x	x	
2			x	x	x	x	
3				x	x	x	
4					x	x	
5						x	
6							
7							

Equipment

tool small.
surface panel number New.
monitor _____. scope _____.

Pre-log calibration at 1635 (date/time)
Run in hole at 1646 (date/time)
Water level at 1650 (date/time)
Casing at 1651 (date/time)
Total depth at 1655 (date/time)
Log start at " (date/time)
Log end at 1750 (date/time)
Post-log calibration at 1755 * (date/time)

* No recal- Compass not triggering

Borehole televiewer field check list

Date: 5/16/90
Time: 16:35
Observer: Moos/Tavares
Well Name : Vorame #1

pre-log calibration:

Time since turn-on 10 minutes.

Test in Al Tank. Fluid is Water.

Magnetic North is _____ degrees azimuth.

Magnetic East is _____ degrees azimuth.

Magnetic South is _____ degrees azimuth.

Magnetic West is _____ degrees azimuth.

place photograph here:

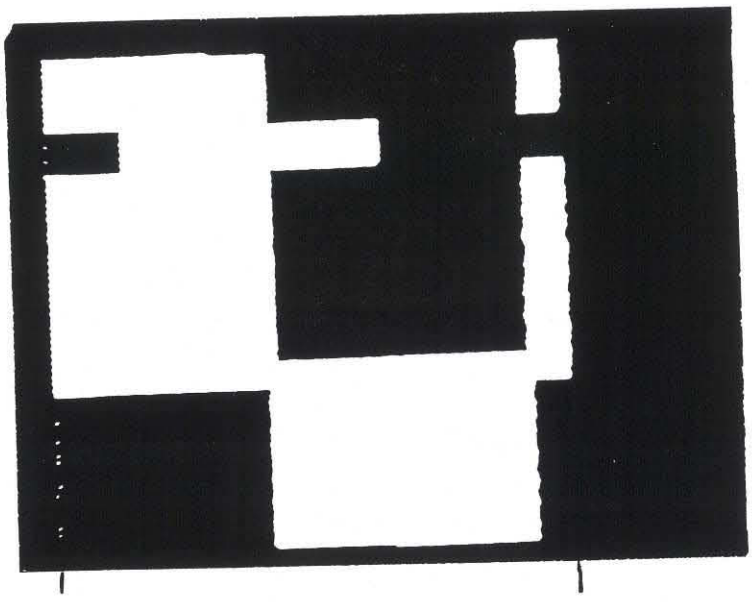

Annotations:

Sleeve on west
Orientation of field affected by trucks...

Borehole televiewer field check list

Date: 5/19/90
Time: 1500
Observer: MOORE / TAVARES
Well Name : WELL - 1

pre-log calibration:

Time since turn-on ~ 30 minutes.

Test in Aluminum tank. Fluid is Water.

Magnetic North is _____ degrees azimuth.

Magnetic East is _____ degrees azimuth.

Magnetic South is _____ degrees azimuth.

Magnetic West is _____ degrees azimuth.

place photograph here:

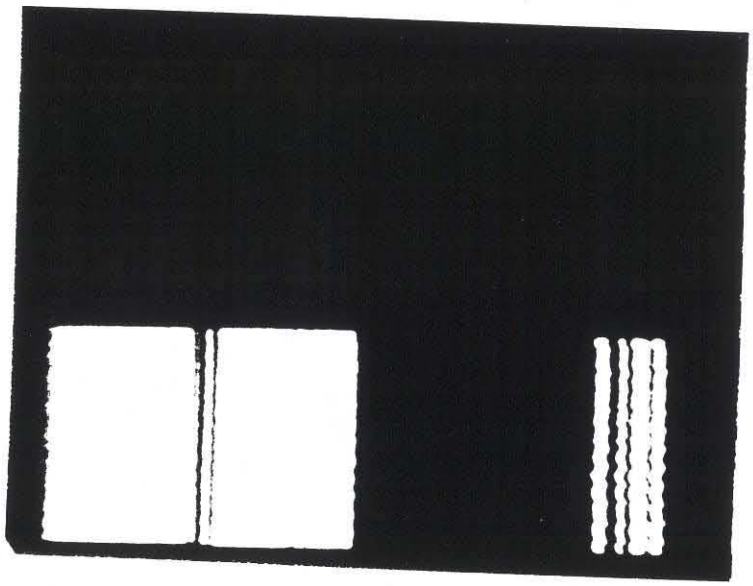

Annotations:

Gate Late
Sleeve West
Absorbin rod East Hi-F (short focus)

Borehole televiewer field check list

Date:_____
Time:_____
Observer:_____
Well Name : NONAME #1

CABLE DEPTHS TO TIE POINTS

DRILLER'S DEPTHS	TIE POINT	MECHANICAL COUNTER	ELECTRONIC COUNTER
	1 1/2' ABOVE GROUND LEVEL	699935	0
?	WATER LEVEL		204
270'/271.5'	CASING 12 3/4 casing		272
548'/549.5'	TOTAL DEPTH 12" hole		549
	OTHER(specify)		
	OTHER(specify)		
	OTHER(specify)		

Borehole televiewer field check list

Date: 5/19/90
Time: 1100
Observer: MOOS/JAVARES
Well Name : INEL-1

Cable:

cable length 21,800
number of conductors 7
resistance (ohms):

	1	2	3	4	5	6	7 armor	armor
1	220	x	x	x	x	x	∞	∞
2	∞	220	x	x	x	x	∞	∞
3	∞	∞	225	x	x	x	∞	∞
4	∞	∞	∞	220	x	x	∞	∞
5	∞	∞	∞	∞	240	x	∞	∞
6	∞	∞	∞	∞	∞	220	∞	∞
7	∞	∞	∞	∞	∞	∞	200	∞
ARMOR	—	—	—	—	—	—	—	0

Equipment

tool Hi Temp
surface panel number Old
monitor _____ scope _____
1st pass 2nd pass

Pre-log calibration at 3:00 pm (date/time)
Run in hole at 3:45 pm (date/time) 17:50
Water level at _____ (date/time)
Casing at 4:35 (date/time) ← 1850 hrs
Total depth at _____ (date/time) 1910 hrs (dinner time)
Log start at _____ (date/time)
Log end at _____ (date/time)
Post-log calibration at _____ (date/time)

Borehole televiewer field check list

Date: 5.19.90

Time: _____

Observer: _____

Well Name : INEL 1

CABLE DEPTHS TO TIE POINTS

DRILLER'S DEPTHS	TIE POINT	MECHANICAL COUNTER	ELECTRONIC COUNTER	
Ø	13 5/8 GROUND LEVEL (TOP OF CASING ~6' ABOVE GL	700008 70000	Ø -9999.5	
	WATER LEVEL	700369	302.5 in 297 out	
3282	TOP OF LINER 9 7/8 CASING		3282 in 3275 out	3275*
6796	TOP OF OPEN HOLE ~~TOTAL DEPTH~~	706790	6782	6785* 6783**
10,333	OTHER(specify) TOP OF 7 7/8 HOLE	710243*	10243*	10230* Rattan
6796	~~OTHER(specify)~~ TOP OF OPEN HOLE OUT	699993	99993	
10,000	OTHER(specify) Marker 12' open hole			

* 2nd run in hole

** 3rd run in hole

Borehole televiewer field check list

Date: 5/20/90
Time: 14:20
Observer: MWD/TAVARES
Well Name : INEL-1

Cable:

POST GEOTHERMAL CABLE CHECK
PRE small BHTV run

cable length 21,800
number of conductors 7
resistance (ohms):

	1	2	3	4	5	6	7 ~~armor~~
1	230	x	x	x	x	x	
2	∞	230	x	x	x	x	
3		∞	230	x	x	x	
4			∞	230	x	x	
5				∞	240	x	
6					∞	230	
7						∞	200
armor							

Equipment

tool Small
surface panel number old
monitor _____. scope _____.

Tool on 2:30

Pre-log calibration at 2:45 (date/time)
Run in hole at 2:50 (date/time)
Water level at 307' 2:58 (date/time)
Casing at 3:10 (liner) (date/time)
Total depth at 9300' (date/time)
Log start at _____ (date/time)
Log end at _____ (date/time)
Post-log calibration at _____ (date/time)

Borehole televiewer field check list

Date: 5·20·90

Time: _____

Observer: _____

Well Name : INEL 1

CABLE DEPTHS TO TIE POINTS

DRILLER'S DEPTHS	Hole Size	TIE POINT	MECHANICAL COUNTER	ELECTRONIC COUNTER IN	OUT
ϕ	13 3/8"	GROUND LEVEL	[illegible]	0	
		WATER LEVEL	700300	303'	
3282	9 3/8"	CASING Liner		3274.5	3275
6796	9 3/8"	Bottom Liner TOTAL DEPTH		6784	6783
10333	12"	OTHER(specify) TD			9300 10236
		OTHER(specify)			
		OTHER(specify)			

444 6/5/90 Time Event

3:45 pm AT INEL 1 - Setting up
Check out Large tool, new surface panel

'Ring out' Cable

								1/TTTT
1	260	∞	∞	∞	∞	∞	∞	∞
1 2		260	∞	∞	∞	∞	∞	∞
1 2 3			260	∞	∞	∞	∞	∞
1 2 3 4				260	∞	∞	∞	∞
1 2 3 4 5					280	∞	∞	∞
1 2 3 4 5 6						260	∞	∞
1 2 3 4 5 6 7							235	∞
								10

4:00 pm Calibration & testing the tool at surface
7:30 pm Shutting down calibration

6/6/90 Tape length 90 min x 5'/min = 450' = 1250(')of tape
5.5'/min = 495.0'
500'/Tape

(0-904)
Tape 1 10,240 - 10,000 + calibration pre
Tape 2 10,000 - 9,500 (0 - 1260)
3 9500 - 9000
4 9000 - 8500 (0 - 1212)
5 8500 - 8000
6 8000 - 7500
7 7500 - 7000 (0 - 1420)
8 7000 - 6785 + calibration post

Borehole televiewer field check list

Date: 6/6/90
Time: 0900
Observer: TAVARES/JOHNSON
Well Name : INEL-1

pre-log calibration:

Time since turn-on 1:00 hr.

Test in Al cal Tank. Fluid is Water.

Magnetic North is — degrees azimuth.

Magnetic East is — degrees azimuth.

Magnetic South is — degrees azimuth.

Magnetic West is degrees azimuth.

place photograph here:

Photographs on following page

Annotations:

WEST

6/6/90 Cont

Time	Event
8:00 Am	At site checking tool calibration
	Got orientation by photographing scope
	with TV signal on channel 1
	Blanking on channel 2
	~~XI Pulse~~ on channel 3 (trigger)
	took polaroid of these signals for
	sleeve in tank and for phenolic rod
	in tank. Phenolic rod in tank used as
	calibration for check:
	HF-1 compass
	HF-2 ✓
	HF-3 ✓
	LF-1 ✓
	LF-2 ✓
	Mark mode not working
11:30 Am	RIH
11:35	Zero Reset does not work on computer EDC1
11:42	0' 699990' ~~0'~~ GL
11:50	304' 303' WL
	3275 TL
	6784 BL
	10236 TD
12:05 pm	0' 699992.5' 0' GL
12:08	303.7' 700296. 303 WL
12:18	3270.5' 703263.0 3275 TL
12:32	6780 706772. 6784 BL
12:55	10236 TD
12:57	10240 710233 10240 5.8'/min
1:00 pm	Tool LF #4

6/6/90 Cont

Time	Event
1:50 pm	10,000 (709992.5) 10,244 - 10,000' TAPE 1 (0 - 904')

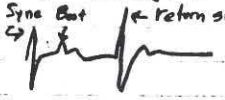

clear water 24.6 μs = 1" round trip

190 - 220 Maybe 16-18 μs/round trip inch

heavy salt 14 μs/round trip inch

base mud

?? → 2:10 10,000 709992.5 Re logging N pulse doubling

3:50 9500 Logging 5.8'/min

Gain → 4:00 9480 LF transducer Gain 3

Change → 4:10 9500 HF Gain 4

4:55 pm 9250 Taking pictures

5:50 9000' Tape 4

7:50 8500' 708492.5' Tape 5 Elevate boom to center tool with approx. 1 ft rise - note Δ 0

9:50 8000' 707992.5' Logging 5.8'/min

11:30 7500' 7492.5' " "

6/7/90 1:10 am 7000' " "

1:50 Am 6780' BL See photo for depth verif.

2:20 Am 3277. Smallest 3270' TL & etc

3270 Next largest

3267. ± largest

2:45 Am 295.5 303.7 WL ?

2:50 99990.1 699982.5' GL

3:30 Post run calibration complete HF #4, Compass

Borehole Televiewer Field Check List: DIGITAL DATA ACQUISITION
SUMMARY SHEET

Date: 7/13/90
Time: 10:00 AM
Operator : C. BARTON

Well Name INEL-1
Well Location INEL IDAHO
Log Date 5/17/90 5/19/90 5/20/90 6/6/90 6/7/90
Magnetic Declination (east of North) 16°
Max Depth 10243
Min Depth 6780
Depth Units FEET
Sweep setting 3.9
Trigger 7.5
Gate width 5.8
Blanking 3.1
T.V. gain FULL
Gate position 7.9
Borehole gain HF
Digitization Delay 150
Digitization Window 100
Tool Specification 0.97
Fluid Velocity 1490
Marker 0
Borehole Deviation OK

Borehole Televiewer Field Check List: DIGITAL DATA ACQUISITION
SUMMARY SHEET

Date: 7/12/90
Time: 3:00 PM
Operator : D. Moos

Well Name USGS-17
Well Location INEL IDAHO
Log Date 5/15/90
Magnetic Declination (east of North) 16°
Max Depth 567
Min Depth 390
Depth Units FEET
Sweep setting 6.4
Trigger 5.2
Gate width 8.5
Blanking 1.5
T.V. gain FULL
Gate position 5.6
Borehole gain HF
Digitization Delay 120
Digitization Window 400
Tool Specification 0.83
Fluid Velocity 1500
Marker 30
Borehole Deviation OK

Borehole Televiewer Field Check List: DIGITAL DATA ACQUISITION
SUMMARY SHEET

Date: 7/9/90
Time: 12:00 PM
Operator : C BARTON

Well Name USGS 7
Well Location INEL IDAHO
Log Date 5/16/90
Magnetic Declination (east of North) 16
Max Depth 895
Min Depth 750
Depth Units FEET
Sweep setting 7.2
Trigger 5.0
Gate width 8.8
Blanking 13.5
T.V. gain ROLL
Gate position 6.8
Borehole gain HF
Digitization Delay 90
Digitization Window 100
Tool Specification 0.83
Fluid Velocity 1500
Marker 30
Borehole Deviation OK

Borehole Televiewer Field Check List: DIGITAL DATA ACQUISITION
SUMMARY SHEET

Date: 7/9/90
Time: 9.00 AM
Operator : C. BARTON

Well Name NONAME
Well Location INEL IDAHO
Log Date 5/16/90
Magnetic Declination (east of North) 16
Max Depth 589
Min Depth 265
Depth Units FEET
Sweep setting 7.9
Trigger 4.9
Gate width 8.2
Blanking 13.8
T.V. gain FULL
Gate position 7.5
Borehole gain HF
Digitization Delay 150
Digitization Window 150
Tool Specification 0.83
Fluid Velocity 1500 M/S
Marker 35
Borehole Deviation UK

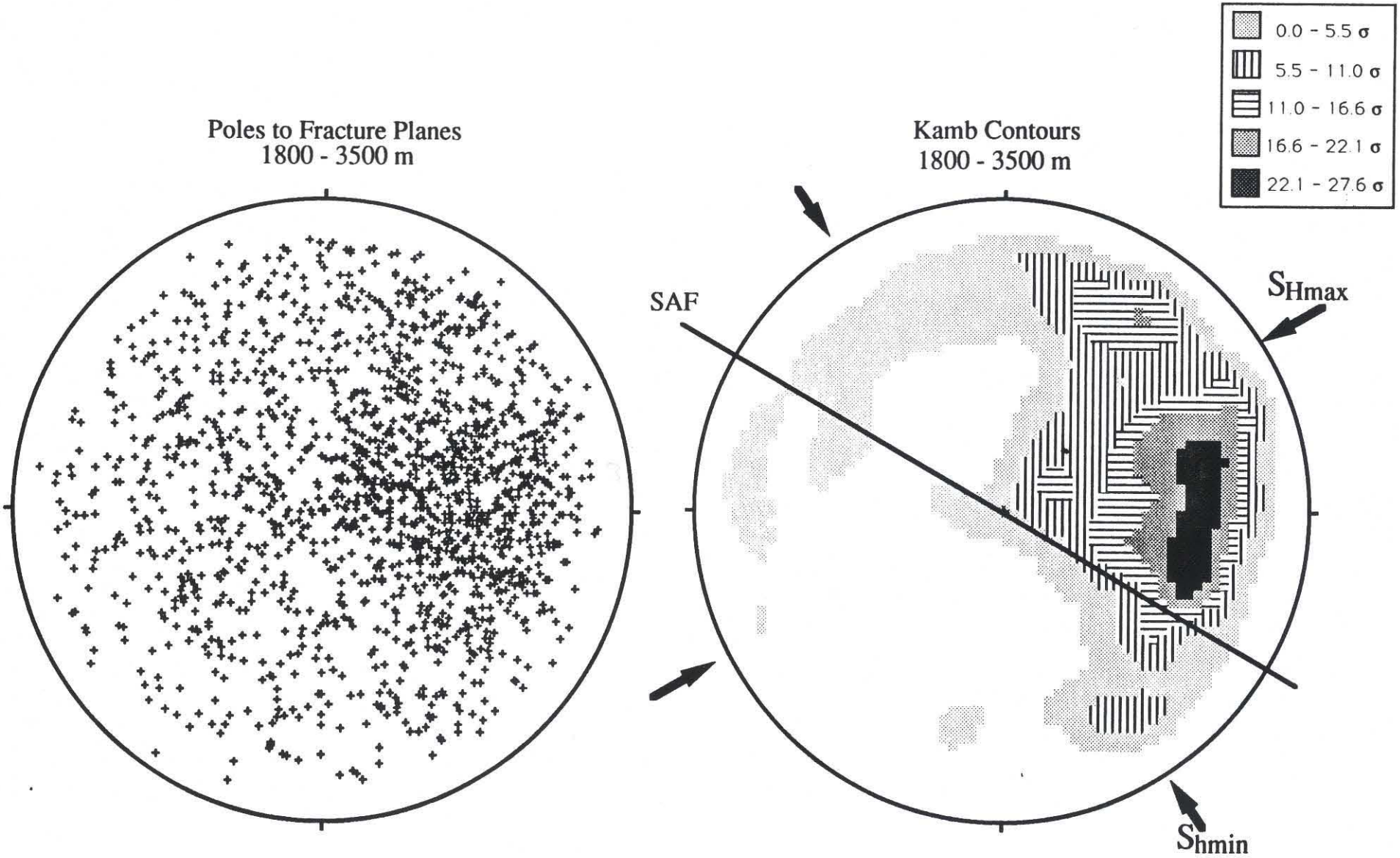
Poles to Fracture Planes
1800 - 3500 m
Kamb Contours
1800 - 3500 m
0.0 - 5.5 σ
5.5 - 11.0 σ
11.0 - 16.6 σ
16.6 - 22.1 σ
22.1 - 27.6 σ
SAF
SHmax
Shmin

Figure 18

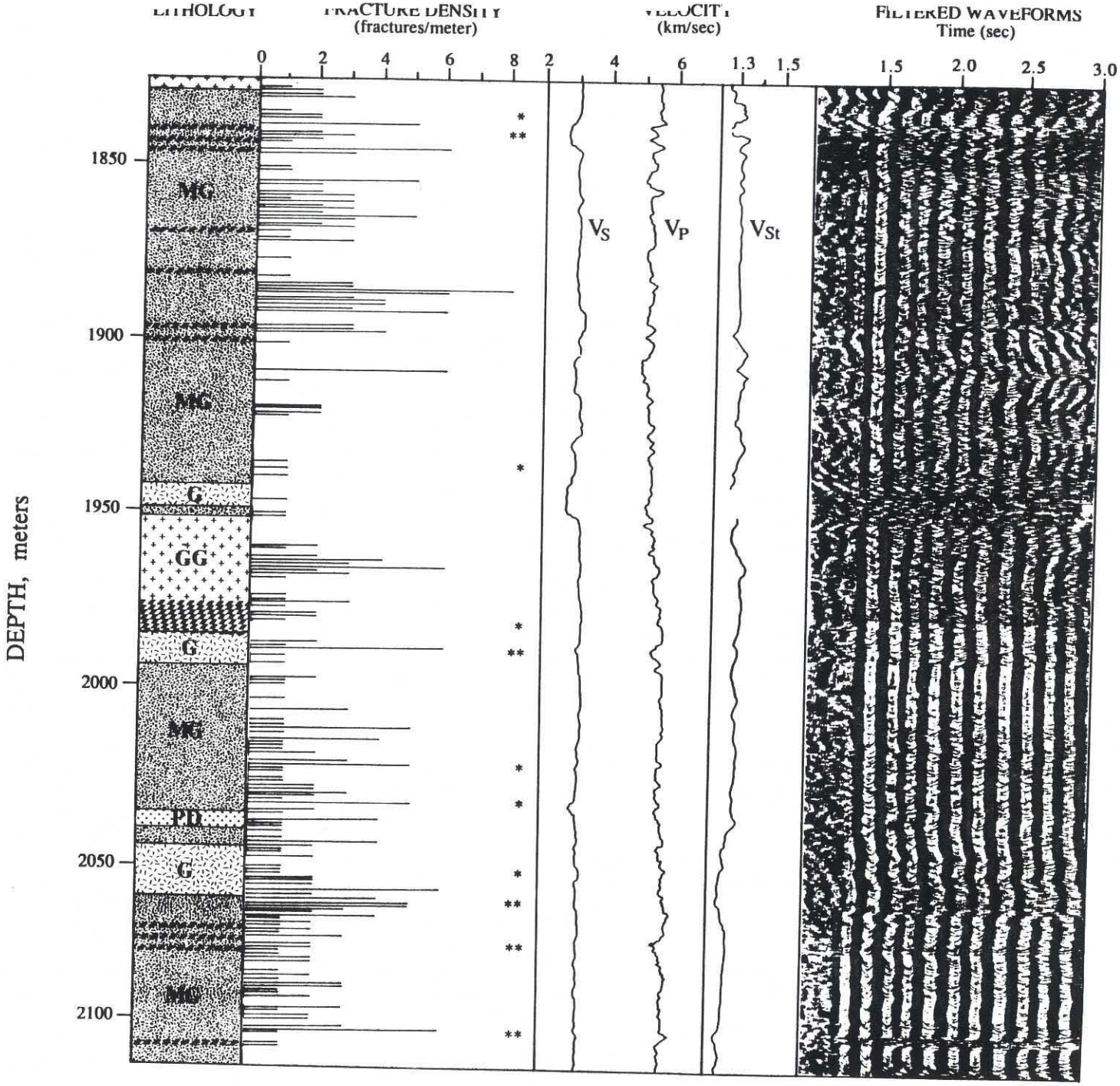
LITHOLOGY
FRACTURE DENSITY
(fractures/meter)
VELOCITY
(km/sec)
FILTERED WAVEFORMS
Time (sec)
0
2
4
6
8
2
4
6
1.3
1.5
1.5
2.0
2.5
3.0
DEPTH, meters
1850
1900
1950
2000
2050
2100
MG
G
GG
PD
V_S
V_P
V_{St}

Figure 19

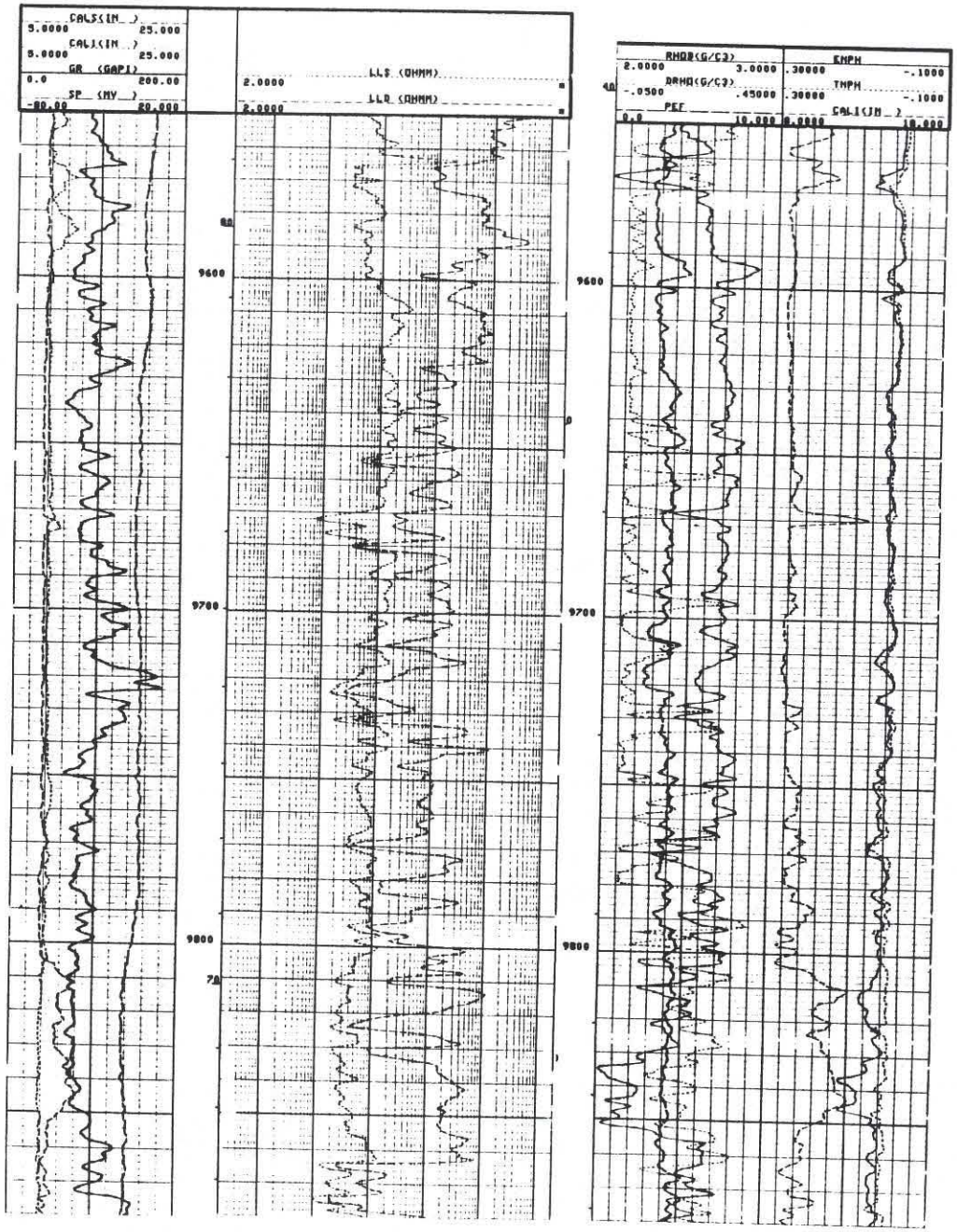

BHTV INTERPRETED SECTION

DIGITAL MANUAL

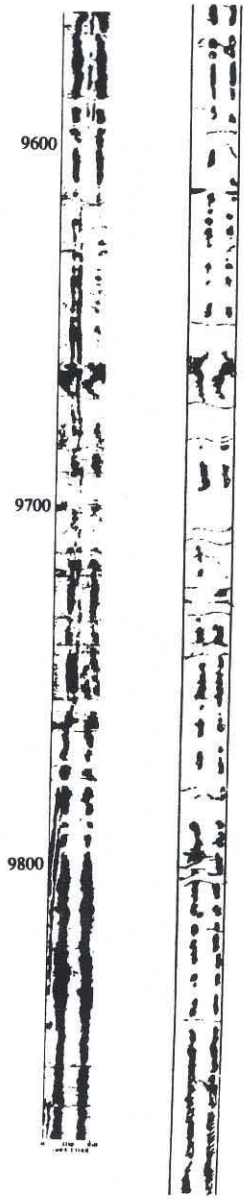

Figure 20

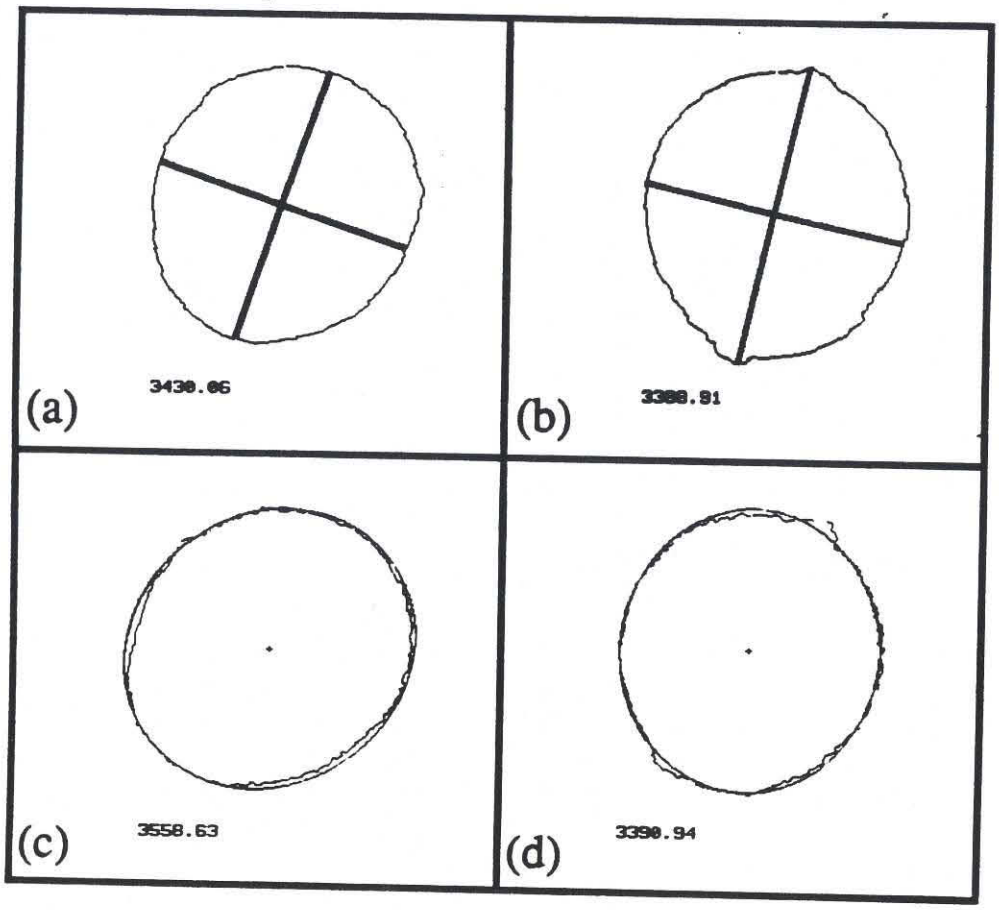

Figure 21

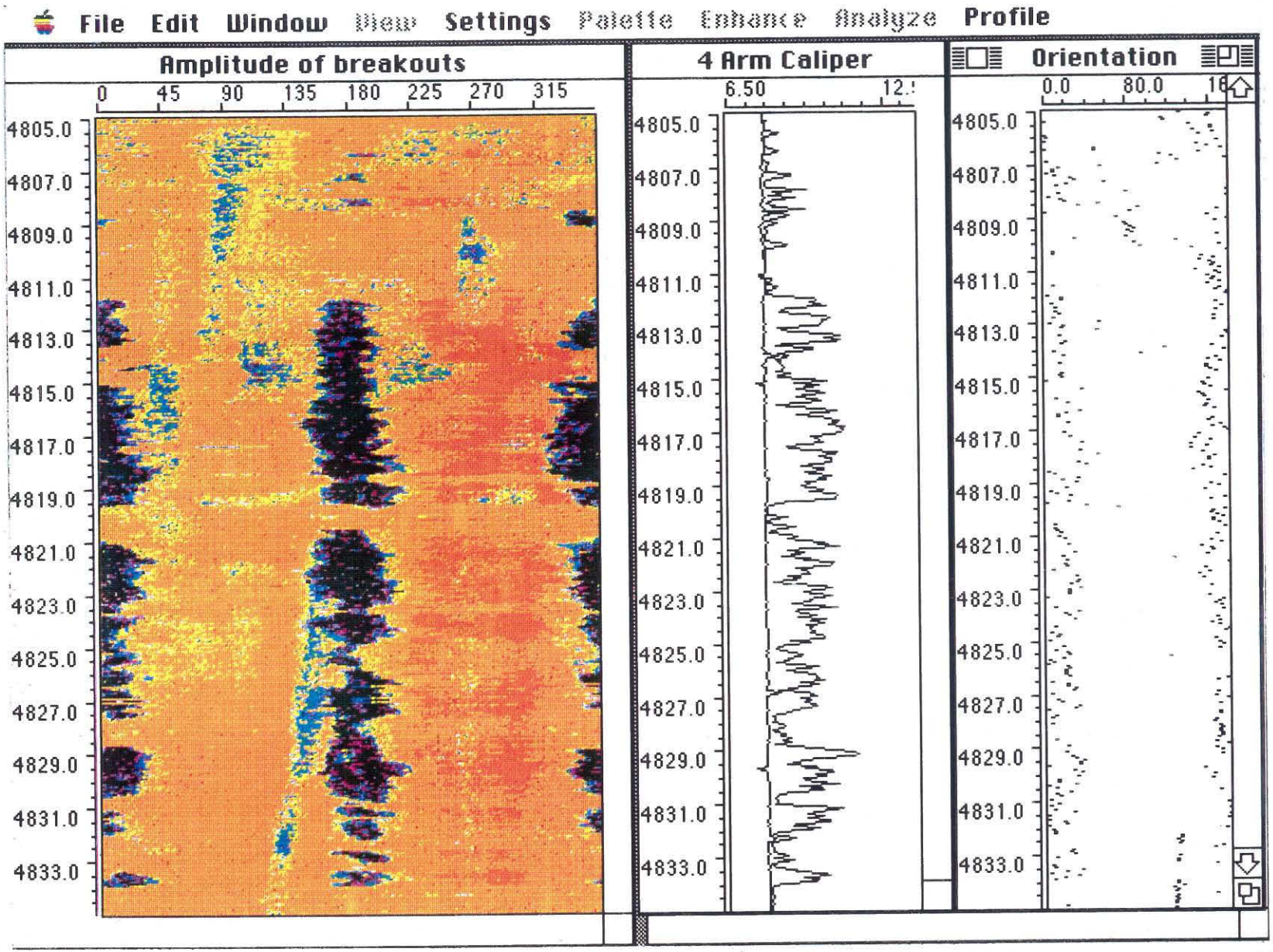
File Edit Window View Settings Palette Enhance Analyze Profile
Amplitude of breakouts
0 45 90 135 180 225 270 315
4805.0 4807.0 4809.0 4811.0 4813.0 4815.0 4817.0 4819.0 4821.0 4823.0 4825.0 4827.0 4829.0 4831.0 4833.0
4 Arm Caliper
6.50
4805.0 4807.0 4809.0 4811.0 4813.0 4815.0 4817.0 4819.0 4821.0 4823.0 4825.0 4827.0 4829.0 4831.0 4833.0
Orientation
0.0 80.0
4805.0 4807.0 4809.0 4811.0 4813.0 4815.0 4817.0 4819.0 4821.0 4823.0 4825.0 4827.0 4829.0 4831.0 4833.0

Figure 22

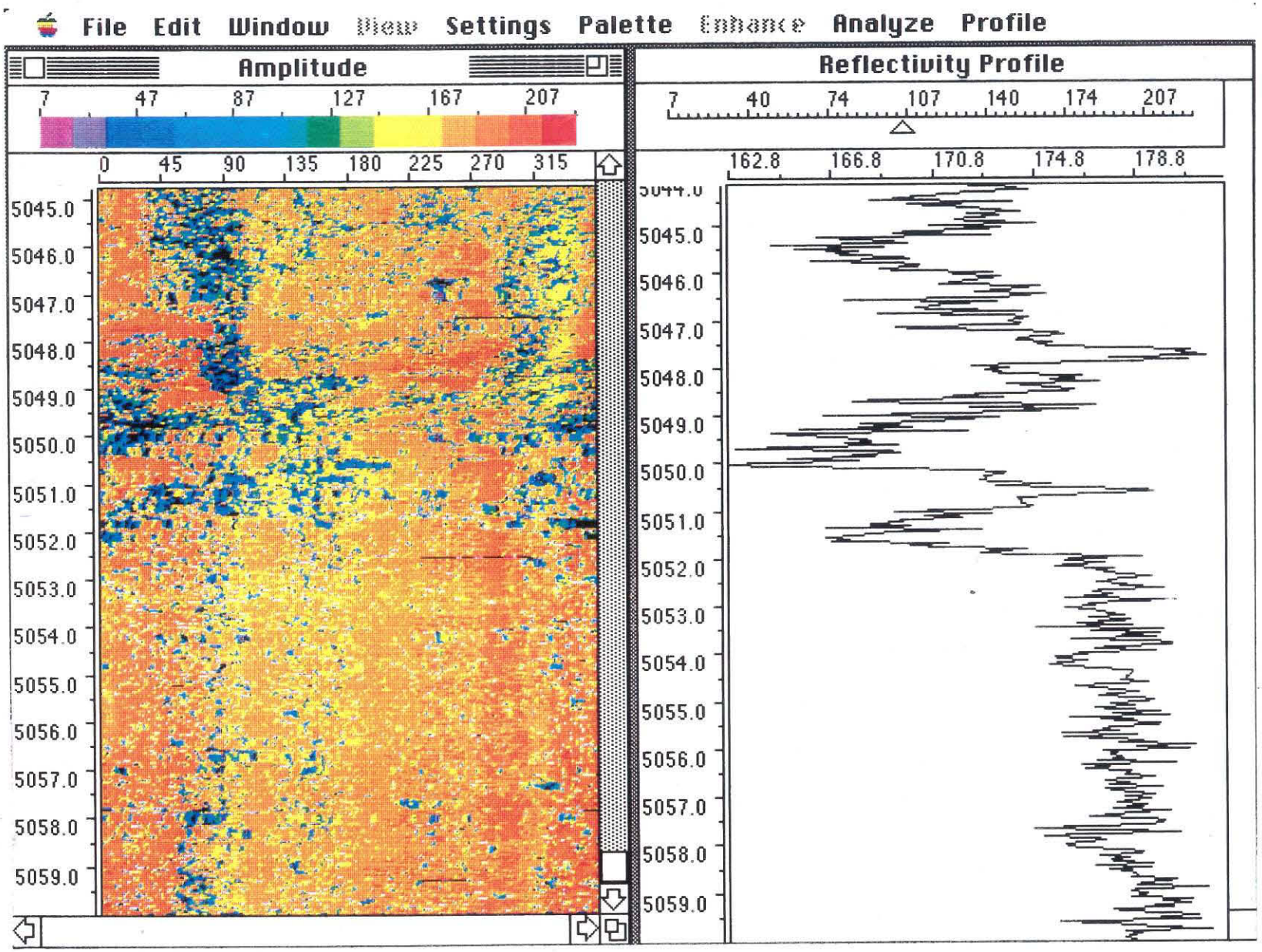
File Edit Window View Settings Palette Enhance Analyze Profile
Amplitude
7 47 87 127 167 207
0 45 90 135 180 225 270 315
5045.0 5046.0 5047.0 5048.0 5049.0 5050.0 5051.0 5052.0 5053.0 5054.0 5055.0 5056.0 5057.0 5058.0 5059.0
Reflectivity Profile
7 40 74 107 140 174 207
162.8 166.8 170.8 174.8 178.8
5045.0 5046.0 5047.0 5048.0 5049.0 5050.0 5051.0 5052.0 5053.0 5054.0 5055.0 5056.0 5057.0 5058.0 5059.0

Figure 23

Appendix V - Moos and Zoback stress estimation paper

The paper included here as Appendix V was published in the July 1990 *Journal of Geophysical Research*, and describes the methodology used to estimate stress magnitudes from the presence or absence of wellbore breakouts and drilling-induced hydraulic fractures.